NAS Technical Report: NAS-2015-01

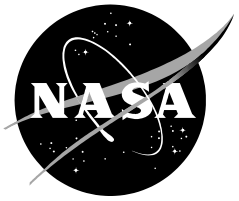

Experimental and Computational Sonic Boom Assessment of Lockheed-Martin N+2 Low Boom Models

Susan E. Cliff
Ames Research Center, Moffett Field, California

Donald A. Durston
Ames Research Center, Moffett Field, California

Alaa A. Elmiligui,
Langley Research Center, Hampton, Virginia

Eric L. Walker
Langley Research Center, Hampton, Virginia

Melissa B. Carter
Langley Research Center, Hampton, Virginia

National Aeronautics and
Space Administration

Ames Research Center
Moffett Field, CA 94035-1000

January 2015

Acknowledgments

The Authors thank John Morgenstern and Mike Buonanno of Lockheed-Martin Aeronautic Company for collaboration and dedication to improving test techniques, and for timely providing grids and *CFD++* computations to NASA. Special thanks to Linda Bangert for her support and guidance through out the course of this work. We also appreciate the support of Michael Aftosmis for adjoint-based solution adapted analyses with *CART3D* and Mike Park for *FUN3D* solutions. James Jensen and William Chan for *OVERFLOW* computations, grid generation, and tunnel layout diagrams. We also greatly appreciate grid generation support from Edward Parlette and Norma Farr for developing Euler and Navier-Stokes surface and volume grids. Shayan Moniyekta, Courtney Winski, and Scott Thomas, for developing scripts and plotting routines. We also thank Maureen Delgado and the wind tunnel crew at NASA Ames Research Center 9- by 7-Foot Supersonic Wind Tunnel for their dedication toward high quality experimental data, and thanks to Ray Hicks for sharing his insight into past sonic wind tunnel testing techniques with NASA.

This report is available in electronic form at

http://www.nas.nasa.gov/ NAS_Technical_Report_NAS-2015-01.pdf

Summary

Near-field pressure signatures were measured and computational predictions made for two low-boom supersonic transport models and five calibration models tested in conjunction with the Lockheed-Martin Aeronautics Company. The calibration models consisted of three axisymmetric bodies, a 70° swept flat plate model, and a vintage 69° swept delta-wing/body model that was tested during the 1970's. The sonic boom pressure signatures were measured in the NASA Ames 9- by 7-Foot Supersonic Wind Tunnel at Mach numbers of 1.6 and 1.7 in 2011 and 2012 during Phases I and II of the NASA High Speed Project N+2 Experimental Systems Validations NASA Research Announcement (NRA) contract with Lockheed-Martin. The low-boom transport models represent designs for a supersonic transport aircraft anticipated to enter service in the 2020-timeframe. Lockheed-Martin designed these aircraft to address environmental and performance goals given in the NRA, specifically for low sonic boom loudness levels and high cruise efficiency. The sonic boom data were measured using a minimally intrusive pressure rail capable of capturing an entire pressure signature without model translation. The Phase II experiment was conducted with relaxed tunnel control constraints to improve the productivity of the test in order to increase the number of runs and test articles. The testing differences are discussed and shown to only have a minimal impact on the quality of the Phase II data. For both phases of testing a variety of new testing techniques were required in addition to spatial averaging of pressure signatures measured at a series of different longitudinal or lateral model positions to reduce wind tunnel distortions and improve the data quality.

High-fidelity numerical simulations of on- and off-track pressure signatures are compared with spatially- and temporally-averaged experimental results. An unstructured tetrahedral grid method that uses a Mach cone aligned outer mesh was the primary method used to compute sonic boom pressure signatures for all of test articles and flight models. In addition, a variety of other computational methods are compared. These include unstructured mixed element (tetrahedral and hexahedral cell) method; overset structured meshes also with Mach aligned cells, and two adjoint-based methods that use Cartesian and tetrahedral cell solution adaptive techniques. Many cases are presented with these different computational approaches for both the wind tunnels models as well as flight vehicle computations of the Phase I and Phase II vehicle concepts. Good agreement between the computational simulations and experiment is seen, as well as good correlations of the computational results.

Sonic boom ground-level signatures are computed using a Burgers-equation solver extrapolation method from near-field experimental and computational data. The ground signatures and perceived loudness metrics compare well, but the extrapolations from experimental data are corrupted by the presence of the strut and require truncation of the signature, which adds uncertainty to the trailing shock of the extrapolated signatures and also to the loudness calculations.

Table of Contents

Summary 1

List of Tables 5

Nomenclature 6

1. Introduction 8

2. Test Objectives 10

3. Facility 11

4. Models 11
   - 4.1. Lockheed-Martin 1021 Model (Phase I Configuration) 13
   - 4.2. Axisymmetric Models (Seeb-ALR, Opt Sig, AS-2) 13
   - 4.3. Lockheed-Martin 1044 Model (Phase II Configuration) 14
   - 4.4. 70° Flat Plate Model 14
   - 4.5. 69° Delta Wing-Body Model 15

5. Instrumentation 15
   - 5.1. RF1 Pressure Rail 15
   - 5.2. Pressure Transducers 16
   - 5.3. Model Balances 16
   - 5.4. Roll Mechanism 17
   - 5.5. Linear Actuator 17

6. Test Techniques 18
   - 6.1. Wind Tunnel Flow Quality 18
   - 6.2. Pressure Rail Correction for Overpressure Coefficient 19
   - 6.3. Phase I Test 19
     - 6.3.1. Spatial Averaging 19
     - 6.3.2. Tunnel Pressure 21
     - 6.3.3. Humidity Levels 21
     - 6.3.4. Rail and Model Positions 22
     - 6.3.5. Model Sizing 22
     - 6.3.6. Sampling Time 22
   - 6.4. Phase II Test 23

7. Experimental Results 23
   - 7.1. Phase I Test 23
     - 7.1.1. Seeb-ALR Model 25
     - 7.1.2. 1021 Model 26
       - 7.1.2.1. 1021 with All Nacelles on Blade Strut, On-track 26
       - 7.1.2.2. 1021 with All Nacelles on Blade Strut, Off-track 27
       - 7.1.2.3. 1021 Without Under-Wing Nacelles on Blade Strut, On-track 27
       - 7.1.2.4. 1021 with All Nacelles on Conventional Sting, On-track 28
       - 7.1.2.5. 1021 with All Nacelles on Conventional Sting, Off-track 28
     - 7.1.3. AS-2 Model 28
     - 7.1.4. Opt Sig Model 29
     - 7.1.5. 1021 Model Repeat Signatures Extrapolated to Ground Level 29
   - 7.2. Phase II Test (New Models) 30
     - 7.2.1. 1044 Model 31
       - 7.2.1.1. 1044 with All Nacelles, Repeatability and Lateral Model Translation Effects for h=32'' data 31

7.2.1.2. 1044 with All Nacelles, Effect of Off-Track Angle at h = 32" ... 32
7.2.1.3. 1044, Effect of Off-Track Angle at h = 54" ... 32
7.2.1.4. 1044, Repeatability at h = 70", On-Track ... 32
7.2.1.5. 1044, Effect of Off-Track Angle at h = 70" ... 33
7.2.1.6. 1044 without Under-Wing Nacelles ... 33
7.2.1.7. 1044 without Center Nacelle ... 33
7.2.2. 70° Flat Plate Model ... 34
7.2.3. 1044 Model Repeat Signatures Extrapolated to Ground Level ... 34
7.3. Phase II Test (Previously Tested Models) ... 35
7.3.1. 1021 Model ... 36
7.3.1.1. 1021 with All Nacelles, Effect of Altitude ... 36
7.3.2. Seeb-ALR Model ... 37
7.3.3. 69° Delta-Wing-Body Model ... 37
7.3.3.1. Effect of Off-Track Angle, Near Zero Alpha, h=25 inches ... 37
7.3.3.1. Effect of Off-Track Angle, Near Zero Alpha, h=32 inches ... 38
7.3.3.2. Effect of Pitch Angle, h=21, and 25 inches ... 38
7.3.3.3. Effect of Pitch Angle, h=32 inches ... 38
7.4. Residual Comparisons of Averaged Signatures from Phase I and II Tests ... 39
7.4.1.1. Waterfall Residual plots for the 1021 Model, h=31 inches, Phase I experiment ... 39
7.4.1.2. Waterfall Residual plots for the 1021 Model, h=25 & 32 inches, Phase II experiment ... 39
7.4.1.3. Waterfall Residual plots for the 1044 Model, h=31 inches. Phase II experiment ... 40
7.4.1.4. Waterfall Residual plots for the 1044 Model, h=70 inches. Phase II experiment ... 40

8. Computational Modeling ... 40
8.1. Computational Tools ... 41
8.1.1. USM3D Methodology ... 41
8.1.2. CART3D Methodology ... 42
8.1.3. FUN3D Methodology ... 42
8.1.4. CFD++ Methodology ... 42
8.1.5. OVERFLOW Methodology ... 43
8.2. Predicted Strut Effects on Force and Moment Data ... 43
8.2.1. 1021 N+2 Phase I computational results ... 43
8.2.2. 1044 N+2 Phase II computational results ... 44

9. Computational/Experimental Pressure Signature Comparisons ... 45
9.1. Phase I Test ... 45
9.1.1. Seeb-ALR Model ... 45
9.1.2. 1021 Model ... 45
9.1.2.1. On-track, all nacelles with blade strut mount, lower α: USM3D analyses ... 46
9.1.2.2. On-track, all nacelles with blade strut mount: USM3D, CART3D FUN3D, and OVERFLOW analyses 46
9.1.2.3. Off-track, all nacelles with blade strut mount: USM3D, CART3D, FUN3D, and OVERFLOW analyses 46
9.1.2.4. 1021 without under-wing nacelles, with blade strut mount: USM3D ... 47
9.1.2.5. 1021, conventional sting with nacelles, on- and off-track ... 48
9.1.3. AS-2 Model ... 48
9.1.4. Opt Sig Model ... 48
9.2. Phase II Test (Newly Constructed Models) ... 49
9.2.1. 1044 Model with All Nacelles on Blade Strut ... 49
9.2.1.1. On-track, h=26.6 inches ... 49
9.2.1.2. On- and off-track, h=32 inches ... 49
9.2.1.3. On- and off-track, h=54 inches, same grid computations ... 50
9.2.1.4. On- and off-track, h=70 inches ... 50
9.2.2. 1044 Model without Under-Wing Nacelle on Blade Strut ... 51

9.2.2.1. On- and Off-track, h = 32 inches 51
9.2.2.2. On-track, h = 70.8 inches 51
9.2.3. 1044 Model without Center Nacelle on Blade Strut 51
9.2.3.1. On- and Off-track, h = 32 inches 51
9.2.4. 70° Flat Plate Model with Blade Strut 52
9.3. Phase II Test (Previously Tested Models) 52
9.3.1. 1021 Model 52
9.3.1.1. Effect of altitude, h=42-, 49-, and 63-inches 52
9.3.2. Seeb-ALR Model 53
9.3.2.1. Effect of altitude, h=56-, and 70-inches 53
9.3.3. 69° Delta Wing-Body Model 53
9.3.3.1. Effect of Off-Track Angle, Near Zero Alpha, h=25 inches 53
9.3.3.2. Effect of Off-Track Angle, Near Zero Alpha, h=32 inches 54
9.3.3.3. Effect of Pitch Angle, h=21, and 25 inches 54
9.3.3.4. Effect of Pitch Angle, h= 32 inches 54

10. Propagated Signatures to Ground Level 55
10.1. Phase I Computational and Experimental Models 55
10.2. Phase II Computational and Experimental Models 55

11. Flight Vehicle Computations 56
11.1. Phase I Flight Vehicle 56
11.1.1. Euler (Inviscid) Analyses 57
11.1.2. Navier-Stokes (Viscous) Sonic Boom Analyses 57
11.1.3. Vehicle Performance (Navier-Stokes and Euler) Analyses 57
11.2. Phase II Flight Vehicle 58
11.2.1. Euler (Inviscid) Analyses 59
11.2.2. Navier-Stokes (Viscous) Analyses 59
11.2.3. Predicted Ground Signatures 59

12. Concluding Remarks 60

13. References 62

14. Figures 67

List of Tables

Table 1. N+2 Supersonic Transport (2020) Goals 9
Table 2. Flight Vehicle Attributes 9
Table 3. Wind Tunnel Model Test Phases 12
Table 4. Wind Tunnel Model Reference Values 12
Table 5. Balance Corrections for N+2 Models with Blade Strut 17
Table 6. Simplified run matrix for the Phase I test T97-0231 24
Table 7. Simplified run matrix for the Phase II test T97-0254 30
Table 8. Simplified run matrix of previously tested models for test T97-0254 35
Table 9. Model 1021 Computed Forces and Moments: M=1.6, α=2.3° 44
Table 10. Model 1021 Computed Forces and Moments: M=1.6, α=2.5° 44
Table 11. Model 1044 Computed Forces and Moments: M=1.7, α=2.1° 44
Table 12. Model 1044 Computed Forces and Moments: M=1.7, α=2.3° 44

Nomenclature

BRC	balance reference center
CFL	Courant-Friedrichs-Lewy, stability parameter for finite difference methods
C_D	drag coefficient
C_L	lift coefficient
C_M	pitching moment coefficient
ΔP/P, dP/P	overpressure coefficient, $(P_L - P_\infty)/P_\infty$
EI NOx	emissions index of *NOx* (Nitrogen Oxides), grams of NO_2 per kg of fuel
EPNdB	Effective perceived noise level in decibels
h	model altitude at model nose, inches
h/L	model altitude non-dimensionalized by model length
H	humidity from tunnel sensors, ppm by weight
L	model reference length, inches
L/D	lift-to-drag ratio
M	Mach number
msec	milliseconds
MRC	moment reference center
MTOW	maximum take-off weight, lbs
P	ground overpressure, psf
P_L	local static (rail) pressure, psf
P_∞	freestream static pressure, psf
P_T	free stream total pressure
PLdB	perceived sound level in decibels
*psf*a	pounds/square foot absolute
Re	Reynolds number, non-dimensional, ρVL/μ
t	time
V	velocity, inches/second
X	longitudinal distance, inches
X_ram	longitudinal distance measured by linear actuator, positive is aft, inches
Z	lateral position, inches
α	angle of attack, degrees
β	angle of sideslip, degrees
ϕ	off-track (azimuthal) or roll angle, degrees

μ	viscosity

Subscripts

Data	Data run, where model pressure signature was measured on the rail
Ref	Reference run, where model pressure signature was not on the rail; also a reference parameter for model geometry
∞	ambient or freestream flow condition

Introduction

Flight at speeds greater than the speed of sound is not permitted over land, primarily because of the noise and structural damage caused by sonic boom pressure waves of supersonic aircraft. Mitigation of sonic boom is a key focus area of the High Speed Project under NASA's Fundamental Aeronautics Program. The project is focusing on technologies to enable future civilian aircraft to fly efficiently with reduced sonic boom, engine and aircraft noise, and emissions. A major objective of the project is to improve both computational and experimental capabilities for design of low-boom, high-efficiency aircraft. NASA and industry partners are developing improved wind tunnel testing techniques and new pressure instrumentation to measure the weak sonic boom pressure signatures of modern vehicle concepts. In parallel, computational methods are being developed to provide rapid design and analysis of supersonic aircraft with improved meshing techniques that provide efficient, robust, and accurate on- and off-body pressures at several body lengths from vehicles with very low sonic boom overpressures. The maturity of these critical parallel efforts is necessary before low-boom flight can be demonstrated and commercial supersonic flight can be realized.

The measurement of the sonic boom pressure signatures of modern low-boom supersonic vehicles in wind tunnels is challenging. Historically, sonic boom pressure signatures were measured in a wind tunnel using needle-like conical probes that measure static pressure at a single point in the flow-field (Ref 1). This technique requires axial translation of the model past the probe to obtain a complete pressure signature of the model (or translation of the probe past the model). Traditional methods used a move-pause data acquisition technique requiring between 40-60 minutes per signature, although a recent effort has shown that near continuous model translation with environmentally controlled pressure transducers and shortened pressure lines can significantly speed up data acquisition time using a probe (Ref 2). However, the single-probe technique is still prone to reduced data accuracy because of small changes in tunnel flow conditions even over short data acquisition times. Humidity, turbulence, ambient pressure variations and stream angle changes during model translation all contribute to measurement uncertainties.

Unlike single point conical probes, pressure rails with hundreds of closely spaced pressure orifices measure a model's entire sonic boom pressure signature at one axial location of the model in the tunnel. Rails offer significant gains in efficiency and precision compared with conventional conical probe testing. Several rails with different cross-sectional shapes have been investigated in the 9- by 7-Foot Supersonic Wind Tunnel at NASA Ames Research Center since 2008 (Ref 1). Initial rail concepts had flat or large-diameter rounded tips that resulted in unknown and inconsistent reflection (i.e., amplification of the pressure signal due to shock reflection off the surface) of a model's pressure signature and unknown rail boundary layer influence on the signature. A pressure rail that effectively eliminates amplification (reflection of model shock waves from its tip) and model reflection from wind tunnel walls was designed in 2010 using CFD analyses (Ref 3) and was designated the reflection factor 1.0 (RF1) rail. This rail is shown in Figures 1.1 and 1.2 attached to the wind tunnel wall in the installation photographs; details of the leading edge of the RF1 rail are shown in Figure 1.2. The rail height prevents impingement of reflected model shock waves, from the wall, on the pressure measuring orifices within the rail tip. The RF1 rail was used in wind tunnel test T97-0231 and T97-0254, in October 2011 (Phase I) and 2012 (Phase II), respectively, at the NASA Ames 9×7-ft wind tunnel to assess the sonic boom pressure signatures of each model concept. While it was initially envisioned that model translation would be unnecessary with a rail concept, testing showed that spatially averaging a series of pressure signatures from several model positions significantly improved measurement accuracy (Refs 4, 5). Both small ambient pressure oscillations and the pressure disturbance caused by shocks emanating from the tunnel structure are nearly eliminated by spatial averaging techniques.

In 2009, NASA published a NASA Research Announcement (NRA) (Ref 6) requesting proposals for "System-Level Experimental Validations for Supersonic Commercial Transport Aircraft Entering Service in the 2020 Time Period." The aircraft concepts were to be designed to second generation "N+2" supersonic vehicle technology with a focus on providing system-level solutions capable of overcoming the efficiency, environmental, and performance barriers to practical supersonic flight. The N+2 environmental and performance goals are given in Table 1.

Table 1. N+2 Supersonic Transport (2020) Goals

Environmental Goals	
Sonic Boom	85 PLdB up to 20° off-track
Airport Noise (cumulative below stage 3)	10–20 EPNdB
Cruise Emissions	< 10 EI NOx
Performance Goals	
Cruise Speed	Mach 1.6–1.8 low-boom flight
Range	4000 nm
Payload (passengers)	35–70 passengers
Fuel Efficiency (passenger-nm per lb of fuel)	3.0

Two companies were awarded NRA contracts: Lockheed-Martin Aeronautics Company (LM) and The Boeing Company. The contracts were executed in two phases, each concluding with wind tunnel test validation of the sonic boom characteristics of their design efforts. This report covers the CFD predictions and experimental measurements for the concepts developed by LM for a large (~240-foot) supersonic transport vehicle designed to carry over 80 passengers. Flight vehicle attributes for LM Phase I and II vehicles are provided in Table 2. The range and fuel efficiency of the vehicles varies with selection of the engine concept. Rolls-Royce North American Technologies, Inc., consulting business known as LibertyWorks™ (RRLW) developed propulsion system definitions under contracts with LM. General Electric (GE) Global Research was also under contract with LM to provide alternative engine nozzles and propulsion systems for these vehicles.

Table 2. Flight Vehicle Attributes

Model	***Phase I***	***Phase II***
Length (ft)	230	244
Span (ft)	84	83.83
Height w/ and w/o gear (ft)	22, 29	23.5, 30.5
Reference area (sq ft)	3,298	3,600
Number of passengers	82 or 100	80
Flight altitude (beginning to end of cruise; ft)	48,500 – 54,800	50,000 – 60,000
Cruise Mach number	1.6	1.7 over land, 1.8 over water
Cruise L/D	9.1	8.7
Range (nm)	4,315 (RRLW) or 5,225 (GE)	5,130
Fuel efficiency	2.86 (RRLW) or 3.13 (GE)	2.94 (on 4,150 nm low boom mission)
MTOW (lb)	290,000	320,000

The first phase of LM's efforts was focused on the reduction of on-track (directly below aircraft in straight and level flight) sonic boom signatures and aerodynamic performance to address the environmental and performance goals specified in the NRA. The Phase I model was further optimized in the interim year between tests, and the resulting Phase II model represented a state-of-the-art design with both on- and off-track low-boom characteristics as well as high performance at cruise flight conditions. Artist renditions of LM vehicle concepts for their Phase 1 (1021 model) and Phase II (1044 model) are shown in Figure 1.3. CAD images of the vehicles in four views (isometric, top, front and side) are shown in Figure 1.4.

The design and execution of these tests were a joint effort with LM and NASA. The Phase I (T97-0231) and Phase II (T97-0254) tests took place in October of 2011 and 2012, respectively, in the 9- by 7-Foot Supersonic Wind Tunnel at NASA Ames Research Center.

NASA provided Computational Fluid Dynamics (CFD) predictions of sonic boom pressure signatures of test articles prior to wind tunnel testing so that the experimentalists had a firm understanding of the expected wind tunnel test results. Predicting accurate sonic boom pressure signatures of weak signals is challenging and significant improvements in the accuracy of sonic boom characteristics have been realized during the High Speed Project. Accurate CFD simulations can be obtained in many ways. One is by providing dense meshes within the sonic boom pressure disturbance along with mesh rotation techniques to align the mesh with the Mach angle, (Ref 7). Another is to provide unstructured mesh adaptation with effective refinement criterion but without cell alignment (Ref 8). A method that allowed for accurate on-track sonic boom computations at large distances used very dense near-body unstructured meshes generated by grid sourcing and subsequent stretching of the mesh at the Mach angle (Ref 9). Solution-adaptive techniques using node centered unstructured mixed element meshes (Refs 10-12), or Cartesian adaptive refinement methods with domain rotation for Euler solutions (Refs 13-16) have also proven to provide accurate solutions. A method that provides anisotropic adapted unstructured mesh optimization for shock capturing has also been successfully used for the compressible Euler equations (Ref 17). Also, structured overset grid methods (Ref 18), or hybrid methods (Refs 19-21) that utilize an unstructured flow solutions in the near-field and structured grid solutions in the far-field can also provide accurate on-track calculations. Grid generation tools that allow stretching of the mesh in addition to alignment to the Mach cone angle (Refs 22-25) offer smaller meshes that maintain density in the axial direction and reduce the effects of dissipation along characteristic lines. The CFD computations provided here use Mach cone aligned prism meshes (Ref 22). Some solution-adaptive (Cartesian and tetrahedral; Refs 12-15) and overset grid computations will also be shown.

In addition to the N+2 models computations and experimental test data given in this report, CFD predictions and experimental comparisons of three axisymmetric calibration models are provided. Two of the bodies were designed and manufactured by the Lockheed-Martin Corporation and the other by The Boeing Company. Furthermore, simulations and experimental results for a 70-degree swept flat plate calibration model and a 1970's vintage 69-degree delta wing body model are reported. The test data for the LM axisymmetric body, delta wing body model, and the Phase I N+2 model, were used for the 1st AIAA Sonic Boom Prediction Workshop held in January 2014 (Refs 26, 27).

Test Objectives

There were three primary objectives for conducting the tests in this experimental validations program:

1. Obtain data to evaluate sonic boom and aerodynamic performance of the LM configurations
2. Improve wind tunnel test techniques for acquiring such data

3. Provide large, high-quality experimental validation database for CFD tool development and improvement of low-boom design methods

The overall purpose of the experimental validations program was to design a viable low-boom supersonic transport aircraft that would meet the NRA environmental and performance goals. LM designed their N+2 transport to meet these goals, but needed high-quality experimental data to evaluate the merits of their design. LM worked with NASA in developing a wind tunnel test program that would meet their needs. Past experience and lessons learned were applied to the test program to get the best data possible, and additional valuable experience was gained for further improvement of the test techniques. The result was a large dataset that Lockheed used to assess their multidisciplinary design and analysis methods for their Phase I transport design reported in Ref 28, and their final N+2 design at the completion of Phase II of the NRA contract, reported in Ref 29. These data also provided NASA and industry the information needed to validate their CFD codes.

Facility

The Ames 9- by 7-Foot Supersonic Wind Tunnel is part of the Unitary Plan Wind Tunnel at NASA Ames Research Center at Moffett Field, California. It is a continuous flow, closed circuit, variable-density tunnel equipped with an asymmetric sliding-block nozzle for setting Mach number (Refs 30-31). The floor of the wind tunnel test section is part of the nozzle block. It translates axially (streamwise) to vary the tunnel throat area while the contoured tunnel ceiling remains stationary. This combination provides a Mach number range from 1.55 to 2.55. The side walls are flat and parallel through the nozzle and test section. The asymmetric nozzle results in slightly larger stream angle variations in the vertical plane, on the order of 0.25 to 0.5 degrees, whereas stream angle in the horizontal plane is generally less than 0.2 degrees. Models are mounted wings vertical in the test section because of the stream angle bias; thus the angle-of-attack plane is horizontal and the sideslip plane is vertical. The wind tunnel model support strut is horizontal, and its side-to-side movement keeps the model in the center of the tunnel as the pitch angle is changed. The forward end of the strut centerbody pivots by means of a mechanical joint (knuckle-sleeve system) to achieve any combination of angle of attack or sideslip within a 15° cone angle.

The tunnel is driven by an 11-stage axial compressor powered by four wound-rotor motors totaling 216,000 hp. The tunnel operates at total pressures between 634 and 3600 psfa with corresponding unit Reynolds numbers between 0.8 and 5.7 million per foot. For the subject series of sonic boom tests, the Mach number and total pressure have been prescribed in the tunnel control system, rather than Mach and Reynolds number, because it is more productive for the 9x7 to run in constant-pressure mode, allowing temperature to float.

An installation photograph of the LM Phase I model in the 9 x 7-foot tunnel is shown in Figure 1.1. The model, RF1 pressure rail, strut and centerbody are visible in the photograph. The RF1 pressure rail is mounted on the north sidewall of the test section to measure the pressure signatures below the model. The wind tunnel strut movement controls the distance from the model to the top of the rail. Throughout this report, the model distance from the rail on the sidewall of the tunnel is referred to as “height,” even though it is a horizontal distance in the 9x7 wind tunnel.

Models

Seven wind tunnel models were tested during the two phases of the Lockheed-Martin NRA contract: three calibration bodies of revolution, two low sonic boom aircraft configurations, a 70-degree swept flat plate calibration model, and a 69-degree delta wing-body model. The axisymmetric bodies are designated Seeb-ALR, Opt Sig, and AS-2, and the low boom concepts are designated the 1021-01 and 1044-02

models. The naming of the low boom concepts with the hyphenation number is specific to Lockheed-Martin's wind tunnel model designation. These will also be referred to as simply the 1021 and 1044 models. Table 3 provides the model and Phase(s) of the experiment in which each model was tested.

Table 3. Wind Tunnel Model Test Phases

Model	*Seeb-ALR*	*Opt Sig*	*AS-2*	*1021*	*1044*	*70° Flat Plate*	*69° Delta*
Phase	I, II	I	I	I, II	II	II	II

The models' reference parameters are provided in Table 4. The X_{Nose} to *MRC* and Z_{Nose} to *MRC* quantities refer to the distance from the model nose to 50% of the Model Reference Center (*MRC*), whereas the X_{Nose} to *BMC* and Z_{Nose} to *BMC* represent the axial and model vertical distance from the model nose to the balance moment center (*BMC*).

Table 4. Wind Tunnel Model Reference Values

Model	*Seeb-ALR*	*Opt Sig*	*AS-2*	*1021*	*1044*	*70° Flat Plate*	*69° Delta*
L_{Ref} (in)	17.68	16.56	18.611	22.365	19.032	9.4	6.8976
S_{Ref} (sq in)	15.552	15.552	15.322	33.177	21.902	33.0	5.131
C_{Ref} (in)	3.6	3.6	2.671	6.628	5.385	6.231	2.519
b_{Ref} (in)	1.4	1.4	0.965	8.055	6.54	6.6	5.131
X_{Nose} to MRC (in)	0	0	11.471	15.626	13.552	7.169	5.117
Z_{Nose} to MRC (in)	0	0	0	0.289	-0.159	1.402	0
X_{Nose} to BMC* (in)	25.026	25.026	24.024	40.841	35.697	24.802	30.343
Z_{Nose} to BMC (in)	0	0	0	4.159	3.550	-4.379	0

**Dimensions from model to balance are with balance level. 1021 model was pitched up 2.5° relative to balance. 1044 model was pitched up 2.1° relative to balance.*

LM's N+2 Phase I low sonic boom aircraft configuration, the 1021 model, is a tri-jet configuration resulting from a design focused on obtaining very low boom on-track with some reduction of overpressures up to 20° off track. During Phase II of the NRA contract, the design was further refined for off-track overpressure reduction, and the Phase II design, the 1044 model, retains the tri-jet but fairly extensive aft deck shape changes as well as other design changes were made to the model.

The LM 1021 and 1044 models were designed with a blade-like swept-strut to minimize model support interference and aft fuselage distortions on the pressure signature imposed by conventional stings. The blade strut, shown in Figure 1.2, is attached to the top of the 1021 model's fuselage just upstream of the center nacelle and is swept greater than the Mach cone angle to minimize the flow disturbance. LM carefully positioned the strut far enough behind the wing leading edge to be shielded without allowing the blade shocks to spill around the leading edge below the model for up to 25 degrees off-track. It was also positioned as close as possible to the center nacelle without causing nacelle ingestion problems. A conventional sting that attached to the lower surface of the model was also tested on the 1021 model during Phase I experiment as a precautionary measure in case LM's predicted benefits of the blade strut

under-estimated the influence of the blade on the pressure signatures. The blade strut proved highly successful during Phase I test and so a conventional sting was not used with the 1044 model during the Phase II test.

1.1. Lockheed-Martin 1021 Model (Phase I Configuration)

The 1021 N+2 model is a 1/125th or (0.8%) scale representation of the Phase I flight vehicle with attributes listed above in Table 2. The model was fabricated using 13-8 high strength stainless steel except the blade strut used Vasco 300 steel because of higher stresses.

Photographs of the 1021 baseline N+2 Phase I model and mounting hardware are shown in Figure 4.1. The upper surface view of the model and a detached blade strut are shown in Figure 4.1(a). The footprint of the blade mount is rectangular with rounded corners and attaches upstream of the tail-mounted nacelle as shown in Figure 1.2. However, a cover plate is assembled to the model in this photo that hides a hollowed-out portion of the body that receives the strut. The photograph of the model and other component lower surfaces are shown in Figure 4.1(b) The underside of the V-tail/nacelle, the aft-body closure component, and the conventional sting are shown detached from the model in Figure 4.1(b). The closed aft-body component is installed when the blade strut is used. The cross sectional area distribution from the forward attachment point to the end of the aft-body closure fixture clearly differs from that of the conventional sting. At the upstream attachment point the cross-sectional areas are equivalent, then differ downstream, where the area tapers to zero for the closed-body, and is nearly constant for the sting mount. These volume changes are expected to result in some contamination of the aft pressure signature data where the contamination begins well upstream of the tail shocks due to the sting's structural requirements to support the model. Both the top blade and sting model supports were designed to position the model at an angle of attack of 2.5° so that the strut pitch angle is near zero and the model can remain nearly equidistant from the pressure rail during axial translation in the tunnel when taking data at angles of attack near 2.5°.

Figure 4.1(c) shows the details of the aft surfaces and nacelle/diverter. The small downward-deflected flaps were required to fine-tune the sonic boom signature rather than to trim the pitching moment of the model. The diverter shape extends to the upper surface and exposed screws mount the nacelle to the lower surface of the wing. The diverter extends beyond the wing trailing edge and diminishes near the base of the nacelle. This photo also shows that boundary layer trip disks were affixed to the upper surface of the wing. The diameters of the trip disks are 0.05 in., with a 0.0075-inch height, and a spacing of 0.2-inch on the inboard section and 0.1-inch on the outboard section of the wing. There is also a small line of disks in front of the centerline nacelle on the upper wing surface, and it appears that one or more of the disks have fallen off. This photograph was taken after both Phase I and II tests and it is not known when the disks came off. The center nacelle and tail are shown in Figure 4.1(d), the inlet lip is blunt and only small fillets between the tail and nacelle components remain after the hand-worked finishing. The lip of the under-wing nacelle and diverter leading edge are shown in Figure 4.1(e). The leading edges of the nacelle and diverter are blunt, but the nacelle lip is much blunter than the diverter leading edge. The nacelle lip is 0.007 inches thick or slightly greater as achieved in the fabrication process.

The Phase I 1021 model was re-tested at the beginning of the Phase II test to verify the test techniques and check long-term repeatability. In addition, higher altitude test data at nearly 70 inches from the model was obtained during the Phase II test with the RF1 rail moved to the aft window blank.

1.2. Axisymmetric Models (Seeb-ALR, Opt Sig, AS-2)

A photograph of the three axisymmetric models tested is shown in Figure 4.2, and their dimensions are provided in the first row of Table 2. The span values provided in the table are the diameters of the

cylindrical portion of the axisymmetric models. The top model in the Figure 4.2 photograph is the Seeb-ALR (aft lift relaxation) axisymmetric body, designed by LM utilizing the work of Seebass, George and Darden (Refs 32, 33) for a low-boom low-drag body with modification to relax the aft-lift requirements (Refs 4, 5). The model in middle of the photograph is the "Opt Sig" (optimum signature) model designed by LM. Its shape is representative of an ideal or optimum pressure signature for low sonic boom for one of LM's target design equivalent areas (volume plus lift distribution). This model was also designed using some of the design philosophy of Darden and Seebass. It possesses very small shape changes with rapid changes in curvature. These curvature variations are more evident when touched than can be seen on the 16.56-inch wind tunnel model. The model in the bottom of the photograph is the Boeing AS-2 axisymmetric "Seeb" body that was designed to produce a sonic boom pressure signature with a small 2-inch flat forward pressure region whereas the LM Seeb-ALR was designed for an 8-inch flat region. The AS-2 model is a true "Seeb" model without alteration of the aft signature.

The Seeb-ALR was re-tested to obtain data at greater altitudes of 56 and 70 inches. A larger number of model positions (39 or 56) were used for averaging with the shorter duration time of 8 seconds to obtain higher quality test data on the model. The model shocks at these altitudes were weaker than the free stream ambient shocks.

1.3. Lockheed-Martin 1044 Model (Phase II Configuration)

During Phase II of the NRA contract, the design was further refined for off-track overpressure reduction. The 1044 model has undergone many design changes from the 1021 that include an extended aft deck and the separation of the V-tail into two canted tails. The model was only tested using the blade strut since this strut was found superior to the conventional sting during the Phase I test. Photographs of the model are shown in Figure 4.3. The upper and lower surfaces of the configuration are shown in 4.3(a) and 4.3(b) with a detached blade strut. An isometric photo from above with the blade strut attached is shown in Figure 4.3(c). The tri-jet model was tested with all nacelles and without either the centerline nacelle or the under-wing nacelles. The model has an aft deck separating the canted vertical tails that which was required to provide good off-track pressure signatures (Figure 4.3(d)). The boundary layer diverters of the under-wing nacelles close in an unconventional manner and extend beyond the end of the aft deck at the base of the canted tails (Figure 4.3(e)) to permit the thin model to withstand the aerodynamic loads in the wind tunnel. Hence these diverter extensions are not found on the flight model. The 1044 model is a smaller 0.65% scale model than the 0.8% scale Phase I model; a side-by-side photo of the Phase I and II models is shown in Figure 4.4 (model lengths are provided in Table 4). The reduced size provides greater flexibility of placement in the tunnel and allowed testing at lower Mach. The Phase I model was larger because it allowed for larger signal-to-noise ratio and improved data accuracy.

1.4. 70° Flat Plate Model

A swept-wing calibration model with a flat lower surface and a planform similar to the1044 model's wing was tested. The blade strut used for the 1044 model attaches to the upper surface of the configuration with the strut base exposed to the freestream tunnel flow as shown in Figure 4.5(a). The flat lower surface is shown in Figure 4.5(b), and pin and attaching screws are visible in the photograph. The leading edge of the model is swept at 69.2°, but it is referred to as 70° to avoid confusion with the 69° delta wing body model. LM designed this model to utilize the flat lower surface to provide a large reflective area that would highlight, in the rail pressures, the impingement of ambient tunnel shocks on the model surface better than could be shown by an axisymmetric calibration model.

1.5. 69° Delta Wing-Body Model

A vintage 1970s model, referred to as the 69° Delta Wing-Body, was retested during the Phase II test. The models geometric surfaces are defined by mathematical functions and it is one of the models from a study of planform effects on sonic boom in 1973 (Ref 34). It has been used in several numerical studies of sonic boom prediction, including the NASA Fundamental Aeronautics Workshop in 2008 (Ref 35). These numerical studies in 2008 were compared with wind tunnel test data from 1973, but an accurate CAD definition for the sting geometry was not available for the computational grids used in 2008. The model tested during the Phase II experiment used a different sting—with a known geometrical shape, but the sting was designed for a larger model.

An upper surface photograph of the model is shown in Figures 4.6(a); the model is symmetric, so the lower surface looks identical except for the lack of the mounting setscrew in the middle of the body. The model attached to the sting is shown in the photographs in Figures 4.6(b) and 4.6(c). The sting shown is larger than desired because the original sting used in 1973 was damaged beyond repair more than a decade before the 2008 study. The small 6.9-inch-long (17.52 cm) model has a sting cavity that is too short to cover the sting-mounted strain gauges. The strain gauges, located just aft of the model, are visible in the photograph of Figure 4.6(b). The gauges are mounted on flat regions cut into the sting surface and are exposed to the free stream under a protective tape, and the surface discontinuities are large enough to affect the aft portion of the sonic boom pressure signatures. The flats are modeled in the computational analyses of the model, but the strain gauges are not. Figure 4.6(c) shows the model and sting in its entirety. The length of the sting typically needs to be around two body lengths to avoid corruption from the down stream model support hardware on the aft model pressure signature. This sting, having been designed for the 12-inch model, is about twice as long as required for this 6.9-inch model.

Instrumentation

Descriptions of the pertinent wind tunnel hardware and instrumentation used for sonic boom testing in both phases of experiments are provided. A computational solution of the flow at Mach 1.6 is used to allow for visualization of the shocks of a model and the RF1 pressure rail in the wind tunnel.

1.6. RF1 Pressure Rail

Sonic boom pressure signatures were measured using the RF1 rail. The rail stands 14 inches tall when measured from the wall. This height prevents impingement of the model shock waves reflected from the wall on the orifices of the rail and provides reflection-free data for model lengths of 35 and 43 inches at Mach 1.6 and 1.8, respectively. The rail has a 0.05-inch radius tip, and a 1-inch base width that results in a small 3.5-degree angle from the tip to the base. It is 90 inches long with an instrumented section 66 inches long that contains 420 pressure orifices of 0.015-inch diameter, spaced 4 mm (approximately 0.16 inches) apart along its tip. A cross sectional cut through the pressure measuring center section of the rail is shown in Figure 5.1 and a CAD drawing of the design is shown in Figure 5.2. The rail is shown attached to two window blanks (flat circular steel plates that replace the windows in the 9×7 wind tunnel) in the drawing. The rail is comprised of three sections: non-instrumented forward and aft sections and a center pressure-measuring section. The individual rail components allow for the inclusion of an additional instrumented rail section to be built to increase productivity and model-in-tunnel placement flexibility.

The 420 pressure orifices with 0.015-inch diameter were manufactured using prefabricated ferrules (metal sleeves) to establish the small orifice size and reduce the manufacturing costs. The ferrules were installed into larger diameter (easier to drill) holes along the tip of the rail. The ferrules connect to metal pressure tubes that are routed through seven machined grooves on one side of the rail that lead the tubes

through slotted window blanks to outside the tunnel. The grooves are shown in purple in the CAD images of Figure 5.2.

A Mach 1.6 flow field simulation of the RF1 rail, the Seeb-ALR body of revolution model, and the wind tunnel wall is shown in Figure 5.3. The computation was performed with *CART3D* (Refs 13-16) in conjunction with the Adjoint ERror Optimization (AERO) module. The computation utilized mesh adaptation to minimize errors along a line sensor placed 0.1 inches above the tip of the RF1 rail. The simulation provides visualization of the pressure field in the symmetry plane of the rail. The mesh is colored by pressure coefficient and rotated to nearly align with the Mach angle of the flow. The model is one body length (17.68 inches) from the rail in the computation. Here it is evident that the model's leading shock reflects from the wall downstream of the model pressure signature on the rail. The figure marks the models signature and reflected signature regions on the rail, and it is clear that there are nearly two body lengths behind the model's signature that offer no contamination from reflected model shocks. Details of the computational assessment of the rail are provided in Ref 3.

1.7. Pressure Transducers

The rail pressures were measured using seven 64-port, 5-psid electronic pressure scanners (ESP) de-ranged to 1.67 psid. The scanners are miniature electronic differential pressure measurement units that contain an array of 64 pressure sensors, one for each 60 rail ports plus 4 monitor ports (not plumbed to the rail). The accuracy of these scanners was determined to be 0.08% of the deranged value, which equates to about 0.0013 psi or 0.187 psf. The measured pressures are converted to pressure coefficients using the tunnel freestream static pressure computed from the Mach number and freestream total pressure measured in the plenum upstream of the test section.

1.8. Model Balances

All the models in the Phase I-II tests except for the 69° delta wing body used the Ames 1.5-inch Task Mk II-D six-component force balance. Upright and inverted runs were conducted for the winged models to correct the angles of attack and sideslip for tunnel flow angularity. The balance was located downstream of the blade strut (Figure 5.4), further behind the model than desired for accurate force and moment measurements, since there was no room for the balance in the model. The center of the balance is 39.875" downstream of the 1021 model nose and 4.131" above the nose, giving larger interaction corrections than desired. The recorded force data have been adjusted using LM-derived force and moment tares (from computed force differences with and without struts) to remove the contributions of the blade and sting forces from the test data. LM provided the tare corrections as a set of slope and offset terms for three of the six force and moment coefficients, which were applied to the data as follows for C_N:

$$C_N = C_{N_{UNC}} + C_{N_{UNC}} * C_{N_{CORR_{SLOPE}}} + C_{N_{CORR_{OFFSET}}}$$

Similar equations were used for C_A, and C_{PM}.

The correction terms provided in Table 5 were applied to the both Phase I and II tests, for the 1021 and 1044 N+2 models, respectively. Post-test detailed CFD analysis of the force and moment coefficient data of the models with and without the model support is provided later in this report. Improved slope and offset correction terms for normal force coefficient can be obtained by evaluation of the CFD and lift coefficient regression fits with reverse pressure signature aging to refine the corrections terms.

Table 5. Balance Corrections for N+2 Models with Blade Strut

Force or Moment Coefficient	*1021 Slope Correction*	*1021 Offset Correction*	*1044 Slope Correction*	*1044 Offset Correction*
C_N	0.0017	0.0172	-0.0406	0.013
C_A	0.0002	-0.0273	-0.0707	-0.0151
C_{PM}	-0.0016	-0.0207	-0.2411	-0.0096

It should be noted that the NASA-derived computational data did not model the blade or sting struts in their entirety or the balance adapter, all of which were metric. Thus, these computations cannot be used to validate the strut effects tare in the experimental data. Hence, the experimental angle of attack was used for CFD comparisons with the experimental data, or lift coefficient predictions from LM's computations were assumed equivalent in the comparisons.

The 69° delta wing body configuration did not use the Mk II-D balance, but instead used two pairs of strain gauges located on flats 1.4 inches apart on the forward end of its sting (see Figure 4.6(c)) to measure model normal force and pitching moment. The sting was made for another model which is longer (12", as opposed to 6.9" for the 69° delta), so the gauges were located slightly behind the 69° delta wing model rather than inside the aft end of it. Thus the gauges were exposed to the flow, and though they were protected from the wind by an epoxy covering, their uneven shape relative to the smooth sting caused small distortions in the pressure signature aft of the model.

1.9. Roll Mechanism

For the LM Phase I and II tests, the model support assembly from the tunnel strut to the model sting consisted of the Ames SR-57 primary adapter, the small model roll mechanism, and the linear actuator.

The small model roll mechanism (SMRM) was originally made for testing with a "kick-sting" for small models, where the kick-sting provides a way of extending the angle-of-attack range beyond what the tunnel strut can provide. The SMRM has a fixed 7.5° bend in it to further accommodate custom angle-of-attack and -sideslip ranges desired by particular tests. This bend has been useful in sonic boom tests in that it allows a model to be moved closer to the rail or to the south wall than would be possible without it, though the bend has not been required for some of the recent sonic boom testing in the 9×7.

1.10. Linear Actuator

A linear actuator was used to translate the model longitudinally (streamwise) in the wind tunnel. This allowed acquisition of multiple pressure signatures at small increments in the *X* direction over a specified distance, such as 26 positions spaced 0.63 inches apart (~4 rail orifices) in a typical *X* sweep. The linear actuator is remotely controlled and its ram translates forward and aft at a rate of 0.7 inches per second over a 24-inch traverse distance. The minimum and maximum (retracted and extended) length of the linear actuator is 44 inches and 68 inches respectively. The linear actuator mounts in the small model roll mechanism with a 2.875-inch diameter male taper, and the model sting mounts in the front of the linear actuator with a 1.05-inch diameter female taper.

A photograph showing the linear actuator and exposed portion of the roll mechanism in the 9×7 wind tunnel is provided in Figure 5.5. The ram of the actuator is shown in its retracted position, where the minimum of 2.625 inches of it is exposed at the front end of the actuator. The tilted-cone-shaped head of the roll mechanism is visible between the primary adapter (at right, partially hidden) and the rear of the

linear actuator. The non-rotating cylindrical body of the roll mechanism is secured in the forward end of the primary adapter.

Test Techniques

The testing techniques differed for the Phase I and Phase II tests. In general, the Phase I experiment was primarily concerned with obtaining the highest quality data possible from the 9x7 wind tunnel, whereas the Phase II test was looking for shortcuts to obtain more efficient testing procedures that would not compromise or minimally reduce the quality of the experimental data. The test techniques that were common to both experiments are first discussed, then the testing methods for the Phase I test are discussed and lastly, in the Phase II section, the testing techniques that differed from the Phase I are provided.

1.11. Wind Tunnel Flow Quality

Ideally, the wind tunnel flow field surrounding the model would be uniform and steady for all model positions in the tunnel. However, this is rarely the case in supersonic wind tunnels, and in the 9x7 wind tunnel, temporal variations and undesired flow angularity and Mach number variation are evident throughout the test section. These features result from the asymmetric sliding-block nozzle, and the fact that the nozzle contours of the floor and ceiling are fixed, meaning that the nozzle was likely optimized for one Mach number and not ideal for the others. Hence, it is not surprising that unsteady characteristic waves emanate from the nozzle through the test section, affecting flow angles, Mach number, and steadiness of the flow. It is not possible to completely correct for these issues, but spatial and temporal averaging have been used to minimize their effects on the sonic boom signatures.

It is difficult in any supersonic wind tunnel to obtain accurate sonic boom data for a model with a very weak pressure field. Free stream turbulence causes model motion fluctuation/vibration and the resulting rounding of the measured pressure signatures. This difficulty is compounded by the large stream angle variations in the 9x7 tunnel test section. Variations of about a third of a degree over small distances of five inches resulting in lift coefficient changes of approximately 0.015 during model translation, representing 10% to 15% changes in lift coefficient for supersonic vehicles. Figure 6.1 illustrates the variation in lift and angle of attack measured over a 16-inch translation for runs 829-854 of the 1021 blade-mounted model at Mach 1.6.

The tunnel free stream pressure waves become significant when measuring models with weak pressure signatures in flow fields around configurations designed for low sonic boom overpressures. The pressure waves of the blade mounted Phase I N+2 model are generally weaker than the tunnel (empty) ambient shock waves. This is evident when comparing ambient tunnel pressure waves with model-induced shocks in retroreflective background-oriented Schlieren (RBOS) images (Ref 36) (Figure 6.2). The image in 6.2(a) was obtained during Phase I test near the design angle of attack. A colored model is superimposed to clarify the position of the model in the image. The bow shock is smaller than the ambient tunnel pressure waves, but the wing, nacelles and tail shocks are stronger than most of the ambient waves. The image in 6.2(b) was taken during Phase II experiment and has the model at 6.9 degrees angle of attack allowing clear image of the stronger bow shock from the increased alpha. Schlieren video also reveals that the tunnel ambient density waves randomly shift position over distances on the order of one-quarter inch on average with some fluctuations up to about 0.5 to 0.75 inches.

1.12. Pressure Rail Correction for Overpressure Coefficient

The RF1 rail measures a complete pressure signature for one model position in the wind tunnel. However, a reference run, with the model moved away from the pressure signature zone of influence of the data run, is necessary. Model locations for example reference and data runs are illustrated in Figure 6.3, where the arrangement of the wind tunnel, LM 1021 model, and rail, are shown in top view. The red model is in the reference run position, and its bow shock strikes the non-instrumented trailing edge portion of the rail. The blue model is in the data run position (nose 31.3 inches above the rail, alpha 2.3°, ram extended 8 in.). Note that the model shocks—drawn at the Mach line angle as an approximation—for this data run fall on the instrumented section of the rail. The shocks fall over the range tunnel stations from -114 to -88 along the rail tip, and the instrumented section of the rail is from -146 to -80 inches. The negative X values indicate that model positions are referenced to the wind tunnel positioning system and are upstream of tunnel zero position (the strut center of rotation). The vertical magenta colored dashed lines on the rail represent the breaks in the rail between the instrumented section and the non-instrumented leading- and trailing-edge sections. It is clear from the figure that the data run model shocks are far enough ahead of those from the reference run to produce valid measurements.

The data and reference pressures use the tunnel static pressure as the free-stream value in the standard definition of pressure coefficient, $\Delta P/P = (P_L - P)/P$, where P is the tunnel static pressure. These pressure signatures are plotted in Figure 6.4(a). The curves in this figure are colored to correspond to the model positions in Figure 6.3. Note the magnitude and tumultuous nature of the pressures measured along the rail; this is an indication of the irregular tunnel ambient flow field. The corrected pressure signature of the model is obtained by subtracting the reference signature from the data signature, as shown in Figure 6.4(b). The multiple-shock shaped pressure signature revealed in the figure shows that the model bow shock is at an approximate X location of -113 and the signature ends at X of approximately -84 inches. The shock at X=-82 is coming from the model support hardware and is not considered part of the model signature. The ambient flow pressure coefficients upstream of the bow shock should theoretically be zero, but there are slight variations from zero in the data due to changes in the wind tunnel flow conditions between the data and reference runs. These variations are indicative of small temporal variations in the tunnel flow between the reference and data runs.

1.13. Phase I Test

NASA and Lockheed-Martin employed several testing techniques in an attempt to improve the accuracy of the data. Listed below are some of the techniques explored:

- Spatially average the data with a series of model positions
- Operate the tunnel at higher total pressure (2300 psf) and maintain within 1 psf
- Reduce the humidity to approximately 230 ppm and maintain within 4 ppm
- Position the model upstream of the leading edge shocks from the RF 1.0 rail
- Increase the model size for a greater signal to noise ratio
- Increase the duration of the reference and data runs

1.13.1. Spatial Averaging

The spatial averaging technique was developed to reduce the effect of tunnel flow field spatial distortions on the data at single model positions during supersonic wind tunnel testing (Refs 1, 4-5). Thus, in the 9×7 wind tunnel the non-uniform flow field causes pressure signatures on the rail to be different for different model positions in the test section. The averaging technique was developed during the 2011 Phase I wind tunnel test where it was discovered that averaging pressure signatures at a series of different model positions nearly eliminates the effect of tunnel flow field distortions on the data. A series of sonic

boom signatures were acquired at 26 model positions and averaged during the Phase I experiment. Figure 6.5 shows a schematic of the model translations and travel distances for the two altitudes (distance between model nose and rail tip) that were used in this test. The model positions in relation to the RF1 rail are shown as well as model and rail shock wave locations for Mach 1.6 flow. For the smaller altitude (21.2 inches from the rail), only 4 inches of model travel could be obtained before the linear actuator ram was fully extended while keeping the model upstream of the rail leading shocks. Thus, the model was only translated forward a distance of one orifice (0.16 in.) for each of the 26 runs (the minimum model translation is the distance between rail orifices for meaningful spatial averaging results). For the larger altitude (31.8 inches), the rail shock is further downstream and allows the model to travel 16 inches, over a distance of 4 orifices (0.63 in.) for each model position.

To enable the signature averaging at multiple model positions, the *X* locations at each point on the signatures need to be aligned. For an *X-sweep*, the *X* values of the rail orifice locations are adjusted by simply adding the ram position:

$$X_{Aligned} = X_{Orifice} + X_{Ram}$$

For a *Z-sweep* (used in the 2012 Phase II test), the *X* values of the rail orifice locations are adjusted by subtracting the height of the model nose at each *Z* position multiplied by the Mach number beta parameter:

$$X_{Aligned} = X_{Orifice} - h_{Nose}\sqrt{M^2 - 1}$$

After the signatures are axially shifted to align each series of pressure signatures, averaging of the data can be accomplished. Summing the aligned signatures, f_i, at each port and dividing by the number of positions, N, results in the arithmatic mean or averaged signature, $\bar{f}$.

$$\bar{f} = \frac{\sum f_i}{N}$$

Figure 6.6(a) shows the experimental pressures for runs 829-854, using reference run 876, for the LM 1021 model with blade strut over a 16-inch traverse with 4-orifice spacing (0.63 in.). The signatures are spread vertically across the page, in what is referred to as a waterfall plot. The bottommost signature is run 829, the 1021 model pressure signature begins at *X*=-113 and ends near -83. Model support and positioning hardware corrupt the signature from *X*=-83 to the end of the pressure measurement. The top signature is run 854, where the model has been translated to the most forward tunnel position. The small incremental translation in *X* for each run can be observed with the forward progression of the model shocks through the run series. The pressures vary with position in the tunnel due to free stream pressure fluctuations, and some of the larger tunnel waves can be identified by small stationary changes in the data. In this figure the topmost 7 pressure signatures show fluctuations at *X*=-124.

Figure 6.6(b) shows aligned pressure signatures for the run series—the result of adding the recorded linear actuator position to each pressure signature. The pressure signatures were also aligned for any changes in altitude. The blue colored pressure signature at the bottom of the plot is the mean or averaged pressure signature of the run series. Since the average value at each point is known, the standard deviation can be computed for each port as follows:

$$\sigma = \sqrt{\frac{\sum (f_i - \bar{f})^2}{N}}$$

The average standard deviation along the rail serves as a figure of merit to determine the best reference run to use. When deciding which reference run to use in forming the spatially averaged signature, the one

with the smallest average standard deviation over the entire signature is selected. Reference runs were taken before and after each series of data runs; usually the reference run *after* the data run usually offered less scatter. Often a reference run chosen this way for one series of data runs also turned out to be a more suitable reference run for another data run series. The choice of the reference run is important to the quality of the corrected signatures for the individual data runs at different tunnel positions, but was less important to the quality of the spatially averaged signatures.

1.13.2. Tunnel Pressure

Operating the test slightly above atmospheric condition at a P_T of 2300 psf, rather than 1450 psf used in tests between 2008 and 2010, has significant advantages. A higher Reynolds number per foot (Re) of 4.43×10^6 is obtained, compared with 2.88×10^6 at 1450 psf. The likelihood of flow separation from the model or blade mounting surfaces is reduced, and the settling time of the rail static pressures is shortened by nearly a factor of two compared with operation at 1450 psf. The higher tunnel pressure also reduces the quantity of dry (~50 ppm) high-pressure air necessary to stabilize humidity, and lower humidity levels are more easily obtained. In addition, it does not require test interruptions for re-pressurizing (in vacuum state) the external tanks (required when operating the tunnel below atmospheric pressure at 1450 psf); these interruptions lasted about 15-20 minutes every couple of hours. However, operating the tunnel at a P_T of 2300 psf requires an increase in power cost, but the aforementioned improvements in accuracy and productivity outweigh the cost increase.

The normal operating mode of the wind tunnel utilizes a coarse pressure valve that automatically adjusts the pressure in the wind tunnel. The total pressure fluctuation was measured in this mode and with the valve fixed after getting on condition. A fine pressure valve solely maintains the pressure in the wind tunnel with the coarse valve fixed. The pressure fluctuations over a 4-minute time interval are plotted in Figure 6.7(a). The P_T has a $\pm$ 2 psf variation with the coarse valve automatically cycling open and closed. The period of each cycle is about 90 seconds. The coarse valve in the fixed position reduced the total pressure variation within 0.5 psf with a cycle period of less than 10 seconds. The tunnel was operated with the coarse valve fixed during Phase I testing to reduce wind tunnel condition variations, but the tunnel was operated in the automated mode with the coarse valve actuating during Phase II testing to expedite testing.

1.13.3. Humidity Levels

Most types of testing in the 9×7 wind tunnel do not require very low humidity or fine control of it, but sonic boom testing is an exception. Humidity is normally brought down to operational levels (~500 ppm by weight, depending on the test requirements) by purging the tunnel of wet air and pumping back up with dry air; though for sonic boom testing, this purging is supplemented by continuously injecting dry, high-pressure air to keep the humidity low.

Maintaining low humidity levels for data and reference runs is of utmost importance to obtain high quality sonic boom data. Higher levels of humidity cause rounding of the signatures and cause spurious pressure signature data including shifts. The pressure signature shifts obtained during long data acquisition probe testing in the early 1990s in the 9×7 wind tunnel were corrected manually by taking ambient flow data points, by retracting the model upstream of the data probe, midway through the signature and at the end of the signature. The raw pressure data was corrected by bi-linearly shifts to account for the changes in pressure due humidity variations. A similar data correction method is discussed in Ref 1 for sonic boom data obtained in 2008.

Typically, approximately 10 lbs/sec of dry air is pumped into the tunnel via a single three-inch diameter pipe pointed downstream located under the wind tunnel strut to reduce the tunnel humidity

levels. By adjusting the amount of high-pressure air entering the tunnel, the humidity level could be stabilized to within 4 ppm during data acquisition. Figure 6.7(b) shows the average humidity for a run series with 30-second duration acquisition times for each model axial position. This run shows a range of less than 4 ppm and an increase in humidity towards the end of the run (X = -167), where the model is in the more forward tunnel location. The overall humidity level that was maintained in the Phase I test was approximately 230 ppm (measured by weight). Stabilizing humidity required a significant amount of time, and reduced test productivity. The payoff of these efforts is reflected in the test data wherein the averaged pressure coefficients upstream of the model bow shock (ambient pressure) are near zero (approximately 0.0002 from zero) throughout the entire test.

1.13.4. Rail and Model Positions

It was observed in a prior wind tunnel test that the data obtained with the RF1 rail on the forward window blank of the test section were superior to the data taken on the aft blank. In order to obtain the most accurate data, the rail was positioned on the forward blank for that entire test. The model support hardware and linear actuator typically require that smaller altitude data be acquired with the rail forward, while data at greater altitudes requires the rail to be mounted on the aft window blank. The reason for the improved data in the forward tunnel position can only be determined by a detailed analysis of tunnel-empty flow field surveys. However, it stands to reason that the larger signal-to-noise ratio with the rail forward is a factor in the improved data, as well as the reduced pressure signature rounding effects from turbulence-induced model vibration, due to smaller shock position differences at the lower model altitude.

The model was also positioned and translated upstream of the rail leading edge shock to eliminate the possibility of the rail leading-edge compression region or subsequent expansion regions affecting the model pressure signatures. Figure 6.5 illustrates the relative positions of the model and rail.

1.13.5. Model Sizing

To further improve the test data the LM 1021 model's size was increased relative to typical prior test configurations; Most sonic boom test articles were 12 inches or less, whereas this model was nearly double that at 22.365 inches. The larger size results in a larger pressure signal relative to the same noise level of the tunnel.

1.13.6. Sampling Time

The sampling time duration of "data" runs (model pressures on rail) were typically 30 or 60 seconds and reference runs were usually 60-90 seconds (although some lasted only 30 seconds). The 90 second duration time was used because during previous tests it was the observed period of the tunnel total pressure variation (refer back to Figure 6.7), and taking the data over 90 seconds provided nearly the same average P_T between data and reference runs. However, during the T97-0231 test entry, the coarse pressure stabilization valve was fixed at a constant setting to reduce the pressure variation from 4 psf to less than 1 psf. The resulting period of pressure oscillation was only 5 seconds with the coarse valve fixed. The benefit of stabilizing the pressure could reduce the need for longer duration runs, but this conjecture needs study.

Averaging the pressure signatures over a series of axial positions had a greater benefit on the quality of the data than increasing the sampling time. Data sampling duration has a strong influence on the quality of the individual data run, but a small effect on the averaged signature. This is demonstrated in Figure 6.8 and 6.9. The data plots near the bottom of Figure 6.8 show the 26 pressure signatures for a run series (black lines), the averaged pressure signature (cyan), and one standard deviation from the averaged data (red) for 30-second duration runs. The test data runs with 2-second sampling times while using the 30-second reference run are plotted above the 30 second duration data in waterfall format (translated 0.02

vertically, with average shown in magenta). The data and reference runs both using 2-second sampling times is shown at the top in the plot (average in green). Comparison of the individual pressure signatures with different sampling times shows that increasing the duration of the sampling time improves the quality of the temporal or individual data runs. It also appears advantageous to use a longer duration for the reference runs than for the data runs. However, the averaged pressure signatures with the various sampling times show only small differences in the averaged data, when overlaid (Figure 6.9). There is almost no difference between the short duration data runs with the longer reference run compared to the longer duration data runs. This highlights a large potential savings in data acquisition time by shortening the sampling time for the overpressure runs in future tests and hence, shorter 6–8 second duration runs were employed in the Phase II testing.

1.14. Phase II Test

During the Phase II test, many of the wind tunnel control measures from the Phase I test were relaxed to allow for a greater number of runs and test articles. Specifically, sampling duration was reduced, and tunnel total pressure and humidity control were relaxed. In addition, the pressure lines from the rail to the pressure transducers were shortened before Phase II testing to reduce the lag time (the time it takes to reach peak pressure levels on the rail). Lag time in the Phase I test was approximately 4 seconds. The length of the pressure tubing from the base of the RF1 rail was attributed to causing the about a factor of two increase in lag time and the tubing was longer than necessary to connect to the pressure transducers outside the tunnel. The pneumatic damping effects of the shorter tubing were not known. However, the benefits of greater productivity outweighed the unknown outcome and time to cut, reconnect and leak check the 420 pressure tubes before the Phase II test.

The benefit of the very tight control on the tunnel total pressure may not have been adequately substantiated and so the tunnel total pressure was put back into automatic control. The humidity control was relaxed to within 10 ppm of 250 ppm. Overall the variation in humidity was about a factor of two greater in Phase II than Phase I, with Phase II approximately 4 ppm and Phase I approximately 2 ppm. It was thought that spatial averaging would remove most of the increased temporal data uncertainty.

Lastly, the model size of the N+2 1044 vehicle is 19.032 inches. It was reduced 3.33 inches in length compared to the Phase I 1021 model. Although this results in a reduced signal-to-noise ratio, LM felt that the quality of the test data in Phase I was better than anticipated and that they could afford to also relax the model size, trading signal to noise ratio for greater model placement flexibility within the confines of the model positioning systems and wind tunnel with a smaller model.

Experimental Results

1.15. Phase I Test

A simplified Run Matrix shown in Table 6 provides an overview of the test. The configuration, Mach number, angle of attack, roll angle, and altitude are provided. In addition, model translation direction is denoted as *X* or *Z* to indicate the sweep direction, along with the wind tunnel test run number range and reference run. The range is denoted with an underscore between the starting and ending run numbers, and the reference run follows a hyphen. The second from the last column in the table shows the figure number of the plotted experimental data. The last column of the table provides the figure number of the computational results overlaid with the experimental results. Cells grouped with a common color in the table indicate that the experimental data within the group are at similar conditions (nearly repeat runs) or runs that are at the essentially the same conditions but differ in off-track angle. Merged cells in the “CFD

Fig. #" column indicate that the data of the rows adjacent are overlaid with one or more computational simulations.

Table 6. Simplified run matrix for the Phase I test T97-0231

Configuration	M	α	h	ϕ	Sweep	Run Series	Exp. Fig. #	CFD Fig. #
Seeb-ALR	1.6	-0.29	20.59	0.47	*X*	195_219-221	7.1	9.1(a)
	1.6	-0.27	20.62	0.46	*X*	553_578-580	7.2	
	1.6	-0.27	31.22	0.30	*X*	581_606-608	7.4	9.1(b)
1021 with all nacelles, blade strut	1.6	2.09	20.69	-2.37	*X*	333_358-359	7.5	9.2
	1.6	1.95	20.61	-4.21	*X*	390_415-387	7.6	
	1.6	2.10	20.75	-0.75	*X*	939_964-938	7.7	
	1.6	2.29	20.71	-0.53	*X*	774_799-828	7.9	9.3
	1.6	2.46	20.79	-0.59	*X*	800_825-828	7.10	
	1.6	2.32	31.33	-0.57	*X*	829_854-876	7.12	9.4
	1.6	2.51	31.35	-0.74	*X*	855_874-876	7.13	
	1.6	2.47	20.80	20.27	*X*	877_902-903	7.15	9.5
	1.6	2.31	20.76	24.56	*X*	748_773-828	7–16	
	1.6	2.30	20.75	47.79	*X*	696_721-828	7.18	9.6
	1.6	2.45	20.86	47.63	*X*	722_747-828	7.19	
1021 without under-wing nacelle, blade	1.6	2.31	20.77	0.20	*X*	631_656-630	7.22	9.7
	1.6	2.58	20.81	-0.66	*X*	657_683-630	7.23	
1021, sting	1.6	2.57	21.10	-1.86	*X*	453_478-507	7.26	9.8
	1.6	2.80	21.19	-2.04	*X*	479_505-507	7.27	
	1.6	2.36	31.51	-0.66	*X*	537_543-544	7.30	9.10
	1.6	2.87	21.21	46.19	*X*	509_534-536	7.31	9.11
AS-2	1.6	-0.27	29.52	-0.15	*X*	918_925-927	7.33	9.12
Opt Sig	1.6	-0.27	20.58	0.24	*X*	989_1014-1017	7.34	9.13

Experimental data are presented in the order shown in the table, which is sorted by configuration type and by run number, but some similar runs (repeats) have been grouped together. Experimental data for each run series in Table 6 are presented with three plots and a table, e.g. Figure 7.1. At the top of each figure, a table gives the nominal model position, orientation, and force and moment coefficients, as well as the range of each of these parameters measured during the run series. The upper left plot is a waterfall

plot of the run series, where the first run in the series is the topmost pressure signature, and the last run, with the model furthest upstream in the tunnel, is the bottommost curve. The pressure signature curves are colored with a rainbow-like variation of colors. The beginning and ending colors of the run series are shown in the figure legend, and the color for the intermediate runs are inherently provided in the figure since each successive run is plotted below the starting run number. The pressure signatures of each run align vertically since they have been shifted by the reported position of the linear actuator. The black solid curve overlaying the initial run at the top of the figure represents the mean pressure signature of the data series.

The plot to the right of the waterfall plot is a wind tunnel layout schematic. Model positions of beginning, ending, and reference run positions are provided in the layout. The blue-colored model and the model supporting hardware represent the placement of the model at the beginning run position. The violet-colored model (without support hardware) is in the ending position of the last run in the run series, and the red-colored model is in the reference run position. Note that the model shocks—drawn at the Mach line angle as an approximation—are displayed as dashed lines for all model positions. The axes of the plot use the wind tunnel positioning system, the negative X values indicate that model positions are upstream of the tunnel zero position (the strut center of rotation). The outline of the RF1 rail is drawn with magenta lines, and the vertical dashed lines on the rail represent the breaks in the rail between the instrumented section and the non-instrumented leading- and trailing-edge sections.

The third and bottommost plot shows all the data from the run series overlaid, with the axes ranges to show details of the models pressure signature. The averaged data shown in black is the final corrected wind tunnel test data for each vehicle. The computed (1-σ) standard deviation of the aligned data from the run series are added and subtracted from the averaged data and displayed as black dashed-line curves.

In each composite plot, the figure title provides the averaged values of pertinent test conditions. In addition, the differences of the total pressure and humidity from the reference run average data are provided. These are labeled as the parameter "-Ref" in the figures, e.g., "H-Ref" provides the average difference in humidity of the reference run from the collective data runs. These two differenced values provide a quick assessment of the data run's tunnel flow conditions compared with those of the reference run. The control of these parameters (humidity and total pressure) is excellent throughout the Phase I test data.

The quality of the averaged pressure signature can be indicated by the variation of the averaged signature *ahead* of the first model shock. This line, sometimes referred to as a leading-zero line, is a result of the difference between the ambient flow of the data runs and the reference run. Theoretically, the ambient flow upstream of the wind tunnel model should produce a pressure signature (leading-zero line) of exactly zero. Thus, the amount of variation from zero in the pressures is an indication of the variation in the tunnel static pressure along that portion of the rail between the reference and data runs. For all run series, the initial data points in the experimental data have more uncertainty because after aligning the signatures they contain fewer data points for the spatial average. This can be visualized in the waterfall plot of Figure 7.1 by observing that the starting and ending pressure signature data points are always misaligned (vertically on the plot) after the pressure signatures have been shifted to align the models pressure signatures. Thus, the first 16 inches of the average will not contain the full set of data points to average. Slight variation in the initial data points are therefore often non-zero but once a few data samples are averaged they quickly settled to a value very near zero for all data taken in Phase I test T97-0231.

1.15.1. Seeb-ALR Model

The Seeb-ALR calibration body of revolution model was tested during both Phase I and Phase II entries. This specialized Seeb model maintained a full 8-inch region of constant pressure on the forward

signature (positive pressures upstream of the main expansion or Y=0 point). It also was designed for a 2-inch region of constant pressure on the aft signature (negative pressures downstream of the main expansion). Experimental data for three run series are provided in Figures 7.1, 7.2, and 7.4. The first two run series (Figures 7.1, 7.2) are essentially repeat runs, both taken at approximately h=20.6 inches, and the third is a run series at h=31.2 (Figure 7.4). The waterfall plots of a model with regions of constant pressure, as in these figures, allows for visualization of wind tunnel ambient shock waves since deviations from the constant pressure level can be seen with close inspection of the plots. The individual runs have small distortions at nearly all positions, but the data in Figure 7.1 was obtained with 30-second duration whereas the data in Figures 7.2 and 7.4 were obtained with full (the largest duration employed) 90-second duration runs. The scatter in the "leading zero" lines is less with the longer duration run (compare the averaged signature plots of Figure 7.1 and 7.2). The averaged data look similar—there is some reduced quality aft of the "tail" shock for the earlier run series, but not for the later run series. This reduced quality is attributed to the position of the reference run. Compare the layout images shown in Figure 7.1 and 7.2—the reference run bow shock is located very close to the tail shock of the beginning run, and is contaminating the aft signature in Figure 7.1, whereas the reference run bow shock is further aft and not affecting the model signature in Figure 7.2. The two repeat run series are overlaid in Figure 7.3. The repeatability of experiment is excellent upstream of the trailing shock where the data is corrupted from the aforementioned proximity of the reference run of Figure 7.1 (black curve in Figure).

The single run series at h=31.2 inches in Figure 7.4 has a very weak pressure signature with a pressure coefficient value of only 0.005 in the flattop region. The upstream ambient pressure signature is well behaved after averaging and the model signature appears to be of high quality.

1.15.2. 1021 Model

The 1021 Model was tested with and without nacelles and with the blade strut model support as well as mounted on a conventional sting to study these different component effects on the sonic boom signatures. Data for each of the various model assemblies are presented in this section.

1.15.2.1. 1021 with All Nacelles on Blade Strut, On-track

Figures 7.5 to 7.19 provide the wind tunnel data for the 1021 model with the blade strut model support. Refer to Table 5 run matrix for primary conditions. Figures 7.5 to 7.7 shows three repeat run series with very small α and h variations of on-track experimental pressures signatures at an altitude of approximately 20.7 inches, h/L=0.93. These run series are slightly below the design angle of attack of 2.3°, and all were obtained using X-sweeps with only a 4-inch total model translation. The data from all three series (each with 26 signatures) are mostly within one-standard deviation of the average. The model support hardware pressures interfere with the experimental data at an X value of approximately -87. The averaged pressure signatures for these run series are overlaid in Figure 7.8. There are only very small differences among these signatures, and the differences could be attributed to the α differences—the forward pressure signature overpressures are arranged according to the experimental α, due to the small lift difference, or the differences could be a result of the small shift in the measured ambient pressure signatures upstream of the model.

On-track data at slightly higher angles of attack, at and slightly above the design angle of attack, are presented in Figures 7.9 and 7.10. The quality of these data is excellent; the individual experimental runs mostly fall within one standard deviation of the average. These experimental pressure signatures are compared in Figure 7.11. The small angle of attack differences are evident in the pressure signatures; the increased lift for the larger α case results in stronger wing overpressures and some changes to the aft pressure signature. Otherwise, the signatures compare well.

On-track pressure signatures at 31.3 inches (h/L=1.4) are presented in Figures 7.12 and 7.13. Pressures outside of one standard deviation are now evident due to the smaller model pressure signal resulting from a reduced signal-to-noise ratio due to the increased distance of the model from the RF1 rail. The two run series are overlaid in Figure 7.14. The 0.2° difference in angle of attack of these two run series result in the expected pressure deviations—larger peak overpressures for the runs at the higher lift coefficient and angle of attack. In spite of the increased scatter of the data the pressure deviations appear only to be coming from the changes in angle of attack.

1.15.2.2. 1021 with All Nacelles on Blade Strut, Off-track

Off-track data at ϕ=20.3° and 24.6° are shown in Figures 7.15 and 7.16. The standard deviation of the experimental data is small for these run series and the averaged pressure upstream of the signature are flat and of value zero. This model has off-track pressure signatures that differ significantly from the on-track, and considerable variation with small changes in off-track angle are observed in the aft portion of the signature. The pressure signatures on-track (ϕ=-0.6°) are compared with the off-track data at ϕ=20.3° and 24.6° in Figure 7.17. The difference in on and off-track data is evident. Thus, though grouped together, the 4.3° difference in off-track angle between the two off-track experimental run series results in different aft signatures that consist of multiple shocks of different strength, rather than an experimental repeatability problem with the data. The angle of attack differences between the off-track run series are not the cause of the discrepancies and are opposite the established trends due to differences in lift or angle-of-attack seen in the comparisons plots of Figures 7.11 and 7.14. The forward portion of the signatures can be attributed to α differences, but the aft signature differences are clearly not due to α changes, since the trailing shocks are now weaker with increased α. These differences are therefore due to the off-track angle differences. Hence, the two series will not be overlaid with CFD in subsequent plots—only the series with the same azimuthal angle will be shown.

Off-track data at approximately 48° are presented for two near-repeat run series in Figures 7.18 and 7.19. The off-track signatures have a strong aft shock (near X = -98) in the averaged pressure signature plots in the figures. These data are well behaved with little variation outside of one standard deviation. The averaged data are compared in Figure 7.20. The experimental data correlate well, and most of the differences are likely attributed to the angle-of-attack disparity between the two run series. There are three small pressure oscillations in the main expansion of the pressure signatures at both test conditions with only slight variation of the signatures. The on- and off-track data are compared directly in Figure 7.21. The changes in the pressure signatures from on-track to off-track are primarily in the reduction of strength of the maximum overpressure shock (thought to be associated with the nacelle) and the increase in strength of the shock aft of the main expansion. The strong aft shock at ϕ=47.6° is about 1.5 times the strength of the on-track aft shock. An associated increase in the loudness level for off-track conditions will accompany the aft shock signal strength for this early design phase of the model (Ref 28). Some reduction of the off-track signature strength is forthcoming in the Phase II design.

1.15.2.3. 1021 Without Under-Wing Nacelles on Blade Strut, On-track

Two experimental run series, near the design angle of attack, are provided for the 1021 model with the under-wing nacelle removed, in Figures 7.22 and 7.23. Both data sets were taken with 90 second duration runs and subsequently little variation is seen in the individual runs with most of the data within one standard deviation of the averaged signatures. The overlaid run series are provided in Figure 7.24. Here we see a small shift in the leading zero line for both of the run series. This can likely be attributed to a small difference in the reference run conditions since both run series use the same reference run correction. The α disparity (0.27°) is greater than most of the other experimental data comparisons, and thus slightly larger pressure differences are seen. The effect that the under-wing nacelle has on the pressure signatures can be clearly seen in an overlay of the model signatures with and without the nacelle

(Figure 7.25), where the flow and model conditions are well matched. The shock associated with the maximum overpressure is actually the bow shock of the under-wing nacelle and possibly some boundary layer diverter pressure disturbance; though much of the diverter is within the thick boundary layer at this Reynolds number. The shocks from the nozzle exit or nacelle base and closure of the diverter is evident in the aft signatures. Also note that the leading zeros line is good for the run series without the nacelles that use a different reference run.

1.15.2.4. 1021 with All Nacelles on Conventional Sting, On-track

The lower surface of the LM 1021 model with detached conventional sting and aft-body closure parts are shown to reveal how the sting attaches to the wing and replaces an aft-body closure component when the blade strut is used (Figure 4.1(b)). The sting mount holds the model at the same angle of attack (2.3°) as the blade strut. Note that the "dog-legged" conventional sting bends abruptly upward about a half body length behind the model—this offset places the model at the Z location relative to the balance as the blade strut does. On-track experimental data at two different angles of attack at h=21.2 inches are provided in Figures 7.26 and 7.27. High quality data were obtained with each run acquired with 90-second duration sampling times. The effects of the angle attack differences are evident in the comparison plot of Figure 7.28. Comparison of the strut difference (blade versus sting) is shown in Figure 7.29. Unfortunately the angles of attack differ and the struts contribute to lift coefficient differences. For example, the blade strut imposes a change of pressure over the upper surface of the wing, as will be shown later in Computational Modeling §8.2**.** However, the forward overpressures align well—providing confidence in matched pitch angle relative to the onset flow. The aft signatures differ beginning at the nacelle shock (x=-102) to the end of the signatures, and the conventional sting interferes with the return-to-ambient flow, from x=-92 on. Computational comparisons of the 1021 model with blade strut, conventional sting, and model without sting/strut are provided in Ref 3, where it is shown that the configuration without sting/strut and blade strut models have nearly identical on-track pressure signatures.

A run series with only eight model positions was taken at an altitude of 31.5 (Figure 7.30). In spite of the small number of runs in the series, the resulting average pressure signature looks of the same quality as averages of more numerous runs.

1.15.2.5. 1021 with All Nacelles on Conventional Sting, Off-track

A complete run series of the 1021 model with the sting mount at an off-track azimuthal angle of 46.2° is presented in Figure 7.31. The influence of the sting on the off-track signatures can be assessed by comparison of the signatures with the blade strut (Figure 7.32). The angle of attack match is imperfect but the lift differences are easily identified as shifted curves owing to the lift differences. The location and amount of disparity of the aft pressures off-track are similar to those seen on-track, compare with Figure 7.29. For the highly-attuned, shaped signature of this model, the accuracy of extrapolated ground signatures from the experimental results with the conventional sting would be questionable.

1.15.3. AS-2 Model

The Boeing AS2 axisymmetric "Seeb" body was designed to produce a sonic boom pressure signature with a small 2-inch flat pressure region whereas the LM Seeb-ALR was designed for an 8-inch flat region. The experimental data shown in Figure 7.33 reveal that there are only 8 experimental runs going into the average signature. The shape within the region of constant pressure ($-90 < X < -87$) varies between the runs, and there is an increase in the range of one-standard deviation from the average in this region. However, the resulting averaged signature does result in a nearly flat region of pressure. Unfortunately, these are the only experimental data available for this model from the Lockheed Phase I and II tests. Additional data are available on this model in reports on experiments with NASA and Boeing (Refs 37-39).

1.15.4. Opt Sig Model

The last model from the Phase I test and the final axisymmetric body studied is the Opt Sig model. The experimental data taken at 20.58 inches from the rail is shown in Figure 7.34. High-quality, 90-second duration run, data were taken for this model. However, the plot of the overlaid run data shows that there are increased scatter at most of the shock peaks where several of the runs are outside of one-standard deviation—the reason for this could be shock movement and misalignment of the signatures before averaging. The multi-shock pressure signature with many small peaky pressures would likely be more sensitive to misaligned signatures than a model with largely flat pressures, but the range of the standard deviation is small indicating that the averaged pressure signature is high quality.

It is fascinating to see that this model, which looks like a cone-cylinder, produces a signature that resembles the pressure signature of a complete configuration. This is because the area distribution of the axisymmetric model possesses very small shape changes with rapid changes in curvature that are so small that they are difficult to see, yet it nearly matches the volume and lift distribution of a complete model similar to the LM 1021 model.

1.15.5. 1021 Model Repeat Signatures Extrapolated to Ground Level

The success of the Phase I experiment can be further assessed by evaluation of the ground level pressures and loudness levels. Although there are a limited number of data run series that are close enough in Mach number, angle of attack, altitude, and roll angle to be considered repeat runs, there are a handful that are close enough to evaluate the changes in ground level sonic boom loudness levels. Note that experimental pressure signatures are truncated before they achieve the return to ambient pressure of a flight model because of model support hardware interference, and this may reduce the accuracy of the following extrapolations.

Experimental pressure signatures for the 1021 Phase I model were extrapolated from the experimental height to the ground assuming a 50,000 ft. flight altitude with standard atmospheric conditions, no winds, and a ground reflection factor of 1.9. The first thee rows for the 1021 model in Table 6 provide three sets of on-track data at similar test conditions that were extrapolated using *sBOOM* (Ref 40). *sBOOM* solves the augmented Burger's equation and has become NASA's new standard method for extrapolation of sonic boom pressures. The perceived loudness (PL) is computed using the *LOUDNESS* code written by Shepherd and Sullivan (Ref 41). The ground pressures for similar runs are shown in Figures 7.35 to 7.37. The on-track experimental data for the 1021 model taken from 20.7 inches below the model at angles of attack of approximately 2° are compared in Figure 7.35. The perceived loudness levels of the entire signature ($PLdB_{wave}$), as well as the front and aft signature contributions to loudness are provided in the figure legends. The computation of the front and aft loudness levels are the result of splitting the complete signature into a front and aft portion, where the separation point is the first time the overpressure crosses zero into the negative pressure domain. In spite of the differences in angle of attack, the "wave" loudness levels are predicted within a range of 1.4 PLdB (between 91.0 and 92.41). There is more variation in the loudness of the aft signatures. The two signatures that are closer in angle of attack agree very well in both ground signature shape, as well as PLdB, with differences of less than 1.26. Figure 7.36 shows the ground-level signatures and PLdBs at slightly larger angles of attack (2.3° and 2.5°). The loudness level increases, as expected, due to the increased lift, with associated loudness levels of 95.06 and 97.02. Figure 7.37 shows propagated results taken at a greater altitude of 31.3 inches with the approximately same spread in angle of attack. The changes due to the different lift coefficients are similar (compare Figures 7.36 and 7.37). The PLdBs of the waves taken from 21 or 31 inches are providing similar loudness levels. This indicates that obtaining the data at 21 inches may be sufficient to capture most all of the three dimensional effects of the model in this situation. The perceived loudness levels are compared with computational prediction later in the report.

1.16. Phase II Test (New Models)

Run matrix Table 7 provides an overview of the new experimental models. Later sections of the report will cover previously tested configurations during the Phase II (T97-0254) test. Cells of a common color in the table indicate that the experimental data for these rows are at similar conditions (nearly repeat runs) or runs that are at the essentially the same conditions but differ in off-track angle.

Table 7. Simplified run matrix for the Phase II test T97-0254

Configuration	M	α	h	ϕ	Sweep	Run Series	Exp. Fig.	CFD Fig.
1044 with all nacelles, blade strut	1.7	2.24	26.59	1.03	*Z*	4865_4913-4864	7.38	9.14
	1.7	2.20	32.64	0.06	*Z*	4276_4326-4275	7.39	9.15
	1.7	2.22	32.59	-0.28	*X*	4788_4813-4787	7.40	
	1.7	2.29	32.64	10.52	*X*	4630_4655-4629	7.42	9.16
	1.7	2.40	32.65	20.15	*X*	4603_4628-4602	7.43	9.17
	1.7	2.46	32.68	30.46	*X*	4576_4601-4575	7.44	9.18
	1.7	2.51	32.64	40.14	*X*	4468_4493-4467	7.45	9.19
	1.7	2.65	32.54	50.42	*X*	4522_4547-4521	7.46	9.20
	1.7	2.77	32.41	60.07	*X*	4549_4574-4548	7.47	9.21
	1.7	1.74	54.76	-0.23	*X*	1818_1894-1895	7.49	9.23
	1.7	1.94	54.77	19.93	*X*	2140_2173-2139	7.50	9.24
	1.7	1.97	54.50	40.03	*X*	2078_2111-2077	7.51	9.25
	1.7	1.99	54.43	60.04	*X*	2016_2049-2015	7.52	9.26
	1.7	1.73	70.68	-0.12	*X*	1555_1631-1632	7.54	9.27
	1.7	1.74	70.70	-0.16	*X*	1713_1751-1712	7.55	
	1.7	2.03	70.85	0.40	*X*	2517_2593-2594	7.56	
	1.7	2.07	70.83	20.10	*X*	2820_2848-2819	7.58	9.28
	1.7	2.18	70.85	39.94	*X*	2790_2818-2789	7.59	9.29
	1.7	2.30	70.59	59.60	*X*	2760_2788-2729	7.60	9.30
1044 without under-wing nacelle, blade strut	1.7	2.17	32.59	0.45	*X*	4933_4958-4932	7.62	9.32
	1.7	2.37	32.69	20.29	*X*	4987_5012-4986	7.63	9.33
	1.7	2.56	32.68	40.14	*X*	5041_5066-5040	7.64	9.34
	1.7	2.71	32.49	60.24	*X*	5095_5120-5121	7.65	9.35
	1.7	1.99	70.77	0.03	*X*	2923_2999-3000	7.68	9.36
1044 without center nacelle, blade strut	1.7	2.25	32.62	0.67	*X*	4119_4144-4145	7.69	9.38
	1.7	2.28	32.66	20.20	*X*	4146_4171-4145	7.70	9-39
	1.7	2.37	32.64	40.31	*X*	4173_4198-4172	7.71	9.40

Configuration	*M*	α	*h*	ϕ	Sweep	Run Series	Exp. Fig.	CFD Fig.
	1.7	2.41	32.39	60.11	*X*	4200_4225-4199	7.72	9.41
70° Flat Plate, blade strut	1.7	-0.03	53.59	0.19	*X*	1360_1398-1359	7.75	9.42
	1.7	-0.05	53.70	0.23	*Z*	1441_1465-1466	7.76	
	1.7	-0.03	53.60	0.20	*X*	1468_1506-1467	7.77	
	1.6	-0.02	54.12	0.20	*Z*	1321_1343-1320	7.79	9.43

1.16.1. 1044 Model

LM's Phase II design, the 1044 model, was tested with and without nacelles mounted on the blade strut to study the individual nacelle effects on the sonic boom pressure signatures. Data for each nacelle arrangement are presented in this section. There are several repeat runs presented for this model at multiple altitudes to evaluate the repeatability of the data using the more expedient testing techniques than used in Phase I.

1.16.1.1. 1044 with All Nacelles, Repeatability and Lateral Model Translation Effects for h=32'' data

The experimental data for the Phase II 1044 tri-nacelle model are shown in Figures 7.38 to 7.40. As expected, the relaxation of some control of the test conditions combined with shorter duration and less pneumatic dampening with the shortened pressure lines results in slightly greater variation of the individual pressure signatures of each run series. Compare the upstream ambient pressure variation in the waterfall and overlaid aligned/average signature plots of these figures with those from the Phase I experiment (Figs 7.5-7.13) and note the scale differences when comparing the signatures. The increase in the individual (temporal) data run variation was expected to have a very small effect on the averaged signatures from the evaluation of the shorter duration run data from the Phase I test (refer to Figures 6.8 and 6.9), but also note that the tunnel humidity and total pressure were more controlled in the Phase I test. The benefit of acquiring 10 times more data during this test entry was the motivation for relaxing tunnel-operating constraints and, as will be seen, did not significantly reduce the data quality.

The experimental data shown in Figure 7.38 was obtained with the model translated across the wind tunnel, changing the altitude of the model during translation rather than the axial position. These are referred to as *Z*-sweeps, and Table 6 indicates the sweep direction as *X* or *Z* for each run series. The data from Figure 7.38 is at the lowest altitude data taken during the test. Several other run series were obtained with *Z*-sweeps during the Phase II test, and the averaged data throughout the entire Phase II test showed very little difference whether longitudinal (*X*) or lateral (*Z*) sweeps were used. Note that there was no scaling of the individual pressure signatures to account for the altitude differences in the averaged data presented in this report. Figures 7.39 and 7.40 are nearly repeat runs in average altitude, angle of attack and roll angles, both run series were obtained with *X*-sweeps, but the data from Figure 7.39 was obtained with half the model translation distance per run. The averaged data from the two series are overlaid in Figure 7.41. The repeatability is strikingly good; most all of the small pressure oscillations are nearly identical. This indicates that there is little benefit to averaging twice the number of spatial runs (51) compared with sampling half the number of runs (26). It also provides some confidence in our ability to obtain high quality data with the relaxation of the aforementioned wind tunnel controls that were used during the Phase I test.

1.16.1.2. 1044 with All Nacelles, Effect of Off-Track Angle at h = 32”

The effect of off-track angle is shown in Figures 7.42 to 7.47, experimental data every 10° in roll or off-track angle to 60°, is provided at an altitude of approximately 32 inches. There are significant differences in the pressure signatures with fairly small differences in roll angle. The on- and off-track averaged signatures are plotted as stacked and overlaid in Figure 7.48. The 1044 model maintains low overpressures off-track up to 20° (the goal prescribed in the NRA), and the cut-off angle is probably nearly 50°. The aft pressure signatures at off-track angles greater than 40° show the emergence of two fairly strong shocks.

1.16.1.3. 1044, Effect of Off-Track Angle at h = 54”

On- and off-track data at an altitude of 54 inches (2.84 body lengths) are presented in Figures 7.49 to 7.52. In order to obtain these signatures the RF1 pressure rail was moved to the aft window blank in the tunnel. This is evident in layout diagrams. At this altitude, the model shocks have reduced in strength by approximately 30 percent compared to the overpressures at 32 inches. The wind tunnel “noise” begins to dominate the pressures—the waterfall plots show several wind tunnel shocks of greater magnitude than the model pressures within the run series. The shocks coming from the wind tunnel align at an angle whereas model shocks align vertically in the experimental waterfall plots. Four dashed lines are drawn across the waterfall plot in Figure 7.50 to identify the aforementioned misaligned pressure waves that are either attributed to ambient shock waves inherent in the wind tunnel or model signatures within the reference run. The waterfall plots of Figure 7.51 and 7.52 shows the same ambient waves even though the model is at a different roll angle. The two lines to the left are thought to be ambient shock waves in the tunnel, whereas the two lines to the right of the plot are from the reference run containing the model signature that is absent in the data runs. The layout diagrams show that the reference run has the model positioned such that wind tunnel model signature is contained within the reference run signature, and so when differencing the negative of the model signature will emerge in the aft averaged signature. Also note that in all four of these data runs, the layout diagrams indicate that the ending data run model position is too far forward in the tunnel, with the bow and forward portion of the model pressure signatures striking upstream of the pressure measuring orifices on the rail. The waterfall plots show that the bow shock has only about two-thirds of the data runs contributing to the averaged pressure signature. The overlaid pressure signatures of the data runs show considerably more scatter (in both signature and σ variation) here than at 32 inches; compare Figures 7.49 to 7.52 with 7.42 to 7.47. The on- and off-track averaged experimental data are compared with a stacked curve plot in Figure 7.53(a), and overlaid in Figure 7.53(b). The averaged data look washed-out but are similar in shape to data at 32 inches—there appears to be no coalescence of shocks but rather attenuation or weakening of the small pressure oscillations compared with the data at 32 inches. The rounding of the bow shock at this altitude may be partially due to the lack of forward pressure data in the averaged signature.

1.16.1.4. 1044, Repeatability at h = 70”, On-Track

The experimental data were obtained at 70.7 inches (h/L=3.71) from the model in Figures 7.54 to 7.56. The RF1 pressure rail remained attached to the aft window blank in the tunnel, placing the data runs signatures further aft on the rail than at 54 inches, and now with full coverage of the model pressure signatures. The three run series shown in the figures can be considered repeat runs. Refer to Table 7, where the tan colored cells show only slight variation in angle of attack and azimuthal angle. The first two run series were taken an hour and 10 minutes apart from each other, and the third run series was obtained 6 hours later, making them short term repeat runs. The standard deviation curves show increased scatter in the runs, and become divergent from the averaged signature near the model’s tail shock. This indicates that the pressure signatures are corrupted by the reference run. The layout diagrams confirm this for these three run series, as they show only a small distance between the models beginning run tail shock and the

bow shock of the reference run. In reality, the reference run's bow shock was located on the instrumented portion of the rail and has encroached on the trailing signatures of the data runs. The averaged pressure signatures of the three repeat runs are overlaid in Figure 7.57. The aft signature is questionable for the reasons just described. The figure shows that the earliest-taken data set (black curve) has non-zero leading points and is shifted vertically above the other two run series in forward and aft pressures, although the signature lies between the other two run series just aft of the maximum overpressure. The run series taken later (blue curve) was obtained at lower humidity levels and with less variation in both humidity and total pressure values compared with the reference run (examine and compare the data quantities presented in the figure titles). The tunnel humidity levels often drop after the tunnel has had time to dry out and this typically results in higher quality data. Note that the humidity levels were 280, 256, and 215 ppm for the three runs in order that the data was taken. The slightly stronger shocks are due, or due in part to the lower humidity levels.

1.16.1.5. 1044, Effect of Off-Track Angle at h = 70"

The experimental data at approximately 20°, 40°, and 60° off-track angle at an altitude of 70.7 inches (*h/L* of 3.71) are presented in Figures 7.58 to 7.60. The layout diagrams show slightly greater distance between the models beginning run tail shock and the bow shock of the reference run; hence a greater portion of the aft signature is realized. The off-track averaged data run series are compared with the on-track run series with the lowest humidity in Figure 7.61. The signatures differ significantly in the aft portion with the largest minimum pressure occurring on-track, but the two aft signature shocks for the 60° off-track run series would be expected to produce a louder boom. Recall that the on-track signature is likely erroneous near *X*=-20 in the figure.

1.16.1.6. 1044 without Under-Wing Nacelles

The under-wing nacelles were removed from the 1044 model for the run series shown in Figures 7.62 to 7.65, and 7.68, but the centerline nacelle remained attached to the upper aft deck of the fuselage. Refer to Figure 4.3 for detailed images of the 1044 wind tunnel model. Figures 7.62 to 7.65 provide the experimental on- and off-track signatures at 32.6 inches. The aft pressure signatures are quite different without the under-wing nacelles. Without the nacelles, two aft shocks emerge for off-track angles of 40° and 60°. These shock occurs near the adjusted *X* positions of -90, and -86 in the aligned overlaid run plots. The extreme off-track angle of 60°, shows the greatest strength of these two aft shocks (Figure 7.65). The full range of on- and off-track averaged near-field signatures without the under-wing nacelles are compared in Figure 7.66. The signatures are then compared with the 1044 model with all nacelles in Figure 7.67. Here the dependence on the lower nacelles to achieve the low sonic boom pressures is observed—to clarify the results, only 0°, 20°, and 40° data are presented.

One run series is presented at an altitude of 70.7 inches (Figure 7.68). To improve the data quality, 76 runs were taken using the full 24-inch length of the linear actuator ram, but the standard deviation from the average is still large because of the large altitude and weak pressure signatures of the model. The aft portion of the signature appears to be corrupted before the trailing shocks are able to return to ambient flow conditions by the model position of the reference run. The layout diagram illustrates that the reference run is positioned both at angle of attack and as close to the wall of the tunnel as possible to avoid its bow shock from encroaching on the data runs trailing shock, but the rapid increase in the standard deviation plot shows that the aft portion of the signature becomes inaccurate before it can return to ambient flow.

1.16.1.7. 1044 without Center Nacelle

The center nacelle that mounts to the crown of the fuselage behind the blade strut was removed from wind tunnel model in the pressure signatures presented in Figures 7.69 to 7.72. The pressure signatures

are taken at the same altitude, h=32 inches, as the data with all nacelles and without the under-wing nacelles. The on- and off-track averaged pressure signatures are overlaid in Figure 7.73. The on-track, 20°, and 40° off-track signatures of the model without the center nacelle are compared with the pressure signatures of the model with all nacelles in Figure 7.74. There is almost no difference with and without the fuselage mounted center nacelle at any of the azimuthal angles. The leading and trailing shocks from the nacelle are shielded by the fuselage and extended aft deck of the 1044 model, and there is no indication in the off-track comparisons of the nacelle shocks. Typically component shielding does not completely extinguish pressure disturbances due to the three-dimensional effects of the flow.

1.16.2. 70° Flat Plate Model

The last new model tested in the Phase II test was the simple flat plate model. Refer to Figure 4.5 for model photographs and to Table 7 for tunnel conditions and model positions. On-track data at h=54 inches was obtained at Mach 1.7 for the first set of plots (Figures 7.75-7.77), and 1.6 for a later plot (Figure 7.79). Figures 7.75 to 7.77 show three repeat runs at Mach 1.7, where the first and third run series presented are axial sweeps, and the second series was obtained with a lateral sweep. The averaged pressure signatures of these three repeat runs are overlaid in Figure 7.78. The Z-sweep averaged run was shifted in X to align with the pressure signatures obtained with X-sweeps. The three signatures agree well, but better agreement is seen in the two axial model translations. The tail shock is slightly weaker for the run series with lateral model translation. But, the average altitude is 53.7 inches for the Z-sweep run and 53.6 for the X-swept runs —this may account for the slightly weaker tail shock of the Z-sweep run.

Experimental data for the Mach 1.6 run series are shown in Figure 7.79. Lateral (from side to side in wind tunnel) model translation was used to acquire this data. The standard deviation from the average is greater at this Mach number than at Mach 1.7, with particularly large variations seen in the strength of the trailing shock. Compare Figure 7.79 with 7.76. The reduced quality of this data series maybe to the large difference in humidity between the data and reference runs (15 ppm compared with 0.2 ppm difference for Figure 7.76).

1.16.3. 1044 Model Repeat Signatures Extrapolated to Ground Level

There are two sets of (on-track) repeat runs, at altitudes of 32- and 70-inches, for the 1044 phase II model; Figures 7.41 and 7.57 compare the pressure signatures at 32- and 70-inches, respectively. One difficultly with extrapolating experimental pressure signatures is determining an appropriate end to the signature because the aft signatures are often corrupted by the presence of the strut and require truncation just upstream of any shocks or pressure changes from its influence. Truncation of the signature adds uncertainty to the trailing shock of the extrapolated signatures and also to the loudness calculations. The experimental pressure signatures at h=32.6 inches were extrapolated to the ground level assuming a 144 foot aircraft and an altitude of 50,000 ft using *sBOOM* and are shown in Figure 7.80. The ground signatures are very similar, yet the overall loudness computations differ by 2.72 decibels, with loudness levels of 96.2 and 98.61. The experimental signatures extrapolated from the 70.8 inches are shown in Figure 7.81. The rogue pressure signature (black curve) may not be valid. Referring back to Figure 7.57, the comparison of repeat runs at h=70 inches, the corresponding run series (runs 1555-1631) were taken earlier in the test and the ambient leading pressures are shifted with positive values of 0.00048 rather than zero. Possible reasons for this are provided in §9.2.1.4. The near field signatures of the other two run series have good leading pressures, however. The experimental data acquired last (runs 2517-2593) shows no upstream ambient pressure oscillations. Thus, the more trusted extrapolation is from this last run series with unchanging leading zeros (blue curve of Figure 7.57). These data were obtained at a 0.3° larger angle of attack than the other run series and the difference between the blue and red curves appears due to the associated lift difference. The characteristic shape of the ground signatures from the two run series with near zero upstream ambient pressures look similar to the two extrapolated signatures taken at h=32.6

(compare Figures 7.80 and 7.81). However, there are differences in the aft pressure signatures, which could also be attributed to the inaccurate data at h=70 because of the close spatial proximity of the reference runs (see Figures 7.54 - 7.56, to see where the standard deviation range becomes disproportionately large). It is difficult to establish which extrapolated data series more accurately represents the models ground signature. The nearer field data (h=32) is more accurate, but there may be remaining three-dimensional effects from the model influencing the pressures at greater altitudes, and the data at 70.8 inches has more scatter that may be erroneously affecting the extrapolated signatures. The PLdB variation is 4.3 (between 94.72 and 99.03) for the signatures extrapolated from h=70.8 inches, and 2.72 (between 96.19 and 98.91) from the data taken from h=32.6 inches.

1.17. Phase II Test (Previously Tested Models)

This section provides the new data from the Phase II test on previously tested wind tunnel models. Table 8 provides the configuration, Mach number, roll angle, and altitude, and range of the run numbers and reference run used for each run series. Two of the Phase I test articles were retested during the Phase II test; the 1021 Phase I model and Seeb-ALR. Re-testing these configurations was motivated by a desire to evaluate long-term repeatability and to obtain data at greater altitudes. In addition, the vintage 69° Delta Wing-Body was retested to acquire data with a known sting, obtain off-track data up to 90° azimuthal angle, and to amass new data for a small range of lift coefficients and altitudes (see Table 8).

Table 8. Simplified run matrix of previously tested models for test T97-0254

Configuration	M	α	h	ϕ	Sweep	Runs	Exp. Fig. #	CFD Fig. #
1021with all nacelles, blade strut	1.6	2.18	24.56	0.12	*X*	3728_3776-3777	7.82	N/A
	1.6	1.97	31.77	0.25	*Z*	3698_3715-3727	7.83	N/A
	1.6	2.14	42.06	0.00	*X*	3801_3839-3840	7.85	9.45
	1.6	1.84	48.65	1.08	*Z*	272_304-271	7.86	9.46
	1.6	2.03	62.84	0.53	*Z*	247_270-271	7.87	9.47
	1.6	2.12	69.63	0.37	*X*	160_200-204	7.88	N/A
Seeb-ALR	1.6	-0.06	56.01	0.41	*Z*	845_900-901	7.90	9.48
	1.6	-0.05	56.02	0.27	*Z*	948_1003-1004	7.91	
	1.6	-0.03	70.02	0.22	*X*	794_832-834	7.93	9.49
69° Delta-Wing-Body	1.7	0.24	24.86	0.16	*X*	5598_5637-5638	7.94	9.50a
	1.7	-0.20	24.75	29.97	*X*	5530_5549-5550	7.95	9.50b
	1.7	-0.18	24.75	60.06	*X*	5551_5570-5571	7.96	9.50c
	1.7	-0.18	24.69	89.87	*X*	5572_5591-5592	7.97	9.50d
	1.7	-0.06	31.64	0.59	*X*	5240_5274-5275	7.99	9.51a
	1.7	-0.17	31.74	29.94	*X*	5284_5301-5275	7.100	9.51b

Configuration	*M*	α	*h*	ϕ	Sweep	Runs	Exp. Fig. #	CFD Fig. #
	1.7	-0.23	31.56	59.74	*X*	5310_5327-5328	7.101	9.51c
	1.7	-0.20	31.61	89.97	*X*	5336_5353-5354	7.102	9.51d
	1.7	0.71	21.33	0.25	*X*	5641_5680-5638	7.104	9.52a
	1.7	2.37	25.21	0.33	*X*	5469_5488-5489	7.105	9.52b
	1.7	3.90	25.49	0.69	*X*	5448_5467-5468	7.106	9.52c
	1.7	1.75	32.10	0.38	*X*	5405_5424-5425	7.108	9.53a
	1.7	3.10	32.33	0.24	*X*	5426_5445-5446	7.109	9.53b

1.17.1. 1021 Model

1.17.1.1. 1021 with All Nacelles, Effect of Altitude

Sonic boom pressure data for the 1021 model in the Phase II test were obtained at six different altitudes between 24.56 and 69.63 inches. The experimental data plots for these run series are presented in Figures 7.82 to 7.83, and 7.85 to 7.87. The data at *h*=24 inches in Figure 7.82 appear of reasonable quality. Unfortunately, this altitude was not obtained in the Phase I test, but data at *h*=20.7 and 31.8 inches were obtained and presented back in Figures 7.15 to 7.19. Comparisons of the waterfall plots from the present run with the Phase I test again show that the quality of the individual runs acquired during the Phase I test with more stringent testing procedures substantially improved the data at each tunnel position. Figure 7.83 is at a repeat condition of two runs from the Phase I test shown in Figures 7.18 to 7.19, but the data for the run in the Phase II test were obtained using a *Z*-sweep rather than an *X*-sweep. Model translation direction has not been shown to affect the quality of the data in previous comparisons, but the angle of attack was slightly low, thus another run from the Phase II test is also overlaid in Figure 7.84. These run series show long-term repeatability, but the pitch angles differ enough to offset the signatures due the lift differences—the pressures rise with increasing angle of attack as expected. There is greater variability in the upstream ambient pressures for the Phase II test as anticipated, but the bow and forebody shocks are in very good agreement. It would have improved the repeatability of the data if the angle of attacks were equivalent.

The test data obtained at altitudes from 42.06 to 69.63 inches are shown in Figures 7.85 to 7.88. The signature in Figure 7.85 (*h*=42) appears to be of good quality. However, the signature in Figure 7.86 (*h*=48) was acquired using *Z*-sweeps and the forward portion of the model's pressure signature is truncated at most of the test altitudes. The layout diagram shows that the ending data run is mostly upstream of the instrumented portion of the rail. Some loss of accuracy of the ambient upstream pressures, bow shock, and forebody pressure signatures is therefore likely. It is difficult to get a wide range of altitudes using the existing rail length, even with the use of the two rail positions in the tunnel. Doubling the length of the rail and having it span both window blanks to (as designed, Ref. 3) would remedy this problem. Better coverage of the model is obtained at *h*=62.84 inches in Figure 7.87, but the reference run interferes with the aft signature—compare the layout diagram in Figure 7.87 with 7.86. The data in Figure 7.88 (*h*=69.63) shows an expected increase in scatter of the individual runs in both waterfall and overlaid data plots, whereby wind tunnel shocks predominate the pressures, yet a reasonable averaged signature emerges from the data. The effect of altitude can be seen in Figure 7.89(a) where the pressure signatures are plotted to same scale and are offset by 0.02. The rail was in the forward window blank position for the smaller three altitudes, and in the aft window blank position for the larger three altitudes. The offset plots

show that standard deviation has a tendency to increase with altitude, but not as dramatically as it appears to when the pressures signatures are scaled to fill the plot area at reduced signal strengths. This indicates that testing of smaller models at greater altitudes would probably not provide accurate sonic boom measurements, unless the shocks within the test section were somehow reduced, and the model vibration/tunnel flow quality were improved. The average pressure signatures are overlaid in Figure 7.89(b) so that the pressure differences with altitude variation can be easily compared.

1.17.2. Seeb-ALR Model

The Seeb-ALR calibration body-of-revolution model was tested at greater altitudes in the Phase II test (56 and 70 inches) with the RF1 rail in the aft position than in the Phase I test (21 and 31 inches) with the rail in the forward tunnel position. Two near repeat runs, at h=56 inches, and tested using lateral model translation (Z-sweeps) are shown in Figures 7.90 and 7.91. The two averaged run series are overlaid in Figure 7.92. There is very good repeatability even at this altitude and low overpressure levels. The data at an altitude of 70 inches are shown in Figure 7.93. The averaged pressure signature looks reasonable, although there are some small wave-like oscillations throughout the signature that may be a result of the shocks from the wind tunnel. Note that there are slightly greater tunnel Reynolds number and total pressure variations between the data and reference runs. The waterfall plot shows wind tunnel shocks that are of the same magnitude or larger than the vertically aligned model shocks in the waterfall plot. Averaging appears to have successfully removed the majority of the pressure oscillations, although the bow and tail shocks appear smeared, from the mirage of aforementioned difficulties in measuring weak pressure signatures at large distances, but smearing from the averaging of misaligned signatures is also likely. Some of the deviation from a truly flat-top pressure signature may also be from small manufacturing differences from the as-designed model. Such deviations would be seen in the lower altitude data, like the sag in overpressure behind the bow shock that is seen at smaller altitudes (Figures 7.1-7.4) as well.

1.17.3. 69° Delta-Wing-Body Model

As previously mentioned, the 69° Delta Wing-Body model from the early 1970s (Ref 34) was tested again during the Phase II test using a new, slightly oversized sting that was designed for a 12-inch model rather than a 6.9-inch model. Refer to Figures 4.6(a-d) to review the photographs that show the exposed strain gauges resulting from the small model's sting cavity being too short to cover the strain gauges on the new sting. The model was tested at Mach 1.7 during this test, rather than Mach 1.68, so direct comparisons can not be made to the results from Ref 34. The configuration was re-tested to obtain high quality experimental data for the First AIAA Sonic Boom Prediction Workshop, held in January 2014.

1.17.3.1. Effect of Off-Track Angle, Near Zero Alpha, h=25 inches

Experimental pressure signatures were obtained by rolling the model to 0°, 30°, 60°, and 90° azimuthal angles and using an inline, retracted-ram reference run. The experimental data are shown in Figures 7.94 to 7.97, and summarized in Figure 7.98 with offset axis or stacked data plots. The layout diagrams in Figures 7.94 to 7.97 show that the model was translated longitudinally in the tunnel and the reference run was obtained with the model positioned behind the data runs at or near the same height. This could be easily accomplished because of the small model size. Inline reference runs were thought to be superior to the reference runs with the models positioned at greater heights particularly when the model is near the sidewalls of the wind tunnel. Keeping the reference run as close to the same Z position in the tunnel would eliminate any possible signature differences due to strut location such as tunnel blockage differences, but this has not been proven to be an issue. The close proximity of the inline reference run to the data runs is observed in the layout diagrams. The reference run is just far enough away from the aft-most data run that the "tail" shock (the large aft shock from the wing trailing edge that recovers to ambient pressure) and a small portion of the sting pressures (just past the strain gauge pressure

oscillations) are free from corruption. The experimental data past an *X* of -93 are considered less accurate than the data ahead of this point in Figures 7.94 to 7.97. The sting strain gauges appear in all the experimental data as a series of small pressure oscillations because the flat regions cut into the sting and the gauges themselves were exposed to the free-stream.

Comparison of the off-track pressures (Figure 7.98) show interesting changes to the aft signatures, where an additional shock from the wing tip of the swept forward trailing edge of the wing emerges and gains strength with increased off-track angle. It would be expected that for this simple model the loudness levels off-track would be less than on-track because of smaller trailing edge shocks, but the 90° off-track data propagated to the ground is predicted to be 0.5 PLdB louder than on-track (Ref 27).

1.17.3.1. Effect of Off-Track Angle, Near Zero Alpha, h=32 inches

On- and off-track data to 90° at *h* near 31.6 inches is shown in Figures 7.99 to 7.102. The run series were reduced to 18 data runs from the original 26 data sets in each series because the reference run could not be retracted far enough behind the data runs to avoid corrupting the aft end of the signature. Reducing the quantity of data runs salvaged the experimental data at this altitude and it does not appear to affect the accuracy. The on-track run series still contains 35 runs, as data were taken at intermediate translation positions compared to the off-track runs. The data quality for all of the run series shown in Figures 7.99 to 7.102 is considered good up to *X*=-83 inches.

A summary plot of these data is shown in Figure 7.103. The characteristic shape of the on- and off-track signatures at *h*=32 inches look similar to those at the closer altitude of *h*=25 inches; compare with Figure 7.98. The data at *h*=32 inches does not shown any signs of shock coalescence, only reduced signature strength or attenuation differences and slightly decreased bow and wing shock slope differences, are seen.

1.17.3.2. Effect of Pitch Angle, h=21, and 25 inches

Refer to Table 7 for the set of runs at various lift coefficients and altitudes. The three orange cells in the table are sorted by altitude and angle of attack, and the experimental data is shown in Figures 7.104 to 7.106, and summarized in Figure 7.107. The data are plotted offset and overlaid in subparts (a) and (b) of the Figure. The expected increase in wing shock strength and the corresponding forward movement of the shock with increasing angle of attack is seen in overlaid signatures (Figure 7.107(b)). Little change in the bow shocks are seen due to the slender forebody of the model, whereas the strength of the tail shock appear mostly due to the altitude differences than increased lift. The pressure oscillation from the model base and sting gauge surface discontinuities differ for the three runs in this complicated region. The data at *h*=21.33 inches are not corrupted by the reference run for at least 7 inches downstream of the model tail shock. The similarity of the “return-to-ambient” pressures indicates that the other two signatures are not greatly affected by the reference run for several inches beyond the onset of the reference run corruption.

1.17.3.3. Effect of Pitch Angle, h=32 inches

Two moderate angles of attack are presented at an altitude of approximately 32 inches in Figure 7.108 and 7.109. The data are compared with offset signatures in Figure 7.110(a), and the averaged data is overlaid in Figure 7.110(b). The signatures are similar, yet differences in wing and tail shock strength are evident due to the change in lift, where the slight forward movements from the stronger wing shock results from the higher pitch angle.

1.18. Residual Comparisons of Averaged Signatures from Phase I and II Tests

The retesting of the 1021 model in the Phase II test provides an opportunity to evaluate the difference or residual of the individual pressure signatures that comprise averaged run data from the computed average pressure signature and compare Phase I and II results on a realistic low sonic boom model.

1.18.1.1. Waterfall Residual plots for the 1021 Model, h=31 inches, Phase I experiment

Two waterfall plots show the residual of each individual run for two repeat runs taken during the Phase I in parts a and b of Figure 7.111. The computed average pressure signature is provided at the top of the waterfall plots in black to provide a reference location of the pressure signatures of the other runs. The residuals of the pressure signatures are aligned as they were in the conventional experimental waterfall plots to show where the signatures of the individual runs vary compared to the average signature. These two runs were introduced in Table 6, which indicates that Figures 7.12 and 7.13 show the pressure signatures of the individual runs and the average. These figures should be compared with the residual values. If all the runs were identical and perfectly aligned with the average signature, then the residual plot for each of the runs would be zero, and a flat line would be shown. A negative pressure indicates that the individual run pressure signature was smaller than average. The plots are also plotted down the page with each subsequent run below the former. It is immediately apparent that the residual from the averaged signature increases in the region of the models pressure signature compared to the ambient upstream flow. These plots reveal that the magnitude of the residual plots is larger in regions of steeper pressure gradients. This indicates that the accuracy of the model shocks is the poorest measured value. Comparing Figure 7.12 with Figure 7.111(a), the individual pressure signatures appear to all be predicting about the same bow shock strength for the model, but the residual plots show many of the residuals with approximately the same magnitude of the averaged pressure signature at the location of the bow shock, but many of opposite sign. This is an indication that the alignment of the models shocks is poor. Residuals with approximately the same magnitude of the averaged pressure signature value identify signature misalignment and make it apparent that this is a source of shock rounding. Comparing the two run series in Figure 7.111 it is observed that most of the first half of the run series have negative values of residual at the bow shock location and the latter half have positive sign. The bow shock maybe increasing with model translation, but it more likely due to signature alignment since the bow shocks appear fairly uniform in the waterfall plots of pressure signature.

1.18.1.2. Waterfall Residual plots for the 1021 Model, h=25 & 32 inches, Phase II experiment

Two run series, at similar conditions as those taken during Phase I, were obtained during Phase II test for the LM 1021 model. The residual waterfall plots are plotted to the same scale as the Phase I data (Figure 7.111) using the same plotting method shown in Figure 7.112. The first two rows of Table 8 correspond to the residuals of the run series displayed in the figure, note that the first run series was taken at an h of 24.56 inches and the second at h of 31.77 inches. Figure 7112(a) shows the residual of a run series that consisted of 77 runs, but only every 4^{th} run is displayed in the plots so that the same scale with the same vertical displacement of the individual plots can be compared for both Phases of experiment. The second run series; part (b) of the figure was acquired with Z-sweeps. It remains apparent when comparing the residual data from the Phase I test (Figure 7.111) with that obtained during Phase II (Figure 7.112) that there is greater scatter in the residual signatures. This is expected due primarily due to the duration of the signature sampling time and to the other aforementioned test technique differences described in S 6.4. The regions within the upstream ambient flow are much more random than in the Phase I experiment.

1.18.1.3. Waterfall Residual plots for the 1044 Model, h=31 inches. Phase II experiment

The 1044 Phase II wind tunnel model residual waterfall plots provided in Figure 7.113 comprise three run series; the first two were acquired with *Z*-sweep model translations and the third with the conventional *X*-sweep translations. Unfortunately, the first run series is at a different altitude than the other two runs, it was taken with the model 26 inches (on average) from the rail, whereas the later two runs were both nominally 32-inches from the rail. The three plots are to the scale and the individual run are separated with identical vertical spacing so that difference is the errors could be compared. There does not seem to be any greater error in the Z-sweep or X-sweep runs. The bow shock misalignment shows that mid-way through the run is where the best alignment is occurring; evidence for this is a sign change in the errors of the bow shock. For example, in Figure 7.113 (a), there are mostly positive errors at the bow shock for the initial runs moving down the waterfall plot, followed by mostly negative errors towards the bottom of the water fall chart. In part (b) there are mostly negative errors followed by positive errors towards the end of the run series in the curves toward the bottom of the figure, and in part (c) we again see mostly positive errors at the bow shock for the initial runs moving down the waterfall plot, followed by mostly negative errors towards the bottom of the water fall chart.

1.18.1.4. Waterfall Residual plots for the 1044 Model, h=70 inches. Phase II experiment

Three run series taken with the 1044 configuration 70 inches from the pressure rail are shown in Figure 7.114, parts (a) through (c). The errors of the individual run minus the average are greater than the computed average signature. 39 pressure signatures acquired using *X*-sweeps were actually used to compute the average for the run series shown in parts (a) and (b), and 75 runs for the signatures in part (c), but every other error plot was eliminated in parts (a) and (b), and two between each plot were eliminated in part (c) of the figure; to clarify and allow for consistent scaling of the plots throughout this section of the report. Compare part (a) of this figure with Figure 7.54 where all 39 signatures are shown and you can see that the close proximity of the reference run compromises the aft signatures before the signatures return to ambient pressure. The companion figure for Figure 7.114 part (b) is Figure 7.55, which shows very similar data as Figure 7.54, but the part (c) companion, Figure 7.56, shows the complete set of runs (75 total). Increasing the number runs for these signatures was done to help reduce the uncertainty, but the effects were not seen in the former standard deviation plots, by comparison of the averaged signatures, or here in the plots of the residual signatures.

These error plots re-affirms that the wind tunnel noise is likely too large to obtain meaningful pressure signatures for models with low overpressure at distances of 70 inches for ultra low sonic boom models of this scale for this particular wind tunnel with the rail in the aft position in the wind tunnel.

Computational Modeling

The sonic boom pressure signatures were computed for each of the wind tunnel test articles. This includes computational results for the 1021 Phase I model geometry with the sting and blade strut model supports, as well as with and without under wing nacelle and boundary layer diverters. The 1044 Phase II model was analyzed with the blade strut and all nacelles, without the center nacelle, and without the under-wing nacelle. Sonic boom pressure signatures can be obtained on configurations of any level of geometric complexity provided a refined volume grid of tetrahedra within a near body cylindrical boundary of surface triangles is supplied and a Mach cone aligned collar grid is constructed. The inner cylindrical meshes were developed using *TetRUSS* (*GridTool* and *V-Grid*) (Ref 42) or *Pointwise* (Ref 43) grid generation methods. Both methods allow for thin, anisotropic cells near the configuration surfaces to support viscous computations, which are necessary to obtain accurate sonic boom pressure signatures at the low wind tunnel Reynolds numbers (Refs 3, 23-24). The mesh density was increased within the sonic boom zone of influence below the model to azimuthal angles of approximately 90 degrees in order to

capture the sonic boom signature out to the cylindrical boundary. Figure 8.1 shows a cylindrical mesh surrounding the 1044 Phase II model developed using *Pointwise*. The increased mesh density on the cylinder surface in the expected zone of influence from the models pressure disturbance is evident in the figure. The Mach Cone Aligned Prism (MCAP) collar grid method (Refs 3, 23-24) was used to append geometrically similar prism cell meshes to the near-body cylindrical boundaries. The inner cylindrical boundaries are used as input to the MCAP software and projected in the radial direction to form a series of prism layers to the far field. The shearing angle of the appended prism mesh is adjusted for the angle of attack and Mach angle to allow for both on- and off-track aligned grids. The symmetry plane with the collar grid appended to the mesh is shown in Figure 8.2. This mesh is aligned for Mach 1.7 flow and 2.1° angle of attack. A smooth gradation of increased stretching from the cylinder boundary (radially) is also evident. The projected prism collar grid maintains the highly refined grid spacing in the axial direction of the inner cylindrical mesh to the far field. Simply increasing the distance of radial projection as successive prism layers are appended to the grid permits radial stretching of the cells and greatly reduces the number of grid points required, while also reducing the effects of numerical dissipation. The MCAP algorithm provides a mesh composed entirely of tetrahedral cells and an automated process to construct grids for accurate sonic boom computations.

1.19. Computational Tools

1.19.1. USM3D Methodology

USM3D (Refs 44-45) is a tetrahedral cell-centered, finite volume Euler and Navier-Stokes (N-S) method. It provides a variety of options for solving the flow equations and several turbulence models for closure of the N-S equations. For the current study, Roe's flux difference splitting scheme was used with a CFL number of 20. Flux limiters were used to preclude oscillations due to shocks and discontinuities by limiting the values of the spatial derivatives. For the present study, at the start of a new solution, the *USM3D* code was computed using the Spalart-Allmaras (SA) turbulence model (Ref 46) with first-order spatial accuracy for 10,000 iterations, and then run for an additional 20,000 iterations with second-order spatial accuracy. Obtaining a well converged, first-order accurate solution before switching to second-order significantly improves the chance of convergence with the code, but it is sometimes not necessary.

USM3D has been successfully used to compute sonic boom pressure signatures at wind tunnel Reynolds numbers (Refs 3,23,24). The success is largely attributed to the use of a Mach MCAP mesh to align the grid cells with the Mach cone angle and stretch along Mach rays. Recall that in the wind tunnel tests, trip disks were attached to N+2 Phase I and II models. The disks were used to energize the boundary layer and reduce the likelihood of flow separation, but not necessarily trip the flow. These small disks were not modeled in any of the computations, and the effect on pressure signature was not evaluated experimentally; the trip disks remained affixed to the model for the entire wind tunnel test. Figure 8.3 shows an oil flow image with many more trip disks on the upper surface of the outboard wing. This was the original distribution of disks, but disks were removed in stages to allow sufficient gaps between the disks in the streamwise direction for more effective boundary layer treatment. Compare the final placement of disks on the outboard wing in Figure 4.1(c). Figure 8.3 also shows trip disks affixed to the blade mount and the center of the wing, upstream of shock impingement from the nacelle. There was also a row of disks on the upper fuselage that are not shown in the photo. The sonic boom pressure data should not be affected by the upper-surface-only mounting of disks. The flow on the wing is not expected to be fully turbulent but in some transient state between laminar and turbulent flow. Thus, in addition to the turbulent simulations, some selected laminar flow computations are presented.

1.19.2. CART3D Methodology

CART3D (Refs 13-16) in conjunction with the Adjoint Error Optimization (AERO) module was used to provide simulations of the Phase I N+2 wind tunnel and flight models. The AERO module extends the capabilities of *CART3D* to include adjoint-based error estimation and automatic mesh refinement. *CART3D* offers high quality Euler sonic boom computations with optimal grids that provide the off-body signatures with reduced numerical errors. The embedded-boundary Cartesian mesh allows for analyses of complex configurations with autonomous mesh generation. The computational mesh typically consists of regular hexahedra everywhere, except for body-intersecting cells, or cut-cells at the surface boundaries.

Mesh adaptation is driven by numerical errors along a pre-specified line within the flowfield domain. The integrated square of the pressures (*dP/P*) along the line is commonly used as the functional for a sonic boom computation. Thus, the length and placement of the line will drive the mesh refinement to minimize the errors in the solution to along the "line sensor". Domain rotation to align the on-track shocks with the Cartesian mesh is necessary to obtain accurate sonic boom pressure signatures without incurring an excessively large computational mesh. A computational symmetry plane mesh colored by pressure coefficient is shown in Figure 8.4 for the Phase I N+2 wind tunnel model. Two on-track line sensors placed at different altitudes (*h/L* of 1.0 and 1.5) are displayed in the figure. The flow solver uses a cell-centered, second-order accurate finite volume method, and the van Leer flux-vector splitting method was employed with the Barth-Jesperson limiter. A five-stage Runge-Kutta scheme and multi-grid were used for convergence to a steady state.

1.19.3. FUN3D Methodology

FUN3D employs a node-based finite volume discretization with a variety of upwind flux functions and turbulence models. For the computations presented here, the Roe flux without eigenvalue limiting and a frozen van Albada limiter was used. *FUN3D* was also used in addition to *CART3D* to compute selected sonic boom pressures on the Phase I N+2 wind tunnel model and flight models. *FUN3D* has available adjoint-based error estimation and automatic mesh refinement capabilities. The *FUN3D*-Adjoint method is an output-adaptive cut-cell method utilizing tetrahedral background grids. The adaptive process, the flow solver, and parallel grid mechanics of the methods are summarized (Refs 47, 48). Exact discrete adjoint solutions are computed on a sonic boom sensor cost function of the square of the pressures (*dP/P*) on a cylindrical surface located at the altitude of the experimental data or location of interest. Inviscid and viscous flow solutions were run using the same MCAP meshes used for *USM3D* computations, without adaptation. Small differences with Mach cone-aligned meshes and solution adaptive approach have been seen, and *FUN3D* can be run with a Mach cone aligned starting mesh before adaption is applied (Ref 12).

1.19.4. CFD++ Methodology

CFD++ is a widely used commercial flow solver that was developed by Metacomp Technologies (Ref 49) and available through the U.S. Army Research Laboratory. It is a sophisticated software product with actively growing and evolving capabilities and features that can treat a variety of CFD problems. It employs a cell-centered finite volume framework that allows for up to 4^{th} order accuracy in time when run in implicit mode, and supports structured, unstructured and overset grids. It allows for mixed element meshes such as hexahedral, triangular prism, pyramid and tetrahedral cells.

LM provided all of the *CFD++* computations and used Euler or RANS (Reynolds-averaged Navier Stokes) solver with the two-equation k-epsilon turbulence model. *CFD++* has a wide range of turbulence model choices and several varieties of the k-epsilon model. LM developed Mach cone aligned meshes with both tetrahedral and hexahedral elements. Use of the hexahedral elements in the near to mid-field allows for less dissipative sonic boom pressure signatures and reduces the computational costs. LM uses

an elliptical shaped near body mesh; elongated to accommodate the wings and shortened to begin aligning cells close to the vehicle surface beneath the model. Images of the grid boundaries in front and a 40° off-track angles for a solutions of a Phase II intermediate design are shown in Figure 8.5. The cells are aligned to the front and aft boundaries that are aligned with the Mach cone angle.

1.19.5. OVERFLOW Methodology

OVERFLOW 2.2 (Refs 50-51), developed by NASA, solves the Reynolds-averaged Navier-Stokes equations. Various turbulence models and convective flux differencing options are available in the code. For the analyses presented here, second order central differencing along with the Spalart-Allmaras turbulence model were used. In order to converge the discrete equations to a steady state, the diagonalized Beam-Warming approximate factorization scheme was used. Each run required between 5,000 and 30,000 time steps to reduce the residual several orders of magnitude depending on model and altitude of interest. Other convective flux discretization options such as Roe and HLLC (Harten Lax Van Leer Contact) upwind methods were also examined with minimal differences in the solutions. Run times were approximately 2 hours using 128 processors (for 5,000 time steps) on the NASA Pleiades super computer for grids with approximately 30 million points.

Overlapping or overset structured meshes are used with the *OVERFLOW* 2.2 solver. The meshes were generated using Chimera grid tools version 2.1 (Ref 52). Free-stream dependent shock-aligned off body grids were used to preserve the shock and expansion waves to the solution extraction lines. This is a more economical approach compared to the automated adaptive mesh refinement methods in *OVERFLOW*. The overset mesh used for the LM 1021 model analysis, in front and symmetry plane views, is shown in Figure 8.6. Here, dense near-body meshes within a cylinder and a cone-shaped outer off-body grid that is rotated to align the cells with the Mach cone angle are used. This offers free-stream on- and off-track alignment. An advantage of this method is that a structured outer Mach cone grid can be rotated to adjust for angle of attack for an exact Mach cone alignment. This Mach-aligned mesh is developed in two dimensions and spun about the axis of the pitch angle. Grid generation of the aligned mesh is robust with no known size limitation of the outer boundary radius. Sonic boom design and analysis have been achieved using *OVERFLOW* with overset-structured meshes (Ref 39).

1.20. Predicted Strut Effects on Force and Moment Data

The experiment used the corrections provided by LM to obtain forces and moments corrected for the blade strut. These corrections were provided in Table 5. The Phase I and II models with and without the blade strut and balance adaptor components were evaluated with *USM3D* using a viscous mesh and the Spalart-Allmaras turbulence model. The surface mesh of the model with the strut and adaptor was split at the balance center and force and moment coefficients upstream of the balance center were computed. Forces and moments over the entire model were obtained for the model without strut and adaptor components.

1.20.1. 1021 N+2 Phase I computational results

The 1021 model force and moment coefficients of the geometry upstream of the balance center are provided in Tables 9 and 10. The strut reduces the lift by 6.4% and increases the drag by 70.7% at the design angle of attack. Computed pressure coefficient contours with and without the blade strut and balance adaptor are shown in Figure 8.7 for side and top views of the models. The adaptor is truncated at the balance center and the integrated force and moment coefficient data are computed up to this location. The computations include the aft adaptor as a separate surface component that is not shown in the figure. Note the annular gap between the blade strut and balance adaptor, which is modeled as it is on the wind

tunnel hardware (Refer to Figure 1.2). This gap contributes significantly to the measured drag since the balance is located behind the gap.

Table 9. Model 1021 Computed Forces and Moments: M=1.6, α=2.3°

Model	*Ref Location*	*CL*	*CD*	*CM*	*CA*	*CY*	*CN*
1021 strut & adaptor	MRC	0.1361	0.04553	-0.02211	0.04003	-0.0347	0.13784
1021	MRC	0.1454	0.02667	-0.00857	0.02081	0.01888	0.14636
1021 strut & adaptor	BRC	0.1361	0.04553	0.48264	0.04003	-0.0347	0.13784
1021	BRC	0.1454	0.02667	0.51423	0.02081	0.01888	0.14636

Table 10. Model 1021 Computed Forces and Moments: M=1.6, α=2.5°

Model	*Ref Location*	*CL*	*CD*	*CM*	*CA*	*CY*	*CN*
1021 strut & adaptor	MRC	0.1357	0.04619	-0.00013	0.03979	-0.0334	0.14757
1021	MRC	0.15487	0.02739	-0.00962	0.02060	0.02067	0.15592
1021 strut & adaptor	BRC	0.1357	0.04619	0.51603	0.03979	-0.0334	0.14757
1021	BRC	0.15487	0.02739	0.54821	0.02060	0.02067	0.15592

1.20.2. 1044 N+2 Phase II computational results

The *USM3D* force and moment coefficients of the1044 model with and without the blade strut and balance adaptor components are provided in Tables 11 and 12 at the design Mach number and angle of attack, and 0.2° greater pitch angle. The strut reduces the lift coefficient by 14.3% and increases the drag 95.3% at the design angle of attack. The strut and adaptor have a greater affect on this model than the 1021 model possibly because of the increased surface area associated with the expanded aft deck on this model. Computed pressure coefficient contours with and without the blade strut and balance adaptor are shown in Figure 8.8. The side and top views of the models are provided in the figure. The adaptor is truncated at the balance center and the integrated force and moment coefficient are computed to this location.

Table 11. Model 1044 Computed Forces and Moments: M=1.7, α=2.1°

Model	*Ref Location*	*CL*	*CD*	*CM*	*CA*	*CY*	*CN*
1044 strut & adaptor	MRC	0.1117	0.05142	-0.0185	0.04728	-0.0518	0.11352
1044	MRC	0.1304	0.02618	-0.0231	0.02138	-0.0146	0.13130
1044 strut & adaptor	BRC	0.1117	0.05142	0.3901	0.04728	-0.0518	0.11352
1044	BRC	0.1304	0.02618	0.4765	0.02138	-0.0146	0.13130

Table 12. Model 1044 Computed Forces and Moments: M=1.7, α=2.3°

Model	*Ref Location*	*CL*	*CD*	*CM*	*CA*	*CY*	*CN*
1044 strut & adaptor	MRC	0.1227	0.05201	-0.0223	0.04704	-0.0510	0.12472
1044	MRC	0.1407	0.02688	-0.0247	0.02121	-0.0159	0.14171
1044 strut & adaptor	BRC	0.1227	0.05201	0.44563	0.04704	-0.0510	0.12472
1044	BRC	0.1407	0.02688	0.51594	0.02121	-0.0159	0.14171

Computational/Experimental Pressure Signature Comparisons

1.21. Phase I Test

The pressure signatures of the four models tested during Phase I wind tunnel testing: Seeb-ALR, 1021, AS-2, and Opt Sig models are compared with CFD solutions in this section. *USM3D* solutions of all of the models are provided, but additionally, *OVERFLOW* solutions are provided for the Seeb-ALR, and 1021 models, and both *FUN3D* and *CART3D* are compared on the various geometry arrangements (sting type and nacelle geometry) of the LM 1021 model. Refer to Table 6 for the basic flow conditions, model position, and figure indices.

1.21.1. Seeb-ALR Model

The LM Seeb-ALR axisymmetric calibration model theoretically should produce a flat top pressure signature with an 8-inch region of non-varying pressures. *USM3D* viscous computations were performed at a Mach number of 1.6 and a Reynolds number of 6.42×10^6 based on the model reference length (17.68 in.) with turbulent flow using the Spalart-Allmaras turbulence model, and run with laminar flow. The Reynolds number used in the computation matched the wind tunnel freestream unit Reynolds number of 4.36×10^6 per foot. *OVERFLOW* computations using the SA turbulence model were also performed at the experimental Reynolds number. Figure 9.1(a) compares two repeat experimental runs, one taken at the start of the wind tunnel test and the second mid-way through the test, with the *USM3D* and *OVERFLOW* computations at h=21 inches. There is good agreement between the computations and experiment, and very good repeatability in the wind tunnel test results. There are very small differences in the strength of the bow shock and some differences in the expansion region of the pressures. Some portion of these differences in the computational results could be due to geometry modeling differences —the *USM3D* surface grid was derived from the "as-designed", where as the *OVERFLOW* grid used an updated surface definition more closely representing the "as-built" model (Refs 25-26). A small nearly flat pressure region just aft of the expansion shows a slight mismatch in pressure level between the experimental and computational results. The laminar flow computation with *USM3D* was performed since it is sometimes found that laminar solutions improve the comparisons with experiment. In this case, the laminar boundary layer model improves the comparison with experiment in the forward flat pressure region, but results in poorer agreement in the expansion region of the aft signature.

An experimental pressure signature at a greater distance (h=31 inches) from the model is compared with *USM3D* and *OVERFLOW* turbulent flow solutions, and a *USM3D* laminar flow computation, with similar results (Figure 9.1(b)). The differences in the expansion are still under investigation.

1.21.2. 1021 Model

The 1021 tri-jet model was evaluated with CFD in all of the experimental arrangements including the modeling of model strut support type and with and without the lower wing mounted nacelle. There were

only two distances from the rail (approximately 21- and 31-inches) where data was obtained and CFD predictions made for this model.

1.21.2.1. On-track, all nacelles with blade strut mount, lower α: USM3D analyses

Computations of the complete 1021 configuration with all nacelles, attached to the blade strut are compared with experiment at an *h/L* of 0.93. *USM3D* viscous computations were performed at a Mach number of 1.6 and a Reynolds number of 8.1×10^6 based on the model reference length (22.4 inches) with laminar and turbulent flow (using the Spalart-Allmaras turbulence model) solutions. The Reynolds number used in the computations match the wind tunnel freestream unit Reynolds number of 4.36×10^6 per foot. In Figure 9.2, three repeat experimental runs are shown in addition to CFD simulations at angles of attack that surround the pitch range of the experimental data. The three repeat experimental runs show excellent repeatability. The computational comparisons with experimental data are very good with most small pressure oscillations predicted by *USM3D* matching the experimental data. The additional computation at α=2.3°, slightly greater than the experimental data, improves the correlation with experiment. The laminar flow computation at alpha 2.1° shows only slight differences in the sonic boom pressure signatures from the turbulent flow solution. Recall that the experimental model had small "trip" disks and that the boundary layer flow on the wing is not fully turbulent but in some state between laminar and turbulent.

1.21.2.2. On-track, all nacelles with blade strut mount: USM3D, CART3D FUN3D, and OVERFLOW analyses

Figure 9.3 and 9.4 are on-track computations closer to the design angle of attack at 21- and 31-inch altitudes, respectively. *USM3D*, *CART3D*, *FUN3D* and *OVERFLOW* are compared with experiment in the figures. The comparisons are stacked vertically for comparisons in parts (a) of figures. Part (b) of these figures overlay all of the computational results for a direct comparison of the methods. Two *USM3D* cases are shown to provide the incremental changes due to small lift differences in both figures. The *CART3D* solutions are high quality inviscid computations, but poorer agreement with experiment is observed because of differences in the development and strength of shocks in the vicinity of the nacelle and diverter on the underside of the wing. The boundary layer is as thick as the diverter height at the low wind tunnel Reynolds number and so diverter shocks are present in the inviscid computation (Ref 53) and absent in experiment and viscous computations. The mismatch in pressure signatures was expected from past experiences with a Gulfstream-designed low boom model (Refs 54-55), where inviscid computations agreed poorly with the low Reynolds number experimental data, but the viscous flow results agreed well (Refs 23-24). The *USM3D*, *FUN3D* and *OVERFLOW* computed pressure signatures are very similar. *FUN3D* was run using the same Mach cone aligned mesh that was developed for *USM3D* computations, and the *OVERFLOW* solution used a specialized overset mesh with Mach cone alignment. With the exception of a small shock aft of the main expansion slightly under predicted by *FUN3D*, the *USM3D*, *FUN3D*, and *OVERFLOW* results appear equivalent at 20.7 inches, but at an *h/L* of 1.4 or the 31-inch altitude (Figure 9.4), the *OVERFLOW* pressure signature does not correlate as well with experiment toward the aft portion of the pressure signature. The reason for this is unknown, but these results look anomalous since other results with this code are good.

1.21.2.3. Off-track, all nacelles with blade strut mount: USM3D, CART3D, FUN3D, and OVERFLOW analyses

Computations at approximately 20- and 48-degrees off-track are compared with experiment for the complete 1021 N+2 configuration with blade strut in Figures 9.5 and 9.6. The pressure signatures change shape rapidly from on-track to off-track with this configuration. The emergence (ϕ=20°) and growth (ϕ=48°) of the main expansion region is evident by comparison of the on-track and off-track pressure

signatures (compare Figures 9.4 to 9.6). This large expansion and ensuing shock result in larger than desired off-track sonic boom loudness levels because the 1021 model design focus was on under-track sonic boom reduction during Phase I of the program. However, the sonic boom loudness level of the 1021 model may meet the environmental goals of the N+2 Supersonic Transport from 0° to 20° since the aft shocks are approaching strengths similar to the on-track runs, and the off-track disturbances travel farther.

Accurate modeling of the aft portion of sonic boom pressure signature is difficult because the pressure field is very complex; multiple vehicle surfaces terminate and the interplay of these trailing shocks coming together as well as the boundary layer effects and flow through the nacelles all affect the pressure signatures. It should be reiterated that the Reynolds number affects the signature; evidence of choked flow between the wing and nacelle is observed in the viscous computations due to the thick boundary layer at experimental conditions. Hence, inviscid-flow computations on this model will differ from viscous computations; this is discussed in detail in Ref 53.

The *USM3D*, *FUN3D* and *OVERFLOW* computations at 20 degrees off-track are compared with experiment at ϕ=20.3 and 24.6°, whereas the *CART3D* solution was obtained at 24.6° in Figure 9.5. In part (a) of the figure each of the four flow codes are individually compared with experiment by offsetting the data. The *USM3D* computations are provided at two angles of attack that surround the experimental pitch angle. The signatures compare fairly well everywhere but the predicted tail shocks are weaker than experiment. The α=2.5° case matches the wing and nacelle shock strengths better, but the tail shock is even weaker with poorer correlation with experiment. It is unclear if the experimental discrepancy in nacelle shock strength is due to a stream angle difference or the azimuthal angle differences. The *CART3D* computation, since it was obtained at the larger off-track angle, results in a stronger tail shock ($-100 < X < 98$) than the other CFD computations. The inviscid solution has two shocks between X of -102 and -100, presumably due to the non-physical prominence of the leading edge of boundary layer diverter. The trailing edge of the diverter may be found near X of -98 inches. The *FUN3D* computation at α=2.3°, ϕ=20° differs from experiment in the same manner as the *USM3D* and *FUN3D* computations. The *OVERFLOW* computation is also very similar to the other viscous results, although it predicts a slightly stronger nacelle shock upstream of the main expansion that is in closer agreement with experiment at ϕ=20.3°.

The computational and experimental results at 48 degrees off-track angle, shown in Figure 9.6, compare well. The *USM3D* computations are at and above the experimental angles of attack, but there is no difference in the strength of the very large trailing shock at 48° off-track angle. The larger alpha case is, however, in better agreement with experiment upstream of the main expansion, and its curve cannot be seen since it is underneath the symbols in the plot. Note that the repeated test conditions show nearly no differences—providing further confidence in the averaged pressure signature obtained with rail-based sonic boom testing. The *CART3D* comparison compares fairly well with experiment at this large off-track angle because the influence from the boundary layer in the vicinity of the nacelle is not fully encountered at this large off-track angle. The *FUN3D* computation achieved greater flow solver convergence than the *USM3D* run, though both used the same mesh, and its signature is similar to *USM3D* where only small pressure differences within the main expansion of the signatures are observed —*USM3D* predicts a small pressure oscillation in this region that is absent in the *FUN3D* solution. *OVERFLOW* computed pressure signature is very similar to those predicted by *USM3D* and *FUN3D*, and its forward signature upstream of the main expansion matches experiment better than the other flow solutions.

1.21.2.4. 1021 without under-wing nacelles, with blade strut mount: USM3D

The under-wing nacelles were removed from the 1021 N+2 configuration and *USM3D* computations were performed with and without turbulence models. The comparisons with experimental data are shown in Figure 9.7. The laminar solutions appear to better match the shock aft of the main expansion, whereas

the Spalart-Allmaras simulations over predict this shock and under predict the expansion at *X*=-100 inches. Again there appears to be a slight offset in the aft wing overpressures between *USM3D* and experiment—the solution at the higher angle of attack agrees better with experiment than the lower. This is likely due to stream angle and lift coefficient differences.

1.21.2.5. 1021, conventional sting with nacelles, on- and off-track

USM3D computations of the 1021 model with the conventional sting model support are compared with experiment in Figures 9.8 to 9.11. The angle of attack range in the first figure is roughly from 2.5° to 2.9°, and the agreement is excellent at 2.9°. The expected difference in pressures due to the lower angle of attack of the computation (2.5°) than experiment (2.58°) are seen on the front side of the maximum overpressure of the signature, which corresponds to slight aft wing lift differences between computation and experiment. The pressure signatures with the sting strut differ from the model mounted on the blade strut; compare Figure 9.8 with Figure 9.3. The SA computations at 2.5° are compared directly in Figure 9.9, as expected, the trailing shocks are stronger with the conventional sting than the blade strut. The on-track pressure signatures of the model with the blade mount offer nearly an identical match to a theoretical flight model pressure signature, and this is shown in Ref 3.

Figure 9.10 shows on-track results at a larger altitude. Excellent agreement between the computational and experimental result is observed. This figure can be compared at similar conditions with the model mounted on the blade strut in Figure 9.4. Figure 9.11 shows an off-track comparison of the sting-mounted model at a roll angle of 46.2°. The large aft shock strength and position are in very good agreement, but there are some small differences in the expansion region that maybe due to boundary layer differences between the computation and experiment in the vicinity of the nacelle.

1.21.3. AS-2 Model

A *USM3D* computation of the AS-2 axisymmetric configuration is compared with experiment in Figure 9.12. The geometry modeled is the as-designed configuration rather than the as-built configuration. The as-built CAD model has a blunt nose tip when zoomed in on the sharp nose and represents the model before any hand finishing was performed during model fabrication. The “as-built” computation (not shown) has slightly larger bow shock strength than the as-designed model. (Ref 3 compares the “as-built” computation with experiment). The discrepancy between the computed bow shock and the measured shock is due to the surface definition not perfectly representing the true “as-built” surface definition, and because of some expected shock rounding of the experimental data. However, the computed forward pressure signature predicts the 2-inch flat pressure region of the design. The experimental results have only a limited number of data runs (6) so the data quality may be slightly compromised. This run series was taken with a lower Reynolds number than all the other data presented in this report in order to match data from a prior test with a different rail.

1.21.4. Opt Sig Model

A *USM3D* computation of the “as-built” Opt Sig axisymmetric configuration is compared with experiment in Figure 9.13. This axisymmetric body provides a very complex pressure signature that would be expected on a complete vehicle rather than a simple body of revolution. The surface definition of the “as-built” model was scanned after hand working the intricate configuration’s shape for a high quality representation of the surface geometry. This body-of-revolution was designed and constructed with extremely small shape changes (bumps) with small but rapid changes in curvature. The small changes in curvature can be more easily felt than seen on the 16.8-inch wind tunnel model. The surface definition used in the computation is a truer representation of the “as-built” configuration, as opposed to the AS-2 model where the final stage of finishing was not captured in the “as-built” surface definition used in the computation. The comparison between the computed and measured bow shock strength is

good. The series of small pressure oscillations both ahead and behind the main expansion are captured accurately with *USM3D*.

1.22. Phase II Test (Newly Constructed Models)

Computational results are compared with the previously shown experimental data for the Phase II wind tunnel test. Refer to Table 7 throughout this section to find the model configuration, flow conditions, run series, and figure number for the experimental and computational/experimental comparisons.

The angle of attack values of experiment to achieve a lift coefficient of approximately 0.12 varied considerably throughout the Phase II test. For the Phase I test, angle of attack was an acceptable metric to compare experimental results to because the model was translated over a limited space in the wind tunnel at only two altitudes. But during the Phase II test, comparisons with lift coefficient are required because the wind tunnel model was placed in many different positions in the tunnel and the angle of attack to achieve the same lift coefficient varied considerably due to slight flow variations in the test section. Refer to Table 7 to see the variation of the average angle of attack for the 1044 model with the blade strut support. The experimental variations of lift coefficient for these runs are mostly within 0.01. Angle of attack increases are seen with increased model roll angles to retain the model cruise lift coefficient. LM provided computations of the 1044 wind tunnel model and has computed a lift coefficient of 0.122 at 2.1° angle of attack. The *USM3D* computations with and without the blade strut provided in §8.2.2 show that the lift coefficient with the blade strut is 0.13, and without the strut 0.11. Both the *USM3D* and the *CFD++* computational results in the subsequent figures are labeled with the lift coefficients that were provided by LM. The reported experimental lift coefficient with non-ideal corrections is reported for comparison.

1.22.1. 1044 Model with All Nacelles on Blade Strut

The as-designed model with two under-wing nacelles and the fuselage/aft deck mounted nacelle were tested on-track close in at h=26.6 inches, and on- and off-track at h=32-, 54-, and 70-inches. *USM3D* turbulent flow computations with the SA turbulence model are compared with laminar flow solutions and *CFD++* with the k-ε turbulence model.

1.22.1.1. On-track, h=26.6 inches

Near-field computations at h=26.6 inches were obtained using *USM3D* with and without turbulence modeling. The turbulent flow computations were obtained with the Spalart-Allmaras model. These computations are compared with the experimental data in Figure 9.14. There is excellent agreement of the bow shock and fore body pressures, but differences in the strength and shock position are observed in the aft signatures from the effects of the different turbulence models. For the most part the aft experimental pressures falls between the two different flow solutions, indicating that the flow is not fully turbulent or laminar due to the wind tunnel model trip disks—refer to the photograph in Figure 4.3(d).

1.22.1.2. On- and off-track, h=32 inches

LM's laminar flow computations with *CFD++* are compared with NASA's *USM3D* results. Turbulent flow solutions with the SA and k-ε turbulence models are compared. Figures 9.15 to 9.21 show 0° to 60° -azimuthal-angle comparisons with experiment. The difference in the laminar and turbulent flow models is mostly seen in the aft pressures and although they differ it is not clear which provides better agreement with experiment. However, the laminar flow results often predict deeper expansions than the turbulent flow results. The model's aft pressure signatures change considerably with off-track angle and CFD computations are able to accurately capture most of these changes. The on-track pressure signatures

up to 40 degrees have many small shocks that change position rapidly with small variation in off-track angle. The pressure signatures at 50 and 60 degrees (Figures 9.20 and 9.21) have stronger shocks with coalesced pressures. Another observation is that stronger shock waves are predicted with *CFD++* than *USM3D*, and that both methods often over predict the experimental shock strength. Hence the *USM3D* pressures are often in closer agreement to the experimental results.

1.22.1.3. On- and off-track, h=54 inches, same grid computations

NASA converted the LM computational mesh used with *CFD++* that is composed of mixed element cells of hexahedra and tetrahedra into a mesh of all tetrahedral cells and obtained *USM3D* computations with the converted mesh. LM uses an elliptically shaped near-body mesh, that when viewed from the front is an ellipse with its minor axis aligned with the symmetry plane of the model so that Mach aligned cells can begin very close to the model (on-track). The symmetry plane of the LM mesh after conversion to tetrahedra is shown in Figure 9.22. Here the close proximity of the Mach aligned cells beneath the model can be seen in this LM mesh. In addition, the inner elliptical mesh is rotated, likely by the angle of attack. In contrast, the NASA mesh is circular in front view and the model is dropped below the center of a cylinder (see Figures 8.1 and 8.2) to allow the Mach-aligned cells to begin closer to the model. The cylinder approach is limited by the maximum radius of the vehicle and model strut support, and can not drop the vehicle to the bottom of the circular cylinder without growing the cylinder radius.

USM3D computational results at approximately 54 inches (*h/L* approximately 2.8) are compared with experiment on-track, and for off-track angle increments of 20 degrees in Figures 9.23 to 9.26. The LM tetrahedral mesh converted from mixed elements is labeled as "LM mesh" in the figures, whereas the *USM3D* with the conventional MCAP are labeled "*USM3D*". The advantage of hexahedral cells is greater computational efficiency and less numerical dissipation. This is likely the reason for the slightly crisper shocks seen in the *CFD++* computational results (Figures 9.15 to 9.21). Here, the all-tetrahedral-cell meshes provide very similar results regardless of elliptical or circular cylinder inner boundary meshes.

For example, negligible differences are observed with the *USM3D* computations using the NASA and LM meshes, on-track (Figure 9.23). The effect of the turbulence model is much greater than the effect of different computational grid. This indicates that it may be unnecessary to use an elliptical mesh if a sufficiently dense cylindrical nearly body mesh is used with MCAP cells. The laminar flow computations are in better agreement with experiment on-track.

At 20° off-track (Figure 9.24), there is greater difference in the signatures due to the different computational grids. The laminar results with the NASA MCAP mesh agree best with experiment. However, at 40° and 60° off-track angles (Figures 9.25 and 19.26), the signature differences due to grid is again negligible, with good correlation with experimental, and minimal differences between the laminar and turbulent flow solutions.

1.22.1.4. On- and off-track, h=70 inches

LM provided *CFD++* turbulent flow computations obtained with the two-equation k-ε model. NASA *USM3D* turbulent flow computations with the Spalart-Allmaras model are compared with laminar flow solutions and *CFD++* in Figures 9.27 to 9.30. The pressure signatures characteristic shapes and signature strength decay are well predicted by CFD, but as expected there is rounding of the experimental shocks due to the increased effects of model vibration as small changes in pitch result in greater variation of shock position on the pressure rail with greater distance, as well as very low signal to tunnel noise ratios.

1.22.2. 1044 Model without Under-Wing Nacelle on Blade Strut

The under-wing nacelle was removed from the 1044 model in the semi-span computational model. A shaded surface grid of the full span model is shown in Figure 9.31. The nacelle boundary layer diverters remain affixed to the lower surface for these computations, and the portion of the exposed diverter under the curved nacelle is concave in shape.

1.22.2.1. On- and Off-track, h = 32 inches

LM *CFD++* simulations with the k-ε turbulent flow model are again compared with *USM3D* turbulent (SA) and laminar flow solutions at h=32 inches for ϕ=0°, 20°, 40°, and 60° in Figures 9.32 to 9.35. The computational meshes used the same surface grids but with the different volume grid approaches as previously discussed. The large differences in the pressure signatures with and without the under-wing nacelle seen in the experimental data are accurately predicted with the computational methods. Good agreement with the experiment is seen on-track in Figure 9.32—all of the small shocks seen in the experimental results are present in the computational results. The comparisons are not as good at 20° off-track angle (Figure 9.33), with no clear advantage of turbulence model. Better agreement is seen at 40° (Figure 9.34), but there are two small pressure oscillations present in the computations that are absent or have coalesced with the other large shocks in the experimental result. Then at 60° off-track (Figure 9.35), the results are quite good with all shocks predicted and small differences in shock strengths.

1.22.2.2. On-track, h = 70.8 inches

A single comparison of experiment with *USM3D* computations at 3.72 body lengths (h=70.8 in.) is shown in Figure 9.36. The weak pressure signal is fairly well predicted, but the computations have slightly stronger aft pressures than experiment. The laminar flow solution shows weaker pressure oscillations in the main expansion region, then comparable trailing shock strengths to the turbulent flow solution.

1.22.3. 1044 Model without Center Nacelle on Blade Strut

The center nacelle, best shown in Figure 4.3(c) and (d), which mounts to the upper aft fuselage behind the blade strut, was removed during the experiment and from the computational surface grids. A shaded image of the surface grids without the centerline nacelle is shown in Figure 9.37.

1.22.3.1. On- and Off-track, h = 32 inches

The computational/experimental pressure signatures are compared at h=32 inches for ϕ=0°, 20°, 40°, and 60° in Figures 9.38 to 9.41. There are some discrepancies between the computational results on-track, though both the laminar and turbulent flow solutions predict the presence of small pressure oscillations in the main expansion region of the pressure signature, the location of these oscillation is predicted too far upstream for the turbulent flow computations and too far aft for the laminar flow results. At 20° and 40° off-track angles (Figures 9.39 to 9.40) there are a few small shocks found in the computational results that are not present in the experimental signatures. The comparisons are better at 60° (Figure 9.41). Aside from the typical shock strength differences between CFD and experiment, the correlation is quite good at this large off-track angle. Both experiment and CFD show a single small compression region within the expansion (near X=-91 inches). It is so small that it appears as a change in the slope of the expansion for the *USM3D* computations. Unfortunately it is difficult to trace the origin of small pressure changes without an adjoint solution, as done in Ref 55.

1.22.4. 70° Flat Plate Model with Blade Strut

The comparisons of the flat plate model are presented in Figures 9.42 and 9.43. *USM3D* computations were performed at Mach 1.7 (Figure 9.42) and Mach 1.6 (Figure 9.43). The expansion/tail shock is fairly accurately predicted at Mach 1.7 with only small differences in the laminar and turbulent flow computations, but at Mach 1.6 the comparisons are poorer. The experimental results (Figure 7.78) at Mach 1.6 show very random pressure signatures for the individual data runs and also a larger than desired change in humidity between reference and data runs (15 ppm). There is a very large difference in tail shock strength within one standard deviation of the averaged data, and the variance curves are added to the comparison plot in Figure 9.43 as black dashed lines—the CFD data is between these curves. Comparing this experimental run series to the data at Mach 1.7 (Figures 7.74 to 7.76), there is higher quality data with much less scatter in the data. Thus, the CFD predictions at Mach 1.6 are likely a better prediction of the pressures than the experimental data. The CFD solutions do not show the drop in pressures between X=-57 to -52 inches that is seen in the experimental results at both Mach 1.7 and 1.6. The cause of this is unknown. Oil flow images using 400 nm purple LED lamps from Innovative Scientific Solutions, Inc., show the surface flow patterns on the configuration upper and lower surfaces in Figure 9.44. The green colored oil is removed by turbulence and pressure from the surface by the strong bow shock from the blunt upper surface strut. The oil flow streaks show the extent of the disturbance from the strut and show well behaved flow on the lower surface. The differences in the forward pressure signatures between CFD and experiment are still not understood.

1.23. Phase II Test (Previously Tested Models)

This section covers the 1021 and Seeb-ALR models that were tested in Phase I and re-tested in the Phase II experiment at the similar and greater altitudes. We also retested the 69° delta Wing-Body configuration in Phase II and present CFD comparisons with the new experimental data. The original experimental data from 1973 is found in Ref 36, and computations from the 1990s can be found in Ref 37.

1.23.1. 1021 Model

Just the as-designed tri-nacelle 1021 configuration mounted on the blade strut was tested in Phase II. *USM3D* computations using the SA turbulence model and laminar flow solutions are compared with the experimental data.

1.23.1.1. Effect of altitude, h=42-, 49-, and 63-inches

USM3D Computations with and without turbulent flow are compared with experiment in Figures 9.45 to 9.47. Note the smaller altitude test cases are not compared with CFD as they were compared with experiment in §9.1.2, and the Phase II experimental results were compared with the Phase I experiment in §7.3.1. The 42.1-inch altitude, Figure 9.45, shows good correlation with experiment. The laminar solution is in better agreement aft of the maximum overpressure, but the maximum overpressure is over predicted by both computations. At 48.7 inches (Figure 9.46), the comparison is good. Fair correlation is seen at 62.8 inches in Figure 9.47. The experimental data appears to have changed its characteristic shape at this altitude. For example the multi-shock forward pressures that steadily grow in overpressure level are now seemingly showing some random variations. This may indicate the altitude limits of experimental testing for this low boom model.

1.23.2. Seeb-ALR Model

Seeb-ALR experimental data were obtained at altitudes of 56- and 70-inches during the Phase II test by moving the RF1 rail to the aft window blank in the experiment. *USM3D* and *OVERFLOW* computations are compared with experiment at these altitudes.

1.23.2.1. Effect of altitude, h=56-, and 70-inches

USM3D (SA and laminar) computations and *OVERFLOW* (SA) analyses are compared with the large altitude experimental data in Figure 9.48 and 9.49. The experimental flat top pressure region begins to deviate from flat at h=54 inches and then at 70 inches becomes wavy. The data at 70 inches are questionable (refer to Figure 7.92), because of the very weak overpressures results in the standard deviation becoming equivalent to half the model signal strength. CFD results compare fairly well at 54 inches, but show poorer agreement at 70 inches. It should be noted that the signatures are plotted to a smaller range than typical, so deviations appear greater due to the plot scale. It may be beyond the signal-to-noise capability of experiment to measure a flat pressure signature of such a weak disturbance at 70 inches. The computational results show flat signatures at all altitudes and are thought to be accurate, whereas the tunnel data are not.

1.23.3. 69° Delta Wing-Body Model

Computations of the 69° Delta Wing-Body configuration are compared with experiment; see Table 8 for the index to experimental data and computational/experimental comparisons. *USM3D* computations using laminar and turbulent flow are compared with *OVERFLOW* turbulent computations and experiment for each of the experimental run series presented in §7.3.3.

1.23.3.1. Effect of Off-Track Angle, Near Zero Alpha, h=25 inches

On- and off-track *USM3D* and *OVERFLOW* pressure signatures for the non-lifting model near α=0° are compared with the wind tunnel test data in Figures 9.50(a)-(d). There is no degradation of the computational results to the extreme off-track angle of 90 degrees, and the position and amplitude of the "tail" shock(s) are well predicted with the computational results. The "tail" shock changes from a single to multiple-shock waveform from on-track to off-track, respectively; except the *OVERFLOW* computation at ϕ=0° has two closely spaced but non-coalesced tail shocks, that can be seen with close inspection of Figure 9.50(a). The *USM3D* and *OVERFLOW* computations were performed with a single grid with Mach cone aligned cells that aligns the cells with the off-track angle. The comparisons are considered very good; some rounding of the experimental shocks are expected due to model vibration and fixed rail-orifice spacing. The signal-to-noise ratio is much larger for this model than the LM low boom N+2 vehicles and this should permit high-quality experimental results. However, a disconcerting observation is the shape of the experimental bow shock as the flow expands around the forebody; a slight pressure oscillation is seen which differs slightly at on- and off-track angles. There may be differences in the wind tunnel model and the computational models (analytically defined surfaces from Ref 34). Another possibility is that the 40-year old model nose may have been damaged and repaired by sanding. Furthermore, the model wing apex discontinuity appears somewhat rounded in the photos shown in Figure 4.6. A rounded wing apex would also result in reduced wing shock strength. Refinement of the computational mesh would make little difference to the result and could increase the discrepancy, and coarsening the mesh would lead to inaccurate results. For better agreement, the model should be measured and an as-tested geometry modeled.

The effect of laminar vs. turbulent flow computations on the pressure signature is small. The laminar flow computations show a slight reduction of wing shock strength compared with the turbulent flow

computations obtained with the Spallart-Allmaras model. As previously mentioned, the tail shock recovery to near ambient pressure in the experimental results shown in Figure 9.97 are corrupt from *X*=-93 to the end of the measured data. The standard deviation increases rapidly beginning at this location. Thus, the computational results in this region are considered more accurate than the experimental. Further evidence of validity of the CFD results is later seen in comparisons with higher quality data at smaller altitudes. It should also be noted that the computations have enough fidelity to identify and accurately compute the pressure oscillations from the modeling of the flat-notched regions on the sting for the strain gauges.

1.23.3.2. Effect of Off-Track Angle, Near Zero Alpha, h=32 inches

An altitude of 32 inches represents an *h/L* of 4.6, which is a significant increase in distance per model length (more than 3-times) than that of the other models tested. Viscous turbulent-flow computations are compared with experiment at on- and off-track angles in Figure 9.51(a)-(d). There is good agreement between the computational methods and dissipation effects are not seen even at this altitude. In fact, the computational signal strength over predicts experiment by a similar amount as was shown at *h*=25 inches (compare with Figure 9.50). There does not appear to be significantly greater rounding of the signatures at 32 inches than at 25 inches, just the reduction in shock strength from increased attenuation. This indicates that pressure signatures at greater altitudes could be still measured with good accuracy for this particular model.

1.23.3.3. Effect of Pitch Angle, h=21, and 25 inches

The data comparison with *USM3D* and *OVERFLOW* computations at the closest altitude measured (*h*=21.2 inches) is shown in Figure 9.52(a). The *USM3D* correlations with experiment are good, including the downstream pressure signatures on the sting, but the magnitude of the wing shock is over predicted. This agreement of the downstream sting pressures aft of *X*=-98 helps affirm that the previous computations (of Figure 9.50 and 9.51) at the altitude of 25 inches are accurate in this region and the experimental data are not. The *OVERFLOW* computation compares less favorably with experiment at this condition; the over predicted wing shock strength is greater than in the non-lifting cases of Figure 9.50.

Comparison of experiment and CFD of the model for two additional lifting conditions, at angles of attack of 2.4° and 3.9° are shown in Figure 9.52(b)-(c). *USM3D* and *OVERFLOW* compare well now, but sharper shocks than experiment are predicted with a slightly greater disparity with experiment at the higher angle of attack. The experimental data bends near the location of the predicted pressure oscillation within the “tail” shock (in Figure. 9.52(b)); this could be due to rounding of the experimental signatures.

1.23.3.4. Effect of Pitch Angle, h= 32 inches

Lifting model comparisons at an increased distance of 32 inches are shown in Figure 9.53(a-b). At these two angles of attack, the turbulent flow computational results predict a pressure oscillation near the middle of the tail shock that is not predicted with the laminar result or experiment (Figure 9.53(a)). The slope or rise time of the bow and wing shocks differ between computations and experiment at both conditions. The computational shocks are nearly vertical and experiment is sloped. Former experimental data from 1973 (Ref 34) shows similar experimental rise times of the bow and wing shocks, measured with a conventional probe, that are shown for the RF1 data shown here. In Figure 9.53(b) the turbulent flow pressure oscillation has shifted to near the minimum overpressure position. The experimental data does not show these small pressure oscillations, and now the laminar flow solution shows a slight jog in the data near this location. The oscillation is likely from the model base shock.

Propagated Signatures to Ground Level

On-track *USM3D* computations for the 1021 and 1044 models are propagated through standard atmospheric conditions to the ground. The ground signatures are taken at the same near-field location as previous experimental data. The computed ground signatures are shown and the noise levels of the CFD extrapolated data are compared with those levels obtained from the experimental data extrapolations from §7.1.5 (1021 model) and §7.2.3 (1044 model).

1.24. Phase I Computational and Experimental Models

Predicted ground pressure signatures from *USM3D* computations of the 1021 model at the cruise angle of attack of 2.3°, and also 2.1° and 2.5°, are compared in Figure 10.1. The near field signatures were extracted at distances of 20.7 in. and 31.3 in. below the model, or in full-scale flight vehicle dimensions, 215.63 ft and 326.25 ft below the aircraft, respectively. All extrapolations used *sBOOM* with a 50,000 ft flight altitude, and the sound levels of the sonic booms were computed with the *LOUDNESS* code. The pressure signatures show an effect from the increased lift with increased bow shock strengths. The ground pressure signatures, whether propagated from 20.7 in. (h/L= 0.93) or 31.3 in. (h/L=1.4) below the model, show very similar results. This indicates that it may be acceptable to take the signature at one body length during design.

The CFD-derived ground pressure signatures from Figure 10.1 should now be compared with the experimental data extrapolations. In Figures 10.2 to 10.4, the loudness levels of the experimentally derived ground signatures of Figures 7.34 to 7.36 are compared to those from the *USM3D* computations. The computational and experimental data are compared separately, grouped by altitude and angle of attack. The range of angle of attack was split into two categories, either a low or high α. Thus, Figure 10.2 compares h=21 in., for lower α (between 1.94° and 2.1°). Figure 10.3 compares h=21 in., at a higher α (between 2.29° and 2.5°), and Figure 10.4 compares h=31 in. data for higher α (between 2.3° and 2.51°). The results from these three figures show that only a 2 to 3 PLdB difference exists between the experimental and computational data extrapolations at similar angles of attack. It would be expected that with less angle of attack variation, the difference in PLdB would be less. It should be noted that there is sensitivity to the aft PLdB loudness results for small changes in the signature truncation location with the CFD computations. The signature must be truncated before the tail shock of wing/body returns to ambient flow to avoid inclusion of the shock from with downstream growth the blade strut or other model support apparatus.

1.25. Phase II Computational and Experimental Models

USM3D and *CFD++* near field pressure signatures of the Phase II 1044 wind tunnel model with blade strut were extrapolated to the ground. The ground signatures are shown in Figure 10.5. *sBOOM* and LOUDNESS tools were used with standard atmospheric conditions, without winds. The input pressure signatures were taken at approximately 1.7 body lengths directly below the model, and assumed to no longer be changing from three-dimensional effects. Small differences due to the pressure changes from laminar and turbulent flow simulations in the computational results can be seen in the ground pressure signatures. The turbulent flow solutions result in stronger bow shocks than the laminar solutions, and the slightly crisper near-field shocks in the *CFD++* solutions are retained in the ground pressures. Note that the computations are of the wind tunnel model rather than the flight model, which differs in shape, and operates at different free-stream Reynolds numbers. Hence, these loudness computations are not representative of the flight model. The trailing pressures must be truncated upstream of the strong compression resulting from the computational modeling of the blade strut model support. The input signatures to *sBOOM* are shown in Figure 10.6. The pressures in the aft region of the *CFD++* laminar

flow solution has some small oscillations that are not present in the other computations, and are probably not accurate, these oscillations may be the reason for the mismatch of the extrapolated pressures shown in Figure 10.5. However, the resulting difference in PLdB is less than 3.0 for all four computations. These particular computations were extrapolated because there is corresponding repeat wind tunnel data at test altitudes of 32 and 70 inches.

The extrapolated CFD results at an altitude of approximately 70 inches were obtained. The signatures were truncated at the inflection point where the blade strut starts interfering with the return to ambient flow in the experiment. *sBOOM* computations were again obtained using a 50,000 ft flight altitude, standard uniform atmosphere, and with a ground reflection factor of 1.9. The extrapolated results are shown in Figure 10.7 (note that LM did not provide a *CFD++* laminar flow solution at this altitude). There is only a 1.67 difference in PLdB level between the computations. The turbulence model has a larger effect than the different solver and grid. The input near-field signatures are shown in Figure 10.8.

Comparison of ground-level PLdB values of both computational and experimental extrapolations from the Phase II test are shown in Figures 10.9 and 10.10 for altitudes of 32- and 70-inches, respectively. There are only small differences in the predicted noise level for these two altitudes. There appears to be a slight increase in predicted noise level for the Phase II model compared with the Phase I model, compare with Figures 10.2 to 10.4. The noise level increase from the front of the pressure wave may be attributed to greater coalescence of the bow shock of the ground signatures. It is not broken into the number of multiple shocks like the Phase I model ground signatures. Compare the Phase II model ground signatures from experimental data extrapolations in Figures 7.79 and 7.80, and CFD extrapolations in Figures 10.5, 10.7, with the experimental extrapolations for the Phase I model Figures 7.34 to 7.36 and the CFD extrapolations in Figure 10.1.

Flight Vehicle Computations

Sonic boom analyses and force predictions for the Phase I (1021) flight vehicle are provided in this section. Near-field inviscid analyses with *CFD++*, *CART3D*, and *USM3D* are provided, in addition to *USM3D*, *FUN3D*, and *CFD++* viscous solutions. The near-field viscous pressure signatures from 1.5 to 2.5 body lengths were propagated using *sBOOM* to ground level. Similarly, sonic boom analyses of the Phase II (1043) flight vehicle were computed with the same codes and extrapolated to ground level.

1.26. Phase I Flight Vehicle

The Phase I flight vehicle is not simply a scaled up version of the 1021 wind tunnel model with the blade strut removed. The flight vehicle configuration has no wing trailing edge thickness whereas the wind tunnel model has blunt trailing edges to meet structural requirements of the small model. Also, the boundary layer diverter height is sized for the Reynolds number and does not poke through the upper surface of the wing as it does on the wind tunnel test article.

Computations with four different CFD codes were obtained on the flight vehicle. Three NASA-developed CFD codes, *USM3D*, *CART3D*, and *FUN3D* were used, and solutions from LM using *CFD++*. Sonic boom signature predictions for the flight vehicle using these codes are shown in Figures 11.1 to 11.12. The computations are compared at two altitudes, an *h/L* of 1.5, 345 feet (4140 inches), and an *h/L* of 2.5, 575 feet (6900 inches). 0°, 20°, and 40° off-track results are compared at these two near-field altitudes.

1.26.1. Euler (Inviscid) Analyses

Pressure signatures from Euler computations using *USM3D*, *CART3D*, *FUN3D*, and *CFD++* are compared in Figures 11.1 to 11.6. The mesh generated for *USM3D* was also used for the *FUN3D* computations, and although *USM3D* is a cell-centered scheme and *FUN3D* is vertex based, there are more cells than points by approximately a factor of seven. It is often the case that a cell-centered scheme requires fewer points to obtain an accurate solution. The *CFD++* grids and solutions were obtained from LM. The comparisons at 1.5 body lengths (Figures 11.1 to 11.3) show excellent correlation with the forward portion of the pressure signatures, but there is considerable variation of the predictions in the aft portion of the signatures. *CART3D* predicts stronger shocks than the other methods, and additional shocks not captured by the other methods.

The *CART3D* results agree better with *USM3D* and *FUN3D* at the greater distance from the configuration, *h/L* of 2.5 (Figures 11.4 to 11.6). Particular the results at 20° off-track angle are in very good agreement. The improved correlation with distance indicates that the crisper or spiky shocks may dissipate or attenuate to the nearly the same levels as the other methods, and is encouraging that all methods may extrapolate to the same ground-level pressure signature. Unfortunately, LM did not provide *CFD++* results at 2.5 body lengths.

1.26.2. Navier-Stokes (Viscous) Sonic Boom Analyses

On and off-track *USM3D* and *FUN3D* computations using the SA turbulence model at 1.5 and 2.5 body lengths are compared in Figures 11.7 to 11.12. *USM3D* and *FUN3D* are using the same viscous mesh and, in general, the pressure signatures from the *FUN3D* solutions appear less dissipative than those from *USM3D*. The positions of all the shocks are in good agreement, but the shock strengths are greater for *FUN3D* primarily in the aft portion of the signatures. Some of this disparity may be attributed to deeper flow solver convergence with *FUN3D* than *USM3D*. The *FUN3D* cases achieved nearly 8 orders magnitude reduction of the residual, whereas *USM3D* convergence flattened after about 3.25 orders drop in convergence. The signature differences from 1.5 to 2.5 body lengths are almost entirely in signal strength for both flow solvers, little to no changes in the characteristic shape of the pressure signatures are seen due to the greater extraction distance below the configuration. The Navier-Stokes computations are providing different results than the Euler results; for example compare Figure 11.1 with 11.7, and Figure 11.4 with 11.10. The differences are in the aft signatures likely due to submerged boundary layer diverters in the viscous computations compared to completely exposed diverters in the Euler solutions.

1.26.3. Vehicle Performance (Navier-Stokes and Euler) Analyses

NASA in-house vehicle performance prediction capabilities were employed to evaluate the LM Phase I model. The study was performed using *USM3D* with specialized viscous meshes generated using *V-Grid* (Ref 42). The grid was designed for drag prediction, and therefore viscous, and it was not stretched or extended to obtain a boom signature.

Figure 11.13 compares computed *USM3D* drag polars using the SA, k-ε, and the Menter's Sheer Stress Transport (SST) (Ref 56) turbulence models with the LM computations using *CFD++* with the k-ε turbulence model. The *USM3D* results with all three turbulence models predict larger drag coefficients than *CFD++*. The best correlations with the LM CFD++ results are with the *USM3D* solutions using the initial SA turbulence model. The drag differs between approximately 15 counts at the lower lift coefficient to within about 5 counts at the largest computed lift coefficient. It was expected that the NASA computations with the k-ε turbulence model would more likely correlate with the LM when the same turbulence model was used, but the k-ε turbulence model solutions increased the drag by approximately 50 counts, shifting the *USM3D* results further away from the LM predictions. The SST

model, since it has shown promise for supersonic prediction, was conducted for a single run. The figure shows that the data point falls in between the SA and the k-ε results. Since experimental data does not exist for this model, further studies were conducted to investigate the differences in the vehicle performance predictions.

Next, a grid convergence study with *USM3D* was attempted, but due to the approximate 3.5° deflection of the flaps, additional grids using the original sourcing (refinement regions) failed around the flap and the intersection of the non-deflected trailing edge above the nacelle. The original grid, at approximately 46 million grid cells, was produced using *V-Grid*. This same approach was shown to provide the correctly sized grid in the similar Boeing Phase 1 drag study (Ref 38). However, after a new grid sourcing was applied to the geometry, two additional grids were produced. The grids created sizes were 36 million and 50 million cells, representing coarser and finer meshes. Figure 11.14 compares the computations with the new grids to the original (baseline) 46 million-cell mesh. The results are very close with the 50 million-grid cell results being less that count of drag different from the baseline grid. As a result of this study and a similar one performed on the Boeing Phase 1 drag model, the baseline grid was used for the remainder of the study.

After investigating the differences in CFD predictions, it was discovered that LM *CFD++ RANS* computations, which does not use Reynolds number as a direct input, resulted in a Reynolds number that was smaller than the *USM3D* value by approximately three million. This difference is believed to be due to round-off error of the *CFD++* input conditions. The initial *USM3D* computation was at a Reynolds number, based on characteristic length, of 133.385 million. A *USM3D* run using the same Reynolds number as LM, 130.074 million, resulted in no significant differences in force computations between *USM3D* and *CFD++* when the Reynolds numbers were properly matched (not shown), an indication that the differences in Reynolds number is not attributing to the drag discrepancies between the flow solvers.

The *CFD++* volume grid consisted of only approximately 12 million grid cells, and the *CFD++* flow solver is a node-based scheme, whereas *USM3D* is a cell-based scheme. Consequently, the *CFD++* grid is similar to running a grid of only approximately two million control volumes with *USM3D*. This is likely too small of a mesh to accurately capture the viscous drag. An inviscid grid was produced for *USM3D* to compare with a LM inviscid computation, and so two *USM3D* Euler computations; at and below the lift coefficient of the CFD++ result are shown in Figure 11.15. *USM3D* still predicts larger drag than CFD++, but the Euler results are much closer. This provides some further evidence that the viscous grid used by *CFD++* was likely insufficient to obtain accurate viscous drag with *CFD++*.

1.27. Phase II Flight Vehicle

The LM flight vehicle, the vehicle designated as the1043, is LM's final flight model designed with flow through nacelles. LM designed a model with powered nacelles subsequent to this design, the 1044, where the configuration was reshaped to accommodate the pressure signature changes from the influence of jet flow. The 1043 vehicle was evaluated with a variety of Euler and Navier-Stokes flow solvers. The computations are performed at the design conditions of Mach 1.7, α=2.1°. Shaded images with the computational surface grid (developed by NASA using *Pointwise* grid generation software) are shown in Figure 11.16. The details of the closeout of the boundary layer diverters for the upper centerline nacelle and the nacelle on the lower surface of the wing are evident in the images. Observe the under wing surface contours that would appear to follow the nacelle shock in the shaded surface grid shown in Figure 11.16(b). Significant performance gains on supersonic vehicles were likely achieved from this detailed wing design in the presence of the nacelle.

1.27.1. Euler (Inviscid) Analyses

CART3D, *USM3D*, *FUN3D*, and *CFD++* Euler computations were preformed on the 1043 flight vehicle. On- and off-track comparisons are shown in Figures 11.17 to 11.19 at 1.5 body lengths (4257.12 in,, 354.76 ft) from the model nose. The *CART3D* mesh was adapted, as in previous solutions for the wind tunnel models, with line sensors placed on-track, and at 20° and 40° off-track angles. The results are expected to represent high quality solutions with minimal computational error, because the mesh adaption algorithm within *CART3D*-AERO is designed to reduce solution errors. *USM3D* and *FUN3D* computations used the same Mach cone aligned mesh, with an inner near-body isotropic mesh with near uniform cells from the configuration's surface grid. The *CFD++* mesh differs from the other meshes and was developed by LM and not provided to NASA.

The pressure signatures at this altitude correlate well—although *CART3D* predicts a small pressure oscillation (compression) within one of the expansion regions near *X*=8200 in., and stronger shocks in the aft portion of the pressure signature, these may be from the aft nacelle surfaces (Figure 11.17). The *CART3D* aft shock difference persists to 20° (Figure 11.18), but the 40° off-track pressure signature comparisons (Figure 11.19) show only small differences in the sharpness of the shocks, but the position and shock's base shape agree among the four flow solutions.

LM did not provide *CFD++* results at *h/L* of 2.5. Similar correlations of *CART3D*, *USM3D*, and *FUN3D* pressure signatures were obtained with overall very good agreement, but more refinement of the shocks in the *CART3D* aft signatures at 0° and 20° off-track angle is observed (Figures 11.20 to 11.22).

1.27.2. Navier-Stokes (Viscous) Analyses

The effects of viscosity were evaluated at the flight Reynolds number of 477.1×10^6. The Reynolds number was computed for a 50,000 ft flight altitude at Mach 1.7. The viscous solvers, *USM3D*, *FUN3D*, and *CFD++* were used, and their overlaid pressures signatures at 1.5 body lengths from the model, on- and off-track are presented in Figures 11.23 to 11.25. There is very good agreement in the forward portion of the pressure signatures (upstream of the first large expansion), but differences in the amplitude of the shocks in the aft signature are observed. The effects from the aft shock strengths on the ground pressures will be evaluated.

Unfortunately, there were problems with the *CFD++* mesh at 2.5 body lengths from the model, so only *USM3D* and *FUN3D* are compared at this altitude (Figures 11.26 to 11.28). It would be expected that the results at 2.5 body lengths would lead to more accurate sonic boom ground extrapolations, and if the *CFD++* pressures at this altitude were available would be in better agreement because sharp peaky pressures are not usually maintained with distance from the model. The *USM3D* results indicate slightly more honed shocks than the *FUN3D* computations on-track and at 20° off-track (Figures 11.26 to 11.27). However, this is reversed at 40° off-track, where *FUN3D* predicts larger shock strengths (Figure 11.28).

1.27.3. Predicted Ground Signatures

The opportunity to assess the ground-level pressure signatures derived from the computational results at flight conditions was afforded for all of the viscous computations. *sBOOM* was run with standard atmospheric temperature and humidity, for a flight altitude of 50,000 ft at Mach 1.7, and a reflection factor of 1.9 at the ground. It used a "double event" two-shock sonic boom (front and aft portions of the signature) loudness calculation. The computational aft boundary of the *CFD++* computation is closer to the model than the *USM3D* and *FUN3D* boundaries as shown in Figure 11.29. The *CFD++* signature truncates at approximately 300 feet compared to nearly 350 feet for the other computations. The computed ground level pressure signatures using these inputs are overlaid in Figure 11.30. The *CFD++*

ground signature differs considerable in the tail shock characteristics because of the foreshortened input signature. There is little difference between the data extrapolated from 1.5 and 2.5 body lengths for the *USM3D* and *FUN3D* simulations. The ground signatures for the flight vehicle at flight conditions can be compared with the wind tunnel model computations (Figures 10.5 and 10.7) at a Reynolds number of 6.74×10^6 (compared to 477.1×10^6 at flight). The forward and aft regions of the ground-level signature are comprised of multiple shocks at flight conditions (Figure 11.30), whereas, nearly an "N-wave" ground signature is computed at wind tunnel test Reynolds number. The bow shock is smooth and steeper to rise than at flight conditions. The tail shock in the wind tunnel model was foreshortened to avoid the blade strut shock, and is likely the cause of the aft pressure differences. The associated total wave, and front and aft signature contributions to the loudness level are compared for the flight vehicle in Figure 11.31. A significant drop in PLdB from the wind tunnel model extrapolations (Figures 10.9 and 10.10) is obtained for the flight models. This exemplifies that propagation inaccuracies can be realized for complex models with highly shaped pressure signatures, that are evaluated at low Reynolds number, and where model support hardware interferes with the "return-to-ambient-flow" region of the signature.

The erroneous ground signature from the *CFD++* foreshortened input pressure signature was corrected by LM. They have developed software tools to establish recovery pressures to free-stream ambient conditions from a truncated waveform. The modified input signatures are shown in Figure 11.32, where the *CFD++* input now smoothly returns to freestream conditions. The ground pressures from extrapolation using the revised inputs are shown in Figure 11.33. The tail shocks are now in excellent agreement, and the only difference is in the position of small pressure oscillation near y=0 of the main expansion wave of the ground pressure signature. The loudness levels are also correlate well now, independent of flow solver, or whether extrapolated from 1.5 or 2.5 body lengths, as shown in Figure 11.34. LM's reported loudness computations of less than 85 PLdB (Ref 29) were preformed with a non-Burgers method (Ref 56) that used an adjustable rise time that matched a regression fit of thirty F-18 boom measurements from one day of testing at the Armstrong Flight Research Center. These predictions were made during the NRA contract period—before they implemented the *sBOOM* code, but since have determined that sBOOM predictions are about 2-4 PLdB louder than predictions made with the Armstrong regression fit risetimes; making the LM predicted loudness very close to the values computed herein.

Concluding Remarks

Two wind tunnel tests were conducted in 2011 and 2012 at the NASA Ames 9- by 7-Foot Supersonic Wind Tunnel to measure the near-field pressure signatures on the following configurations: Lockheed-Martin Phase I and II low-boom configurations, three calibration bodies-of-revolution, a 70° swept plate model, and a vintage 69° delta-wing/body configuration. The sonic boom test data were obtained using a minimally intrusive pressure rail. The sonic boom data obtained by the rail instrumentation was compared with high-fidelity numerical simulations of off-body pressures. The test results showed very good agreement between the computational and experimental data when a variety of new testing techniques including spatial averaging of a series of pressure signatures were employed.

The use of the RF1 pressure rail combined with spatial averaging of aligned signatures with different axial positions and constant altitude eliminated the wind tunnel distortions seen in the individual pressure signatures at most fixed model positions in the wind tunnel. The rail data were, as predicted, free from model shock reflections. The data from the Phase I test proved that accurate data with reasonable acquisition time is obtainable in the Ames 9- by 7-Foot Supersonic Wind Tunnel.

Evaluation of the Phase I test data revealed that data runs with 2-second duration acquisition times are of the same accuracy as 30-second duration times when a series of data runs are averaged. By decreasing

the duration of the sampling time of the data runs at each model position during the Phase II test resulted in substantial productivity gains with little effect on the accuracy of the experimental data. It was also shown during the Phase II test that for the small number of runs with both longitudinal and lateral model translation sweeps resulted in nearly equivalent quality pressure signatures. The availability of lateral model translation provides greater model placement flexibility and a wider range of test altitudes. However, longitudinal translation is still the preferred method since shock coalesce differences are theoretically possible with altitude changes using lateral translation.

Wind tunnel test pressure signatures are subject to inaccuracies for estimation of sonic boom loudness levels of complete configuration models due to the low experimental Reynolds number and some contamination of the model support hardware. Reliance on computational analysis of vehicles at flight Reynolds numbers without model support hardware is required for estimation of sonic boom loudness levels. Additional inaccuracies stem from poor replicas of the flight vehicles due to wind tunnel model structural requirements and model fabrication limitations. However, wind tunnel testing remains invaluable for providing validation data that gives confidence in the CFD methods to predict the sonic boom pressures of complex vehicles.

In general, however, the experimental shock waves have some rounding due to free stream turbulence within the wind tunnel that causes model motion fluctuation/vibration. This is compounded by stream angle variations (approximately 0.33 of a degree) in the 9×7 tunnel test section. Angle variations result in lift coefficient changes of approximately 0.015 during model translation, representing a 10 -15% change in lift coefficient for these configurations. The variation in lift coefficient will also affect the relative strength and position of model shocks, and result in possible signature misalignment when simply shifting the data based on actuator ram and model nose position, and Mach number. Averaging misaligned pressure signatures will result in further rounding of shocks, especially those with crisp—small base thicknesses.

USM3D was the computational evaluation method used to evaluate all of the configurations tested during Phase I and II wind tunnel tests. *CART3D*, *FUN3D*, *CFD++*, and *OVERFLOW* flow solutions were compared with *USM3D* computations and experiment. There was good agreement between all flow codes and experiment. The key to accurate sonic boom analyses lies in the computational mesh, with less importance on the flow solver. All computations relied on off-body Mach cone aligned cells or nearly aligned cells with additional mesh adaptation. Stretching of aligned cells was also used with all flow codes to improve efficiency and reduce numerical dissipation. All solutions presented herein closely matched the experimental pressures obtained with the RF1 rail, regardless of flow solver.

Navier-Stokes computations were shown to predict some differences in sonic boom pressures compared with Euler computations. The extent that viscous flow affects the sonic boom pressure signatures is configuration and Reynolds number dependent. Simple models with simple sonic boom pressure signatures, such as bodies of revolution or analytic models, like the delta wing body configuration show little difference to Navier-Stokes computations. But, the LM low boom N+2 designs require complex vehicle shapes in order to achieve low boom loudness levels. Differences in Euler and Navier-Stokes computations were seen even at flight conditions where a thin boundary layer would be expected to not greatly affect the pressure signatures. This indicates that any future flight demonstration vehicle should be evaluated and perhaps even designed with Navier-Stokes computations.

Computational methods were able to acutely predict the sonic boom levels, and the next step towards realization of civilian supersonic transportation is to assess numerical simulations of propulsion effects on sonic boom with as needed wind tunnel tests, then perform detailed computational analyses of flight vehicles with propulsion effects modeling. This would be followed by a vehicle flight demonstration test of a manned low-boom aircraft with front and rear shaped pressure signatures.

References

[1] Durston, D., Cliff, S., Wayman, T., Merret J., Elmiligui, A., and Bangert, L., "Near-Field Sonic Boom Test on Two Low-Boom Configurations Using Multiple Measurement Techniques at NASA Ames," *AIAA Paper 2011-3333*, 29th AIAA Applied Aerodynamics Conference, Honolulu, HI, June 2011.

[2] Wilcox, F. J., Jr.; and Elmiligui, A. A., "Experimental Measurements of Sonic Boom Signatures Using a Continuous Data Acquisition Technique," *NASA /TP-2013-218035*, August 2013.

[3] Cliff, S., Elmiligui, A., Aftosmis, M., Thomas, S., Morgenstern, J., and Durston, D., "Design and Evaluation of a Pressure Rail for Sonic Boom Measurements in Wind Tunnels," Seventh International Conference on Computational Fluid Dynamics (ICCFD7), *ICCFD-2006*, Big Island, HI, July 2012.

[4] Morgenstern, J. M., "Distortion Correction for Low Sonic Boom Measurement in Wind Tunnels," *AIAA Paper 2012-3216*, 33rd Applied Aerodynamics Conference, June 2012.

[5] Morgenstern, J. M., "How to Accurately Measure Low Sonic Boom or Model Surface Pressures in Supersonic Wind Tunnels," *AIAA Paper 2012-3215*, 33rd Applied Aerodynamics Conference, June 2012.

[6] NASA Langley Research Center Supersonics Project, "Request for Proposal for Potential Order for System-Level Experimental Validations for Supersonic Commercial Transport Aircraft Entering Service in the 2018–2020 Time Period," *NASA Program Announcement Number NNH08ZEA001N-SUP3*, August 2009

[7] Cliff, S., Thomas, S., McMullen, M., Melton, J., and Durston, D., "Assessment of Unstructured Euler Methods for Sonic Boom Pressure Signatures Using Grid Refinement and Domain Rotation," *NASA/TM-2008-214568*, Sept. 2008

[8] Choi, S., Alonso, J. J., and Van der Weide, E., "Numerical and Mesh Resolution Requirements for Accurate Sonic Boom Prediction," *AIAA Journal of Aircraft,* Vol. 46, No. 4, July-Aug. 2009

[9] Carter, M. B., and Deere, K. A., "Grid Sourcing and Adaptation Study Using Unstructured Grids for Supersonic Boom Prediction," *AIAA Paper 2008-6595*, 26th AIAA Applied Aerodynamics Conference, Honolulu, Hawaii, August 2008.

[10] Jones, W.T., Nielsen, E. J., and Park M. A., "Validation of 3D Adjoint Based Error Estimation and Mesh Adaption for Sonic Boom Prediction," *AIAA Paper 2006-1150*, 44th AIAA Aerospace Sciences Meeting and Exhibit, Reno, NV, January 2006.

[11] Park M. A., and Darmofal, D. L., "Validation of an Output-Adaptive Tetrahedral Cut-Cell Method for Sonic Boom Prediction," *AIAA Journal Vol. 48, No. 9, Sept. 2010. [DOI 10.2514/1.J050111]*

[12] Park, M. A., "Low Boom Configuration Analysis with FUN3D Adjoint Simulation Framework," *AIAA Paper 2011-3337*, 29th AIAA Applied Aerodynamics Conference, Honolulu, HI, June 2011.

[13] Aftosmis, M. J., and Berger, M. J., "Multilevel Error Estimation and Adaptive H-Refinement for Cartesian meshes with embedded boundaries," *AIAA Paper 2002-0863*, 40th AIAA Aerospace Sciences Meeting and Exhibit, Reno NV, Jan. 2002.

[14] Nemec, M., and Aftosmis, M. J., "Adjoint Error-Estimation and Adaptive Refinement for Embedded-Boundary Cartesian Meshes," *AIAA Paper 2007-4187*, 18th AIAA CFD Conference, Miami FL, June 2007.

[15] Wintzer, M., Nemec, M., and Aftosmis, M. J., "Adjoint-based Adaptive Mesh Refinement for Sonic Boom Prediction," *AIAA Paper 2008-6593*, 26th AIAA Applied Aerodynamics Conference, Honolulu HI, June 2008.

[16] Aftosmis, M. J., Nemec, M., and Cliff, S. E., "Adjoint-based Low Boom Design with CART3D," *AIAA Paper 2011-3500*, 29th AIAA Applied Aerodynamics Conference, Honolulu, HI, June 2011.

[17] Louisville, A., Dervieux, A., and Alauzet, F., "Fully Anisotropic Goal-Oriented Mesh Adaptation for 3D Steady Euler Equations," *Journal of Computational Physics Volume 229 Issue 8, pages 2866-2897*, April 2010.

[18] Haering, E., Murray, J., Purifoy, D., Graham, D., Meredith, K., Ashburn, C., and Stucky, M.,, "Airborne Shaped Sonic Boom Demonstration Pressure Measurements with Computational Fluid Dynamics Comparisons," *AIAA Paper 2005-0009*, 2005.

[19] Laflin, Kelly R., Klausmeyer, Steven M., and Chaffin, Mark, "A Hybrid Computational Fluid Dynamics Procedure for Sonic Boom Prediction," *AIAA Paper 2006-3168*, 24th AIAA Applied Aerodynamics Conference, San Francisco, CA, June 2006.

[20] Waithe, Kendrick A., "Application of USM3D for Sonic Boom Prediction by Utilizing a Hybrid Procedure," *AIAA Paper 2008-129*, Jan. 2008

[21] Howe, Donald C., "Hybrid CART3D/OVERFLOW Near-Field Analysis of a Low Boom Configuration with Wind Tunnel Comparisons," *AIAA Paper 2011-3336.*

[22] Campbell, R. L., Carter, M. B., Deere, K. A. and Waithe, K. A., "Efficient Unstructured Grid Adaptation Methods for Sonic Boom Prediction," *AIAA Paper 2008-7327*, 26th AIAA Applied Aerodynamics Conference, Honolulu HI, Aug. 2008.

[23] Cliff, S.E., Elmiligui, A. A.,Campbell, R. L., and Thomas, S. D., "Evaluation of Refined Tetrahedral Mesh with Projected, Stretched, and Sheared Prism Layers for Sonic Boom analysis, *AIAA Paper 2011-3338*, 29th AIAA Applied Aerodynamics Conference, Honolulu, HI, June 2011

[24] Cliff, S.E., Elmiligui, A., Campbell, R. L., and Thomas, S. D., "Refined Tetrahedral Meshes with Mach Cone Aligned Prisms for Sonic Boom Analysis." To be published in the AIAA Journal of Aircraft.

[25] Park, M. A., Campbell, R. L., Elmiligui, A. A, Cliff, S. E., and Nayani, S. N., "Specialized CFD Grid Generation Methods for Near-Field Sonic Boom Prediction", *AIAA Paper 2014-0115*, SciTech 2014, 52nd Aerospace Sciences Meeting, National Harbor, Maryland, Jan. 13-17, 2014.

[26] Cliff, S. E., Durston, D. A., Chan, W. M., Elmiligui, A. A., Moini-Yekta, S., and Jensen, J. C., "Computational and Experimental Assessment of Models for the First AIAA Sonic Boom Prediction Workshop", *AIAA Paper 2014-0560*, SciTech 2014, 52nd Aerospace Sciences Meeting, National Harbor, Maryland, Jan 13-17, 2014.

[27] Park, M. A., and Morgenstern, J. M., "Summary and Statistical Analysis of the First AIAA Sonic Boom Prediction Workshop," *AIAA Paper 2014-2006*, 32nd AIAA Applied Aerodynamics Conference, Atlanta, GA, June 16-20, 2014.

[28] Morgenstern, J., Norstrud, N., Sokhey J., Martens, S., and Alonso, J., "Advanced Concept Studies for Supersonic Commercial Transports Entering Service in the 2018 to 2020 Period", Phase I Final Report, *NASA/CR—2013-217820*, February 2013.

[29] Morgenstern, J., "Final Report for the NASA N+2 Supersonic Validations Phase II: Advanced Concepts Studies for Supersonic Commercial Transports Entering Service in the 2018 to 2020 Period", Contract No.: NNC10CA02C, CDRL No. 11, Submittal No. 02, SOW Para: 3.11, DID: NPR 2200.2, Document No. PMF-01766, Revision 5, May 29, 2014.

[30] Test Planning Guide for High Speed Wind Tunnels, http://www.nasa.gov/sites/default/files/643643main_HSpeedTestPlanGuide.pdf.
NASA Ames Wind Tunnel Operations Division report number A027-9391-XB2, rev. 5, April 27, 2005

[31] Reed, T. D., Pope, T. C., and Cooksey, J. M.: "Calibration of Transonic and Supersonic Wind Tunnels", *NASA CR-2920*, November 1977.

[32] Darden, C. M., "Sonic Boom Minimization with Nose-Bluntness," *NASA /TP-1348*, 1979.

[33] George, A. R., and Seebass, R., "Sonic Boom Minimization Including Both Front and Rear Shocks," *AIAA J. Vol. 9, No. 10*, Oct. 1971, pp. 2091-2903.

[34] Hunton, L. W., Hicks, R. M., and Mendoza, J. P., "Some Effects of Wing Planform on Sonic Boom," *NASA TN D-7160*, January 1973.

[35] Park M. A., Aftosmis, M. J., Campbell, R. L., Carter, M. B., Cliff, S. E., and Bangert, L. S. "Summary of the 2008 NASA Fundamental Aeronautics Program Sonic Boom Prediction Workshop," *Journal of Aircraft*, *Vol. 51 No. 3, (2014), pp. 987-1001. [DOI 10.2514/1.C032589]*

[36] Heineck, J. T., Schairer, E. T., Walker, L. A., Kusher L. K., "Retroreflective Background Oriented Schlieren (RBOS)," ISV14-14-14th International Symposium on Flow Visualization, EXCO Daegu, Korea, June, 2010.

[37] Durston, D., Elmiligui A., Cliff, S., Winski, C, Carter, M., Walker, E., "Experimental and Computational Sonic Boom Assessment of Boeing N+2 Low Boom Models", *AIAA Paper 2015-2140*, 32nd AIAA Applied Aerodynamics Conference, Atlanta, GA, June 2015.

[38] Durston, D., Elmiligui A., Cliff, S., Winski, C, Carter, M., Walker, E., "Experimental and Computational Sonic Boom Assessment of Boeing N+2 Low Boom Models", NASA TP (to be published).

[39] Magee, T. E., Shaw, S. G., and Fugal, S. R., "Experimental Validations of a Low-Boom Aircraft Design," *AIAA Paper 2013-0646*, 51st AIAA Aerospace Sciences Meeting, Fort Worth Region, TX, Jan. 2013.

[40] Rallabhandi, S. K., "Advanced Sonic Boom Prediction using the Augmented Burgers Equation," *AIAA Journal of Aircaft, Vol. 48 No. 4*, pp: 1245-1253, July-August, 2011.

[41] Shepherd, K. P., and Sullivan, B. M., "A Loudness Calculation Procedure Applied to Shaped Sonic Booms," *NASA /TP 3134*, 1991.

[42] Pirzadeh, S., "Advanced Unstructured Grid Generation for Challenging Aerodynamics Applications," *AIAA Paper 2008-7178*, Aug. 2008.

[43] Pointwise Software, http://www.pointwise.com, 213 South Jennings Avenue, Fort Worth, Texas 76104-1107.

[44] Frink, N. T., Pirzadeh, S. Z., Parikh, P. C., Pandya, M. J., and Bhat, M. K., "The NASA Tetrahedral Unstructured Software System," *The Aeronautical Journal*, *Vol. 104, No. 1040*, October 2000, pp. 491-499.

[45] Frink, N. T., "Assessment of an Unstructured-Grid Method for Predicting 3-D Turbulent Viscous Flows," *AIAA Paper 96-0292*, 34th Aerospace Sciences Meeting, Reno NV, Jan. 1996.

[46] Spalart, P, and Allmaras, S.A., "One-Equation Turbulence Model for Aerodynamic Flows," *AIAA Paper 92-0439*, 30th Aerospace Sciences Meeting and Exhibit, Reno NV, Jan. 1992.

[47] Park, M. A., and Darmofal, D. L., "Validation of an Output-Adaptive, Tetrahedral Cut-Cell Method for Sonic Boom Prediction," *AIAA Journal, Vol. 48, No. 9*, Sept. 2010, pp. 1928-1945.

[48] Park, M. A. and Darmofal, D. L., "Parallel Anisotropic Tetrahedral Adaptation," *AIAA Paper 2008-917*, 2008.

[49] Metacomp Technologies, Inc. CFD++ Users Manual, 28632-B Roadside Drive, Suite 255, Agoura Hills, CA, 91301, USA.

[50] Nichols, R., and Buning, P., "User's Manual for OVERFLOW 2.1," Version 2.1t, August 2008.

[51] Nichols, R., Tramel, R., and Buning, P., "Solver and Turbulence Model Upgrades to OVERFLOW 2 for Unsteady and High-Speed Applications", *AIAA Paper 2006-2824*, 24th AIAA Applied Aerodynamics Conference, San Francisco, California, June, 2006.

[52] Chan, W., Gomez, R., Rogers S., and Buning, P., "Best Practices in Overset Grid Generation", *AIAA Paper 2002-3191*, 32nd AIAA Fluid Dynamics Conference and Exhibit, St. Louis, MO, June 24-26, 2002.

[53] Afosmis, M. J., and Nemec M., "Cart3D Simulations for the First AIAA Sonic Boom Prediction Workshop," *AIAA Paper 2014-0558,* AIAA Science and Technology Forum and Exposition (SciTech2014), National Harbor, MD, January 2014.

[54] Wayman, T. R., Waithe, K. A., Howe, D. C., Bangert, L. S., and Wilcox, F., "Near-Field Acoustic Test on a Low Boom Configuration in Langley's 4x4 Wind Tunnel," *AIAA Paper 2011-3331*, 29th AIAA Applied Aerodynamics Conference, Honolulu, HI, June, 2011.

[55] Waithe, K. A., "Design of a Wind Tunnel Mount for a Low Boom Test," *AIAA Paper 2011-3334*, 29th AIAA Applied Aerodynamics Conference, Honolulu, HI, June, 2011.

[56] Menter, F. R., "Improved Two-Equation k-omega Turbulence Models for Aerodynamic Flows, *NASA /TM-103975*, Oct. 1992.

[57] Stevens, S. S., "Perceived Levels of Noise by Mark VII Decibels (E)", *J. Acoust Soc Am, Vol. 51, No. 2, Pt. 2*, Feb. 1972, pp. 575-601.

Figures

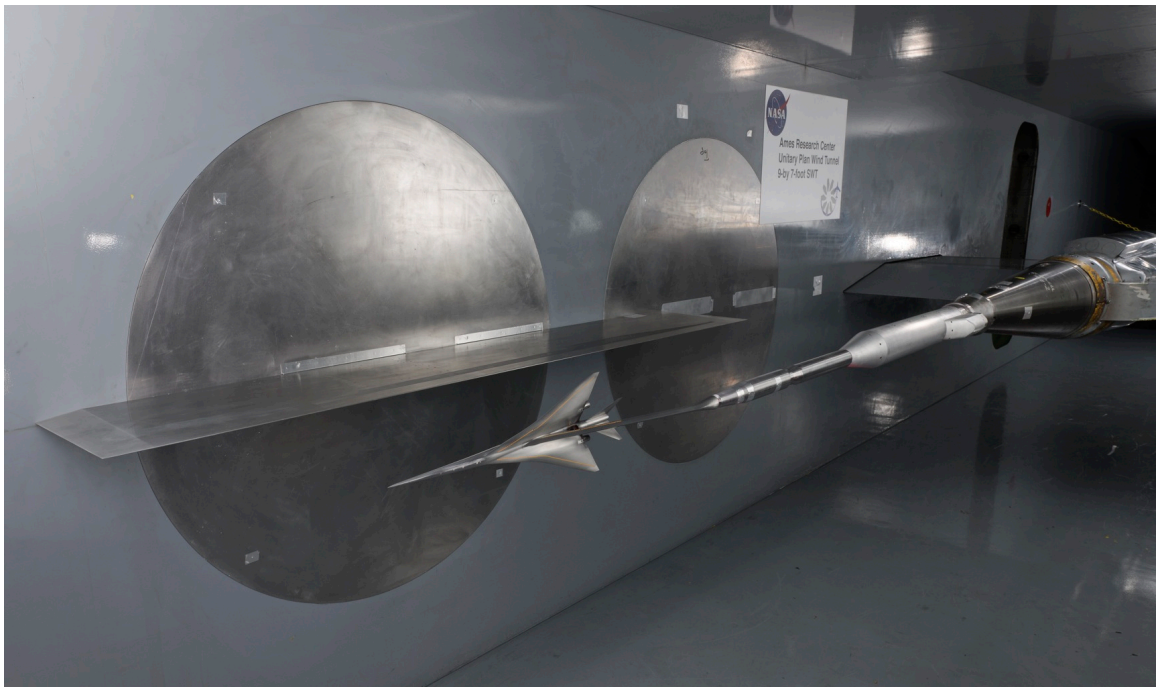

Figure 1.1. Installation photograph of the Lockheed Phase I 1021 model, and RF1 pressure rail in the NASA Ames 9- by 7-foot Supersonic Wind Tunnel

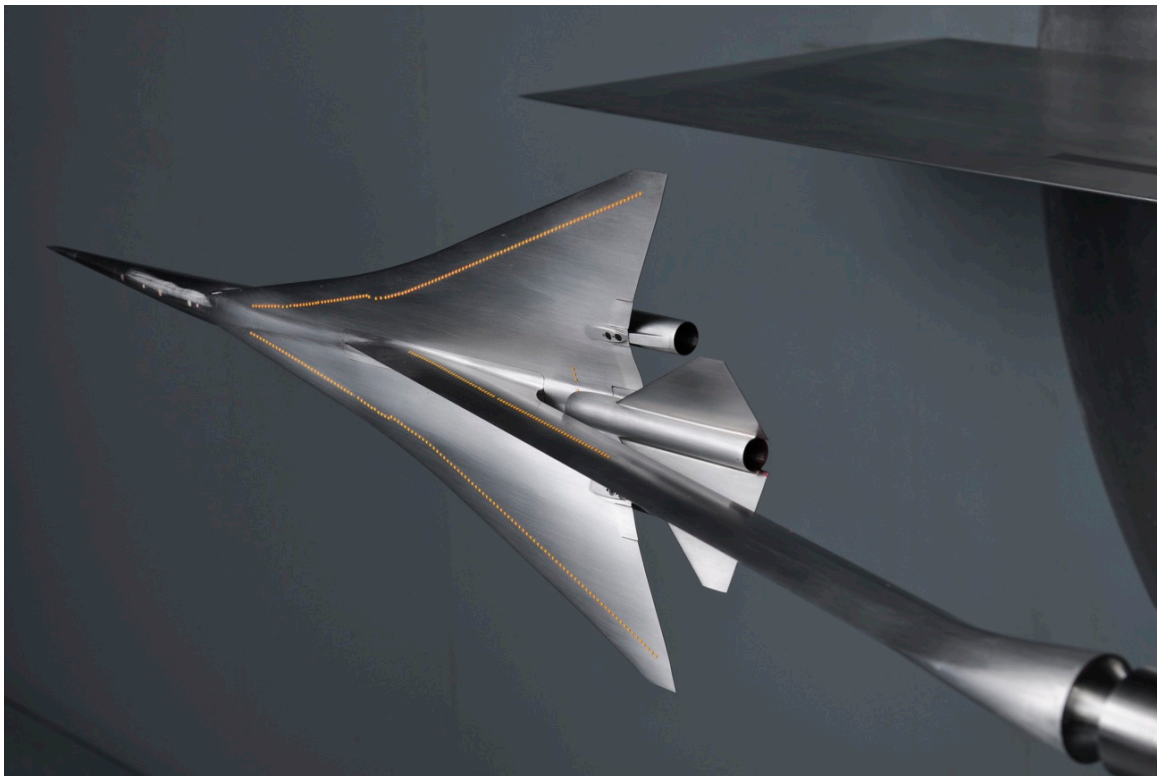

Figure 1.2. Photograph of the Lockheed Phase I 1021 model with blade strut and leading edge portion of the RF1 rail in the Ames 9 by 7-foot Supersonic Wind Tunnel

(a) Phase I concept

(b) Phase II concept

Figure 1.3. Artist's concepts of Lockheed Phase I and II N+2 low-boom supersonic transport configurations

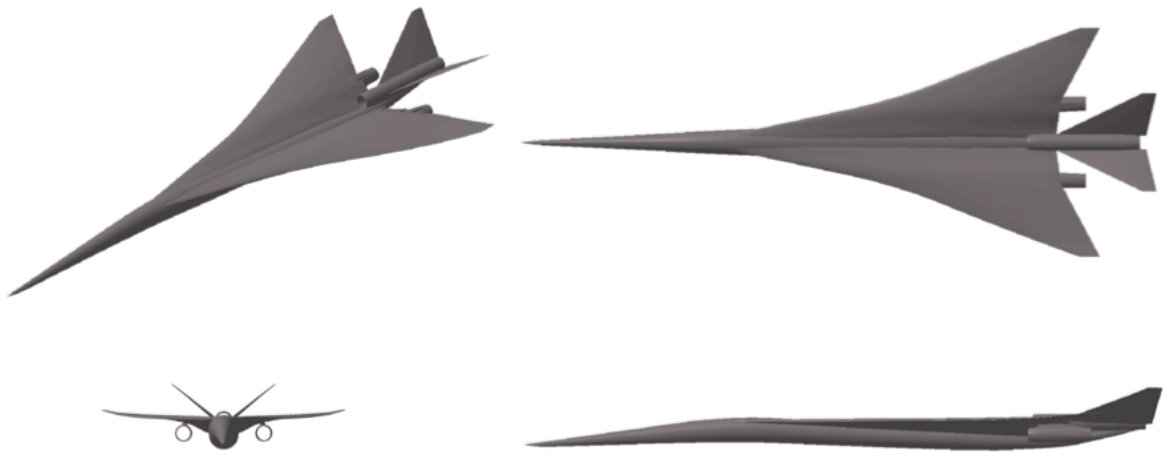

(a) Phase I 1021 configuration

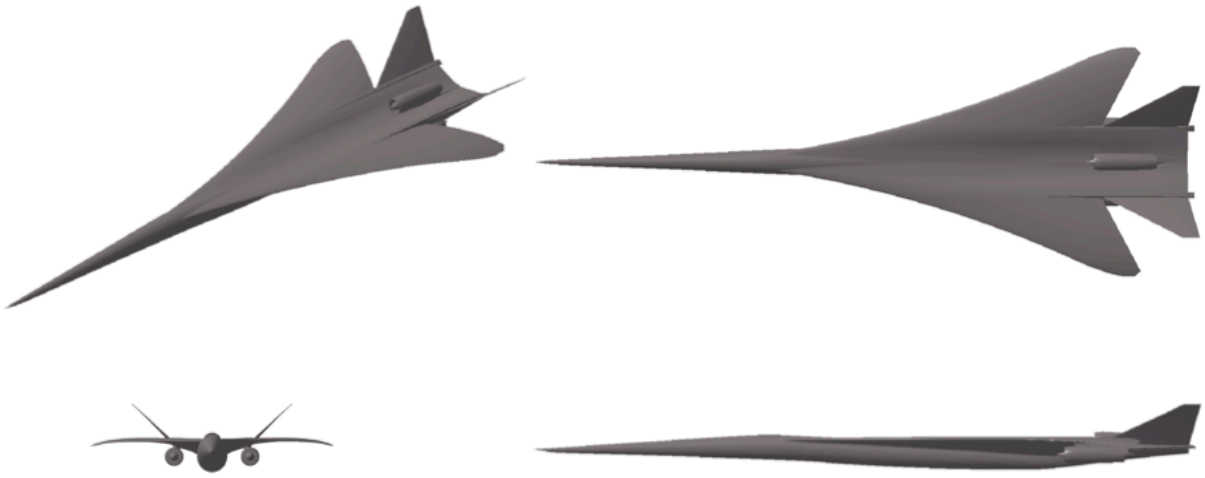

(b) Phase II 1043 configuration

Figure 1.4. Four-view CAD images of Lockheed Martin Phase I and II N+2 configurations

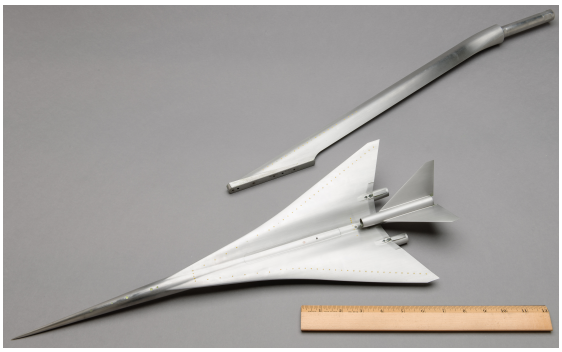

(a) Upper surface, with detached blade strut

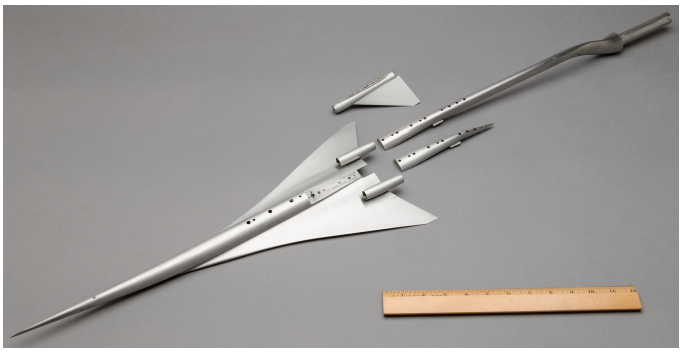

(b) Lower surface, with detached V-tail/nacelle, conventional sting, and aft-body closure parts

(c) Aft region of model

(d) Center nacelle and tail of model

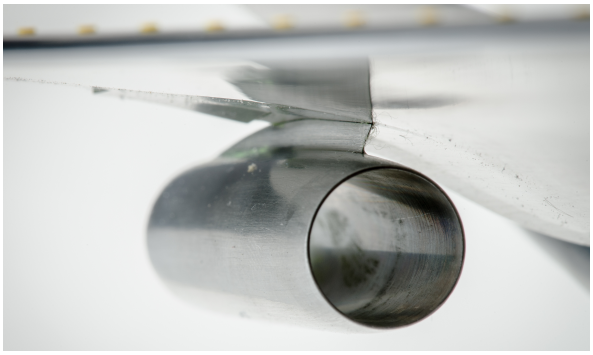

(e) Under wing nacelle and boundary layer diverter

Figure 4.1. Photographs of Lockheed N+2 1021 model

Figure 4.2. Photograph of axisymmetric wind tunnel test models, top to bottom: Seeb-ALR, Opt Sig, AS2

(a) Upper surface, with detached blade strut

(b) Lower surface

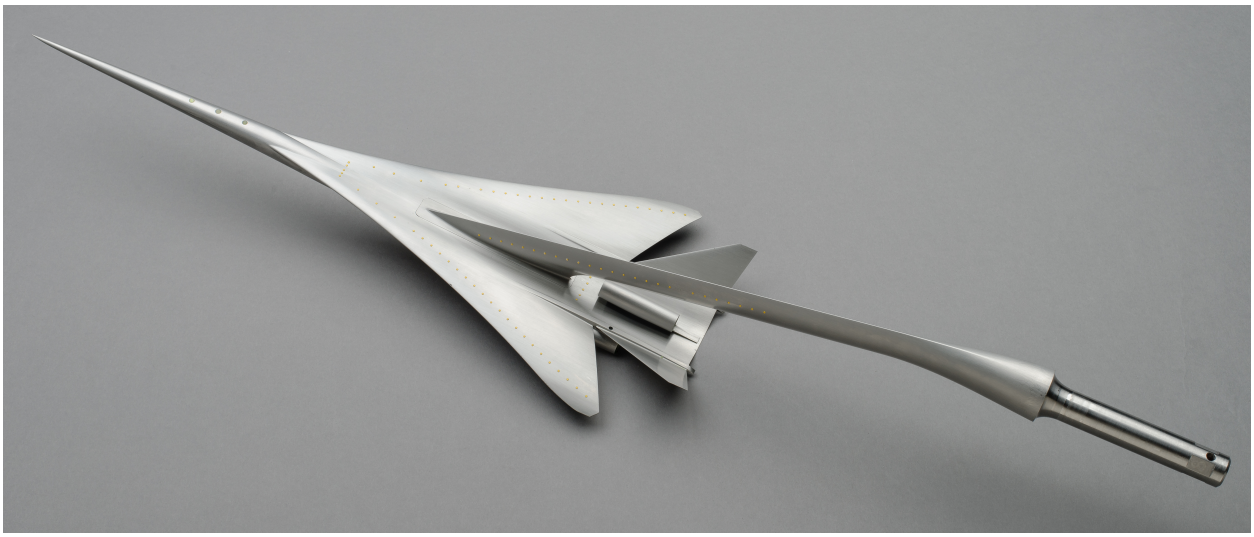

(c) Upper surface (isometric view) of the Phase II model with attached blade strut

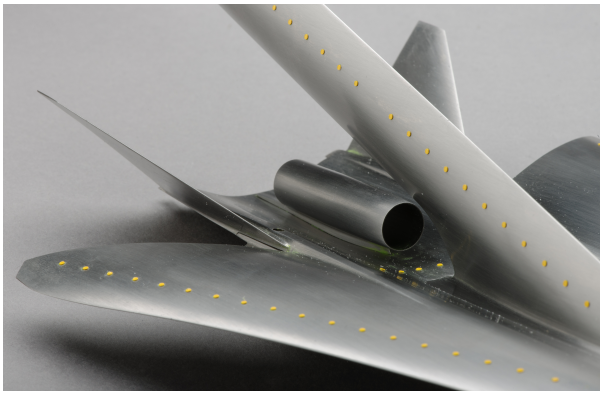

(d) Aft region (upper surfaces) with attached blade strut

(e) Aft region (lower surfaces) with attached blade strut

Figure 4.3. Photographs of Lockheed N+2 1044 model

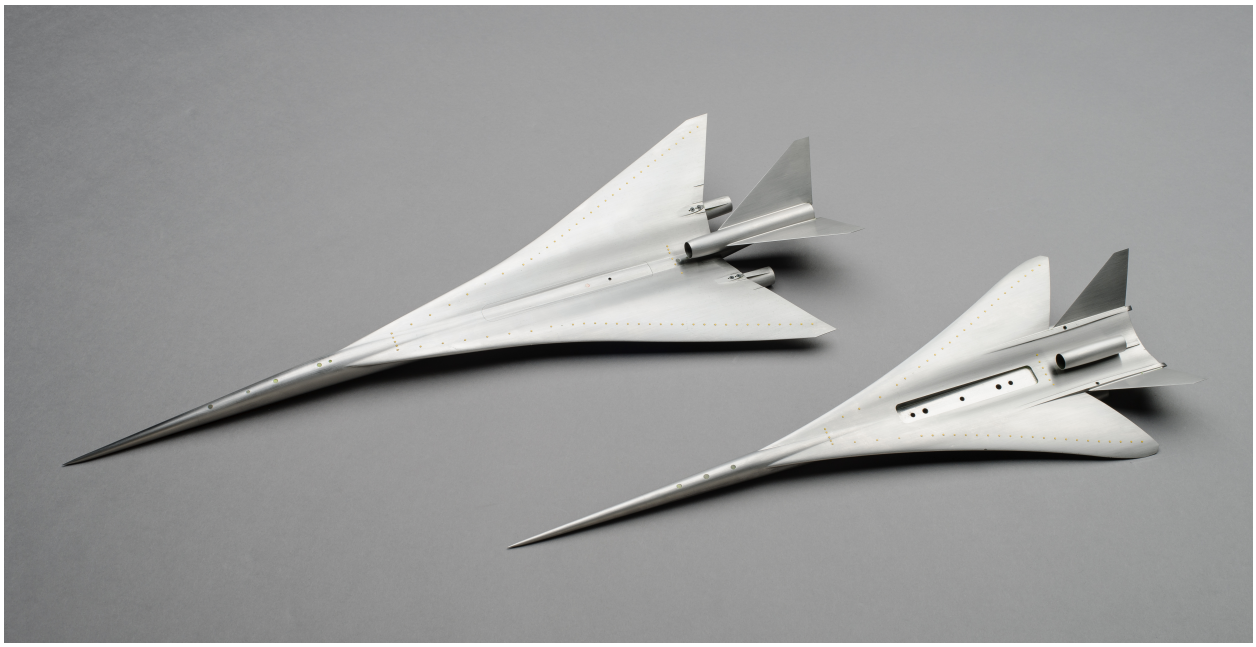

Figure 4.4. Comparison of Phase I (upper left) and Phase II (lower right) wind tunnel models

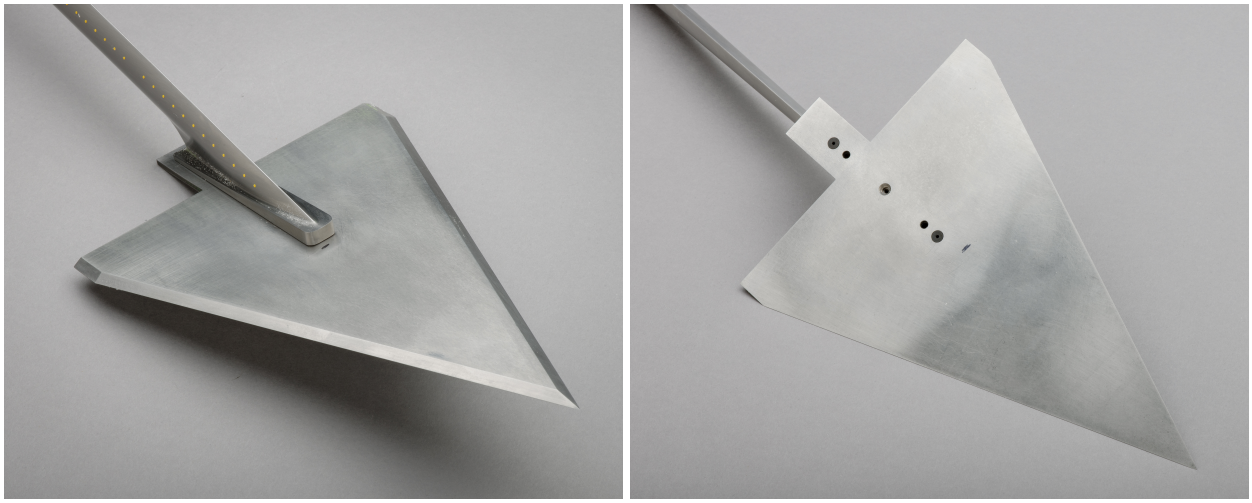

(a) Upper surface (b) Lower surface

Figure 4.5. Photographs of 70° flat plate calibration model

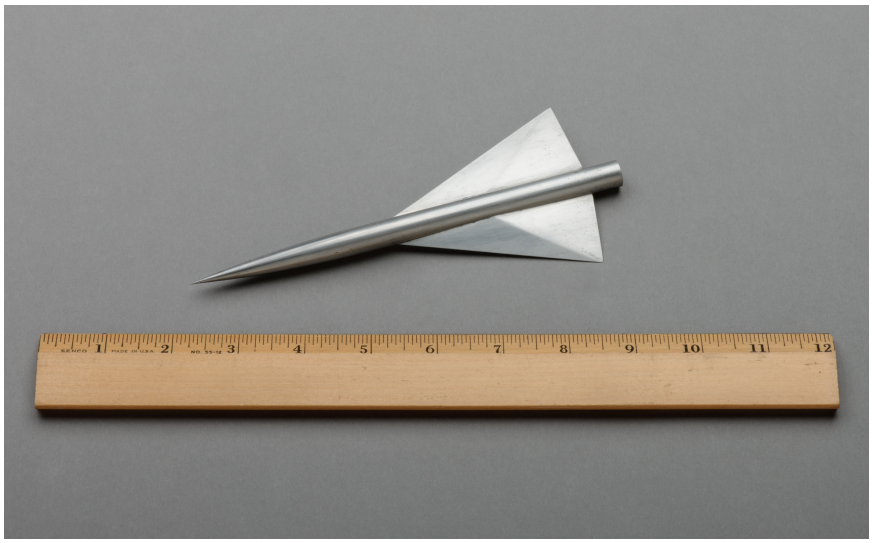

(a) Upper surface of the model

(b) Exposed strain gauges on sting behind model

(c) Model with entire sting

Figure 4.6. Photographs of the 69° Delta Wing-Body model (concluded)

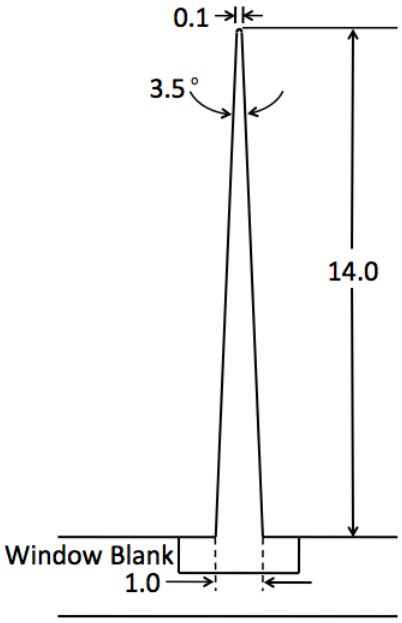

Figure 5.1. Cross section of the rail with dimensions in inches

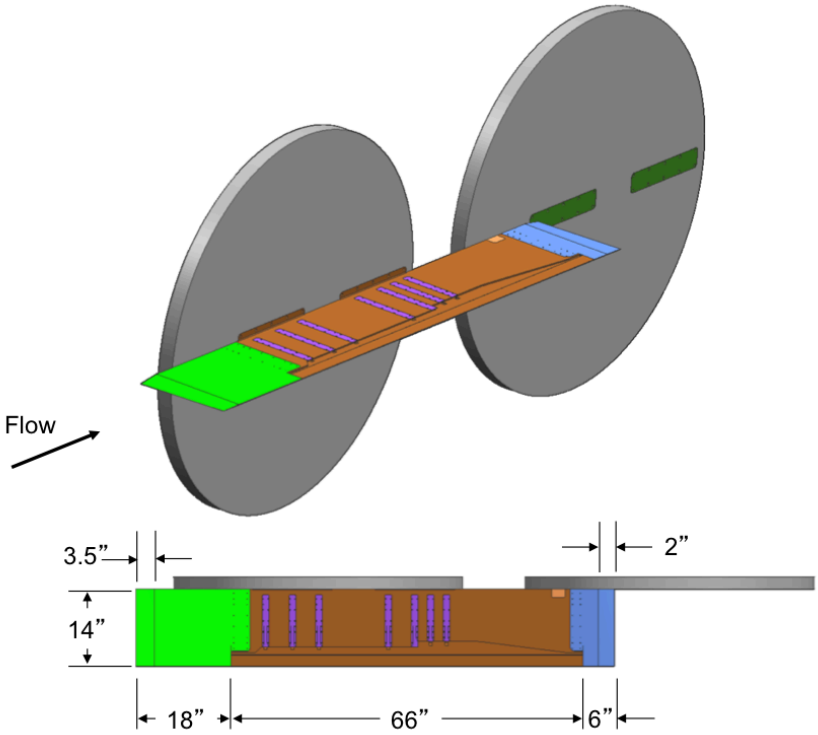

Figure 5.2. Isometric and top view of the RF1 rail design

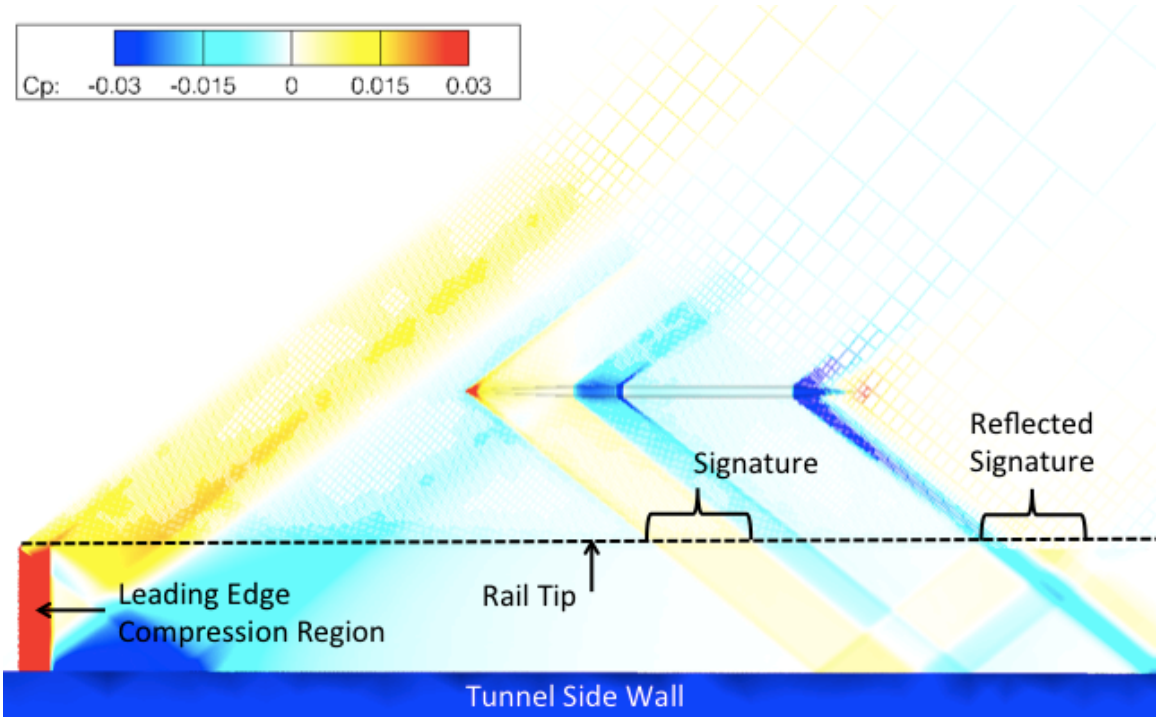

Figure 5.3. CART3D-AERO computation of the Seeb-ALR, RF 1.0 rail, and wall. M=1.6, α=0°, h=17.68 inches

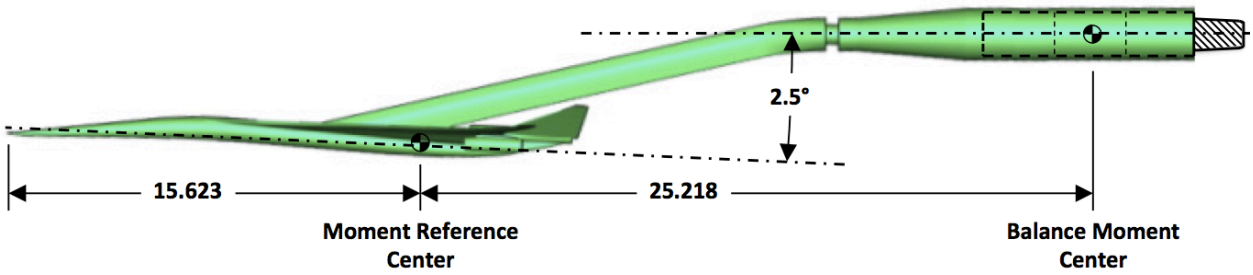

Figure 5.4. Lockheed 1021 with balance mounted aft of blade strut (dimensions in inches)

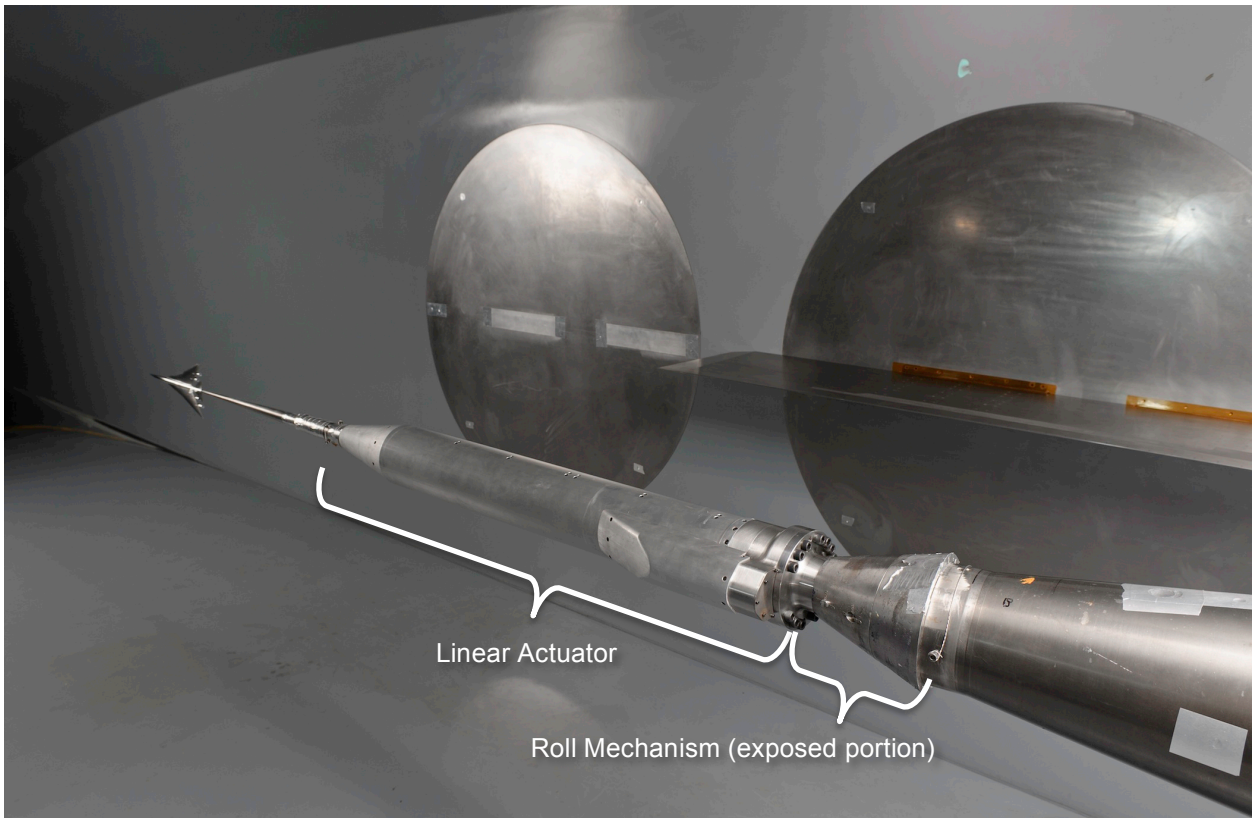

Figure 5.5. View of linear actuator and roll mechanism in 9x7 wind tunnel, with Ames LBWT model mounted on sting and RF1 pressure rail in background (ACD10-0230-006.jpg)

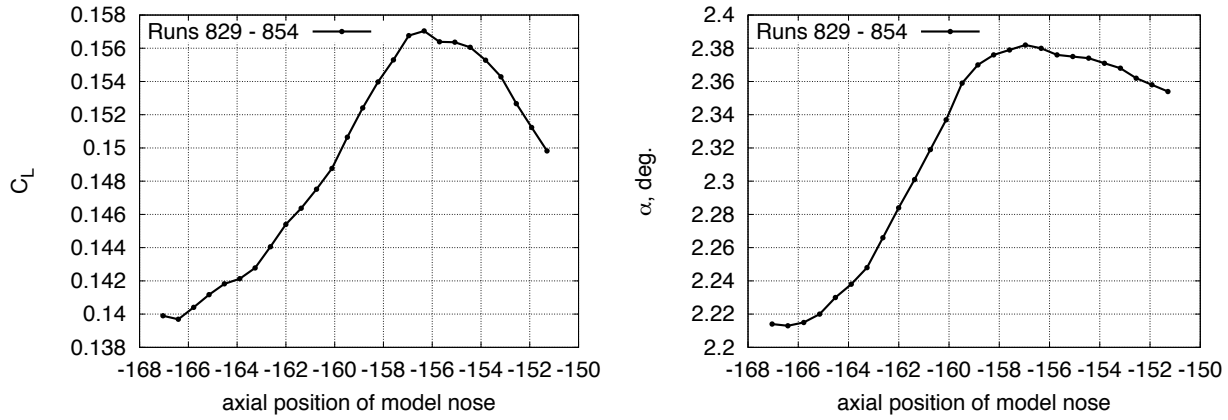

(a) Lift coefficient variation (b) Angle-of-attack variation

Figure 6.1. Lift coefficient variation and angle of attack variation over 16 in traverse of the N+2 model, *M*=1.6

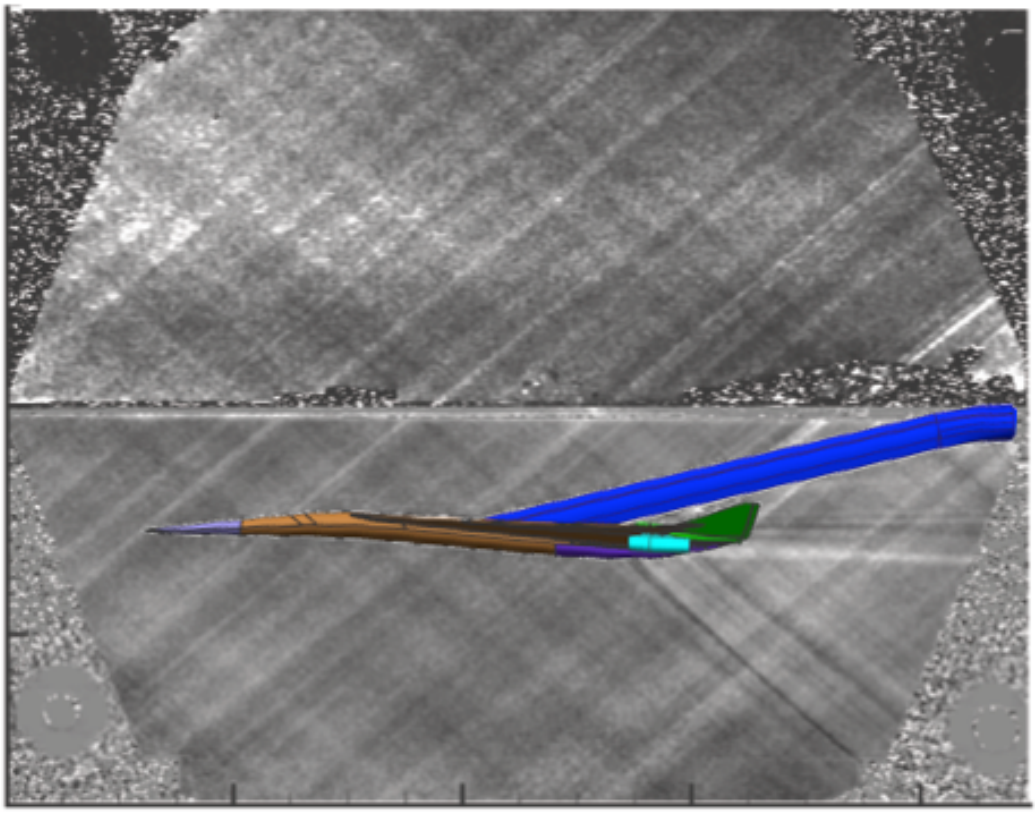

(a) LM 1021 model with blade mount, and RF1 rail (centered vertically), colored model superimposed

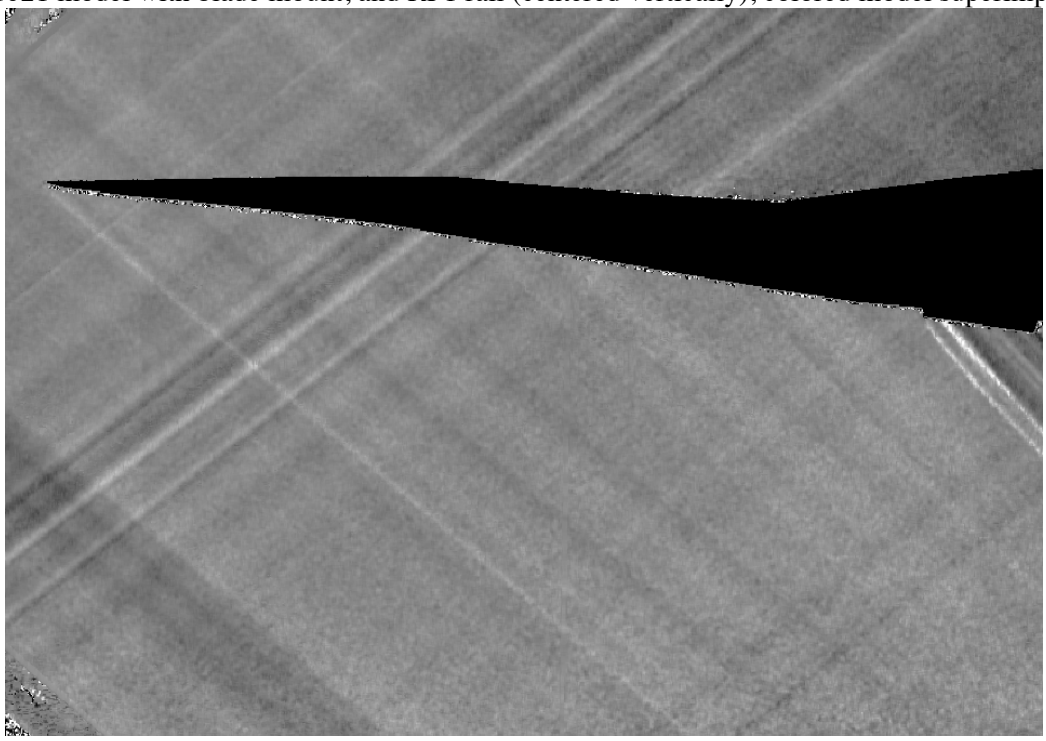

(b) Forward portion of LM 1021 model at 6.9° angle of attack and different tunnel position

Figure 6.2. Retroreflective background oriented Schlieren images of the Lockheed 1021 model with blade mount in 9x7 wind tunnel, M=1.6

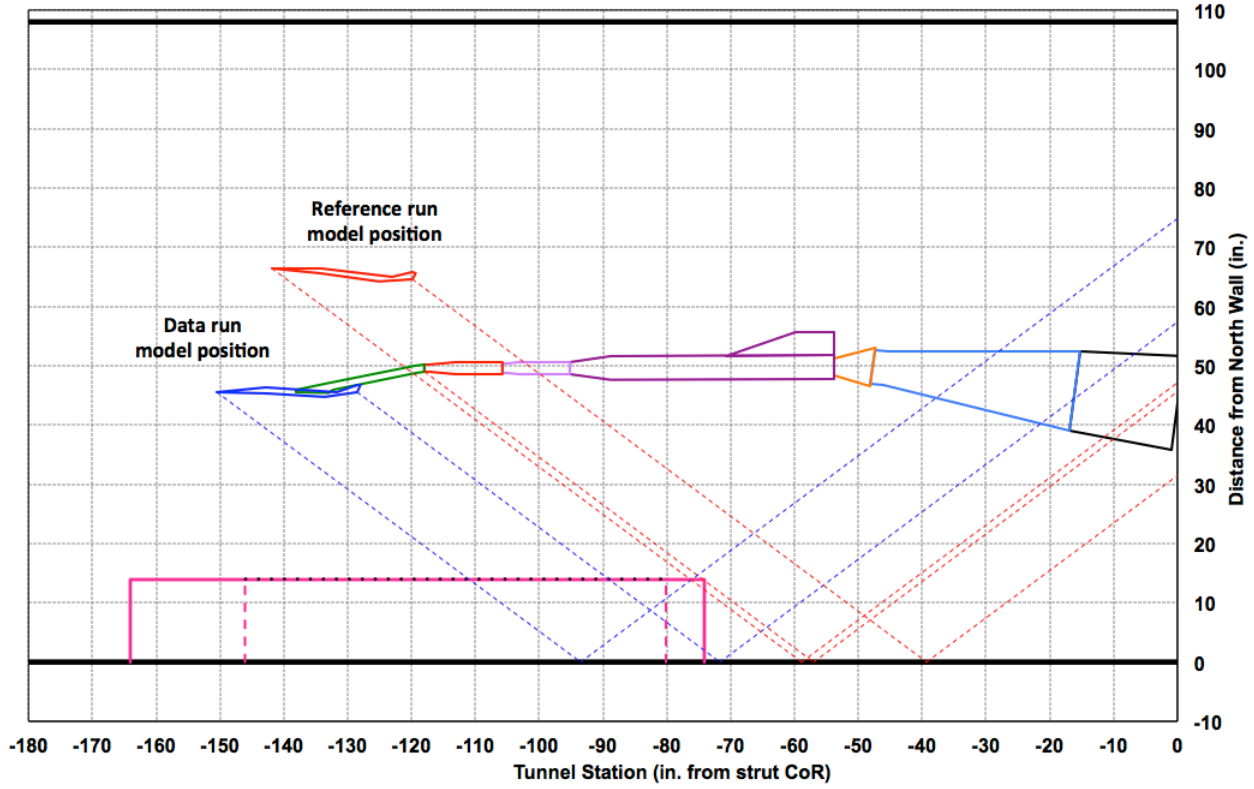

Figure 6.3. 9x7 wind tunnel layout showing model positions for reference and data runs relative to RF1 rail and tunnel walls.

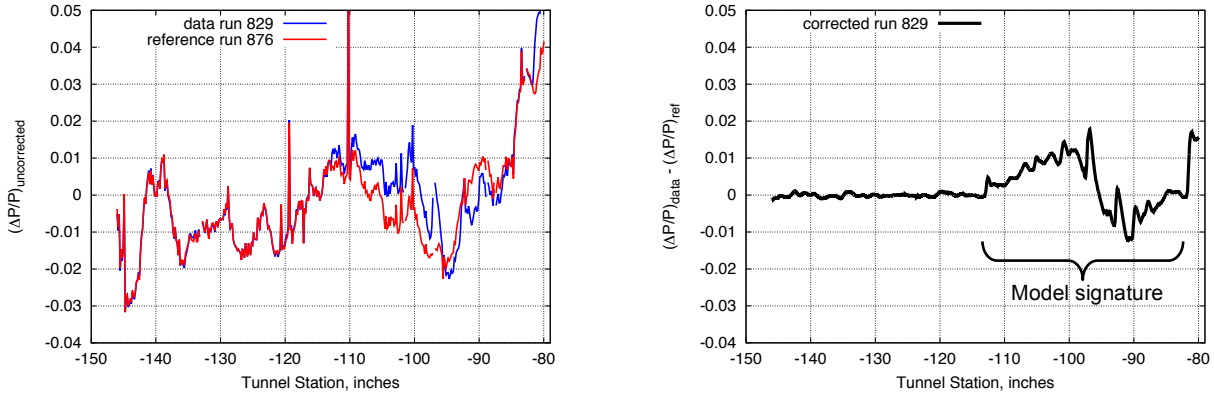

(a) Uncorrected pressure signatures for data and reference runs

(b) Resultant pressure signature from difference between data and reference runs

Figure 6.4. Differencing technique to obtain corrected pressure signature coefficient with rail

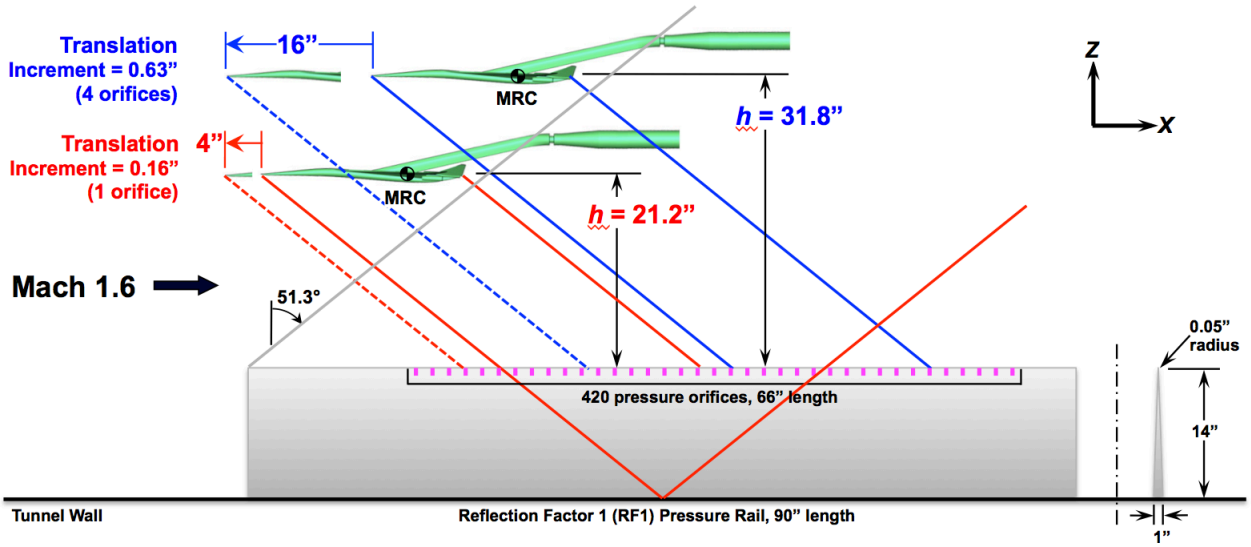

Figure 6.5. Model and rail layout for translation series at test altitudes of 21.2 and 31.8 inches for Mach 1.6 flow

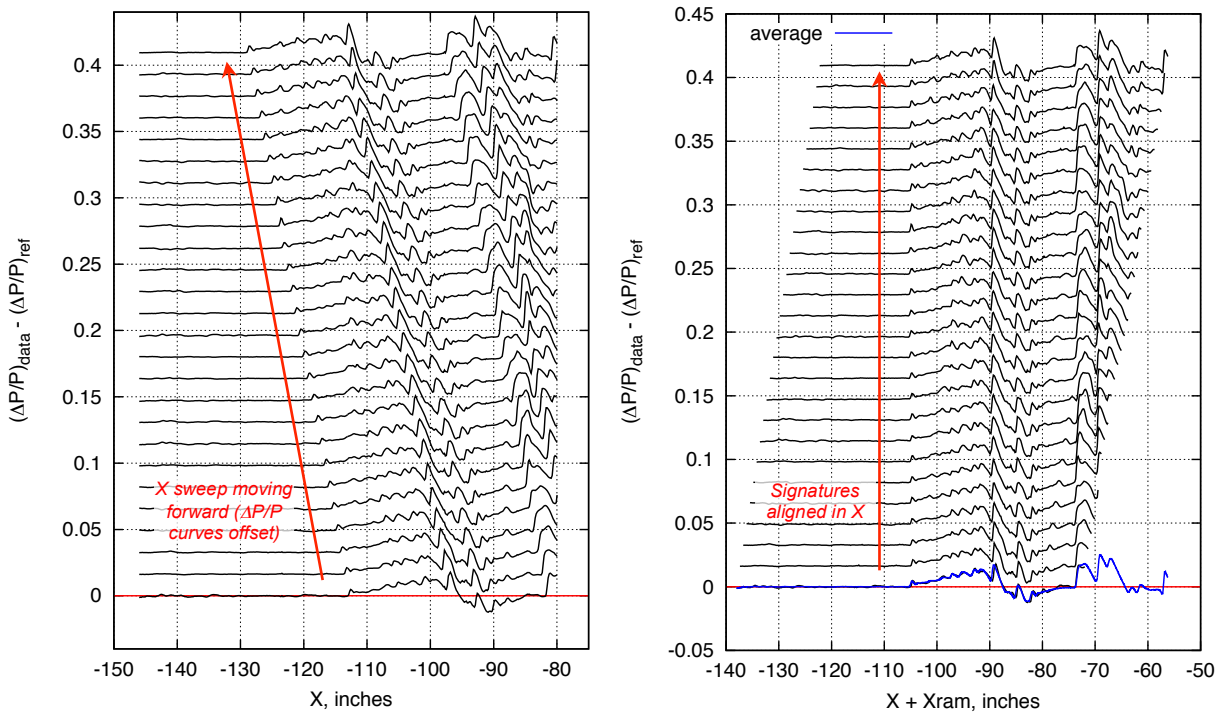

(a) Non-aligned waterfall plot (b) Aligned waterfall plot with average

Figure 6.6. Waterfall plots of pressure signatures for run series 829_854-876 translated over a 16-inch axial traverse, M=1.6, h=31.33 inches.

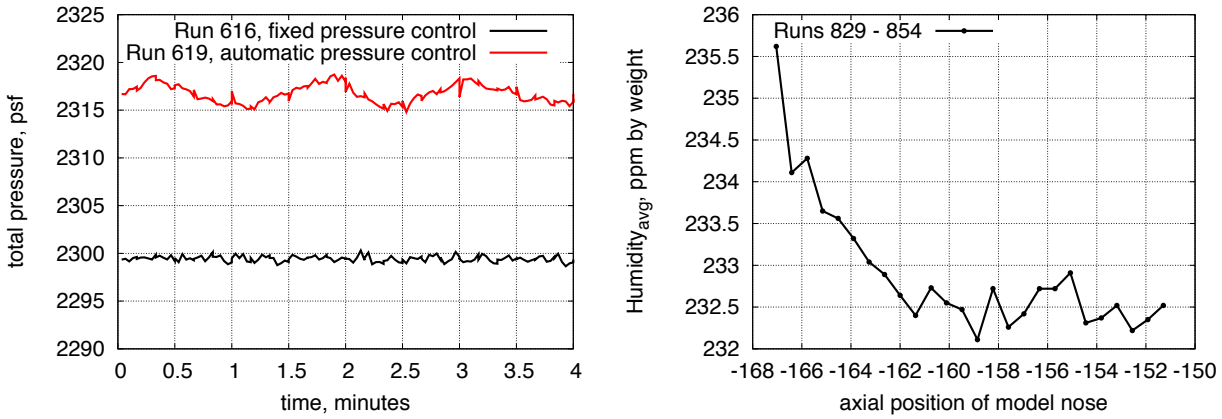

a). P_T time history with fixed or auto control b) Humidity variation within a run series

Figure 6.7. Wind tunnel total pressure and humidity time histories

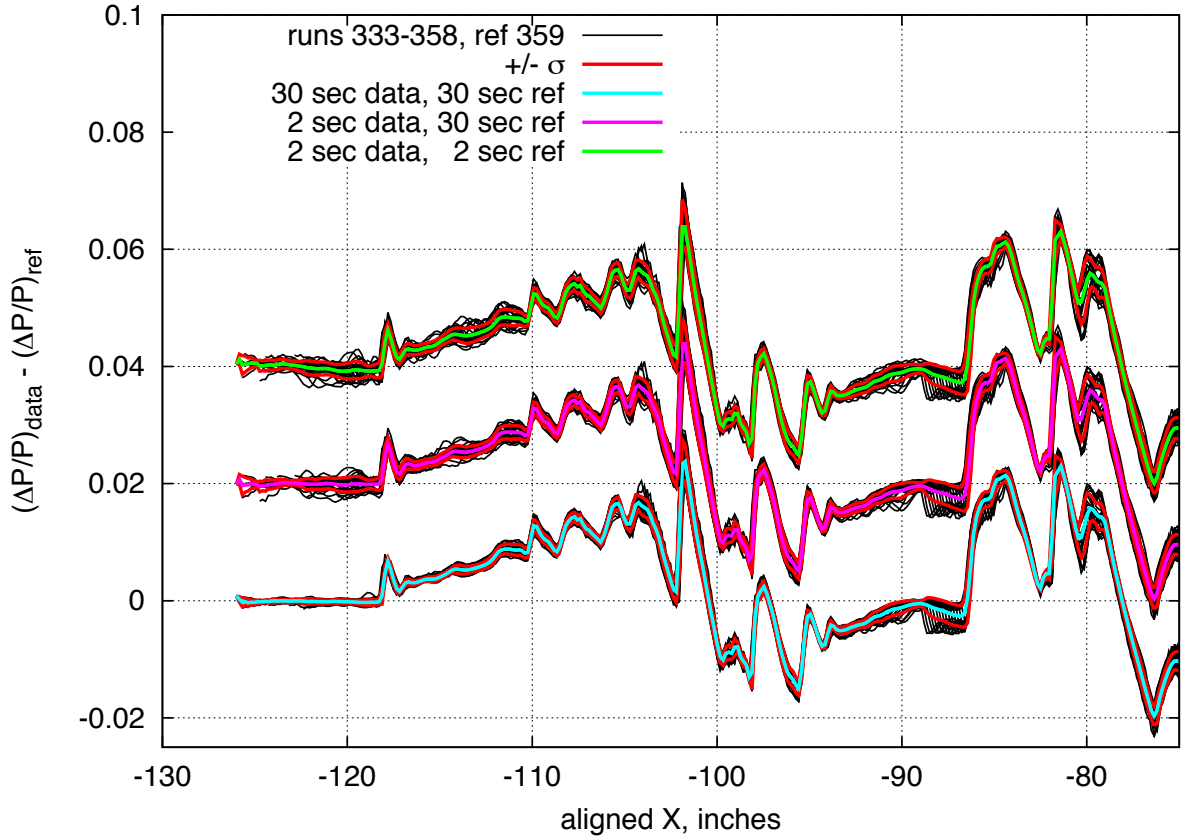

Figure 6.8. Aligned pressure signatures for runs 333-358, ref 359 with 30-second and 2-second duration data. Plots offset vertically by 0.02

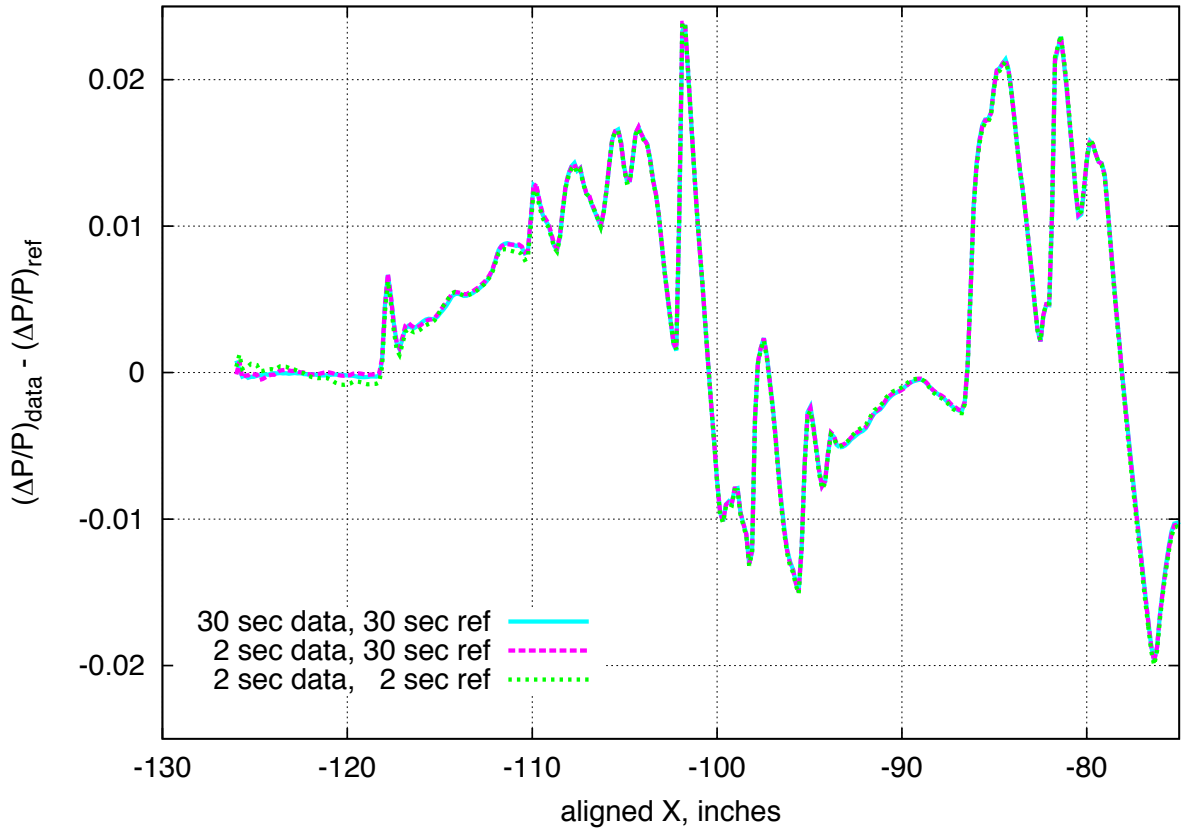

Figure 6.9. Averaged experimental pressure signatures comparing 30- and 2- second sampling time durations

***X_ram*, in**	***h*, in**	***h/L***
12.00 [-0.00 : 24.00]	20.59 [20.54 : 20.65]	1.16 [1.16 : 1.17]
***α*, deg**	***β*, deg**	***ϕ*, deg**
-0.29 [-0.29 : -0.28]	0.17 [0.13 : 0.22]	0.47 [0.17 : 0.82]
CL	***CD***	***CM***
-0.012 [-0.020 : -0.006]	0.09645 [0.07791 : 0.12098]	0.185 [0.101 : 0.302]

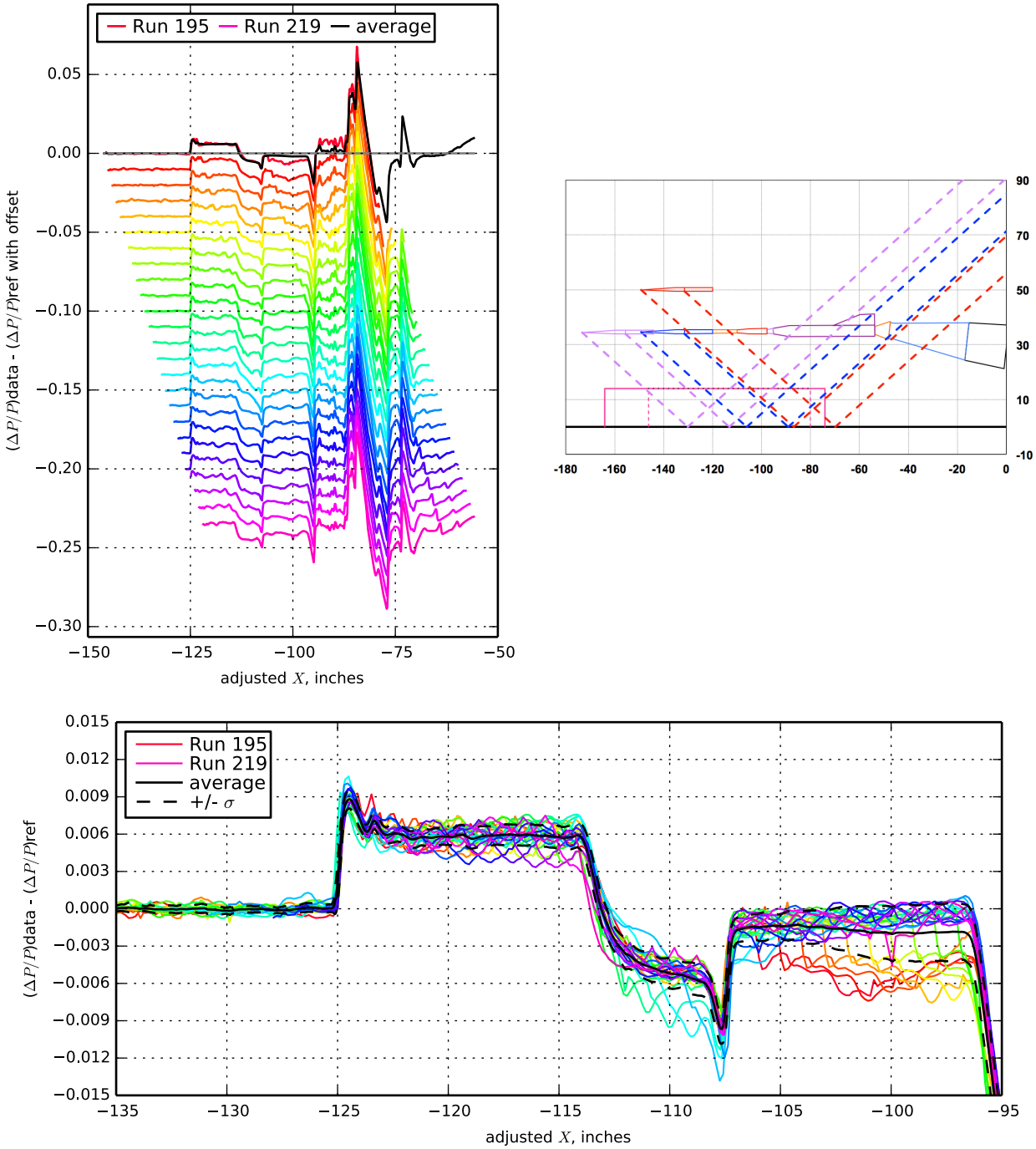

Figure 7.1. Seeb-ALR, Runs 195-219:221, Mach 1.6, Duration 30 sec, Re 6.42x10^6, T -79.51° F, PT 2300.39 psf, PT-Ref 0.07 psf, H 336.01 ppm, H-Ref -2.15 ppm

***X_ram*, in**	***h*, in**	***h/L***
12.46 [-0.00 : 24.00]	20.62 [20.59 : 20.67]	1.17 [1.16 : 1.17]
***α*, deg**	***β*, deg**	***ϕ*, deg**
-0.27 [-0.28 : -0.26]	0.17 [0.13 : 0.22]	0.46 [0.14 : 0.81]
CL	***CD***	***CM***
-0.002 [-0.006 : 0.006]	0.08684 [0.08355 : 0.09163]	0.031 [-0.073 : 0.087]

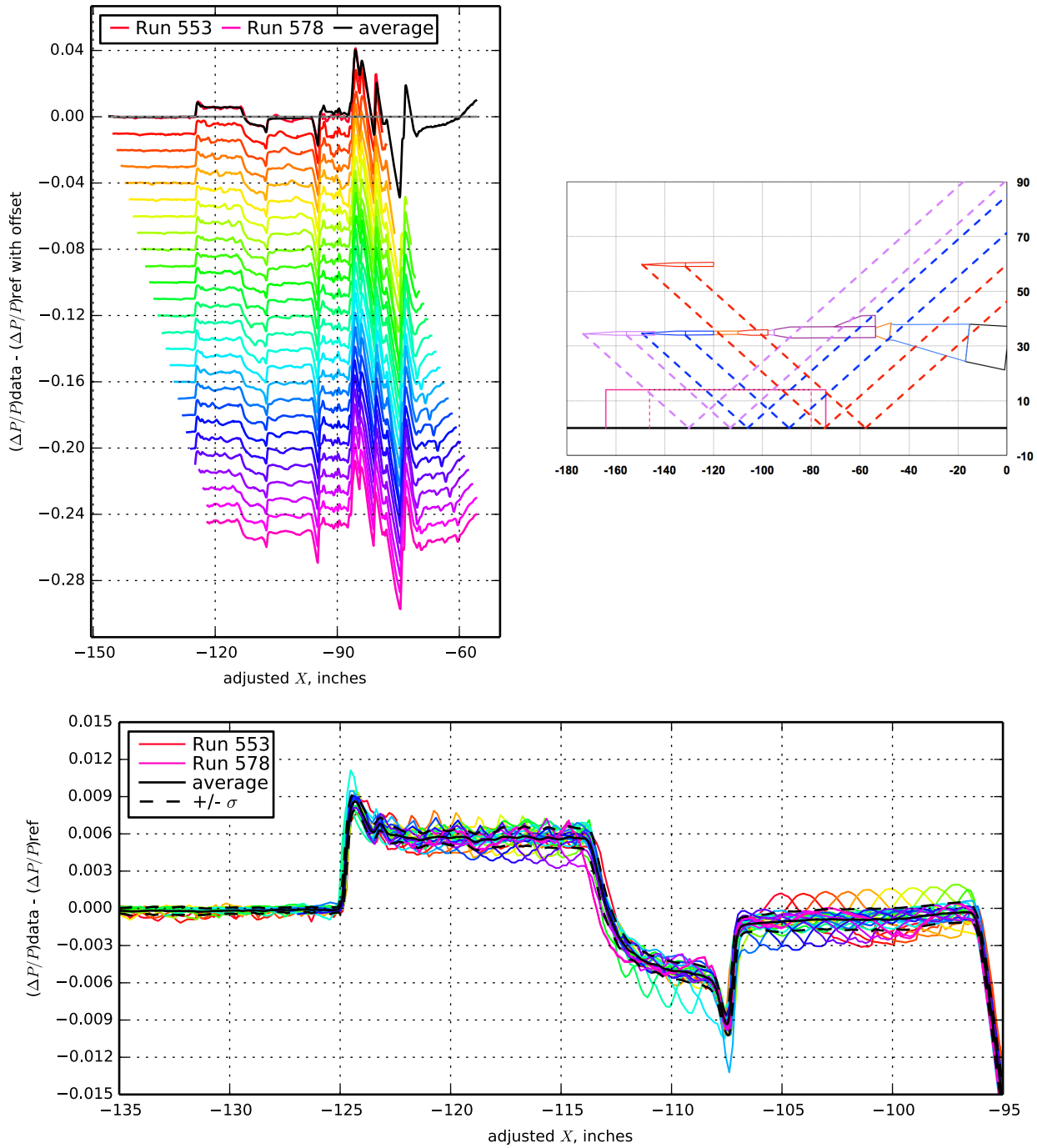

Figure 7.2. Seeb-ALR, Runs 553-578:580, Mach 1.6, Duration 90 sec, Re 6.43x10^6, T -81.62° F, PT 2298.92 psf, PT-Ref 0.37 psf, H 255.30 ppm [254.51 : 257.41], H-Ref 1.45 ppm

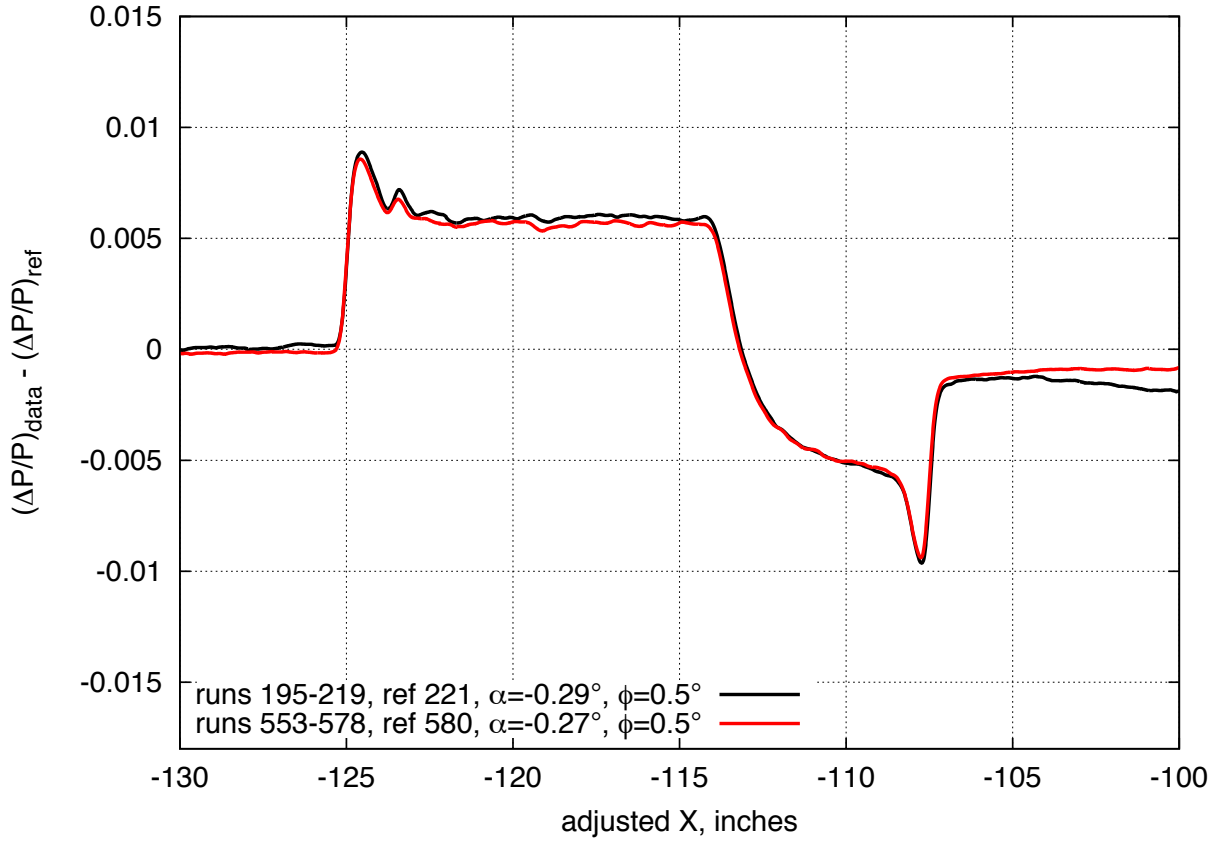

Figure 7.3. Comparison of near-repeat run series pressure signatures for the Seeb-ALR model, on-track, M=1.6, h=20.6 inches

***X_ram*, in**	***h*, in**	***h/L***
12.46 [-0.00 : 24.00]	31.22 [31.17 : 31.27]	1.77 [1.76 : 1.77]
***α*, deg**	***β*, deg**	***ϕ*, deg**
-0.27 [-0.28 : -0.27]	0.17 [0.13 : 0.21]	0.30 [0.09 : 0.53]
CL	***CD***	***CM***
0.001 [-0.006 : 0.008]	0.08390 [0.07944 : 0.08955]	-0.015 [-0.120 : 0.093]

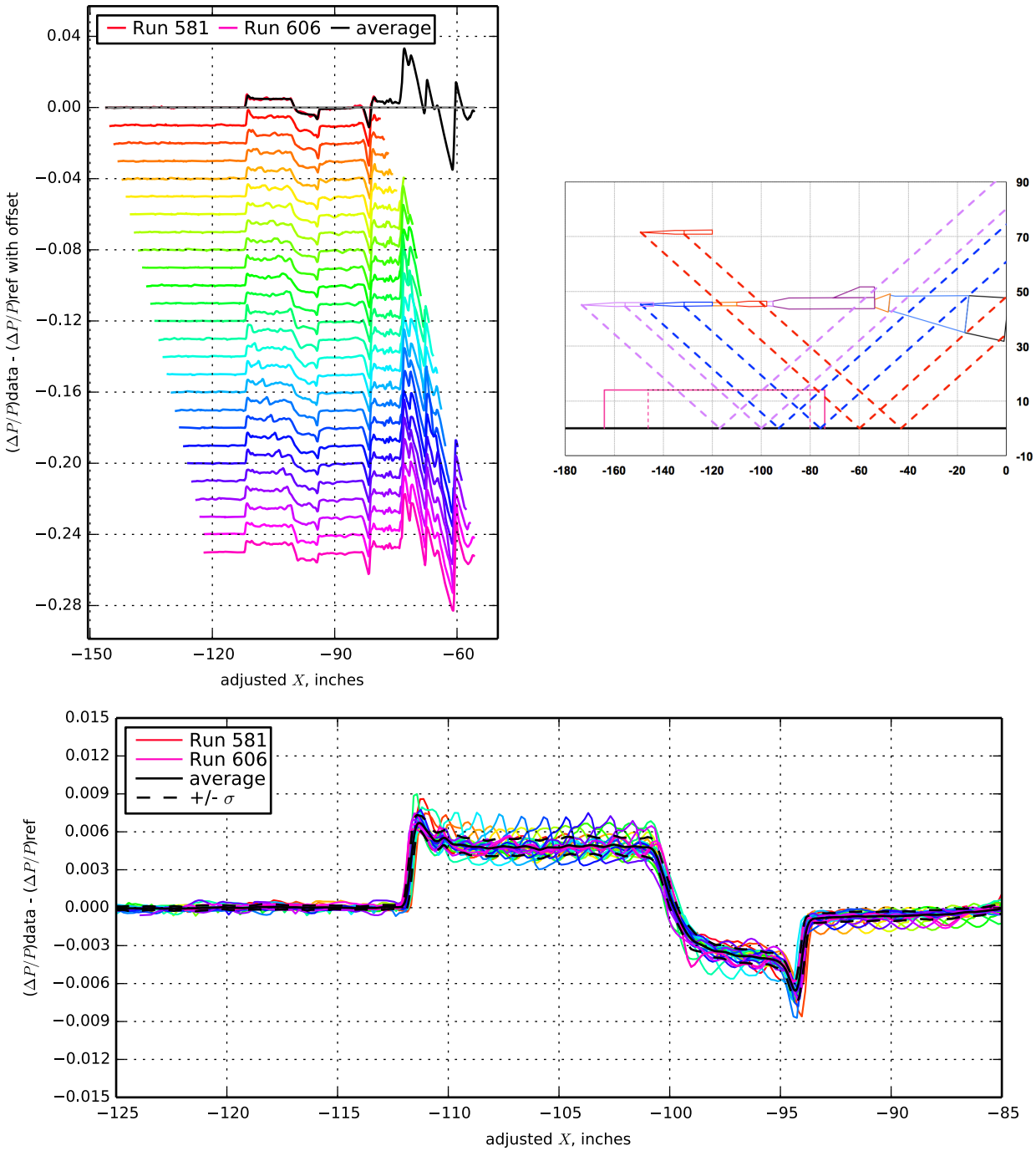

Figure 7.4. Seeb-ALR, Runs 581-606:608, Mach 1.6, Duration 90 sec, Re 6.42x10^6, T -79.83° F, PT 2298.11 psf, PT-Ref -0.89 psf, H 252.05 ppm [250.87 : 253.68], H-Ref -0.09 ppm

***X_ram*, in**	***h*, in**	***h/L***
21.97 [20.00 : 23.94]	20.69 [20.67 : 20.72]	0.92 [0.92 : 0.93]
***α*, deg**	***β*, deg**	***ϕ*, deg**
2.09 [2.03 : 2.18]	-0.12 [-0.19 : -0.09]	-2.37 [-2.42 : -2.32]
CL	***CD***	***CM***
0.143 [0.138 : 0.149]	0.01952 [0.01928 : 0.02002]	-0.113 [-0.120 : -0.104]

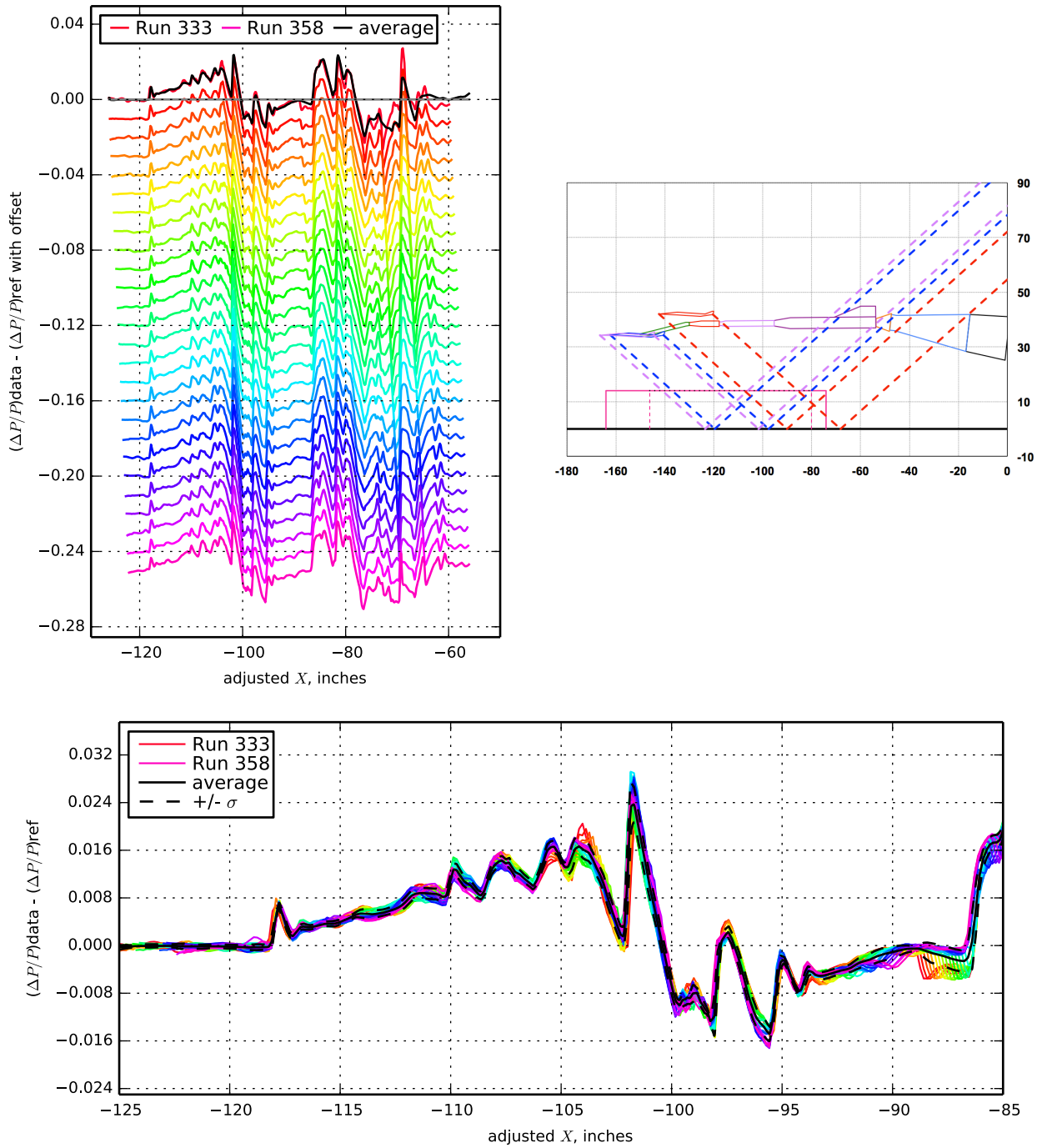

Figure 7.5. 1021 model with blade strut, Runs 333-358:359, Mach 1.6, Duration 30 sec, Re 8.09x10^6, T -78.02° F, PT 2299.62 psf, PT-Ref -0.07 psf, H 202.26 ppm [200.36 : 204.07], H-Ref -2.19 ppm

***X_ram*, in**	***h*, in**	***h/L***
21.97 [20.00 : 23.94]	20.61 [20.60 : 20.64]	0.92 [0.92 : 0.92]
***α*, deg**	***β*, deg**	***ϕ*, deg**
1.95 [1.90 : 2.04]	-0.41 [-0.48 : -0.38]	-4.21 [-4.23 : -4.18]
CL	***CD***	***CM***
0.136 [0.131 : 0.144]	0.02223 [0.01903 : 0.02585]	-0.108 [-0.120 : -0.095]

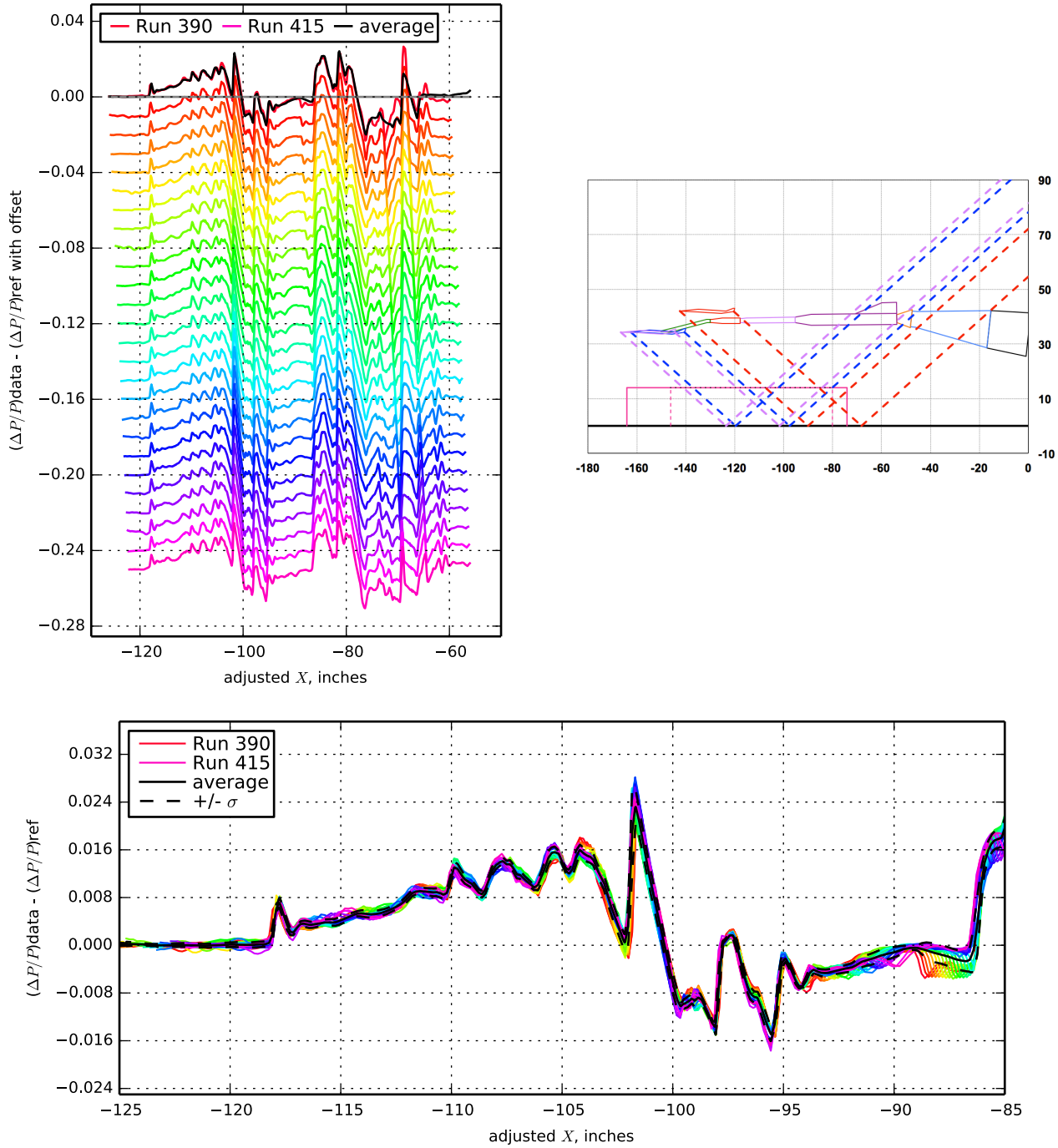

Figure 7.6. 1021 model with blade strut, Runs 390-415:387, Mach 1.6, Duration 30 sec, Re 8.06x10^6, T -76.95° F, PT 2300.19 psf, PT-Ref -0.36 psf, H 212.86 ppm [211.89 : 214.33], H-Ref 0.55 ppm

***X_ram*, in**	***h*, in**	***h/L***
21.97 [20.00 : 23.94]	20.75 [20.73 : 20.78]	0.93 [0.93 : 0.93]
***α*, deg**	***β*, deg**	***ϕ*, deg**
2.10 [2.05 : 2.19]	0.19 [0.12 : 0.24]	-0.75 [-1.75 : -0.47]
CL	***CD***	***CM***
0.147 [0.142 : 0.152]	0.02201 [0.02170 : 0.02273]	-0.122 [-0.128 : -0.113]

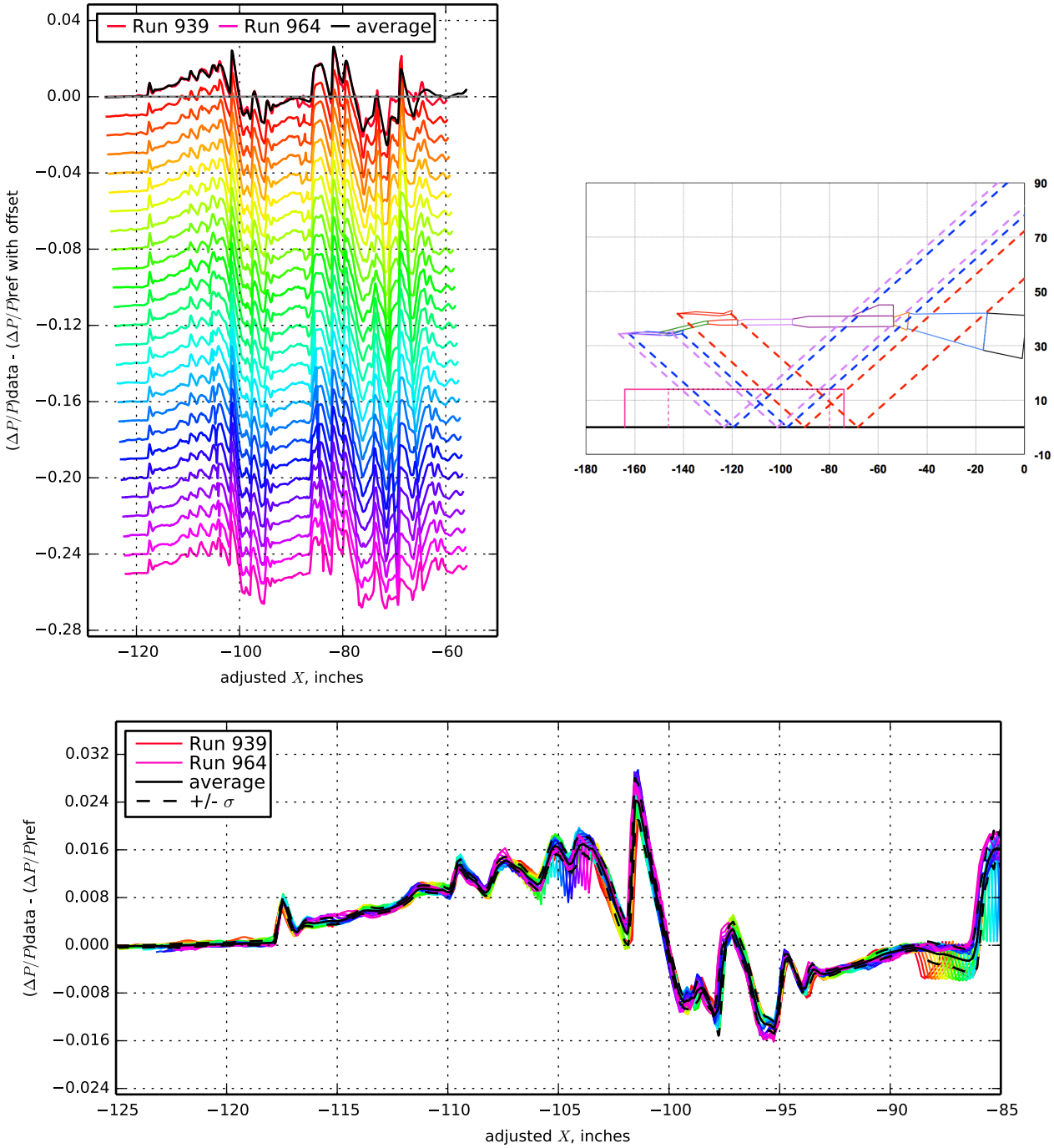

Figure 7.7. 1021 model with blade strut, Runs 939-964:938, Mach 1.6, Duration 90 sec, Re 8.16x10^6, T -81.47° F, PT 2298.83 psf, PT-Ref -0.41 psf, H 232.53 ppm [230.52 : 236.53], H-Ref -1.21 ppm

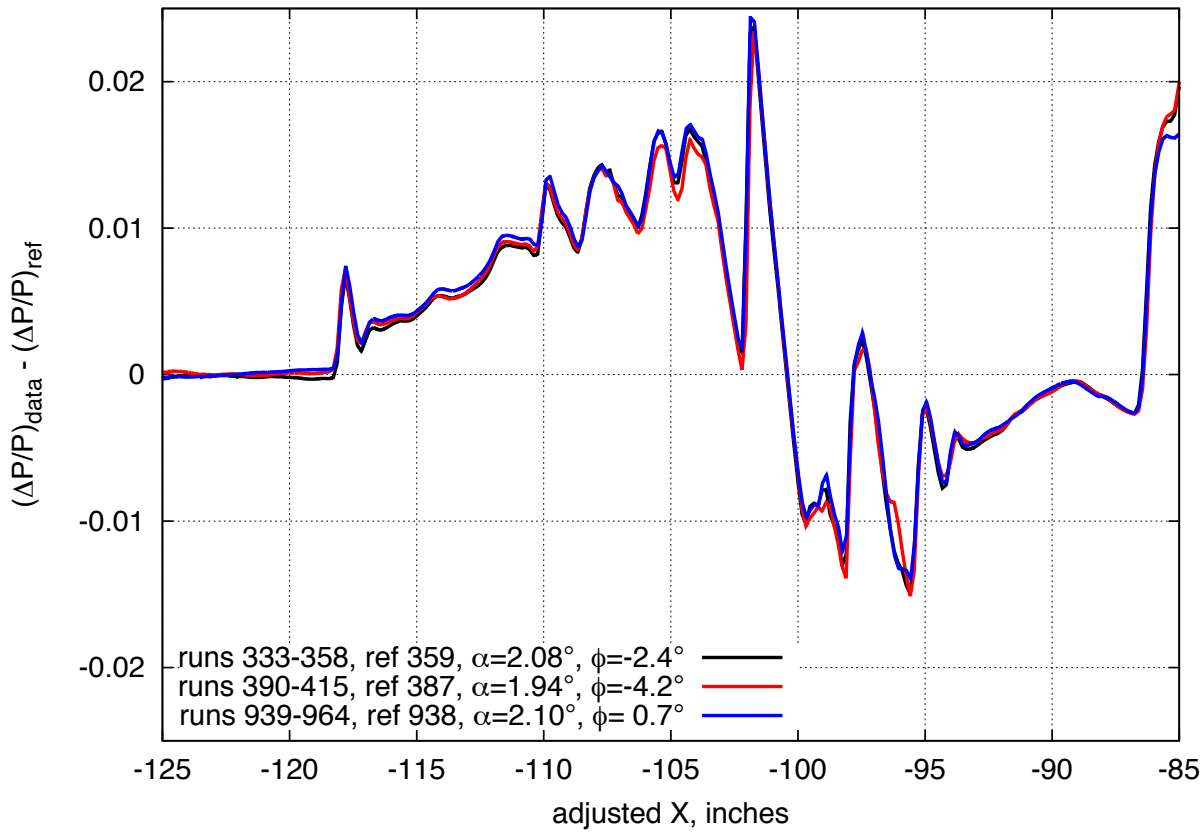

Figure 7.8 Comparison of near-repeat run series pressure signatures for the 1021 model with all nacelles on blade strut, below the design angle-of-attack conditions, on-track, M=1.6, h=20.7 inches

***X_ram*, in**	***h*, in**	***h/L***
21.97 [20.00 : 23.94]	20.71 [20.68 : 20.75]	0.92 [0.92 : 0.93]
***α*, deg**	***β*, deg**	***ϕ*, deg**
2.29 [2.23 : 2.38]	0.20 [0.12 : 0.23]	-0.53 [-1.60 : -0.33]
CL	***CD***	***CM***
0.148 [0.145 : 0.154]	0.01690 [0.01602 : 0.01805]	-0.104 [-0.110 : -0.098]

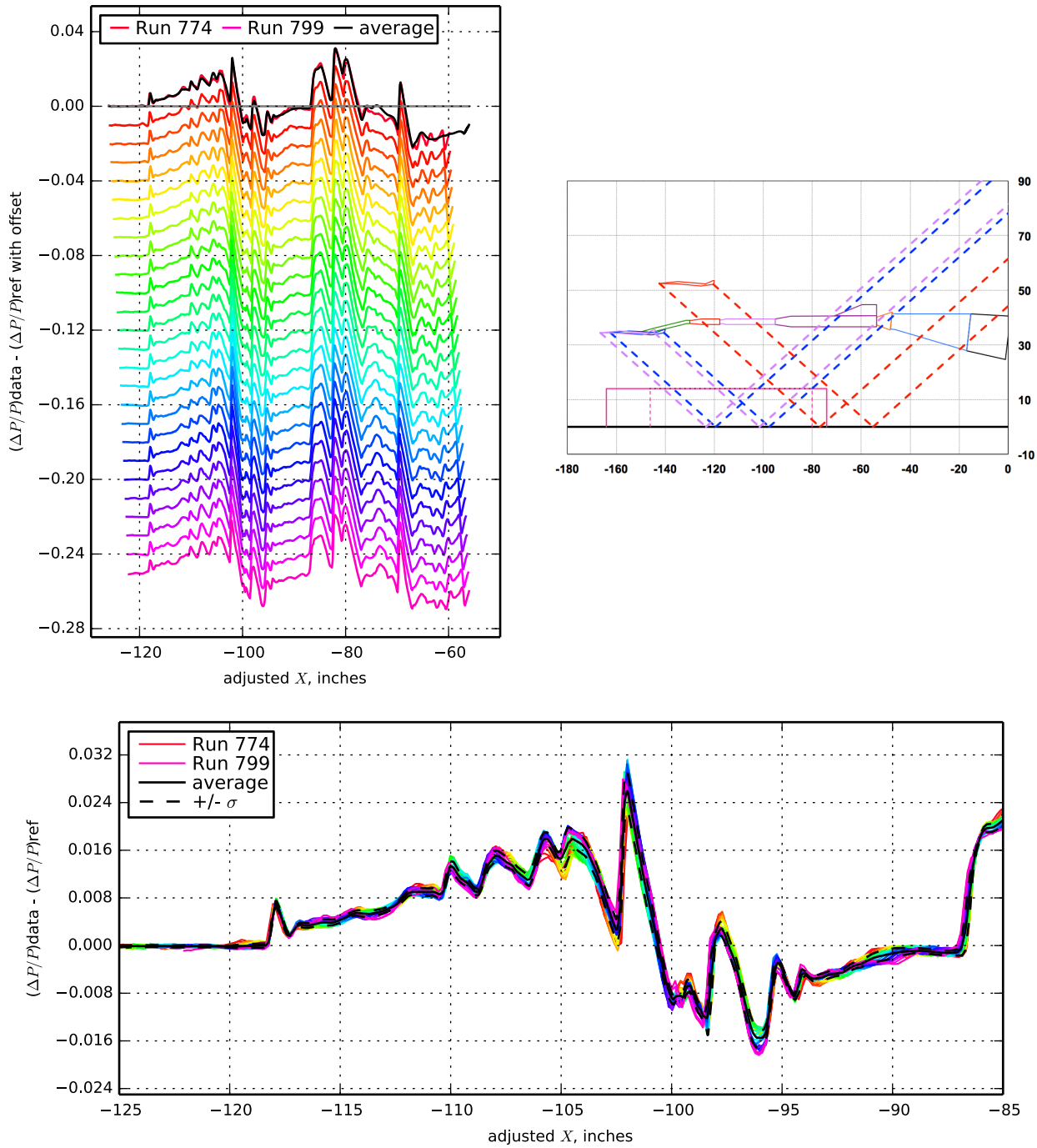

Figure 7.9. 1021 model with blade strut, Runs 774-799:828, Mach 1.6, Duration 90 sec, Re 8.16x10^6, T -80.36° F, PT 2298.76 psf, PT-Ref -0.21 psf, H 235.3 ppm [234.0 : 236.4], H-Ref 3.78 ppm

***X_ram*, in**	***h*, in**	***h/L***
21.98 [20.00 : 23.94]	20.79 [20.75 : 20.83]	0.93 [0.93 : 0.93]
***α*, deg**	***β*, deg**	***ϕ*, deg**
2.46 [2.40 : 2.55]	0.16 [0.09 : 0.20]	-0.59 [-0.67 : -0.53]
CL	***CD***	***CM***
0.156 [0.151 : 0.163]	0.02097 [0.01856 : 0.02252]	-0.103 [-0.115 : -0.094]

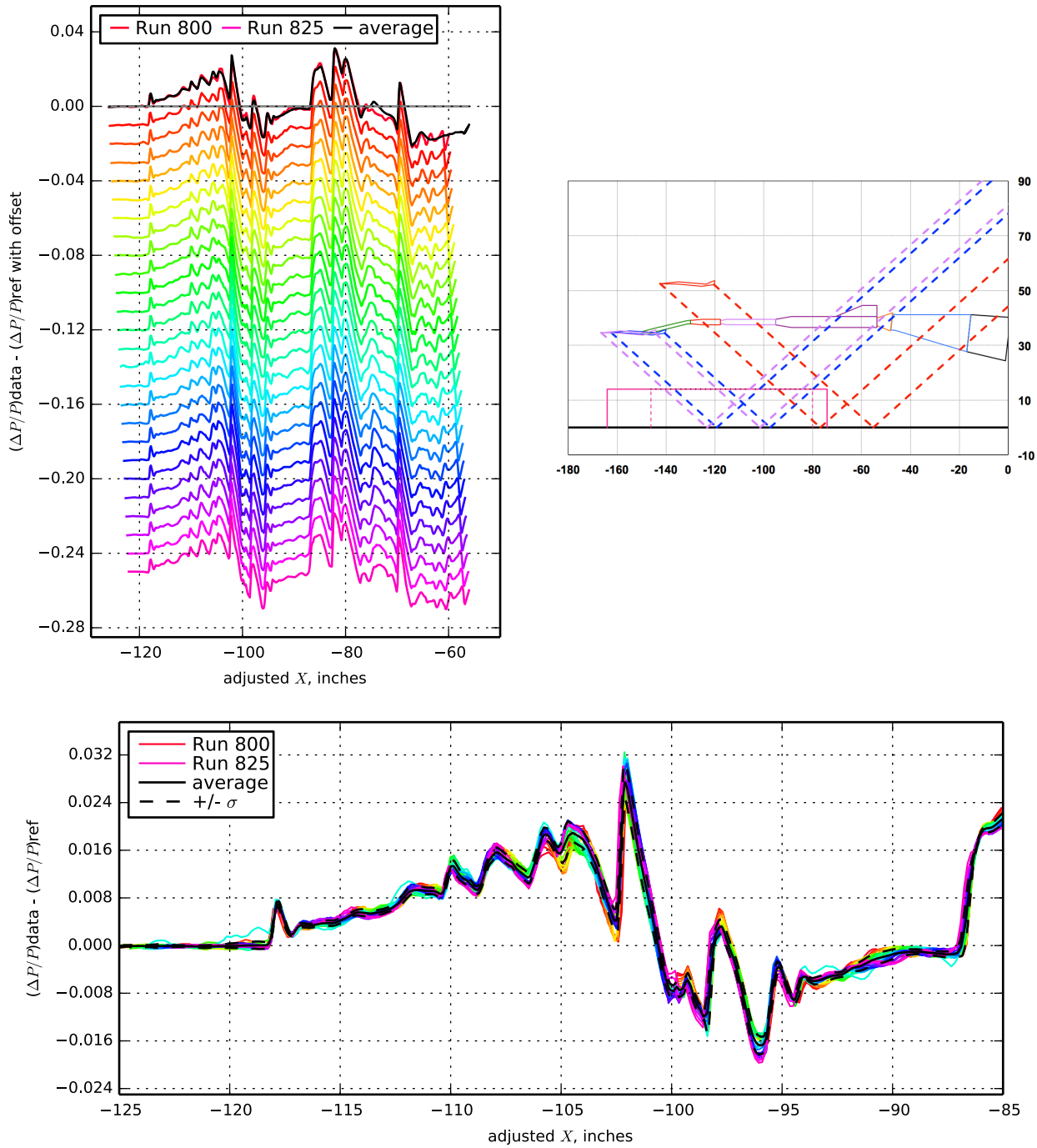

Figure 7.10. 1021 model with blade strut, Runs 800-825:828, Mach 1.6, Duration 90 sec, Re 8.16x10^6, T -80.46° F, PT 2298.66 psf, PT-Ref -0.08 psf, H 238.0 ppm [235.6 : 241.9], H-Ref 6.46 ppm

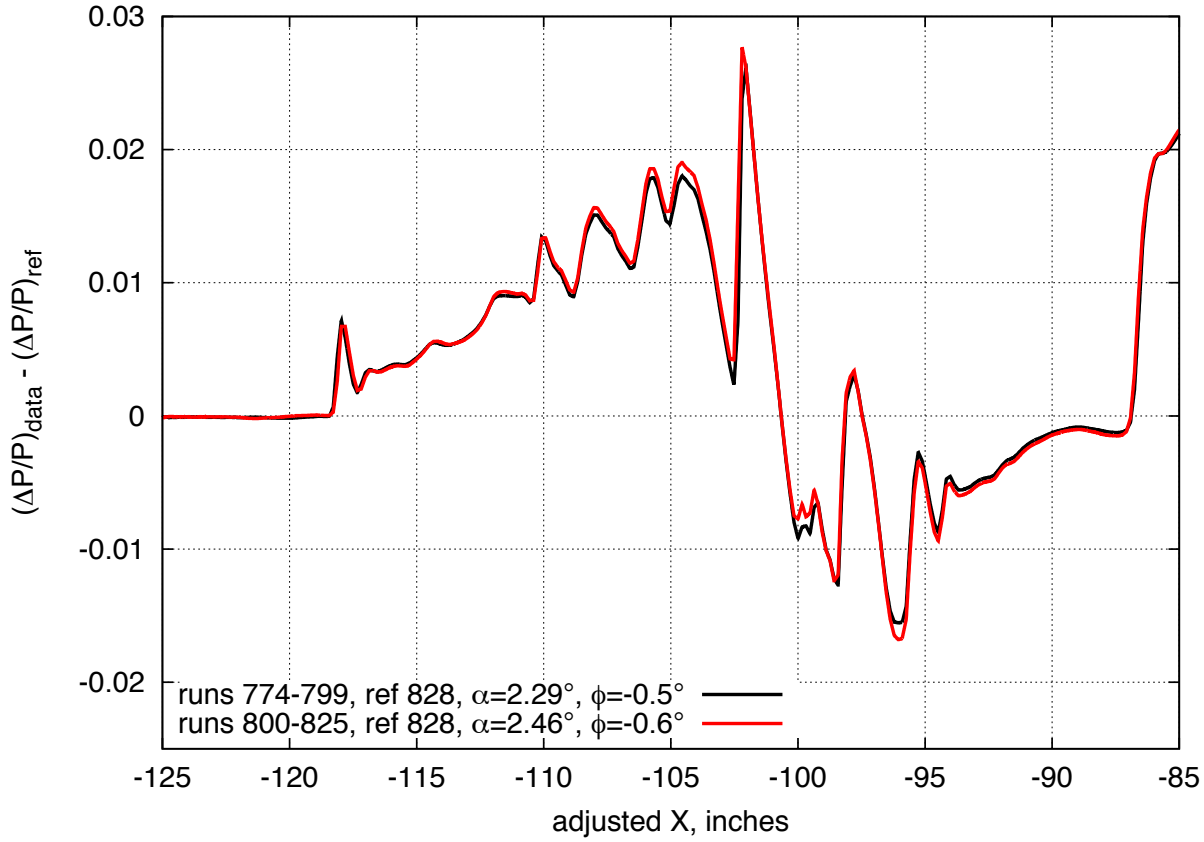

Figure 7.11 Comparison of near-repeat run series pressure signatures for the 1021 model with all nacelles on blade strut, near design angle-of-attack conditions, on-track, M=1.6, h=20.7 inches

***X_ram*, in**	***h*, in**	***h/L***
15.88 [8.00 : 23.75]	31.33 [31.32 : 31.36]	1.40 [1.40 : 1.40]
***α*, deg**	***β*, deg**	***ϕ*, deg**
2.32 [2.21 : 2.38]	-0.41 [-0.59 : -0.17]	-0.57 [-0.69 : -0.43]
CL	***CD***	***CM***
0.149 [0.140 : 0.157]	0.02080 [0.01997 : 0.02171]	-0.099 [-0.110 : -0.083]

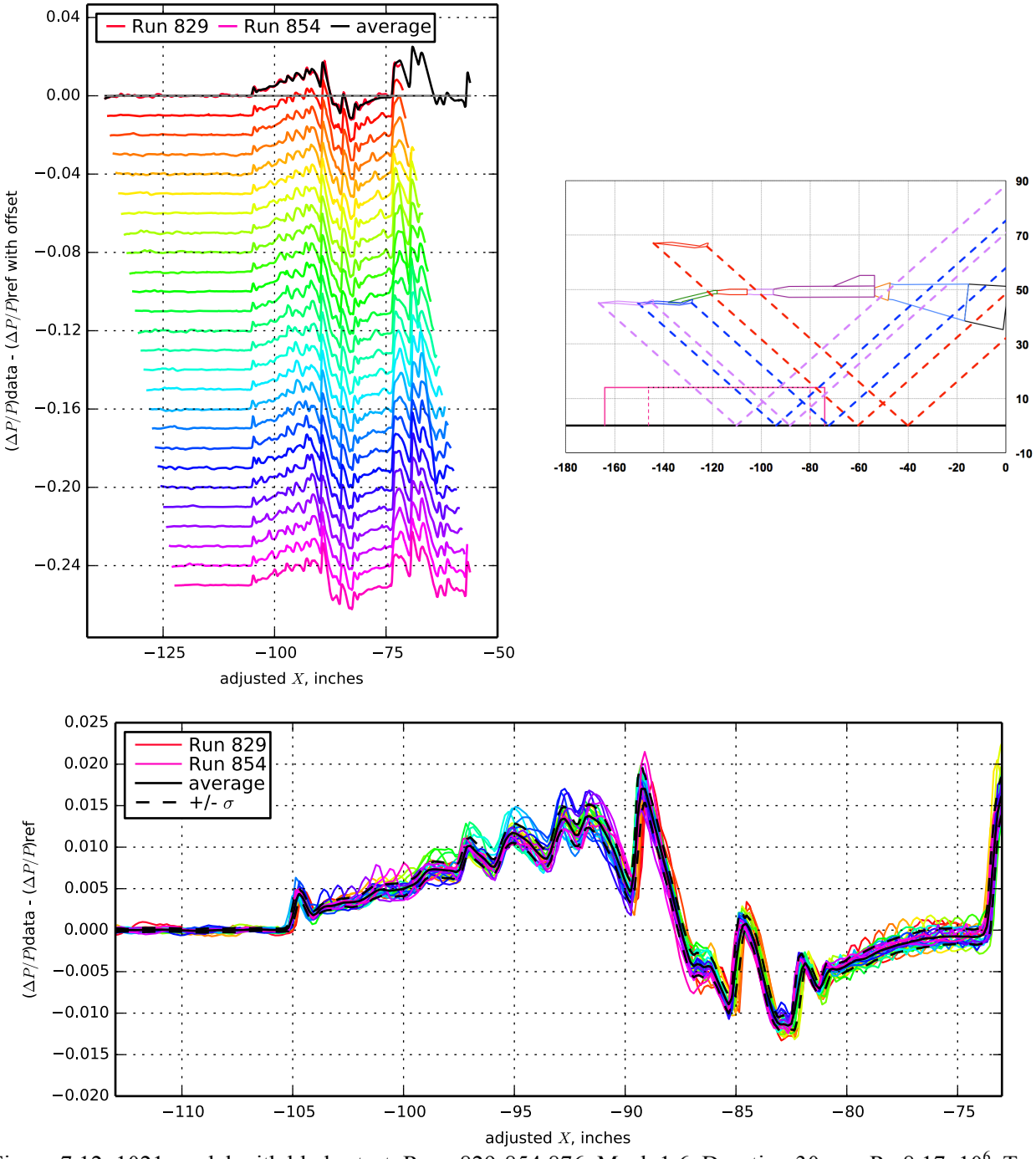

Figure 7.12. 1021 model with blade strut, Runs 829-854:876, Mach 1.6, Duration 30 sec, Re 8.17x10^6, T -80.49° F, PT 2299.36 psf, PT-Ref -0.15 psf, H 232.9 ppm [232.1 : 235.6], H-Ref 0.82 ppm

***X_ram*, in**	***h*, in**	***h/L***
13.99 [8.00 : 19.97]	31.35 [31.31 : 31.38]	1.40 [1.40 : 1.40]
***α*, deg**	***β*, deg**	***ϕ*, deg**
2.51 [2.42 : 2.55]	-0.50 [-0.63 : -0.32]	-0.74 [-0.82 : -0.65]
CL	***CD***	***CM***
0.160 [0.152 : 0.165]	0.02109 [0.02036 : 0.02191]	-0.105 [-0.112 : -0.096]

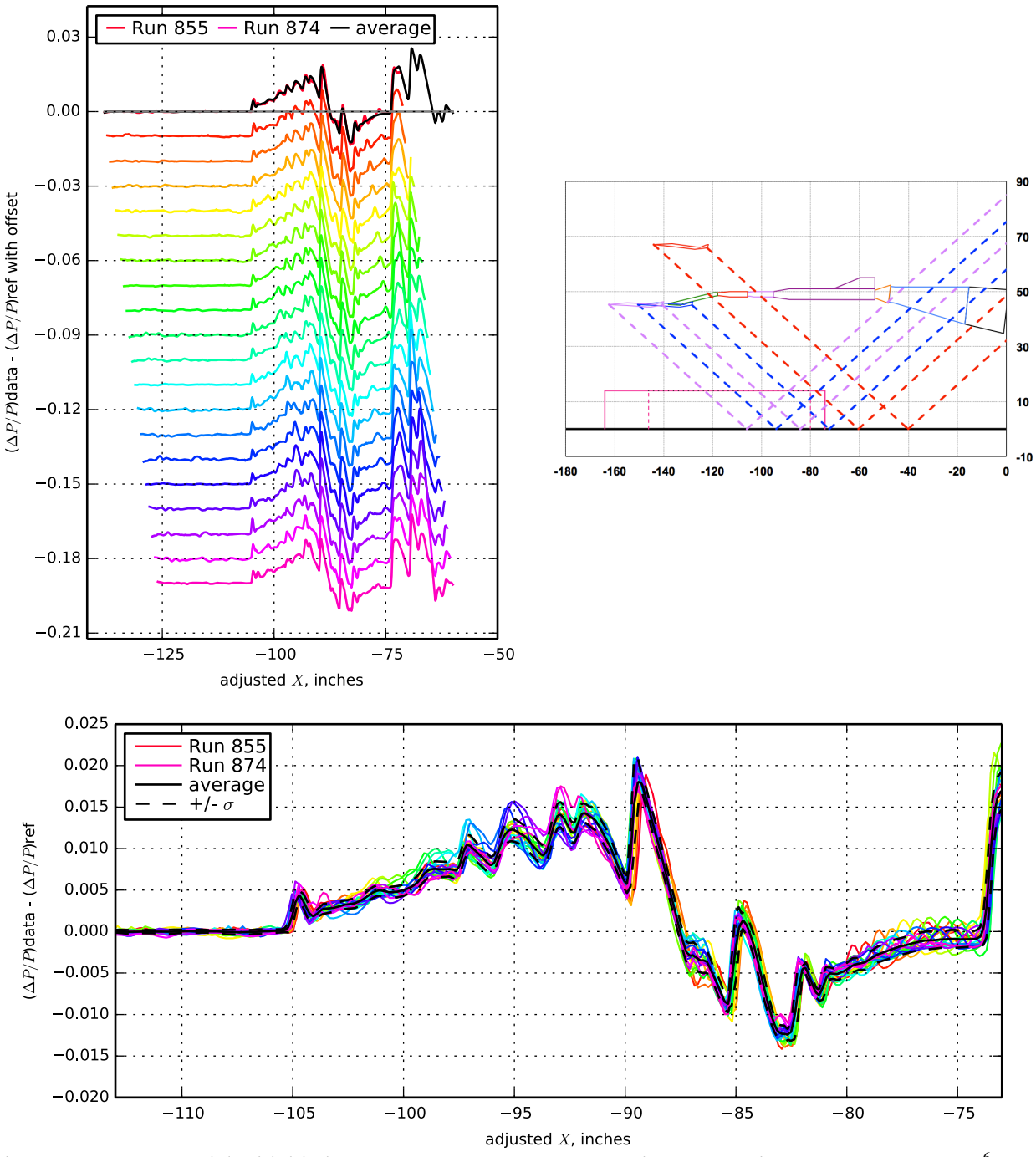

Figure 7.13. 1021 model with blade strut, Runs 855-874:876, Mach 1.6, Duration 30 sec, Re 8.17x10^6, T -80.46° F, PT 2299.70 psf, PT-Ref 0.22 psf, H 233.8 ppm [232.1 : 235.5], H-Ref 1.68 ppm

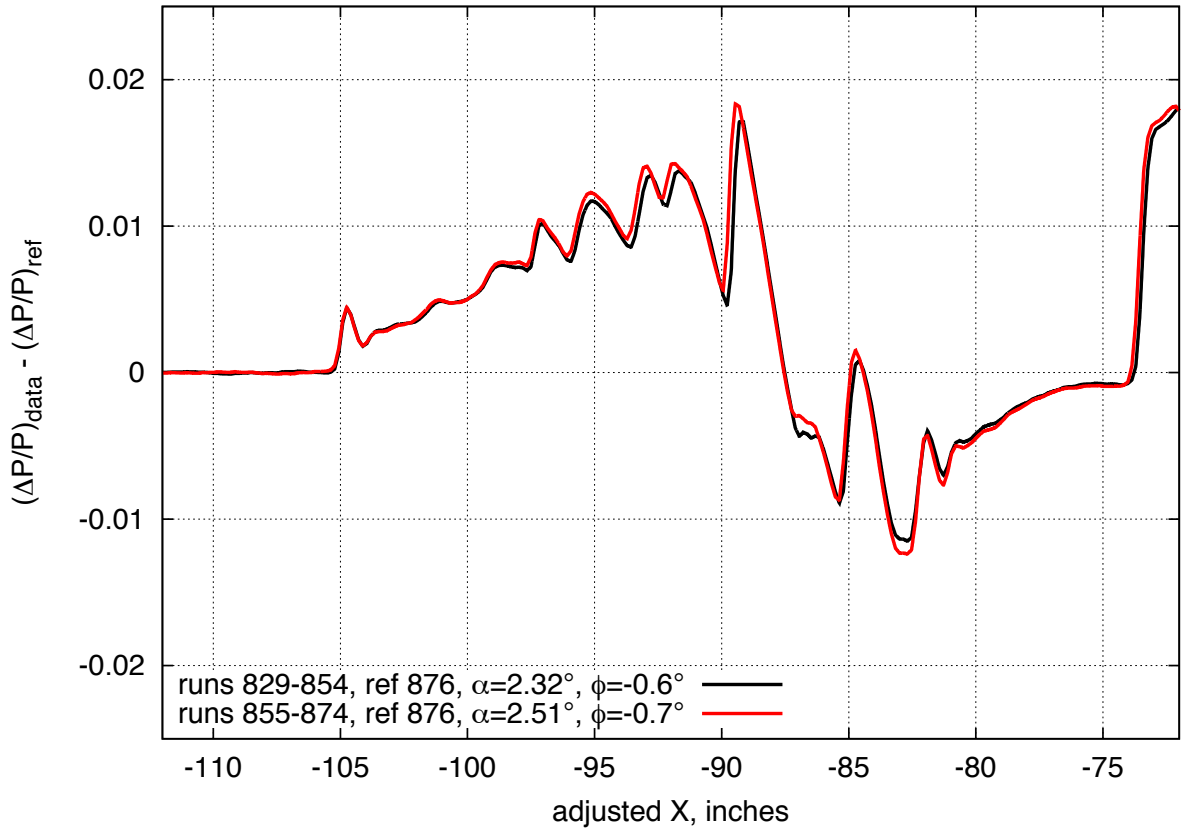

Figure 7.14. Comparison of near-repeat run series pressure signatures for the 1021 model with all nacelles on blade strut, near and above design angle-of-attack conditions, on-track, M=1.6, h=31.4 inches

***X_ram*, in**	***h*, in**	***h/L***
21.97 [20.00 : 23.94]	20.80 [20.76 : 20.83]	0.93 [0.93 : 0.93]
***α*, deg**	***β*, deg**	***ϕ*, deg**
2.47 [2.42 : 2.58]	-0.01 [-0.08 : 0.03]	20.27 [20.23 : 20.30]
CL	***CD***	***CM***
0.155 [0.150 : 0.160]	0.02206 [0.02146 : 0.02258]	-0.106 [-0.114 : -0.099]

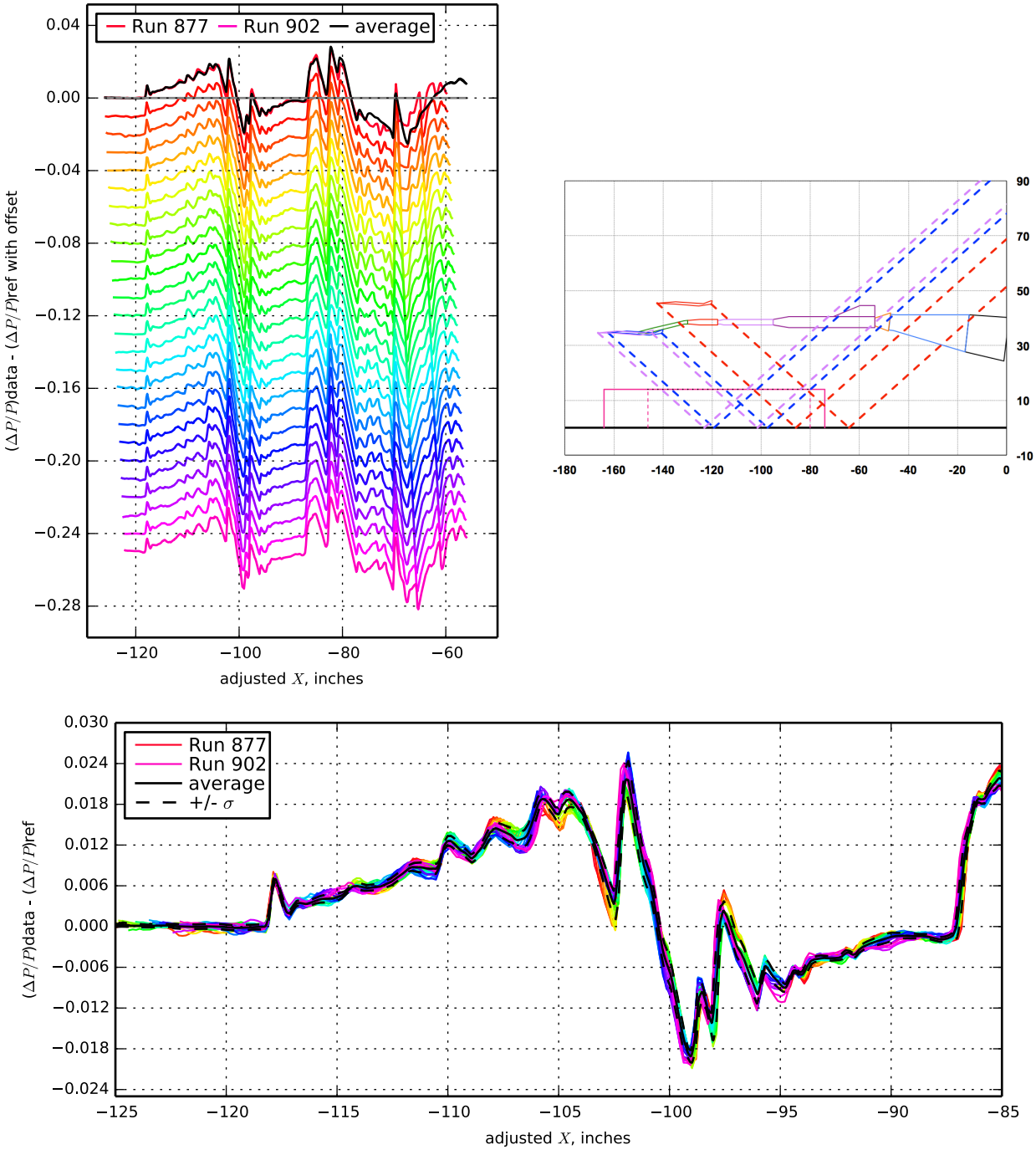

Figure 7.15. 1021 model with blade strut, Runs 877-902:903, Mach 1.6, Duration 30 sec, Re 8.16x10^6, T -80.09° F, PT 2299.68 psf, PT-Ref 0.15 psf, H 231.0 ppm [230.2 : 231.8], H-Ref 1.89 ppm

***X_ram*, in**	***h*, in**	***h/L***
21.97 [20.00 : 23.94]	20.76 [20.72 : 20.78]	0.93 [0.93 : 0.93]
***α*, deg**	***β*, deg**	***ϕ*, deg**
2.31 [2.25 : 2.41]	0.24 [0.17 : 0.29]	24.56 [24.52 : 24.59]
CL	***CD***	***CM***
0.148 [0.142 : 0.153]	0.01849 [0.01765 : 0.01961]	-0.110 [-0.118 : -0.102]

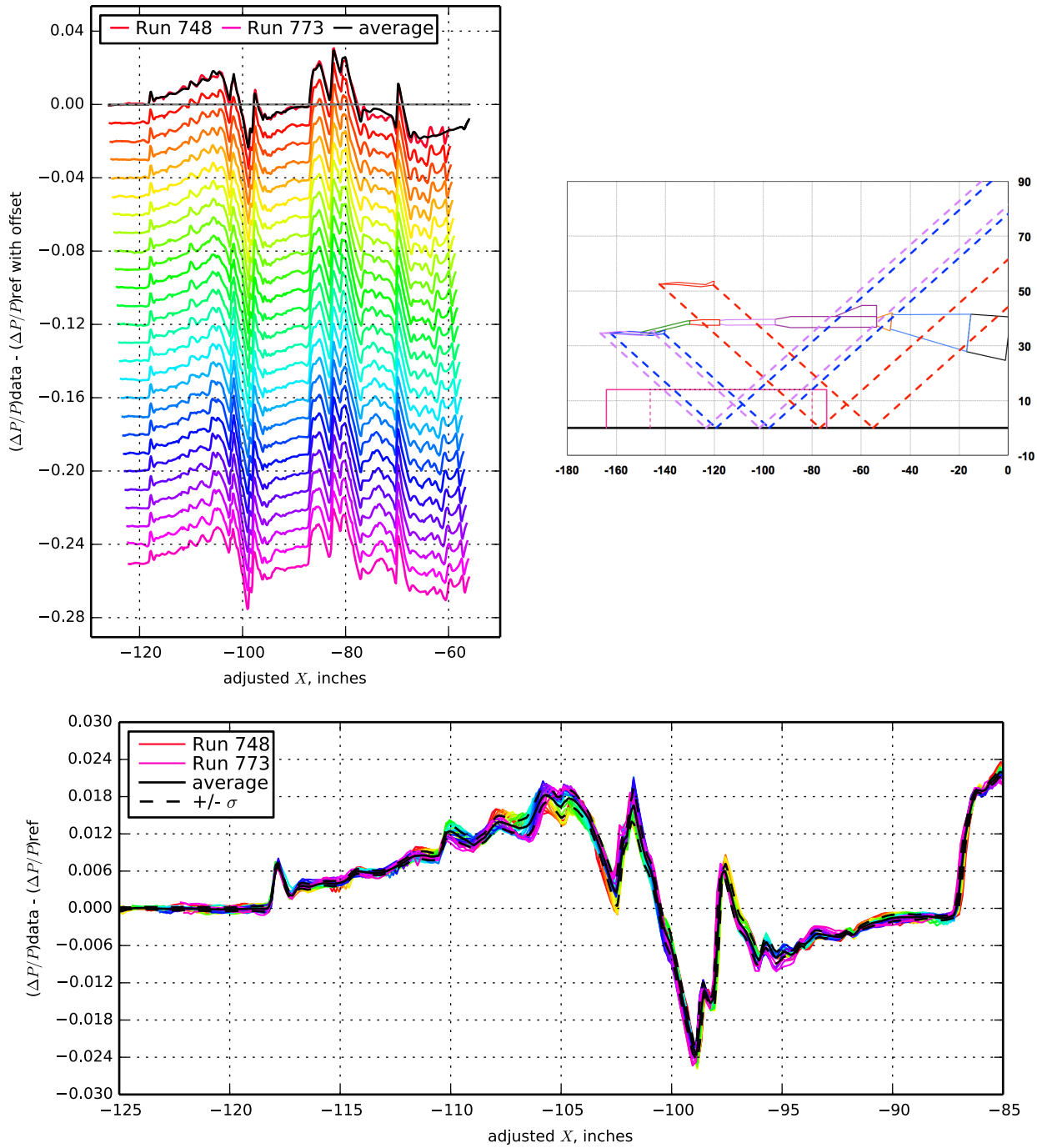

Figure 7.16. 1021 model with blade strut, Runs 748-773:828, Mach 1.6, Duration 30 sec, Re 8.16x10^6, T -80.36° F, PT 2299.36 psf, PT-Ref -0.04 psf, H 236.5 ppm [235.8 : 237.0], H-Ref 4.91 ppm

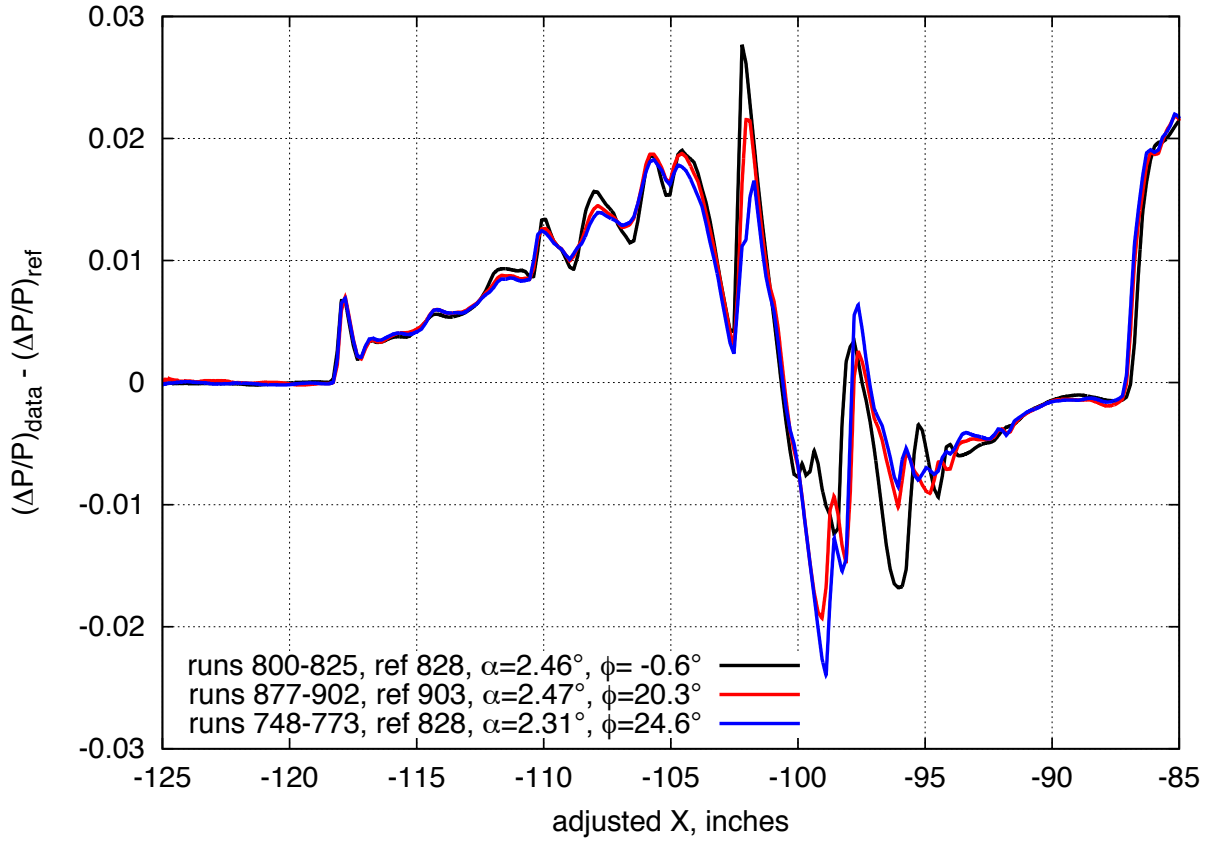

Figure 7.17. Comparison of off-track (ϕ=20.3° and 24.6°) to on-track ((ϕ=-0.6°) pressure signatures for the 1021 model with all nacelles on blade strut, near and above design angle-of-attack conditions, *M*=1.6, *h*=20.8 inches

***X_ram*, in**	***h*, in**	***h/L***
21.97 [20.00 : 23.94]	20.75 [20.70 : 20.77]	0.93 [0.92 : 0.93]
***α*, deg**	***β*, deg**	***ϕ*, deg**
2.30 [2.26 : 2.41]	0.11 [0.08 : 0.15]	47.79 [46.85 : 47.97]
CL	***CD***	***CM***
0.147 [0.142 : 0.149]	0.02073 [0.01967 : 0.02237]	-0.109 [-0.116 : -0.101]

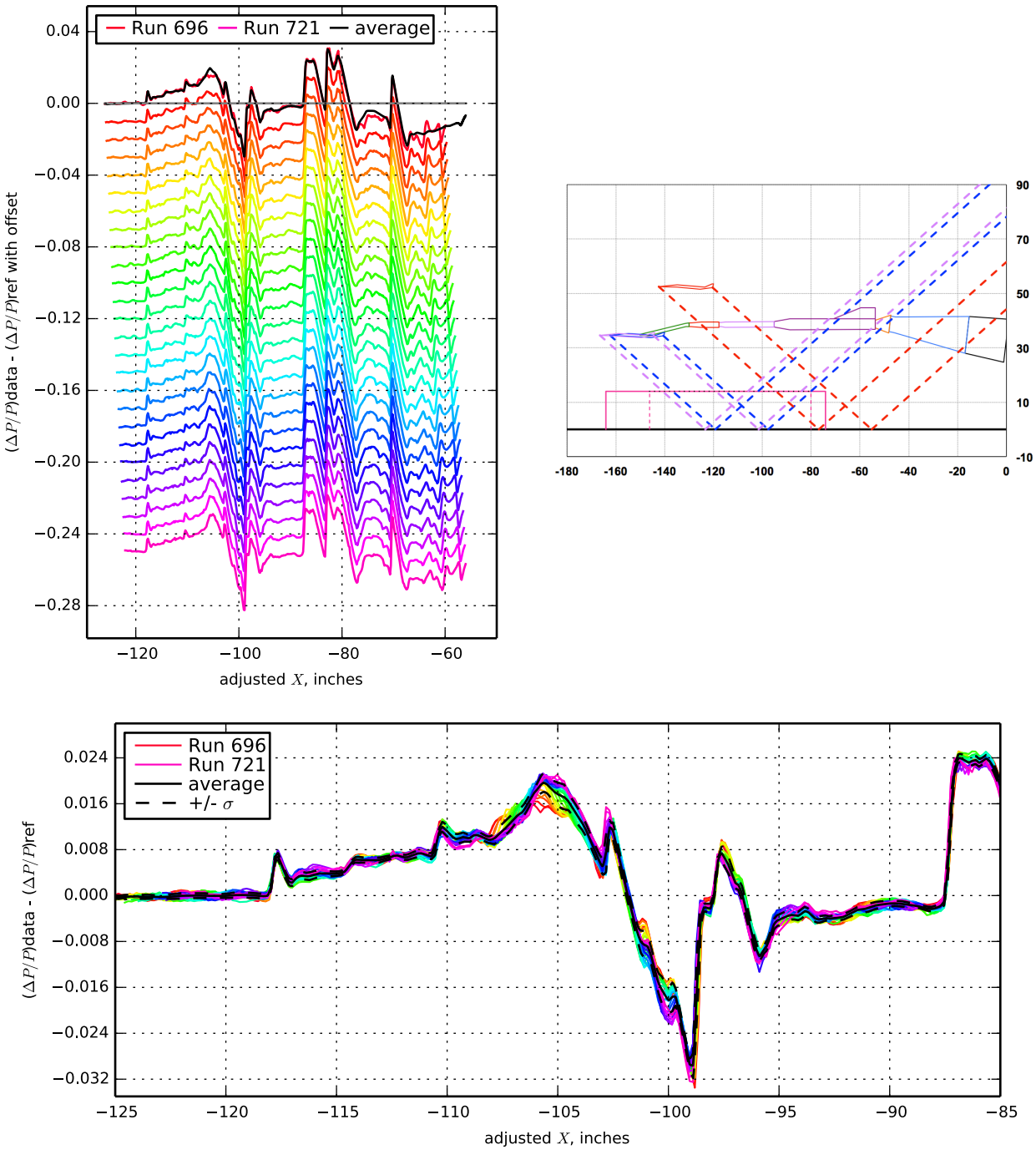

Figure 7.18. 1021 model with blade strut, Runs 696-721:828, Mach 1.6, Duration 30 sec, Re 8.18x10^6, T -81.22° F, PT 2298.71 psf, PT-Ref -0.60 psf, H 237.4 ppm [233.7 : 238.7], H-Ref 5.84 ppm

***X_ram*, in**	***h*, in**	***h/L***
21.97 [20.00 : 23.94]	20.86 [20.83 : 20.87]	0.93 [0.93 : 0.93]
***α*, deg**	***β*, deg**	**□, deg**
2.45 [2.41 : 2.56]	0.19 [0.15 : 0.22]	47.63 [47.59 : 47.69]
CL	***CD***	***CM***
0.153 [0.148 : 0.156]	0.02043 [0.01943 : 0.02160]	-0.110 [-0.118 : -0.101]

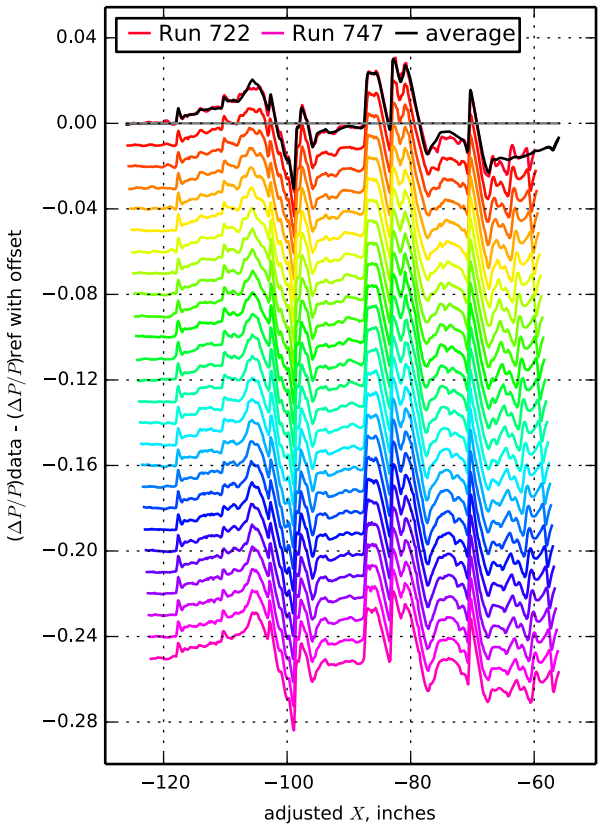

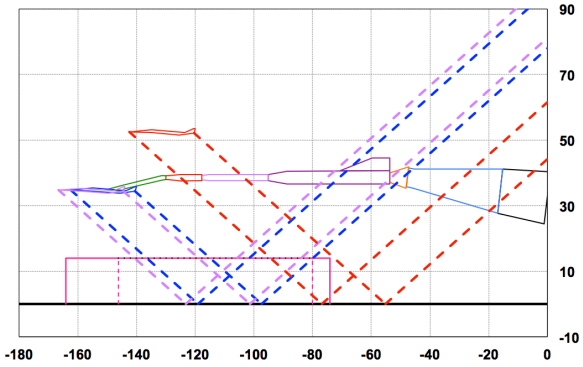

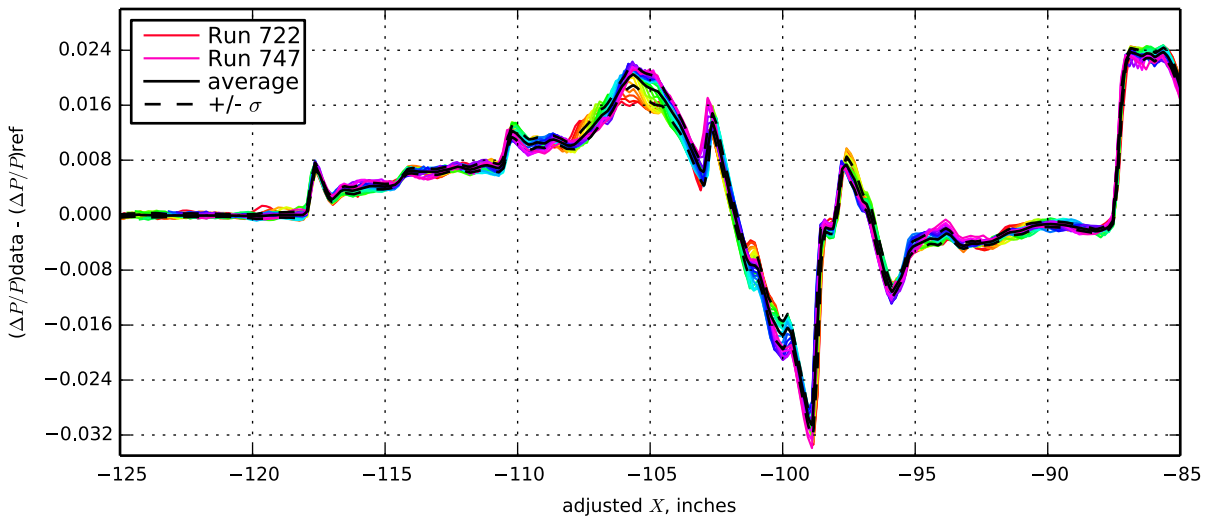

Figure 7.19. 1021 model with blade strut, Runs 722-747:828, Mach 1.6, Duration 30 sec, Re 8.17x10^6, T -80.72° F, PT 2299.16 psf, PT-Ref -0.05 psf, H 236.0 ppm [234.3 : 237.9], H-Ref 4.41 ppm

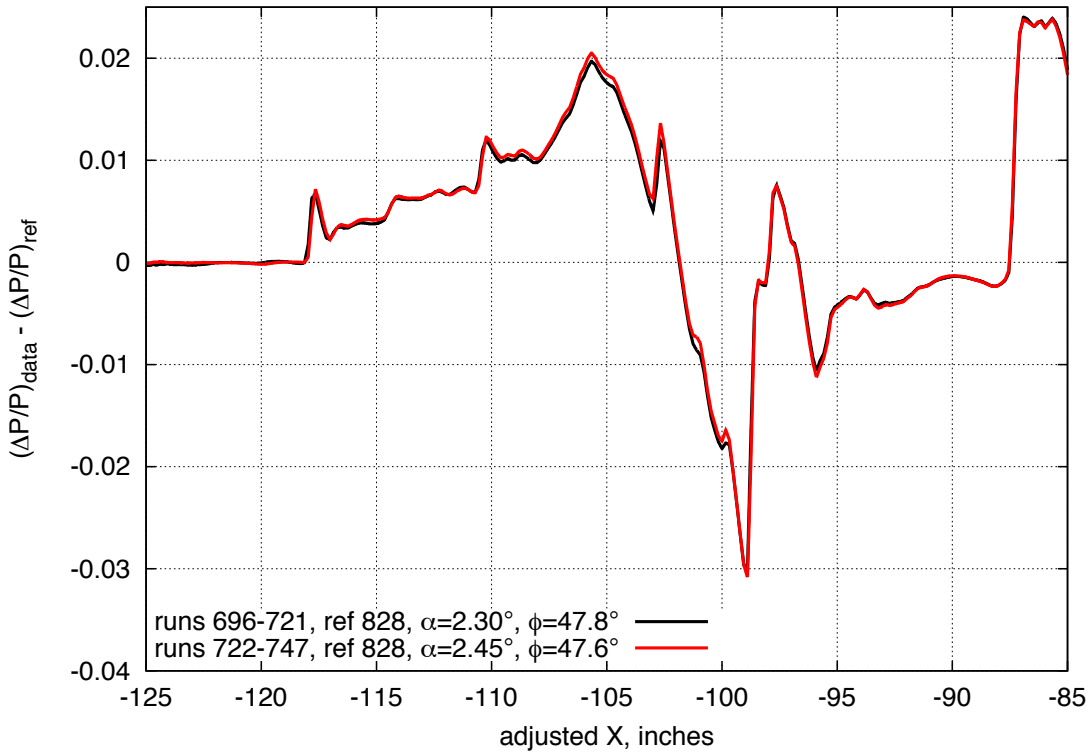

Figure 7.20. Comparison of off-track (ϕ=48°) pressure signatures for the 1021 model with all nacelles on blade strut, near and above design angle-of-attack conditions, *M*=1.6, *h*=20.8 inches

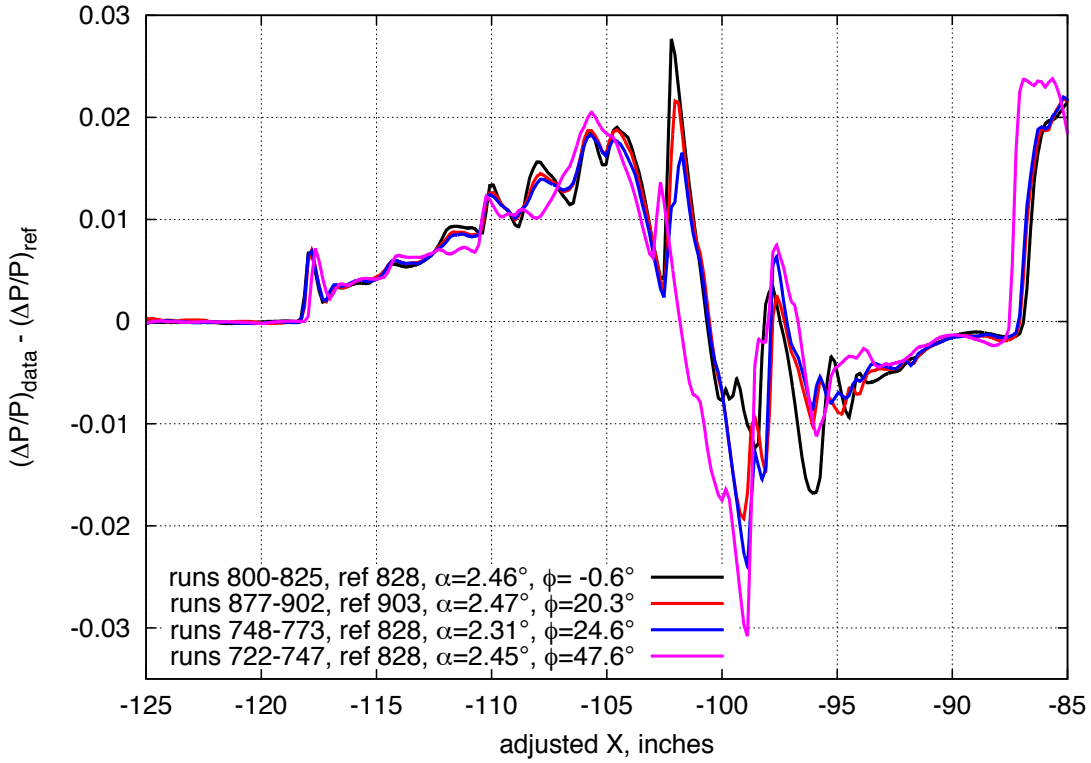

Figure 7.21. Comparison of on- and off-track pressure signatures for the 1021 model with all nacelles on blade strut, above design angle-of-attack, *M*=1.6, *h*=20.8 inches

***X_ram*, in**	***h*, in**	***h/L***
21.97 [20.00 : 23.94]	20.77 [20.74 : 20.81]	0.93 [0.93 : 0.93]
***α*, deg**	***β*, deg**	***ϕ*, deg**
2.31 [2.25 : 2.40]	0.27 [0.20 : 0.32]	0.20 [0.11 : 0.27]
CL	***CD***	***CM***
0.145 [0.140 : 0.151]	0.01860 [0.01839 : 0.01915]	-0.113 [-0.122 : -0.103]

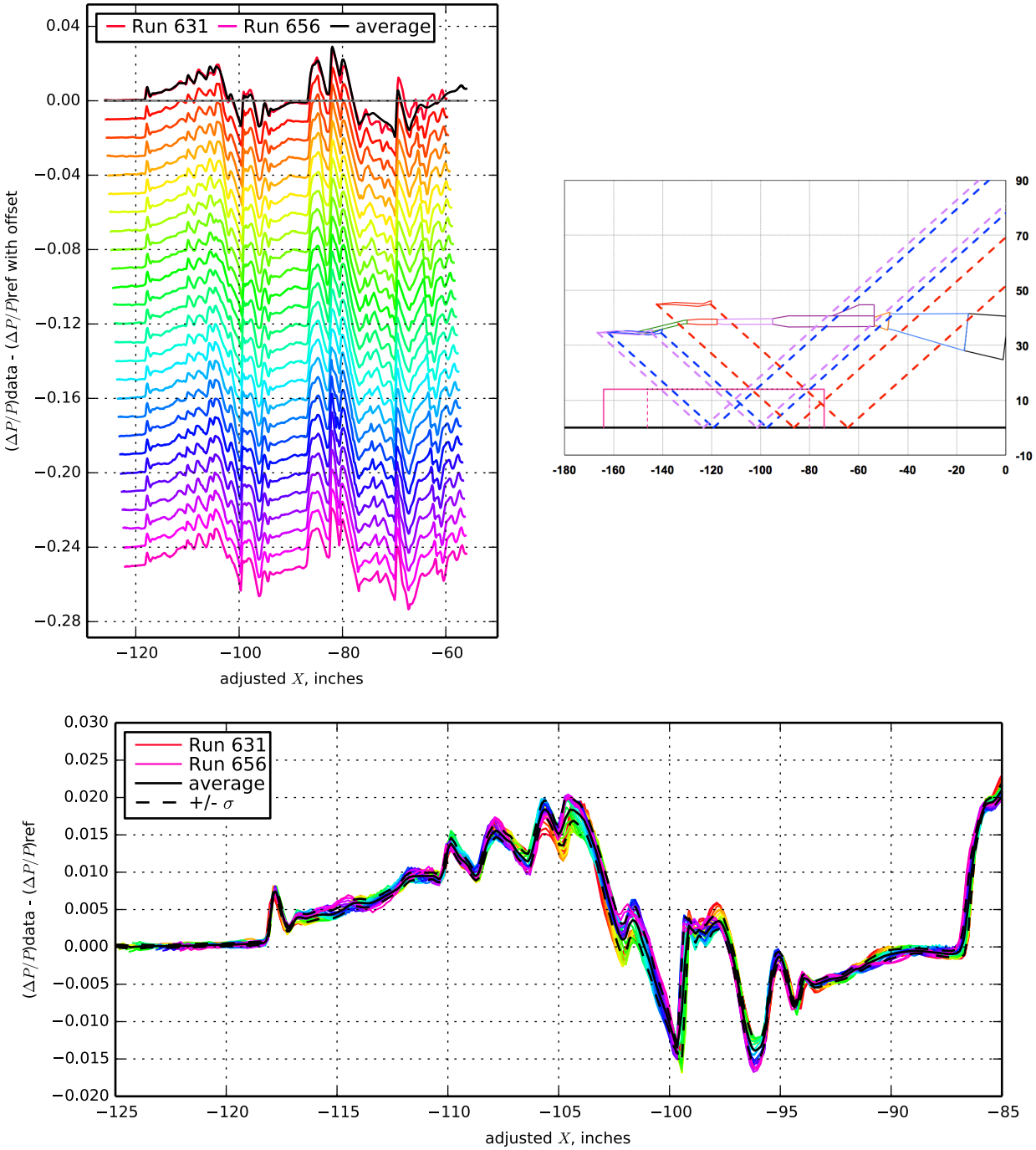

Figure 7.22. 1021 model on blade strut without under-wing nacelle, Runs 631-656:630, Mach 1.6, Duration 90 sec, Re 8.09x10^6, T -78.85° F, PT 2299.56 psf, PT-Ref 0.13 psf, H 251.7 ppm [249.3 : 254.2], H-Ref -0.32 ppm

***X_ram*, in**	***h*, in**	***h/L***
21.97 [20.00 : 23.94]	20.81 [20.78 : 20.86]	0.93 [0.93 : 0.93]
***α*, deg**	***β*, deg**	***ϕ*, deg**
2.58 [2.53 : 2.67]	0.14 [0.07 : 0.18]	-0.66 [-0.73 : -0.59]
CL	***CD***	***CM***
0.158 [0.153 : 0.164]	0.02104 [0.02040 : 0.02181]	-0.115 [-0.124 : -0.109]

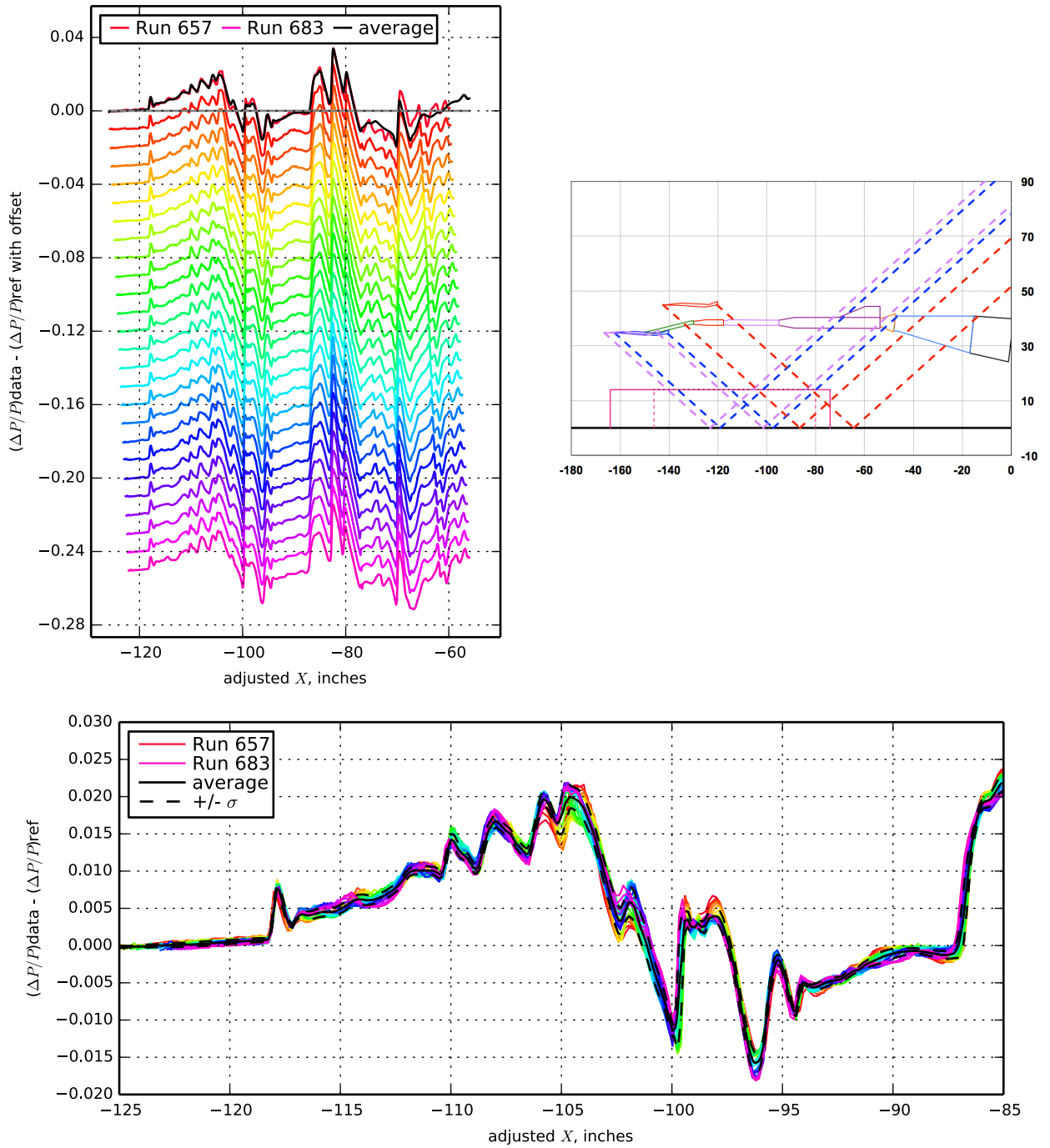

Figure 7.23. 1021 model on blade strut without under-wing nacelle, Runs 657-683:630, Mach 1.6, Duration 90 sec, Re 8.06x10^6, T -77.16° F, PT 2300.22 psf, PT-Ref 0.63 psf, H 251.2 ppm [249.8 : 253.5], H-Ref -0.80 ppm

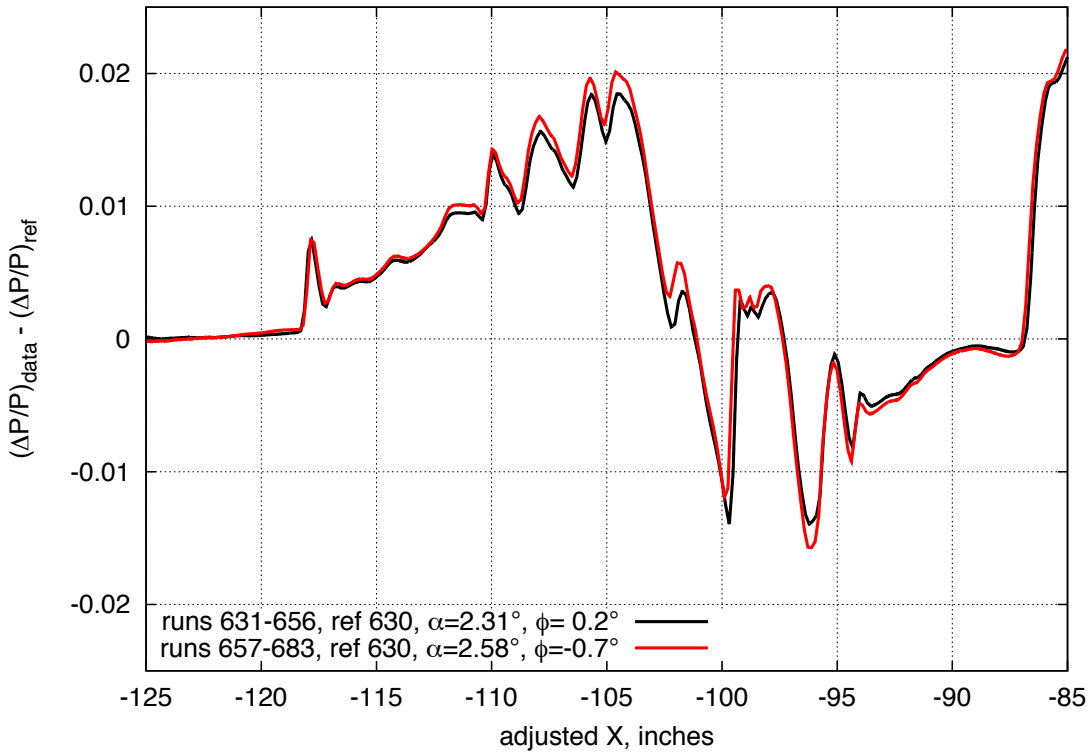

Figure 7.24. Comparison of near-repeat run series for the 1021 model without the under-wing nacelle, on blade strut, near and above design angle-of-attack conditions, on-track, M=1.6, h=20.8 inches

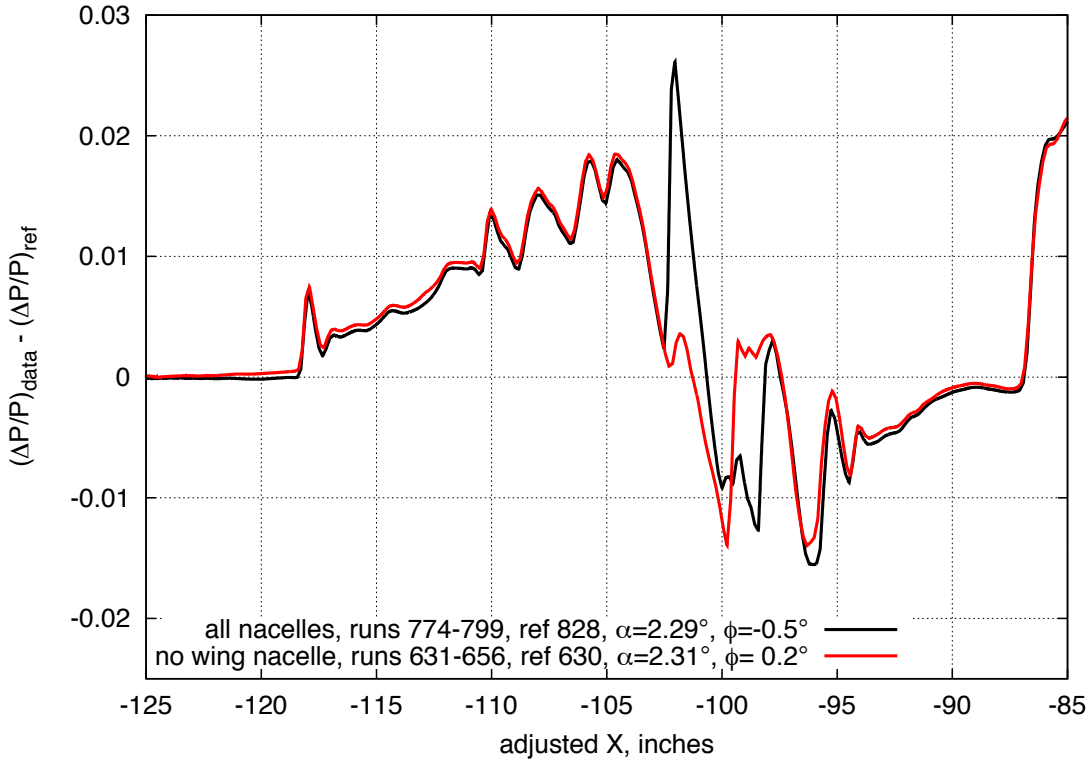

Figure 7.25. Comparison of 1021 model with all nacelles and without the under-wing nacelle, at design conditions, on-track, M=1.6, h=20.8 inches

***X_ram*, in**	***h*, in**	***h/L***
21.97 [20.00 : 23.94]	21.10 [21.06 : 21.15]	0.94 [0.94 : 0.94]
***α*, deg**	***β*, deg**	***ϕ*, deg**
2.57 [2.49 : 2.69]	-0.06 [-0.15 : -0.02]	-1.86 [-1.90 : -1.83]
CL	***CD***	***CM***
0.149 [0.143 : 0.157]	0.02579 [0.02494 : 0.02626]	0.004 [-0.006 : 0.012]

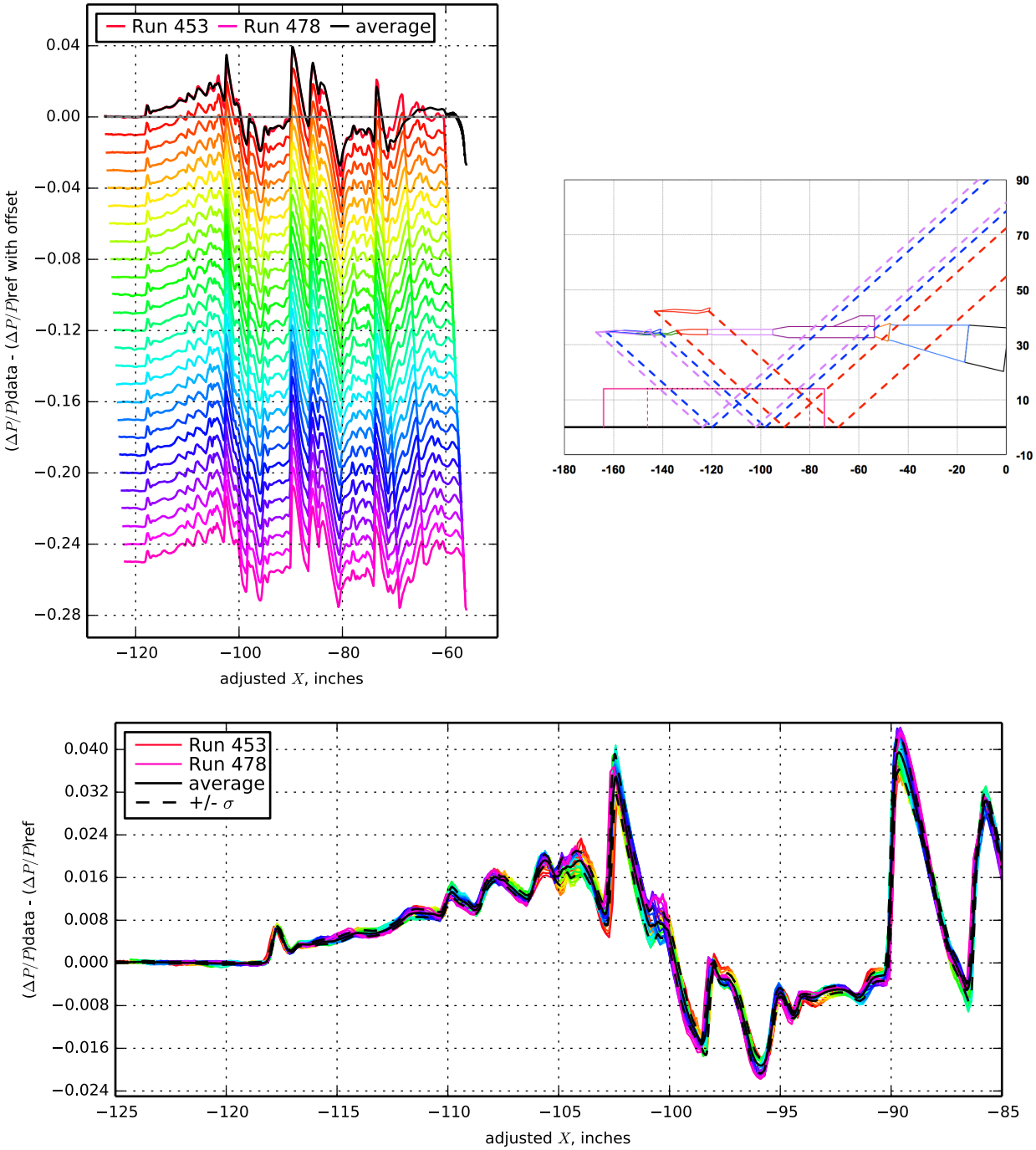

Figure 7.26. 1021 model on sting, Runs 453-478:507, Mach 1.6, Duration 90 sec, Re 8.07x10^6, T -77.72° F, PT 2299.35 psf, PT-Ref -0.34 psf, H 256.7 ppm [253.8 : 258.8], H-Ref -0.62 ppm

***X_ram*, in**	***h*, in**	***h/L***
21.93 [20.00 : 23.94]	21.19 [21.15 : 21.26]	0.95 [0.94 : 0.95]
***α*, deg**	***β*, deg**	***ϕ*, deg**
2.80 [2.72 : 2.93]	-0.09 [-0.18 : -0.05]	-2.04 [-2.08 : -2.02]
CL	***CD***	***CM***
0.159 [0.153 : 0.168]	0.02710 [0.02608 : 0.02785]	0.006 [-0.006 : 0.013]

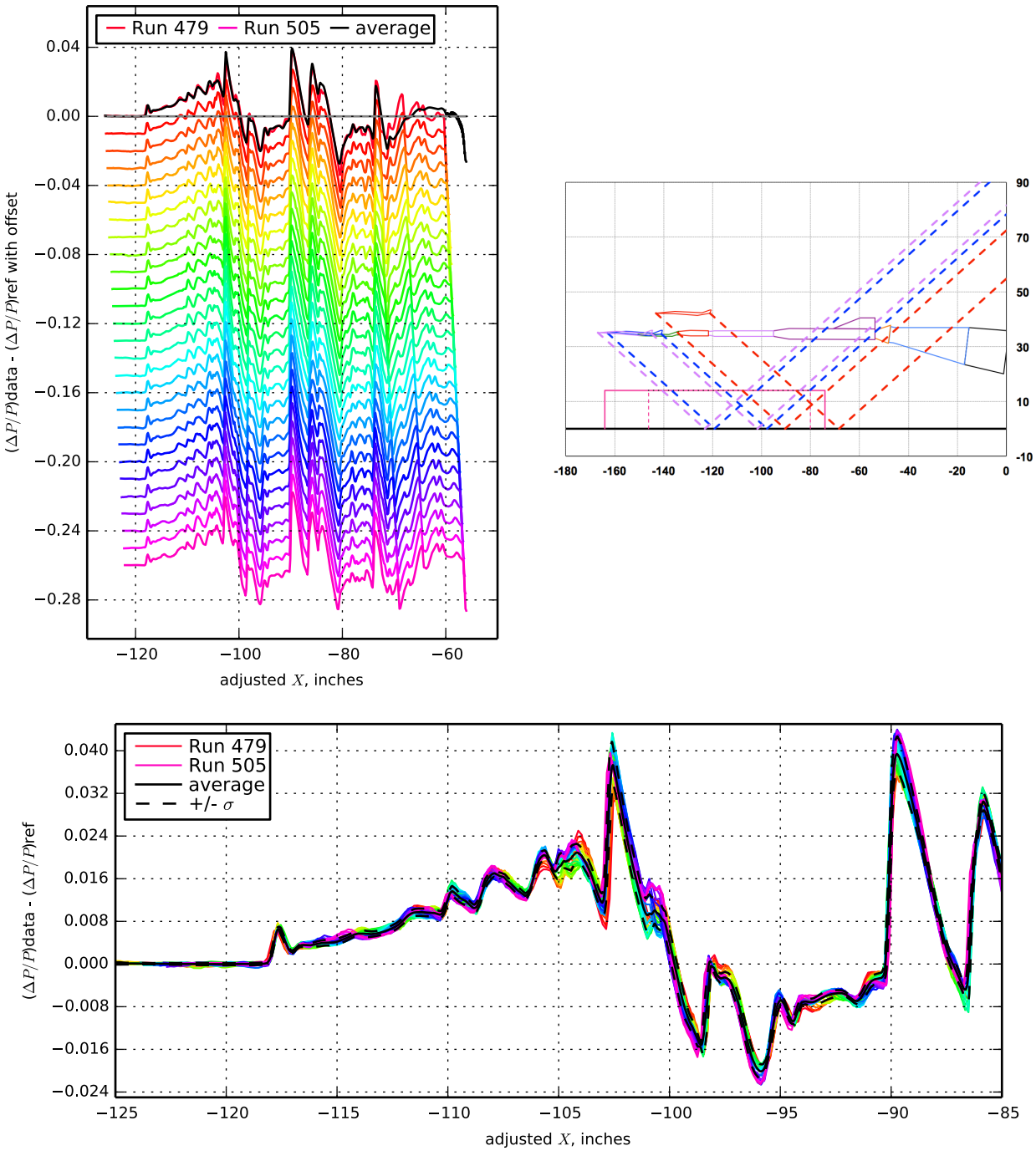

Figure 7.27. 1021 model on sting, Runs 479-505:507, Mach 1.6, Duration 90 sec, Re 8.05x10^6, T -77.10° F, PT 2299.79 psf, PT-Ref -0.13 psf, H 257.3 ppm [255.8 : 261.8], H-Ref -0.04 ppm

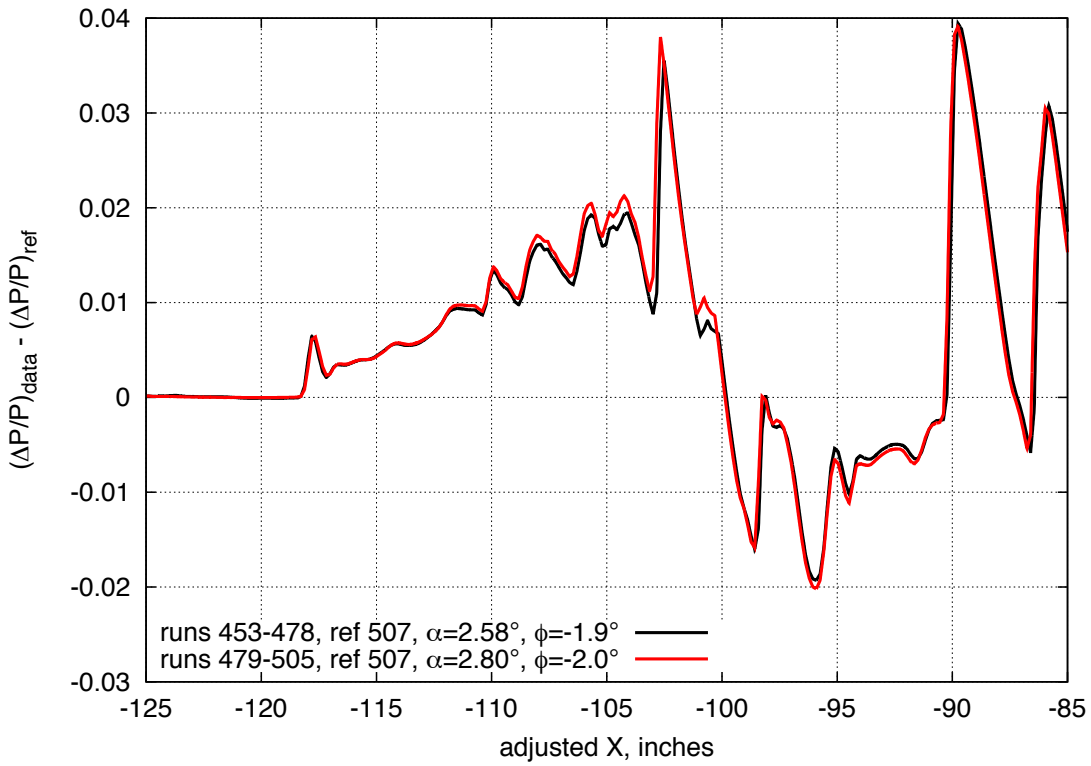

Figure 7.28. Comparison of the 1021 model on conventional sting, above design angle-of-attack conditions, on-track, M=1.6, h=21.2 inches

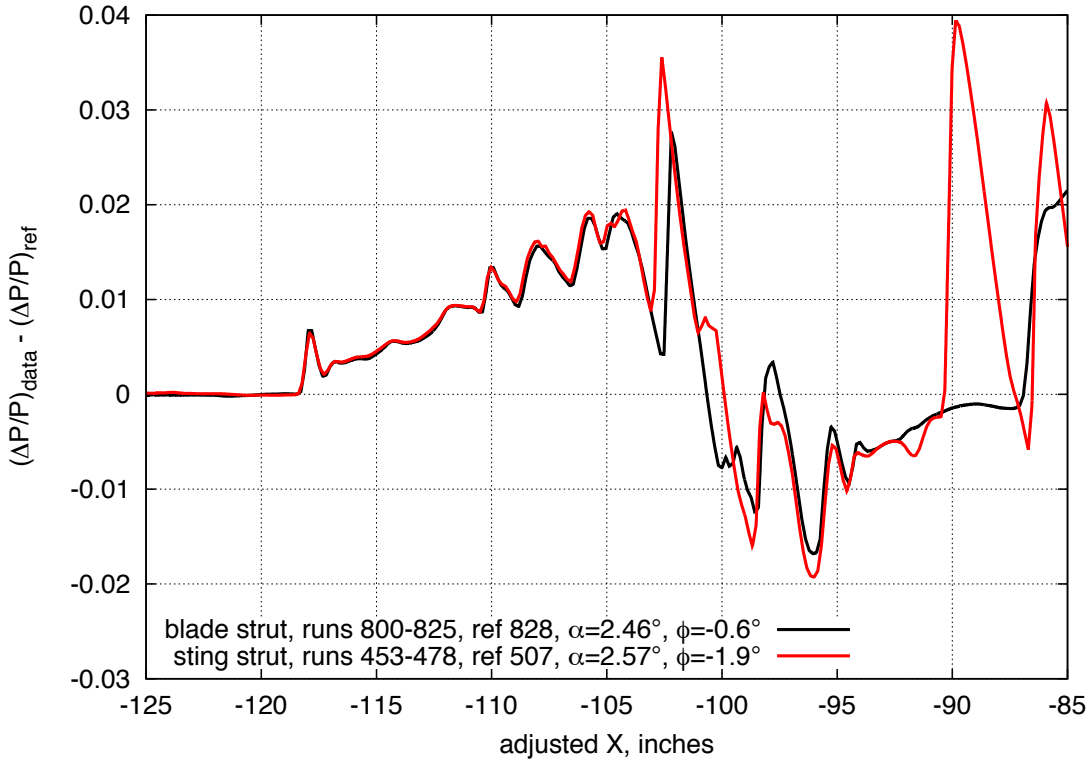

Figure 7.29. Comparison of the 1021 model on blade and conventional sting struts, above design angle-of-attack conditions, on-track, M=1.6, h=21.2 inches

***X_ram*, in**	***h*, in**	***h/L***
19.32 [15.00 : 23.98]	31.51 [31.44 : 31.60]	1.41 [1.40 : 1.41]
***α*, deg**	***β*, deg**	***ϕ*, deg**
2.36 [2.27 : 2.49]	-0.37 [-0.52 : -0.21]	-0.66 [-0.73 : -0.59]
CL	***CD***	***CM***
0.142 [0.135 : 0.152]	0.02054 [0.01997 : 0.02093]	-0.010 [-0.019 : -0.001]

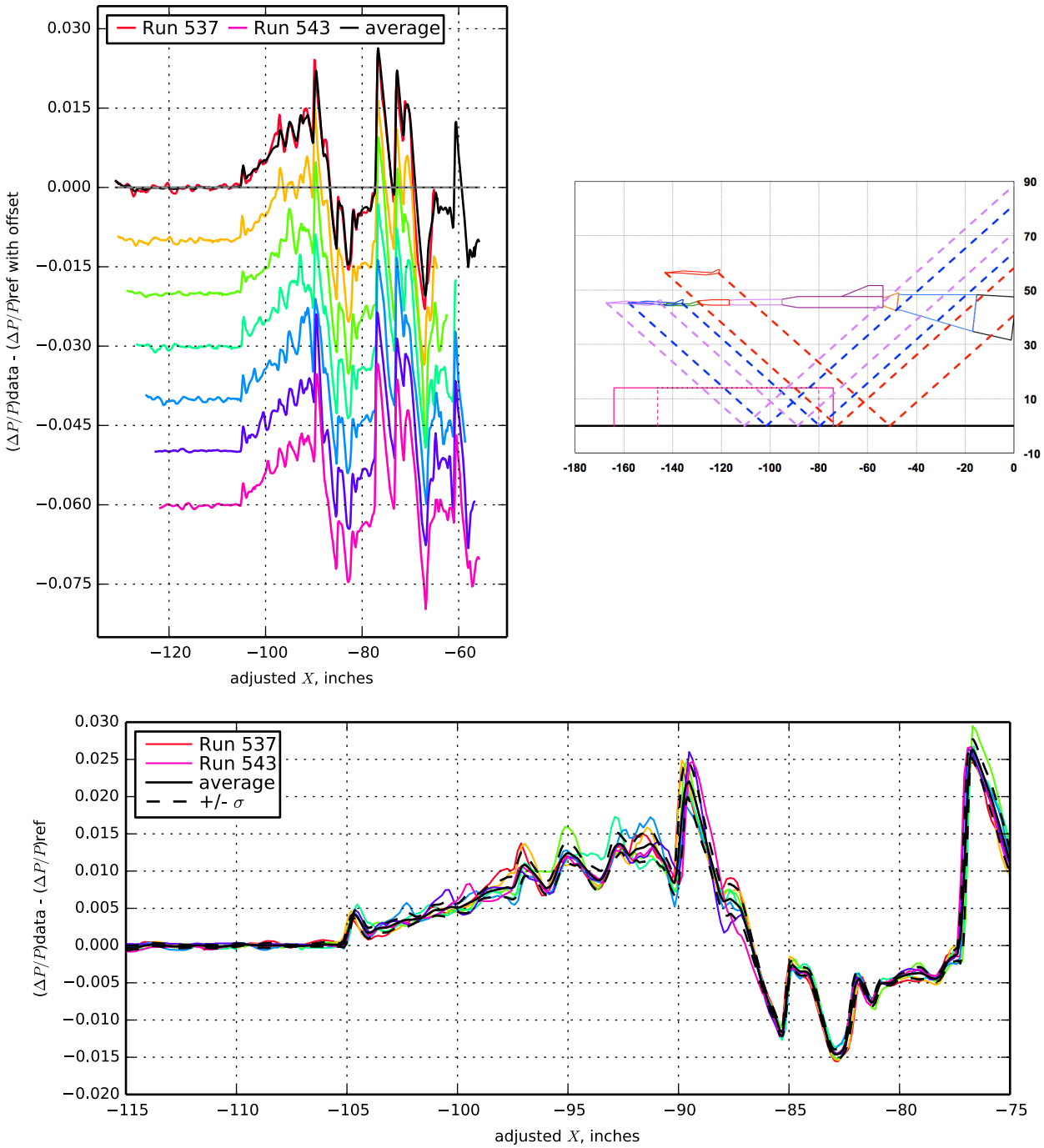

Figure 7.30. 1021 model on sting, Runs 537-543:544, Mach 1.6, Duration 30 sec, Re 8.05x10^6, T -76.43° F, PT 2300.46 psf, PT-Ref 0.06 psf, H 258.4 ppm [258.0 : 259.2], H-Ref -0.67 ppm

***X_ram*, in**	***h*, in**	***h/L***
21.97 [20.00 : 23.94]	21.21 [21.16 : 21.25]	0.95 [0.94 : 0.95]
***α*, deg**	***β*, deg**	***ϕ*, deg**
2.87 [2.81 : 3.00]	0.49 [0.42 : 0.53]	46.19 [45.32 : 46.30]
CL	***CD***	***CM***
0.154 [0.148 : 0.159]	0.02655 [0.02577 : 0.02703]	0.001 [-0.006 : 0.008]

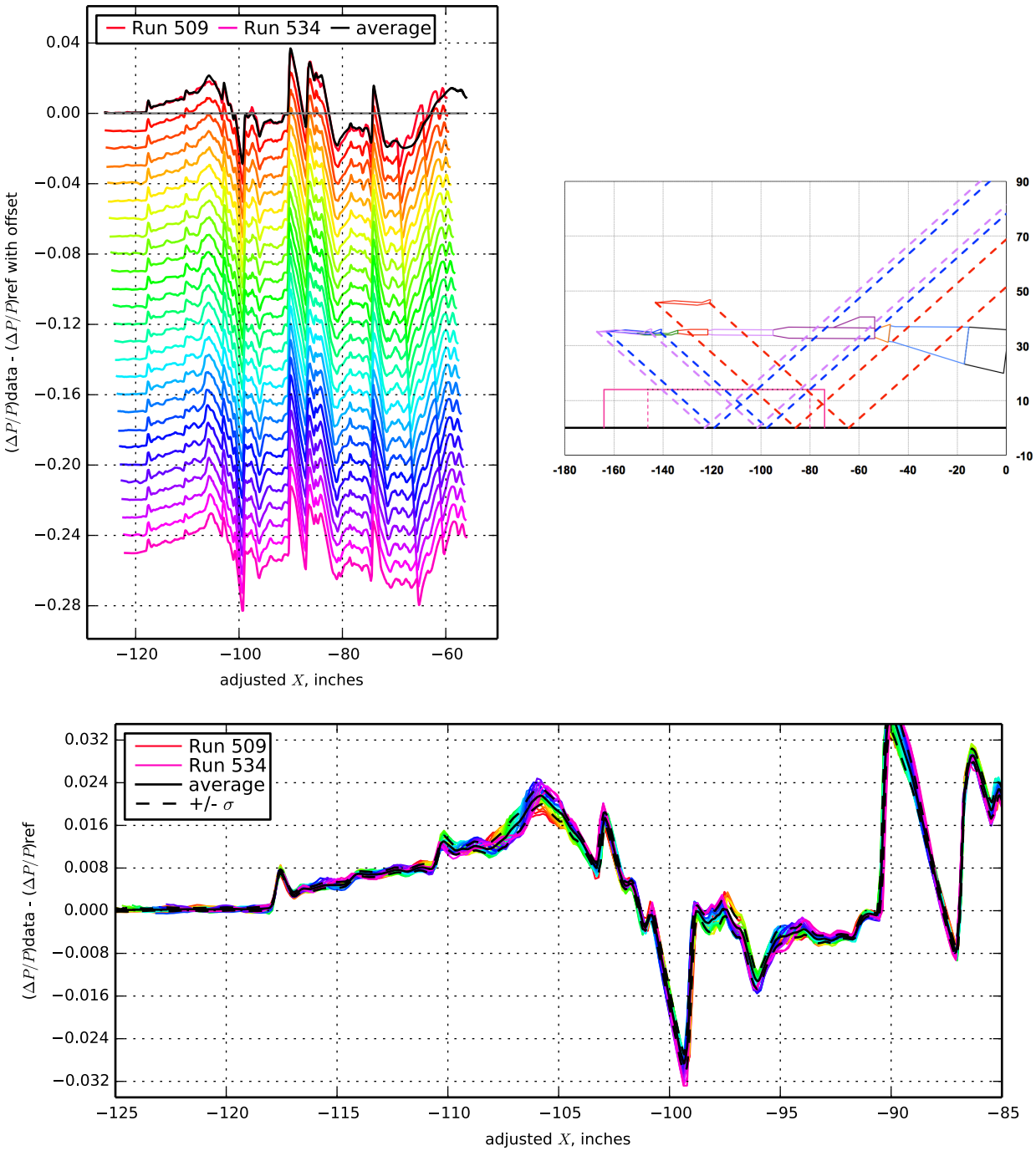

Figure 7.31. 1021 model on sting, Runs 509-534:536, Mach 1.6, Duration 30 sec, Re 8.05x10^6, T -76.60° F, PT 2300.22 psf, PT-Ref -0.18 psf, H 257.8 ppm [256.3 : 260.7], H-Ref 0.14 ppm

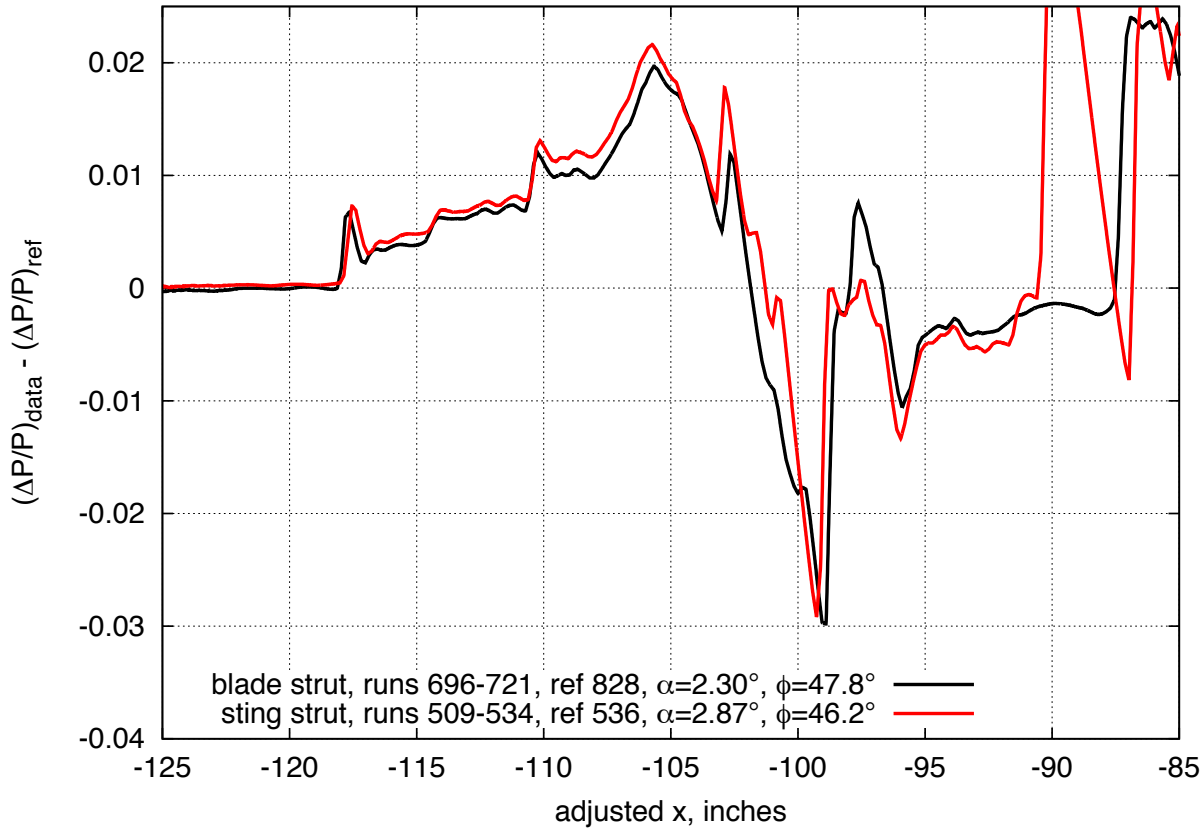

Figure 7.32. Off-track comparison of the 1021 model on blade and conventional sting struts, at and above design angle-of-attack conditions, M=1.6, h=21.2 inches

***X_ram*, in**	***h*, in**	***h/L***
11.25 [-0.00 : 24.00]	29.52 [29.47 : 29.56]	1.59 [1.58 : 1.59]
***α*, deg**	***β*, deg**	***ϕ*, deg**
-0.27 [-0.28 : -0.26]	0.06 [0.05 : 0.08]	-0.15 [-0.22 : -0.07]
CL	***CD***	***CM***
-0.011 [-0.019 : -0.004]	0.05885 [0.05450 : 0.06409]	0.126 [0.054 : 0.204]

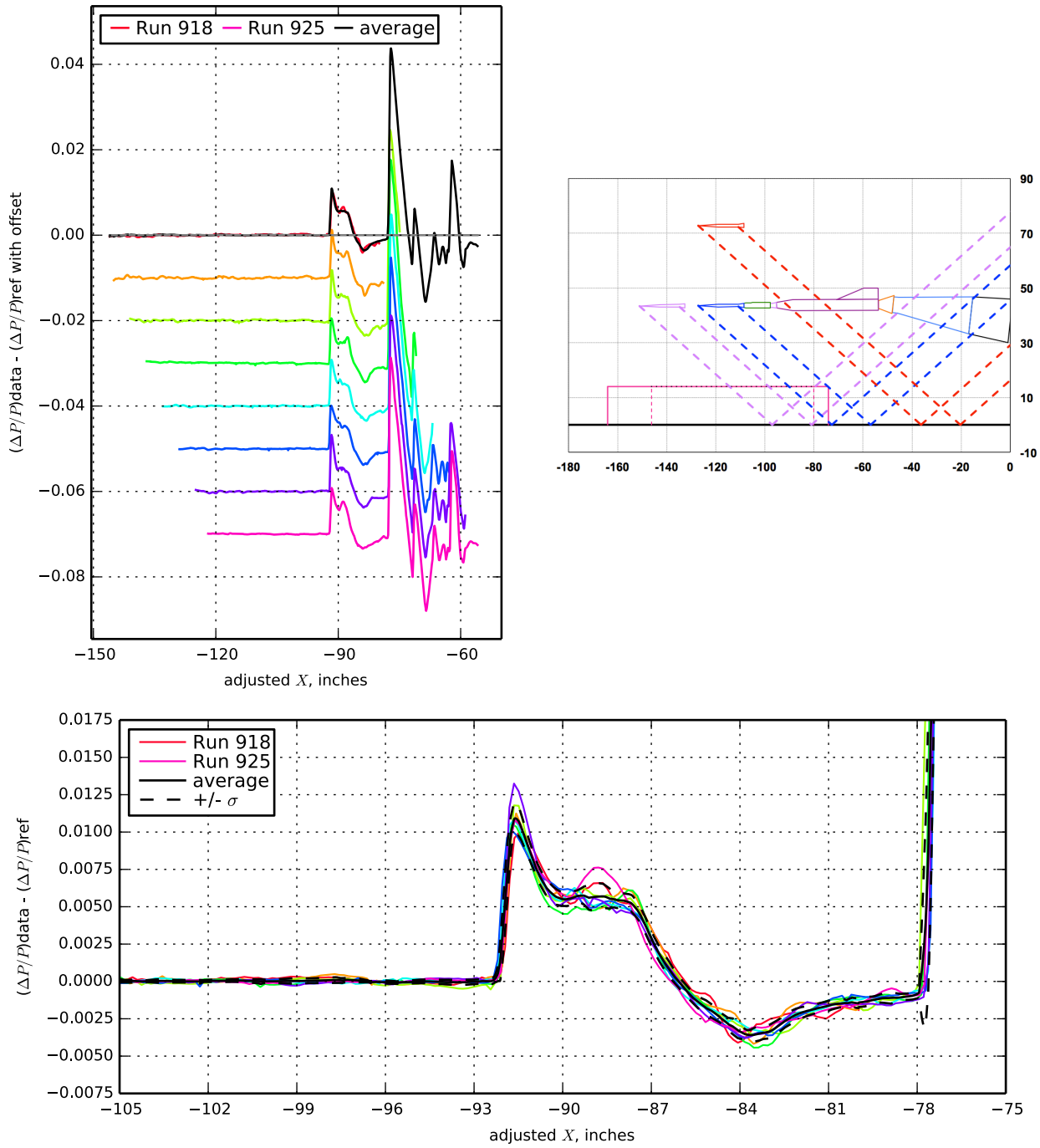

Figure 7.33. AS-2, Runs 918-925:927, Mach 1.6, Duration 90 sec, Re 4.40x10^6, T -87.72° F, PT 1451.38 psf, PT-Ref -0.13 psf, H 217.6 ppm [217.3 : 217.9], H-Ref -0.19 ppm

***X_ram*, in**	***h*, in**	***h/L***
20.93 [18.96 : 22.90]	20.58 [20.57 : 20.58]	1.24 [1.24 : 1.24]
***α*, deg**	***β*, deg**	***ϕ*, deg**
-0.27 [-0.27 : -0.26]	0.14 [0.13 : 0.14]	0.24 [0.20 : 0.29]
CL	***CD***	***CM***
-0.003 [-0.009 : 0.001]	0.06098 [0.05885 : 0.06233]	0.051 [-0.001 : 0.110]

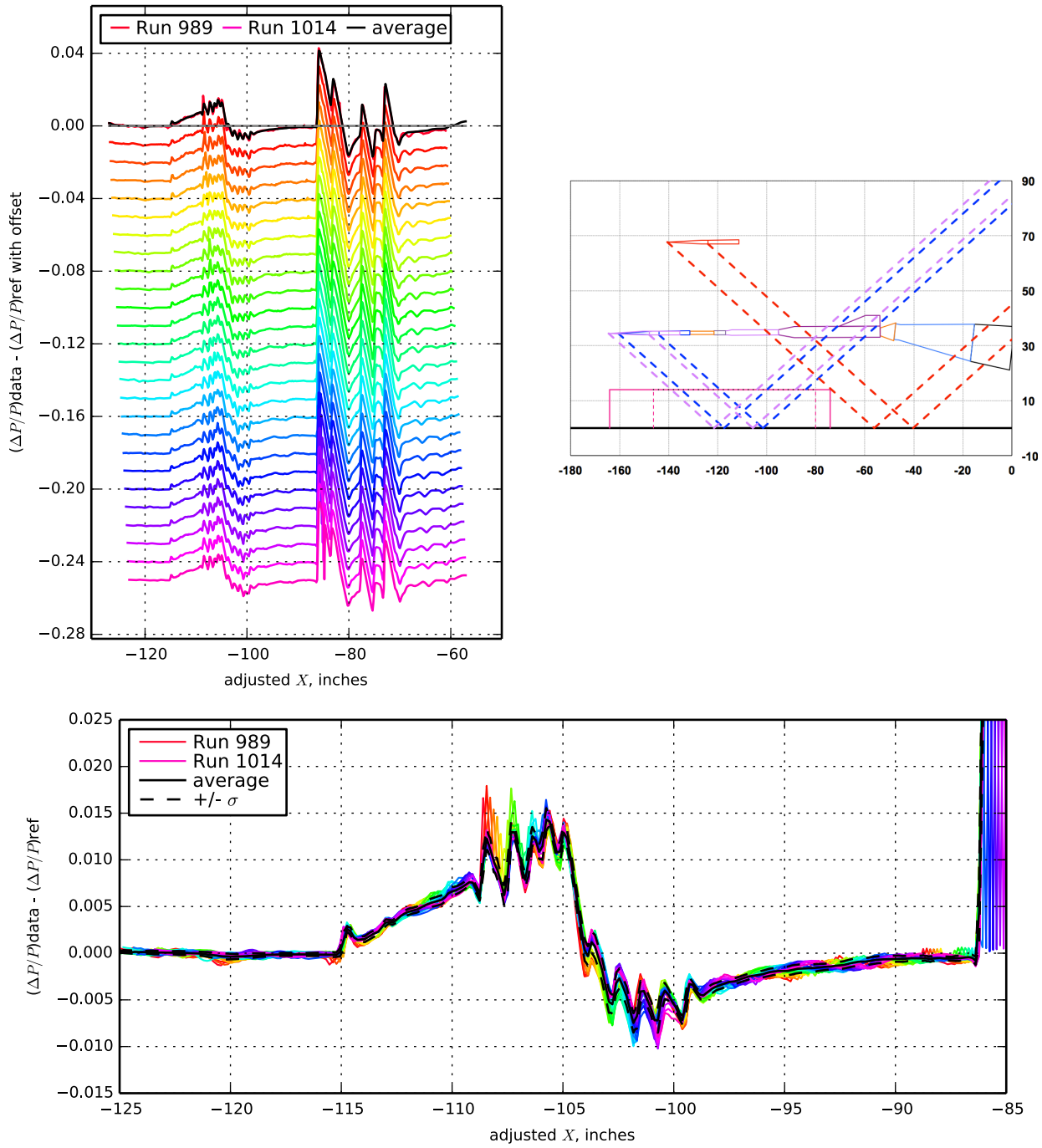

Figure 7.34. Opt Sig, Runs 989-1014:1017, Mach 1.6, Duration 90 sec, Re 6.03x10^6, T -80.21° F, PT 2299.99 psf, PT-Ref -0.35 psf, H 201.1 ppm [198.7 : 203.9], H-Ref -0.75 ppm

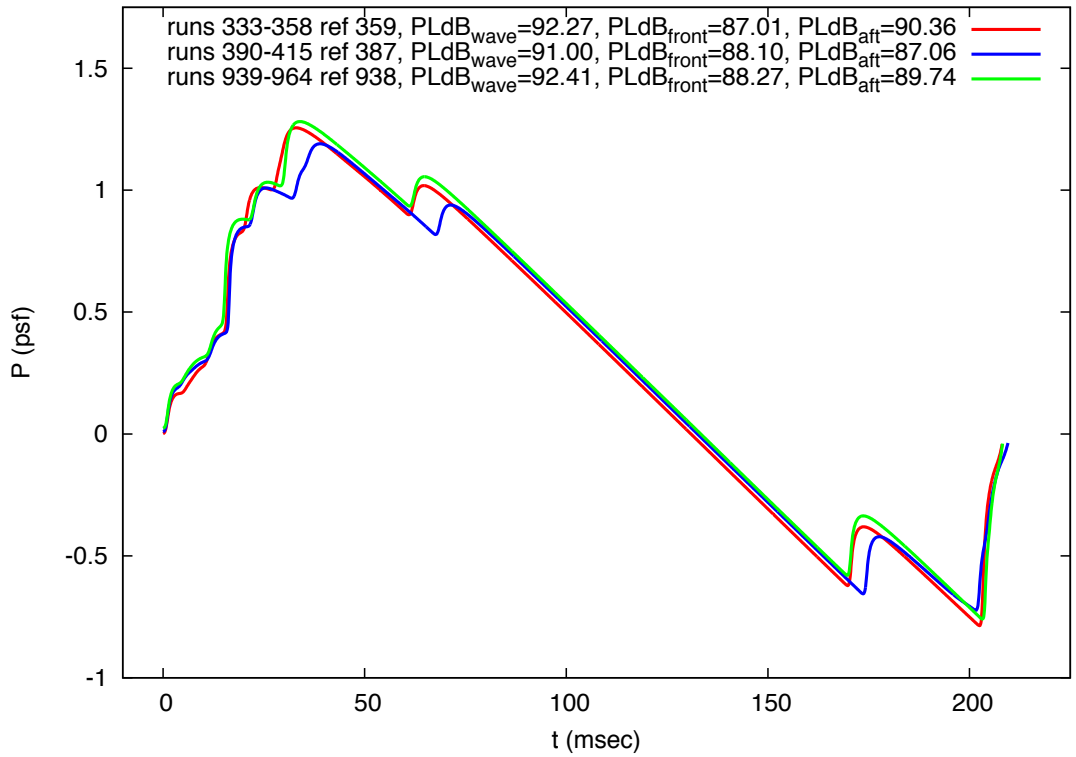

Figure 7.35. Extrapolated pressures of 1021 Phase I model to ground, M=1.6, h=50,000 ft. Near-field signatures taken at h of [20.6: 20.8] inches, and α of [1.94 : 2.10] degrees

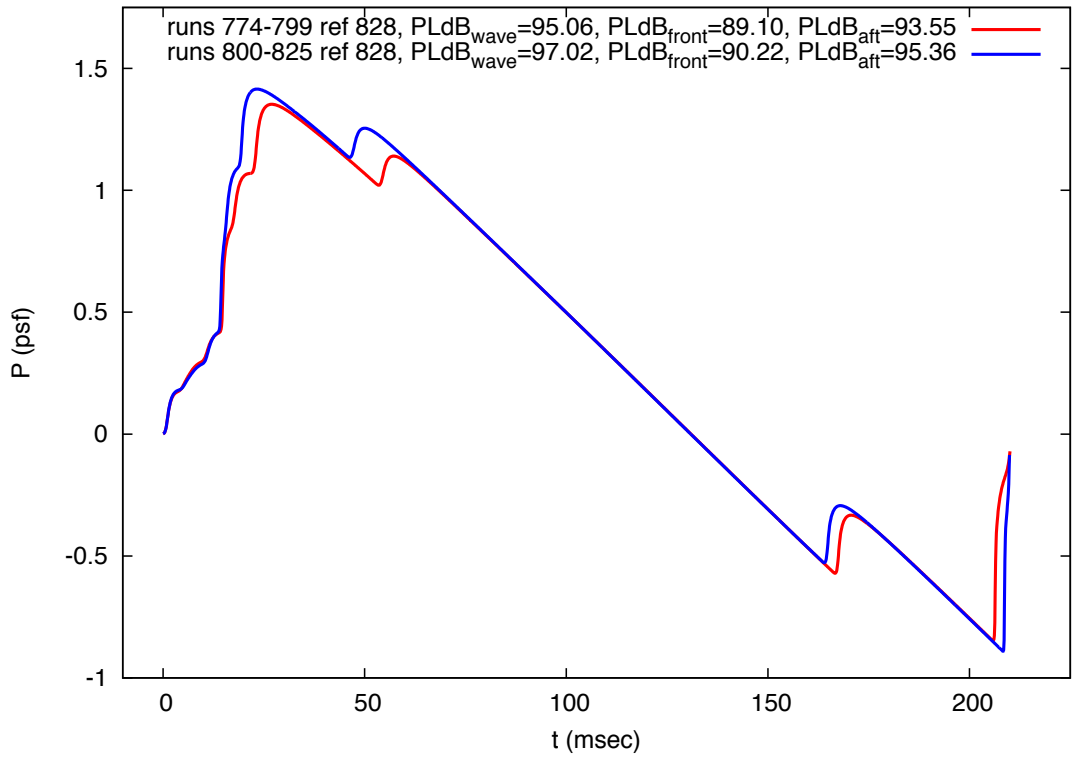

Figure 7.36. Extrapolated pressures of 1021 Phase I model to ground, M=1.6, h=50,000 ft. Near-field signatures taken at h of [20.7 : 20.8] inches, and α of [2.29 : 2.46] degrees

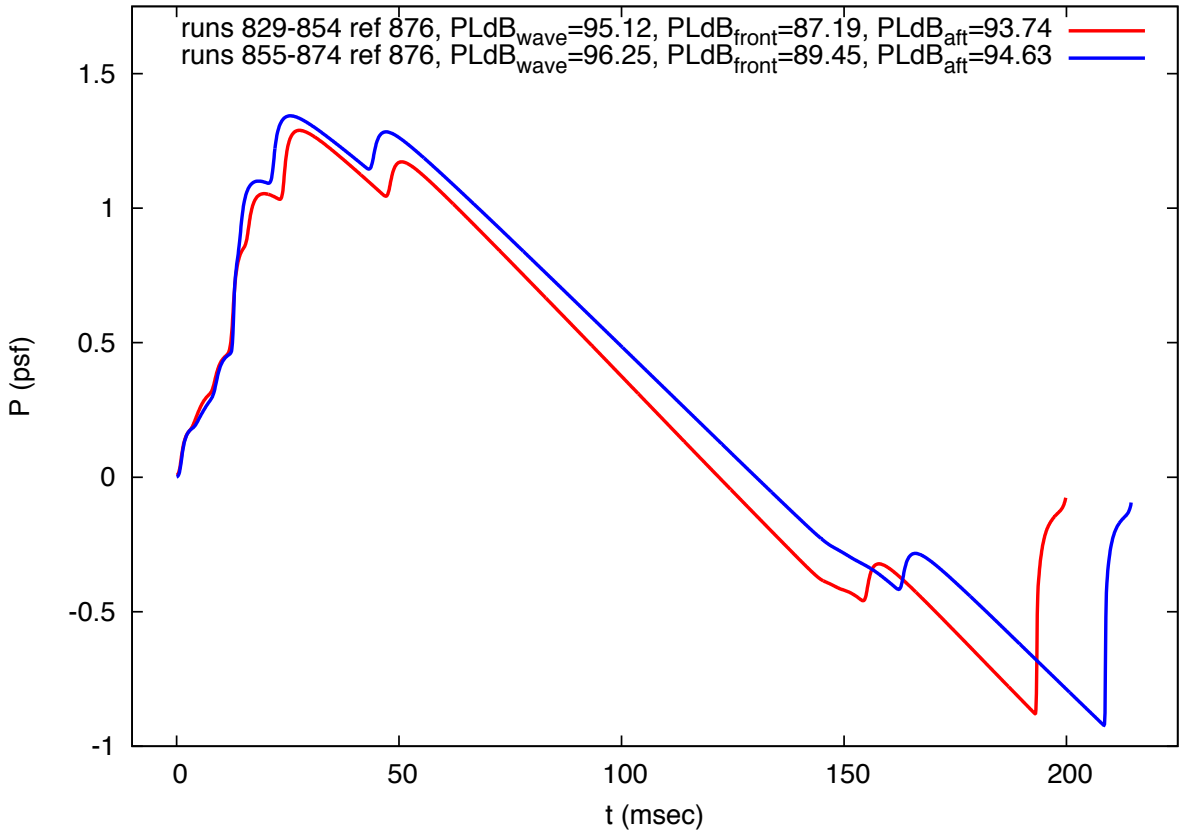

Figure 7.37. Extrapolated pressures of 1021 Phase I model to ground, M=1.6, h=50,000 ft. Near-field signatures taken at h of [31.3 : 31.4] inches, and α of [2.31 : 2.50] degrees

***X_ram*, in**	***h*, in**	***h/L***
18.00 [18.00 : 18.00]	26.59 [20.54 : 32.61]	1.40 [1.08 : 1.71]
***α*, deg**	***β*, deg**	***ϕ*, deg**
2.24 [2.22 : 2.26]	0.48 [0.47 : 0.49]	1.03 [0.44 : 1.84]
CL	***CD***	***CM***
0.129 [0.122 : 0.132]	0.06159 [0.06015 : 0.06330]	-0.262 [-0.285 : -0.230]

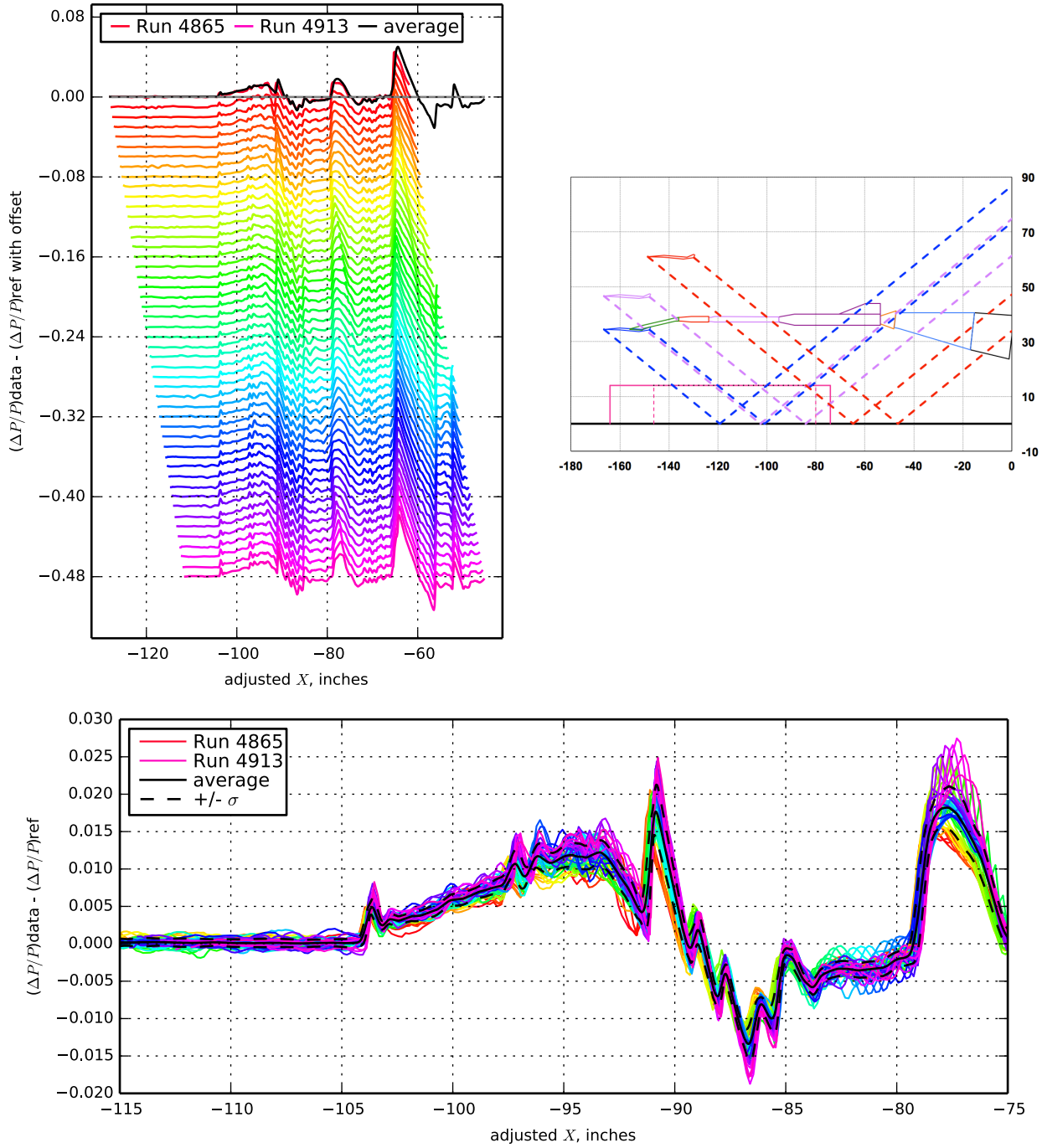

Figure 7.38. 1044 model with blade strut, Runs 4865-4913:4864, Mach 1.7, Duration 6 sec, Re 6.76x10^6, T -97.55° F, PT 2299.67 psf, PT-Ref -5.71 psf, H 184.3 ppm [183.6 : 184.9], H-Ref -0.62 ppm

***X_ram*, in**	***h*, in**	***h/L***
15.88 [8.00 : 23.75]	32.64 [32.57 : 32.73]	1.71 [1.71 : 1.72]
***α*, deg**	***β*, deg**	***ϕ*, deg**
2.20 [2.14 : 2.26]	-0.13 [-0.15 : -0.12]	0.06 [-0.01 : 0.11]
CL	***CD***	***CM***
0.123 [0.119 : 0.130]	0.06188 [0.06051 : 0.06318]	-0.238 [-0.250 : -0.222]

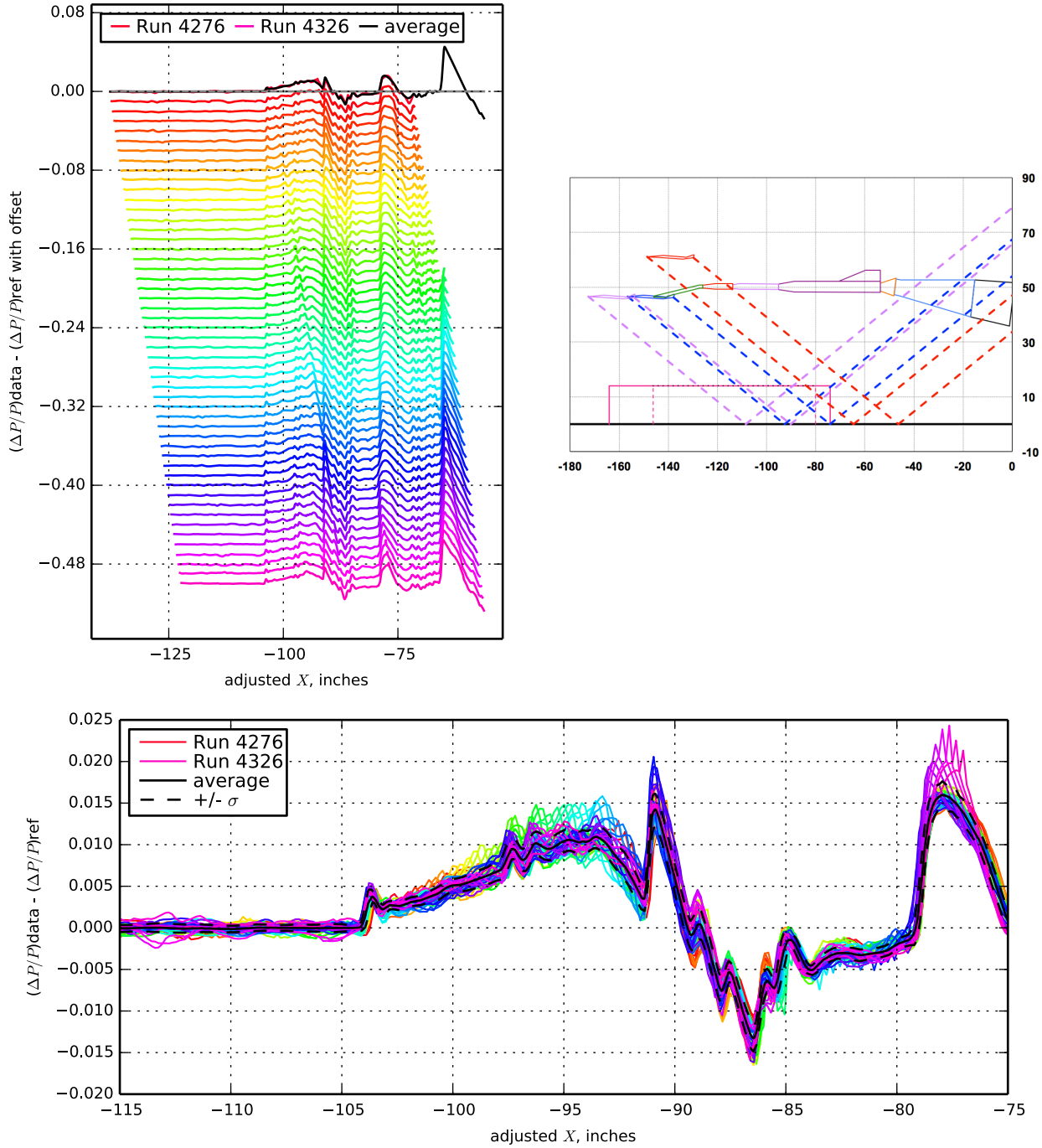

Figure 7.39. 1044 model with blade strut, Runs 4276-4326:4275, Mach 1.7, Duration 6 sec, Re 6.81x10^6, T -99.47° F, PT 2299.19 psf, PT-Ref 0.16 psf, H 213.6 ppm [211.7 : 215.1], H-Ref -4.09 ppm

***X_ram*, in**	***h*, in**	***h/L***
15.88 [8.00 : 23.75]	32.59 [32.52 : 32.70]	1.71 [1.71 : 1.72]
***α*, deg**	***β*, deg**	***ϕ*, deg**
2.22 [2.17 : 2.29]	-0.61 [-0.62 : -0.59]	-0.28 [-0.34 : -0.25]
CL	***CD***	***CM***
0.125 [0.120 : 0.132]	0.06153 [0.06005 : 0.06293]	-0.241 [-0.253 : -0.227]

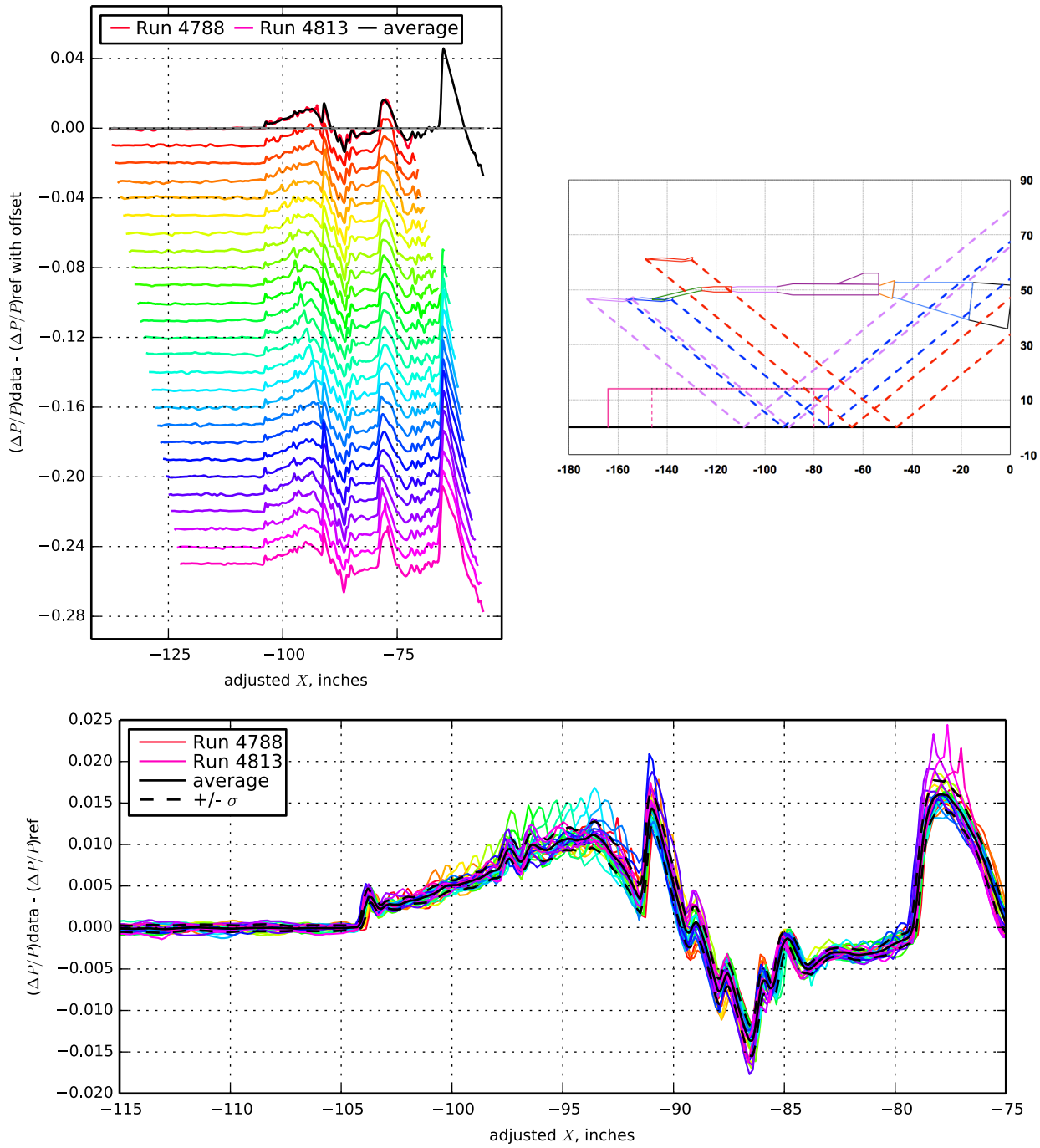

Figure 7.40. 1044 model with blade strut, Runs 4788-4813:4787, Mach 1.7, Duration 6 sec, Re 6.77x10^6, T -97.87° F, PT 2299.64 psf, PT-Ref 0.00 psf, H 181.2 ppm, H-Ref -0.02 ppm

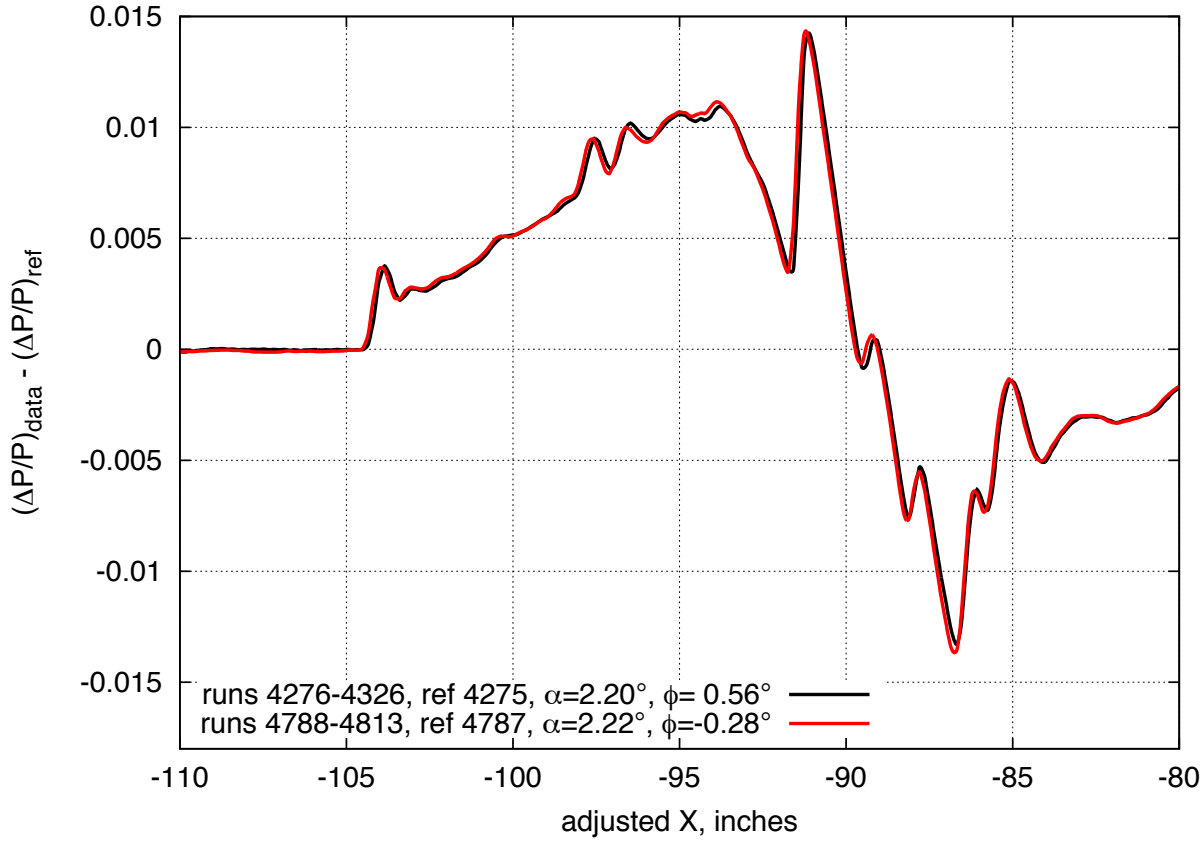

Figure 7.41. Comparison of near-repeat run series pressure signatures for the 1044 Phase II model with blade strut, on-track, M=1.7, h=32.6 inches

***X_ram*, in**	***h*, in**	***h/L***
15.88 [8.00 : 23.75]	32.64 [32.55 : 32.76]	1.72 [1.71 : 1.72]
***α*, deg**	***β*, deg**	***ϕ*, deg**
2.29 [2.24 : 2.35]	0.53 [0.51 : 0.56]	10.52 [10.32 : 10.70]
CL	***CD***	***CM***
0.124 [0.119 : 0.128]	0.06240 [0.06156 : 0.06411]	-0.239 [-0.256 : -0.228]

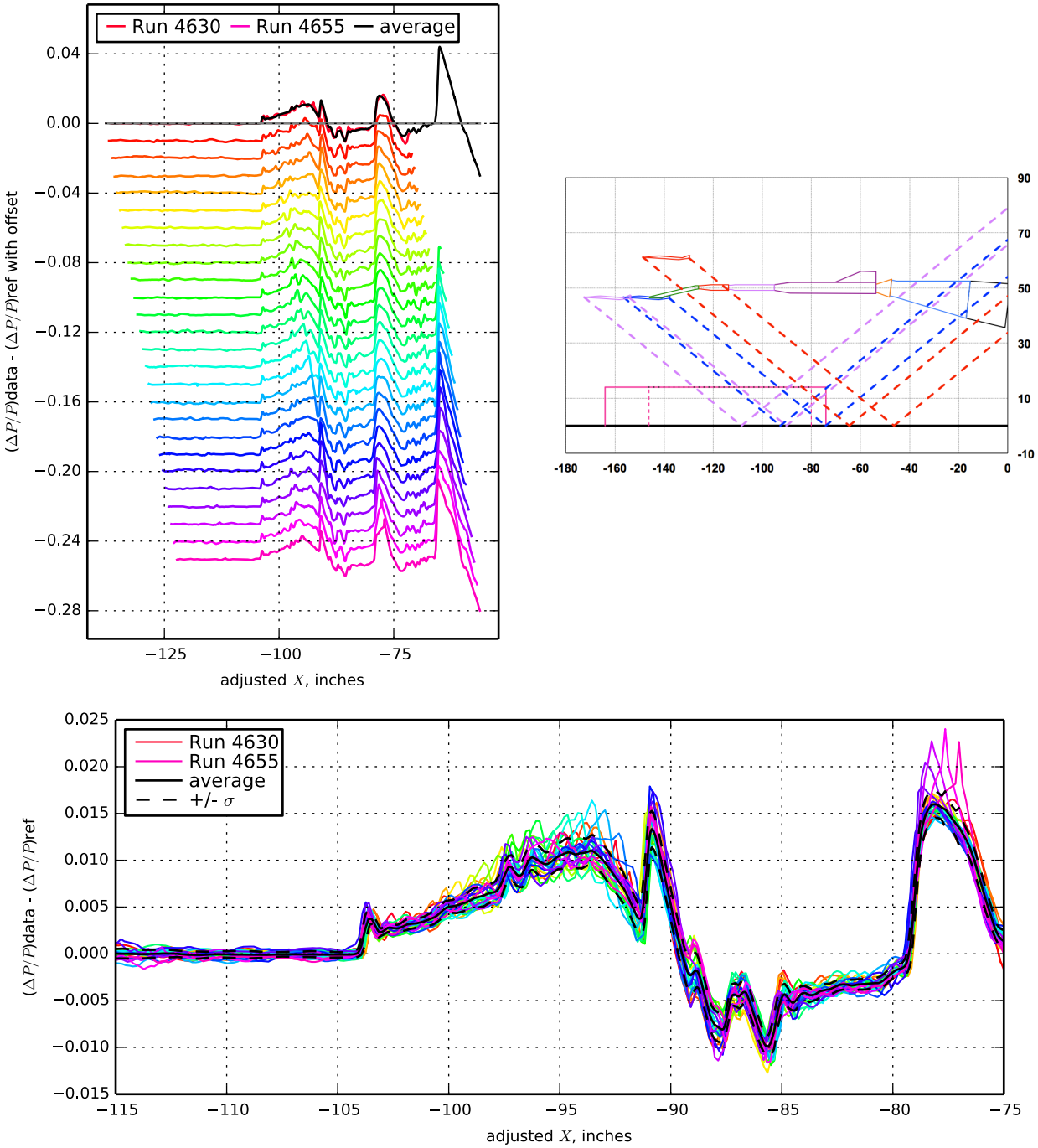

Figure 7.42. 1044 model with blade strut, Runs 4630-4655:4629, Mach 1.7, Duration 6 sec, Re 6.79x10^6, T -98.78° F, PT 2299.80 psf, PT-Ref -0.44 psf, H 227.9 ppm [227.3 : 228.6], H-Ref 0.28 ppm

***X_ram*, in**	***h*, in**	***h/L***
15.88 [8.00 : 23.75]	32.65 [32.54 : 32.79]	1.72 [1.71 : 1.72]
***α*, deg**	***β*, deg**	***ϕ*, deg**
2.40 [2.36 : 2.46]	0.39 [0.36 : 0.41]	20.15 [20.01 : 20.27]
CL	***CD***	***CM***
0.125 [0.121 : 0.130]	0.06266 [0.06188 : 0.06439]	-0.244 [-0.264 : -0.232]

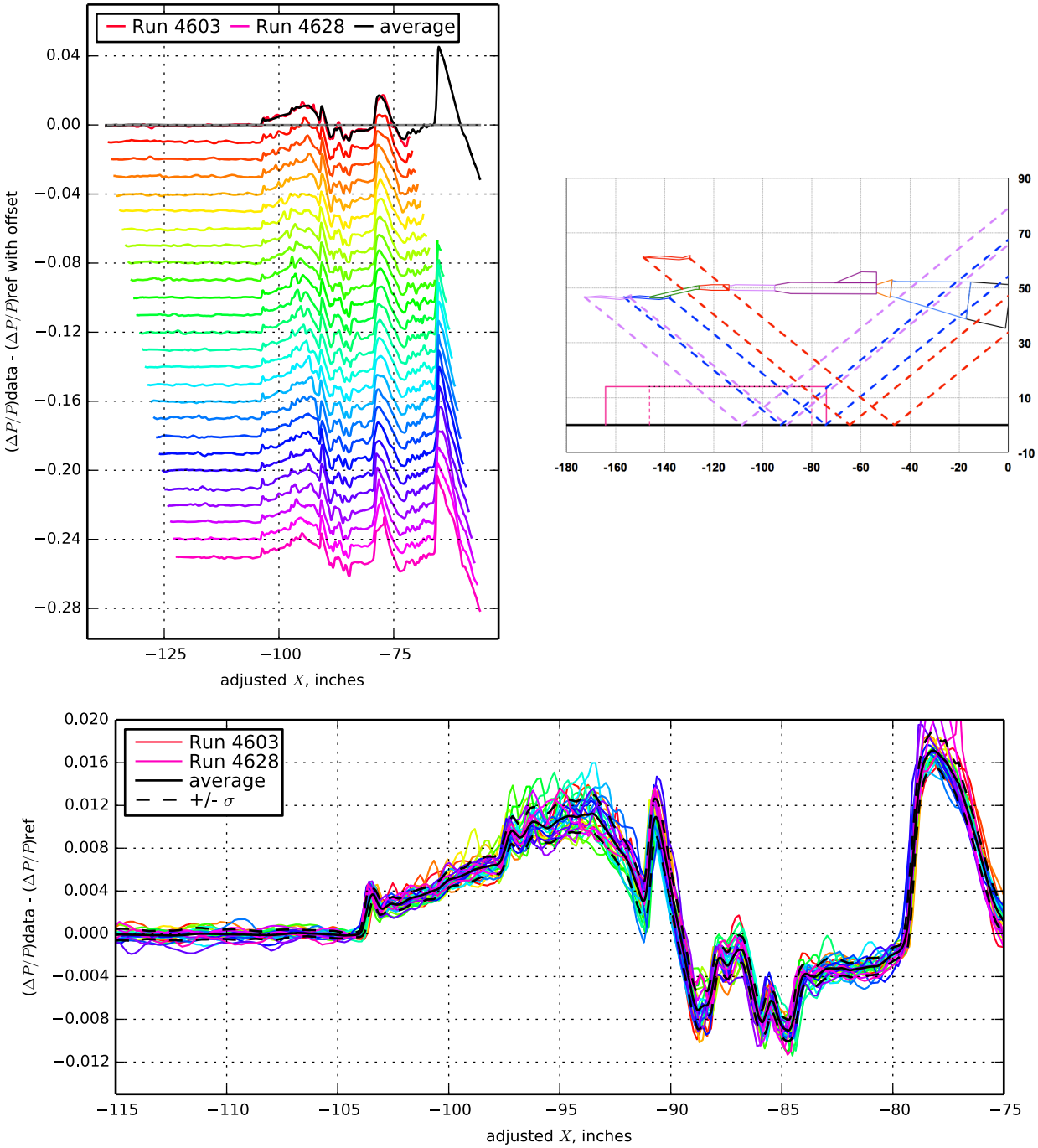

Figure 7.43. 1044 model with blade strut, Runs 4603-4628:4602, Mach 1.7, Duration 6 sec, Re 6.79x10^6, T -98.90° F, PT 2299.83 psf, PT-Ref -0.19 psf, H 224.1 ppm [223.3 : 225.2], H-Ref 0.82 ppm

***X_ram*, in**	***h*, in**	***h/L***
15.88 [8.00 : 23.75]	32.68 [32.56 : 32.82]	1.72 [1.71 : 1.72]
***α*, deg**	***β*, deg**	***ϕ*, deg**
2.46 [2.41 : 2.50]	0.45 [0.43 : 0.48]	30.46 [30.35 : 30.59]
CL	***CD***	***CM***
0.122 [0.118 : 0.126]	0.06298 [0.06203 : 0.06470]	-0.238 [-0.256 : -0.226]

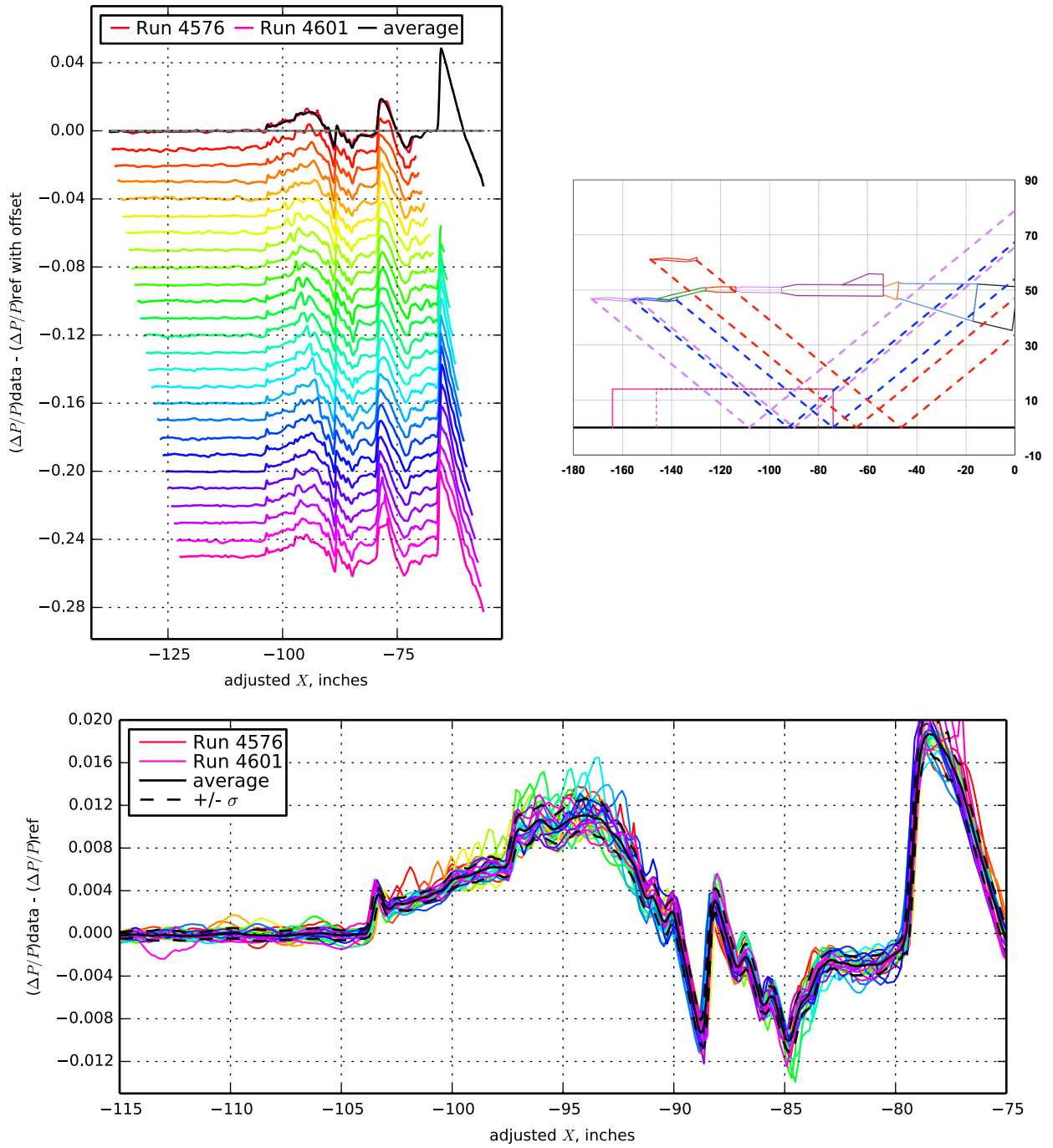

Figure 7.44. 1044 model with blade strut, Runs 4576-4601:4575, Mach 1.7, Duration 6 sec, Re 6.80x10^6, T -99.09° F, PT 2299.84 psf, PT-Ref 0.15 psf, H 227.1 ppm [222.8 : 227.9], H-Ref 2.75 ppm

***X_ram*, in**	***h*, in**	***h/L***
15.88 [8.00 : 23.75]	32.64 [32.51 : 32.78]	1.71 [1.71 : 1.72]
***α*, deg**	***β*, deg**	***ϕ*, deg**
2.51 [2.48 : 2.54]	0.54 [0.52 : 0.58]	40.14 [40.05 : 40.27]
CL	***CD***	***CM***
0.120 [0.116 : 0.123]	0.06340 [0.06236 : 0.06511]	-0.234 [-0.253 : -0.224]

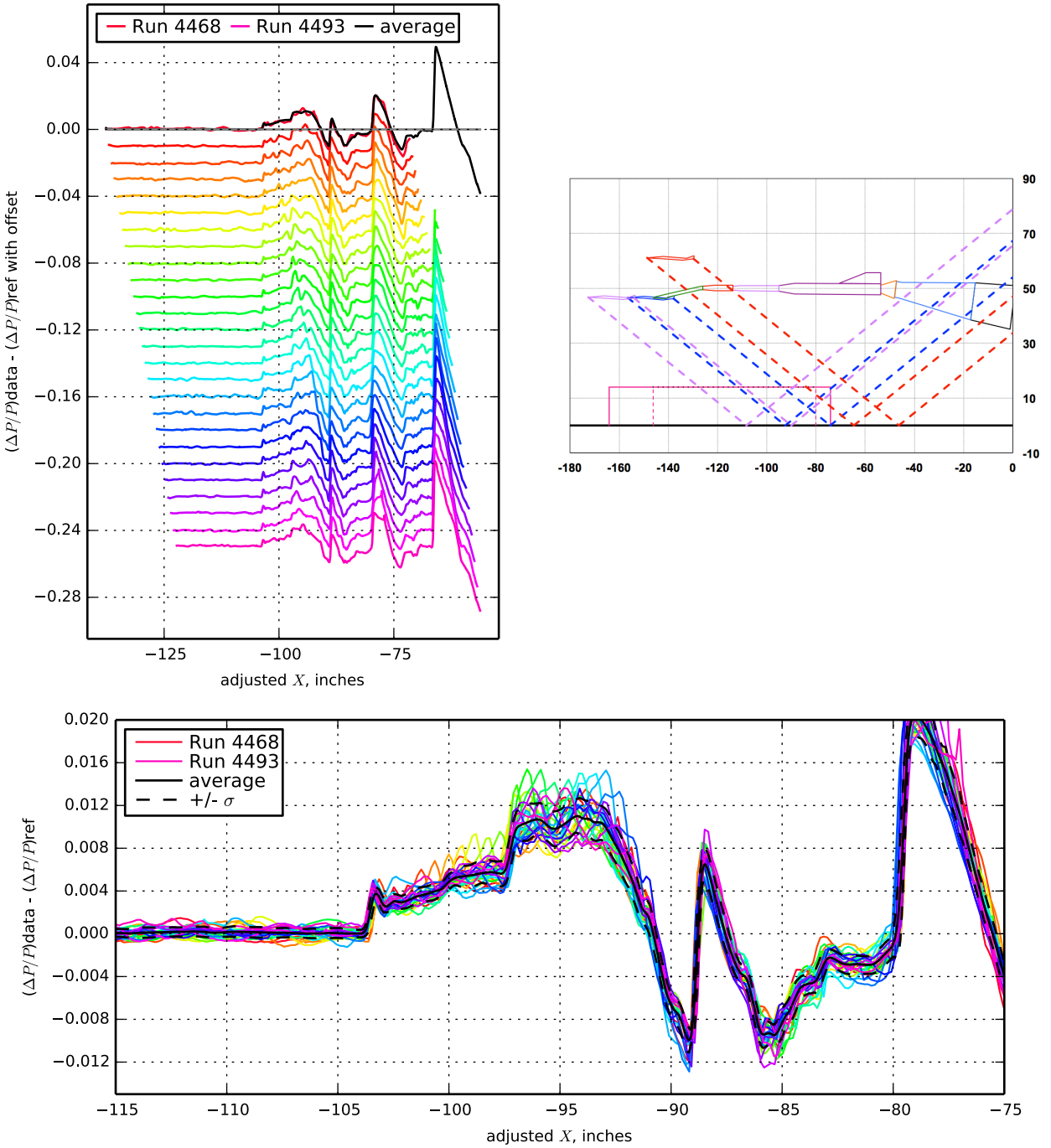

Figure 7.45. 1044 model with blade strut, Runs 4468-4493:4467, Mach 1.7, Duration 6 sec, Re 6.80x10^6, T -99.35° F, PT 2299.34 psf, PT-Ref 0.26 psf, H 218.3 ppm [216.5 : 219.8], H-Ref 0.34 ppm

***X_ram*, in**	***h*, in**	***h/L***
15.88 [8.00 : 23.75]	32.54 [32.42 : 32.68]	1.71 [1.70 : 1.72]
***α*, deg**	***β*, deg**	***ϕ*, deg**
2.65 [2.62 : 2.68]	0.30 [0.28 : 0.33]	50.42 [50.40 : 50.46]
CL	***CD***	***CM***
0.121 [0.118 : 0.124]	0.06357 [0.06273 : 0.06513]	-0.238 [-0.251 : -0.230]

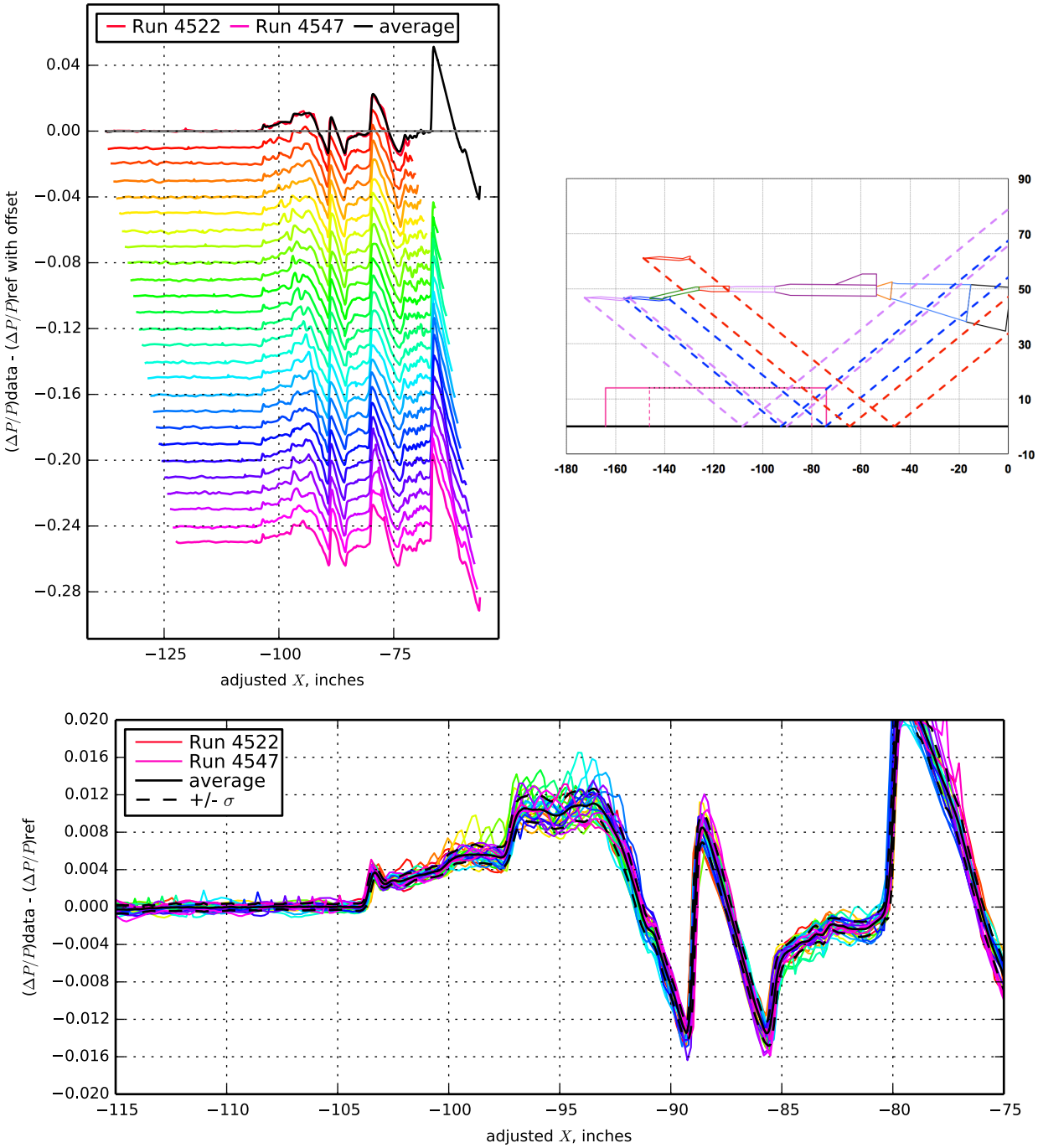

Figure 7.46. 1044 model with blade strut, Runs 4522-4547:4521, Mach 1.7, Duration 6 sec, Re 6.81x10^6, T -99.44° F, PT 2299.75 psf, PT-Ref 0.32 psf, H 226.9 ppm [225.7 : 228.3], H-Ref -0.97 ppm

***X_ram*, in**	***h*, in**	***h/L***
15.88 [8.00 : 23.75]	32.41 [32.30 : 32.54]	1.70 [1.70 : 1.71]
***α*, deg**	***β*, deg**	***ϕ*, deg**
2.77 [2.73 : 2.80]	0.21 [0.19 : 0.23]	60.07 [60.02 : 60.16]
CL	***CD***	***CM***
0.122 [0.117 : 0.126]	0.06371 [0.06272 : 0.06513]	-0.238 [-0.247 : -0.227]

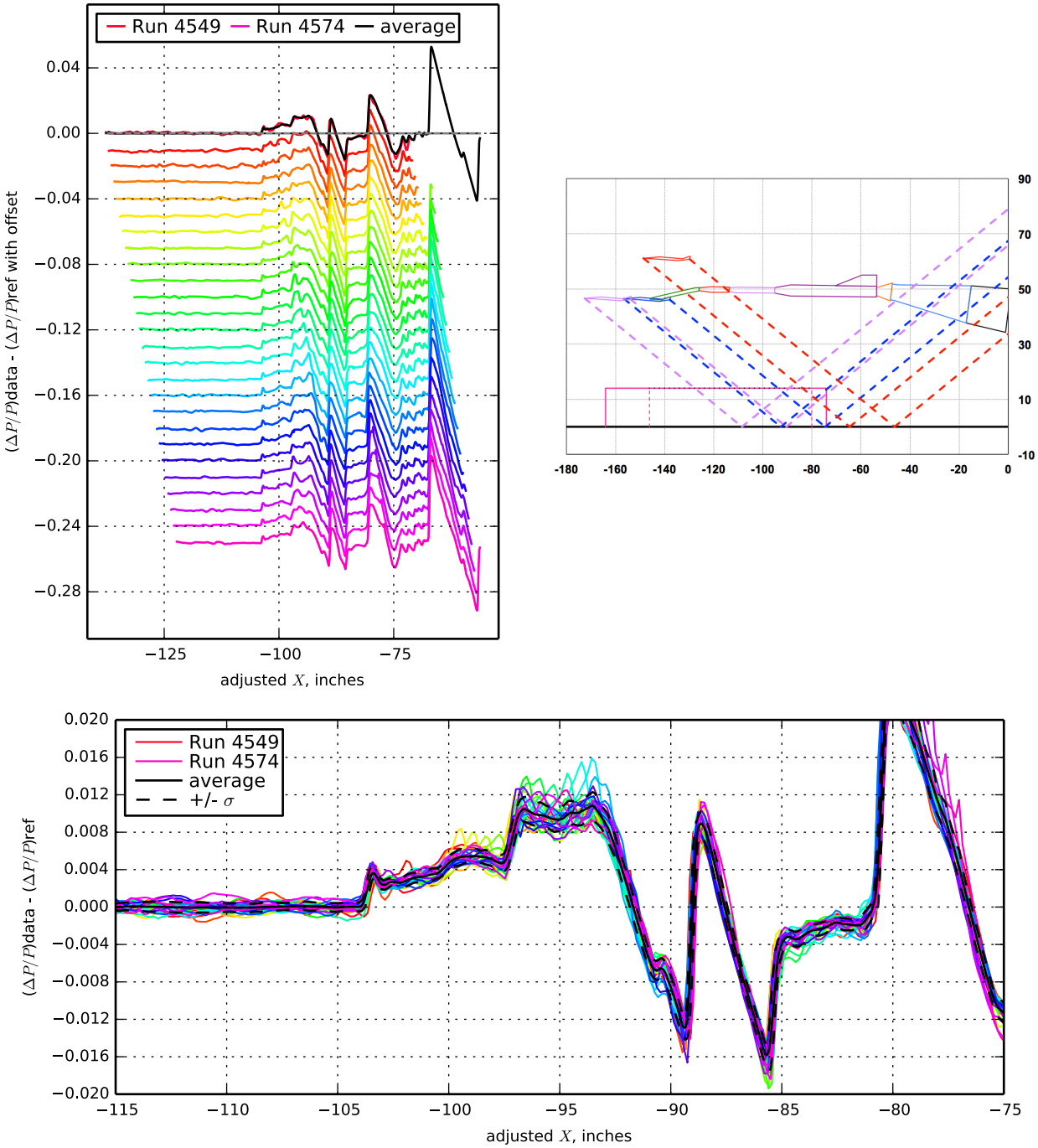

Figure 7.47. 1044 model with blade strut, Runs 4549-4574:4548, Mach 1.7, Duration 6 sec, Re 6.81x10^6, T -99.37° F, PT 2299.74 psf, PT-Ref -0.29 psf, H 225.3 ppm [224.9 : 226.2], H-Ref -2.90 ppm

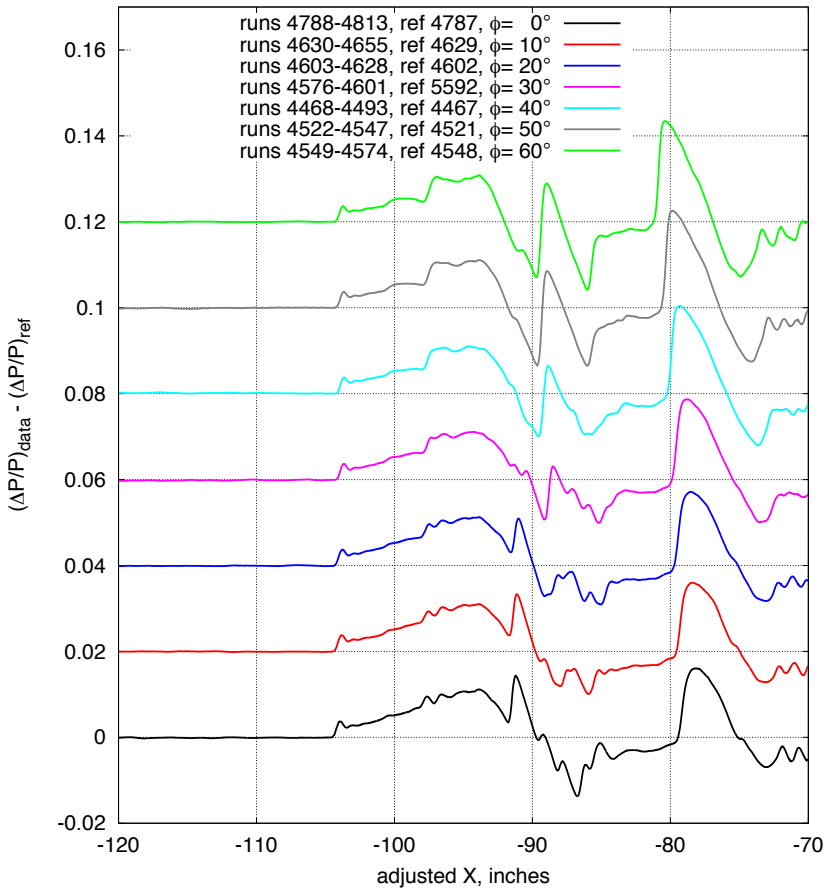

a) Stacked average data

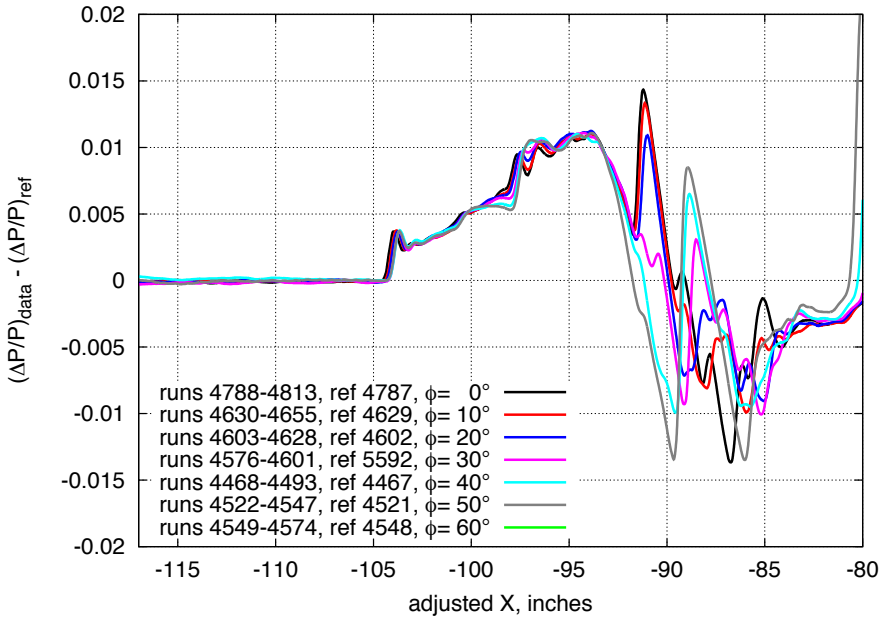

b) Overlaid average data

Figure 7.48. Comparison of on- and off-track pressure signatures for the 1044 Phase II model with blade strut, M=1.7, h=32 inches

***X_ram*, in**	***h*, in**	***h/L***
11.97 [-0.01 : 23.94]	54.76 [54.73 : 54.83]	2.88 [2.88 : 2.88]
***α*, deg**	***β*, deg**	***ϕ*, deg**
1.74 [1.71 : 1.79]	-0.18 [-0.23 : -0.10]	-0.23 [-0.29 : -0.13]
CL	***CD***	***CM***
0.106 [0.096 : 0.113]	0.03637 [0.03552 : 0.03759]	-0.111 [-0.121 : -0.093]

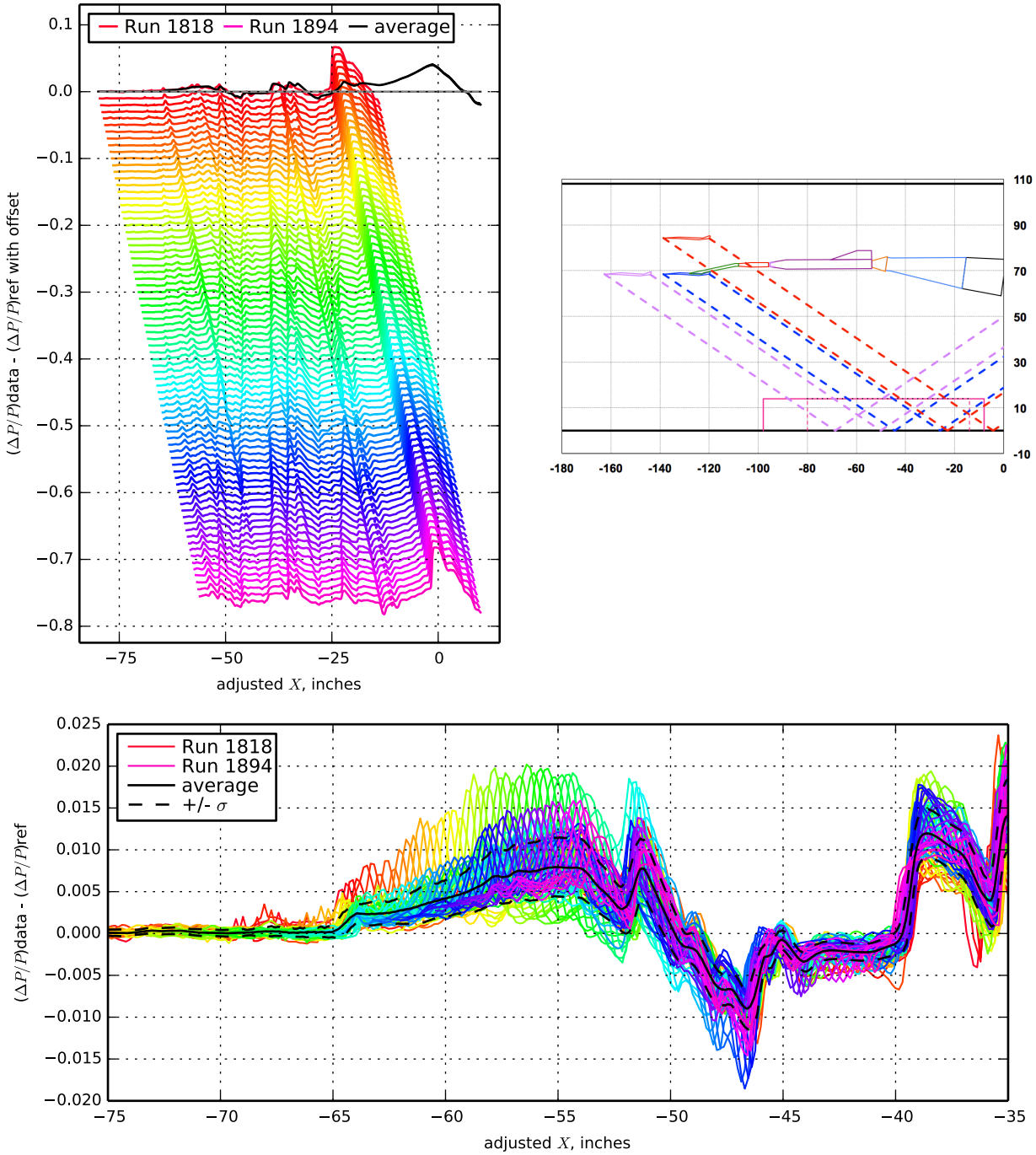

Figure 7.49. 1044 model with blade strut, Runs 1818-1894:1895, Mach 1.7, Duration 6 sec, Re 6.74x10^6, T -96.79° F, PT 2299.87 psf, PT-Ref -0.51 psf, H 251.1 ppm [249.5 : 252.8], H-Ref 1.99 ppm

***X_ram*, in**	***h*, in**	***h/L***
13.55 [3.15 : 23.94]	54.77 [54.73 : 54.84]	2.88 [2.88 : 2.88]
***α*, deg**	***β*, deg**	***ϕ*, deg**
1.94 [1.92 : 1.95]	-0.22 [-0.28 : -0.16]	19.93 [19.87 : 20.01]
CL	***CD***	***CM***
0.103 [0.096 : 0.112]	0.03679 [0.03603 : 0.03784]	-0.099 [-0.111 : -0.086]

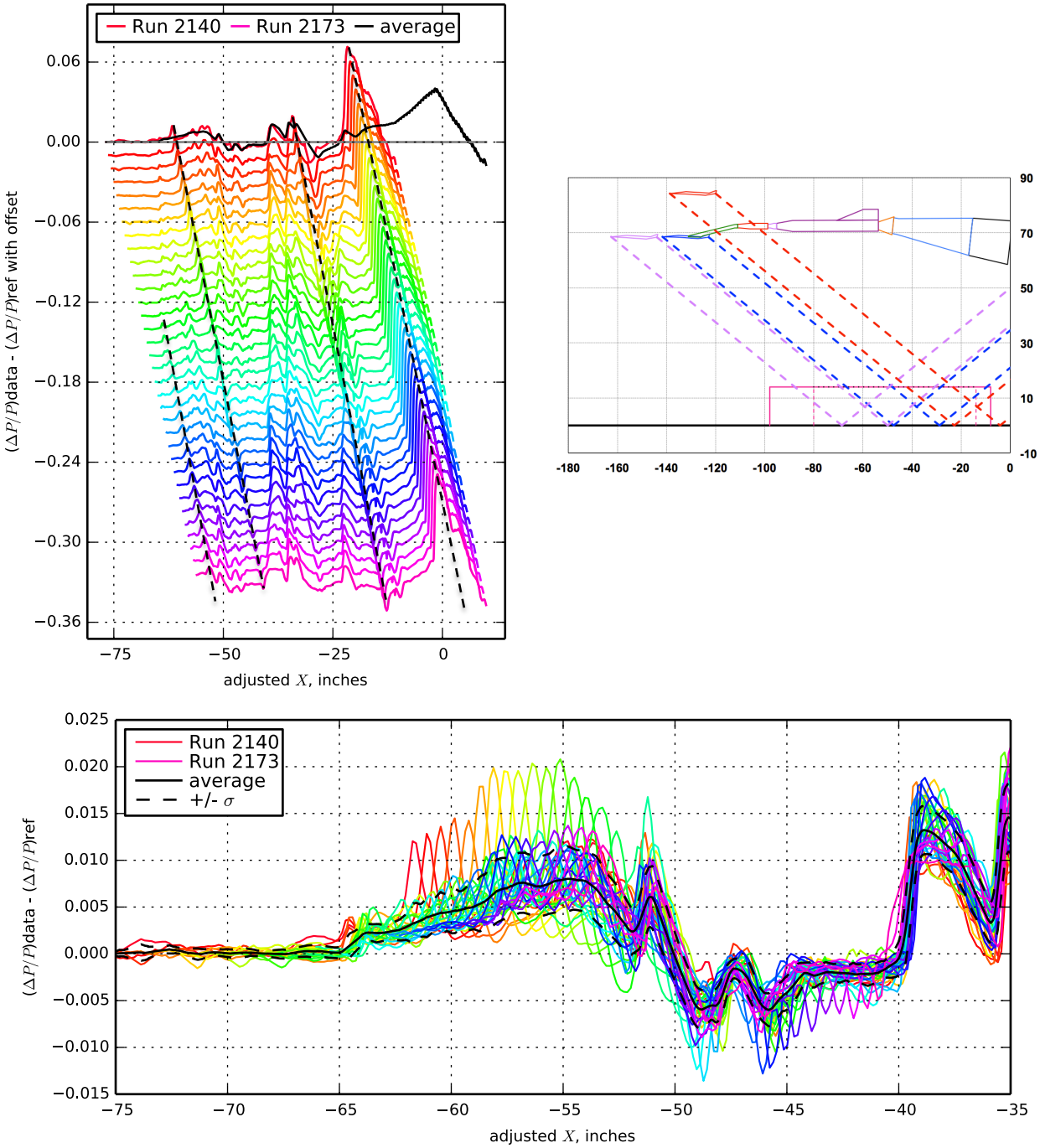

Figure 7.50. 1044 model with blade strut, Runs 2140-2173:2139, Mach 1.7, Duration 6 sec, Re 6.74x10^6, T -96.92° F, PT 2299.81 psf, PT-Ref -0.95 psf, H 220.8 ppm [219.8 : 221.9], H-Ref -0.14 ppm

***X_ram*, in**	***h*, in**	***h/L***
13.54 [3.15 : 23.94]	54.50 [54.48 : 54.52]	2.86 [2.86 : 2.86]
***α*, deg**	***β*, deg**	***ϕ*, deg**
1.97 [1.96 : 1.99]	-0.52 [-0.56 : -0.47]	40.03 [39.99 : 40.08]
CL	***CD***	***CM***
0.096 [0.084 : 0.111]	0.03707 [0.03624 : 0.03794]	-0.096 [-0.114 : -0.085]

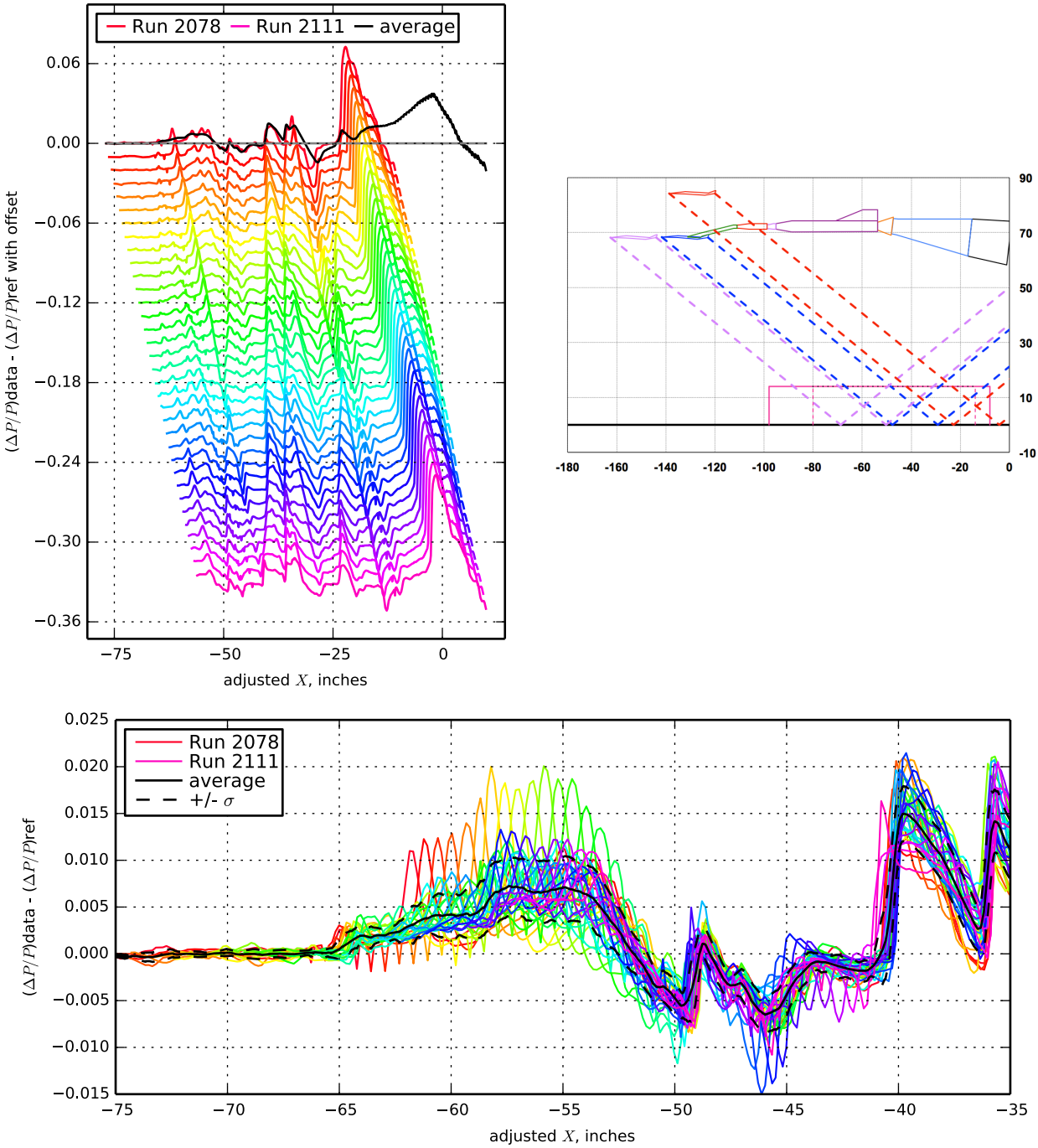

Figure 7.51. 1044 model with blade strut, Runs 2078-2111:2077, Mach 1.7, Duration 6 sec, Re 6.75x10^6, T -97.15° F, PT 2299.93 psf, PT-Ref -0.54 psf, H 225.7 ppm [224.9 : 226.6], H-Ref -2.57 ppm

***X_ram*, in**	***h*, in**	***h/L***
13.54 [3.14 : 23.94]	54.43 [54.40 : 54.48]	2.86 [2.86 : 2.86]
***α*, deg**	***β*, deg**	***ϕ*, deg**
1.99 [1.97 : 2.01]	-0.21 [-0.24 : -0.18]	60.03 [59.96 : 60.13]
CL	***CD***	***CM***
0.091 [0.076 : 0.109]	0.03735 [0.03627 : 0.03823]	-0.093 [-0.116 : -0.076]

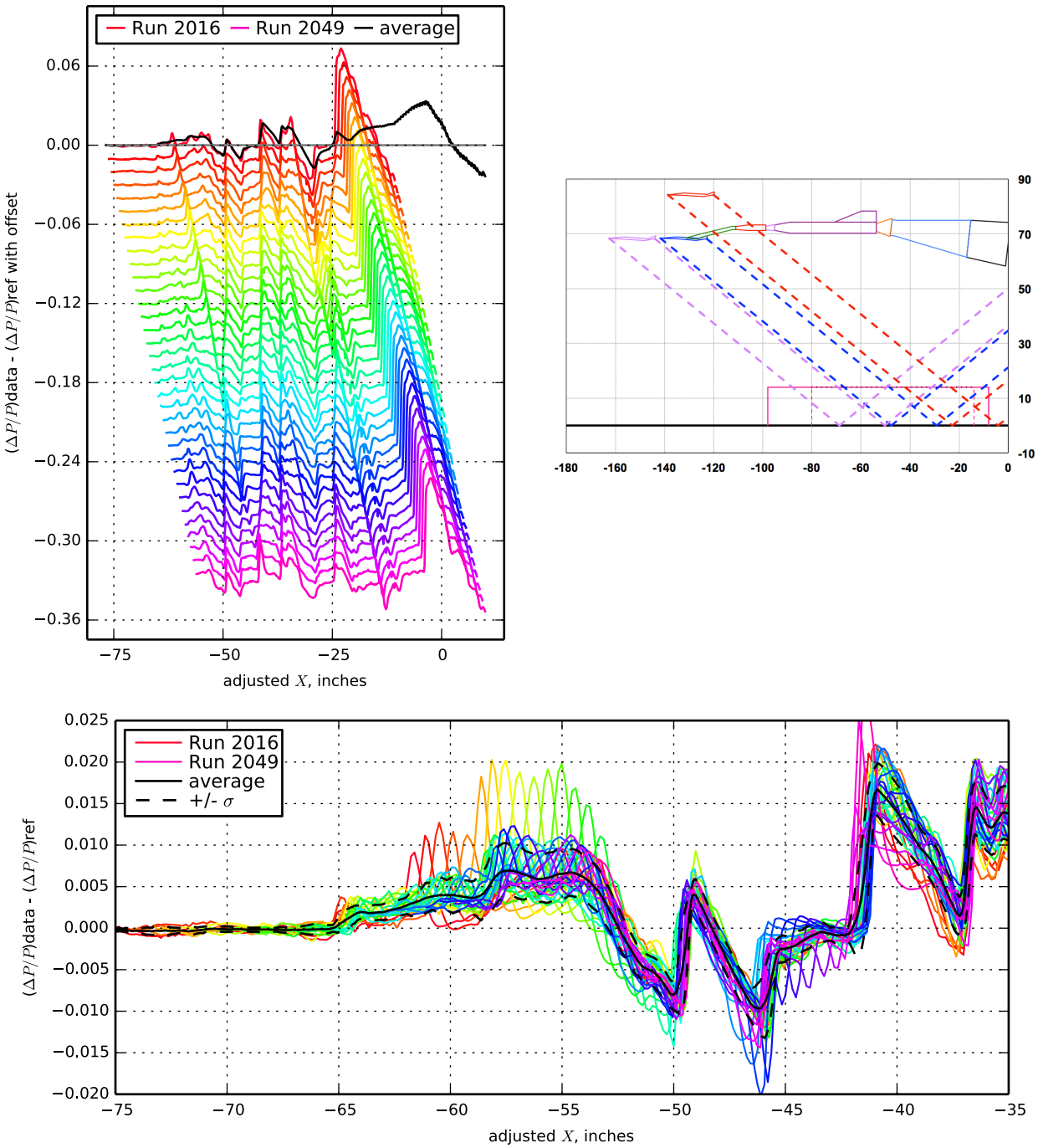

Figure 7.52. 1044 model with blade strut, Runs 2016-2049:2015, Mach 1.7, Duration 6 sec, Re 6.74x10^6, T -96.86° F, PT 2299.89 psf, PT-Ref -0.56 psf, H 233.7 ppm [232.9 : 234.8], H-Ref -4.21 ppm

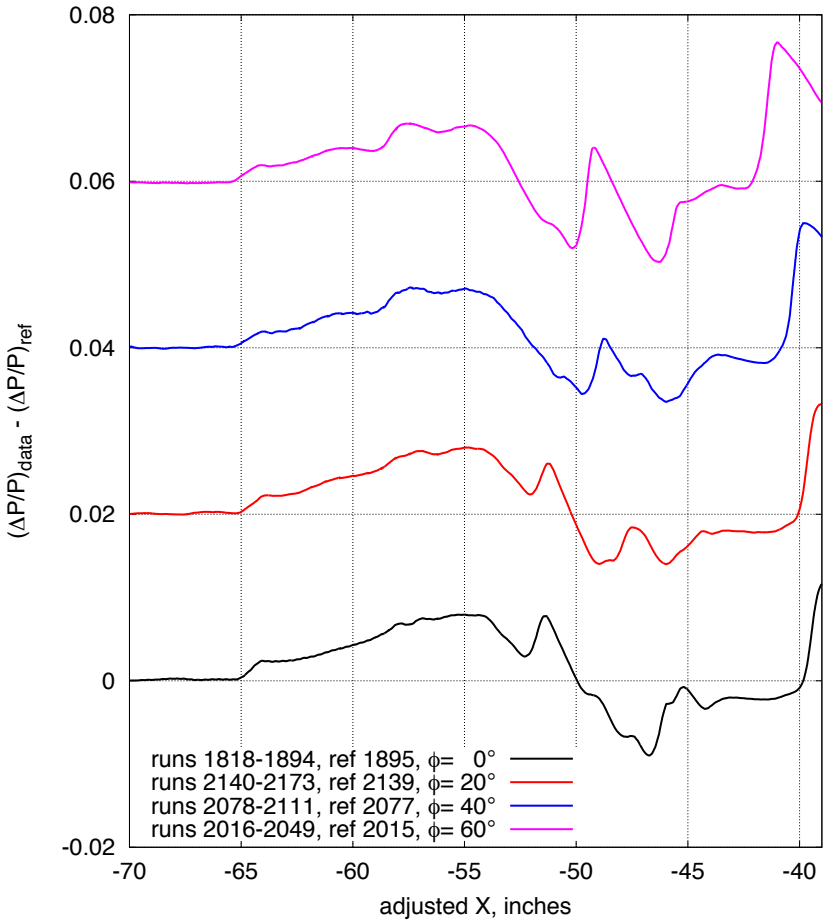

a) Stacked averaged data

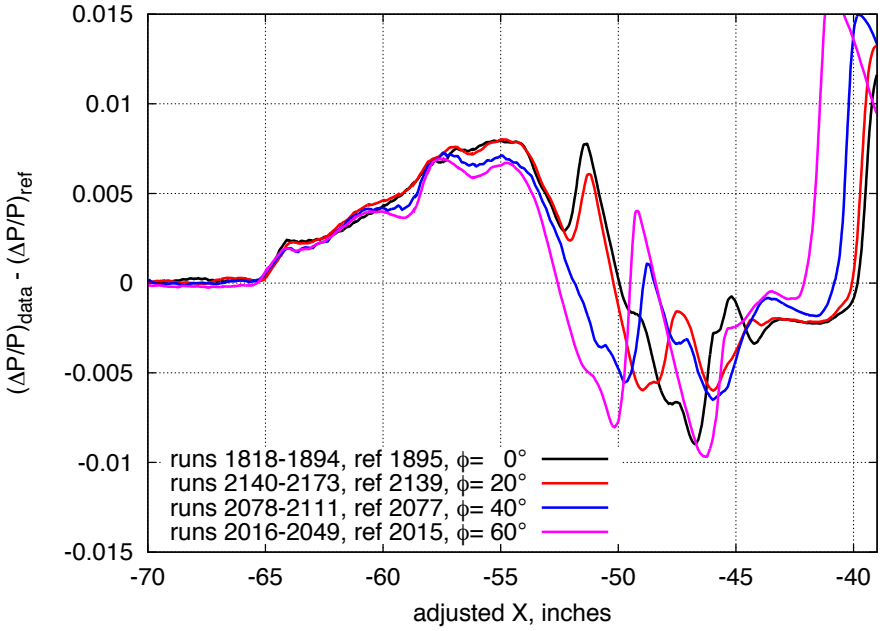

b) Overlaid averaged data

Figure 7.53. Comparison of on- and off-track pressure signatures for the 1044 Phase II model with blade strut, M=1.7, h=54 inches, lower lift coefficient data

***X_ram*, in**	***h*, in**	***h/L***
11.97 [-0.01 : 23.94]	70.68 [70.63 : 70.74]	3.71 [3.71 : 3.72]
***α*, deg**	***β*, deg**	***ϕ*, deg**
1.73 [1.68 : 1.77]	-0.16 [-0.21 : -0.10]	-0.12 [-0.17 : -0.07]
CL	***CD***	***CM***
0.105 [0.095 : 0.113]	0.03734 [0.03530 : 0.03867]	-0.120 [-0.139 : -0.107]

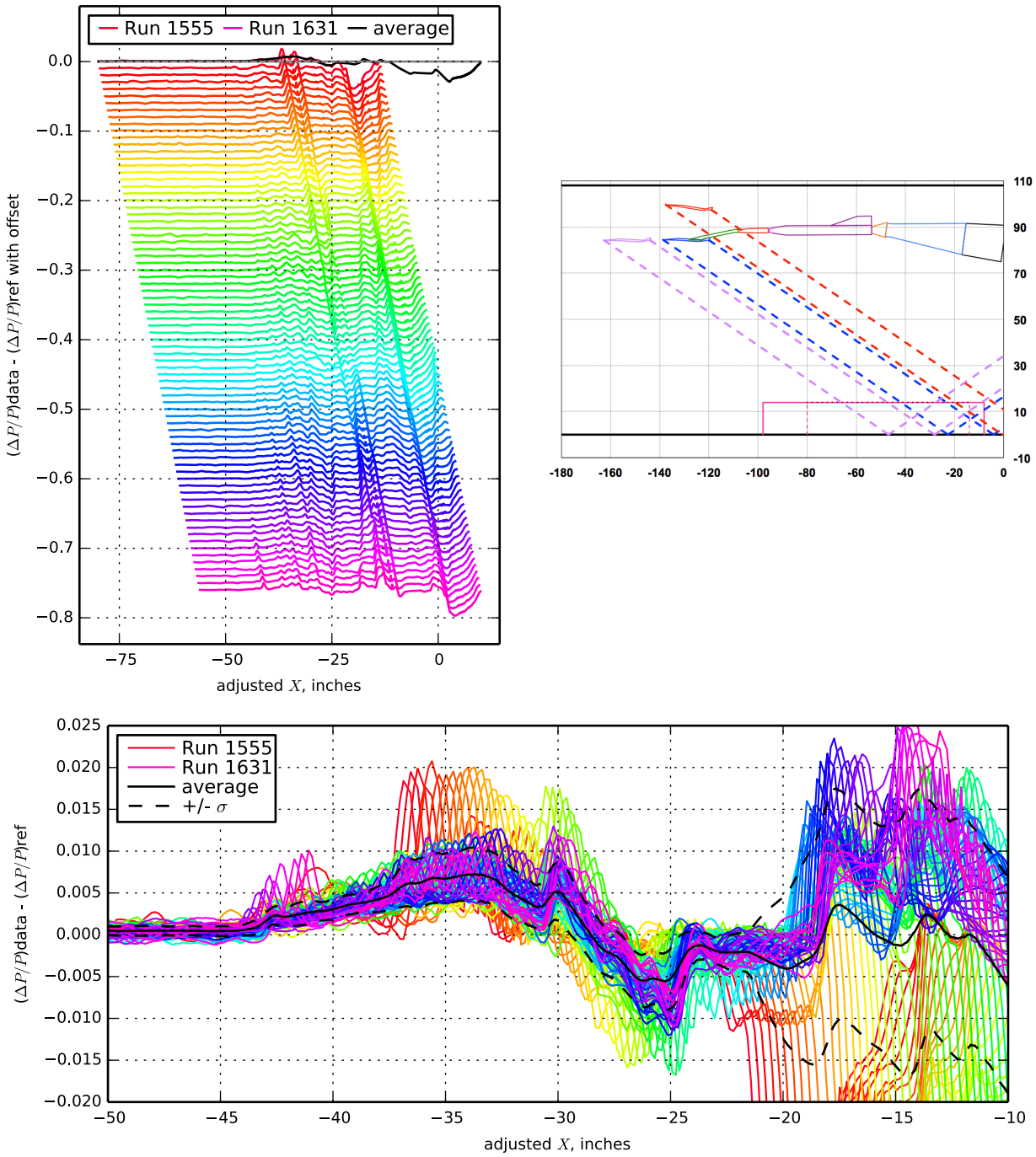

Figure 7.54. 1044 model with blade strut, Runs 1555-1631:1632, Mach 1.7, Duration 6 sec, Re 6.77x10^6, T -97.68° F, PT 2302.89 psf, PT-Ref -0.07 psf, H 280.8 ppm [277.0 : 284.9], H-Ref 4.87 ppm

***X_ram*, in**	***h*, in**	***h/L***
11.97 [-0.01 : 23.94]	70.70 [70.65 : 70.76]	3.71 [3.71 : 3.72]
***α*, deg**	***β*, deg**	***ϕ*, deg**
1.74 [1.69 : 1.78]	0.93 [0.87 : 0.99]	-0.16 [-0.37 : 0.06]
CL	***CD***	***CM***
0.103 [0.094 : 0.110]	0.03712 [0.03556 : 0.03798]	-0.114 [-0.128 : -0.101]

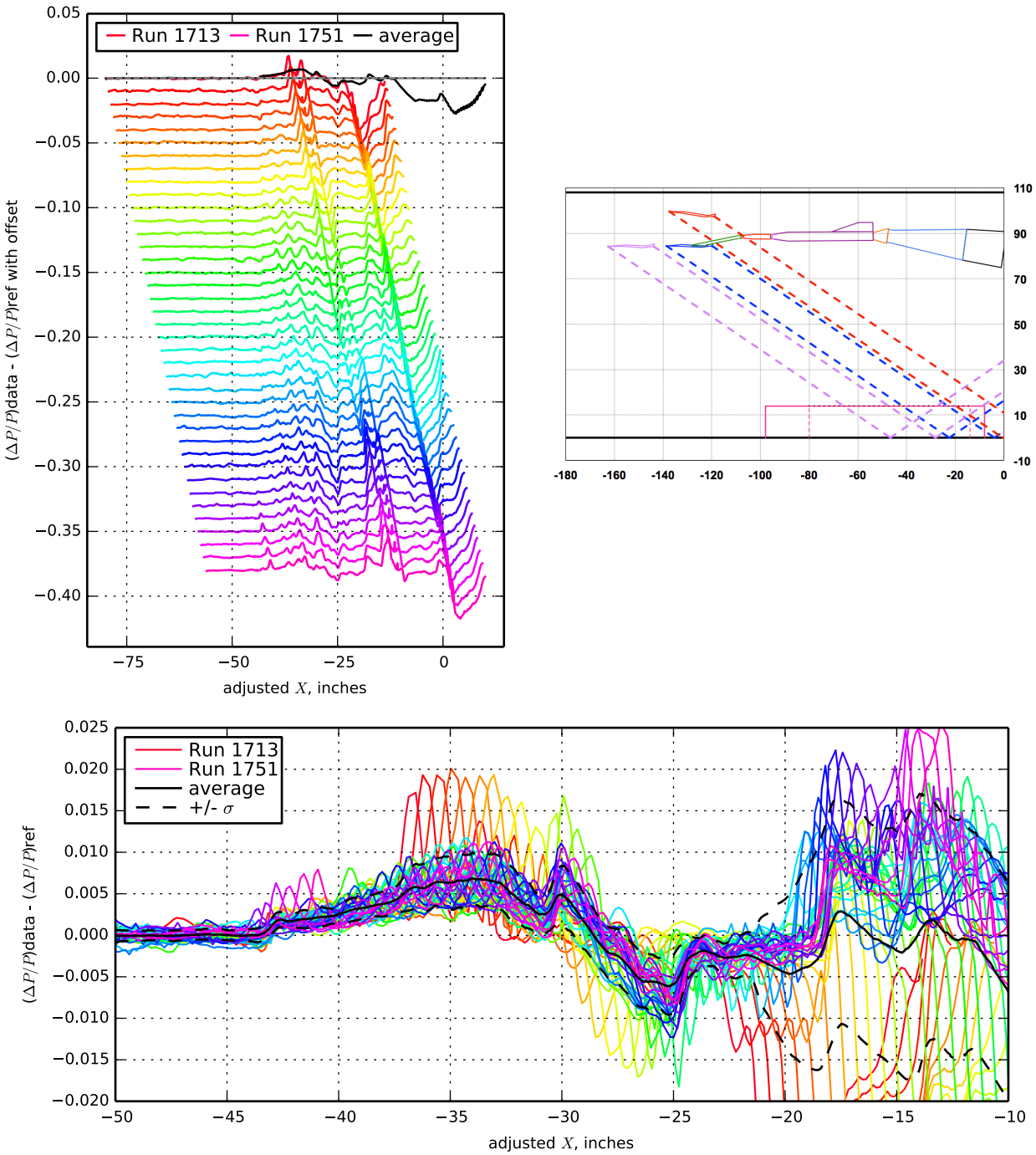

Figure 7.55. 1044 model with blade strut, Runs 1713-1751:1712, Mach 1.7, Duration 6 sec, Re 6.75x10^6, T -97.12° F, PT 2300.34 psf, PT-Ref -1.34 psf, H 256.6 ppm [255.8 : 257.5], H-Ref -4.96 ppm

***X_ram*, in**	***h*, in**	***h/L***
11.97 [-0.01 : 23.94]	70.85 [70.76 : 70.97]	3.72 [3.72 : 3.73]
***α*, deg**	***β*, deg**	***ϕ*, deg**
2.03 [1.98 : 2.08]	0.12 [0.07 : 0.18]	0.40 [0.32 : 0.50]
CL	***CD***	***CM***
0.115 [0.105 : 0.124]	0.03654 [0.03476 : 0.03776]	-0.111 [-0.128 : -0.098]

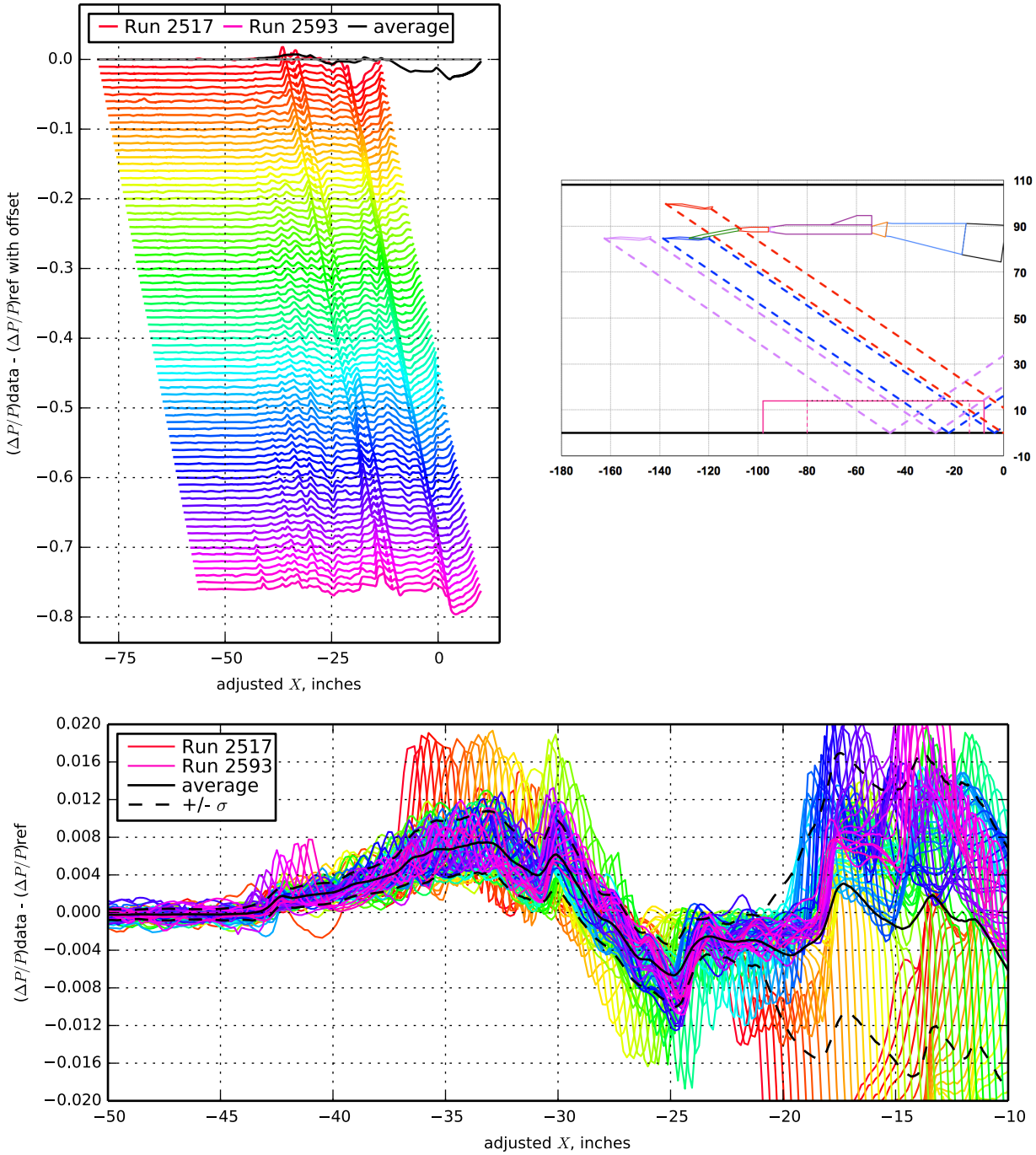

Figure 7.56. 1044 model with blade strut, Runs 2517-2593:2594, Mach 1.7, Duration 6 sec, Re 6.73x10^6, T -96.31° F, PT 2299.73 psf, PT-Ref -0.75 psf, H 215.0 ppm [214.3 : 215.9], H-Ref -0.86 ppm

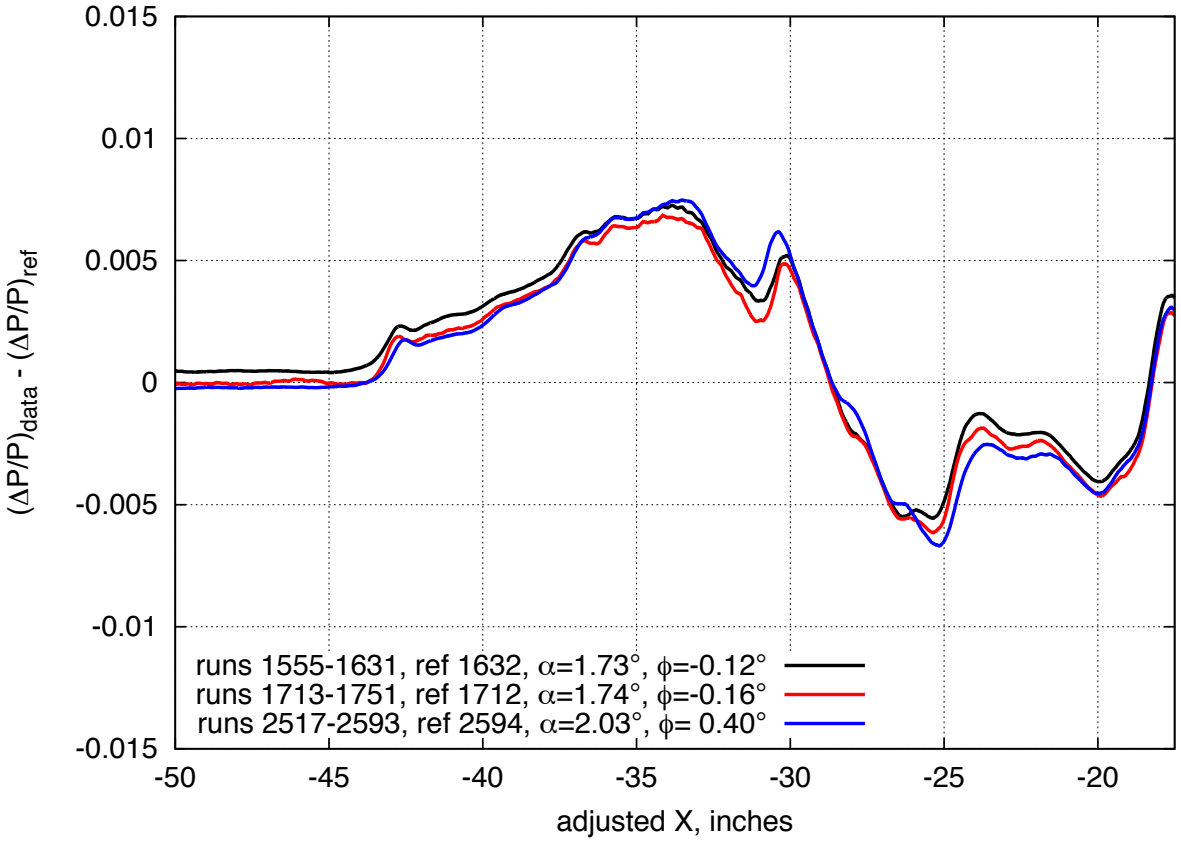

Figure 7.57. Comparison of near-repeat on-track pressure signatures for the 1044 Phase II model with blade strut, M=1.7, h=70.7 inches

***X_ram*, in**	***h*, in**	***h/L***
13.23 [4.41 : 22.05]	70.83 [70.72 : 70.95]	3.72 [3.72 : 3.73]
***α*, deg**	***β*, deg**	***ϕ*, deg**
2.07 [2.04 : 2.11]	0.32 [0.27 : 0.34]	20.10 [20.02 : 20.17]
CL	***CD***	***CM***
0.108 [0.102 : 0.114]	0.03741 [0.03642 : 0.03843]	-0.099 [-0.107 : -0.092]

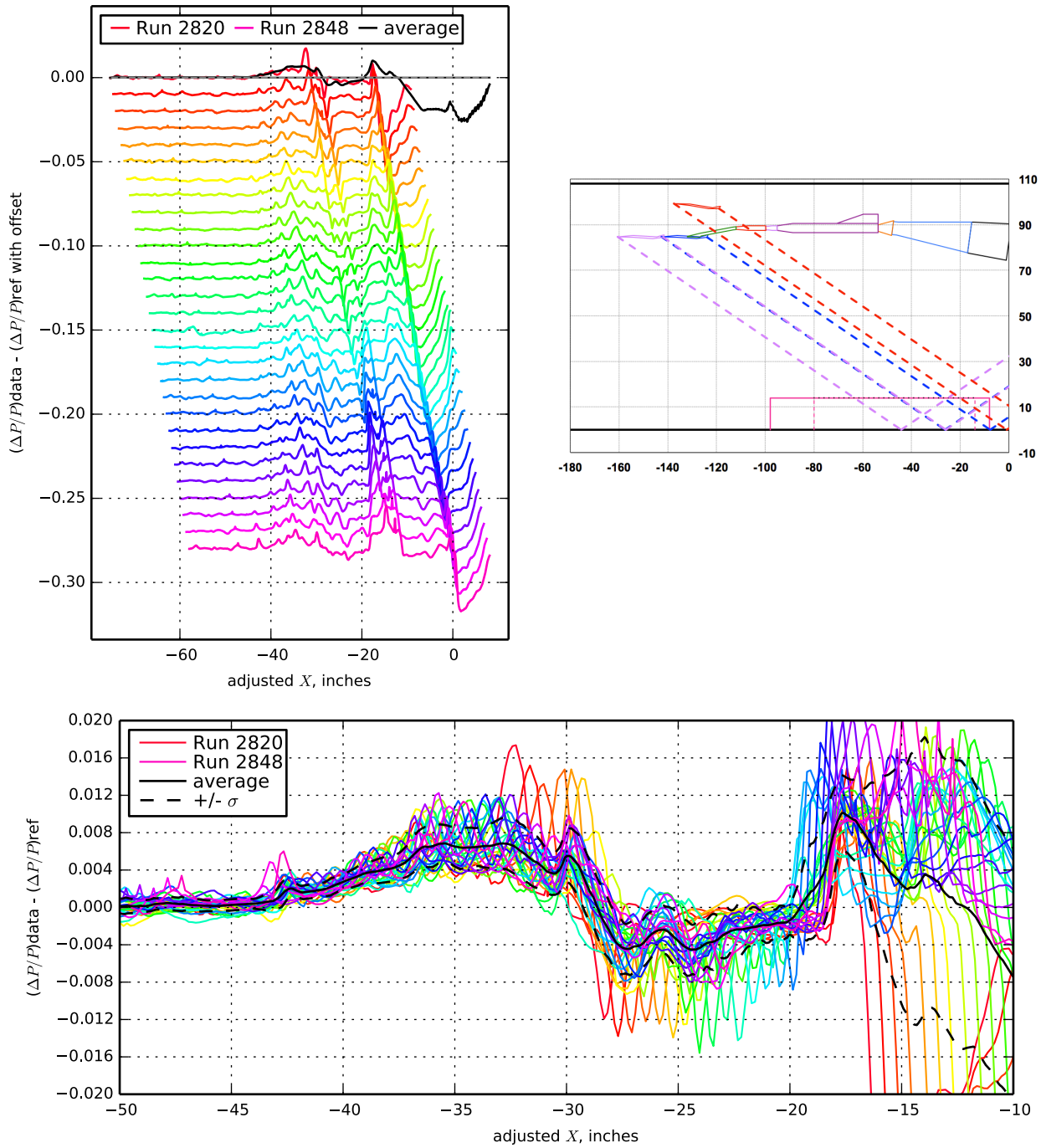

Figure 7.58. 1044 model with blade strut, Runs 2820-2848:2819, Mach 1.7, Duration 6 sec, Re 6.70x10^6, T -95.04° F, PT 2299.83 psf, PT-Ref 0.37 psf, H 238.4 ppm, H-Ref 1.58 ppm

***X_ram*, in**	***h*, in**	***h/L***
13.23 [4.41 : 22.05]	70.85 [70.70 : 71.00]	3.72 [3.72 : 3.73]
***α*, deg**	***β*, deg**	***ϕ*, deg**
2.18 [2.15 : 2.20]	0.49 [0.45 : 0.52]	39.94 [39.87 : 40.01]
CL	***CD***	***CM***
0.106 [0.102 : 0.108]	0.03792 [0.03697 : 0.03878]	-0.098 [-0.109 : -0.089]

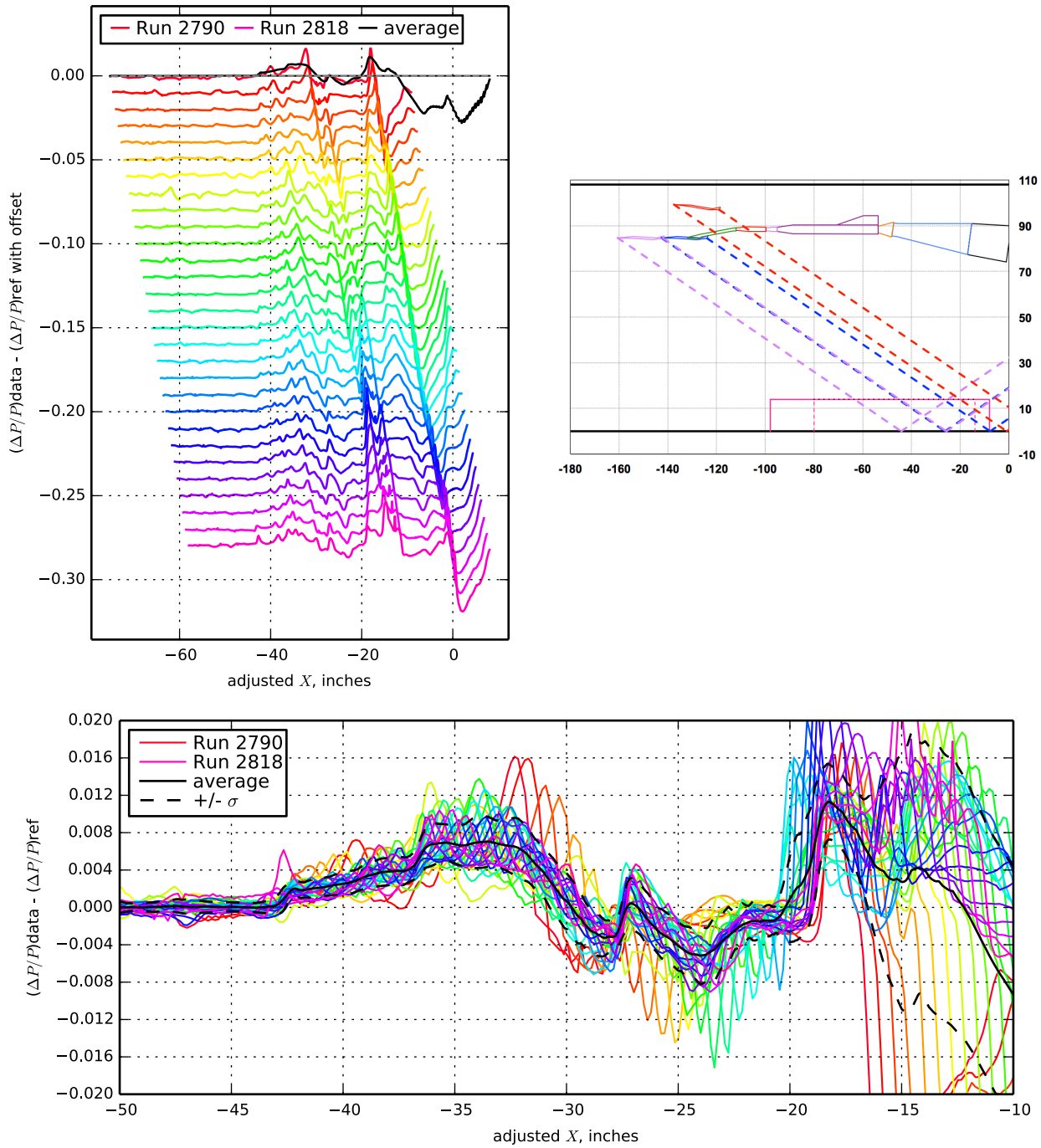

Figure 7.59. 1044 model with blade strut, Runs 2790-2818:2789, Mach 1.7, Duration 6.1 sec, Re 6.69×10^6, T -94.92° F, PT 2299.92 psf, PT-Ref -0.87 psf, H 235.9 ppm, H-Ref 2.05 ppm

***X_ram*, in**	***h*, in**	***h/L***
13.23 [4.41 : 22.05]	70.59 [70.48 : 70.70]	3.71 [3.70 : 3.71]
***α*, deg**	***β*, deg**	***ϕ*, deg**
2.30 [2.29 : 2.31]	0.12 [0.09 : 0.15]	59.60 [59.58 : 59.62]
CL	***CD***	***CM***
0.107 [0.103 : 0.111]	0.03840 [0.03742 : 0.03916]	-0.100 [-0.115 : -0.091]

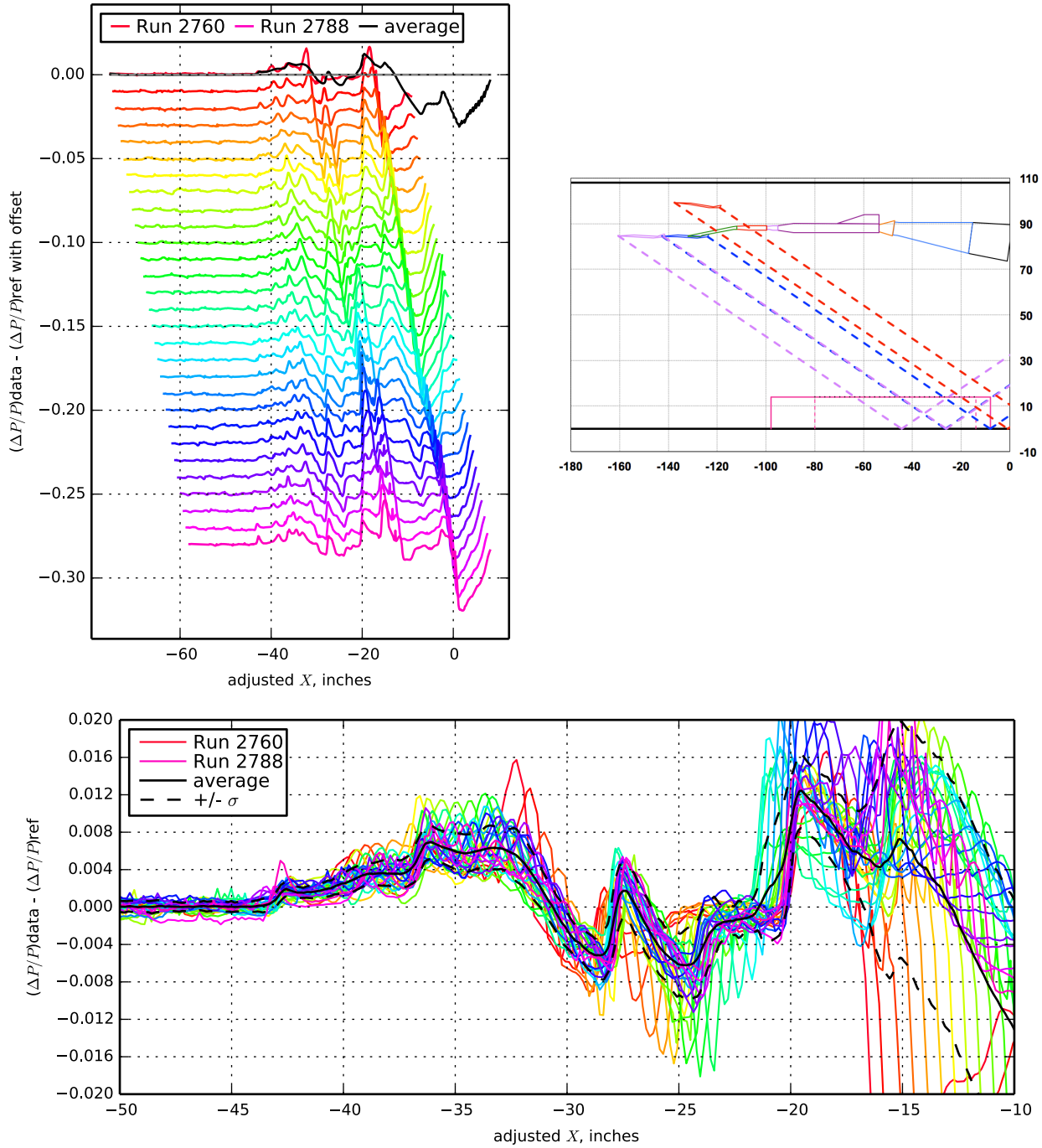

Figure 7.60. 1044 model with blade strut, Runs 2760-2788:2729, Mach 1.7, Duration 6 sec, Re 6.69x10^6, T -94.79° F, PT 2299.87 psf, PT-Ref 0.17 psf, H 232.9 ppm, H-Ref 2.23 ppm

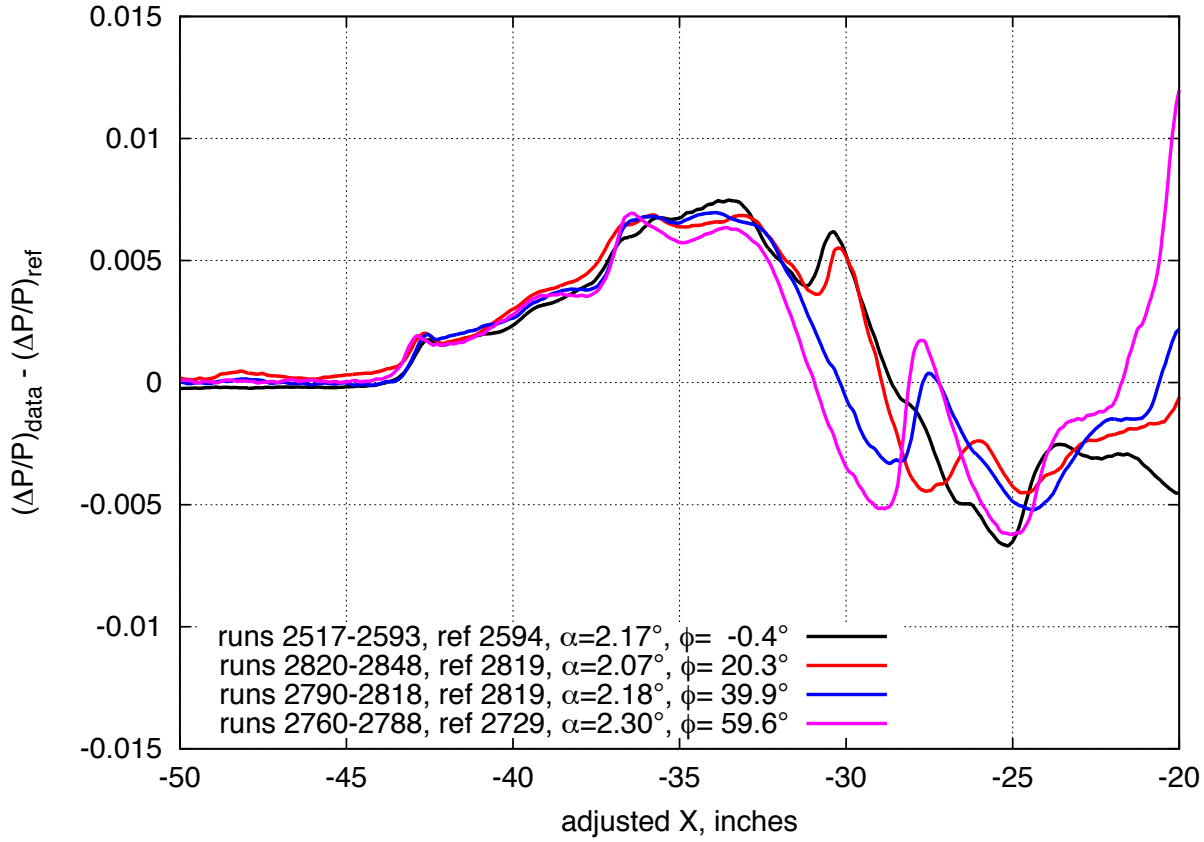

Figure 7.61. Comparison of on- and off-track pressure signatures for the 1044 Phase II model with blade strut, M=1.7, h=70.7 inches

***X_ram*, in**	***h*, in**	***h/L***
15.88 [8.00 : 23.75]	32.59 [32.53 : 32.68]	1.71 [1.71 : 1.72]
***α*, deg**	***β*, deg**	***ϕ*, deg**
2.17 [2.13 : 2.23]	0.59 [0.57 : 0.60]	0.45 [0.24 : 0.67]
CL	***CD***	***CM***
0.116 [0.111 : 0.121]	0.06003 [0.05931 : 0.06156]	-0.218 [-0.231 : -0.205]

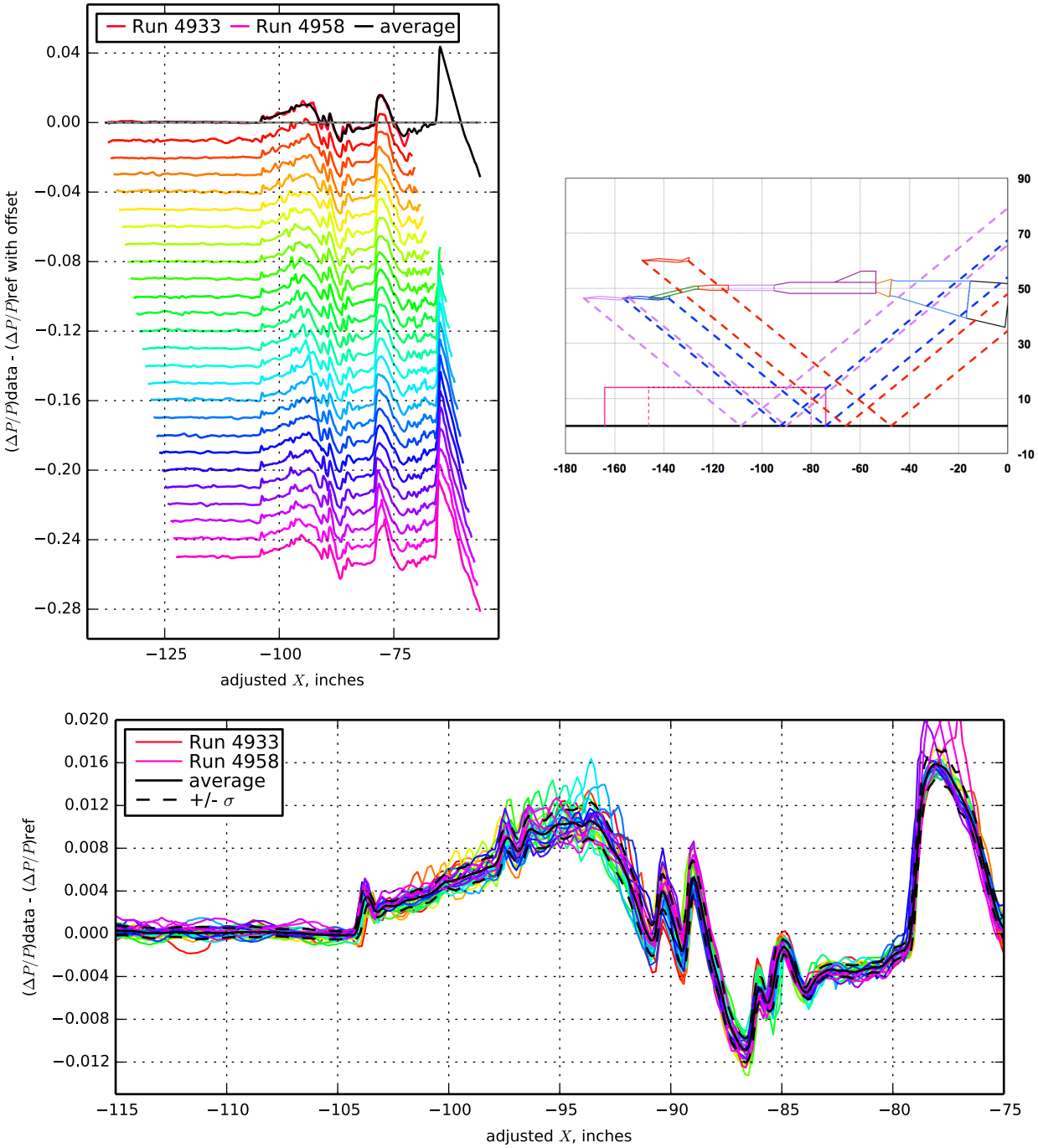

Figure 7.62. 1044 model without under-wing nacelle on blade strut, Runs 4933-4958:4932, Mach 1.7, Duration 6 sec, Re 6.77x10^6, T -98.10° F, PT 2299.65 psf, PT-Ref 0.40 psf, H 278.5 ppm [276.8 : 280.2], H-Ref -2.52 ppm

***X_ram*, in**	***h*, in**	***h/L***
15.88 [8.00 : 23.75]	32.69 [32.57 : 32.82]	1.72 [1.71 : 1.72]
***α*, deg**	***β*, deg**	***ϕ*, deg**
2.37 [2.32 : 2.41]	0.65 [0.63 : 0.69]	20.29 [20.11 : 20.50]
CL	***CD***	***CM***
0.117 [0.114 : 0.121]	0.06059 [0.05965 : 0.06208]	-0.228 [-0.247 : -0.217]

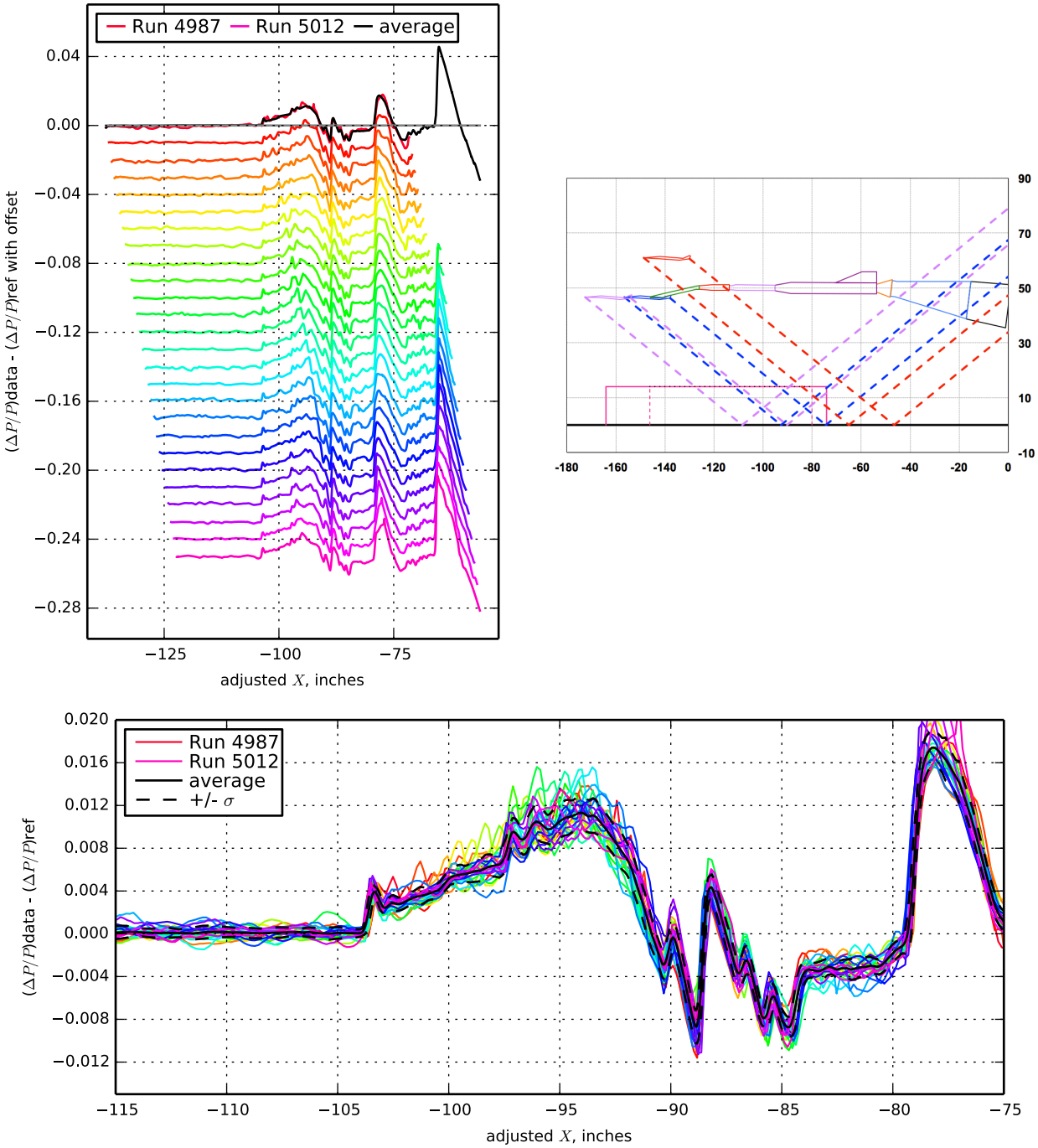

Figure 7.63. 1044 model without under-wing nacelle on blade strut, Runs 4987-5012:4986, Mach 1.7, Duration 6 sec, Re 6.73x10^6, T -96.48° F, PT 2298.94 psf, PT-Ref 0.44 psf, H 257.6 ppm [255.9 : 259.4], H-Ref -4.70 ppm

***X_ram*, in**	***h*, in**	***h/L***
15.88 [8.00 : 23.75]	32.68 [32.54 : 32.85]	1.72 [1.71 : 1.73]
***α*, deg**	***β*, deg**	***ϕ*, deg**
2.56 [2.53 : 2.59]	0.69 [0.68 : 0.73]	40.13 [40.02 : 40.28]
CL	***CD***	***CM***
0.117 [0.114 : 0.119]	0.06152 [0.06047 : 0.06314]	-0.228 [-0.249 : -0.219]

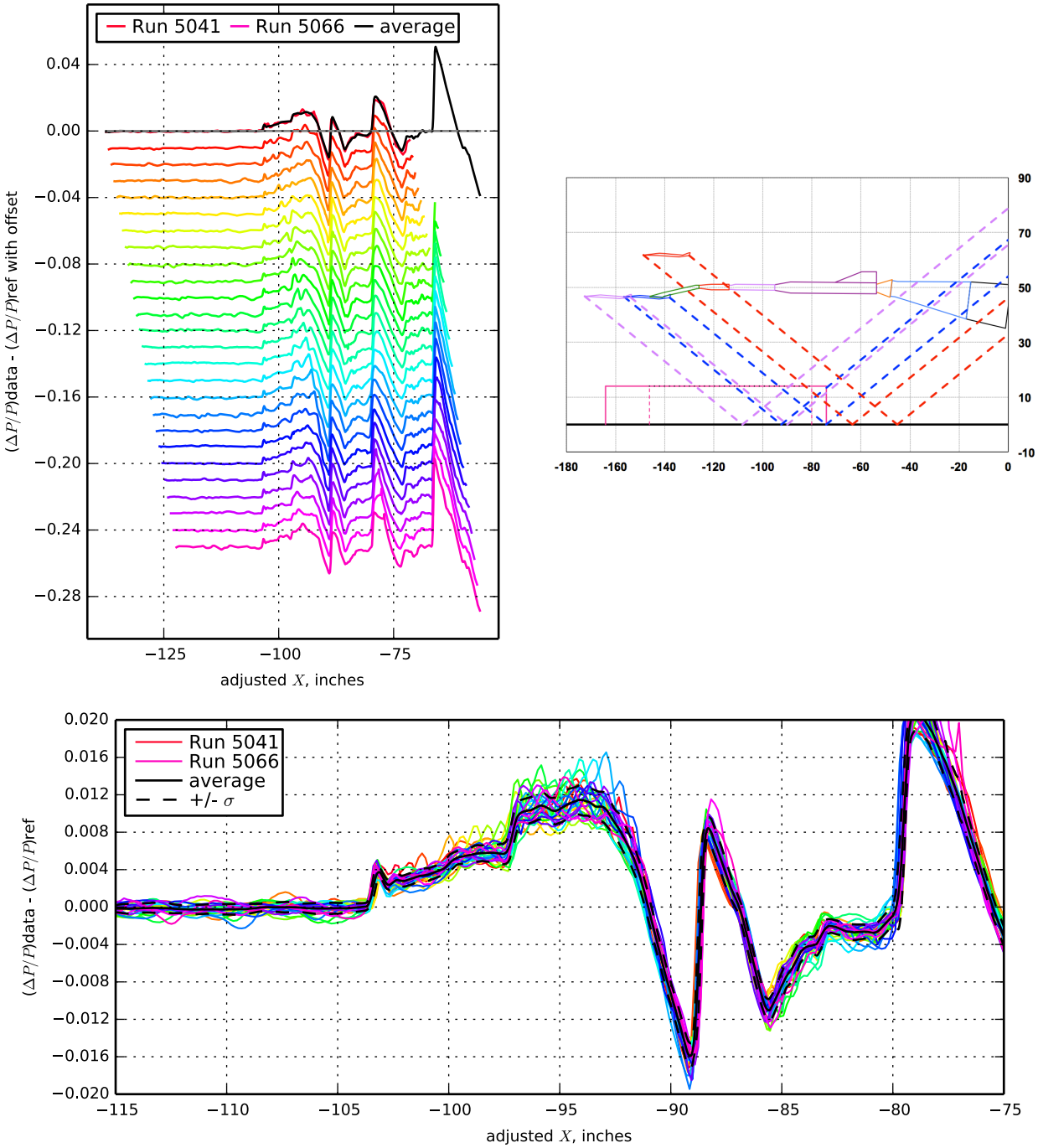

Figure 7.64. 1044 model without under-wing nacelle on blade strut, Runs 5041-5066:5040, Mach 1.7, Duration 6 sec, Re 6.72x10^6, T -96.09° F, PT 2298.99 psf, PT-Ref -0.07 psf, H 243.5 ppm [242.0 : 244.8], H-Ref -4.39 ppm

***X_ram*, in**	***h*, in**	***h/L***
15.88 [8.00 : 23.75]	32.49 [32.36 : 32.63]	1.71 [1.70 : 1.71]
***α*, deg**	***β*, deg**	***ϕ*, deg**
2.71 [2.68 : 2.74]	0.41 [0.39 : 0.44]	60.24 [60.20 : 60.30]
CL	***CD***	***CM***
0.115 [0.109 : 0.119]	0.06211 [0.06117 : 0.06354]	-0.225 [-0.235 : -0.212]

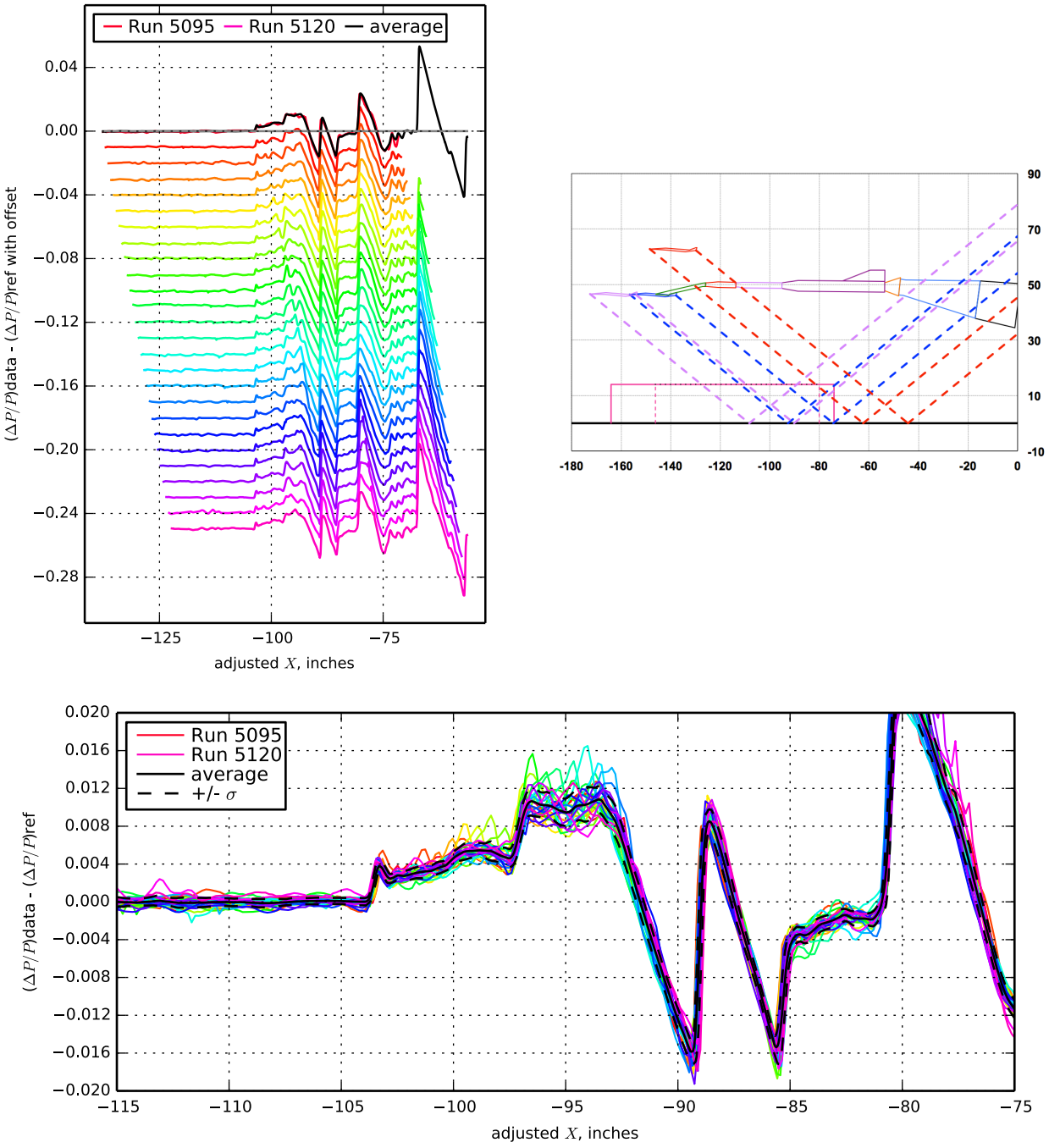

Figure 7.65. 1044 model without under-wing nacelle on blade strut, Runs 5095-5120:5121, Mach 1.7, Duration 6 sec, Re 6.71x10^6, T -95.51° F, PT 2298.89 psf, PT-Ref 0.15 psf, H 229.3 ppm [228.3 : 230.4], H-Ref 1.25 ppm

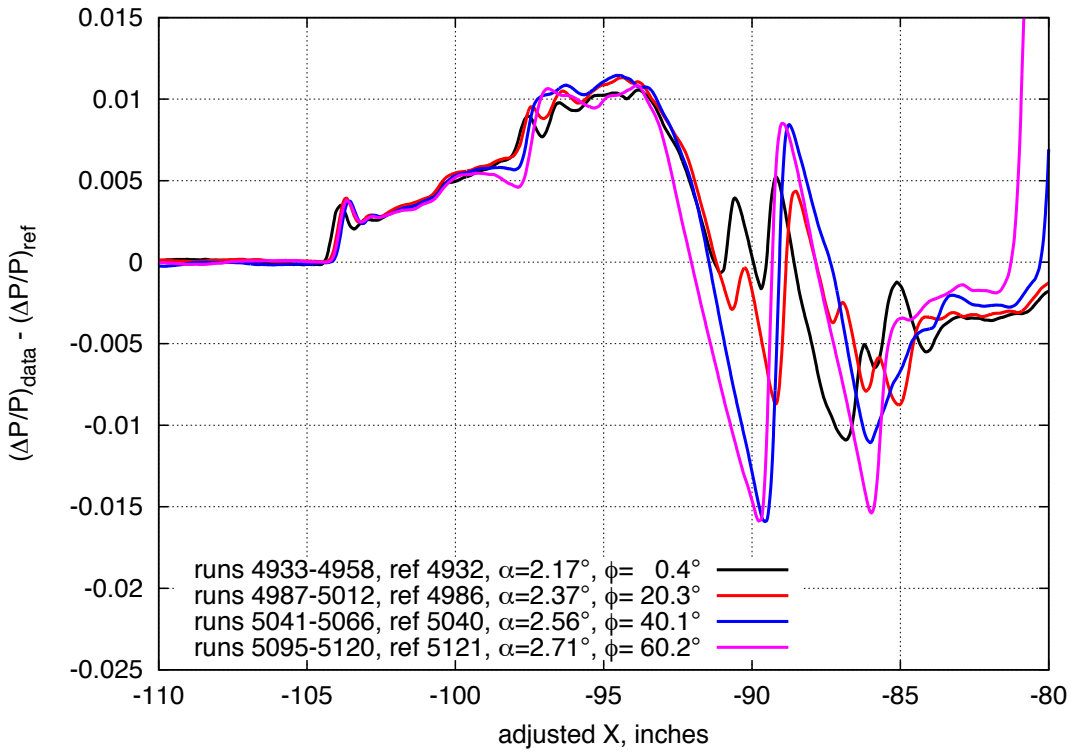

Figure 7.66. Comparison of on- and off-track pressure signatures for the 1044 Phase II model without under-wing nacelles on blade strut, M=1.7, h=32 inches

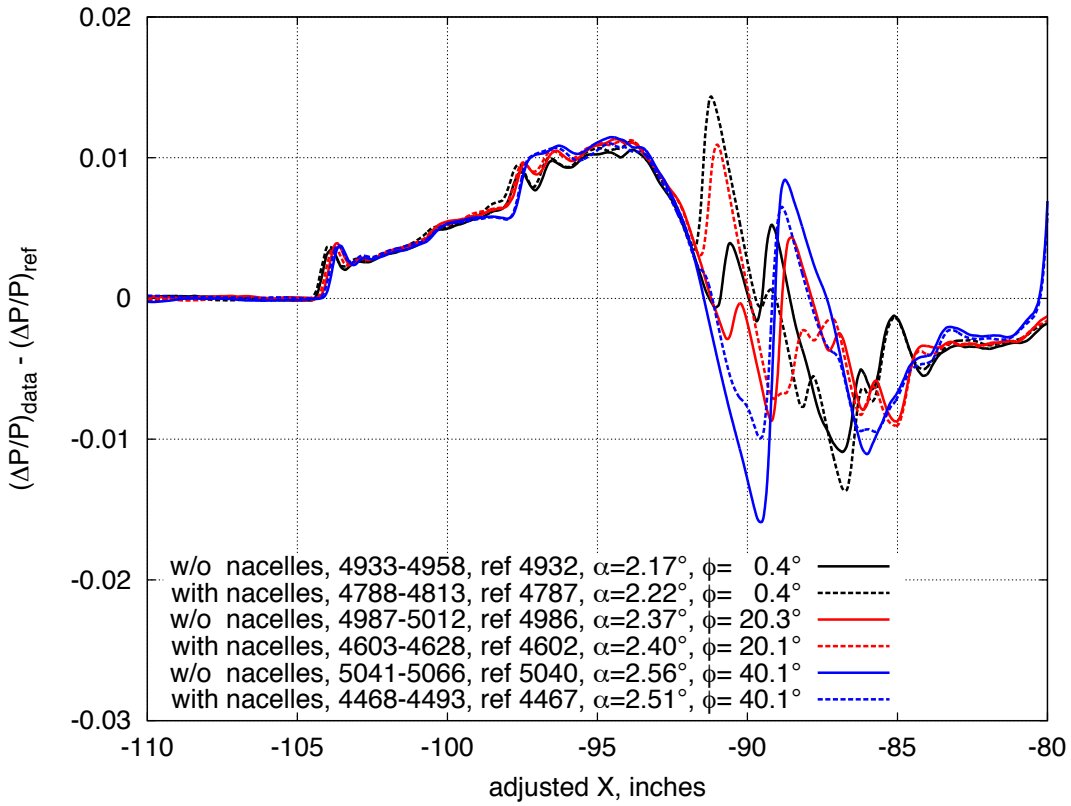

Figure 7.67. Comparison of pressure signatures with and without under-wing nacelles, on- and off-track, for the1044 phase II model, M=1.7, h=32 inches

***X_ram*, in**	***h*, in**	***h/L***
11.97 [-0.01 : 23.94]	70.77 [70.69 : 70.89]	3.72 [3.71 : 3.72]
***α*, deg**	***β*, deg**	***ϕ*, deg**
1.99 [1.95 : 2.04]	-0.09 [-0.13 : -0.04]	0.03 [-0.02 : 0.09]
CL	***CD***	***CM***
0.113 [0.104 : 0.123]	0.03614 [0.03427 : 0.03738]	-0.127 [-0.144 : -0.114]

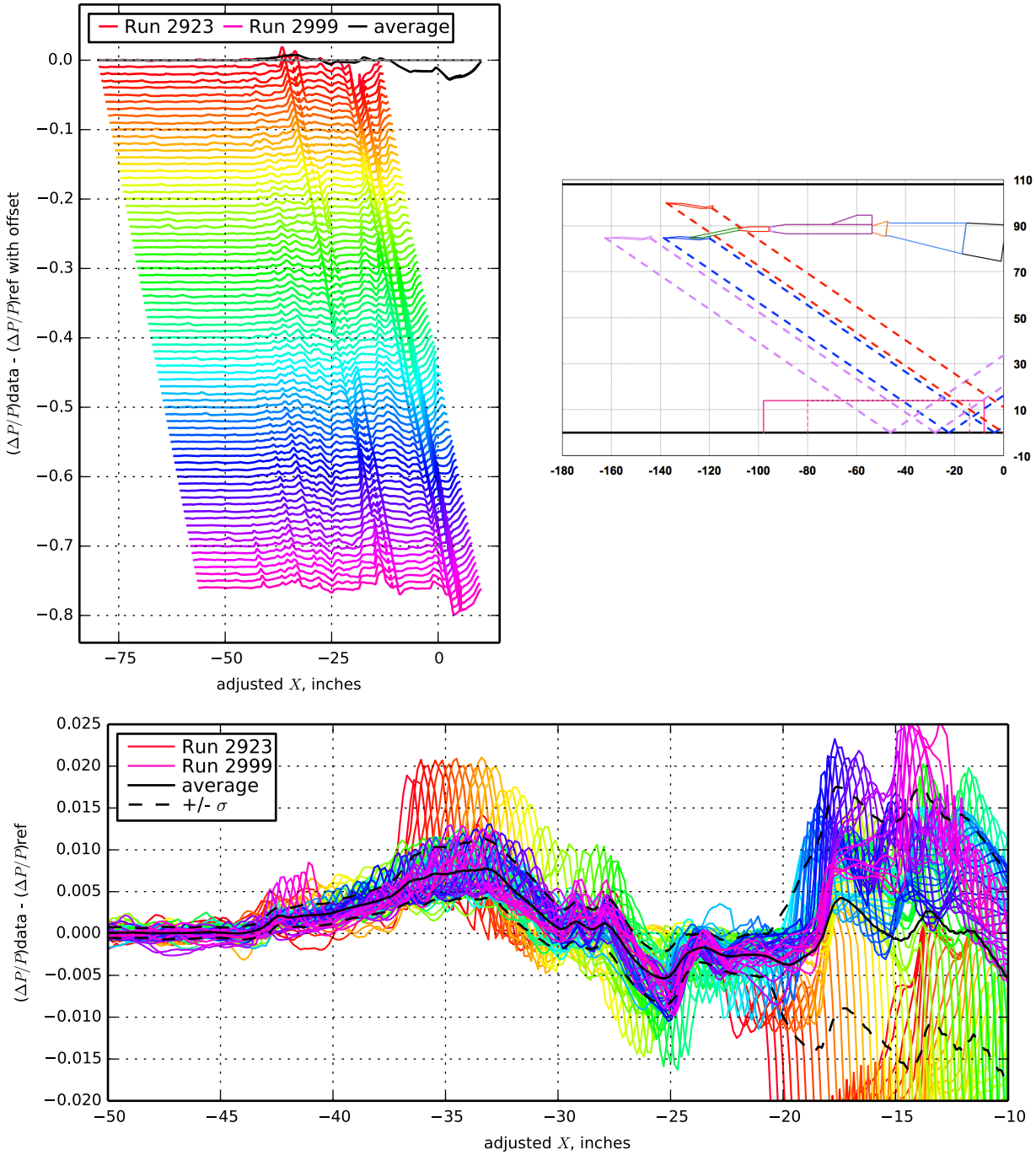

Figure 7.68. 1044 model without under-wing nacelle on blade strut, Runs 2923-2999:3000, Mach 1.7, Duration 6 sec, Re 6.75x10^6, T -97.08° F, PT 2302.03 psf, PT-Ref -5.52 psf, H 267.6 ppm [265.8 : 269.9], H-Ref 3.35 ppm

***X_ram*, in**	***h*, in**	***h/L***
15.88 [8.00 : 23.75]	32.62 [32.55 : 32.72]	1.71 [1.71 : 1.72]
***α*, deg**	***β*, deg**	***ϕ*, deg**
2.25 [2.21 : 2.31]	0.54 [0.51 : 0.56]	0.67 [0.48 : 0.87]
CL	***CD***	***CM***
0.130 [0.125 : 0.135]	0.06034 [0.05914 : 0.06218]	-0.246 [-0.262 : -0.232]

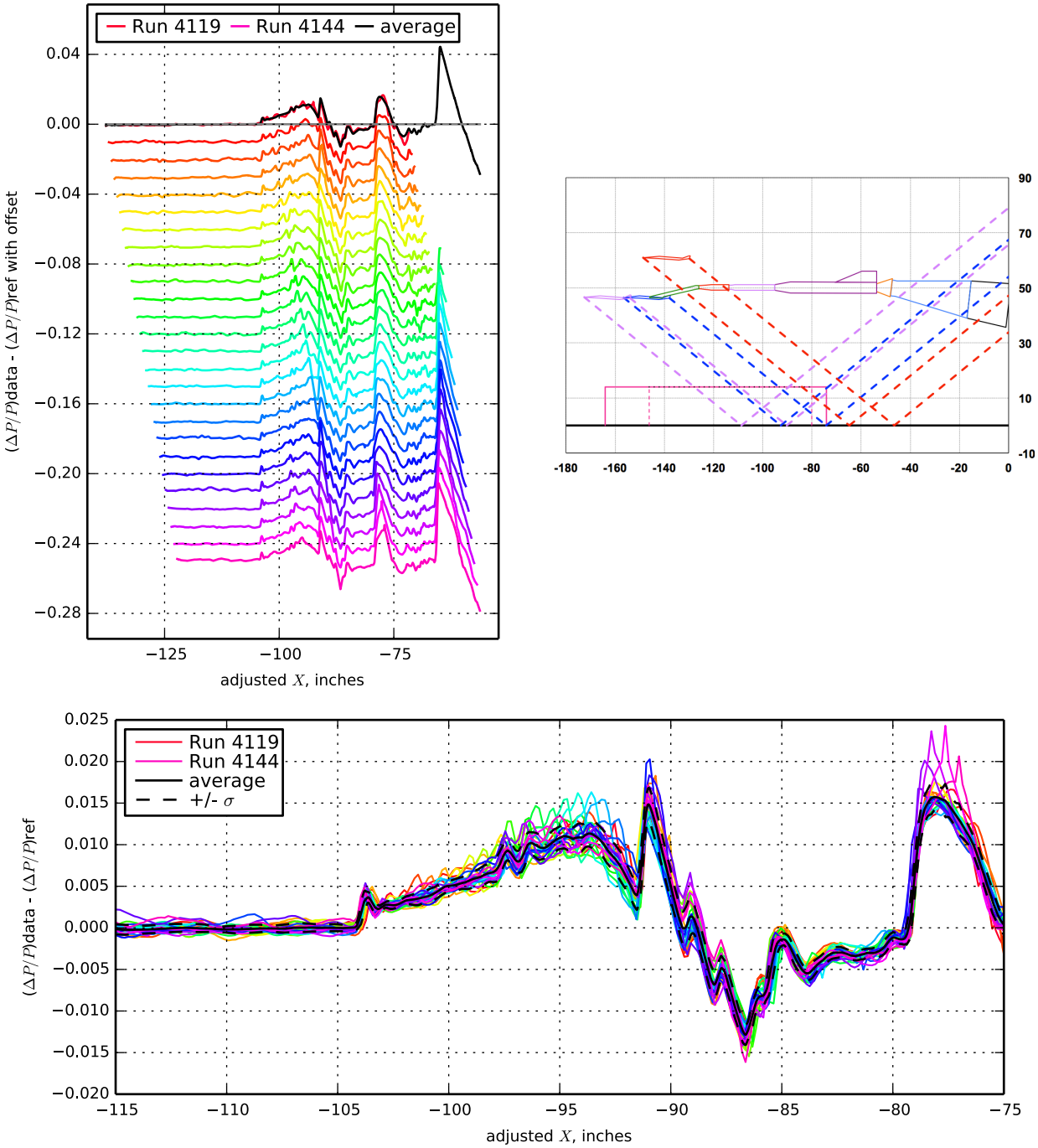

Figure 7.69. 1044 model without center nacelle on blade strut, Runs 4119-4144:4145, Mach 1.7, Duration 6 sec, Re 6.77x10^6, T -97.97° F, PT 2297.91 psf, PT-Ref 0.14 psf, H 246.4 ppm [244.9 : 247.5], H-Ref 2.12 ppm

***X_ram*, in**	***h*, in**	***h/L***
15.88 [8.00 : 23.75]	32.66 [32.55 : 32.79]	1.72 [1.71 : 1.72]
***α*, deg**	***β*, deg**	***ϕ*, deg**
2.28 [2.24 : 2.34]	0.63 [0.60 : 0.68]	20.20 [20.01 : 20.41]
CL	***CD***	***CM***
0.122 [0.118 : 0.128]	0.06058 [0.05955 : 0.06219]	-0.237 [-0.256 : -0.226]

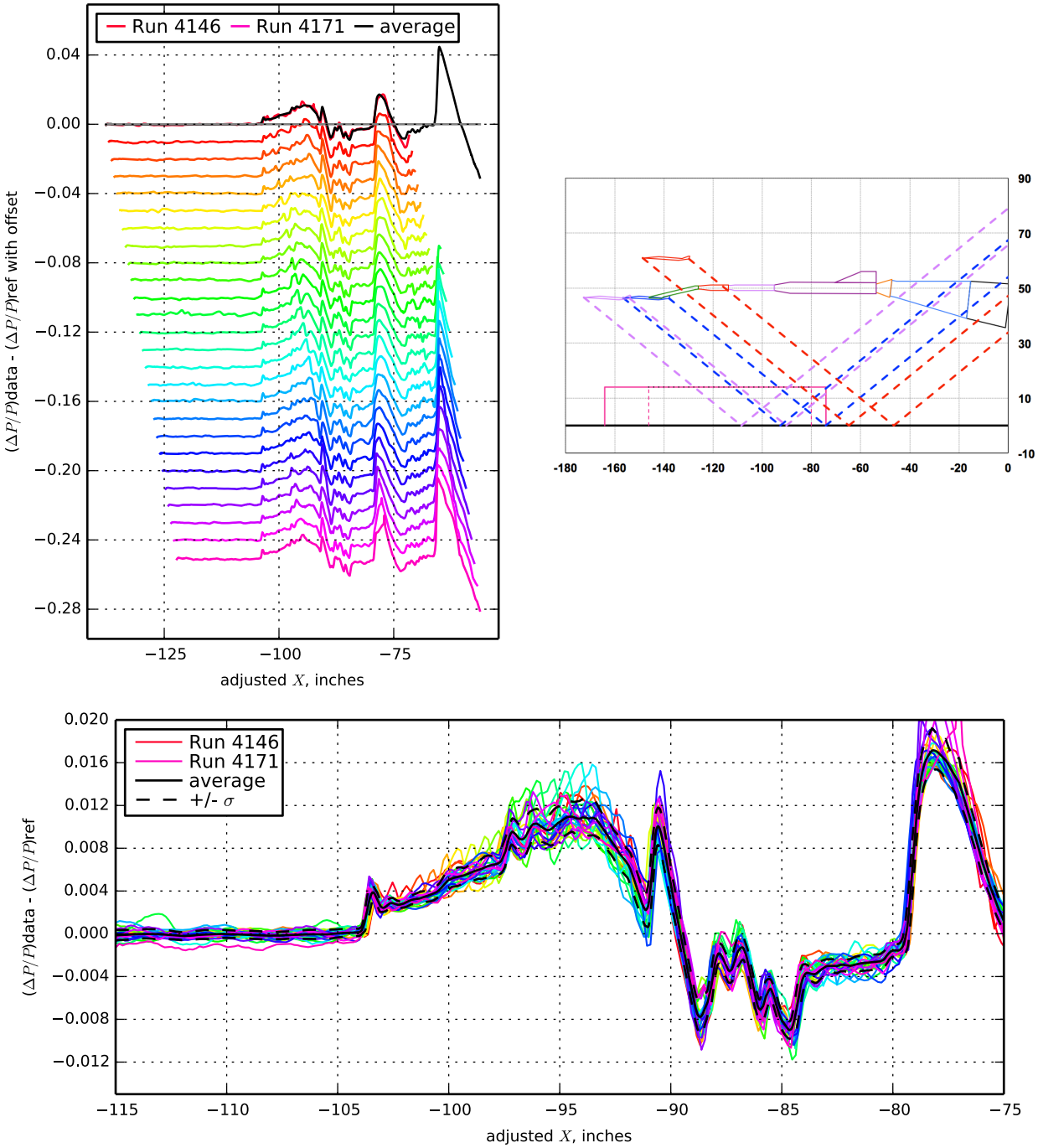

Figure 7.70. 1044 model without center nacelle on blade strut, Runs 4146-4171:4145, Mach 1.7, Duration 6 sec, Re 6.75x10^6, T -97.47° F, PT 2297.34 psf, PT-Ref -0.43 psf, H 242.0 ppm [241.4 : 242.7], H-Ref -2.22 ppm

***X_ram*, in**	***h*, in**	***h/L***
15.88 [8.00 : 23.75]	32.64 [32.51 : 32.78]	1.71 [1.71 : 1.72]
***α*, deg**	***β*, deg**	***ϕ*, deg**
2.37 [2.34 : 2.39]	0.66 [0.63 : 0.72]	40.31 [40.17 : 40.51]
CL	***CD***	***CM***
0.117 [0.114 : 0.119]	0.06131 [0.06012 : 0.06304]	-0.227 [-0.245 : -0.217]

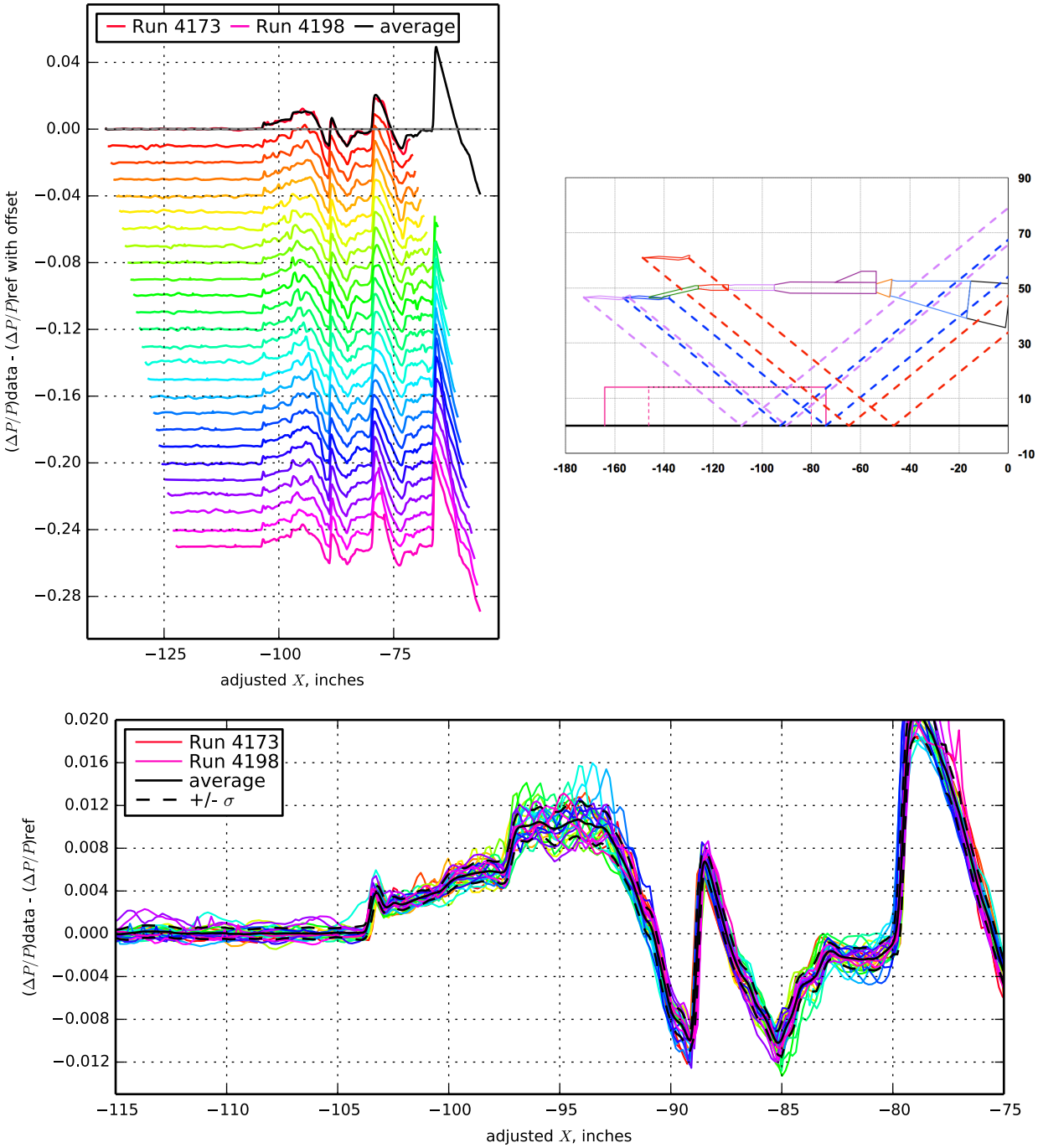

Figure 7.71. 1044 model without center nacelle on blade strut, Runs 4173-4198:4172, Mach 1.7, Duration 6 sec, Re 6.74x10^6, T -97.15° F, PT 2297.20 psf, PT-Ref 0.01 psf, H 240.0 ppm, H-Ref -1.06 ppm

***X_ram*, in**	***h*, in**	***h/L***
15.88 [8.00 : 23.75]	32.39 [32.29 : 32.51]	1.70 [1.70 : 1.71]
***α*, deg**	***β*, deg**	***ϕ*, deg**
2.41 [2.38 : 2.43]	0.33 [0.30 : 0.38]	60.11 [60.04 : 60.21]
CL	***CD***	***CM***
0.107 [0.103 : 0.110]	0.06173 [0.06071 : 0.06333]	-0.203 [-0.215 : -0.192]

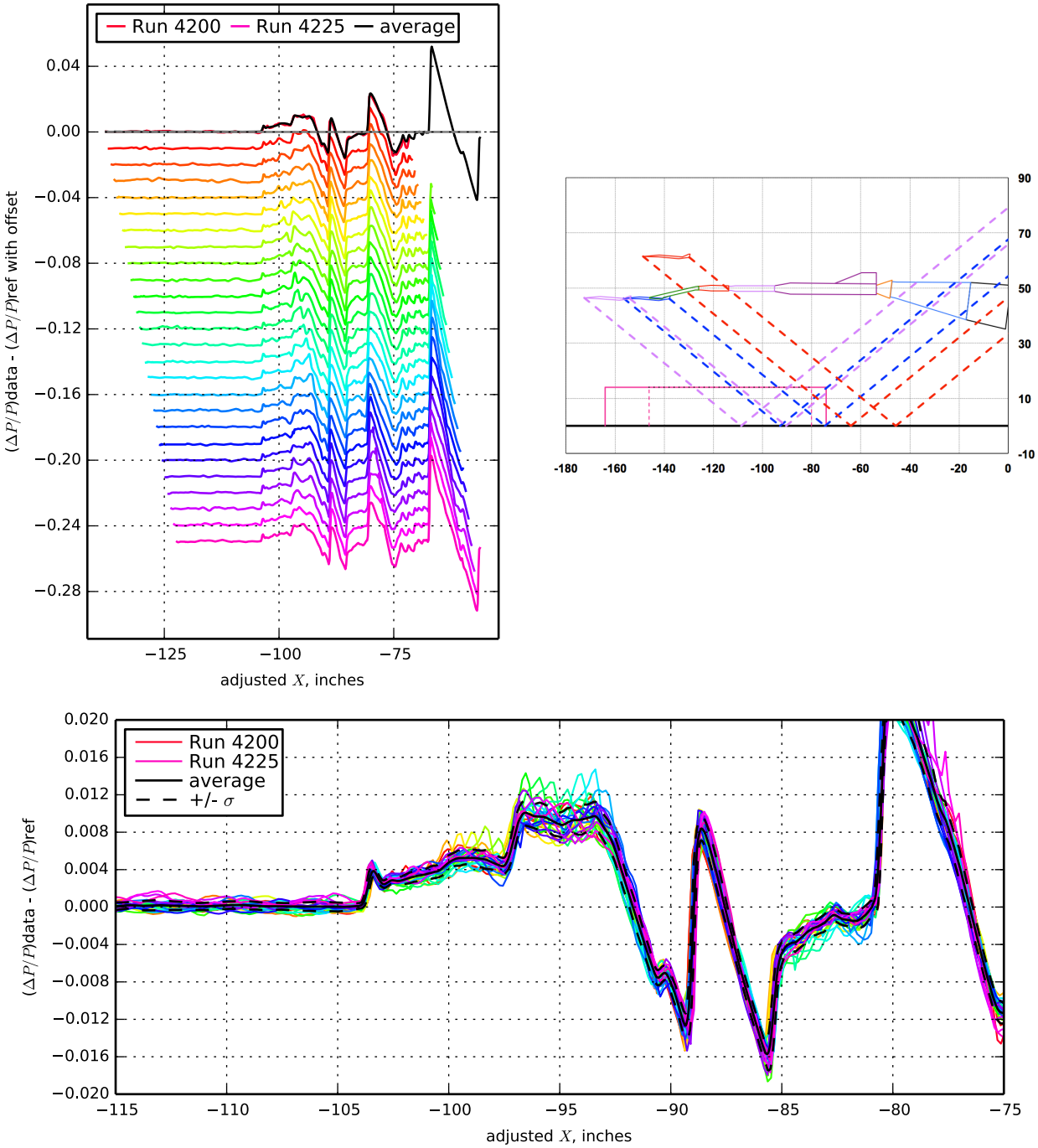

Figure 7.72. 1044 model without center nacelle on blade strut, Runs 4200-4225:4199, Mach 1.7, Duration 6 sec, Re 6.74x10^6, T -96.94° F, PT 2297.26 psf, PT-Ref 0.02 psf, H 241.5 ppm [240.5 : 242.3], H-Ref 2.17 ppm

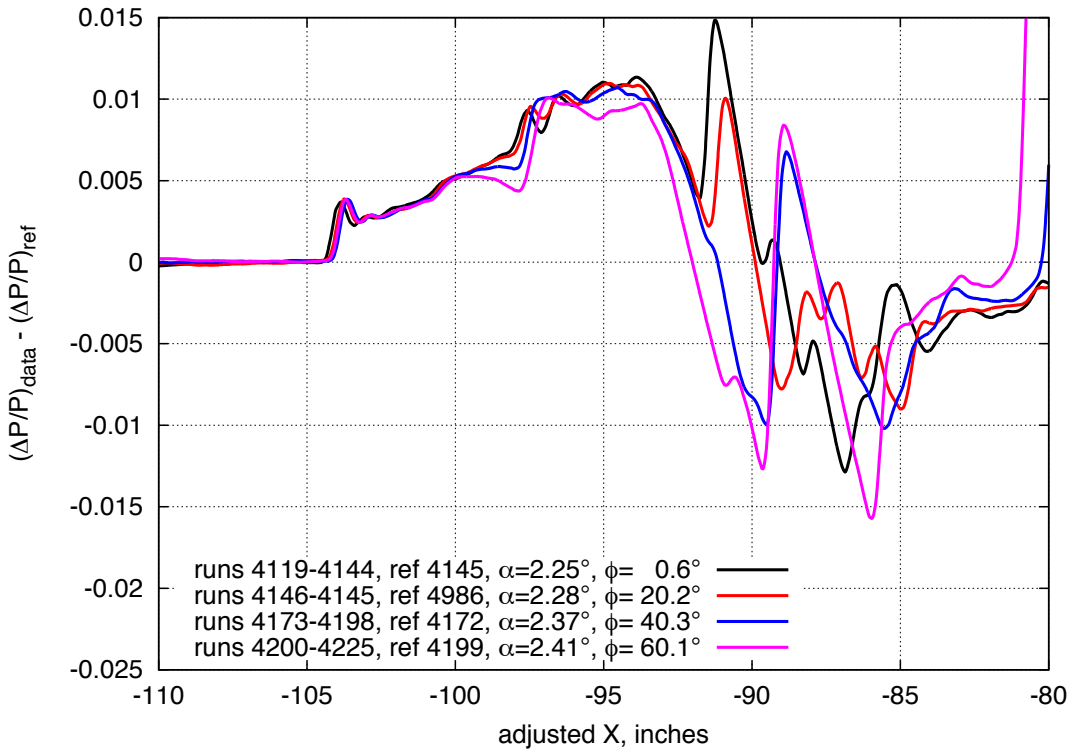

Figure 7.73. Comparison of on- and off-track pressure signatures for the 1044 Phase II model without center nacelle on blade strut, M=1.7, h=32 inches

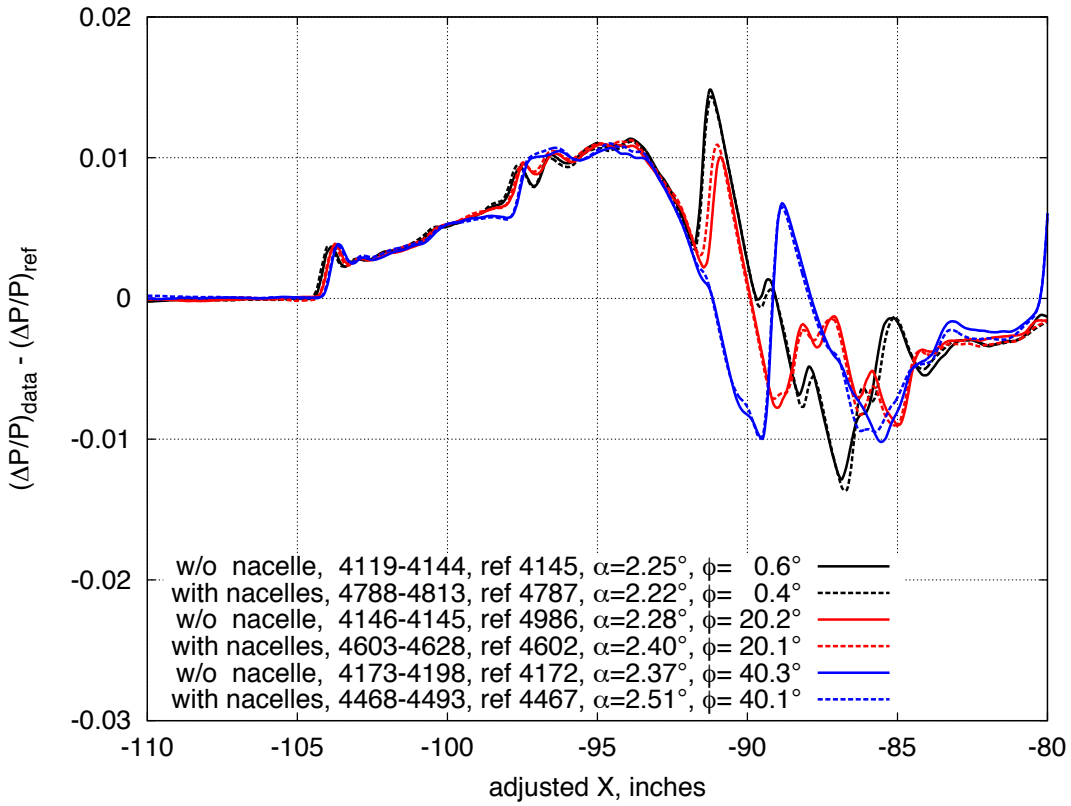

Figure 7.74. Comparison of pressure signatures with and without center nacelle, on- and off-track, for the1044 phase II model, M=1.7, h=32 inches

***X_ram*, in**	***h*, in**	***h/L***
12.22 [-0.01 : 23.94]	53.58 [53.17 : 54.04]	5.70 [5.66 : 5.75]
***α*, deg**	***β*, deg**	***ϕ*, deg**
-0.03 [-0.05 : -0.01]	0.09 [0.03 : 0.14]	0.19 [0.10 : 0.25]
CL	***CD***	***CM***
-0.030 [-0.036 : -0.026]	0.02493 [0.02419 : 0.02573]	-0.001 [-0.008 : 0.012]

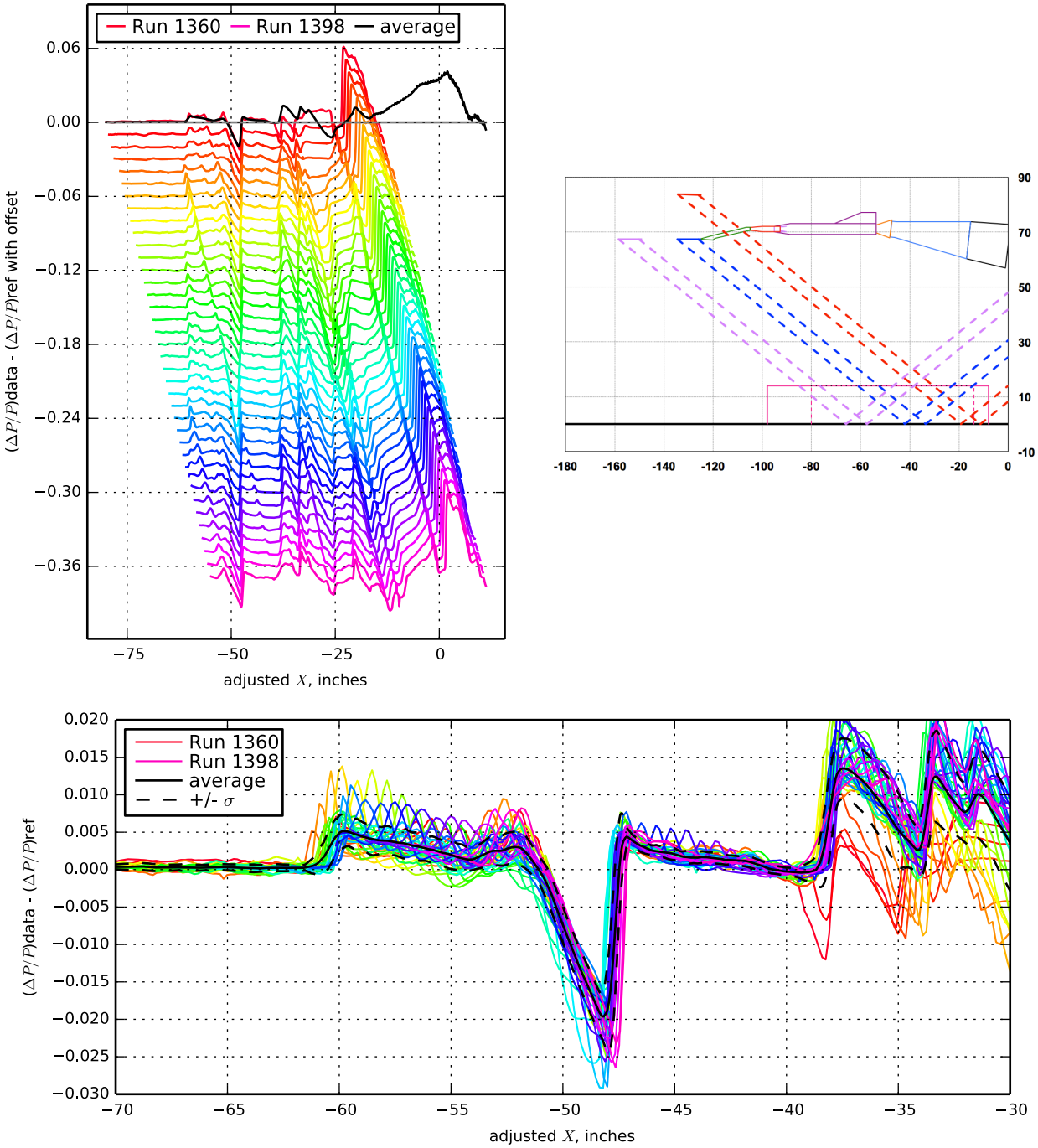

Figure 7.75. 70° Flat plate model on blade strut, Runs 1360-1398:1359, Mach 1.7, Duration 8 sec, Re 3.34×10^6, T -97.98° F, PT 2298.80 psf, PT-Ref -0.92 psf, H 250.0 ppm [248.5 : 251.8], H-Ref -4.67 ppm

***X_ram*, in**	***h*, in**	***h/L***
-0.01 [-0.01 : -0.01]	53.70 [42.70 : 64.71]	5.71 [4.54 : 6.88]
***α*, deg**	***β*, deg**	***ϕ*, deg**
-0.05 [-0.07 : -0.04]	0.10 [0.08 : 0.13]	0.23 [0.17 : 0.30]
CL	***CD***	***CM***
-0.033 [-0.037 : -0.029]	0.02432 [0.02400 : 0.02458]	0.001 [-0.005 : 0.009]

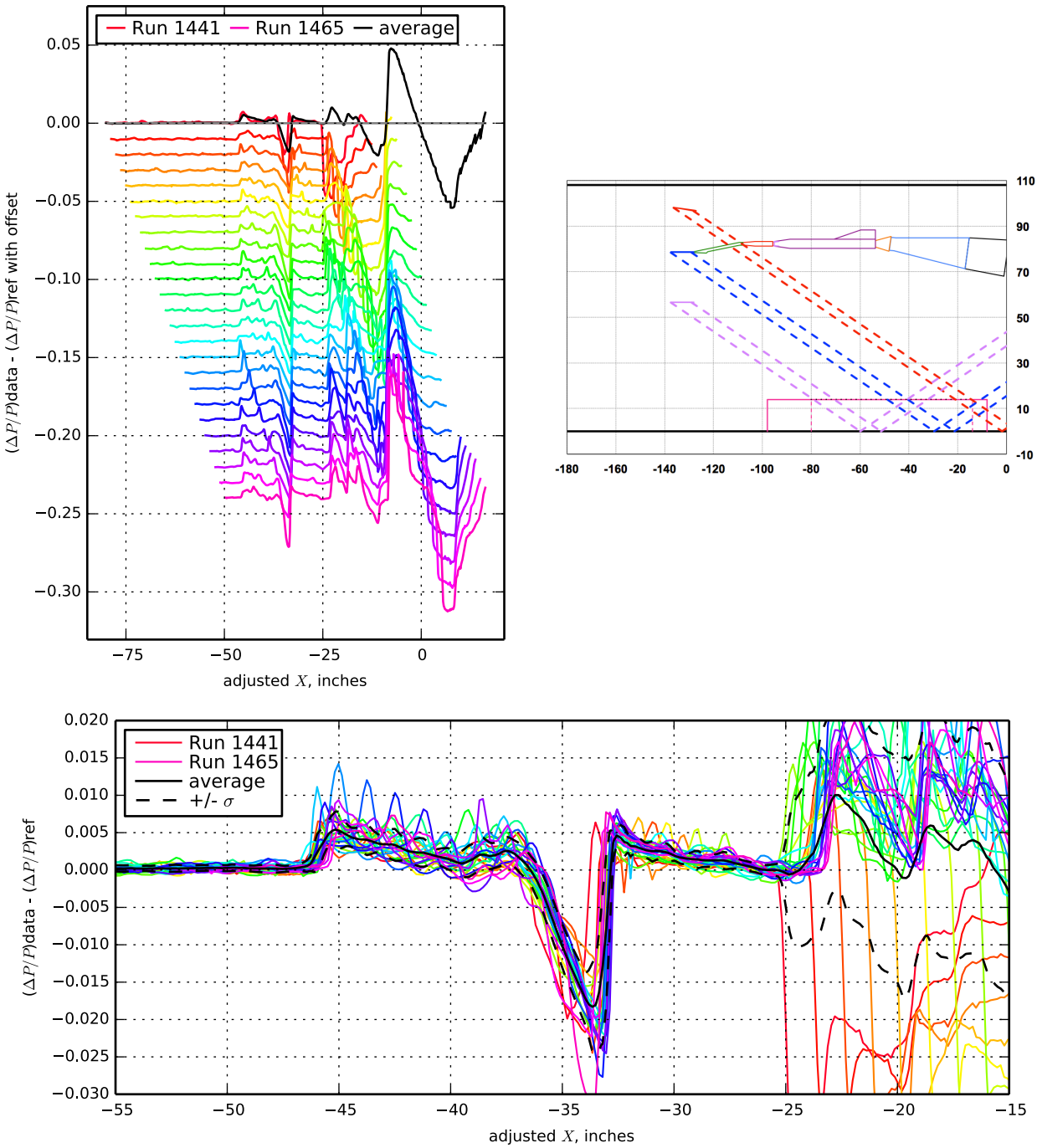

Figure 7.76. 70° Flat plate model on blade strut, Runs 1441-1465:1466, Mach 1.7, Duration 8 sec, Re 3.34×10^6, T -97.80° F, PT 2298.92 psf, PT-Ref -0.19 psf, H 238.6 ppm [237.8 : 239.6], H-Ref -0.22 ppm

***X_ram*, in**	***h*, in**	***h/L***
11.97 [-0.01 : 23.94]	53.60 [53.17 : 54.04]	5.70 [5.66 : 5.75]
***α*, deg**	***β*, deg**	***ϕ*, deg**
-0.03 [-0.05 : -0.01]	0.10 [0.03 : 0.15]	0.20 [0.11 : 0.26]
CL	***CD***	***CM***
-0.030 [-0.035 : -0.025]	0.02491 [0.02423 : 0.02572]	-0.001 [-0.009 : 0.011]

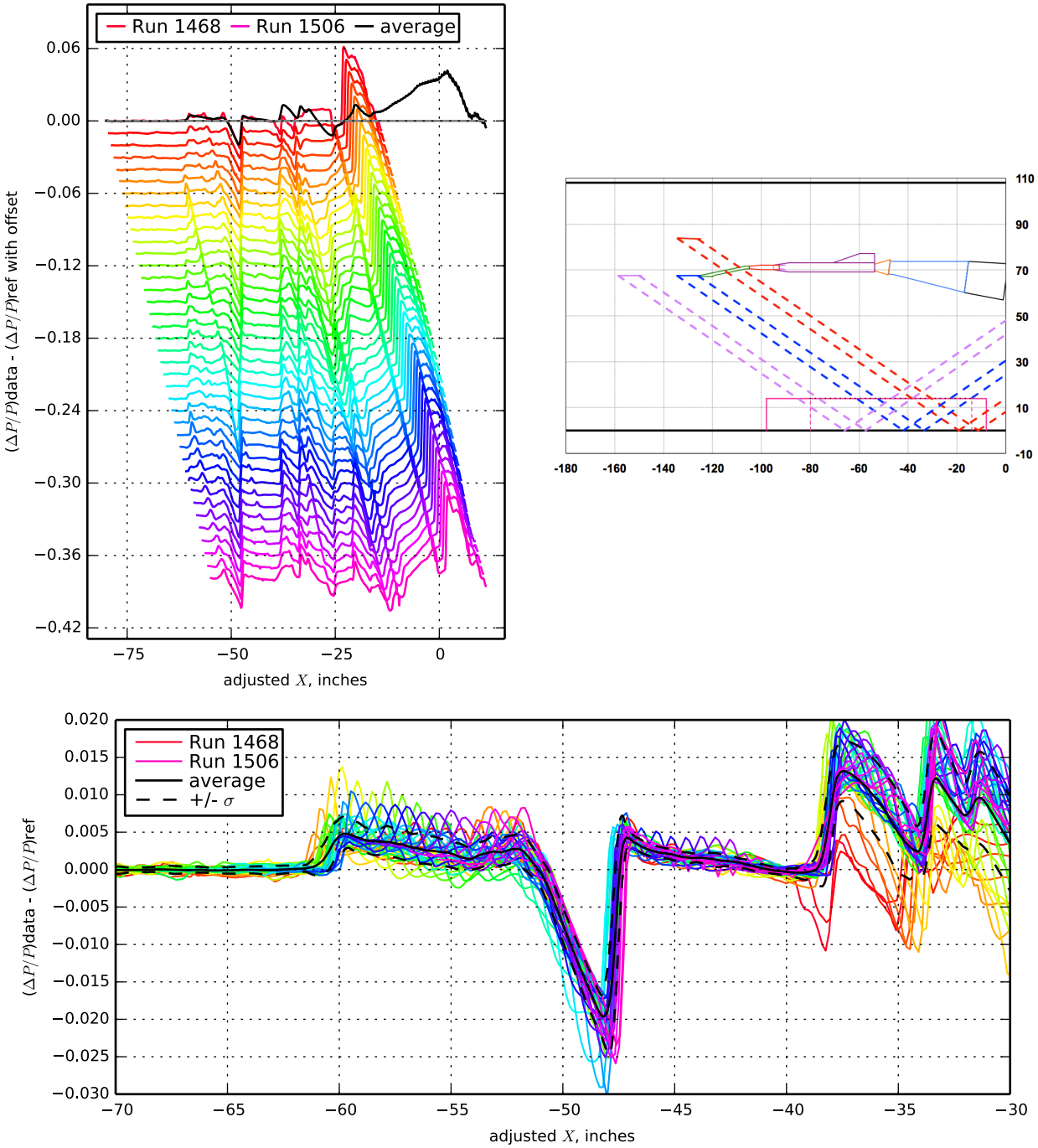

Figure 7.77. 70° Flat plate model on blade strut, Runs 1468-1506:1467, Mach 1.7, Duration 8 sec, Re 3.34x10^6, T -97.61° F, PT 2298.75 psf, PT-Ref -0.11 psf, H 234.7 ppm [233.7 : 235.8], H-Ref -2.01 ppm

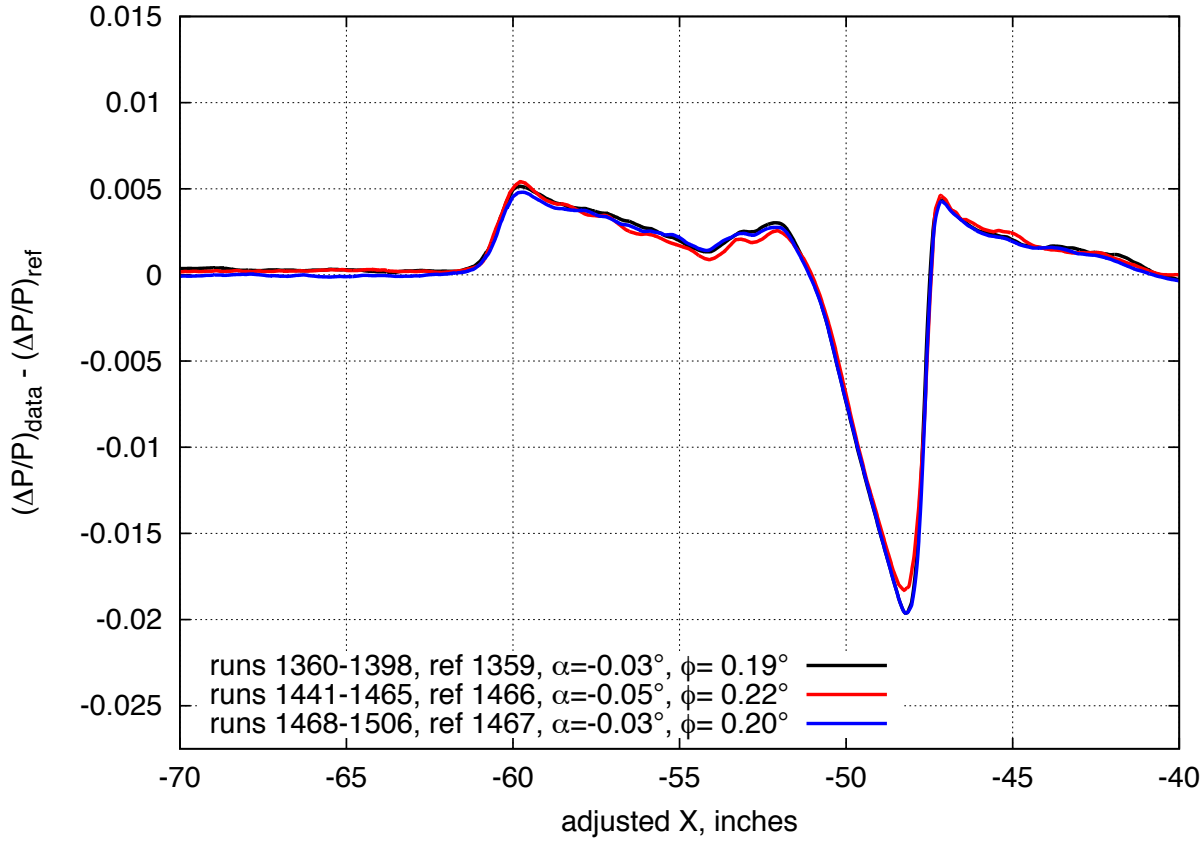

Figure 7.78. Comparison of on-track pressure signatures for the 70° flat plate model, M=1.7, h=54.6 inches

***X_ram*, in**	***h*, in**	***h/L***
-0.01 [-0.01 : -0.01]	54.12 [43.04 : 65.19]	5.76 [4.58 : 6.94]
***α*, deg**	***β*, deg**	***ϕ*, deg**
-0.02 [-0.04 : -0.01]	0.09 [0.07 : 0.13]	0.20 [0.15 : 0.28]
CL	***CD***	***CM***
-0.028 [-0.033 : -0.024]	0.02409 [0.02373 : 0.02448]	-0.007 [-0.011 : -0.001]

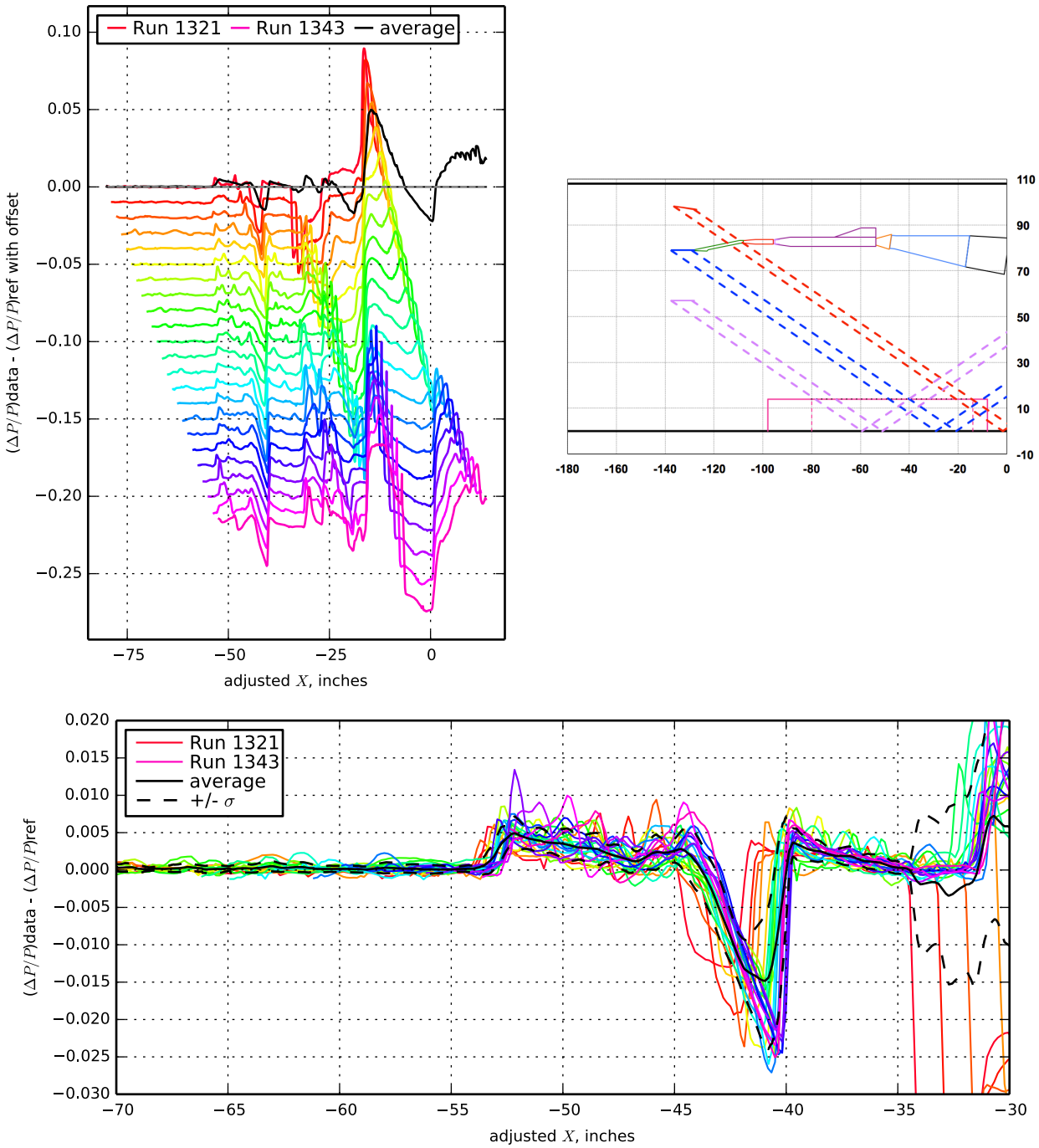

Figure 7.79. 70° Flat plate model on blade strut, Runs 1321-1343:1320, Mach 1.6, Duration 8 sec, Re 3.45x10^6, T -82.18° F, PT 2299.77 psf, PT-Ref -1.86 psf, H 272.2 ppm [271.1 : 275.2], H-Ref -15.03 ppm

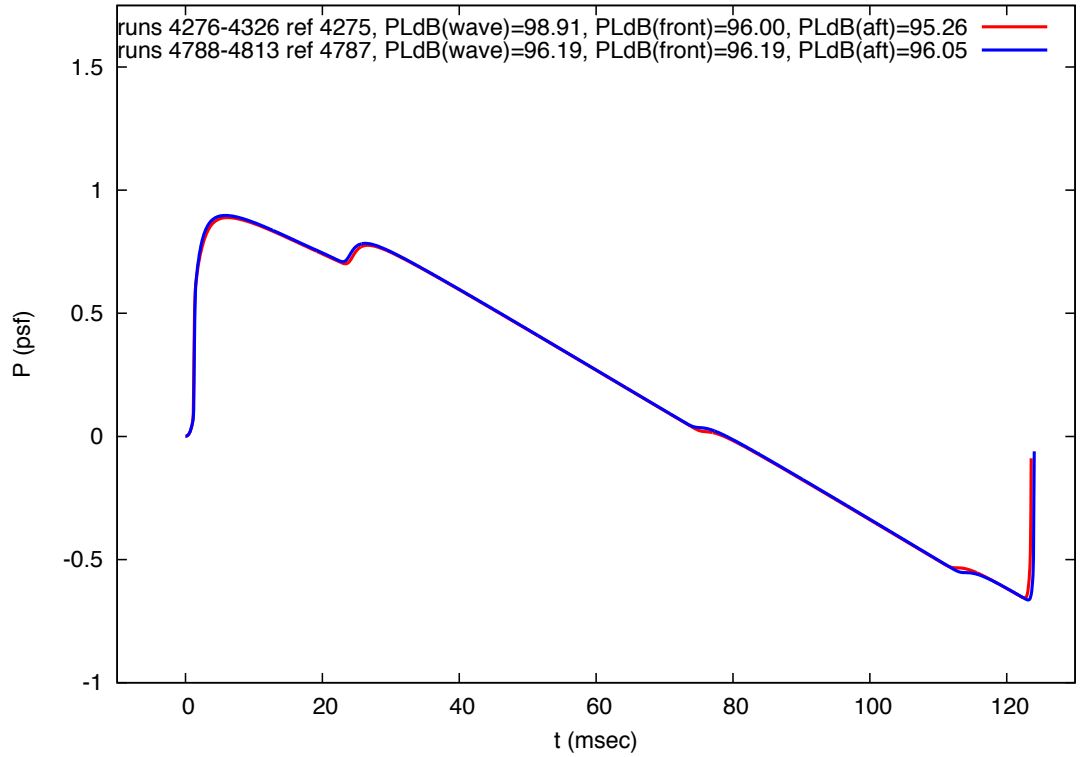

Figure 7.80. Extrapolated pressures of 1044 Phase II model to ground, M=1.7, h=50,000 ft. Near-field signatures taken at h = 32.6 inches, α avg [2.20 : 2.20] degrees

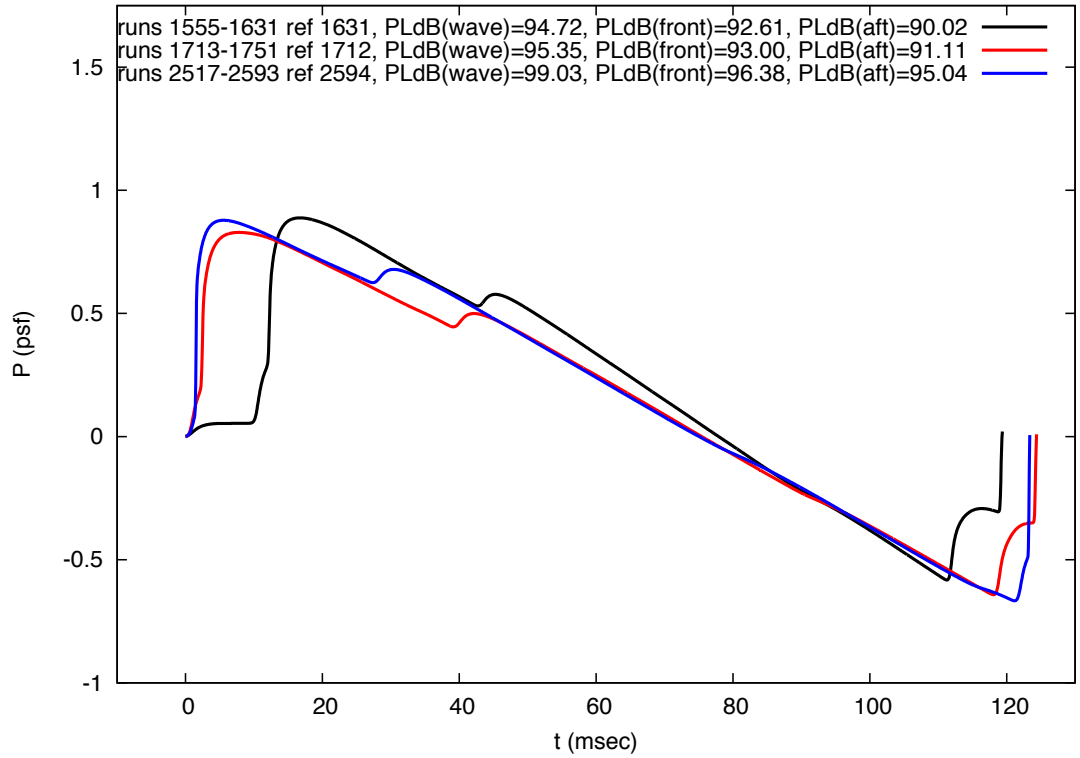

Figure 7.81. Extrapolated pressures of 1044 Phase II model to ground, M=1.7, h=50,000 ft. Near-field signatures taken at h = 70.8 inches, α avg. [2.07:2.30] degrees

***X_ram*, in**	***h*, in**	***h/L***
24.00 [24.00 : 24.00]	24.56 [18.56 : 30.56]	1.10 [0.83 : 1.36]
***α*, deg**	***β*, deg**	***ϕ*, deg**
2.18 [2.14 : 2.23]	-0.05 [-0.06 : -0.03]	0.12 [0.08 : 0.19]
CL	***CD***	***CM***
0.149 [0.138 : 0.161]	0.01726 [0.01610 : 0.01850]	-0.134 [-0.148 : -0.119]

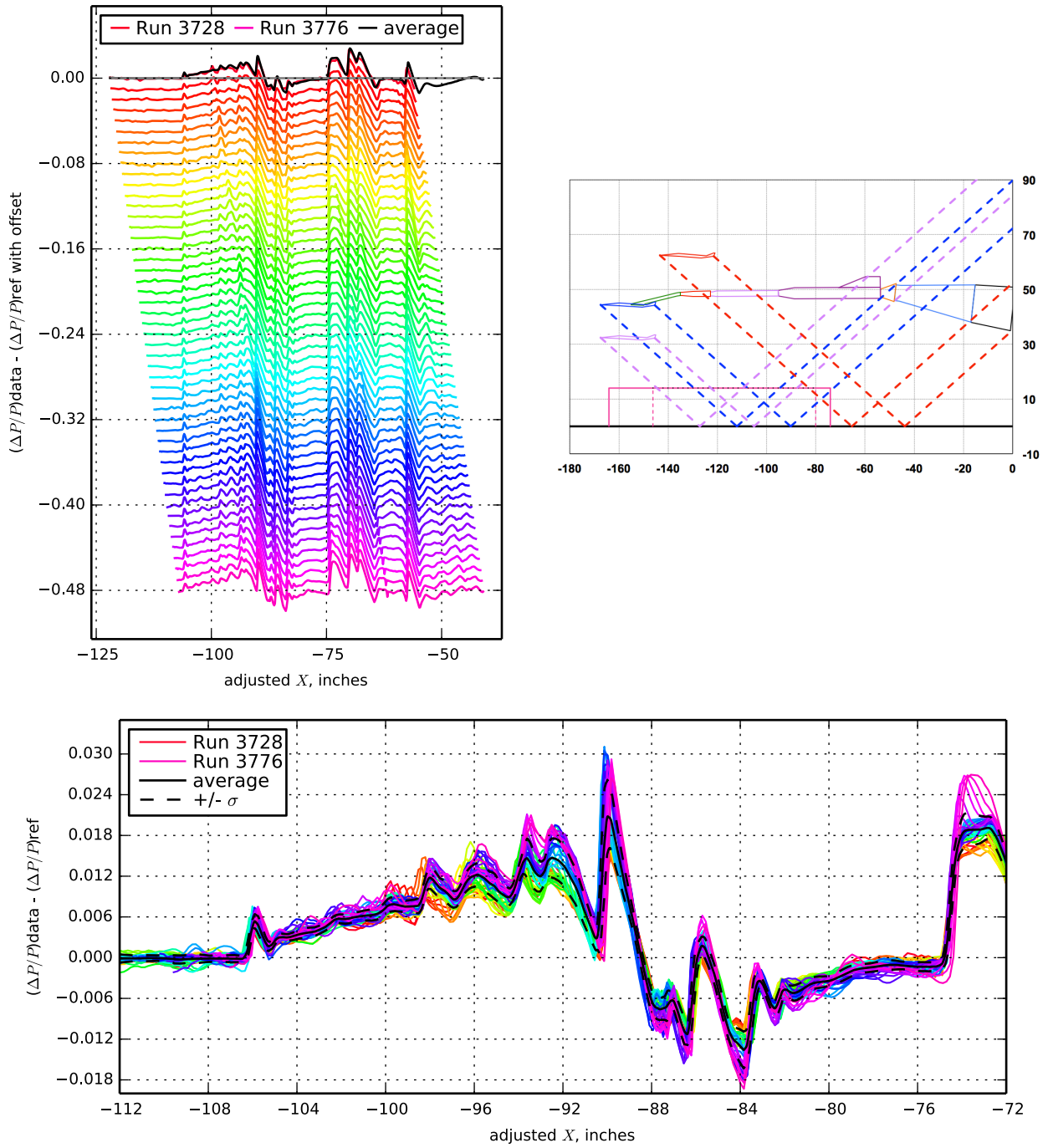

Figure 7.82. 1021 model with blade strut (re-tested), Runs 3728-3776:3777, Mach 1.6, Duration 6 sec, Re 8.15×10^6, T -79.84° F, PT 2299.56 psf, PT-Ref 0.71 psf, H 266.4 ppm [265.6 : 267.4], H-Ref 0.27 ppm

***X_ram*, in**	***h*, in**	***h/L***
17.61 [14.93 : 20.29]	31.77 [31.75 : 31.80]	1.42 [1.42 : 1.42]
***α*, deg**	***β*, deg**	***ϕ*, deg**
1.97 [1.96 : 1.97]	-0.04 [-0.08 : -0.03]	0.25 [0.16 : 0.29]
CL	***CD***	***CM***
0.136 [0.132 : 0.142]	0.01671 [0.01574 : 0.01723]	-0.128 [-0.133 : -0.121]

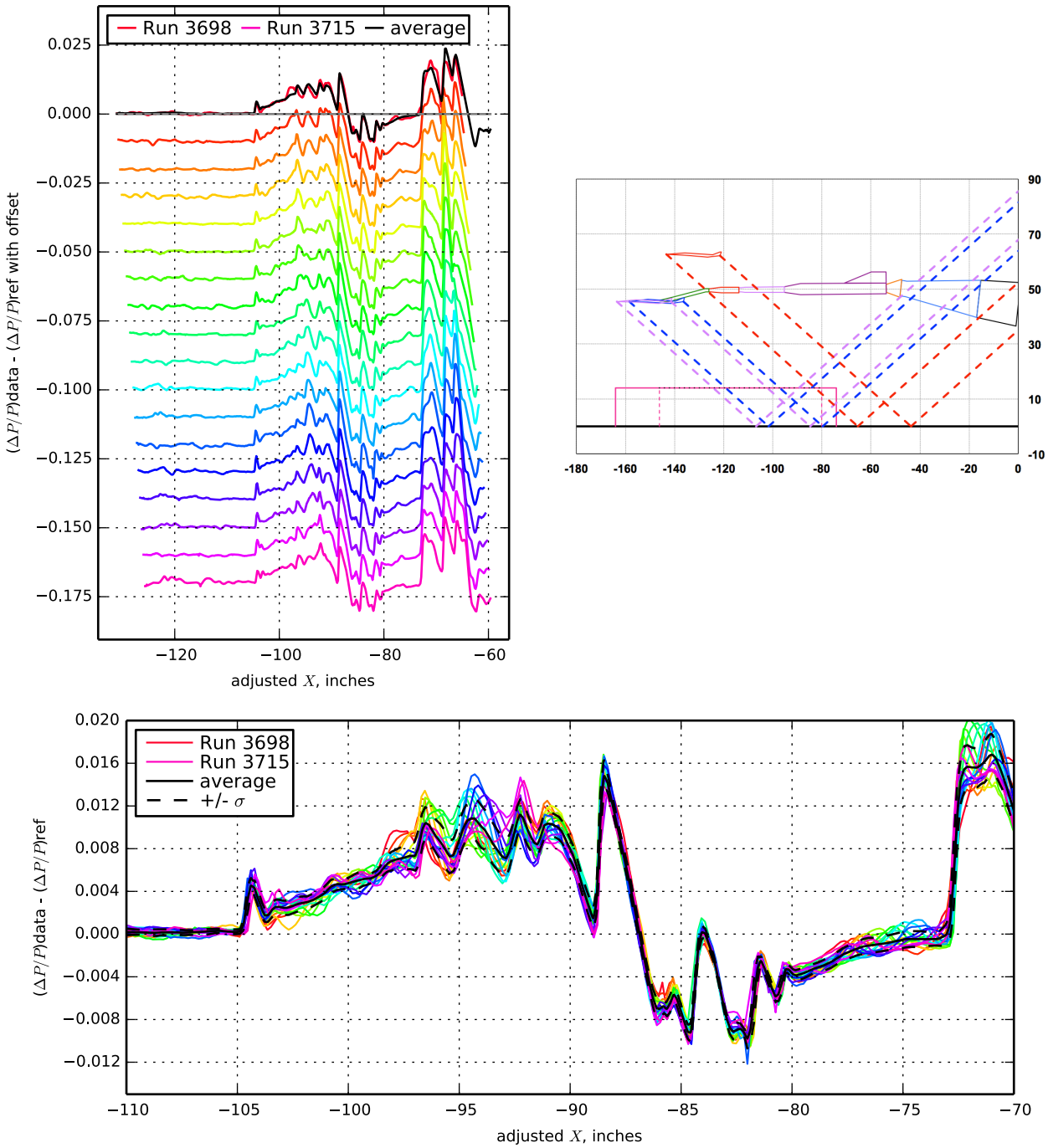

Figure 7.83. 1021 model with blade strut (re-tested), Runs 3698-3715:3727, Mach 1.6, Duration 6 sec, Re 8.16×10^6, T -80.26° F, PT 2299.75 psf, PT-Ref -0.51 psf, H 270.4 ppm, H-Ref 0.93 ppm

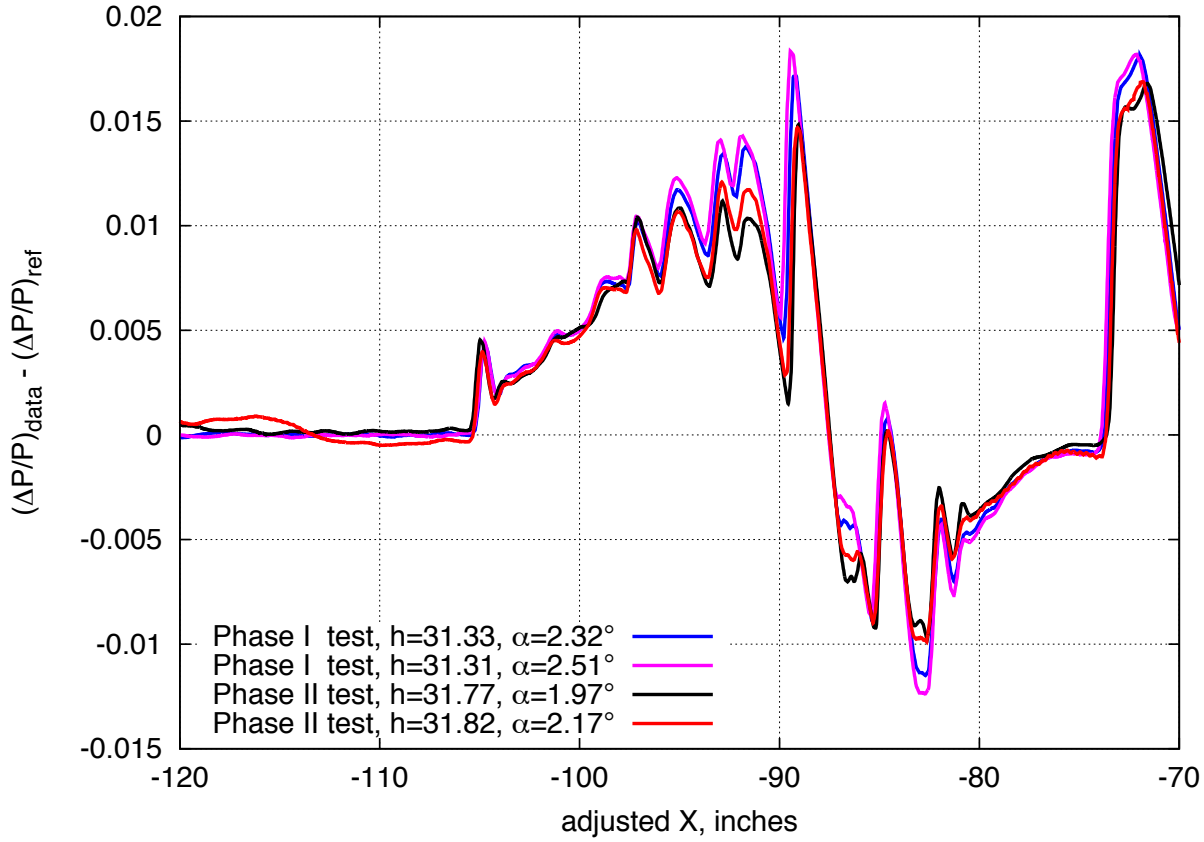

Figure 7.84. Long-term repeatability of the 1021 wind tunnel model, M=1.6

***X_ram*, in**	***h*, in**	***h/L***
17.99 [12.00 : 23.97]	42.06 [42.01 : 42.12]	1.88 [1.88 : 1.88]
***α*, deg**	***β*, deg**	***ϕ*, deg**
2.14 [2.09 : 2.21]	-0.10 [-0.16 : -0.07]	0.00 [-0.10 : 0.07]
CL	***CD***	***CM***
0.144 [0.137 : 0.151]	0.01776 [0.01728 : 0.01852]	-0.122 [-0.127 : -0.116]

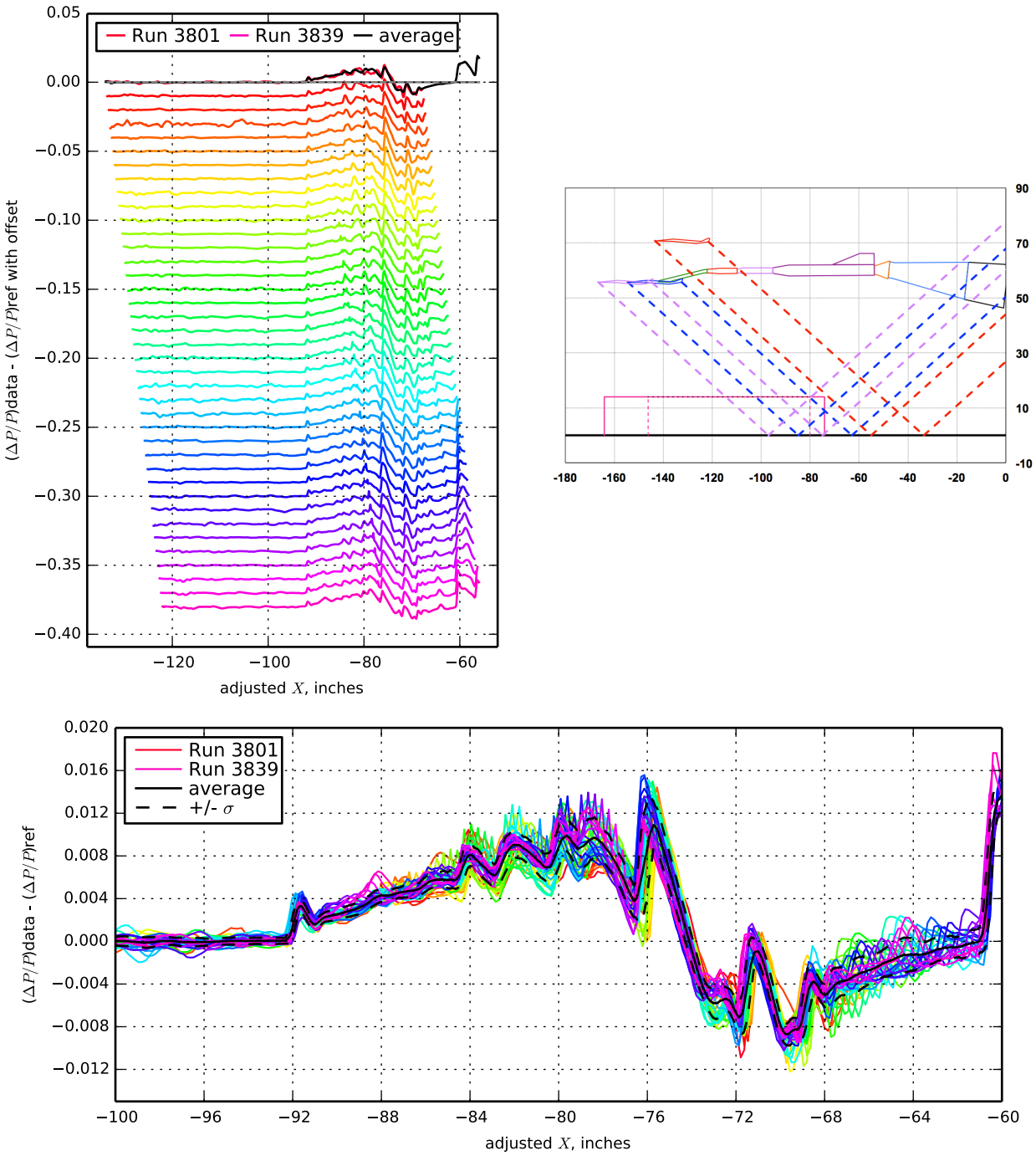

Figure 7.85. 1021 model with blade strut (re-tested), Runs 3801-3839:3840, Mach 1.6, Duration 6 sec, Re 8.15×10^6, T -80.02° F, PT 2298.95 psf, PT-Ref 0.38 psf, H 263.1 ppm [262.2 : 263.8], H-Ref 0.89 ppm

***X_ram*, in**	***h*, in**	***h/L***
-0.01 [-0.01 : -0.01]	48.65 [40.61 : 56.70]	2.17 [1.81 : 2.53]
***α*, deg**	***β*, deg**	***ϕ*, deg**
1.84 [1.81 : 1.86]	0.30 [0.28 : 0.31]	1.08 [0.92 : 1.28]
CL	***CD***	***CM***
0.138 [0.131 : 0.144]	0.01643 [0.01586 : 0.01691]	-0.131 [-0.134 : -0.127]

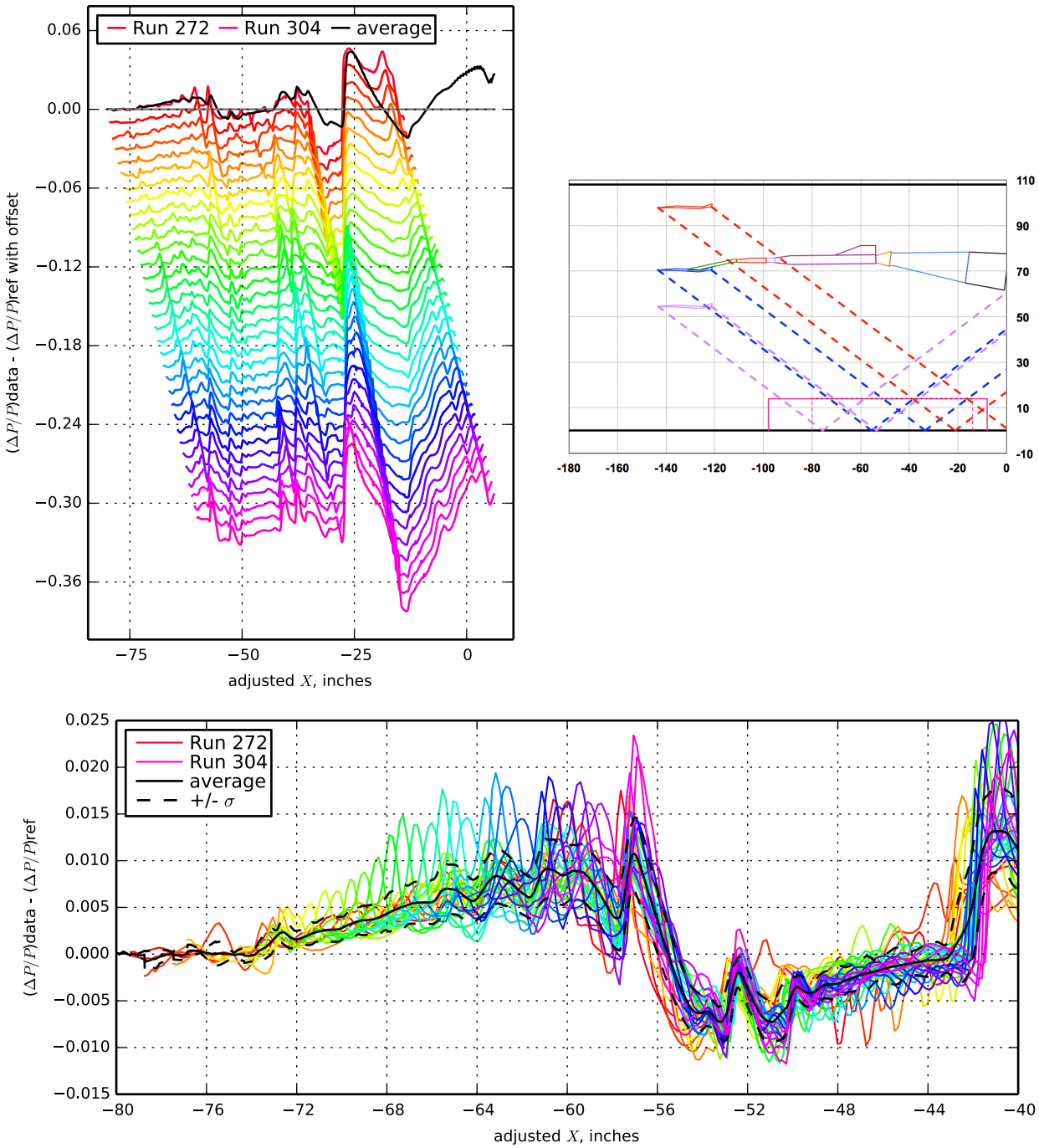

Figure 7.86. 1021 model with blade strut (re-tested), Runs 272-304:271, Mach 1.6, Duration 6 sec, Re 8.26×10^6, T -81.40° F, PT 2316.71 psf, PT-Ref -0.83 psf, H 213.7 ppm [213.0 : 214.3], H-Ref 0.30 ppm

***X_ram*, in**	***h*, in**	***h/L***
8.00 [8.00 : 8.00]	62.84 [57.08 : 68.64]	2.81 [2.55 : 3.06]
***α*, deg**	***β*, deg**	***ϕ*, deg**
2.03 [2.01 : 2.06]	0.12 [0.10 : 0.14]	0.53 [0.47 : 0.59]
CL	***CD***	***CM***
0.146 [0.142 : 0.153]	0.01840 [0.01820 : 0.01858]	-0.132 [-0.133 : -0.130]

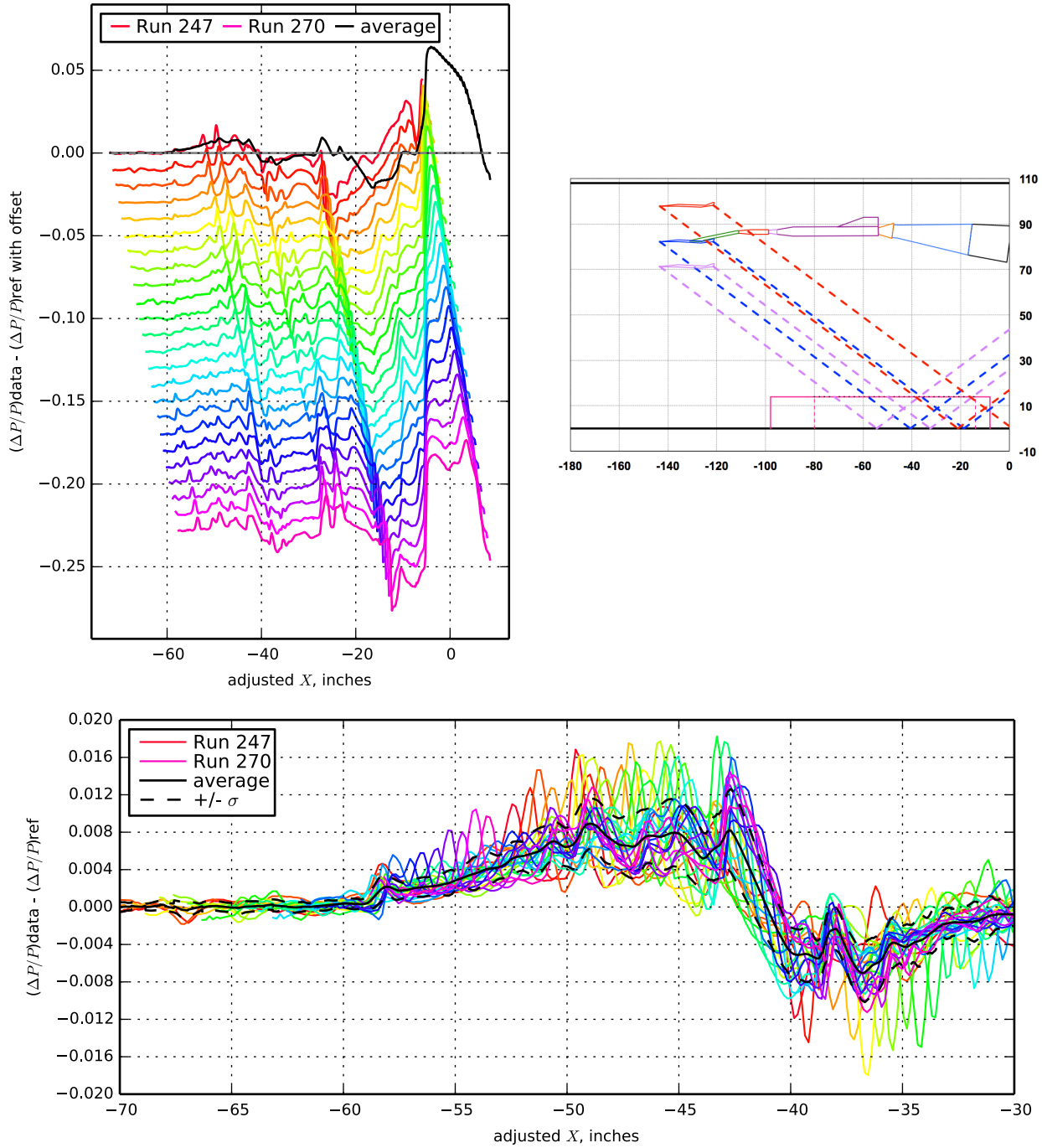

Figure 7.87. 1021 model with blade strut (re-tested), Runs 247-270:271, Mach 1.6, Duration 6 sec, Re 8.26×10^6, T -81.41° F, PT 2316.79 psf, PT-Ref -0.75 psf, H 212.3 ppm, H-Ref -1.13 ppm

***X_ram*, in**	***h*, in**	***h/L***
20.76 [17.61 : 23.91]	69.63 [69.59 : 69.67]	3.11 [3.11 : 3.11]
***α*, deg**	***β*, deg**	***ϕ*, deg**
2.12 [2.08 : 2.16]	0.09 [0.07 : 0.10]	0.37 [0.34 : 0.40]
CL	***CD***	***CM***
0.153 [0.148 : 0.159]	0.01918 [0.01853 : 0.01986]	-0.131 [-0.132 : -0.130]

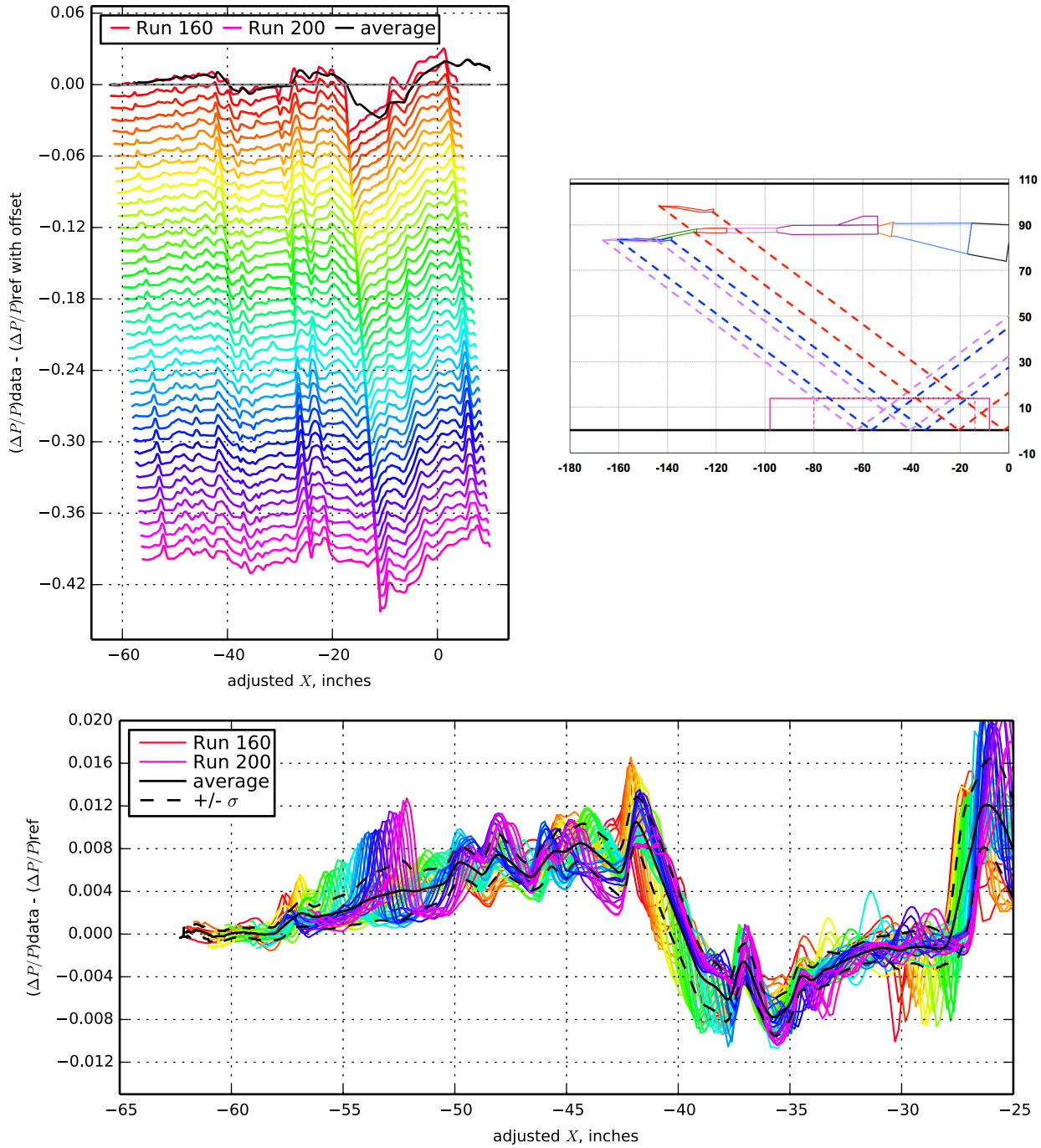

Figure 7.88. 1021 model with blade strut (re-tested), Runs 160-200:204, Mach 1.6, Duration 6 sec, Re 8.26×10^6, T -81.53° F, PT 2316.78 psf, PT-Ref 0.66 psf, H 207.9 ppm, H-Ref -0.03 ppm

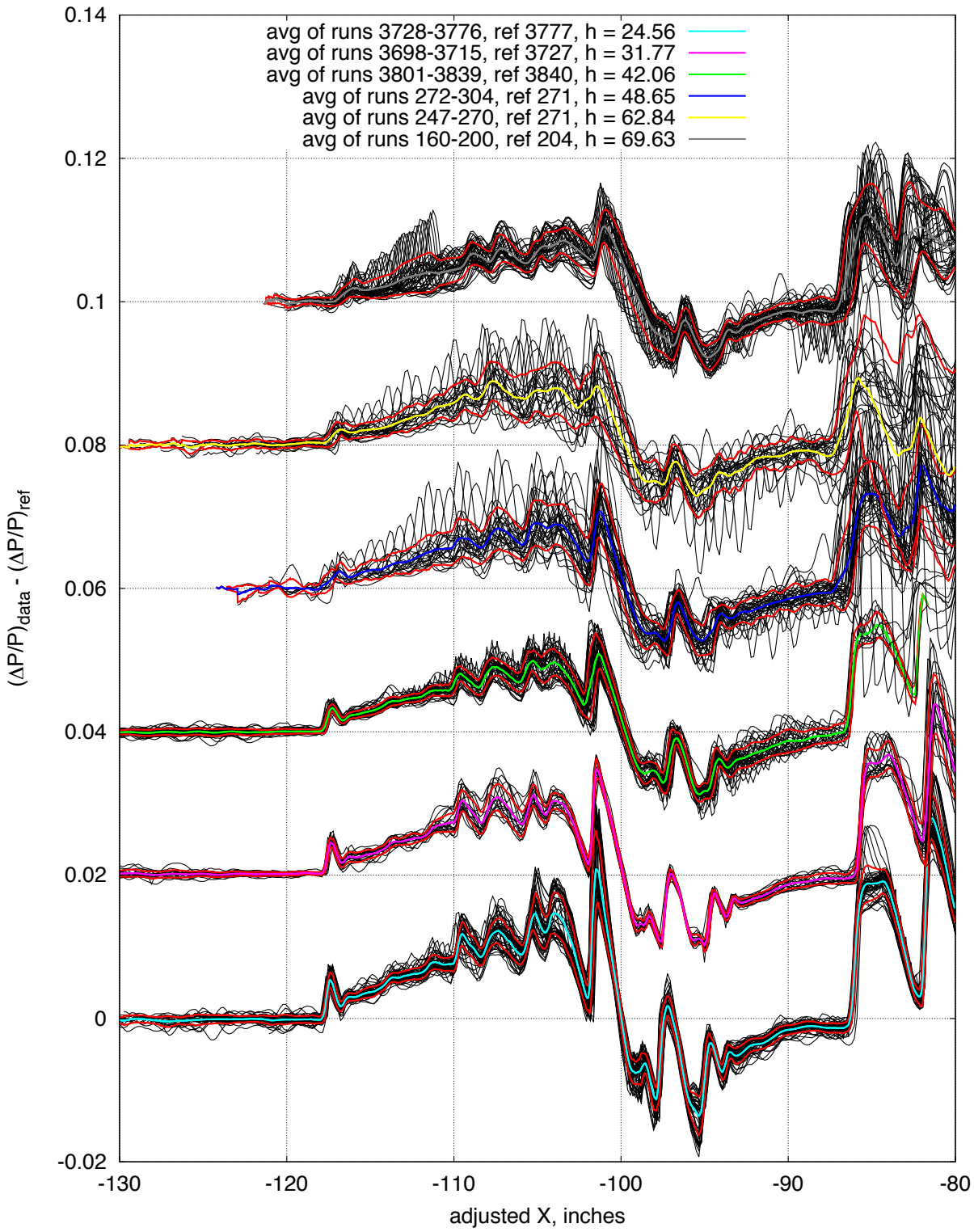

a) Stacked individual and averaged data

Figure 7.89. Effect of altitude h[24.56:69.63] inches for the on-track pressure signature for the1021 model re-tested in the phase II experiment, M=1.6, α[1.84:2.18] degrees (continues)

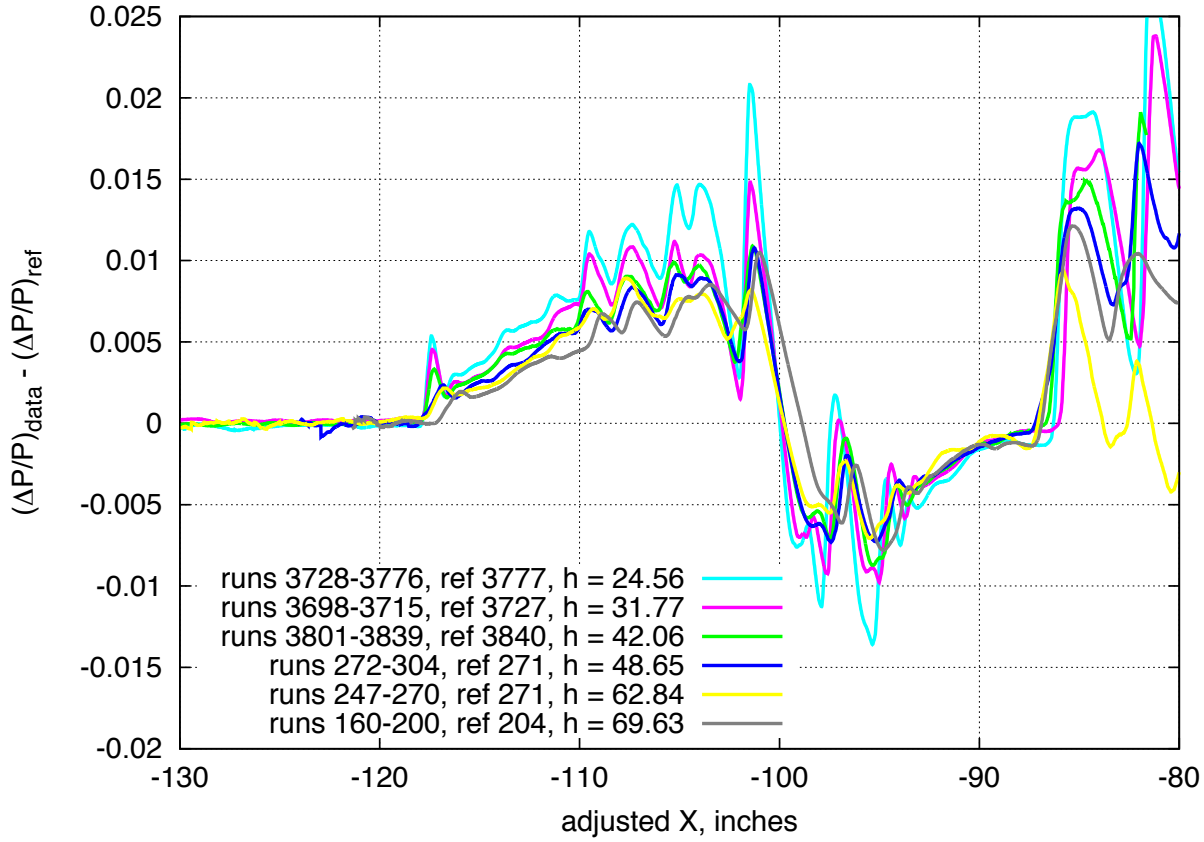

b) Overlaid averaged data

Figure 7.89. Effect of altitude h[24.56:69.63] inches for the on-track pressure signature for the1021 model re-tested in the phase II experiment, M=1.6, α[1.84:2.18] degrees (concluded)

***X_ram*, in**	***h*, in**	***h/L***
-0.01 [-0.01 : -0.01]	56.01 [42.16 : 69.87]	3.17 [2.38 : 3.95]
***α*, deg**	***β*, deg**	***ϕ*, deg**
-0.06 [-0.06 : -0.06]	0.21 [0.21 : 0.21]	0.41 [0.32 : 0.53]
CL	***CD***	***CM***
-0.002 [-0.004 : -0.001]	0.04939 [0.04771 : 0.05080]	0.016 [0.001 : 0.046]

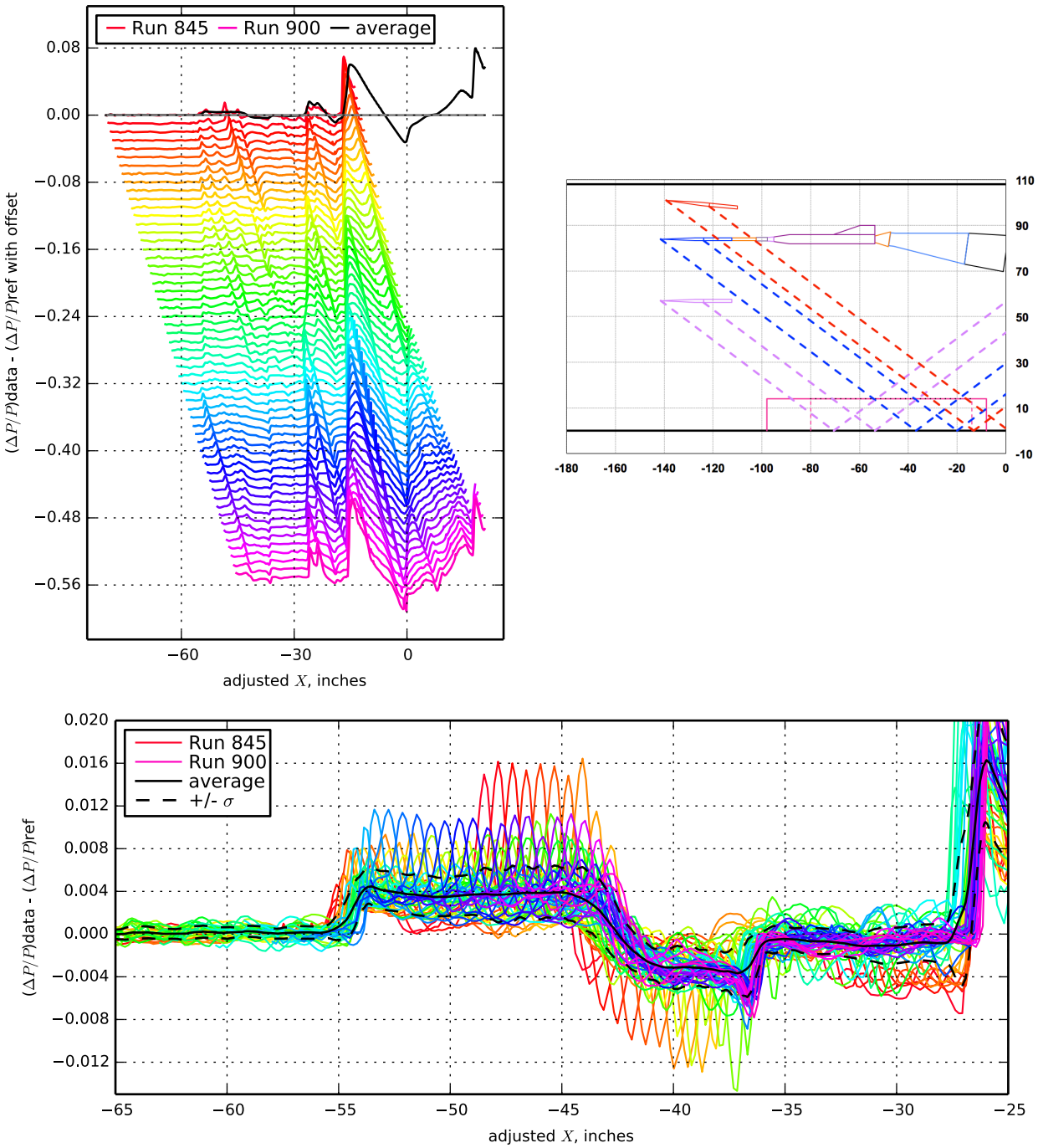

Figure 7.90. Seeb-ALR (re-tested), Runs 845-900:901, Mach 1.6, Duration 8 sec, Re 6.49x10^6, T -82.47° F, PT 2297.28 psf, PT-Ref -0.52 psf, H 272.6 ppm [270.5 : 275.0], H-Ref -1.29 ppm

***X_ram*, in**	***h*, in**	***h/L***
-0.01 [-0.01 : -0.01]	56.02 [42.16 : 69.88]	3.17 [2.38 : 3.95]
***α*, deg**	***β*, deg**	***ϕ*, deg**
-0.05 [-0.06 : -0.05]	0.15 [0.15 : 0.15]	0.27 [0.21 : 0.35]
CL	***CD***	***CM***
-0.002 [-0.004 : -0.000]	0.04935 [0.04766 : 0.05084]	0.007 [-0.011 : 0.037]

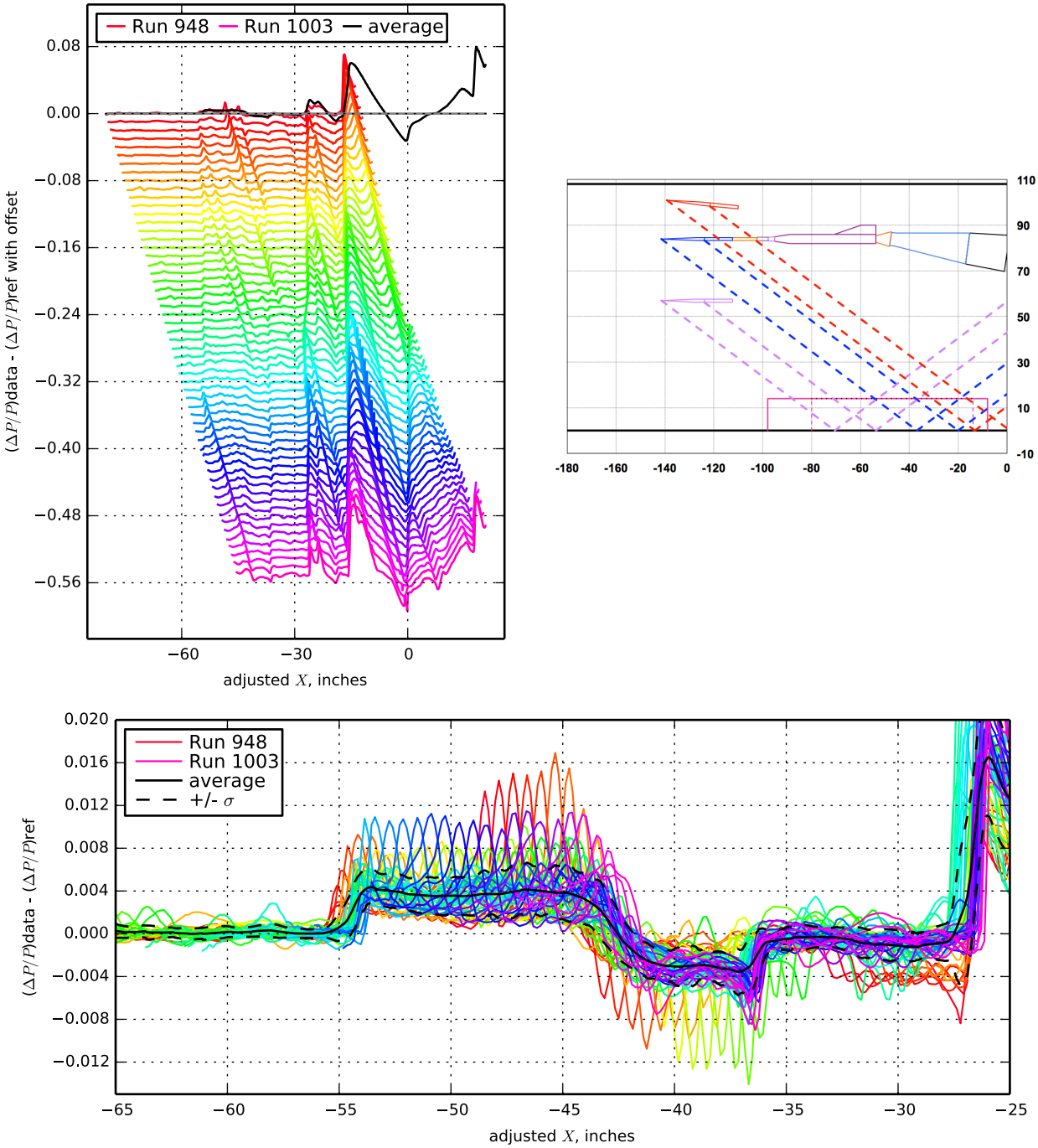

Figure 7.91. Seeb-ALR (re-tested), Runs 948-1003:1004, Mach 1.6, Duration 8.1 sec, Re 6.47x10^6, T -81.74° F, PT 2297.33 psf, PT-Ref -0.68 psf, H 272.9 ppm [271.5 : 274.5], H-Ref 1.43 ppm

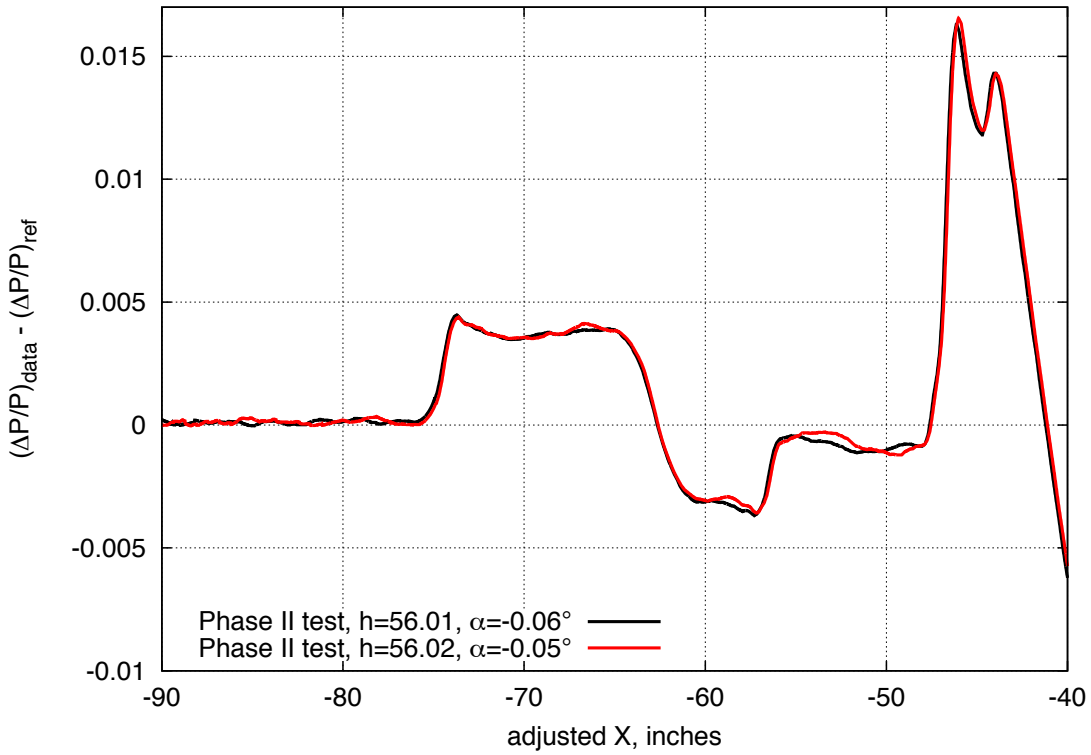

Figure 7.92. Short-term repeatability of the Seeb-ALR at an altitude of 56 inches

***X_ram*, in**	***h*, in**	***h/L***
11.97 [-0.01 : 23.94]	70.02 [70.02 : 70.03]	3.96 [3.96 : 3.96]
***α*, deg**	***β*, deg**	***ϕ*, deg**
-0.03 [-0.03 : -0.02]	0.15 [0.12 : 0.19]	0.22 [0.15 : 0.30]
CL	***CD***	***CM***
-0.003 [-0.004 : -0.002]	0.05335 [0.05021 : 0.05435]	0.020 [0.006 : 0.036]

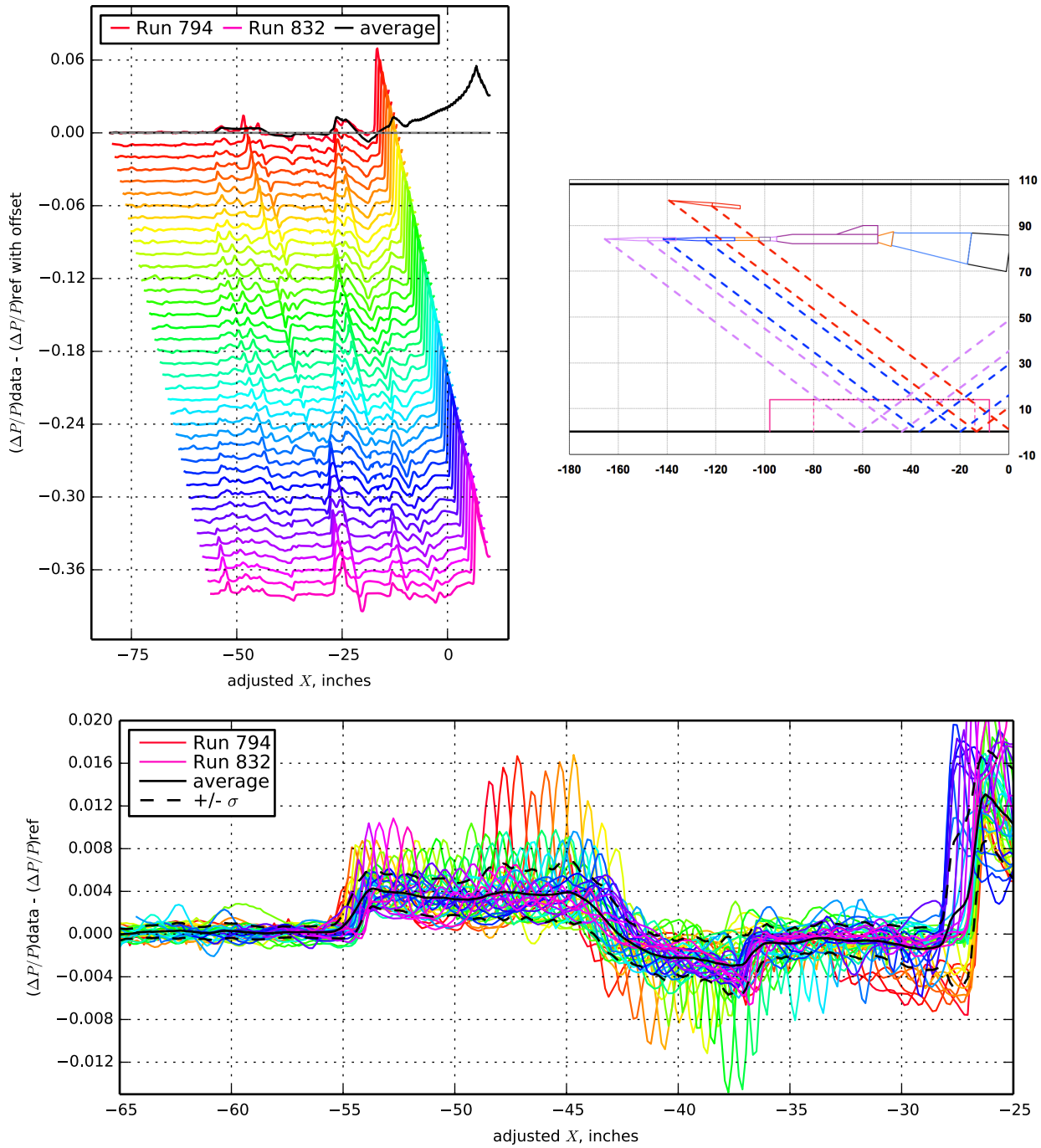

Figure 7.93. Seeb-ALR (re-tested), Runs 794-832:834, Mach 1.6, Duration 8 sec, Re 6.49x10^6 [6.47x10^6 : 6.51x10^6], T -82.20° F, PT 2301.91 psf, PT-Ref 4.41 psf, H 259.6 ppm [253.9 : 266.6], H-Ref 4.66 ppm

***X_ram*, in**	***h*, in**	***h/L***
17.76 [11.52 : 23.91]	24.86 [24.84 : 24.87]	3.60 [3.60 : 3.61]
***α*, deg**	***β*, deg**	***ϕ*, deg**
0.24 [0.22 : 0.27]	-0.09 [-0.09 : -0.08]	0.16 [0.14 : 0.18]
CL	***CD***	***CM***
0.015 [0.000 : 0.027]	0.26507 [0.25252 : 0.28277]	-0.210 [-0.383 : 0.024]

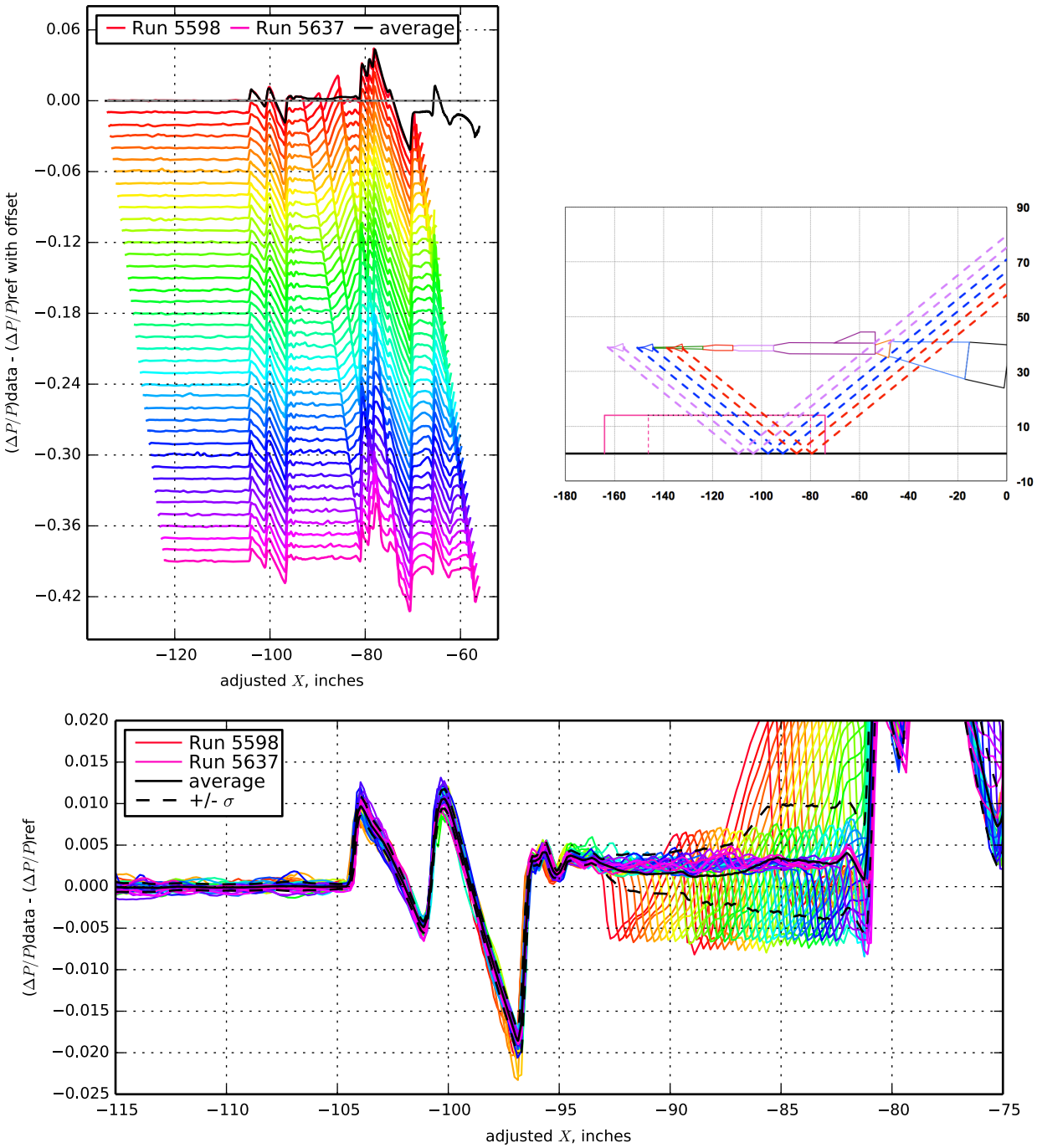

Figure 7.94. 69° Delta wing body, Runs 5598-5637:5638, Mach 1.7, Duration 6 sec, Re 2.43x10^6, T -95.08° F, PT 2302.30 psf, PT-Ref 0.53 psf, H 231.7 ppm, H-Ref -0.10 ppm

***X_ram*, in**	***h*, in**	***h/L***
17.77 [11.78 : 23.75]	24.75 [24.72 : 24.78]	3.59 [3.58 : 3.59]
***α*, deg**	***β*, deg**	***ϕ*, deg**
-0.20 [-0.23 : -0.18]	-0.12 [-0.13 : -0.11]	29.97 [29.95 : 29.99]
CL	***CD***	***CM***
0.007 [-0.004 : 0.016]	0.26738 [0.25552 : 0.28363]	-0.301 [-0.452 : -0.114]

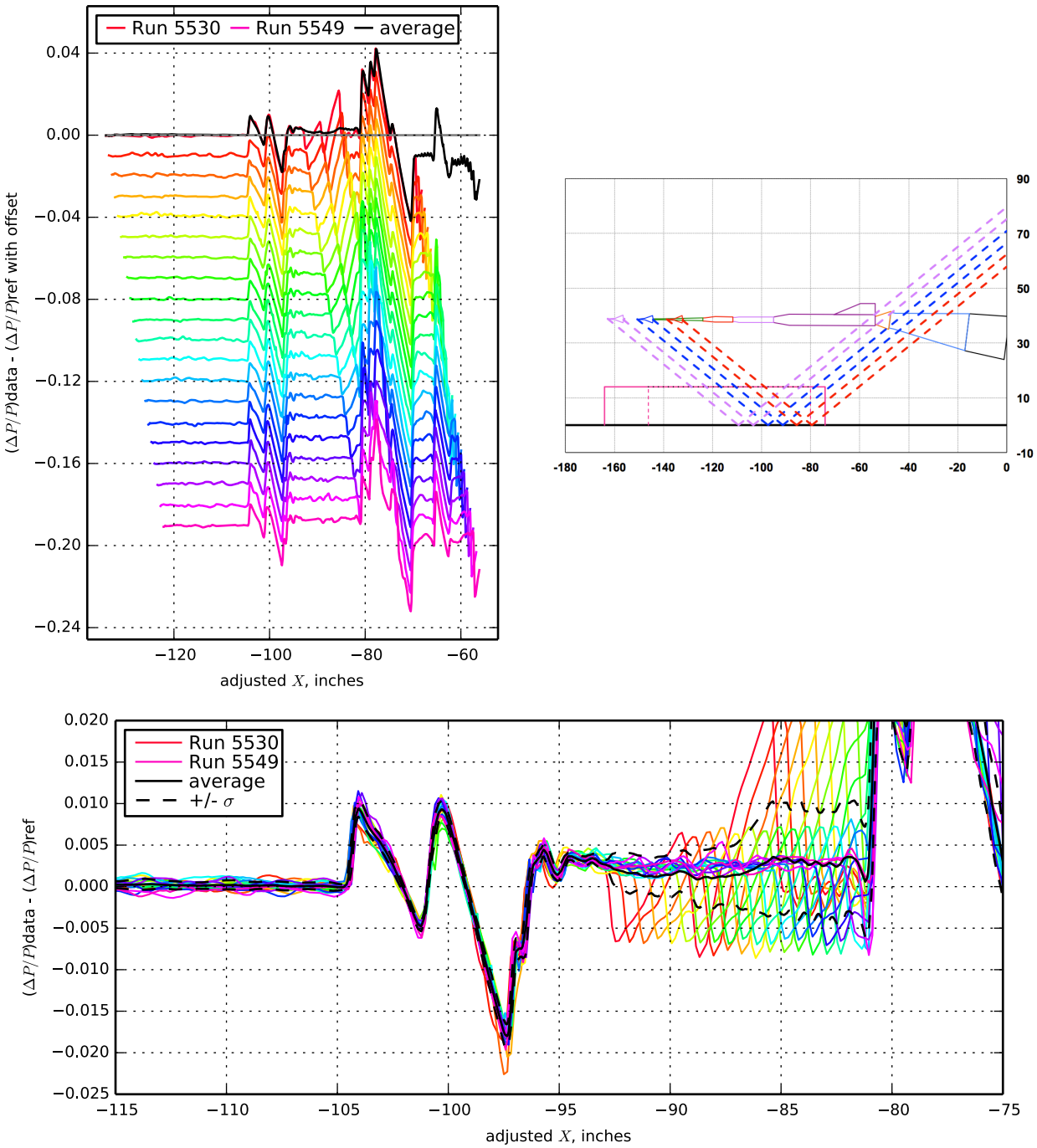

Figure 7.95. 69° Delta wing body, Runs 5530-5549:5550, Mach 1.7, Duration 6 sec, Re 2.43x10^6, T -94.57° F, PT 2302.87 psf, PT-Ref -0.27 psf, H 232.2 ppm, H-Ref 0.28 ppm

***X_ram*, in**	***h*, in**	***h/L***
17.77 [11.78 : 23.75]	24.75 [24.73 : 24.78]	3.59 [3.58 : 3.59]
***α*, deg**	***β*, deg**	***ϕ*, deg**
-0.18 [-0.21 : -0.17]	-0.23 [-0.25 : -0.22]	60.06 [60.02 : 60.10]
CL	***CD***	***CM***
0.008 [-0.001 : 0.012]	0.26618 [0.25387 : 0.28308]	-0.302 [-0.410 : -0.167]

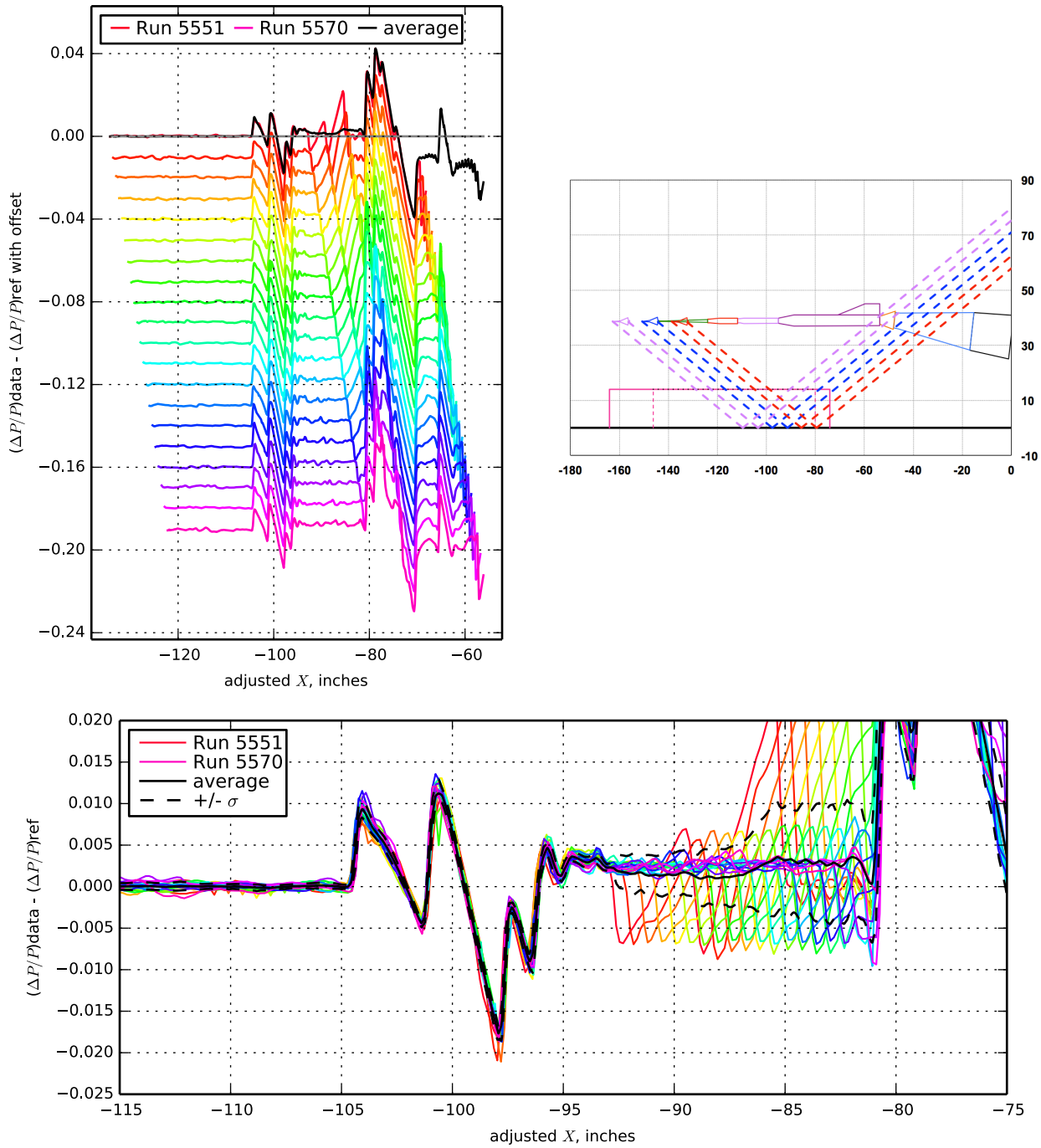

Figure 7.96. 69° Delta wing body, Runs 5551-5570:5571, Mach 1.7, Duration 6 sec, Re 2.43x10^6, T -94.60° F, PT 2302.37 psf, PT-Ref 0.50 psf, H 232.2 ppm, H-Ref 0.02 ppm

***X_ram*, in**	***h*, in**	***h/L***
17.77 [11.78 : 23.75]	24.69 [24.63 : 24.74]	3.58 [3.57 : 3.59]
***α*, deg**	***β*, deg**	***ϕ*, deg**
-0.18 [-0.20 : -0.15]	-0.50 [-0.52 : -0.48]	89.87 [89.83 : 89.90]
CL	***CD***	***CM***
0.006 [-0.000 : 0.010]	0.26581 [0.25431 : 0.28187]	-0.228 [-0.291 : -0.165]

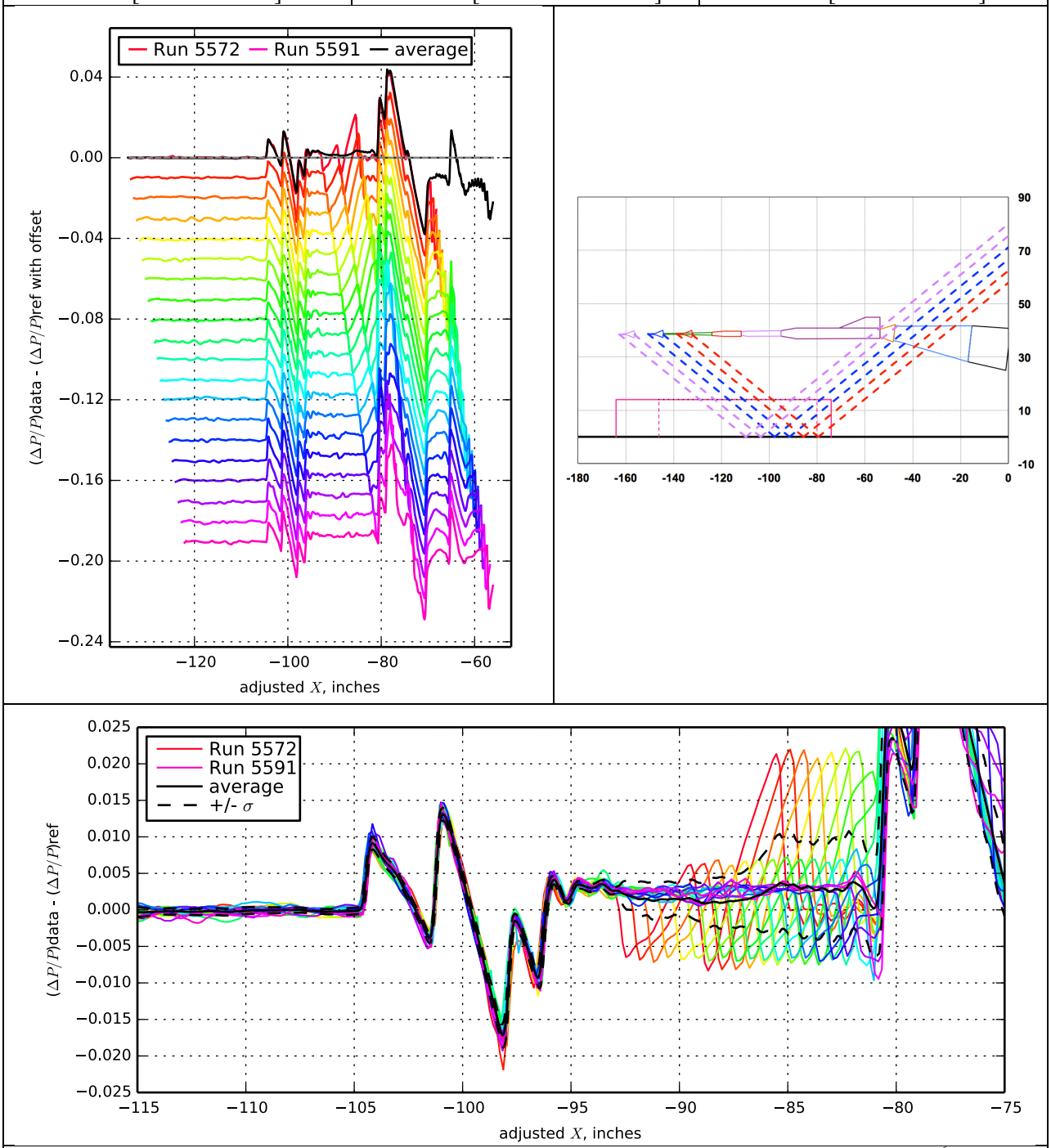

Figure 7.97. 69° Delta wing body, Runs 5572-5591:5592, Mach 1.7, Duration 6 sec, Re 2.43x10^6, T -94.59° F, PT 2302.30 psf, PT-Ref -0.63 psf, H 232.5 ppm, H-Ref 0.14 ppm

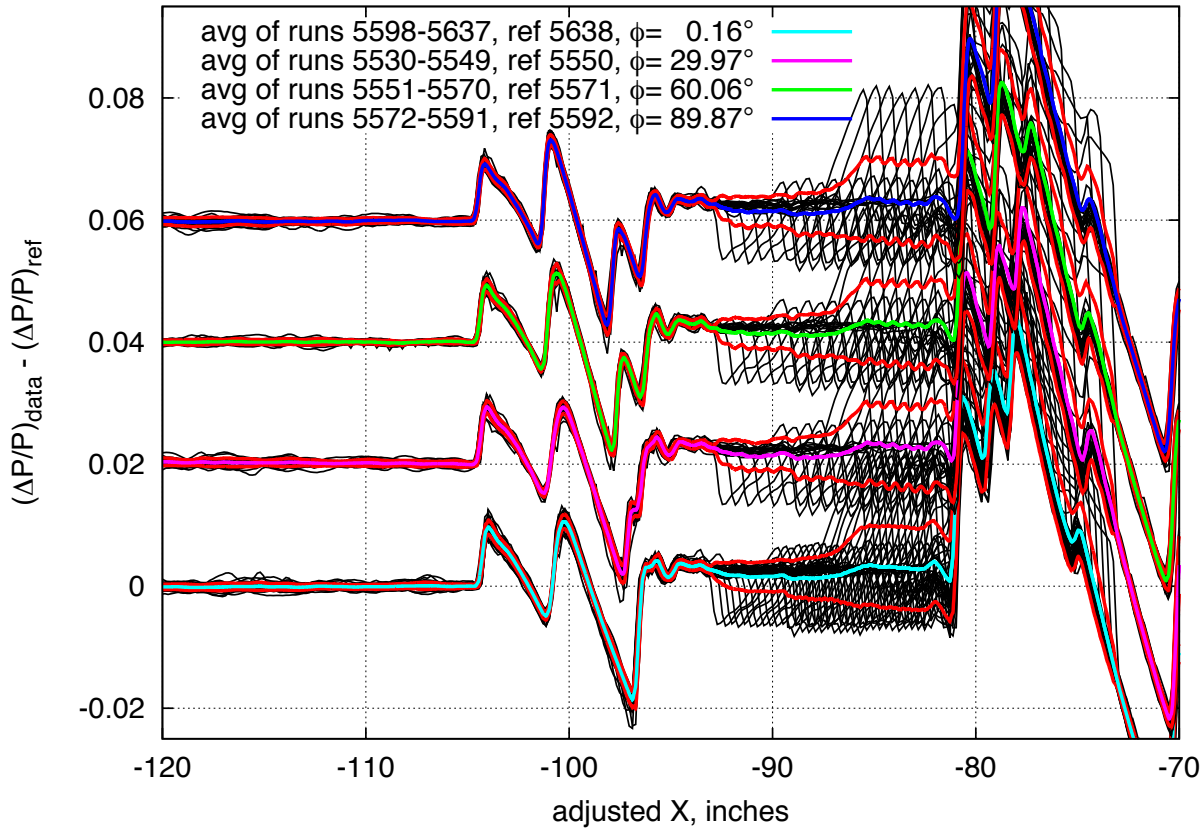

Figure 7.98. Effect of off-track angle for the 69° Delta Wing Body model, M=1.7, near zero angle of attack, α[-0.20 : 0.24] degrees, at h[24.69 : 24.86] inches

***X_ram*, in**	***h*, in**	***h/L***
18.40 [13.04 : 23.75]	31.64 [31.62 : 31.66]	4.59 [4.58 : 4.59]
***α*, deg**	***β*, deg**	***ϕ*, deg**
-0.06 [-0.08 : -0.03]	0.36 [0.36 : 0.36]	0.59 [0.53 : 0.67]
CL	***CD***	***CM***
-0.011 [-0.020 : -0.007]	0.26548 [0.26135 : 0.26939]	-0.042 [-0.128 : 0.094]

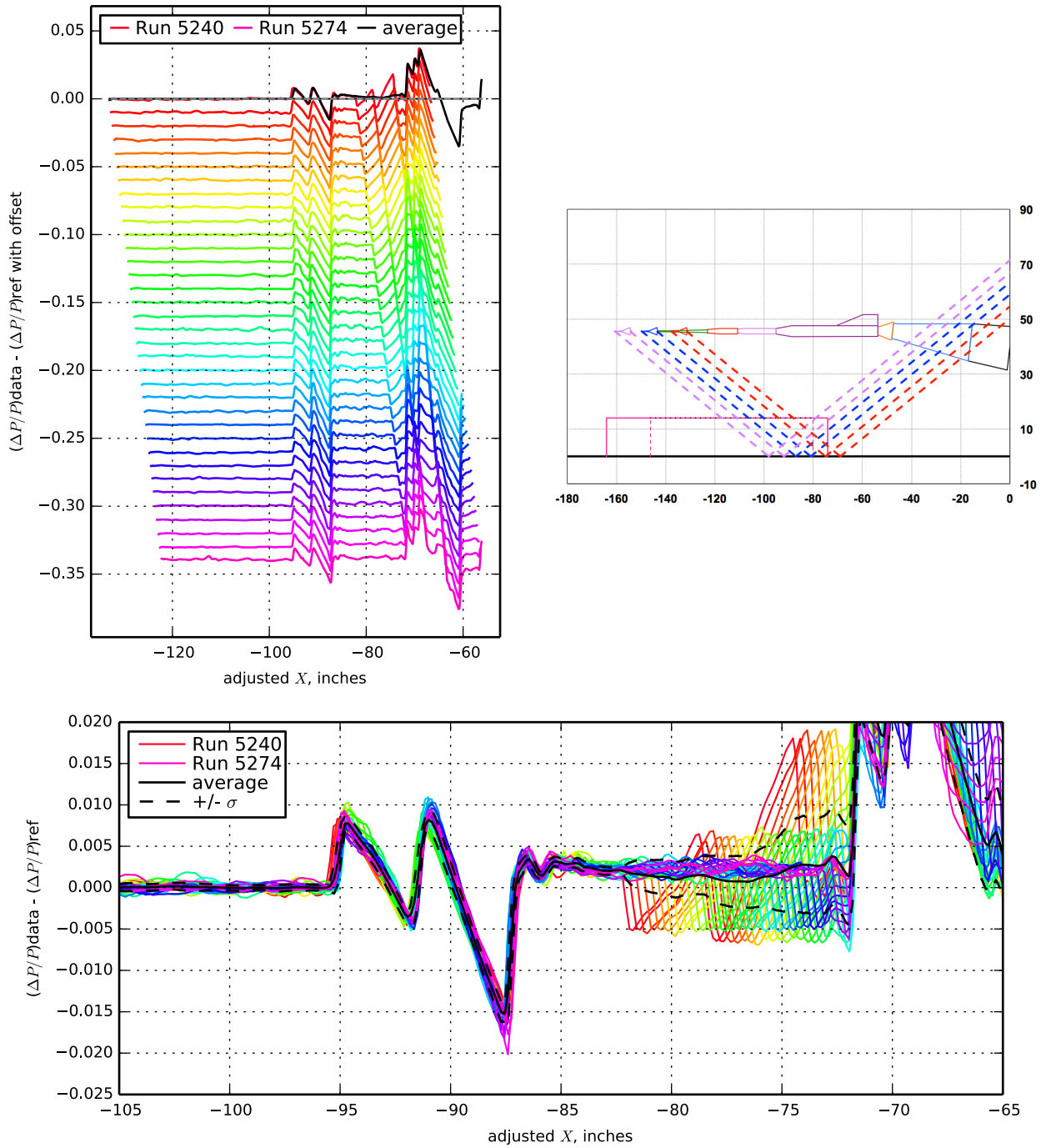

Figure 7.99. 69° Delta wing body, Runs 5240-5274:5275, Mach 1.7, Duration 6 sec, Re 2.44x10^6, T -95.71° F, PT 2302.83 psf, PT-Ref -0.38 psf, H 252.0 ppm, H-Ref -0.63 ppm.

***X_ram*, in**	***h*, in**	***h/L***
18.40 [13.04 : 23.75]	31.74 [31.72 : 31.77]	4.60 [4.60 : 4.61]
***α*, deg**	***β*, deg**	***ϕ*, deg**
-0.17 [-0.19 : -0.14]	-0.40 [-0.41 : -0.40]	29.94 [29.88 : 29.99]
CL	***CD***	***CM***
-0.007 [-0.015 : -0.002]	0.26643 [0.26132 : 0.27031]	-0.166 [-0.264 : -0.011]

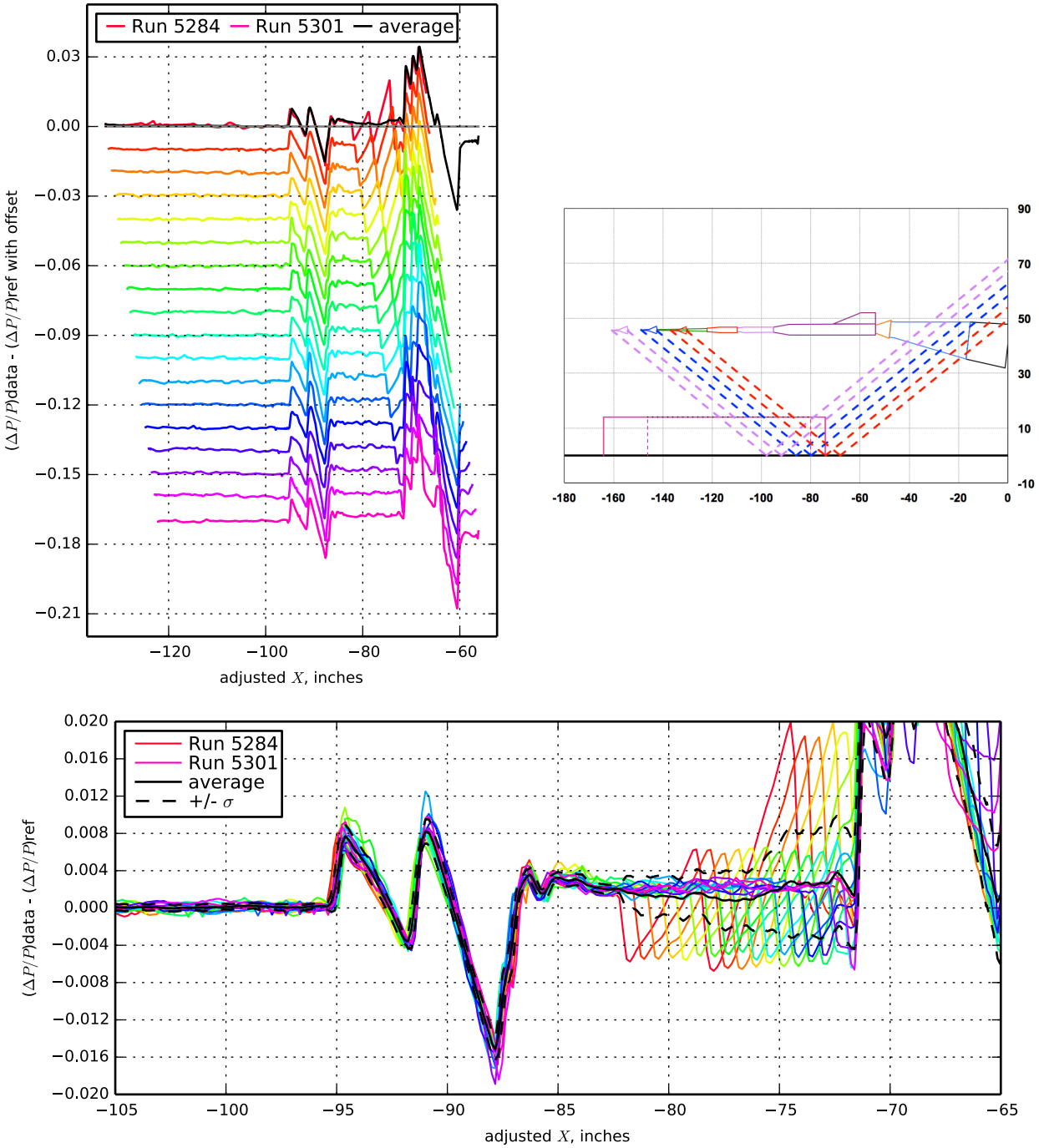

Figure 7.100. 69° Delta wing body, Runs 5284-5301:5275, Mach 1.7, Duration 6 sec, Re 2.43x10^6, T -95.41° F, PT 2302.75 psf, PT-Ref -0.46 psf, H 252.1 ppm, H-Ref -0.54 ppm.

***X_ram*, in**	***h*, in**	***h/L***
18.40 [13.04 : 23.75]	31.56 [31.48 : 31.65]	4.58 [4.56 : 4.59]
***α*, deg**	***β*, deg**	***ϕ*, deg**
-0.23 [-0.25 : -0.18]	-0.95 [-0.96 : -0.95]	59.74 [59.62 : 59.82]
CL	***CD***	***CM***
-0.004 [-0.009 : -0.001]	0.26762 [0.26363 : 0.27117]	-0.215 [-0.301 : -0.078]

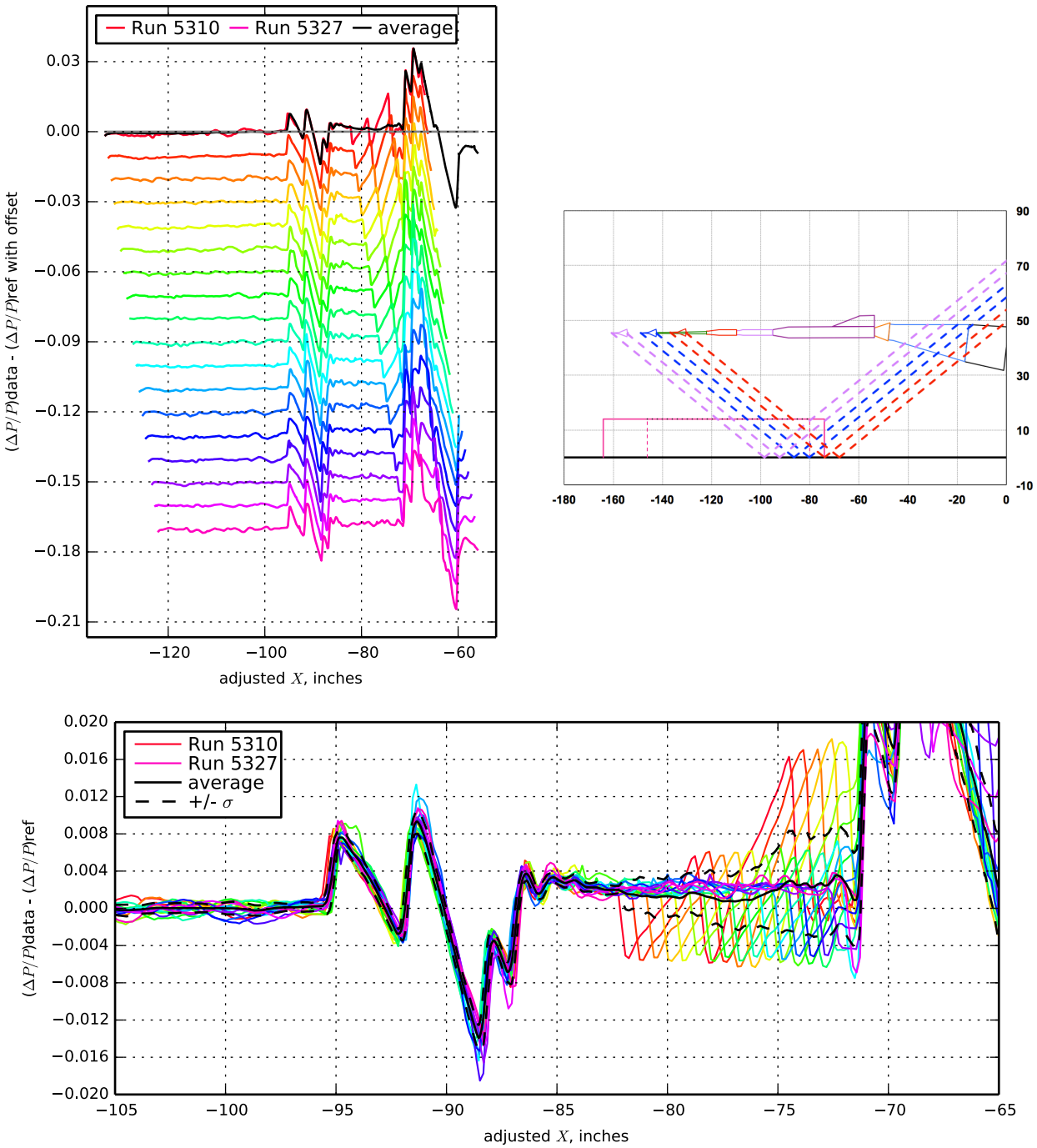

Figure 7.101. 69° Delta wing body, Runs 5310-5327:5328, Mach 1.7, Duration 6 sec, Re 2.43x10^6, T -95.23° F, PT 2302.90 psf, PT-Ref -0.79 psf, H 248.4 ppm, H-Ref 0.64 ppm.

***X_ram*, in**	***h*, in**	***h/L***
18.40 [13.04 : 23.75]	31.61 [31.53 : 31.69]	4.58 [4.57 : 4.59]
***α*, deg**	***β*, deg**	***ϕ*, deg**
-0.20 [-0.23 : -0.17]	-0.72 [-0.73 : -0.71]	89.97 [89.93 : 90.00]
CL	***CD***	***CM***
0.003 [-0.001 : 0.006]	0.26710 [0.26393 : 0.26973]	-0.226 [-0.264 : -0.157]

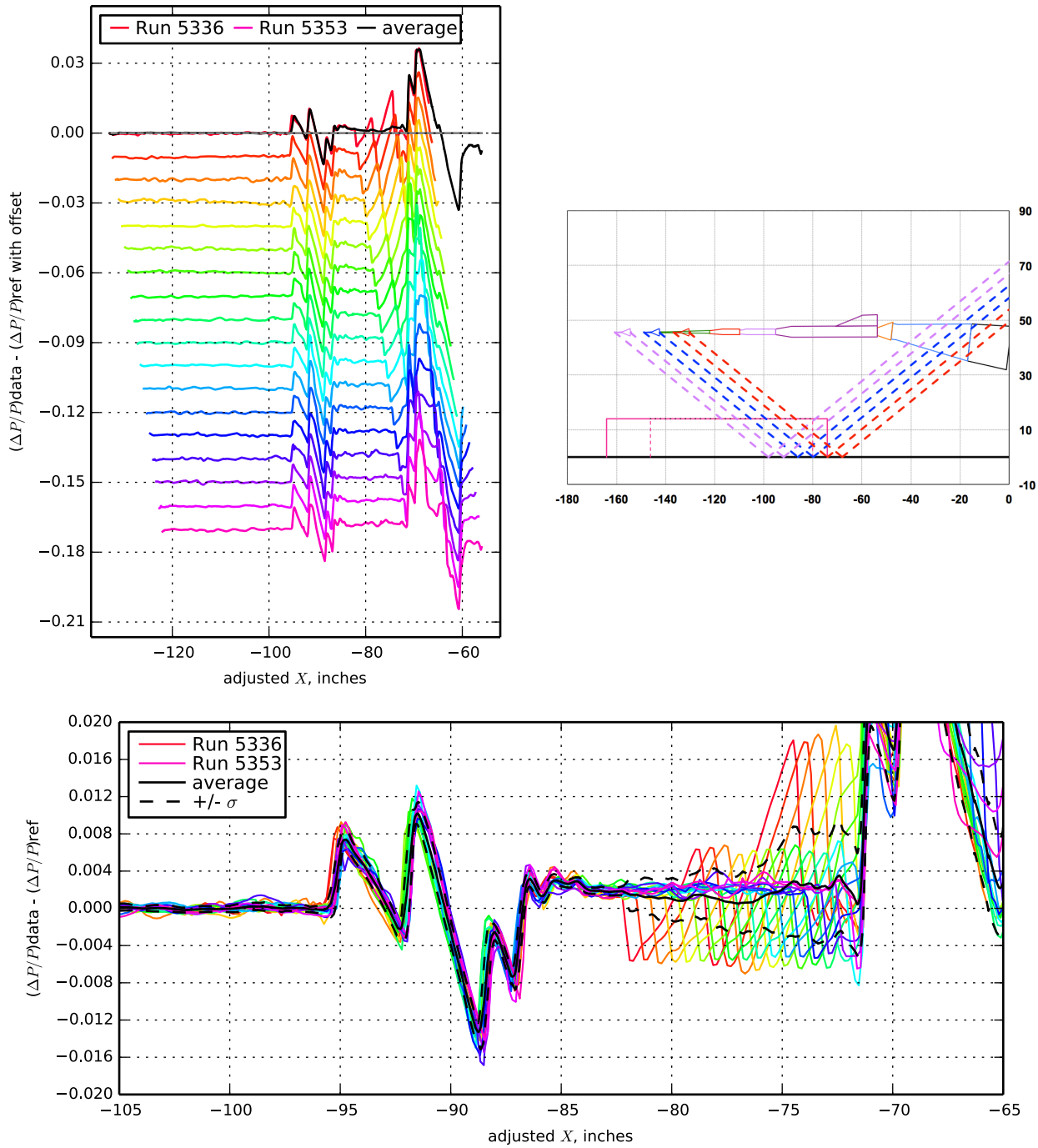

Figure 7.102. 69° Delta wing body, Runs 5336-5353:5354, Mach 1.7, Duration 6 sec, Re 2.43x10^6, T -95.16° F, PT 2302.70 psf, PT-Ref -0.61 psf, H 246.3 ppm, H-Ref 0.61 ppm.

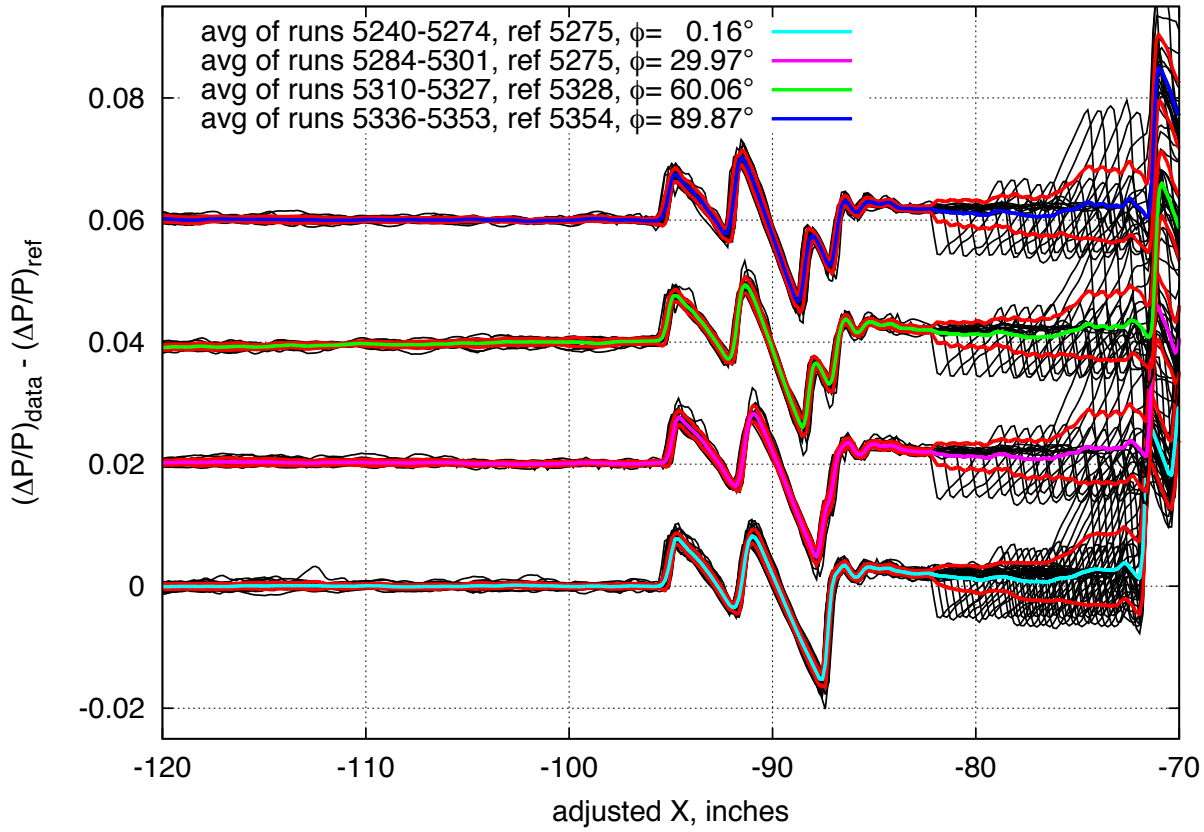

Figure 7.103. Effect of off-track angle for the 69° Delta Wing-Body model, M=1.7, near zero angle of attack, α [-0.22-0.06] degrees, h [31.56-31.74] inches

***X_ram*, in**	***h*, in**	***h/L***
17.61 [11.47 : 23.75]	21.33 [21.26 : 21.39]	3.09 [3.08 : 3.10]
***α*, deg**	***β*, deg**	***ϕ*, deg**
0.71 [0.69 : 0.73]	-0.02 [-0.02 : -0.01]	0.25 [0.25 : 0.26]
CL	***CD***	***CM***
0.017 [-0.005 : 0.046]	0.27692 [0.25950 : 0.28601]	-0.078 [-0.456 : 0.187]

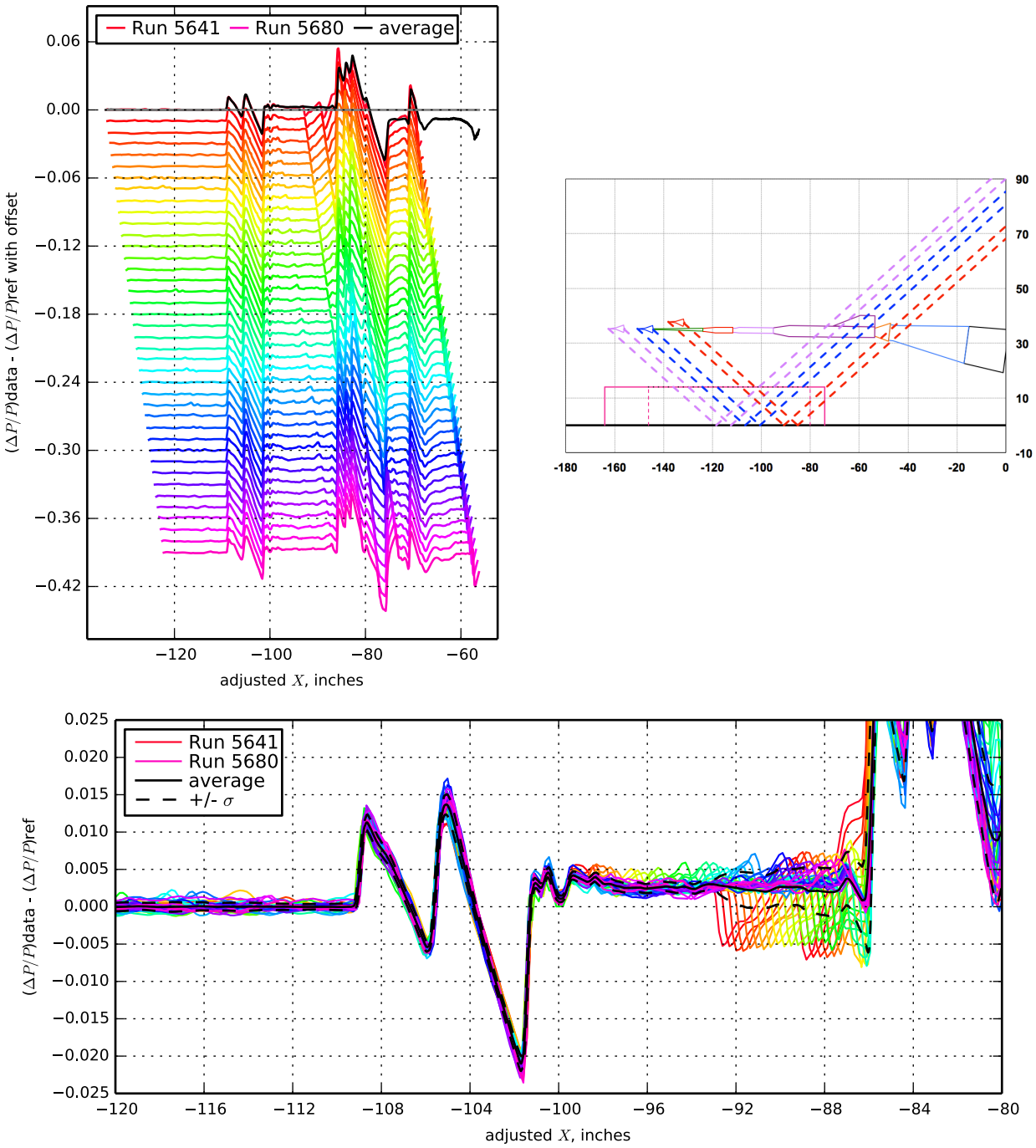

Figure 7.104. 69° Delta wing body, Runs 5641-5680:5638, Mach 1.7, Duration 6 sec, Re 2.43x10^6, T -95.13° F, PT 2302.32 psf, PT-Ref 0.56 psf, H 232.8 ppm [230.6 : 235.7], H-Ref 1.03 ppm

***X_ram*, in**	***h*, in**	***h/L***
17.77 [11.78 : 23.75]	25.21 [25.01 : 25.39]	3.65 [3.63 : 3.68]
***α*, deg**	***β*, deg**	***ϕ*, deg**
2.37 [2.33 : 2.39]	0.41 [0.41 : 0.42]	0.33 [0.24 : 0.43]
CL	***CD***	***CM***
0.101 [0.078 : 0.117]	0.28072 [0.26401 : 0.29618]	-0.502 [-0.700 : -0.209]

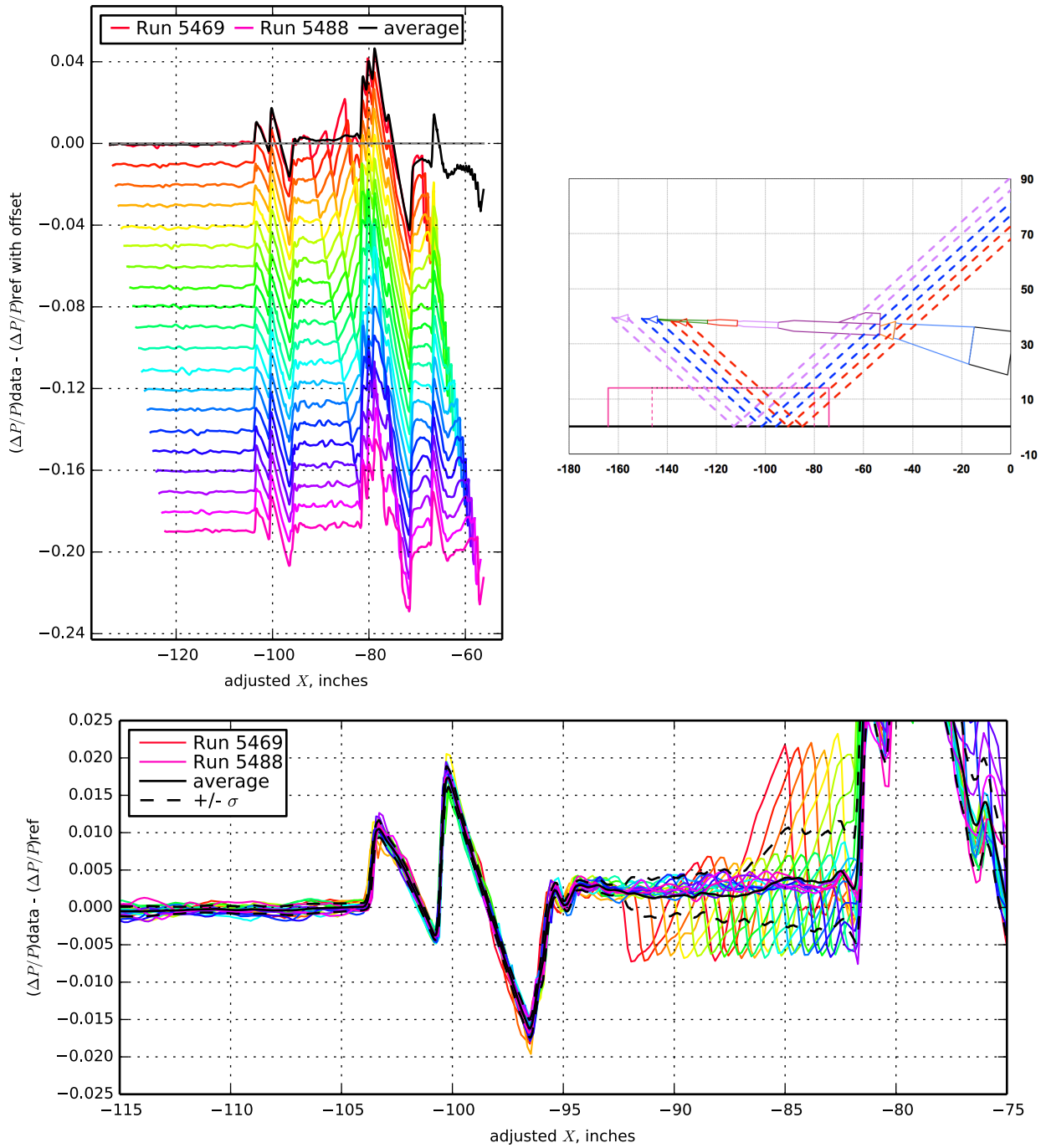

Figure 7.105. 69° Delta wing body, Runs 5469-5488:5489, Mach 1.7, Duration 6 sec, Re 2.43x10^6, T -94.56° F, PT 2302.85 psf, PT-Ref 0.19 psf, H 235.9 ppm, H-Ref 0.56 ppm

***X_ram*, in**	***h*, in**	***h/L***
17.77 [11.78 : 23.75]	25.49 [25.15 : 25.81]	3.70 [3.65 : 3.74]
***α*, deg**	***β*, deg**	***ϕ*, deg**
3.90 [3.88 : 3.93]	0.72 [0.72 : 0.72]	0.69 [0.53 : 0.84]
CL	***CD***	***CM***
0.179 [0.151 : 0.200]	0.29537 [0.27712 : 0.30742]	-0.826 [-1.050 : -0.473]

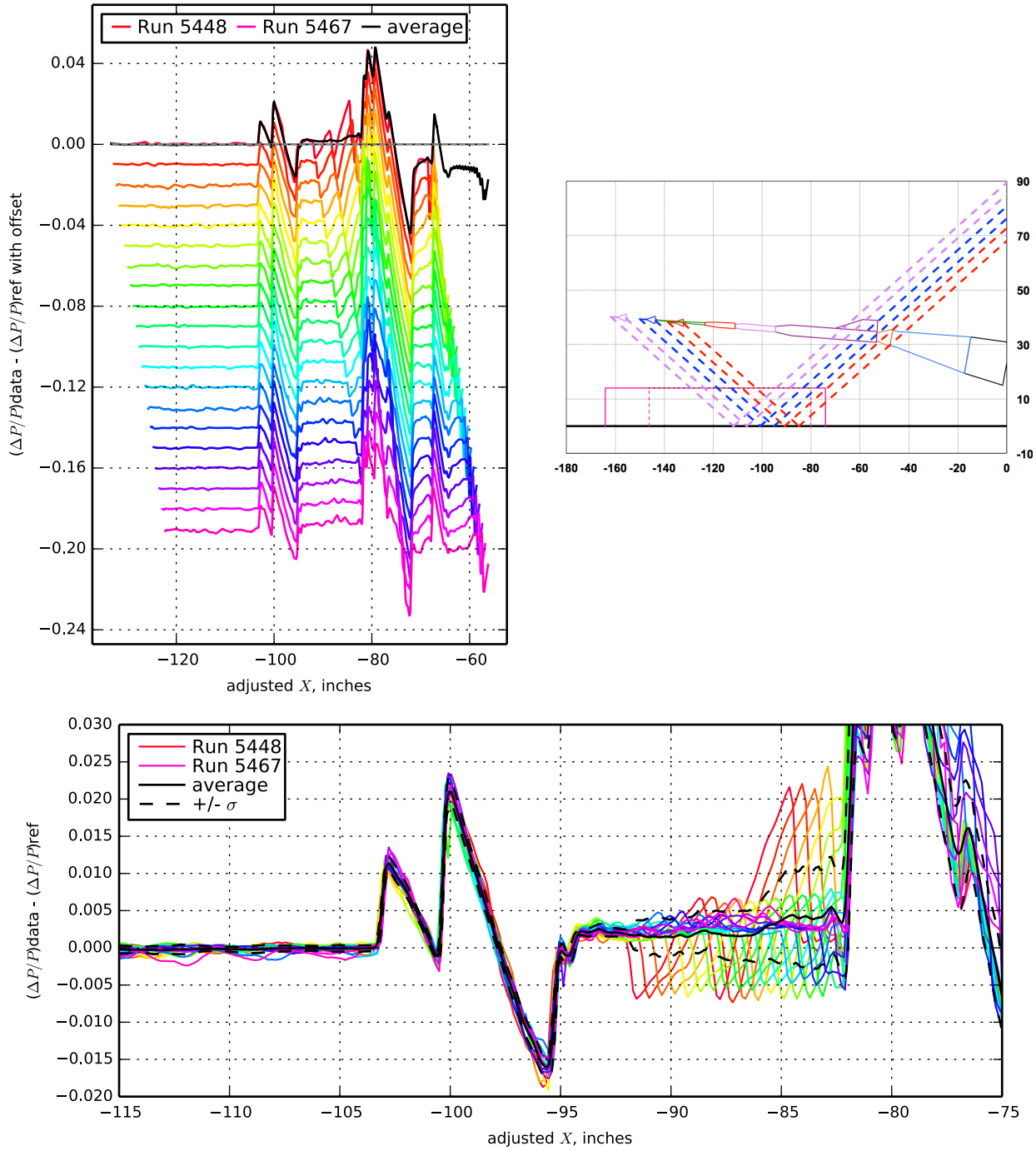

Figure 7.106. 69° Delta wing body, Runs 5448-5467:5468, Mach 1.7, Duration 6 sec, Re 2.43x10^6, T -94.79° F, PT 2302.80 psf, PT-Ref 0.66 psf, H 237.4 ppm, H-Ref 0.48 ppm

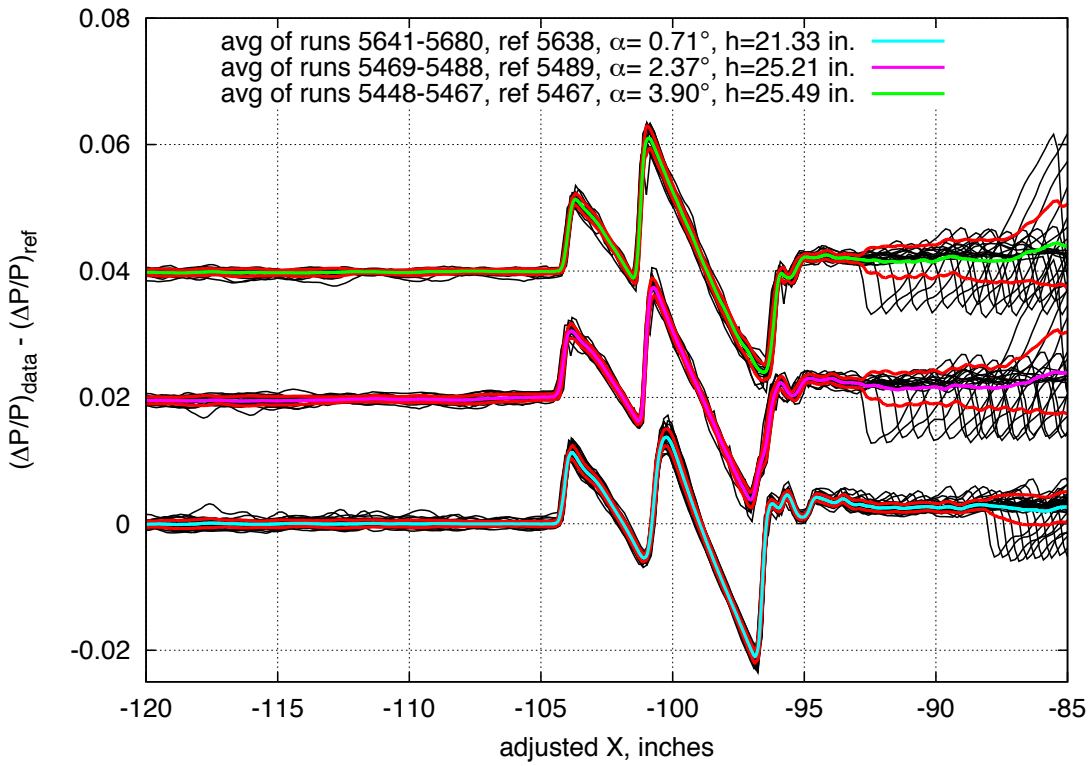

a) Stacked individual and averaged data

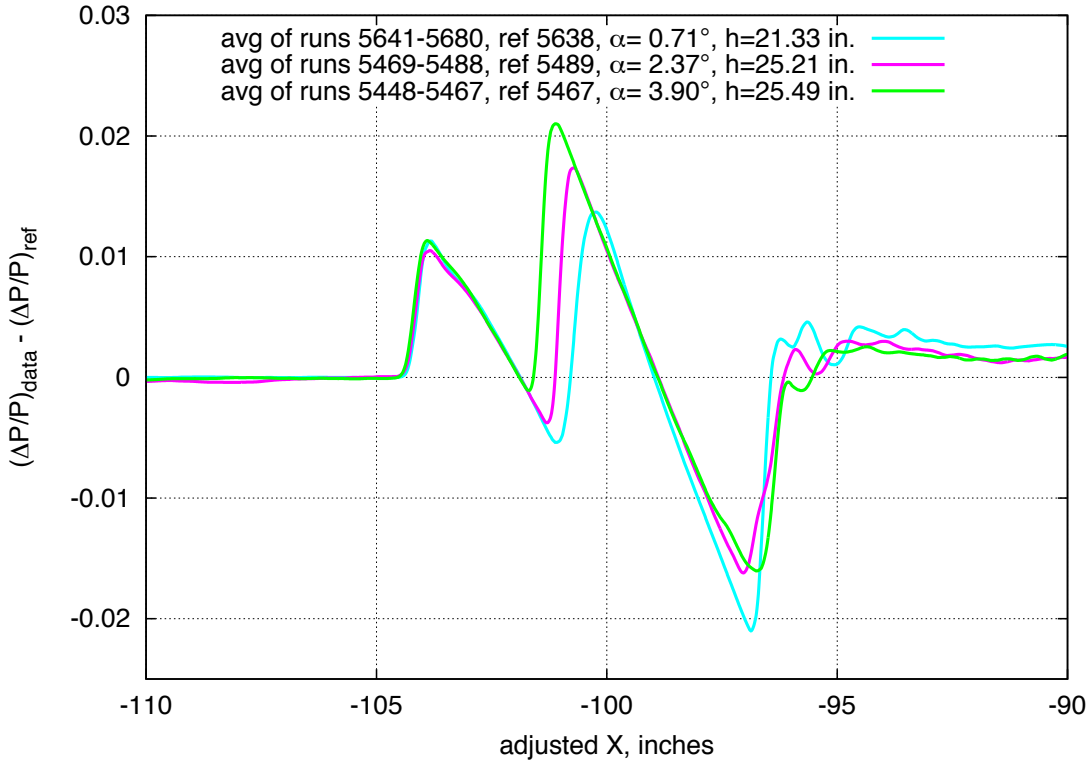

b) Overlaid averaged data

Figure 7.107. 69° Delta Wing, on-track pressure signatures, h [21.33: 25.49], α [0.71: 3.90]°, M=1.7

***X_ram*, in**	***h*, in**	***h/L***
17.77 [11.78 : 23.75]	32.10 [31.98 : 32.27]	4.65 [4.64 : 4.68]
***α*, deg**	***β*, deg**	***ϕ*, deg**
1.75 [1.72 : 1.79]	0.36 [0.36 : 0.36]	0.38 [0.31 : 0.45]
CL	***CD***	***CM***
0.065 [0.055 : 0.081]	0.26888 [0.26368 : 0.27431]	-0.325 [-0.431 : -0.188]

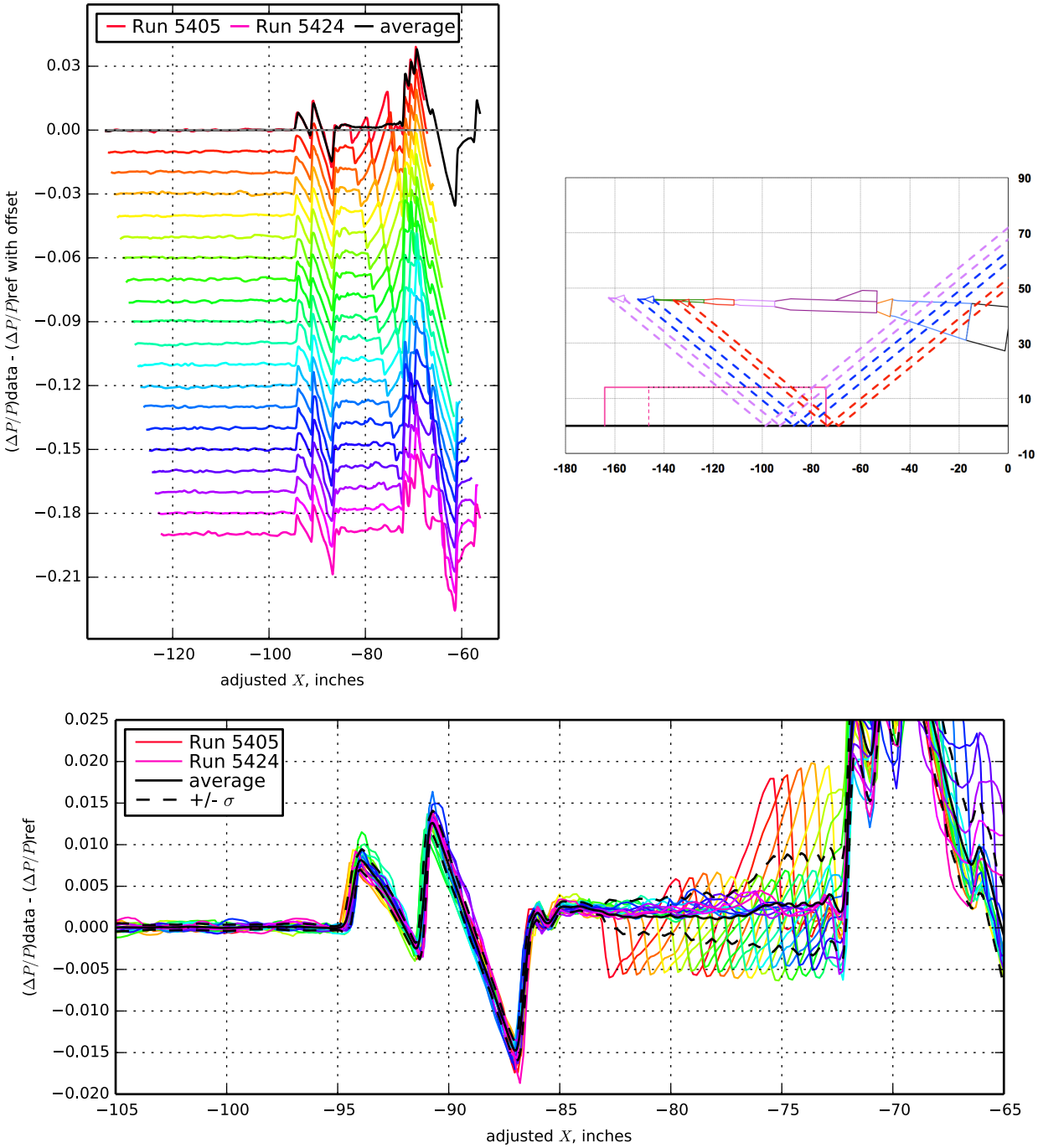

Figure 7.108. 69° Delta wing body, Runs 5405-5424:5425, Mach 1.7, Duration 6 sec, Re 2.43x10^6, T -94.82° F, PT 2302.68 psf, PT-Ref -0.12 psf, H 241.5 ppm, H-Ref 0.50 ppm

***X_ram*, in**	***h*, in**	***h/L***
17.77 [11.78 : 23.75]	32.33 [32.09 : 32.61]	4.69 [4.65 : 4.73]
***α*, deg**	***β*, deg**	***ϕ*, deg**
3.10 [3.07 : 3.15]	0.54 [0.54 : 0.54]	0.24 [0.14 : 0.33]
CL	***CD***	***CM***
0.134 [0.126 : 0.151]	0.27780 [0.27344 : 0.28161]	-0.633 [-0.747 : -0.514]

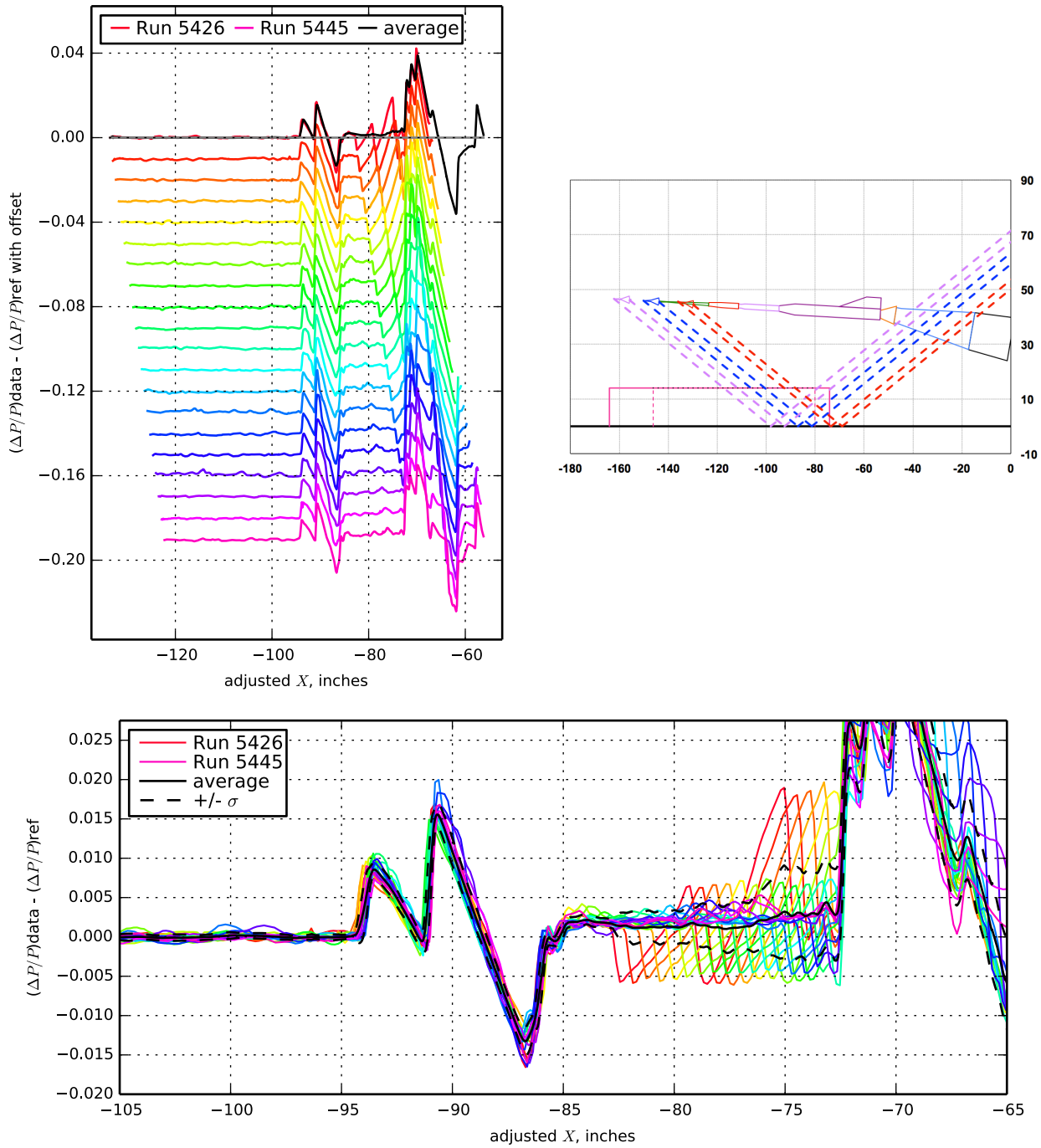

Figure 7.109. 69° Delta wing body, Runs 5426-5445:5446, Mach 1.7, Duration 6 sec, Re 2.43x10^6, T -94.83° F, PT 2302.70 psf, PT-Ref 0.43 psf, H 239.9 ppm, H-Ref 0.25 ppm

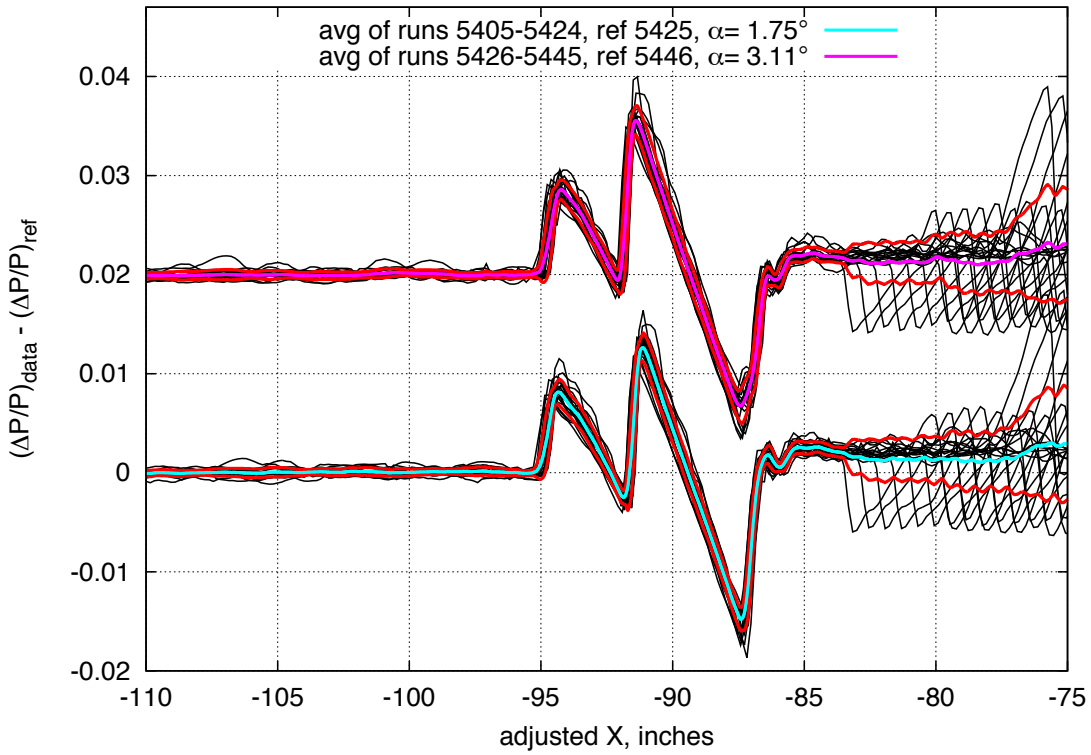

a) Stacked individual and averaged data

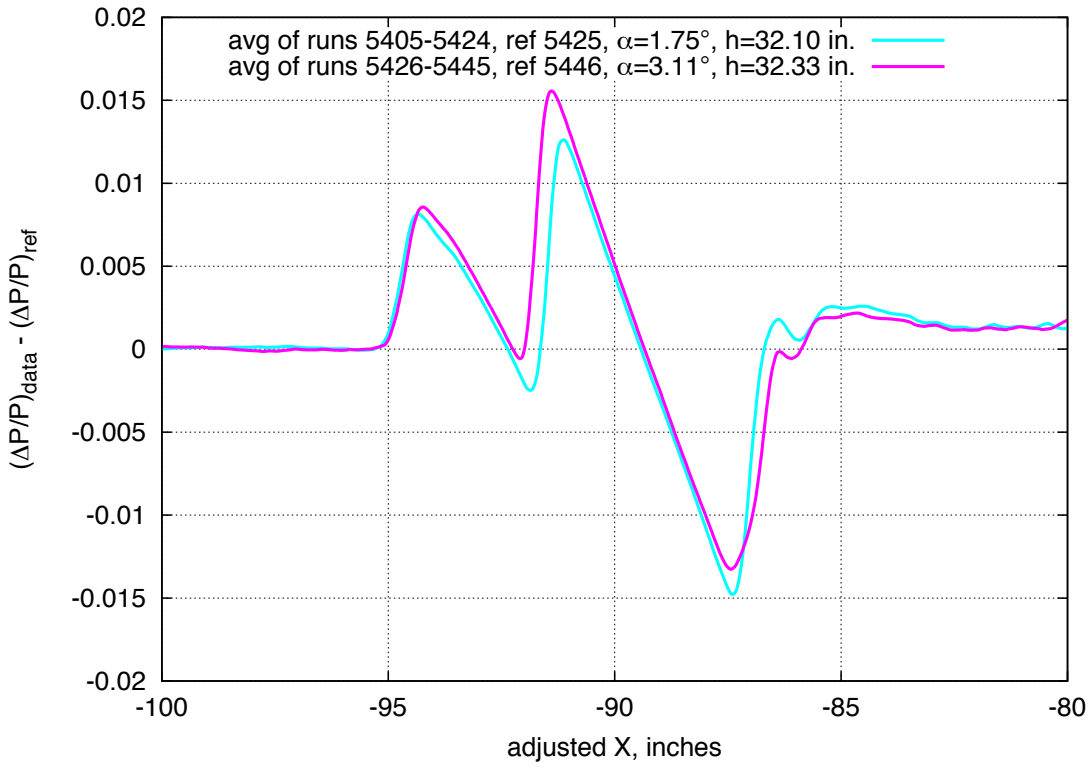

b) Overlaid averaged data

Figure 7.110. 69° Delta Wing, on-track pressure signatures, M=1.7, h [32.10 : 32.33] inches

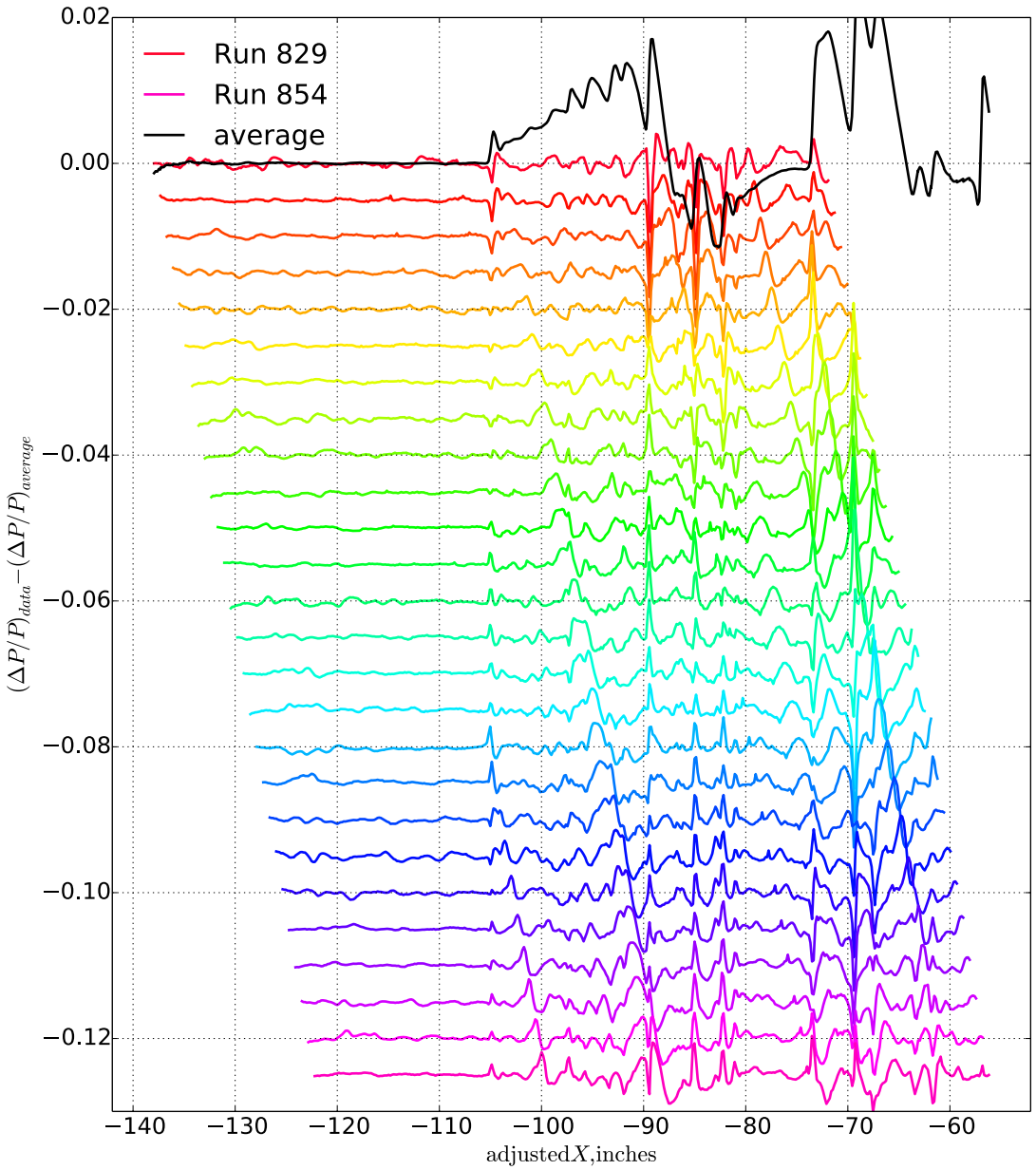

a) Residual and averaged data for run series 829_854-876

Figure 7.111 Phase I test residuals from the 1021 Model, M=1.6, h= 31 inches (continues)

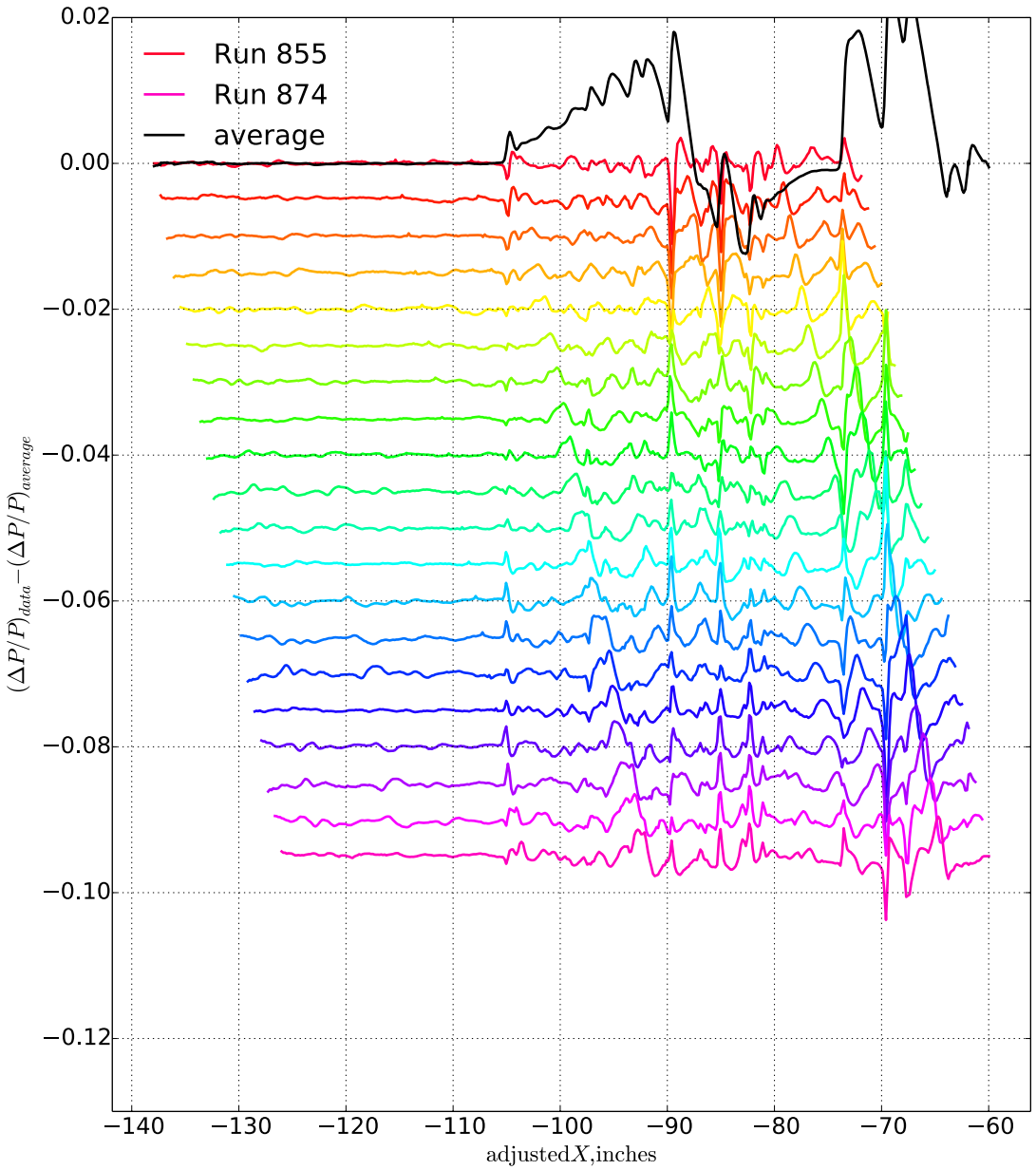

b) Residual and averaged data for run series 855_874-876

Figure 7.111 Phase I test residuals from the 1021 Model, *M*=1.6, *h*= 31 inches (concluded)

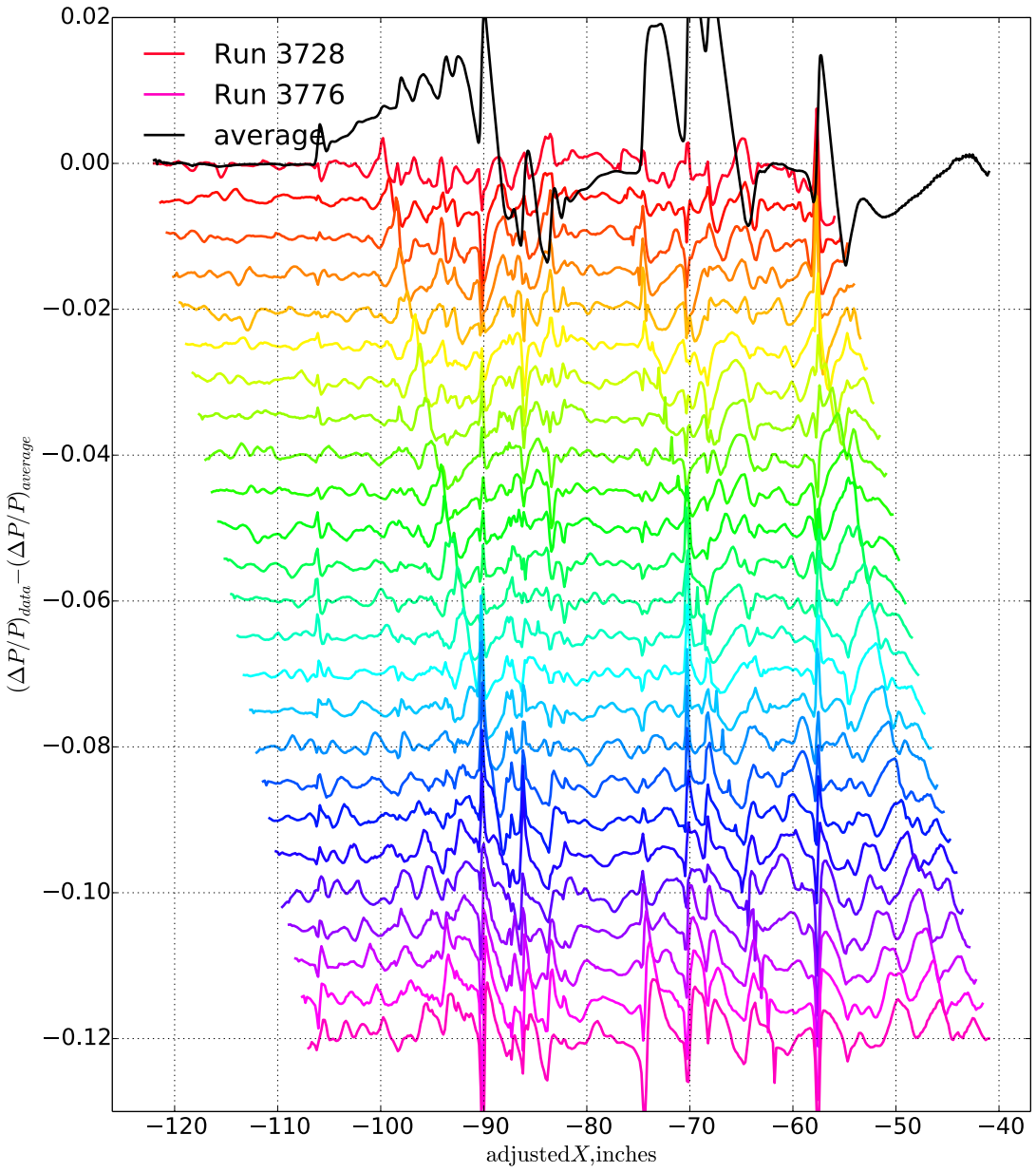

a) Residual and averaged data for run series 3728-3776-3777, from Phase II test at *h*=24.56 inches

Figure 7.112 Phase II test residuals from the 1021 Model, *M*=1.6, *h*=25 and 32 inches (continues)

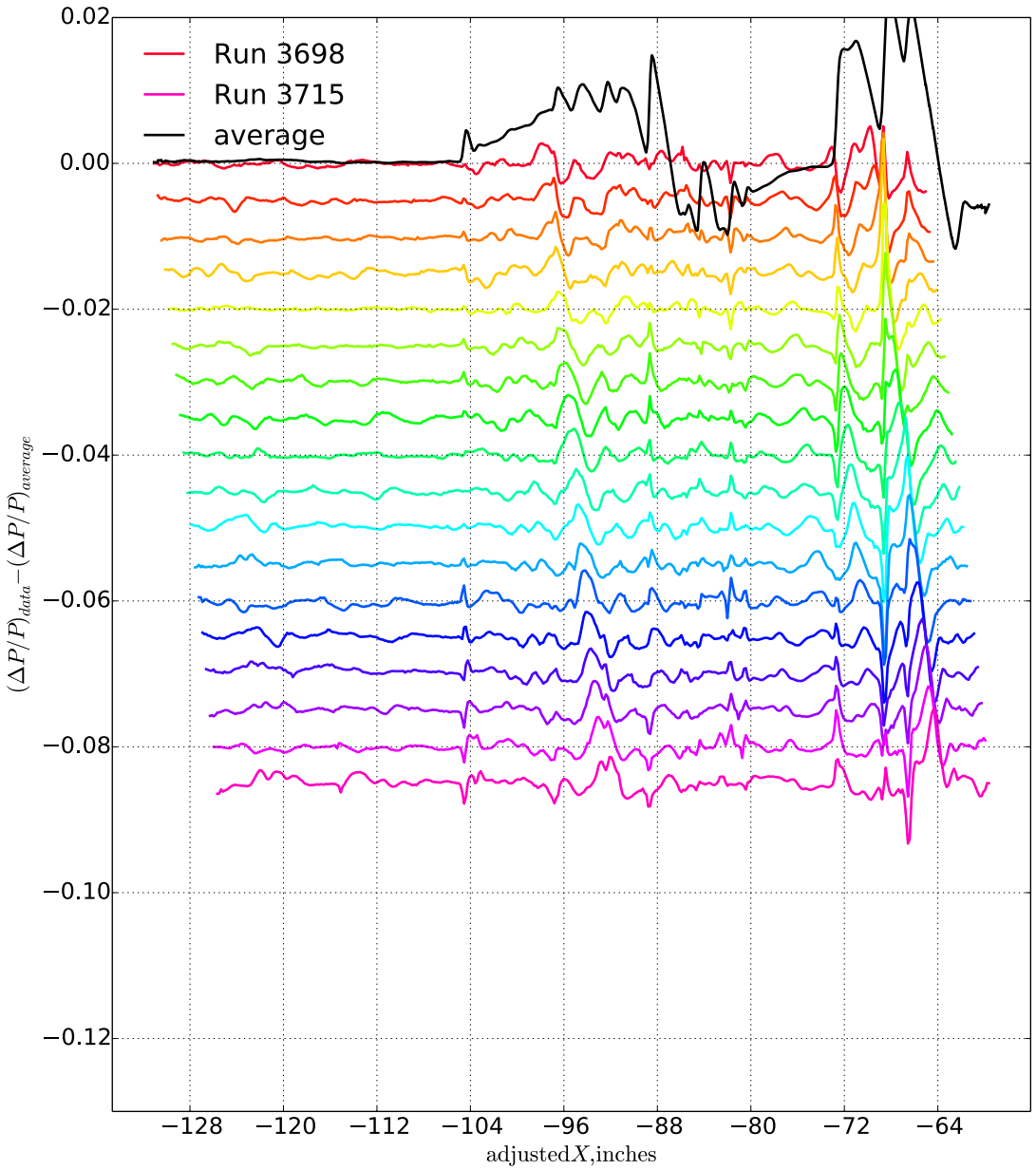

b) Residual and averaged data for run series 3698_3715-3727, from Phase II test at *h*=31.77 inches

Figure 7.112 Phase II test residuals from the 1021 Model, *M*=1.6, *h*=25 and 32 inches (concluded)

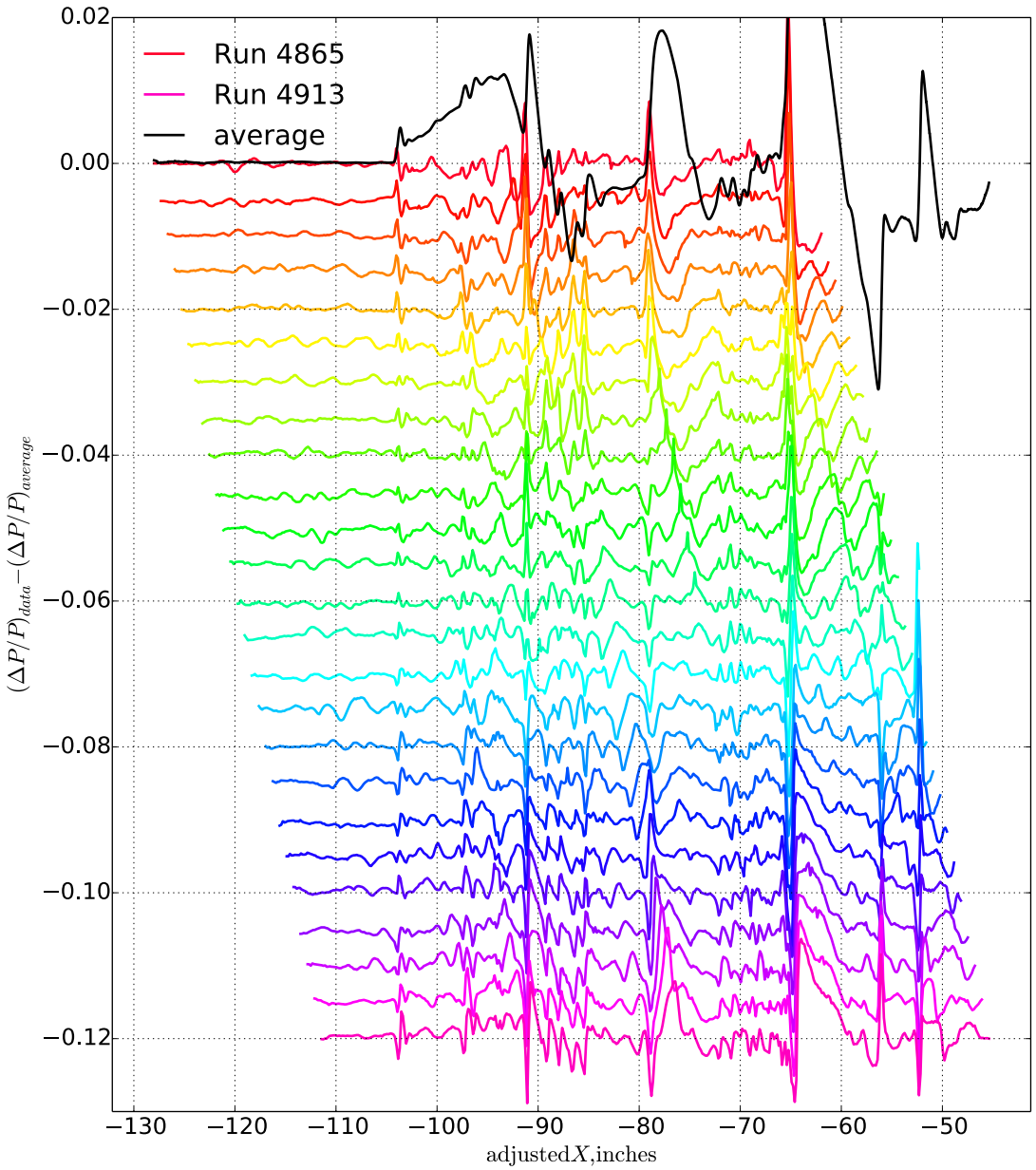

a) Residual and averaged data for run series 4865_4913-4864, *h*=26.59 inches, *Z*-sweep
Figure 7.113 Phase II test residuals from the 1044 Model, *M*=1.6, *h*=26 and 33 inches (continues)

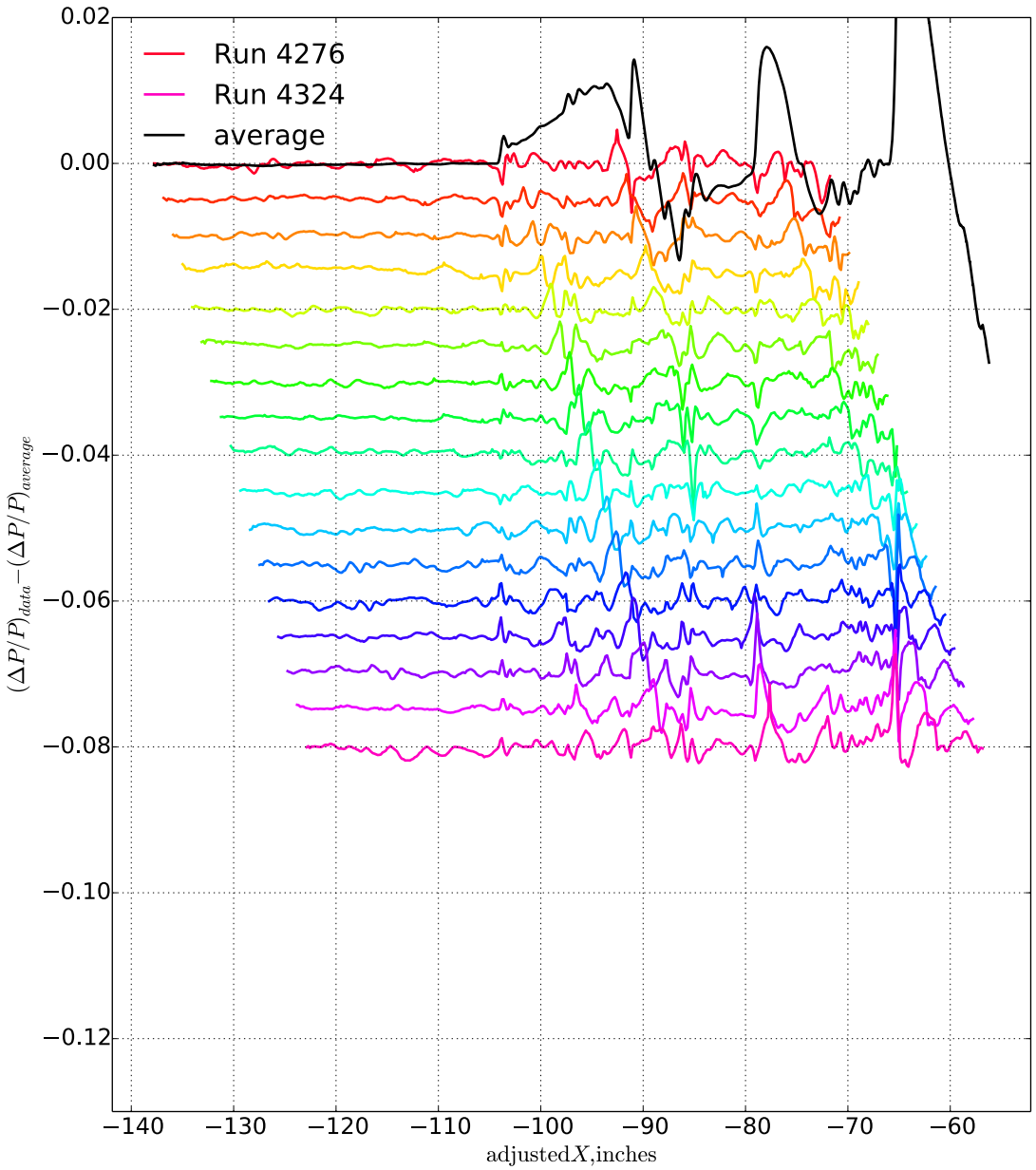

b) Residual and averaged data for run series 4276_4326-4275, *h*=32.64 inches, *Z*-sweep
Figure 7.113 Phase II test residuals from the 1044 Model, *M*=1.6, *h*=26 and 33 inches (continues)

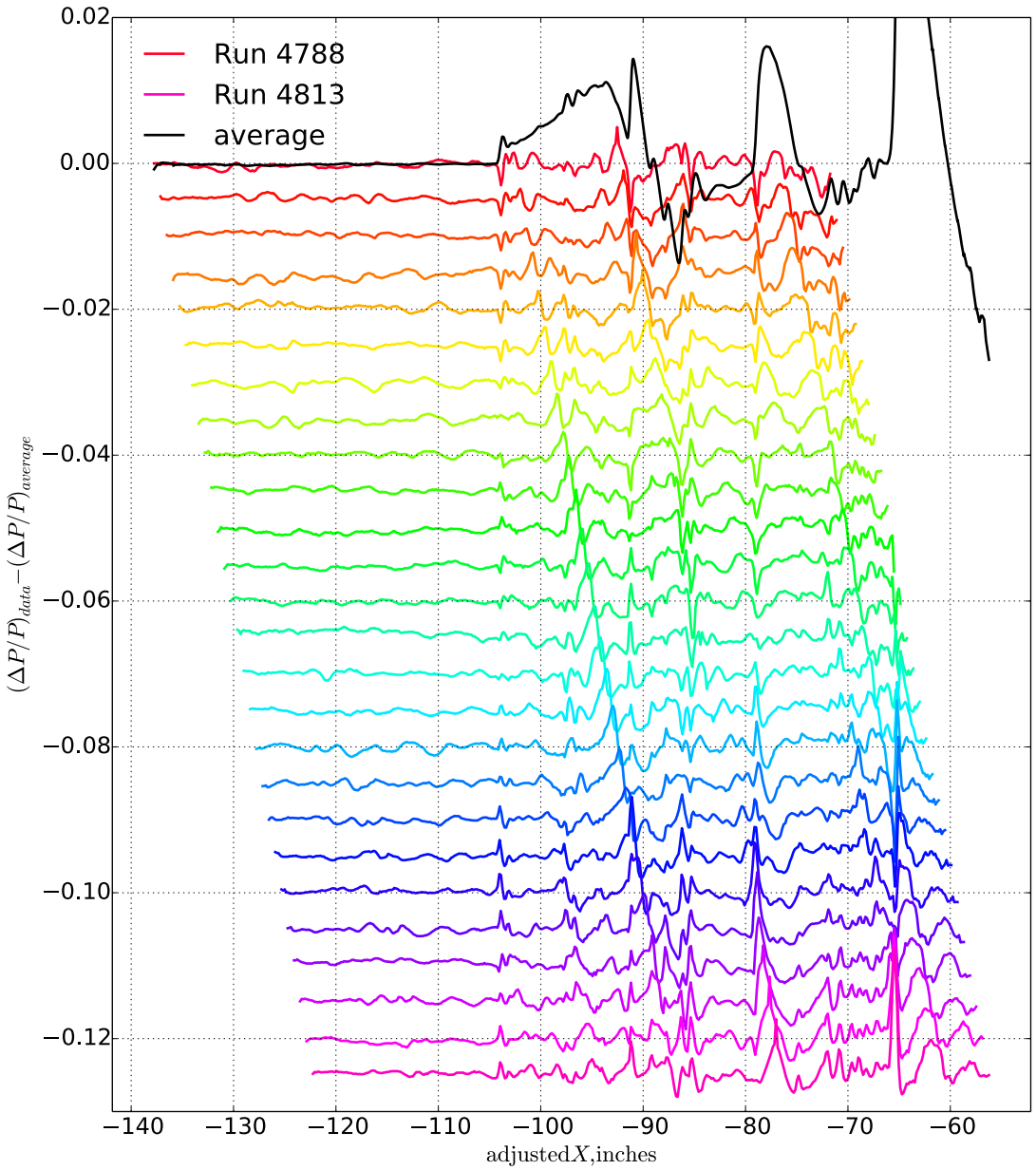

c) Residual and averaged data for run series 4788_4813-4787, *h*=32.59 inches, *X*-sweep
Figure 7.113 Phase II test residuals from the 1044 Model, *M*=1.6, *h*=26 and 33 inches (concluded)

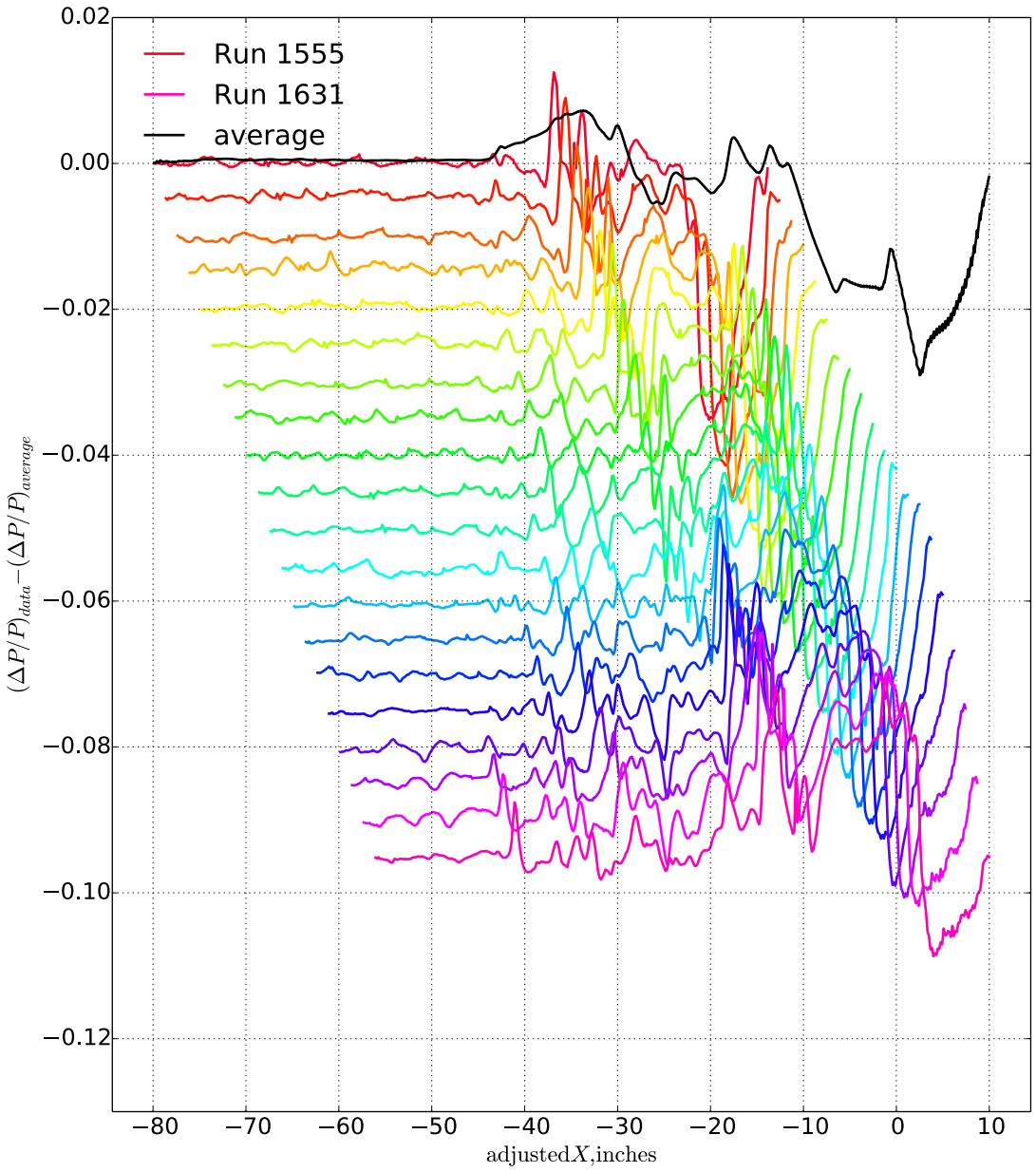

a) Residual and averaged data for run series 1555_1631-1632, *h*=70.68, *X*-sweep
Figure 7.114 Phase II test residuals from the 1044 Model, *M*=1.6, *h*=71 inches (continues)

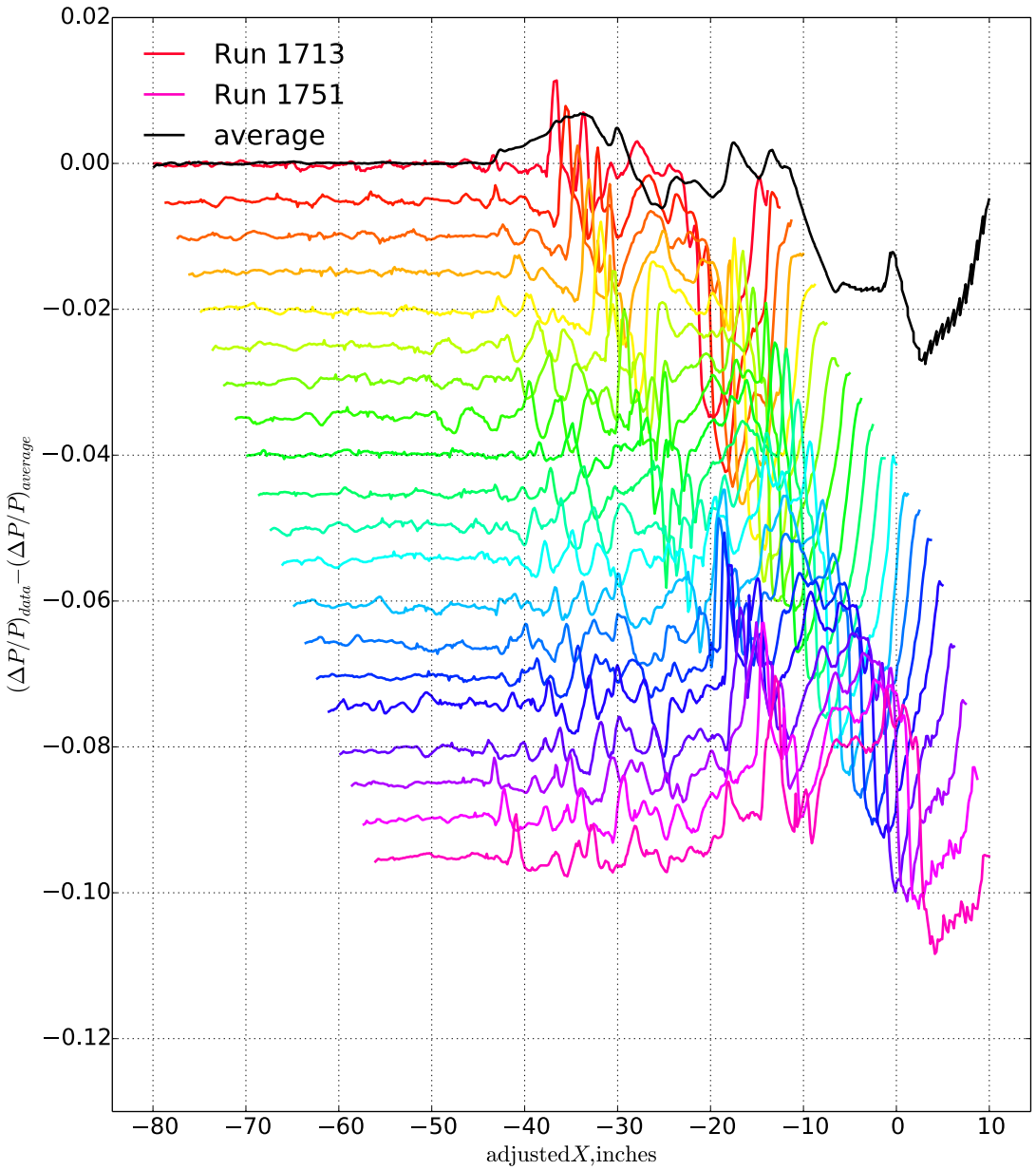

b) Residual and averaged data for run series 1713_1751-1712, *h*=70.70, *X*-sweep
Figure 7.114 Phase II test residuals from the 1044 Model, *M*=1.6, *h*=71 inches (continues)

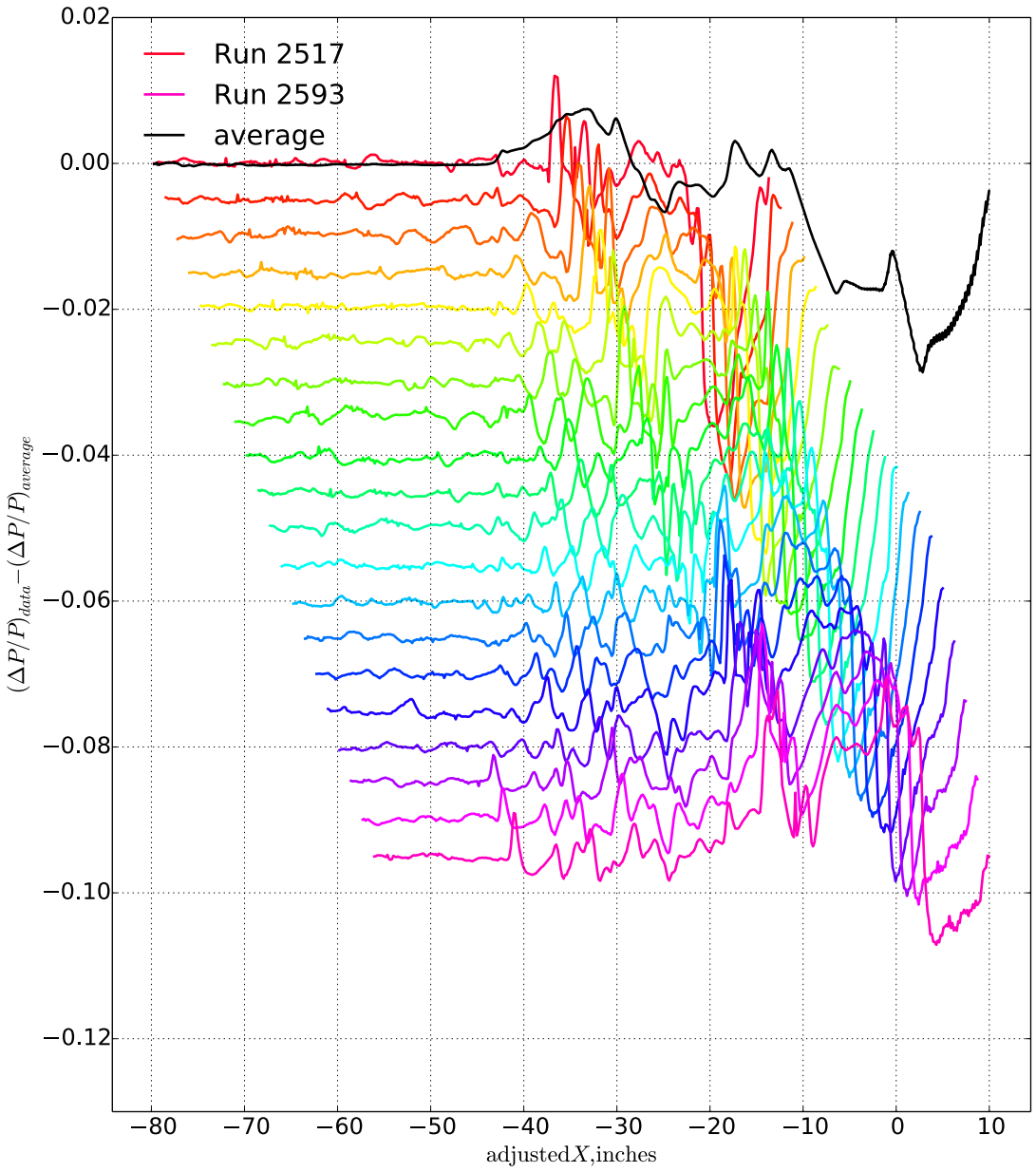

c) Residual and averaged data for run series 2517_2593-2594, h=70.85, X-sweep
Figure 7.114 Phase II test residuals from the 1044 Model, M=1.6, h=71 inches (concluded)

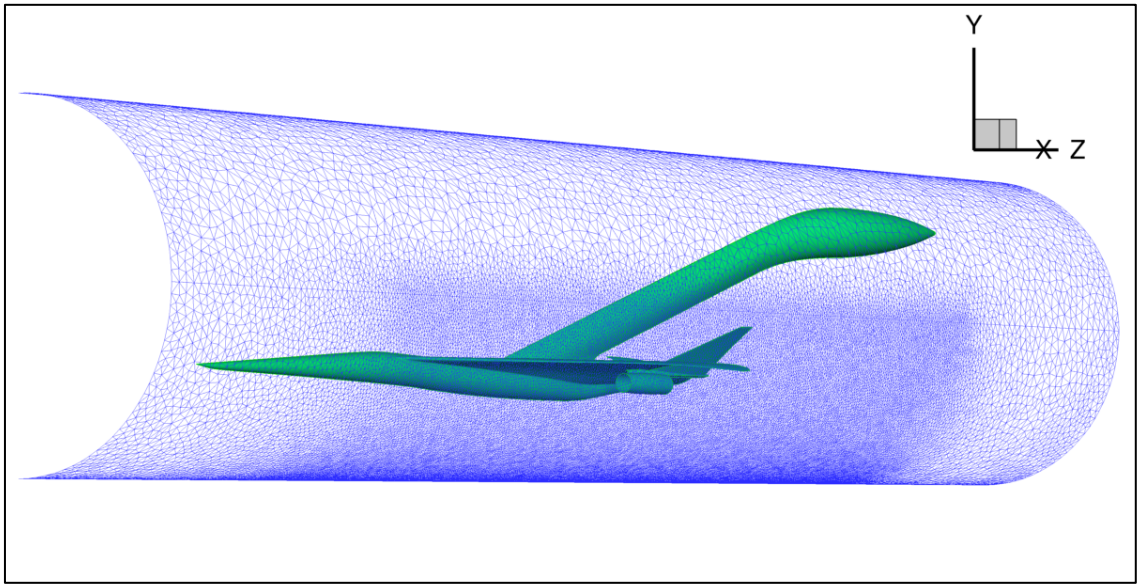

Figure 8.1. Cylindrical near-body mesh surrounding the 1044 phase II model

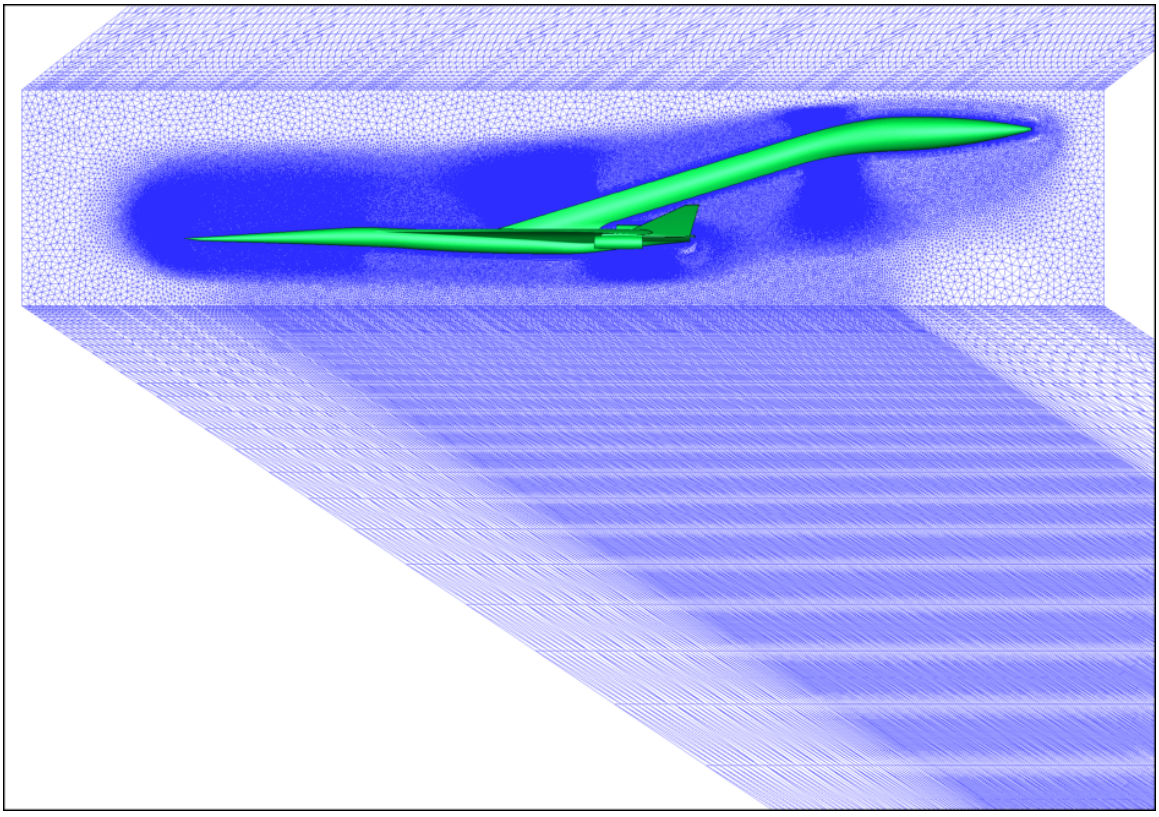
Figure 8.2. Symmetry plane with outer aligned prism collar grid appended to near-body tetrahedral mesh

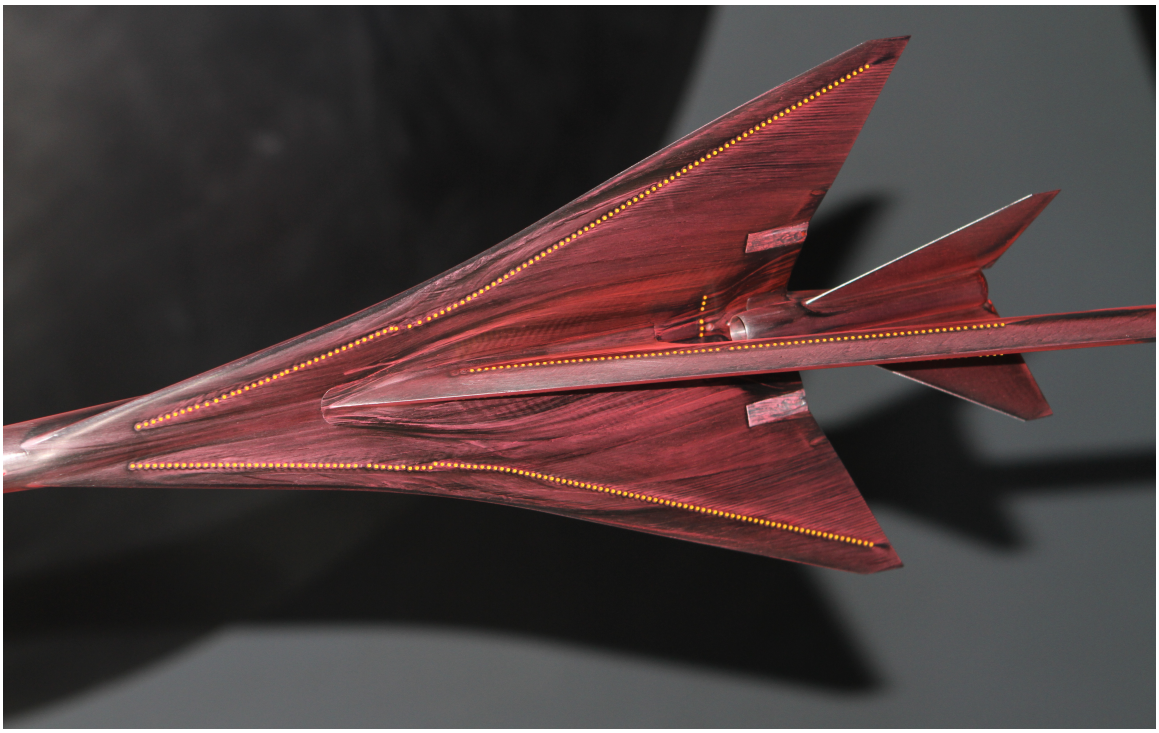

Figure 8.3. Trip disks on LM N+2 model with oil flows

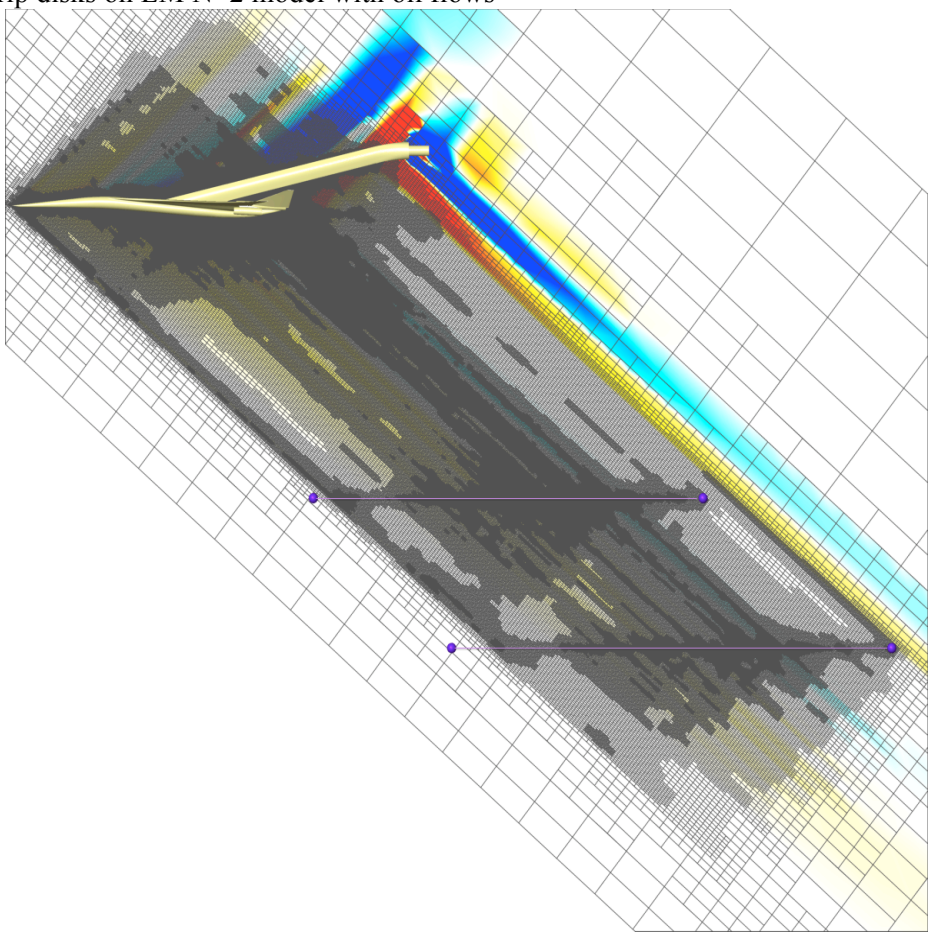

Figure 8.4. CART3D Mach-aligned solution-adaptive mesh for the phase I 1021 model. M=1.6, α=2.3°

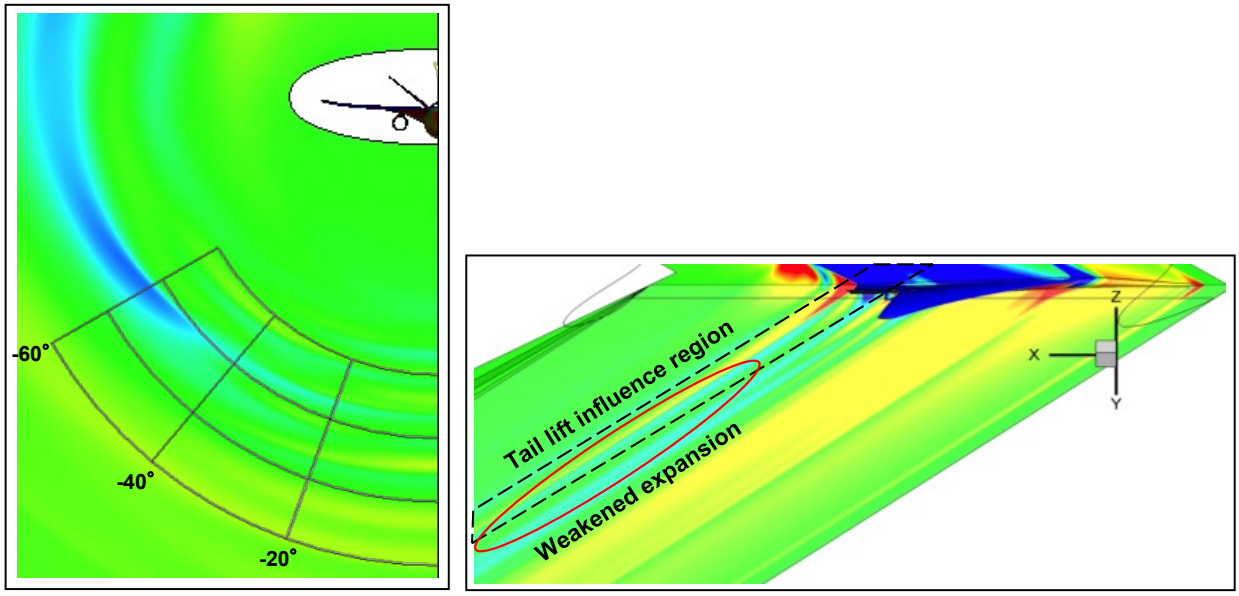

Figure 8.5. CFD++ grid boundaries, front and 40° off-track solutions of a phase II intermediate design

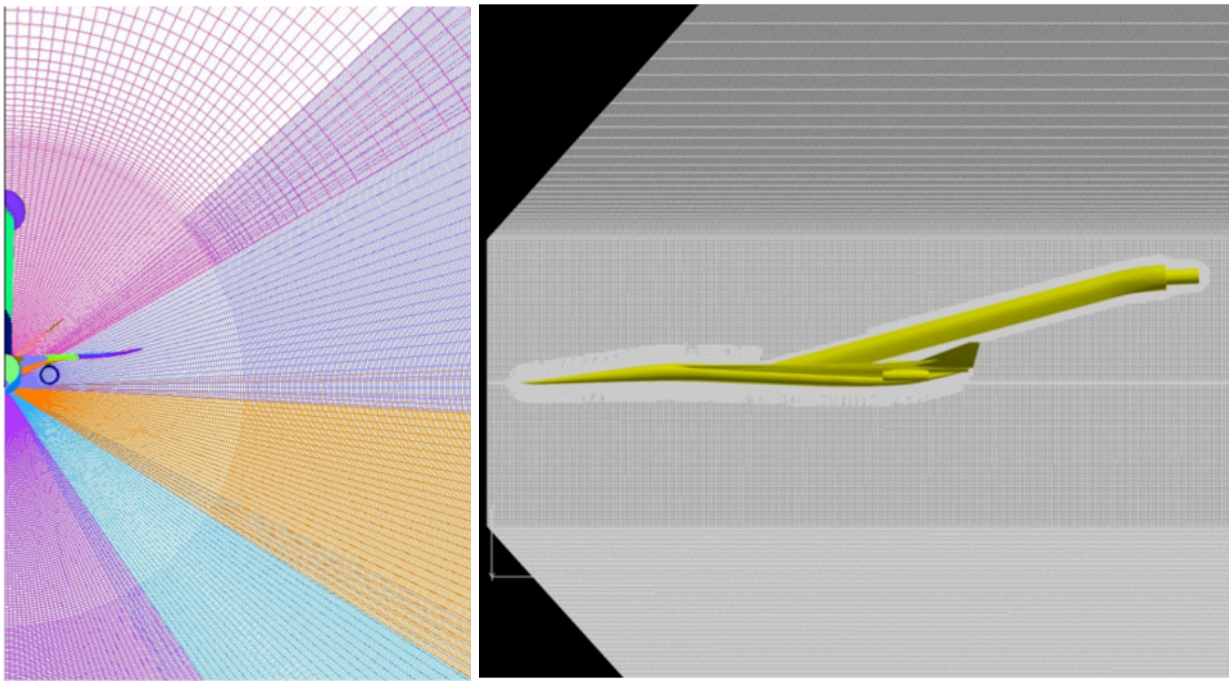
Figure 8.6. OVERFLOW overset mesh in front (left) and symmetry plane (right) for the phase I 1021 model.

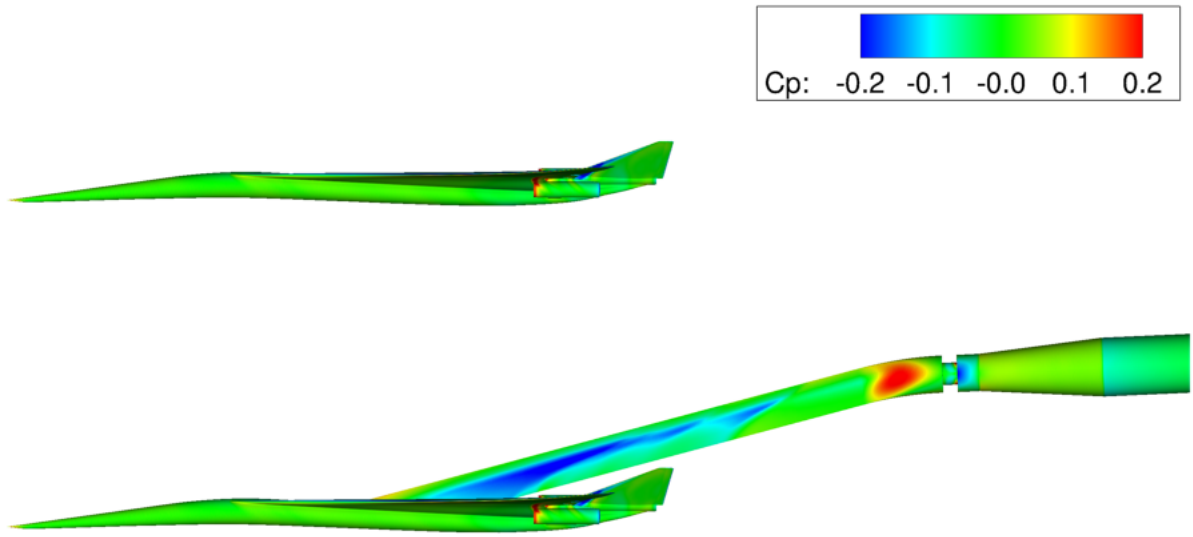

a) Side view of 1021 model

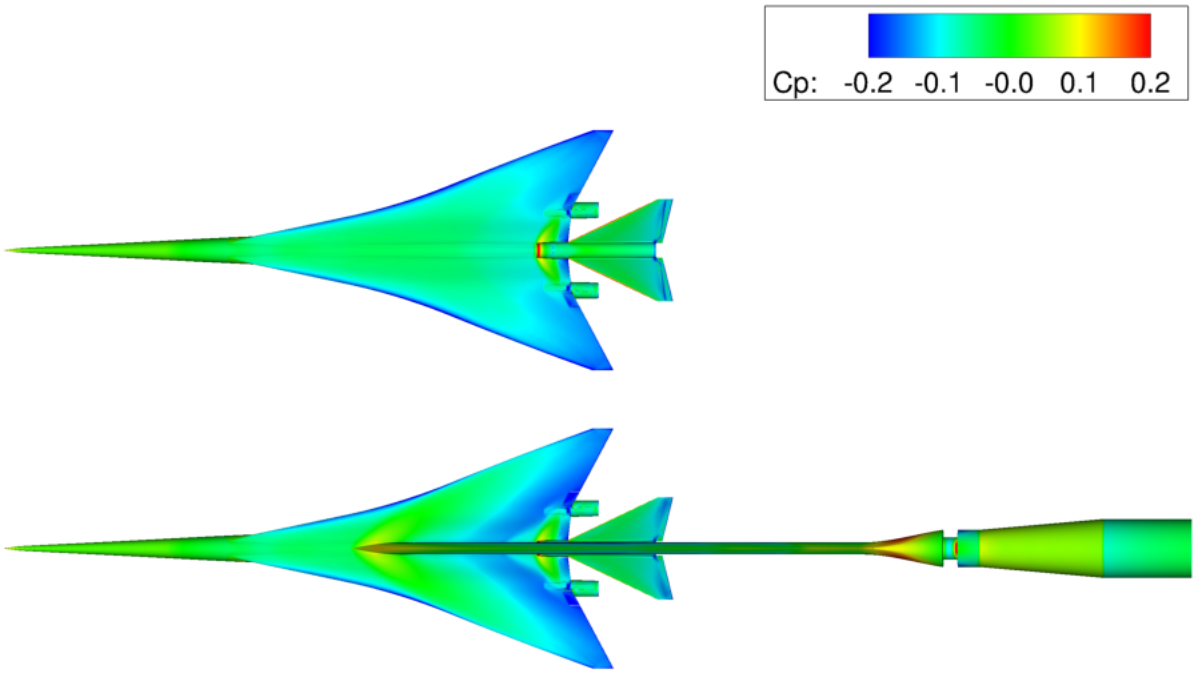

b) Top view of 1021 model

Figure 8.7. Computed pressures of the 1021 phase I model with and without blade support and balance adaptor. M=1.6, α=2.3°

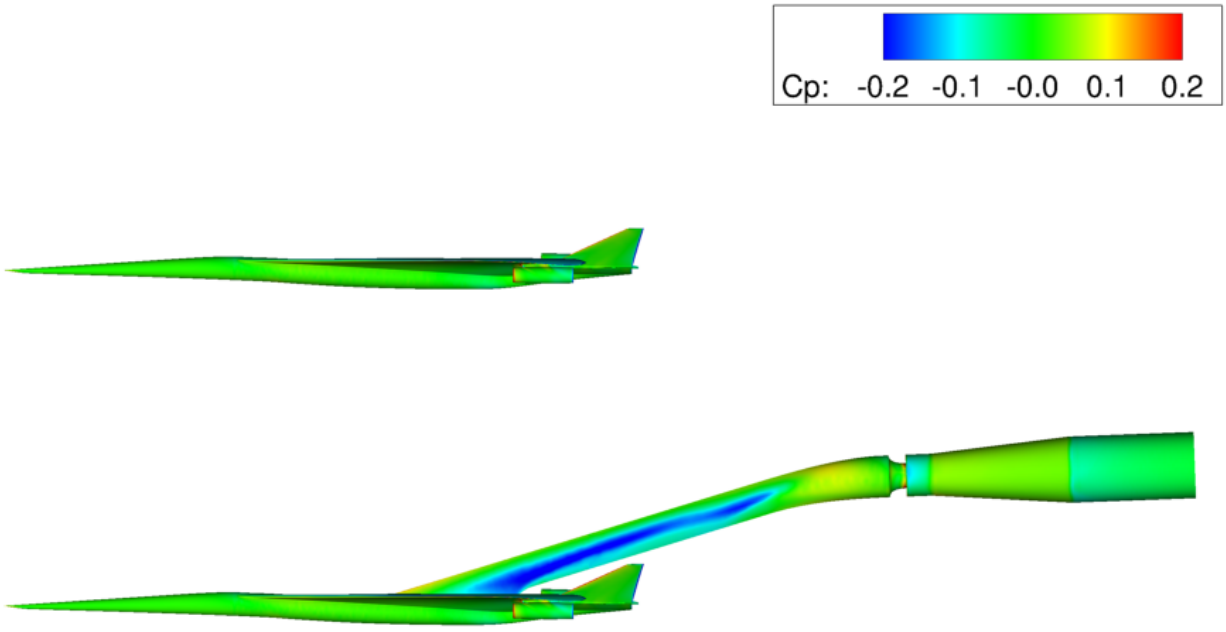

a) Side view of 1044 model

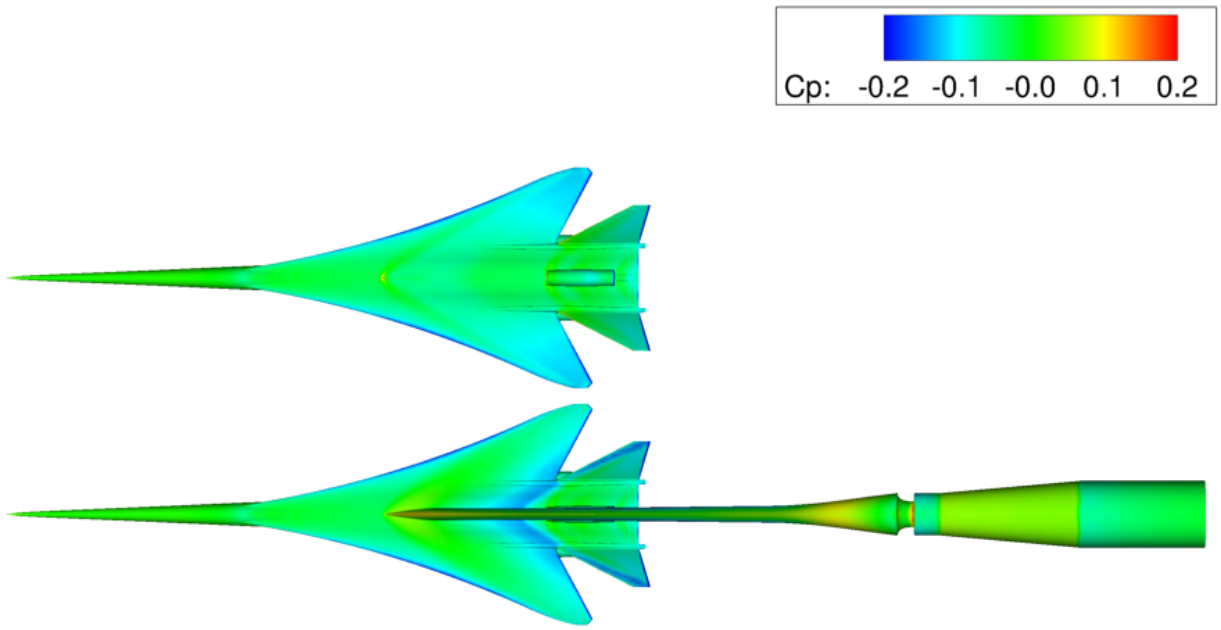

b) Top view of 1044 model

Figure 8.8. Computed pressures of the 1044 phase II model with and without blade support and balance adaptor. M=1.7, α=2.1°

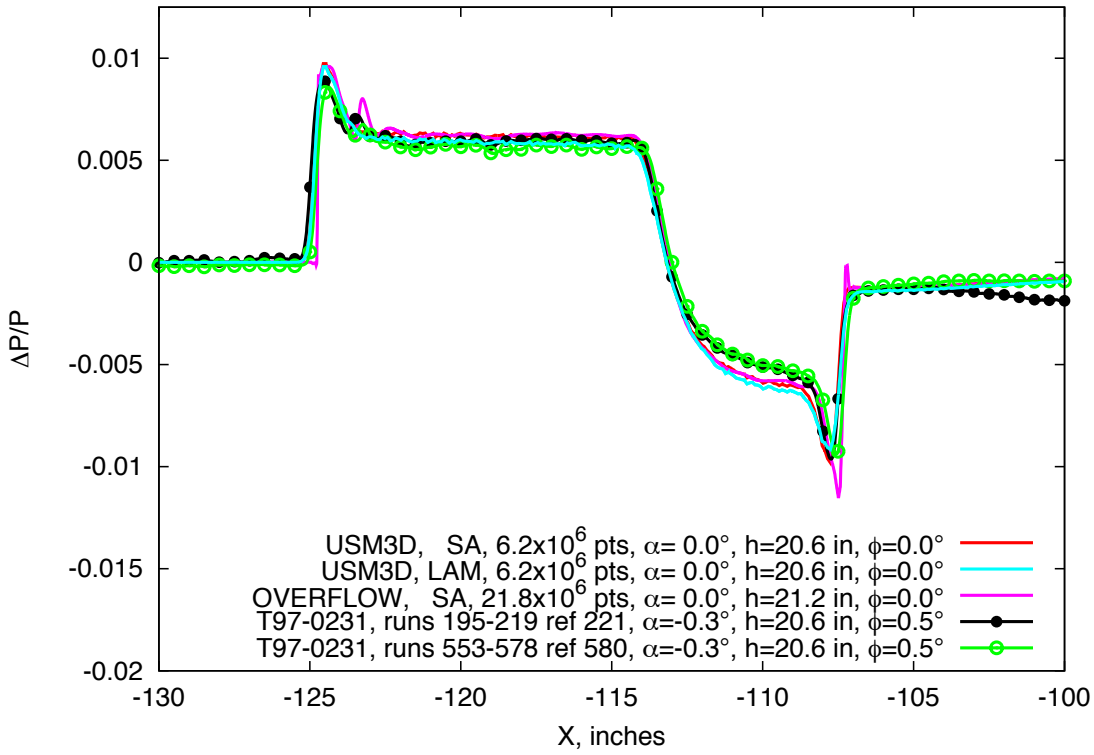

a) h=20.6 inches

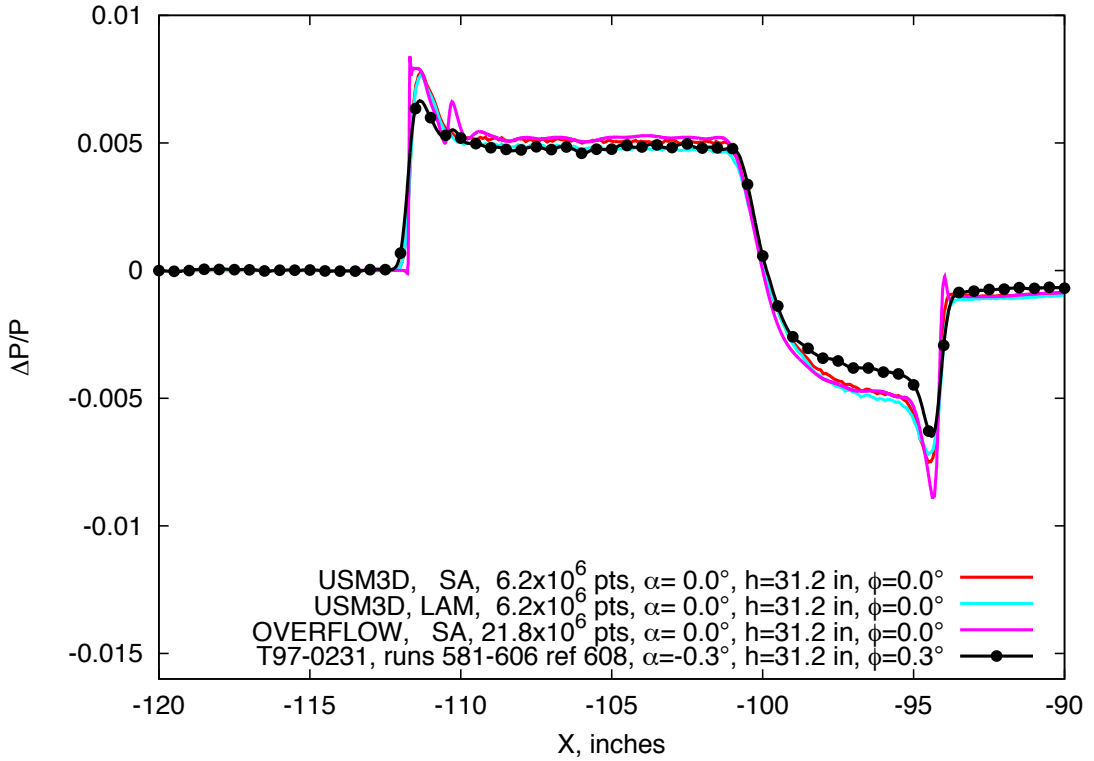

b) h=31.2 inches

Figure 9.1. Seeb-ALR experimental data compared with USM3D and OVERFLOW computations, M=1.6, Re=6.42x10^6

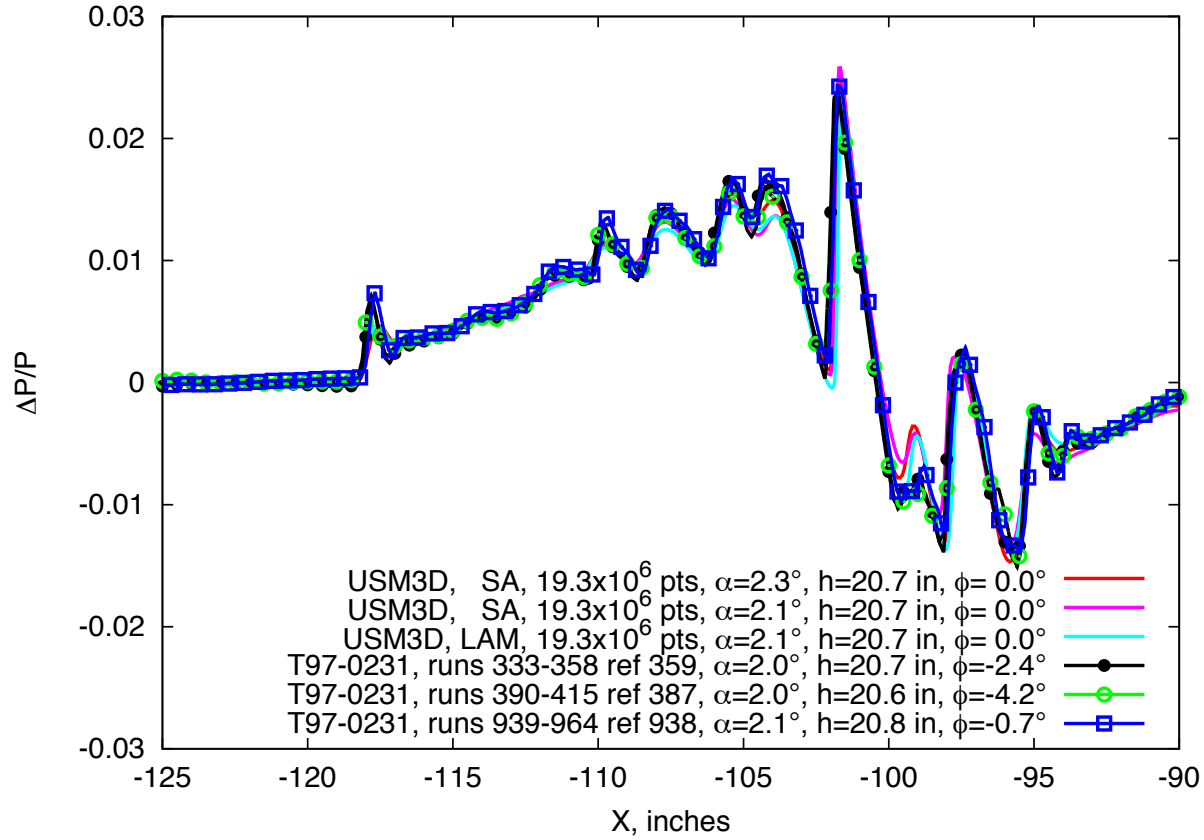

Figure 9.2. 1021 model with all nacelles, blade strut, experimental data compared with USM3D computation, M=1.6, Re=8.10x10^6

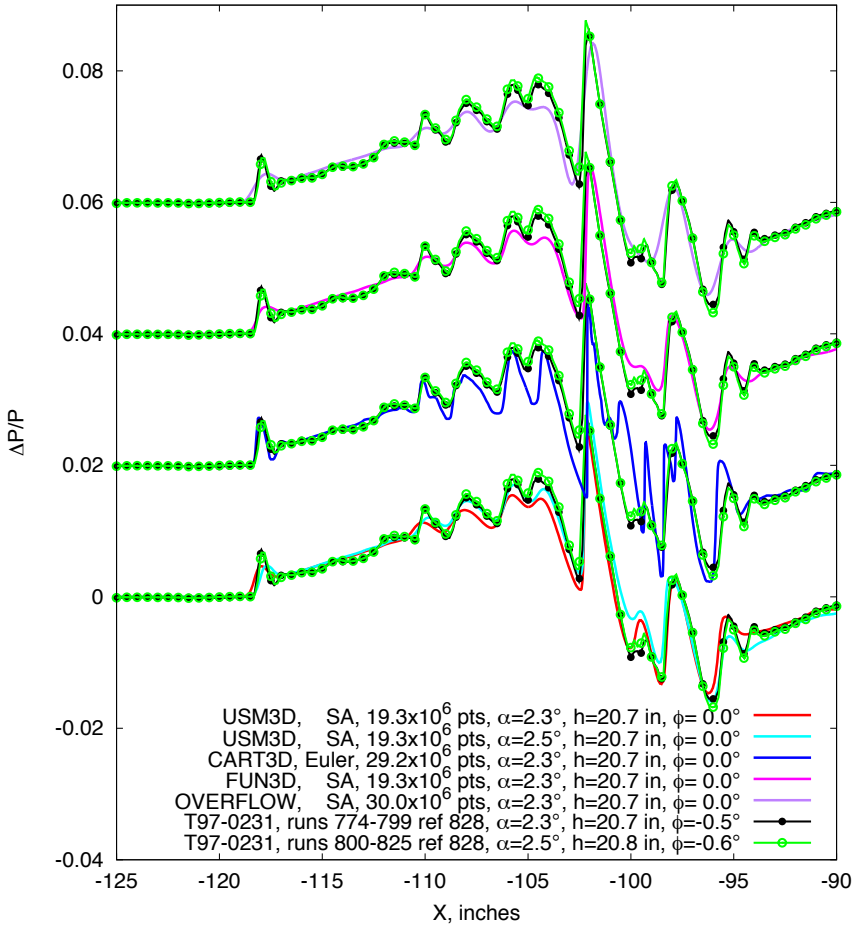

a) CFD compared with experiment, stacked

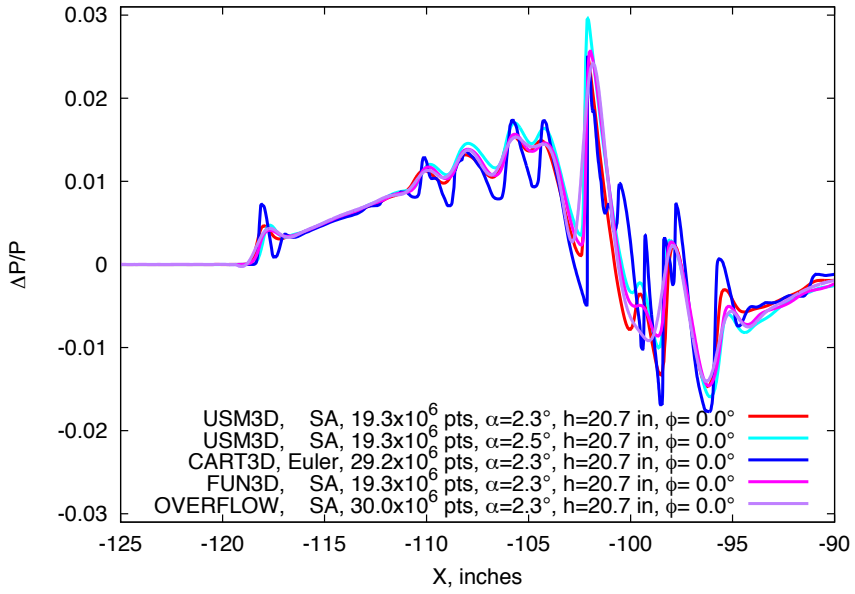

b) CFD compared

Figure 9.3. 1021 model with all nacelles, blade strut, computational and experimental comparisons, M=1.6, h=20.7 in., Re=8.10x10^6

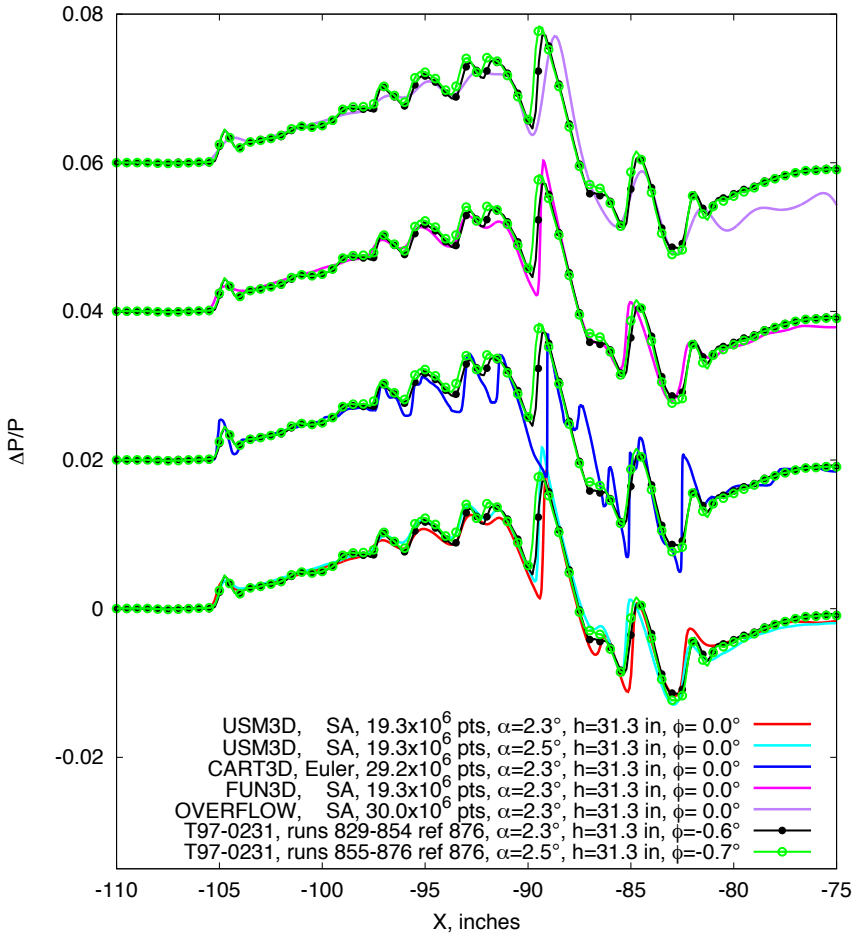

a) CFD compared with experiment, stacked

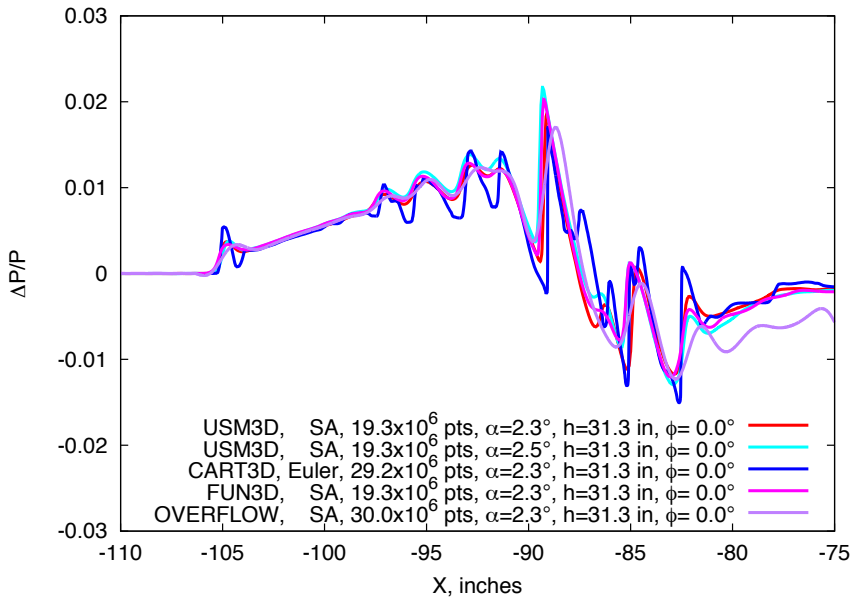

b) CFD compared

Figure 9.4. 1021 model with all nacelles, blade strut, computational and experimental comparisons, M=1.6, h=31.3 in., Re=8.10x10^6

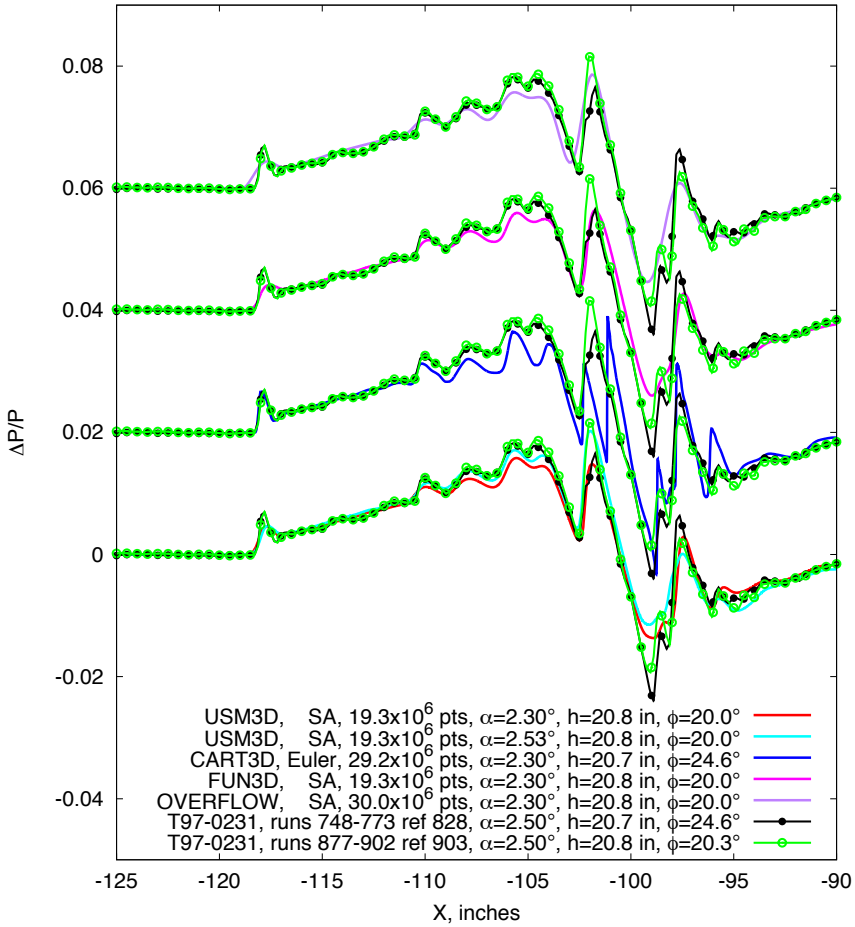

a) CFD compared with experiment, stacked, ϕ=20° and 24.6°

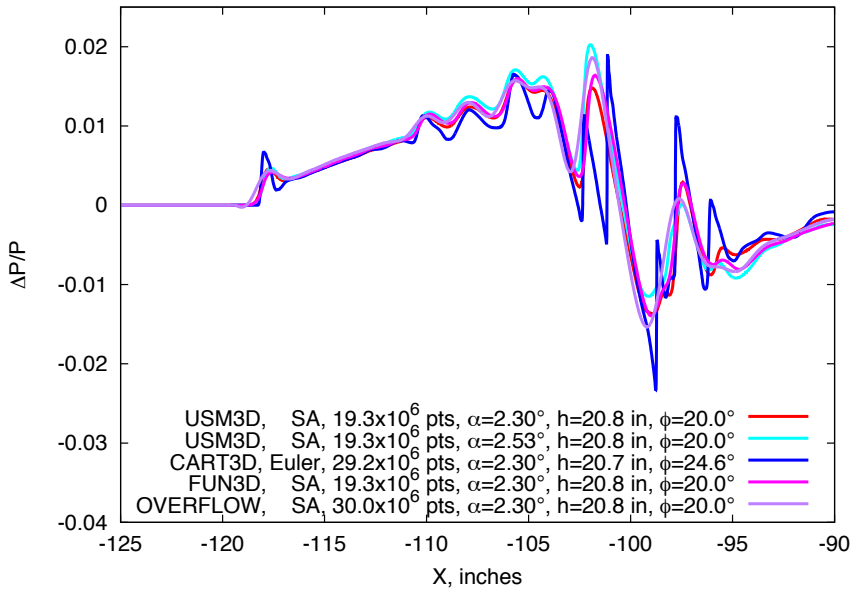

b) CFD compared, ϕ=20° and 24.6°

Figure 9.5. 1021 model with all nacelles, blade strut, computation and experimental comparisons, M=1.6, ϕ=20° and 24.6°, h=20.7 in., Re=8.10x10^6

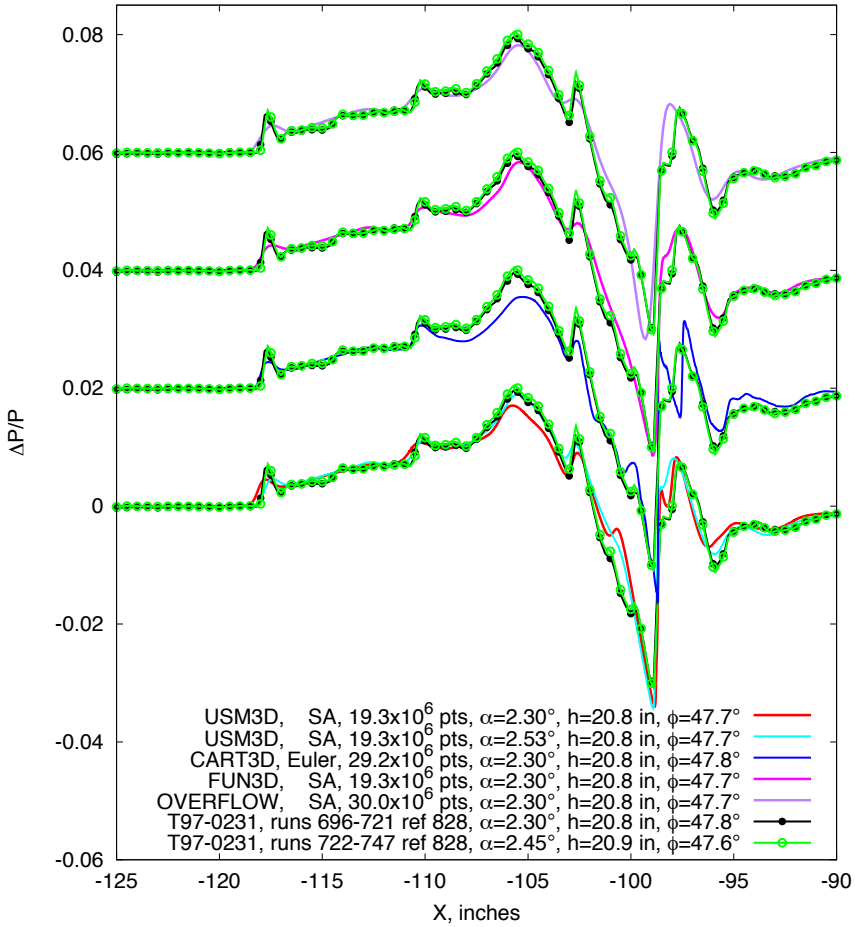

a) CFD compared with experiment, stacked, ϕ=48°

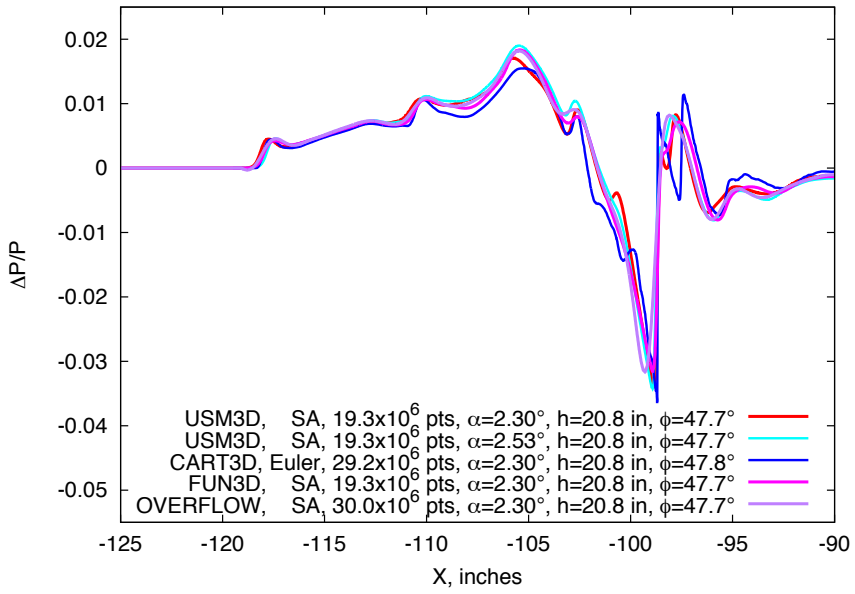

b) CFD compared, ϕ=48°

Figure 9.6. 1021 model with all nacelles, blade strut, computational and experimental data comparisons, M=1.6, ϕ=48°, h=20.8 in., Re=8.10x10^6

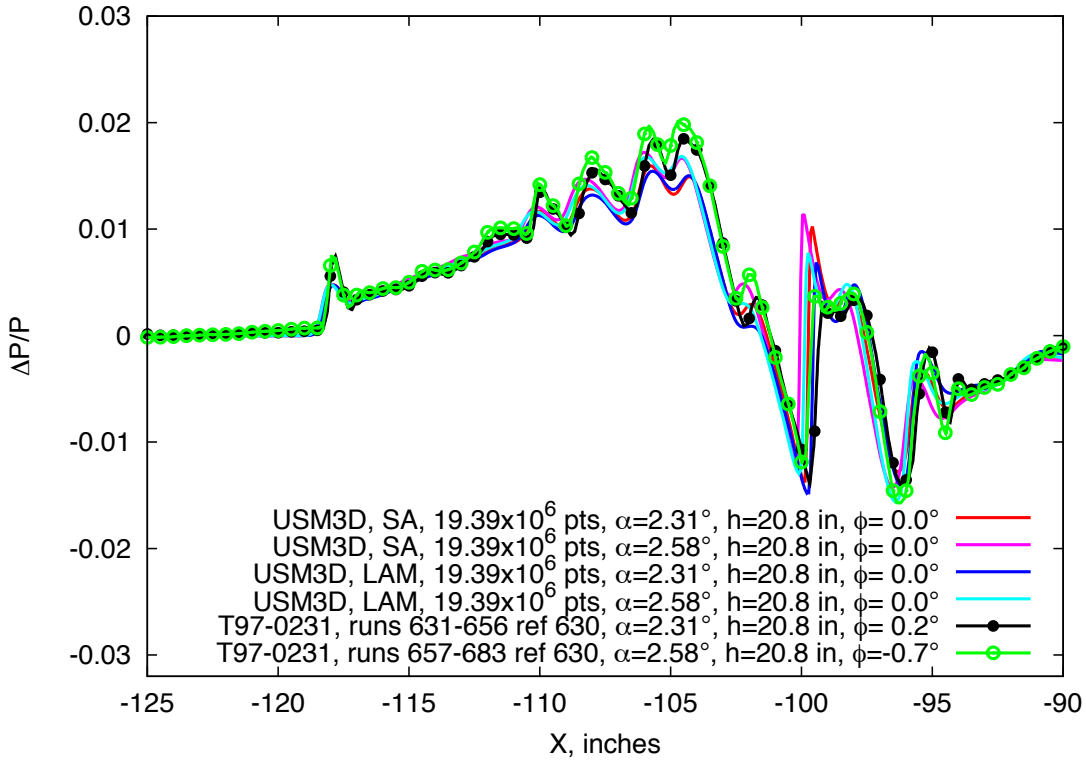

Figure 9.7. 1021 model without under-wing nacelle, on blade strut, experimental data compared with USM3D laminar and turbulent flow simulations, M=1.6, h=20.8 in., Re=8.10x10^6

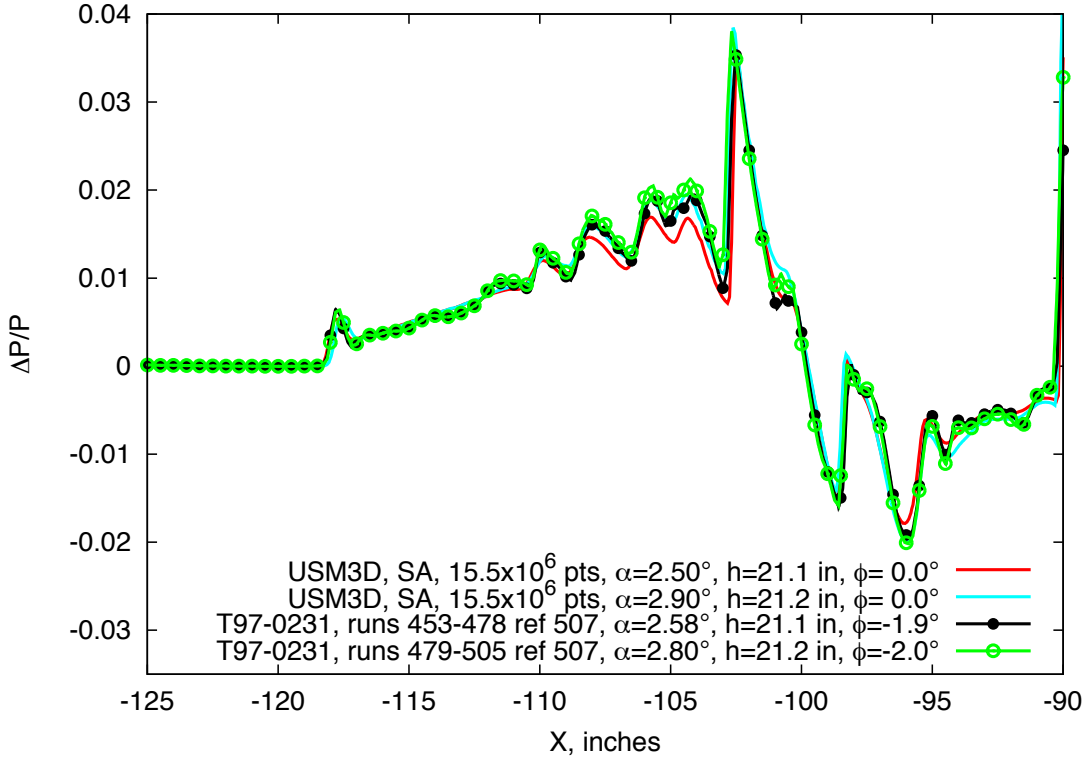

Figure 9.8. 1021 model with all nacelles, on sting strut, experimental data compared with USM3D computations, M=1.6, h=21.1 in., Re=8.10x10^6

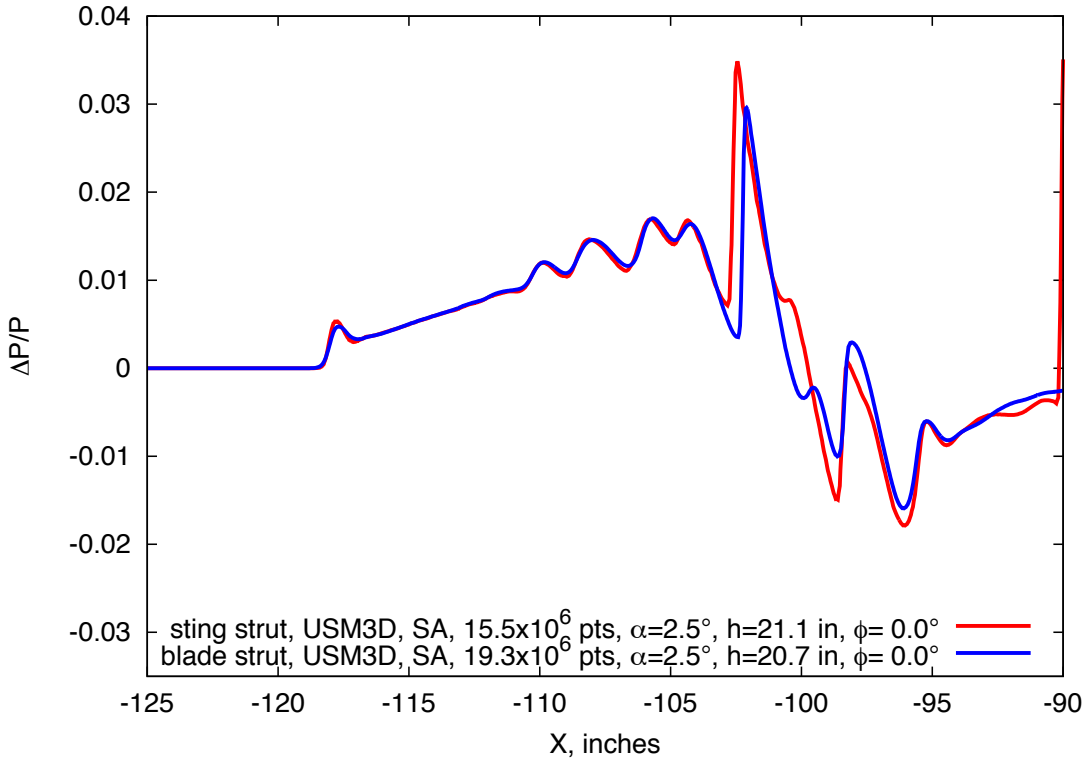

Figure 9.9. Comparison of the 1021 model with all nacelles, on sting and blade struts, USM3D computations, M=1.6, h=21 in., Re=8.10x10^6

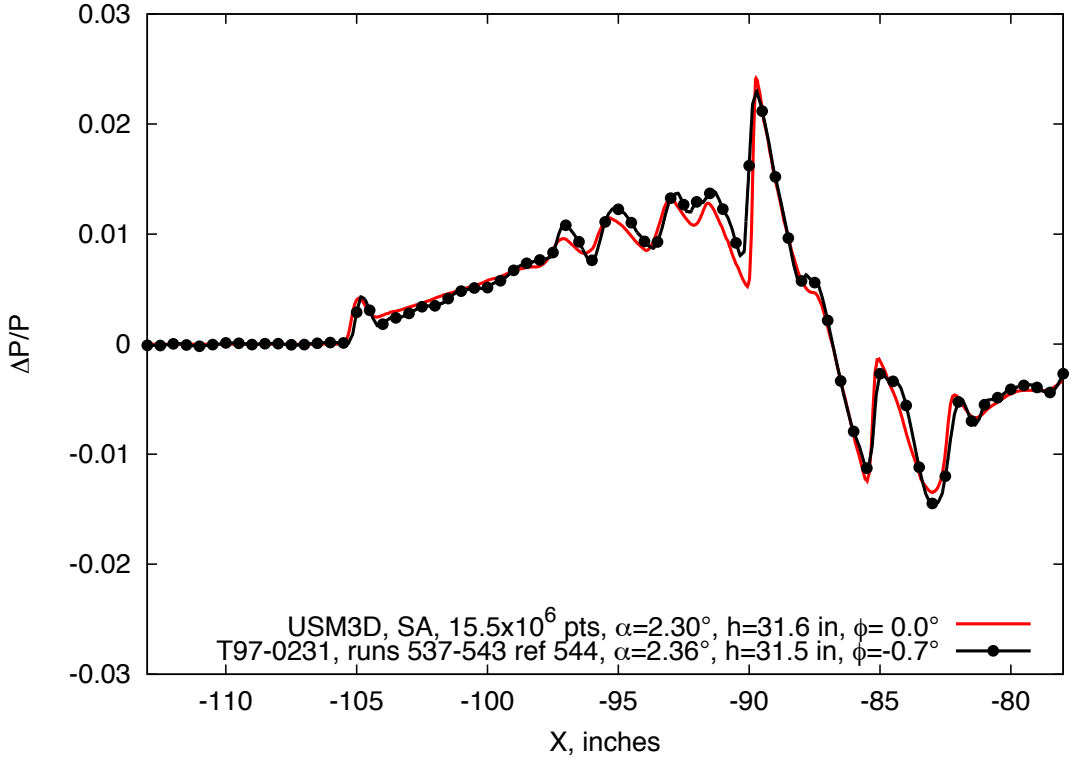

Figure 9.10. 1021 model with all nacelles, on sting strut, experimental data compared with USM3D computation, M=1.6, h=31.6 in., Re=8.10x10^6

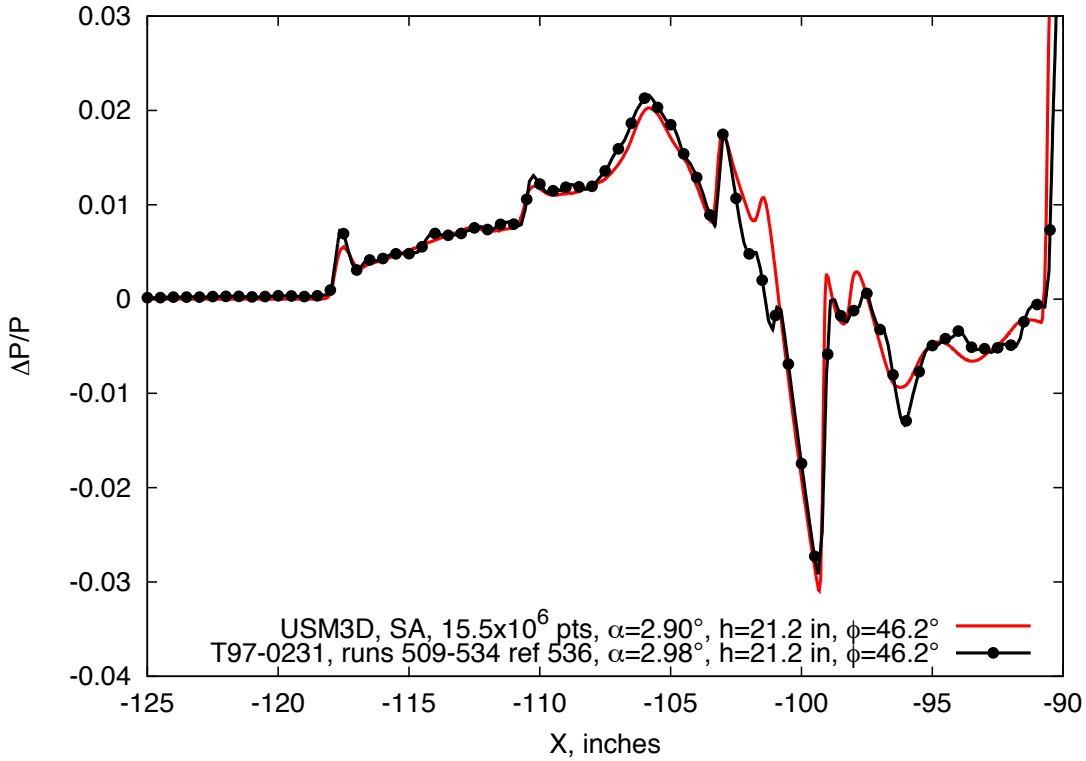

Figure 9.11. 1021 model with all nacelles, on sting strut, experimental data compared with USM3D computation, M=1.6, h=21.2 in., ϕ=46.2°, Re=8.10x10^6

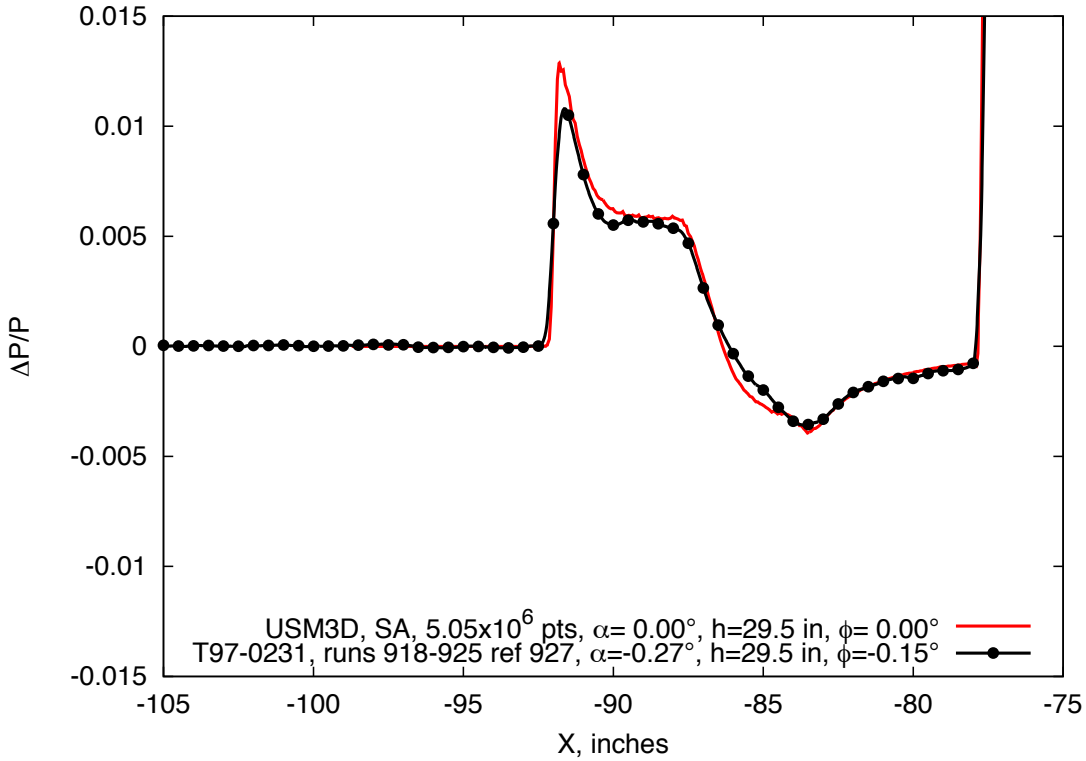

Figure 9.12. Boeing AS-2, experimental data compared with USM3D computation, M=1.6, h=29.5 in, Re=4.40x10^6

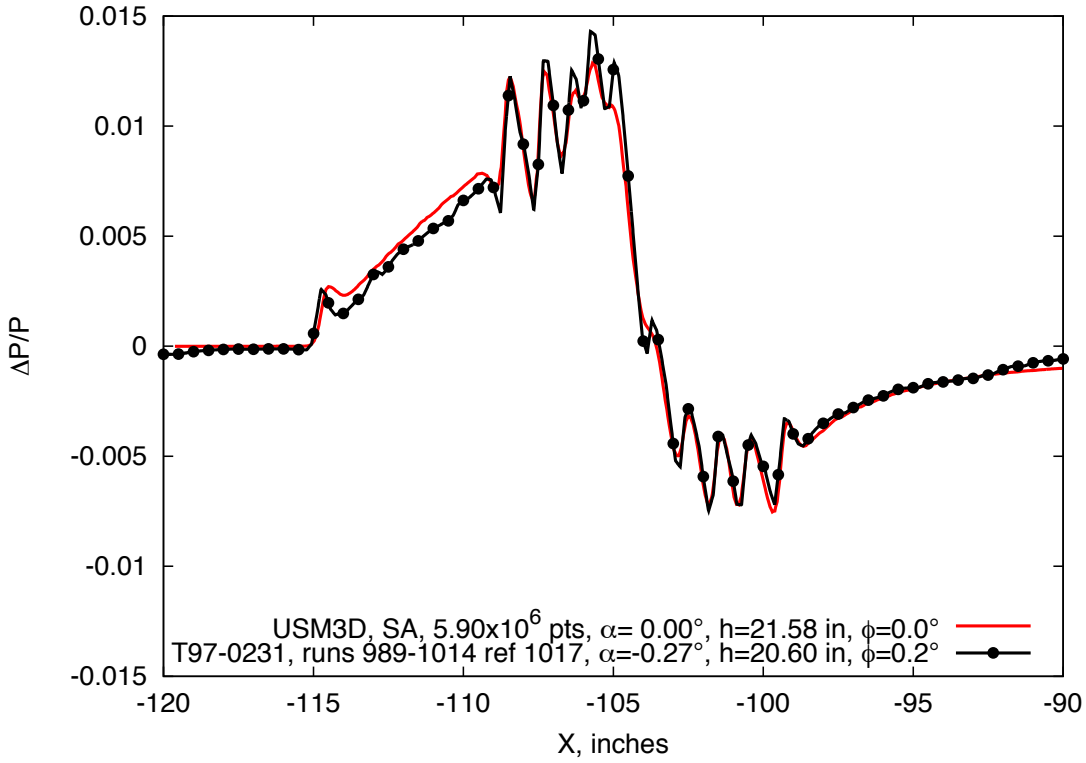

Figure 9.13. Lockheed Opt Sig, experimental data compared with USM3D computation, M=1.6, h=21 in., Re=6.03x10^6

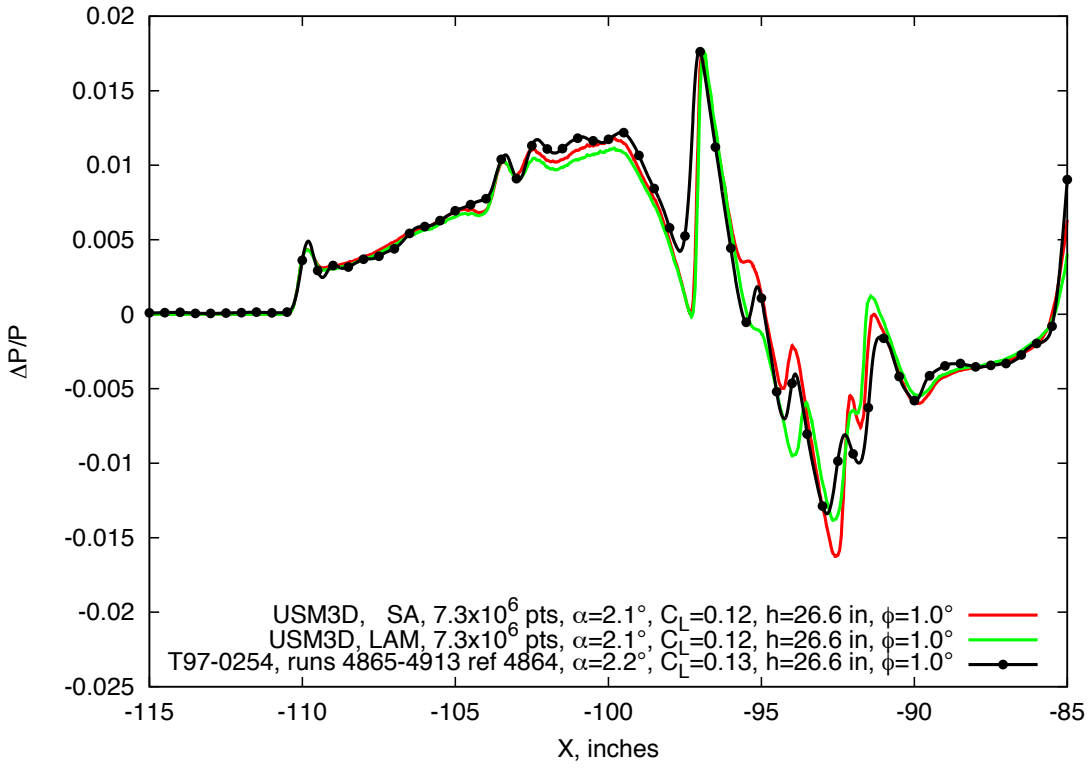

Figure 9.14. 1044 model, blade, experimental data compared with USM3D computations with laminar and turbulent solutions, M=1.7, h=26.6 in., ϕ=0°, Re=6.76 x10^6

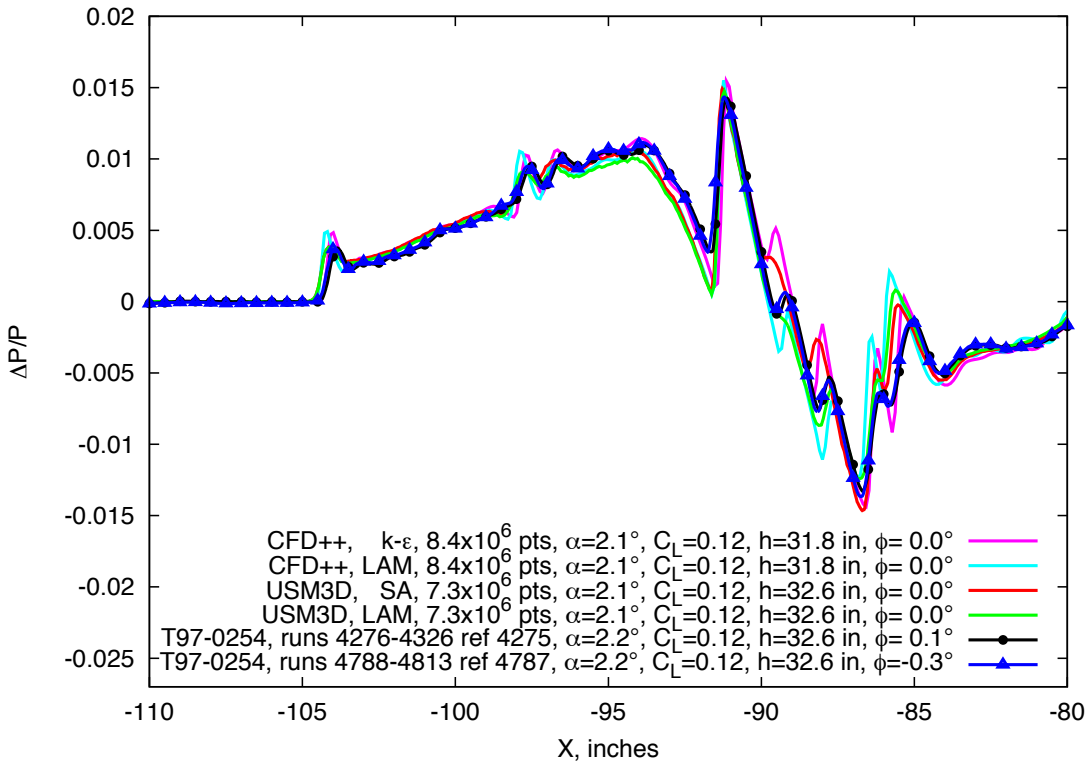

Figure 9.15. 1044 model, blade, experimental data compared with CFD++, and USM3D computations with laminar and turbulent solutions, M=1.7, h=32.6 in., ϕ=0°, Re=6.81x10^6

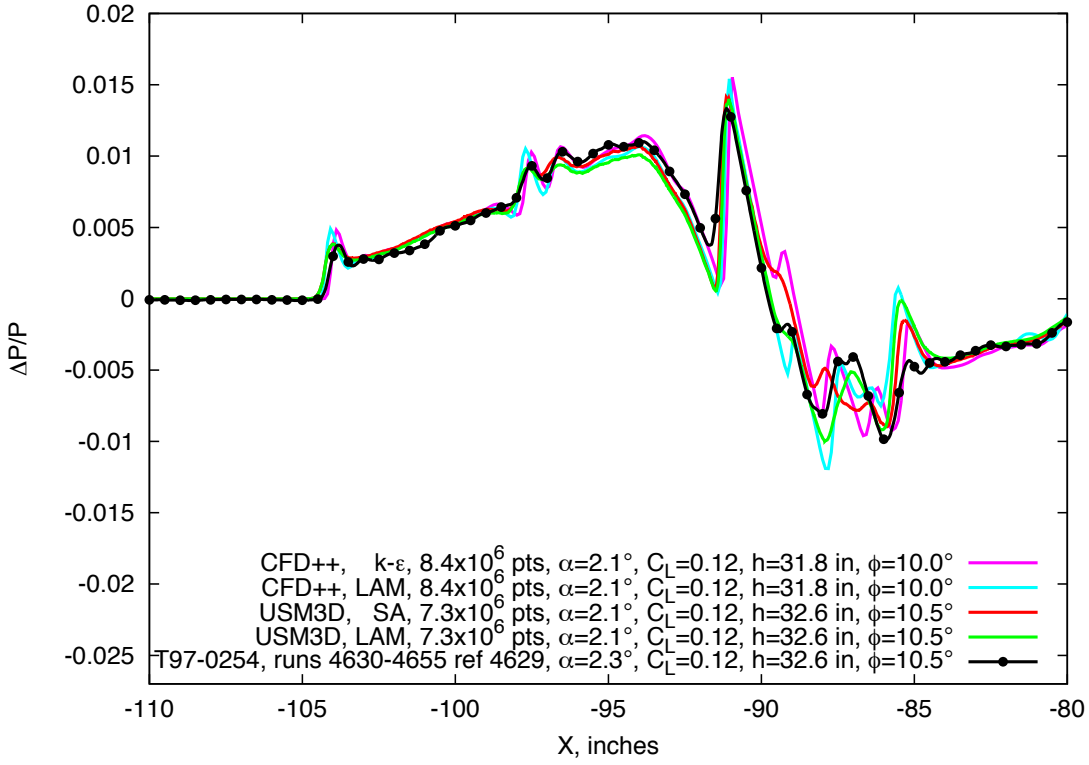

Figure 9.16. 1044 model, blade, experimental data compared with CFD++, and USM3D computations with laminar and turbulent solutions, M=1.7, h=32.6 in., ϕ=10°, Re=6.79x10^6

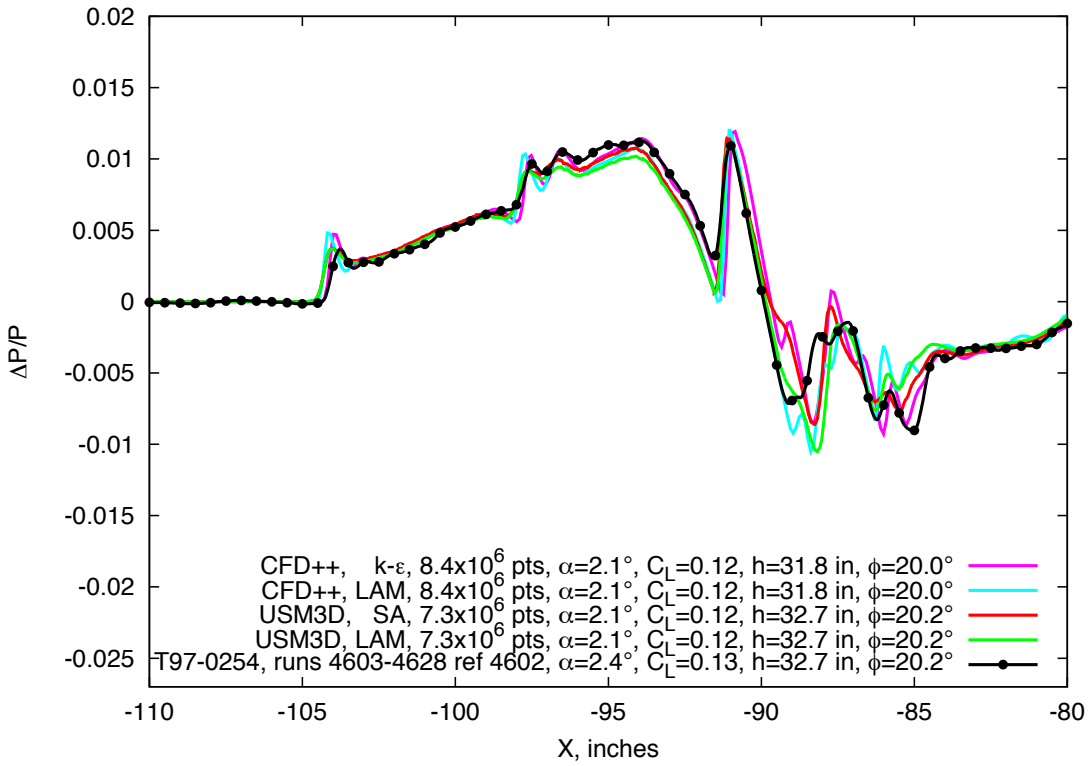

Figure 9.17. 1044 model, blade, experimental data compared with CFD++, and USM3D computations with laminar and turbulent solutions, M=1.7, h=32.7 in., ϕ=20°, Re=6.79 x10^6

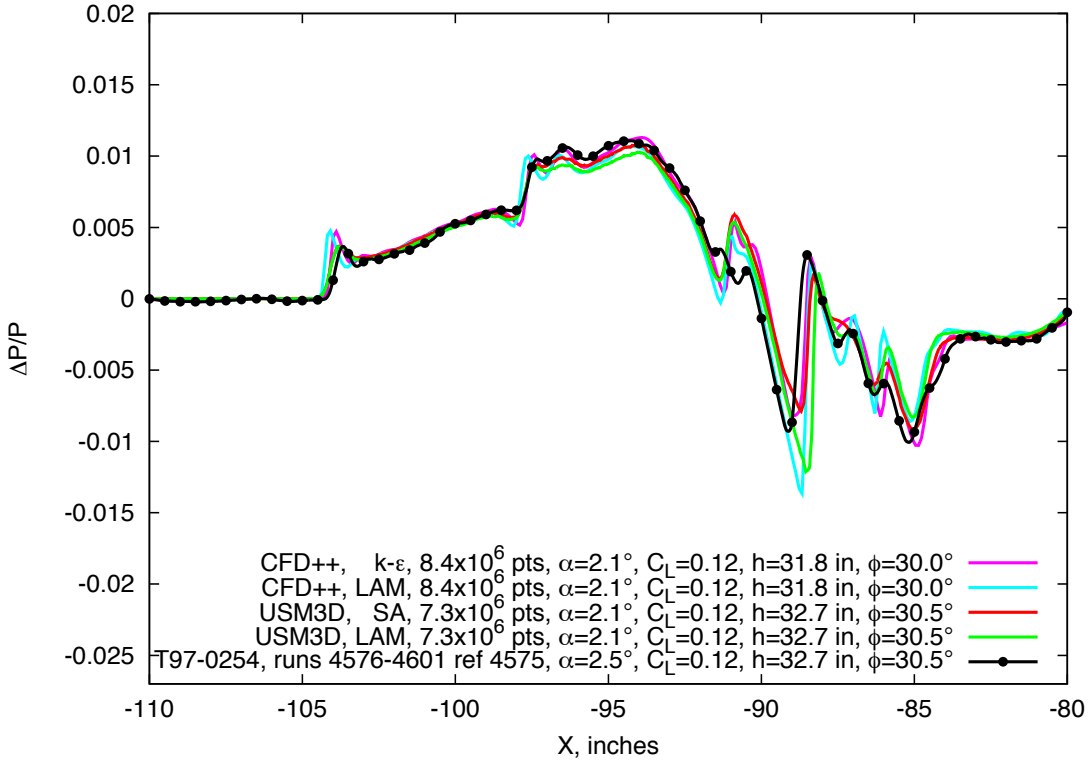

Figure 9.18. 1044 model, blade, experimental data compared with CFD++, and USM3D computations with laminar and turbulent solutions, M=1.7, h=32.7 in., ϕ=30°, Re=6.80 x10^6

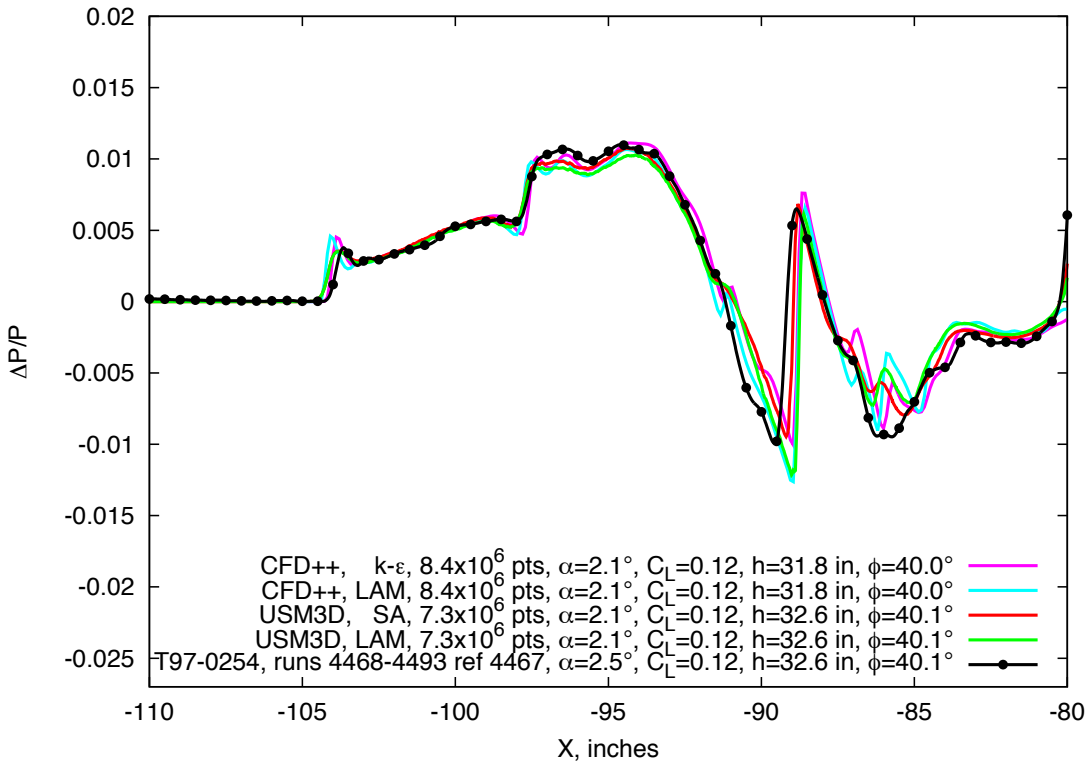

Figure 9.19. 1044 model, blade, experimental data compared with CFD++, and USM3D computations with laminar and turbulent solutions, M=1.7, h=32.6 in., ϕ=40°, Re=6.80 x10^6

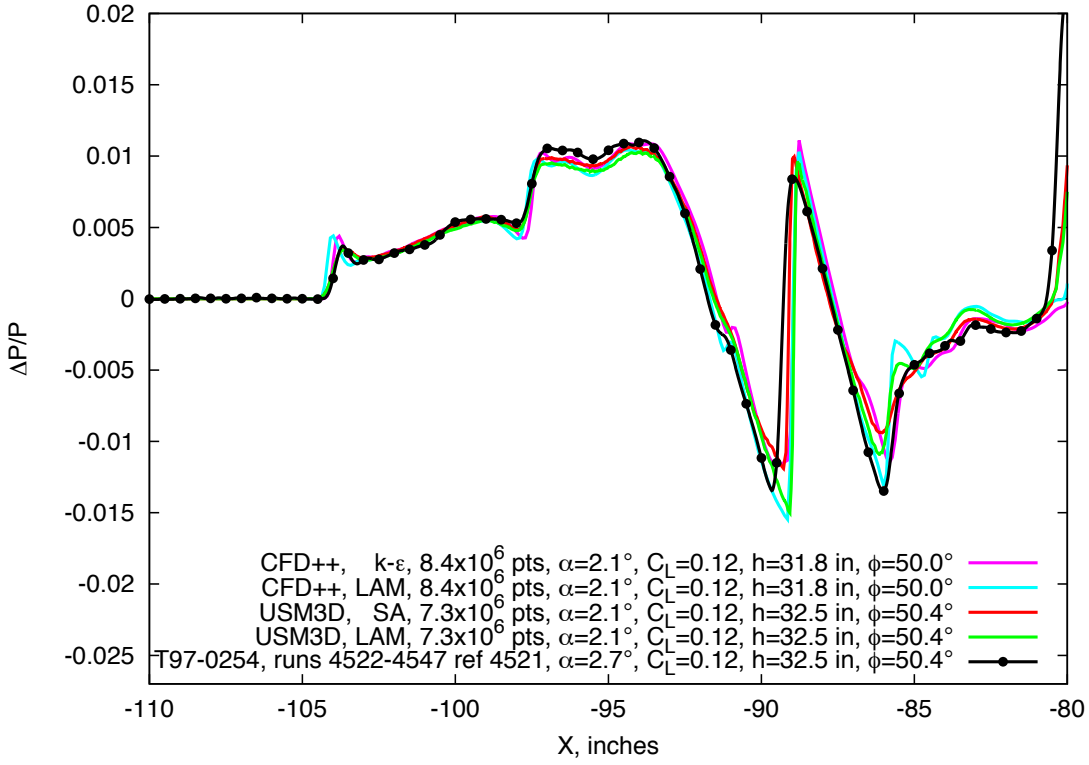

Figure 9.20. 1044 model, blade, experimental data compared with CFD++, and USM3D computations with laminar and turbulent solutions, M=1.7, h=32.5 in., ϕ=50°, Re=6.81 x10^6

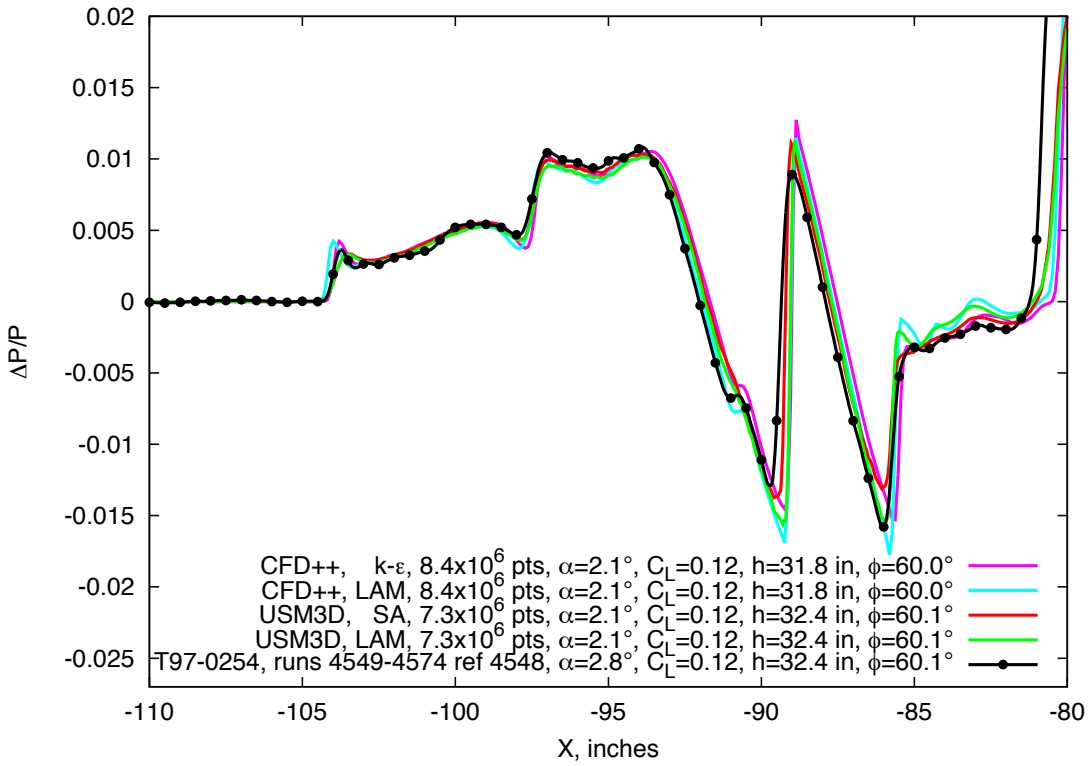

Figure 9.21. 1044 model, blade, experimental data compared with CFD++, and USM3D computations with laminar and turbulent solutions, M=1.7, h=31.8 in., ϕ=60°, Re=6.81 x10^6

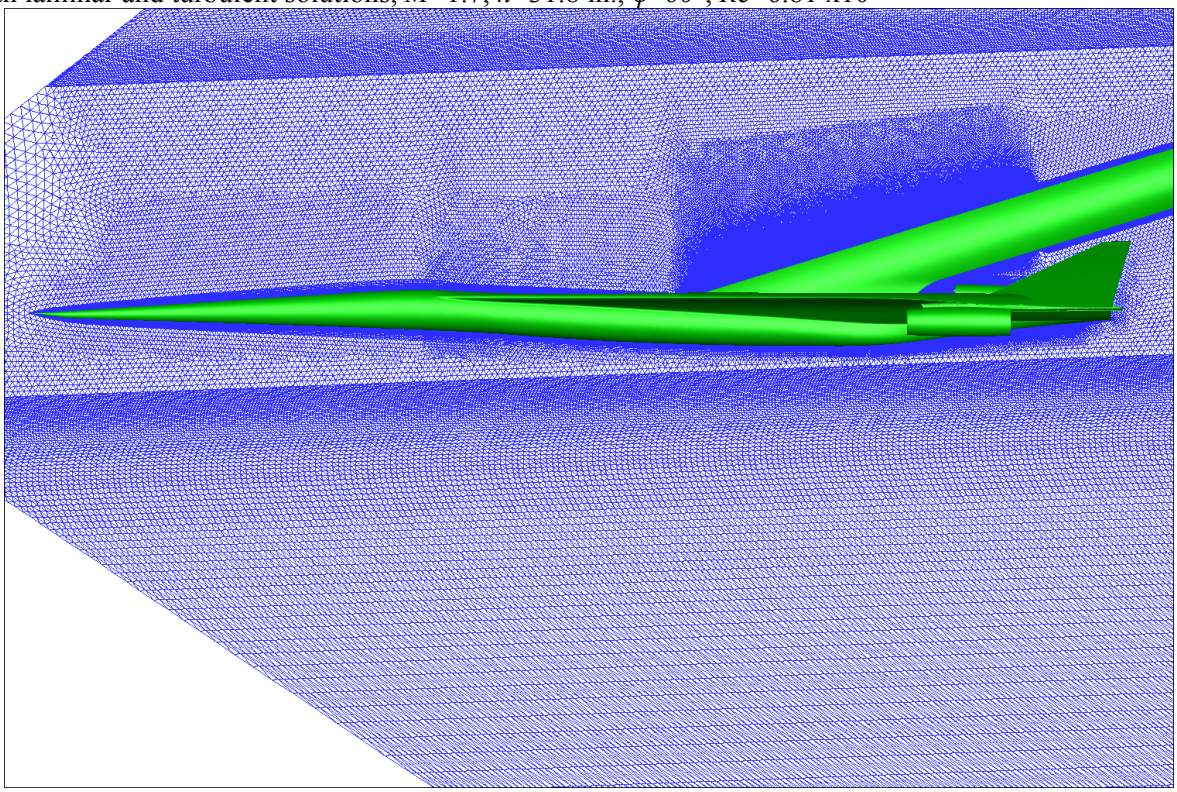

Figure 9.22. Lockheed near-body symmetry plane mesh after conversion from mixed element to tetrahedral cells

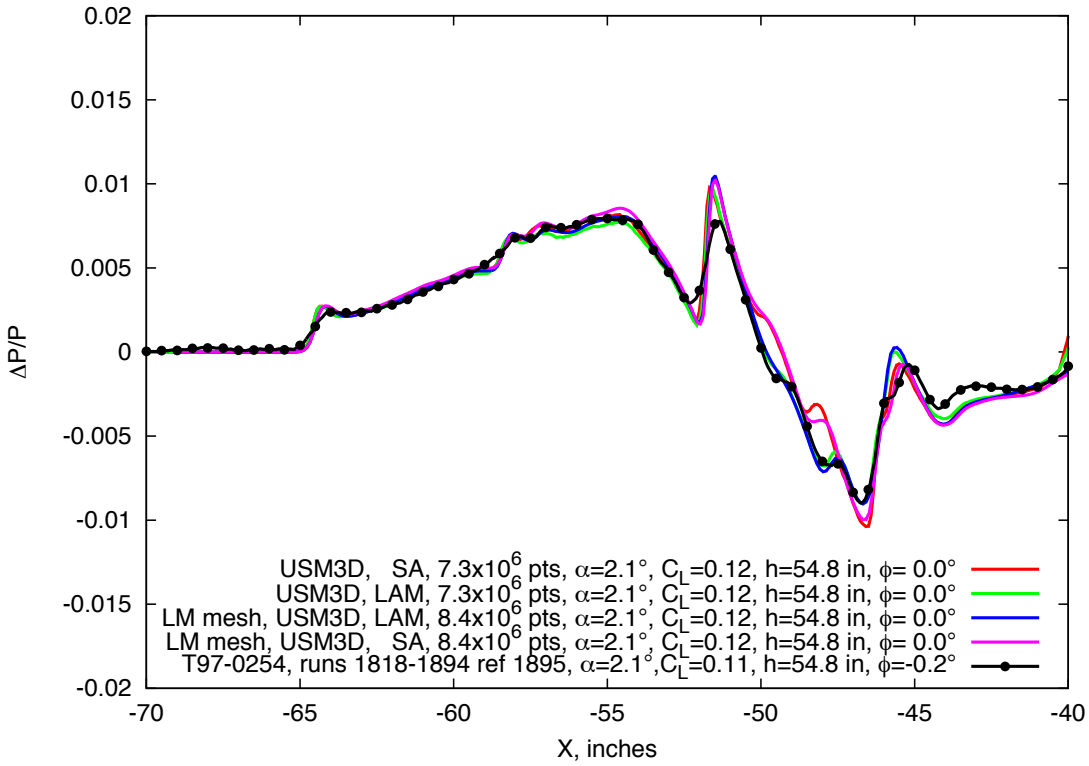

Figure 9.23. 1044 model, blade, experimental data compared with USM3D computations using Lockheed and NASA meshes, laminar and turbulent solutions, M=1.7, h=54.8 in., ϕ=0°, Re=6.74 x10^6

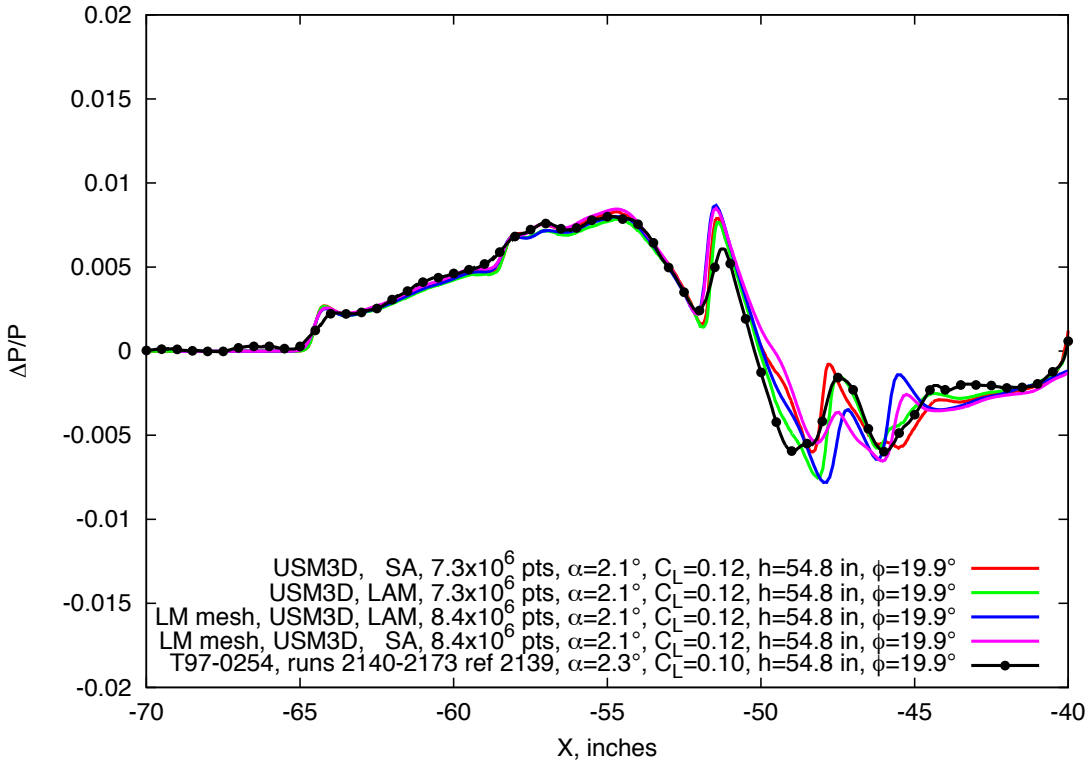

Figure 9.24. 1044 model, blade, experimental data compared with USM3D computations using Lockheed and NASA meshes, laminar and turbulent solutions, M=1.7, h=54.8 in., ϕ=20°, Re=6.74 x10^6

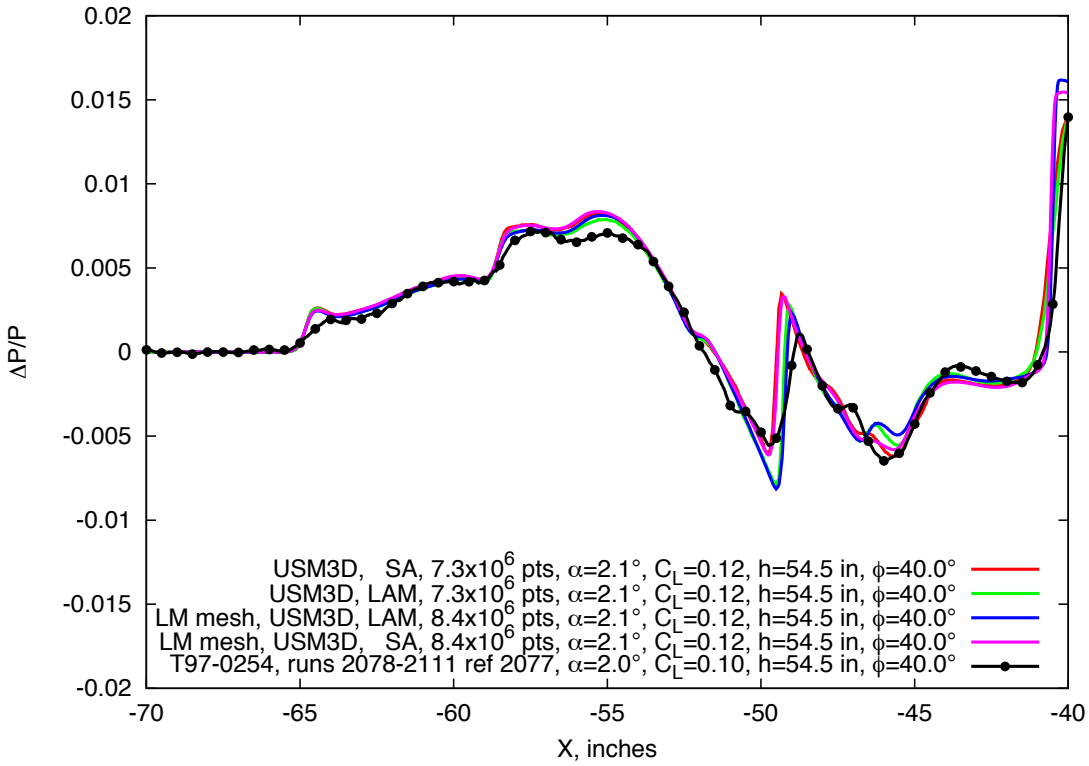

Figure 9.25. 1044 model, blade, experimental data compared with USM3D computations using Lockheed and NASA meshes, laminar and turbulent solutions, M=1.7, h=54.5 in., ϕ=40°, Re=6.75 x10^6

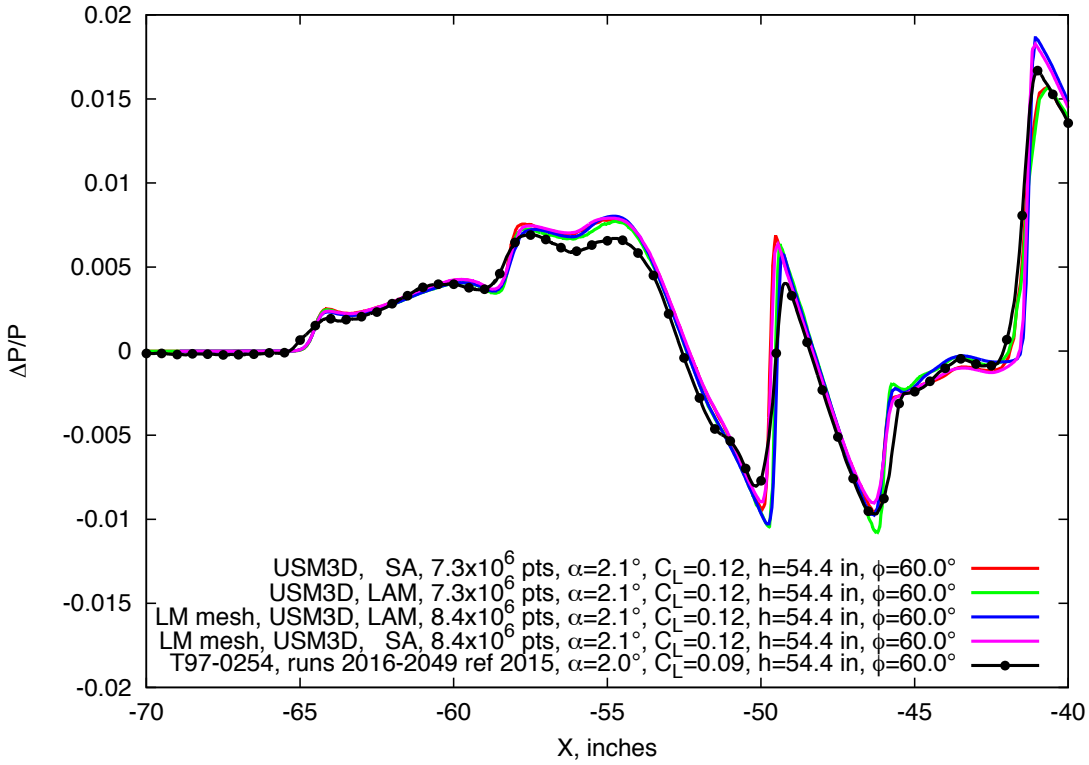

Figure 9.26. Lockheed 1044, blade, experimental data compared with USM3D computations using Lockheed and NASA meshes, laminar and turbulent solutions, M=1.7, h=54.4 in., ϕ=60°, Re=6.74 x10^6

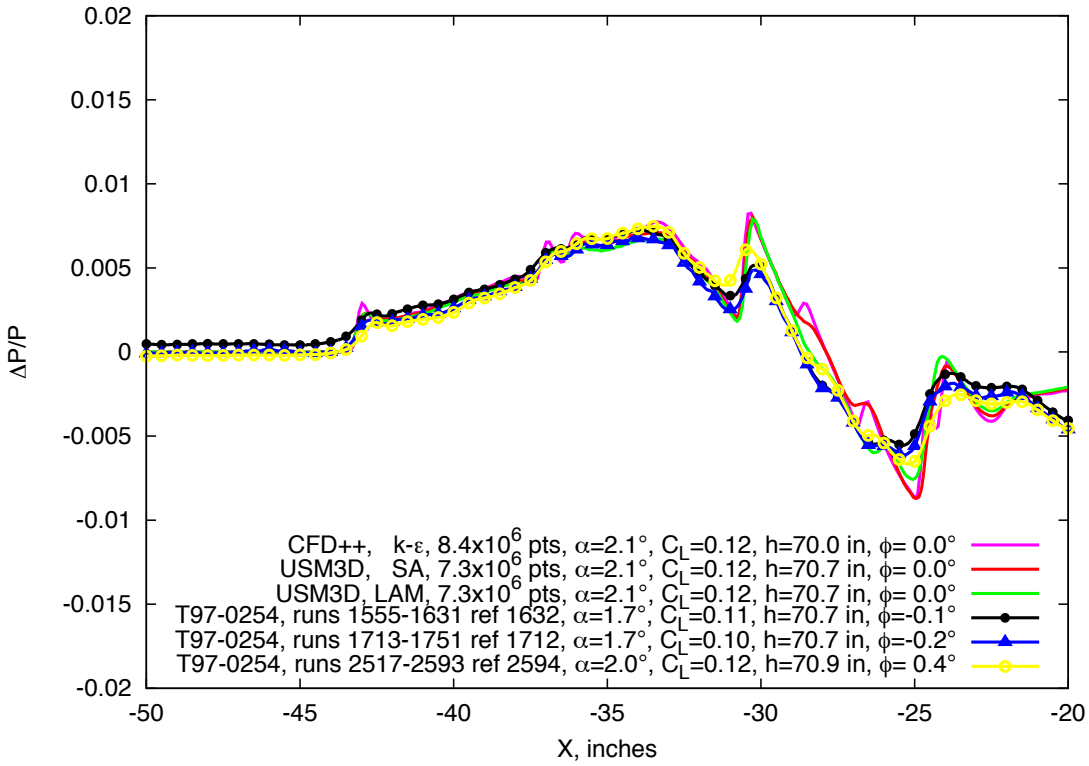

Figure 9.27. 1044 model, blade, experimental data compared with laminar and turbulent flow solutions, M=1.7, h=70.7 in., ϕ=0°, Re=6.77 x10^6

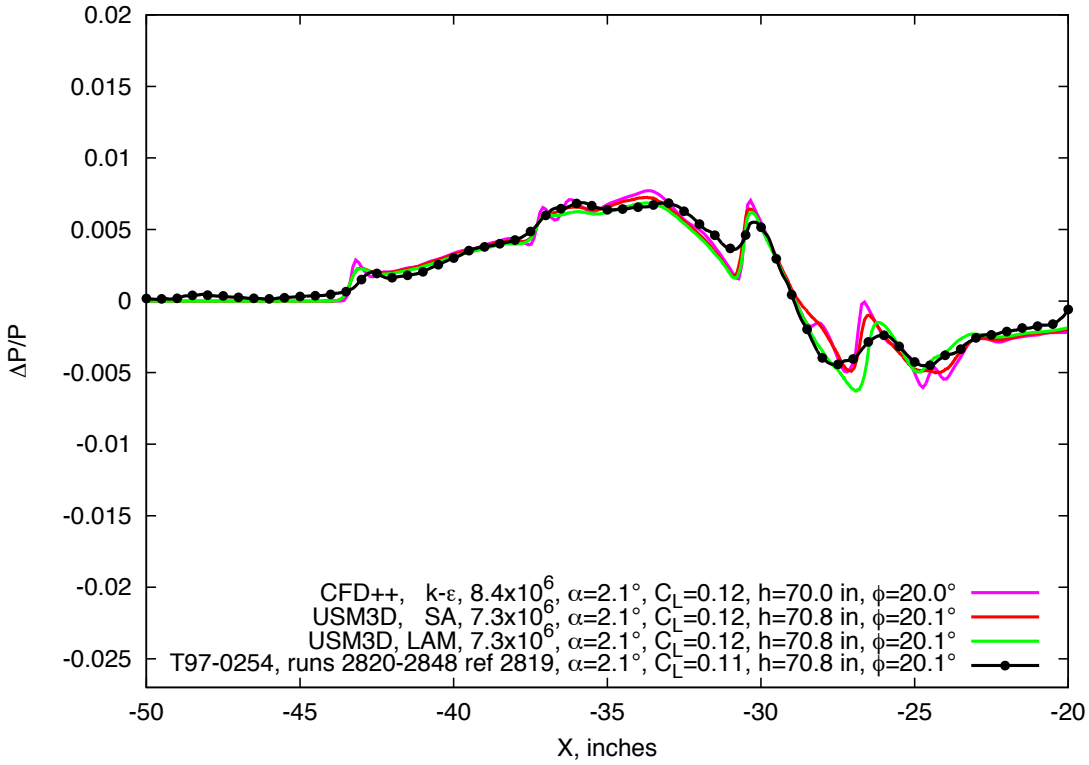

Figure 9.28. 1044 model, blade, experimental data compared with laminar and turbulent flow solutions, M=1.7, h=70.8 in., ϕ=20°, Re=6.70 x10^6

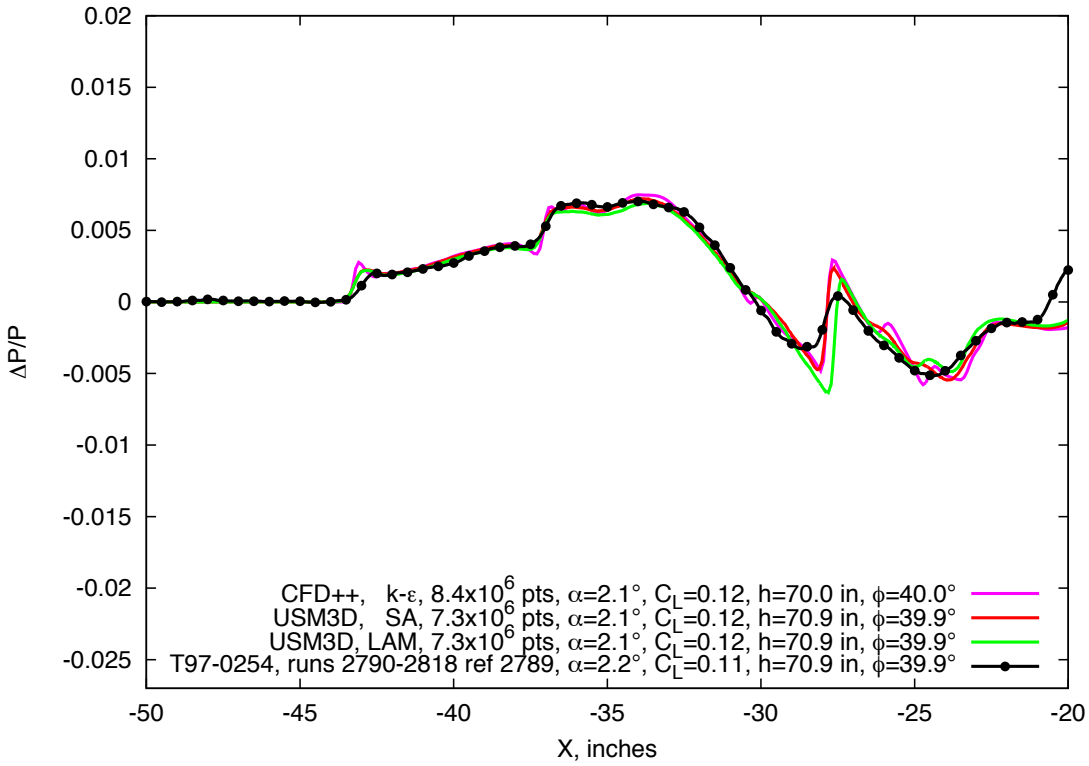

Figure 9.29. 1044 model, blade, experimental data compared with laminar and turbulent flow solutions, M=1.7, h=70.9 in, ϕ=40°, Re=6.69 x10^6

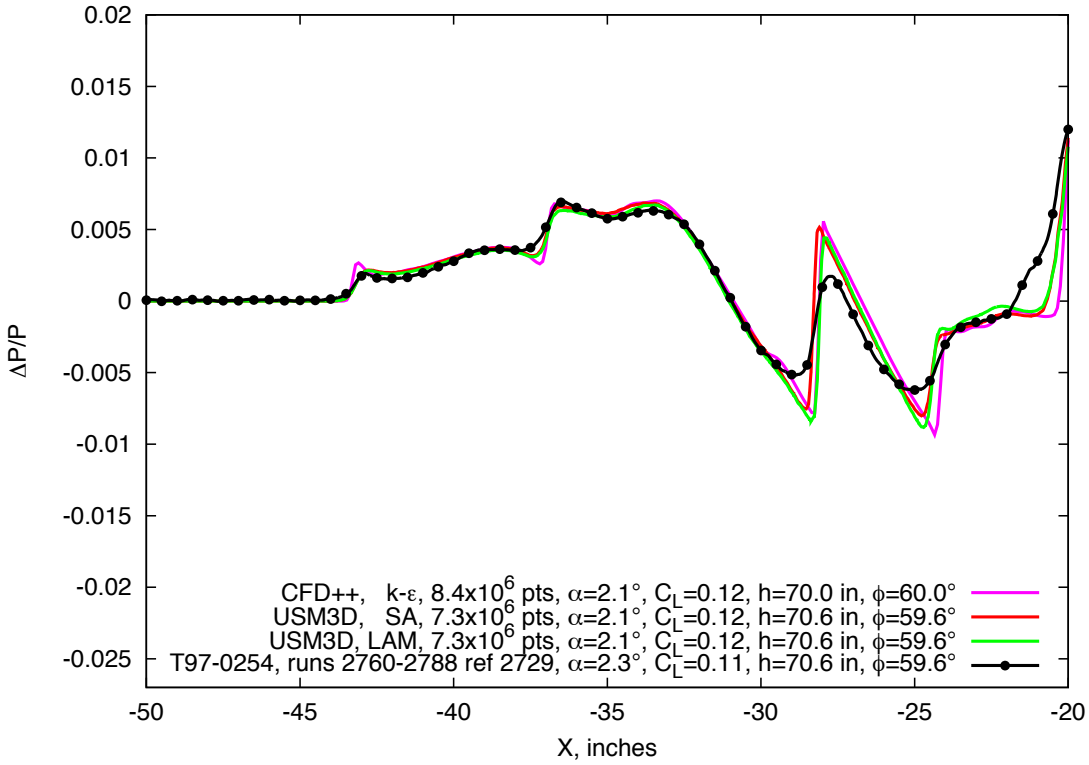

Figure 9.30. 1044 model, blade, experimental data compared with laminar and turbulent flow solutions, M=1.7, h=70.6 in., ϕ=60°, Re=6.69 x10^6

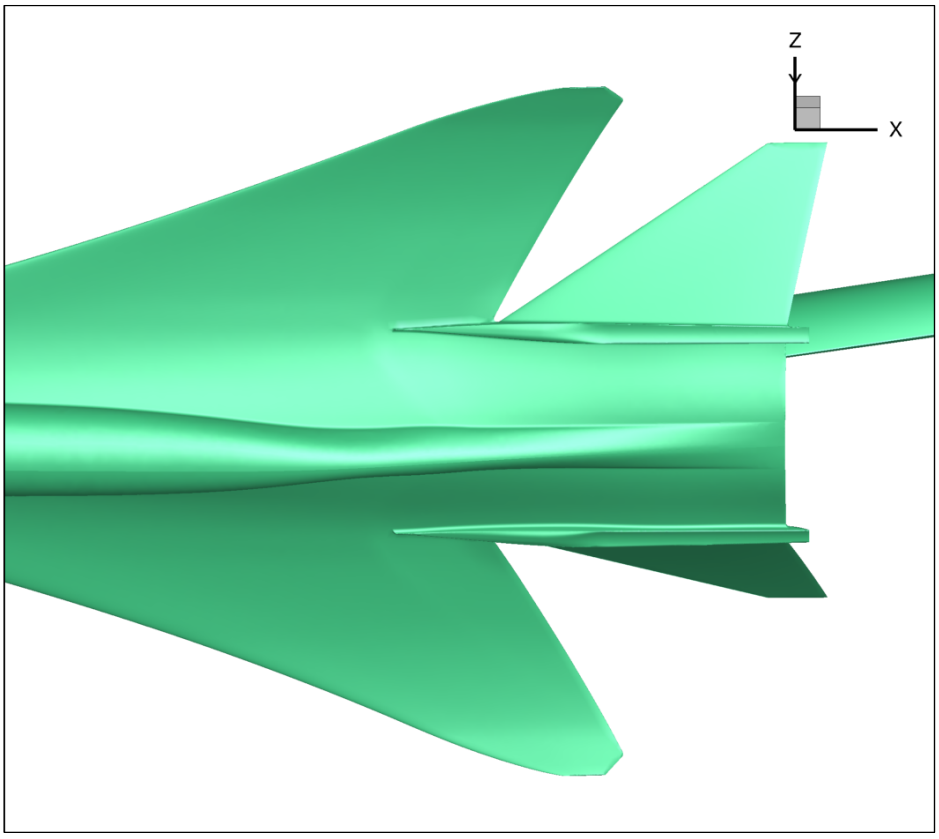

Figure 9.31. Computational surface mesh of the 1044 model without under-wing nacelles.

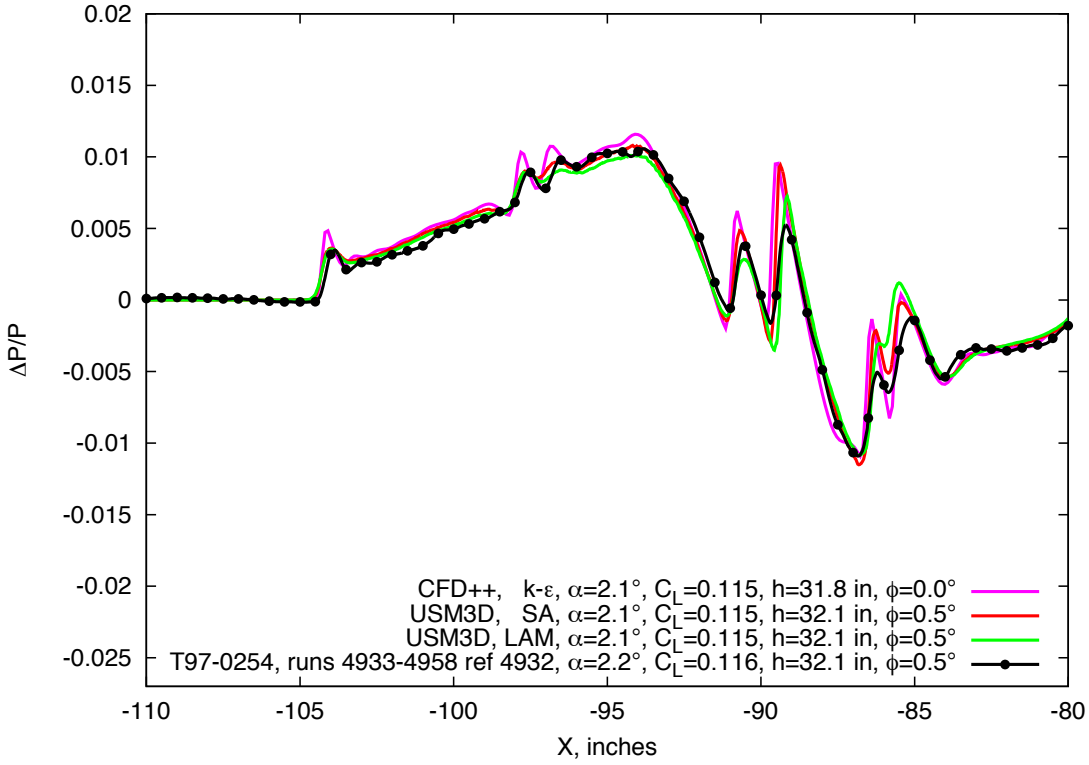

Figure 9.32. 1044 model without under-wing nacelle, blade, experimental data compared with laminar and turbulent flow solutions, M=1.7, h=32.1 in., ϕ=0°, Re=6.73 x10^6

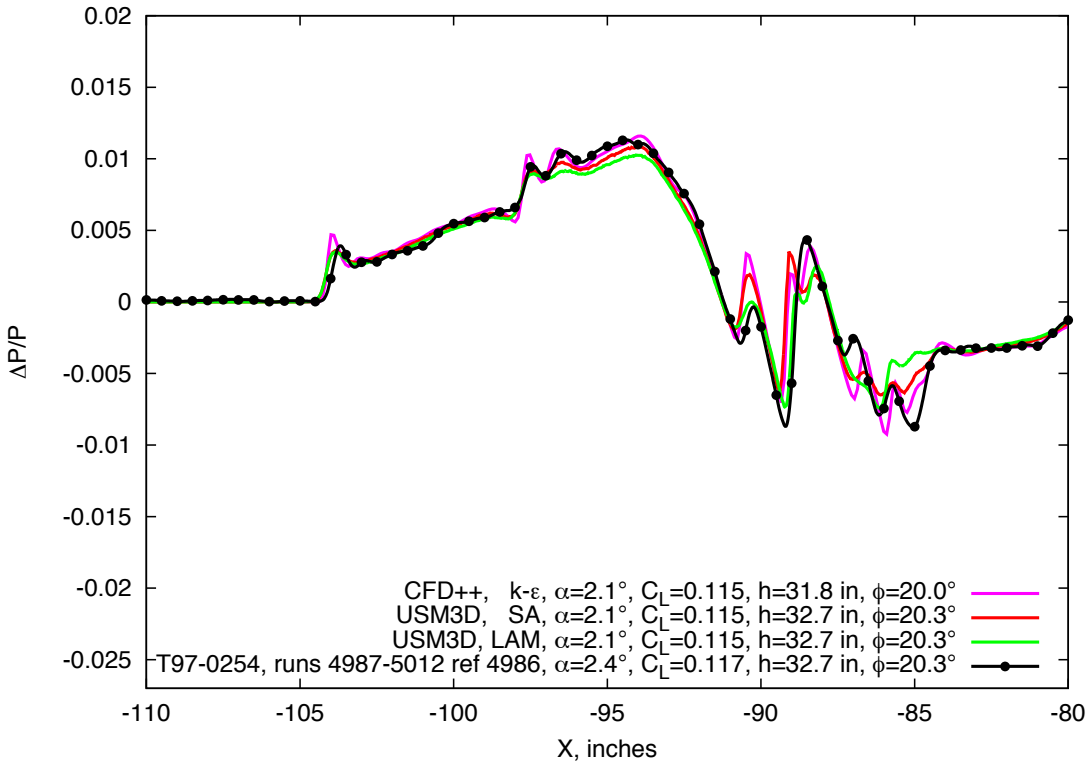

Figure 9.33. 1044 model without under-wing nacelle, blade, experimental data compared with laminar and turbulent flow USM3D solutions, M=1.7, h=32.7 in., ϕ=20°, Re=6.73 x10^6

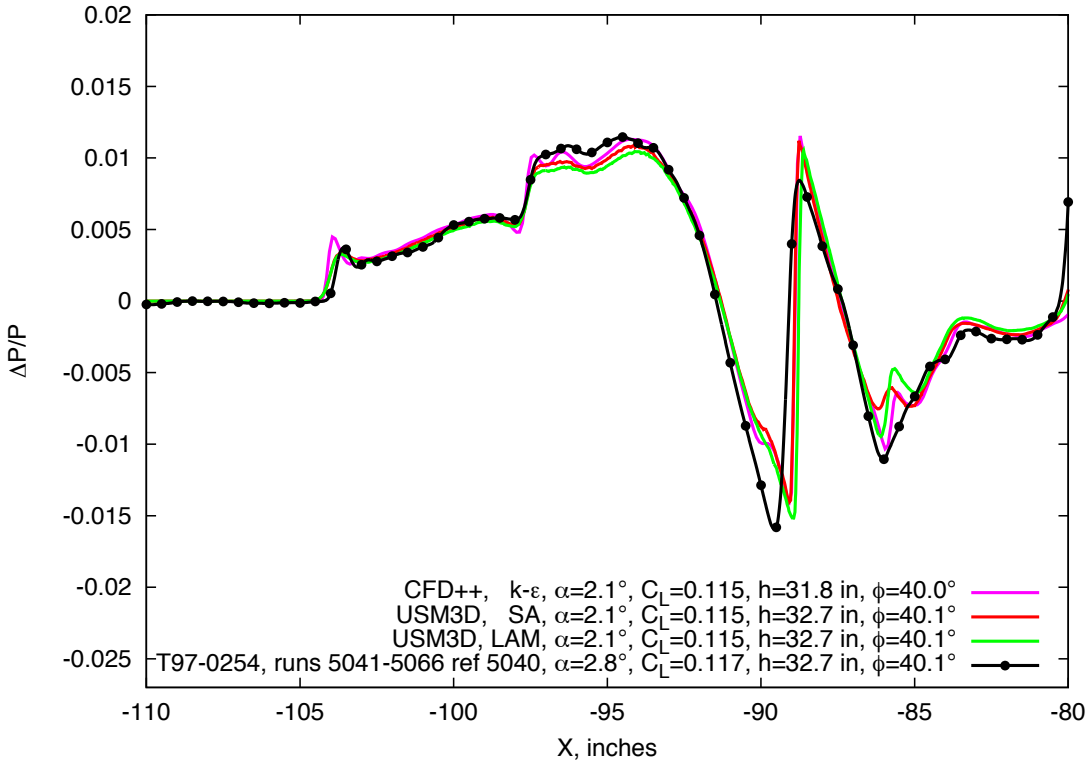

Figure 9.34. 1044 model without under-wing nacelle, blade, experimental data compared with laminar and turbulent flow solutions, M=1.7, h=32.7 in., ϕ=40°, Re=6.72 x10^6

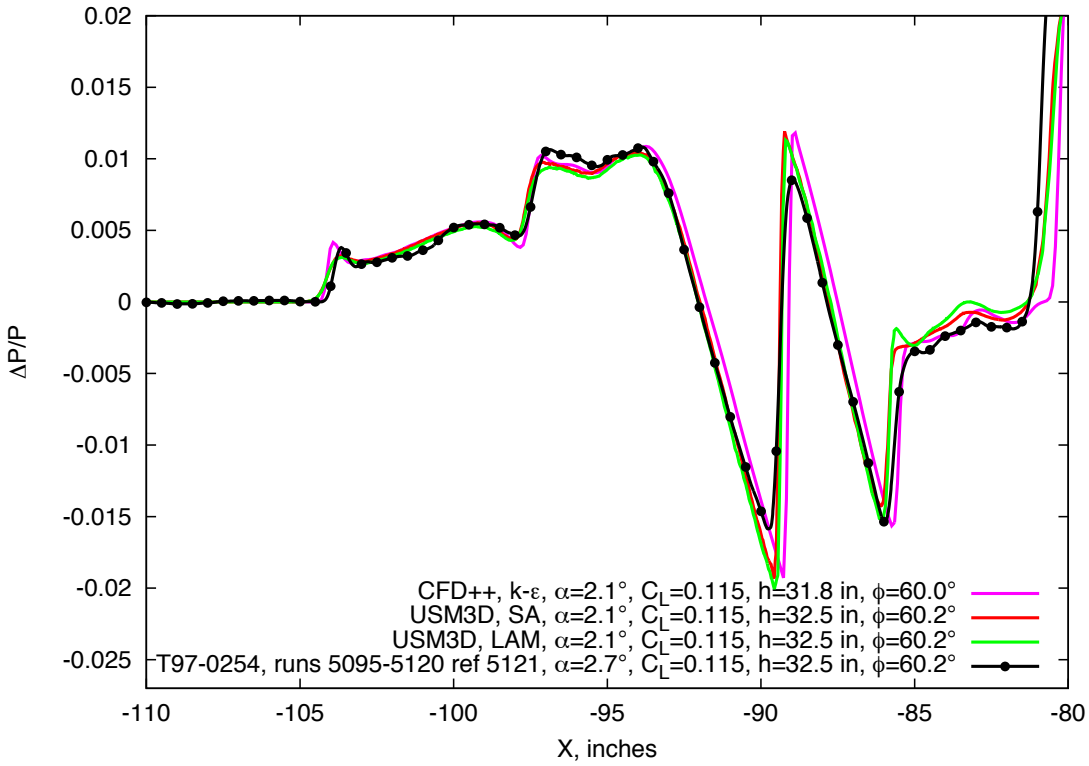

Figure 9.35. 1044 model without under-wing nacelle, blade, experimental data compared with laminar and turbulent flow solutions, M=1.7, h=32.5 in., ϕ=60°, Re=6.71 x10^6

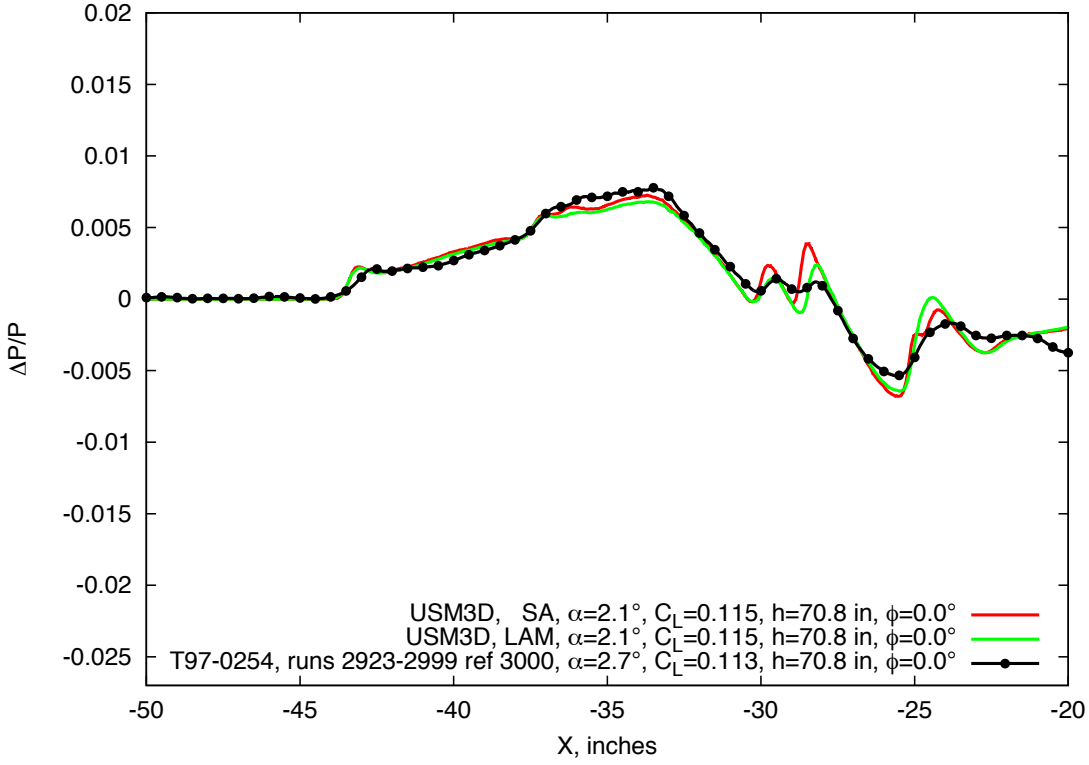

Figure 9.36. 1044 model without under-wing nacelle, blade, experimental data compared with laminar and turbulent flow solutions, M=1.7, h=70.8 in., ϕ=0°, Re=6.75 x10^6

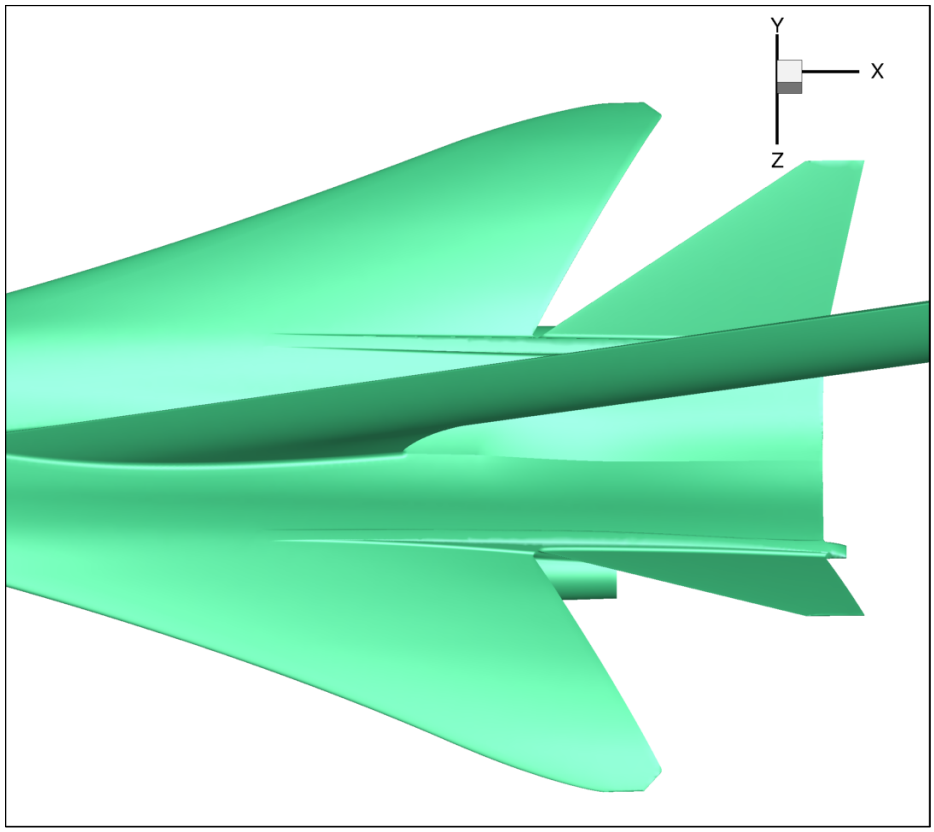

Figure 9.37. Computational surface mesh of the 1044 model without the centerline nacelle.

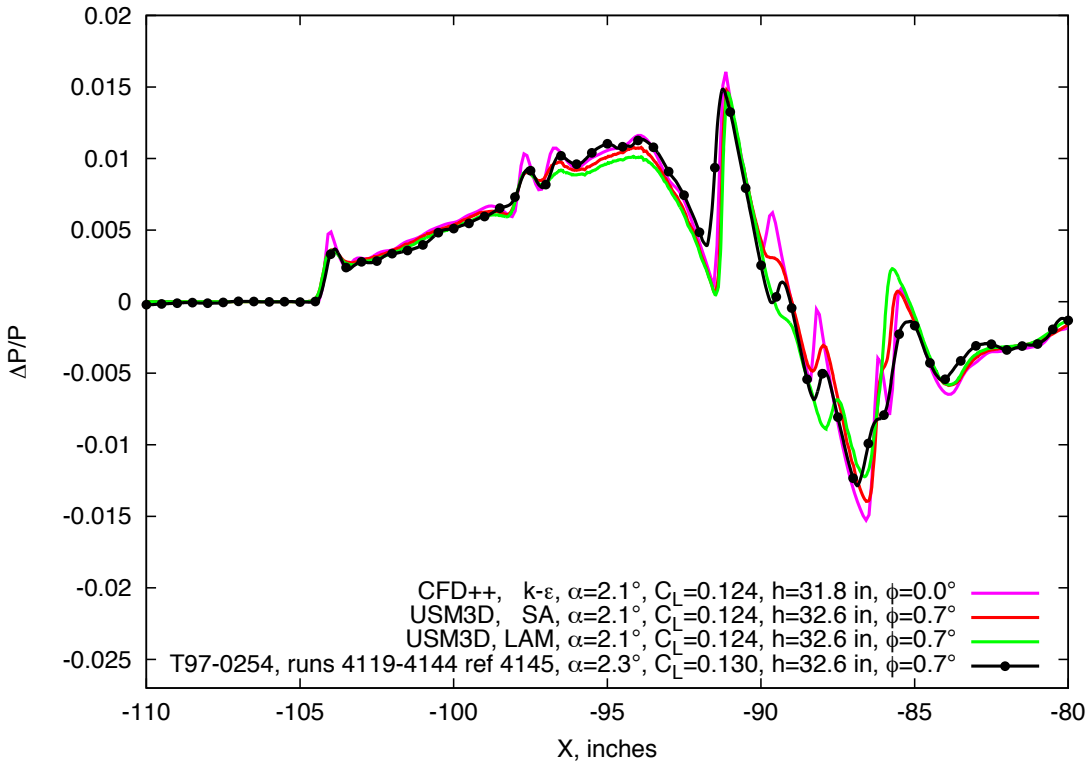

Figure 9.38. 1044 model without center nacelle, blade, experimental data compared with laminar and turbulent flow solutions, M=1.7, h=32.6 in., ϕ=1°, Re=6.77 x10^6

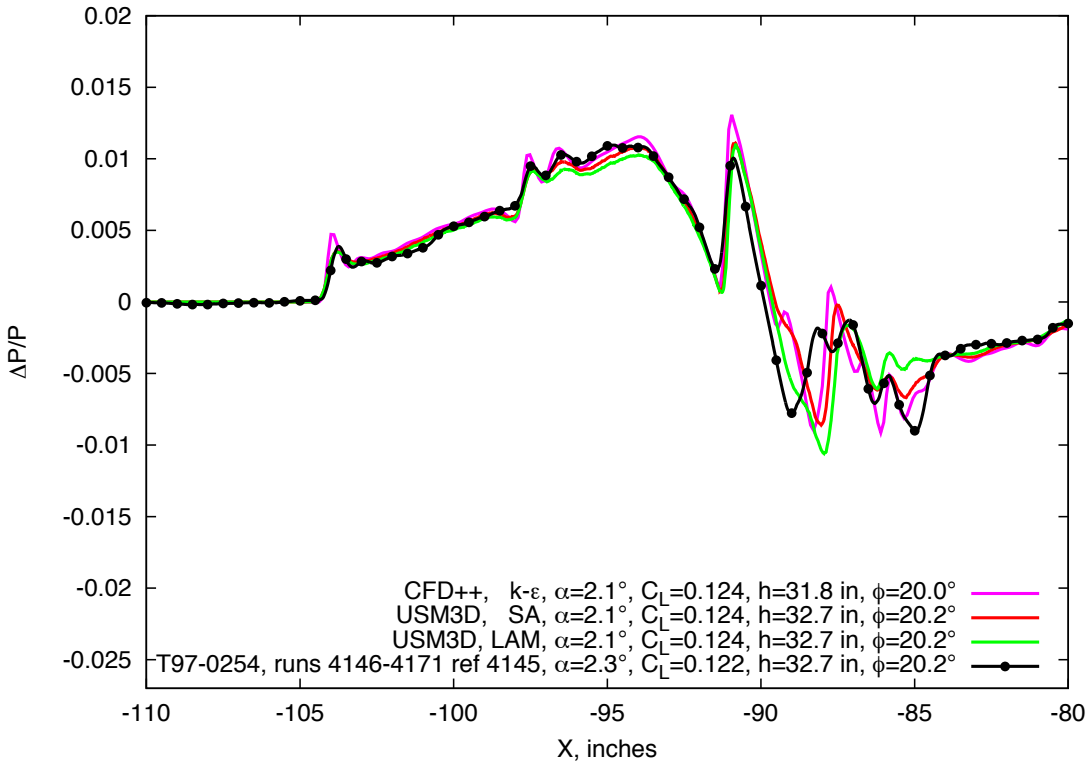

Figure 9.39. 1044 model without center nacelle, blade, experimental data compared with laminar and turbulent flow solutions, M=1.7, h=32.7 in., ϕ=20°, Re=6.75 x10^6

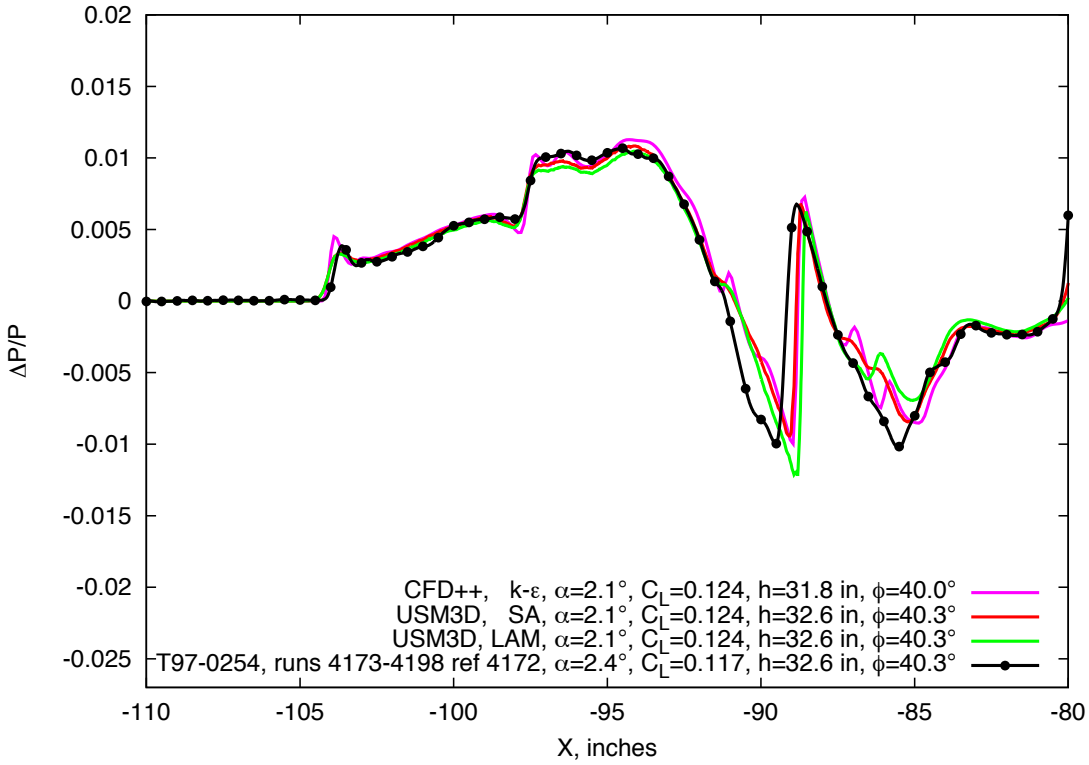

Figure 9.40. 1044 model without center nacelle, blade, experimental data compared with laminar and turbulent flow solutions, M=1.7, h=32.6 in., ϕ=40°, Re=6.74 x10^6

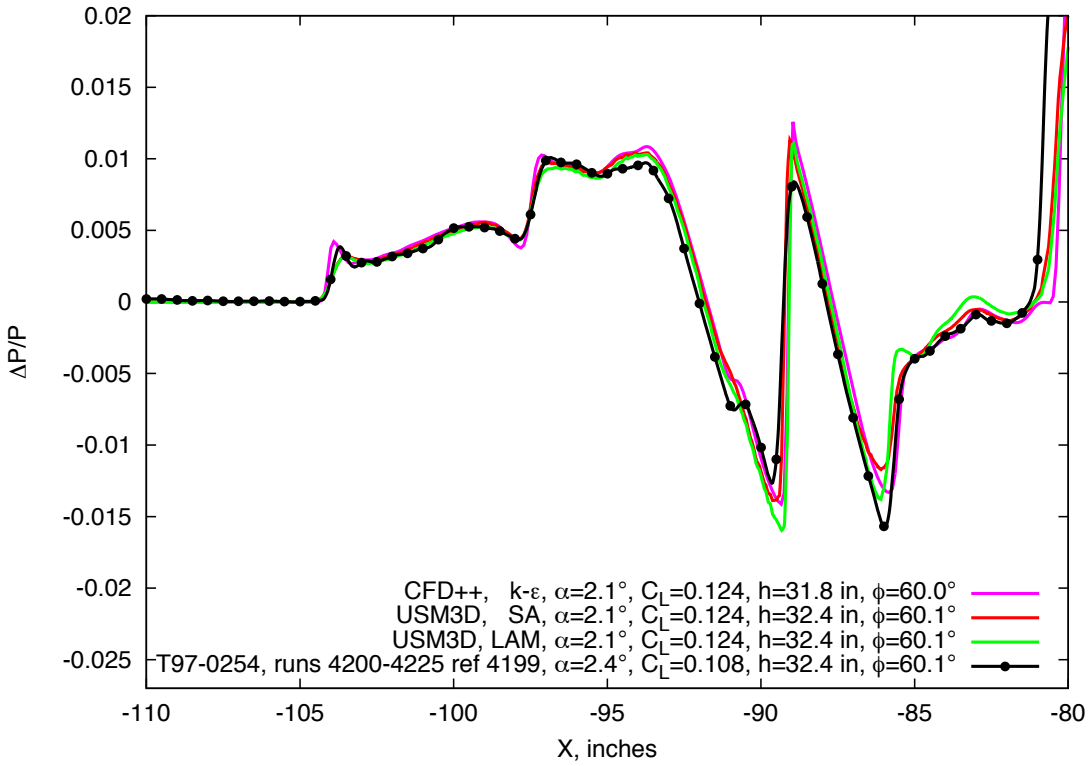

Figure 9.41. 1044 model without center nacelle, blade, experimental data compared with laminar and turbulent flow solutions, M=1.7, h=32.4 in., ϕ=60°, Re=6.74 x10^6

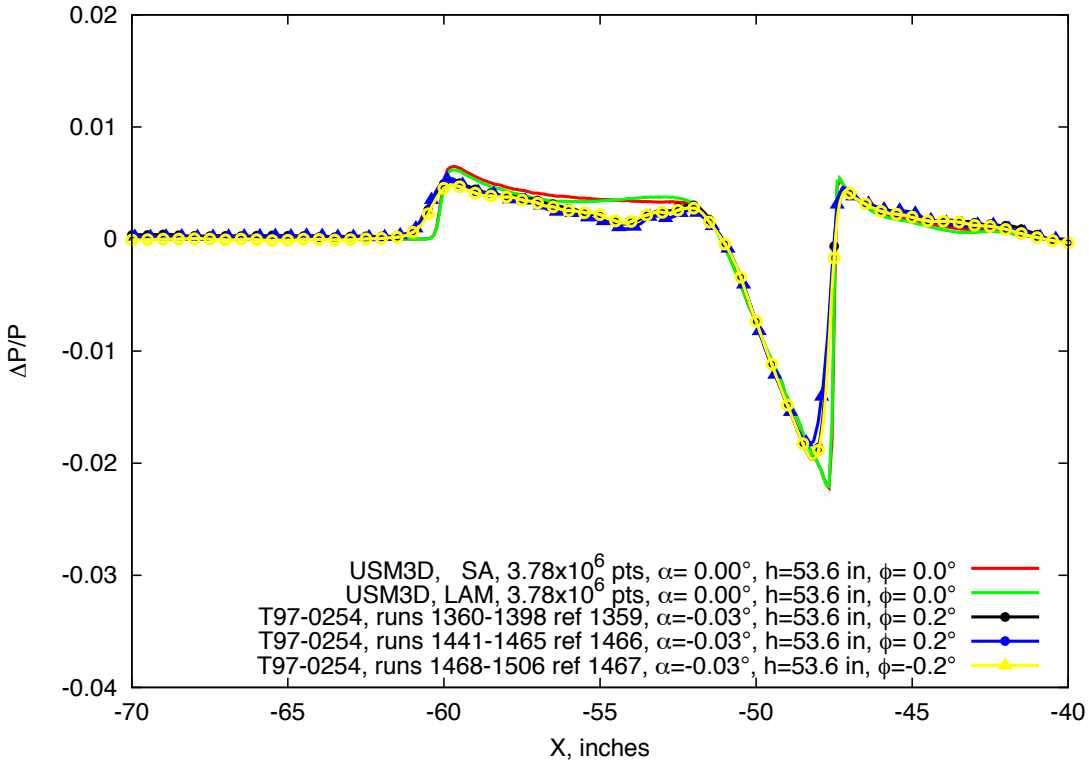

Figure 9.42. 70° Flat Plate, blade, experimental data compared with laminar and turbulent flow solutions, M=1.7, h=53.6 in., ϕ=0°, Re=3.34 x10^6

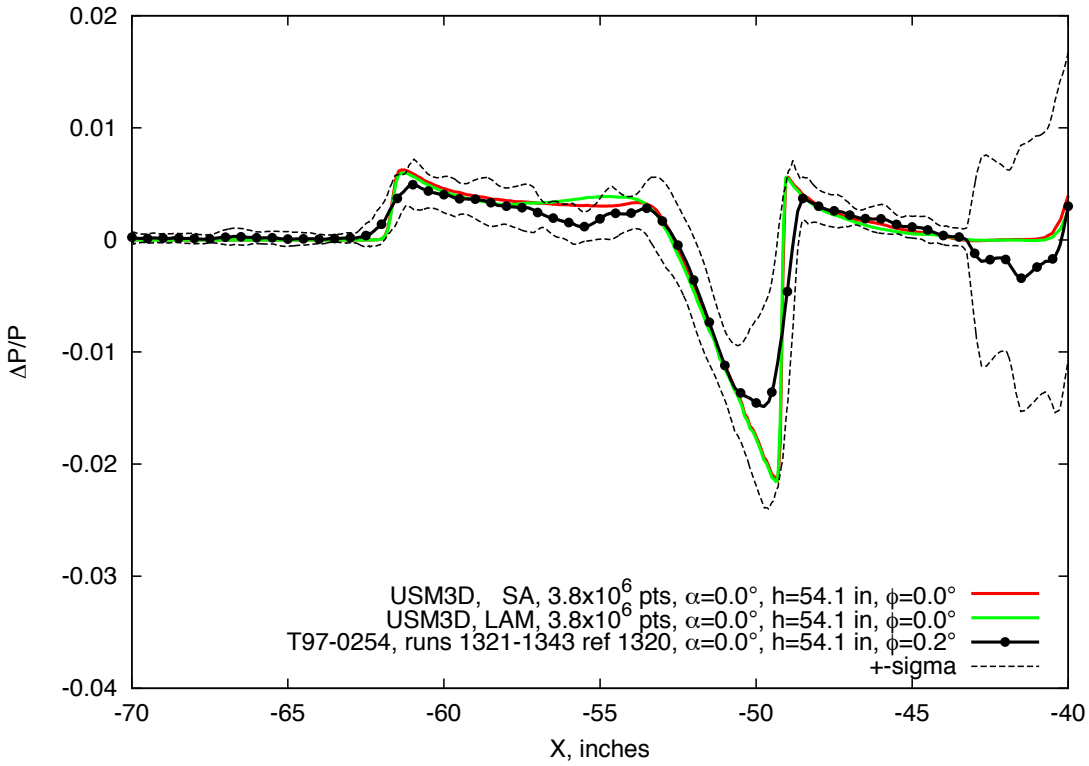

Figure 9.43. 70° Flat Plate, blade, experimental data compared with laminar and turbulent flow solutions, M=1.6, h=54.1 in., ϕ=0°, Re=3.45 x10^6

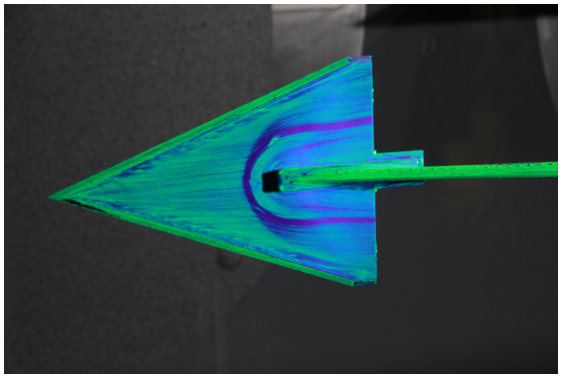

(a) Upper surface

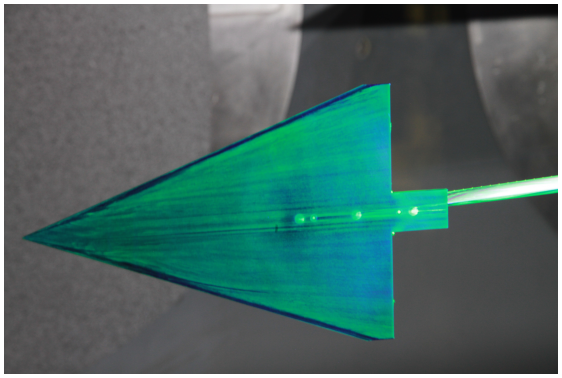

(b) Lower surface

Figure 9.44. Oil flow images of the 70° Flat Plate Model, M=1.7

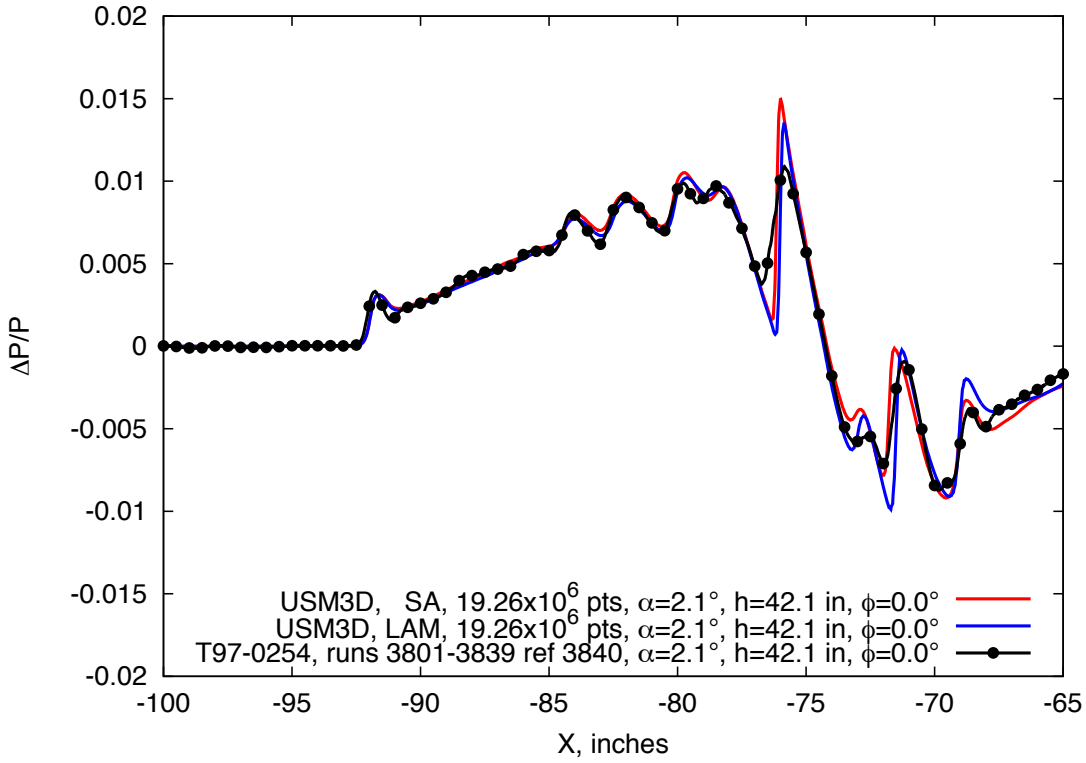

Figure 9.45 1021 model, blade, experimental data compared with laminar and turbulent flow solutions, M=1.6, h=42.1 in., ϕ=0°, Re=8.15 x10^6

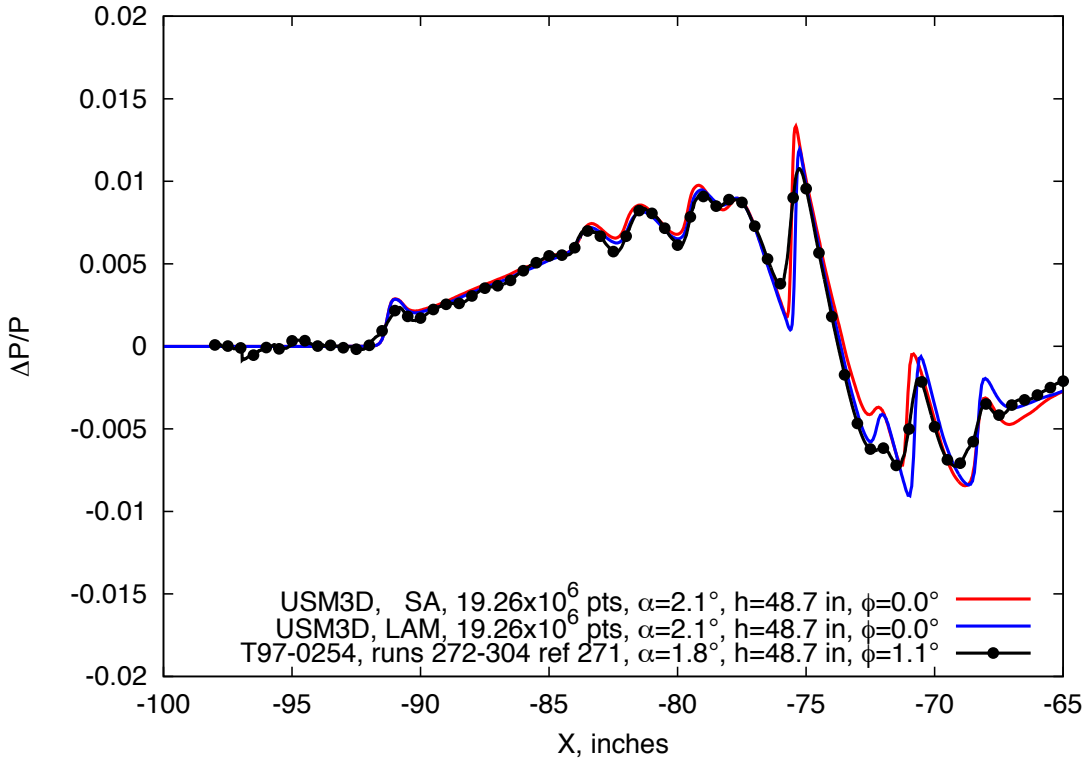

Figure 9.46. 1021 model, blade, experimental data compared with laminar and turbulent flow solutions, M=1.6, h=48.7 in., ϕ=0°, Re=8.15 x10^6

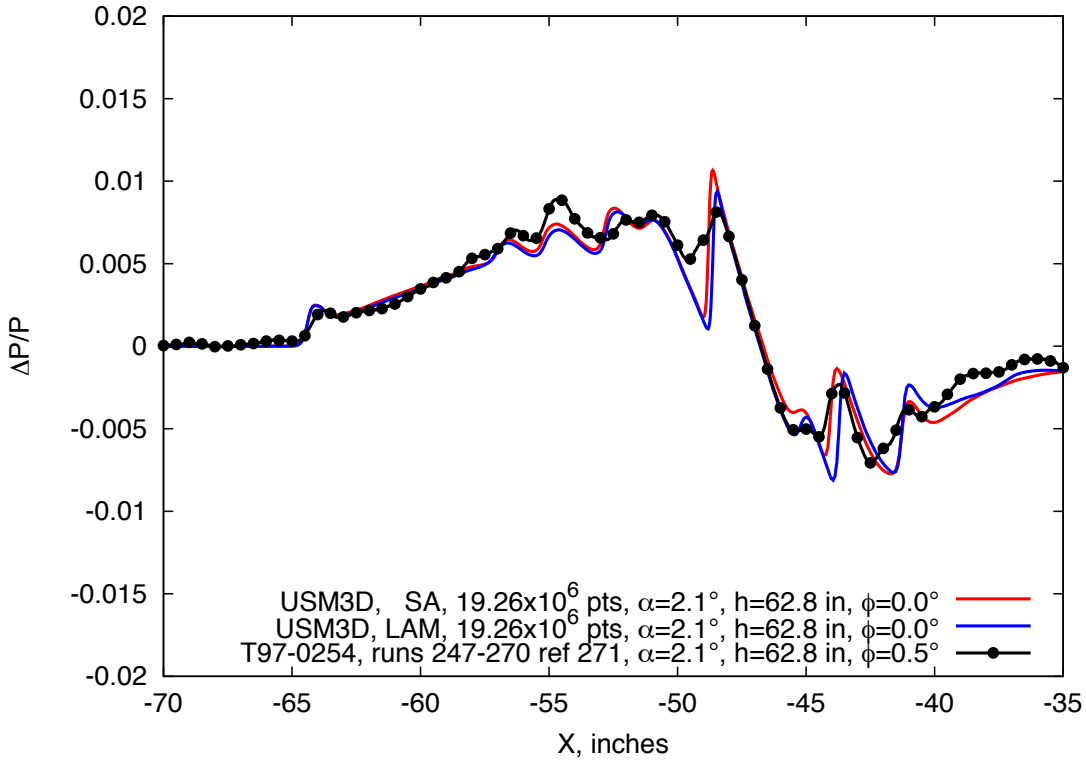

Figure 9.47. 1021 model, blade, experimental data compared with laminar and turbulent flow solutions, M=1.6, h=62.8 in., ϕ=0°, Re=8.15 x10^6

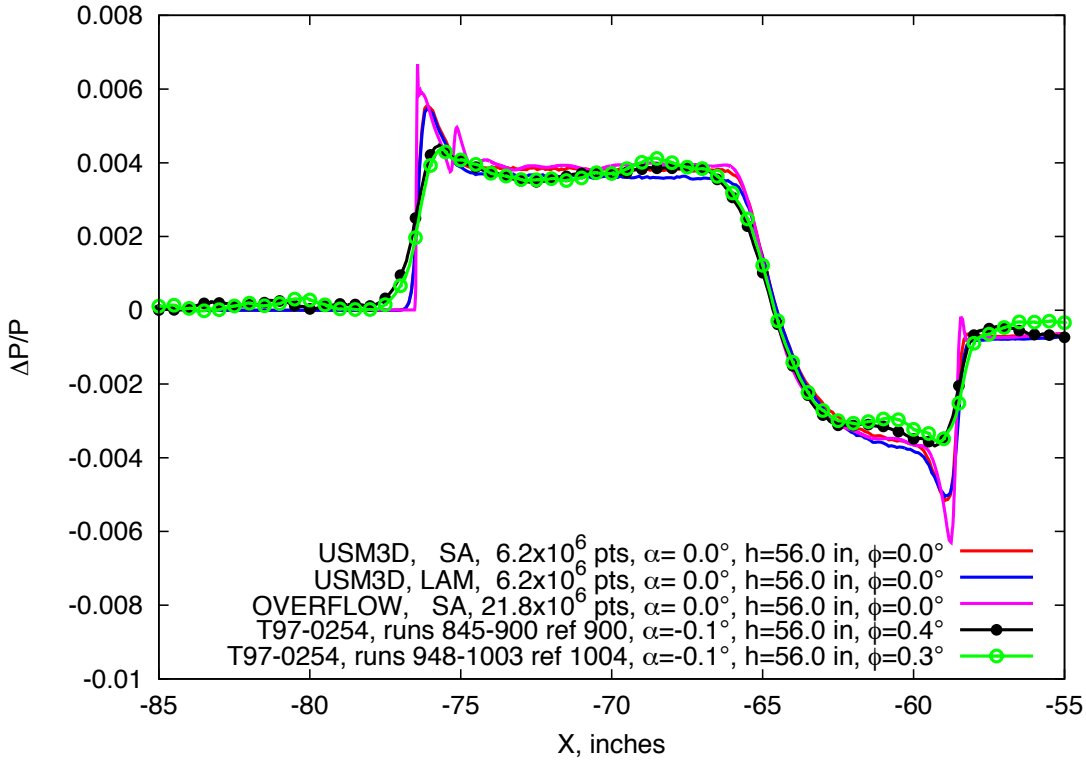

Figure 9.48. Lockheed Seeb-ALR, experimental data compared with USM3D and OVERLFLOW computations, M=1.6, α=0, h=56 in., Re=6.42x10^6

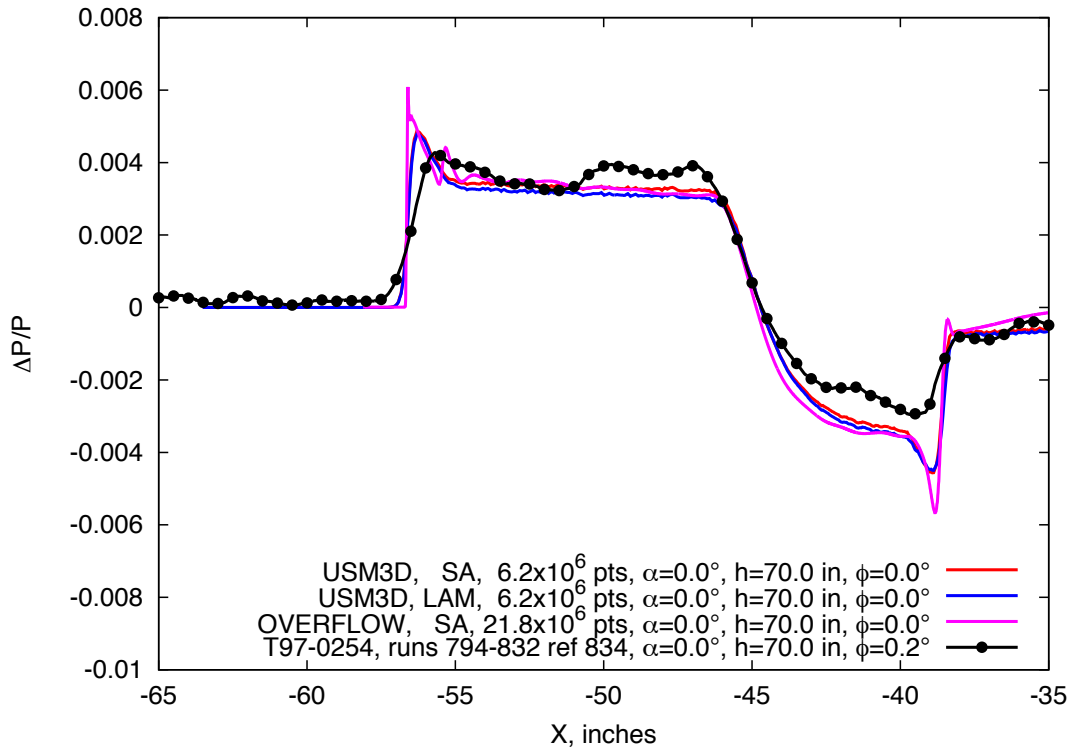

Figure 9.49. Lockheed Seeb-ALR, experimental data compared with USM3D and OVERLFLOW computations, M=1.6, α=0, h=70 in., Re=6.42x10^6

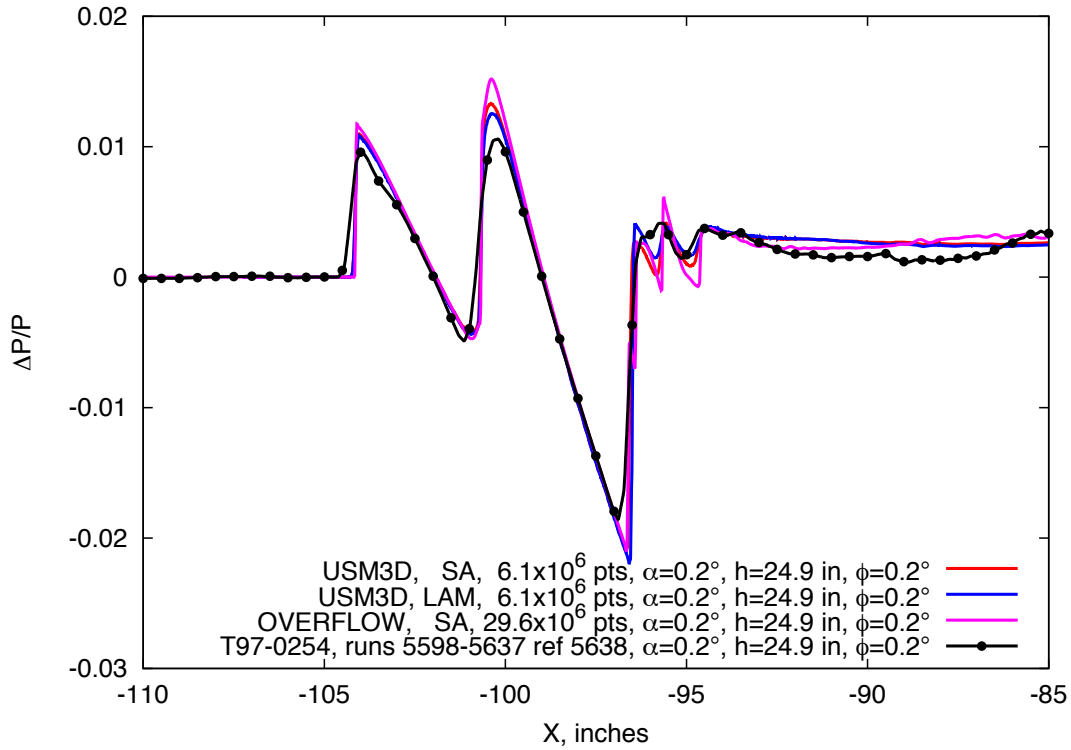

(a) ϕ=0°

Figure 9.50. 69° Delta Wing-Body, experimental data compared with USM3D and OVERFLOW solutions, M=1.7, h=25 in., Re=2.43x10^6 (continues)

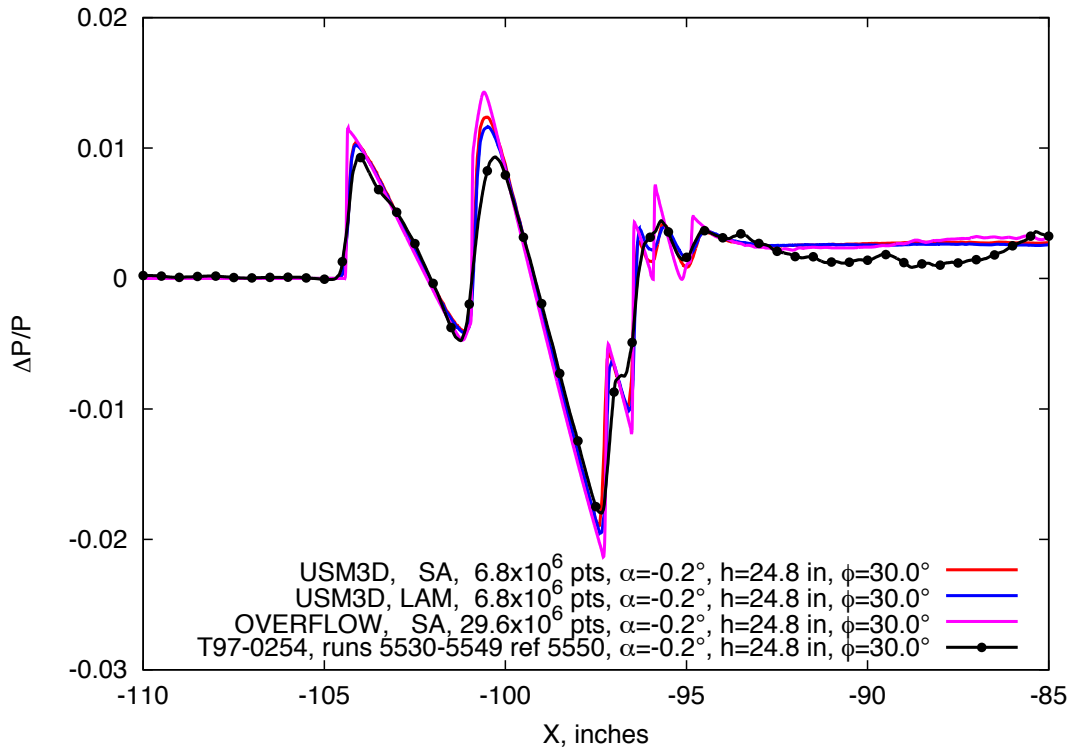

(b) ϕ=30°

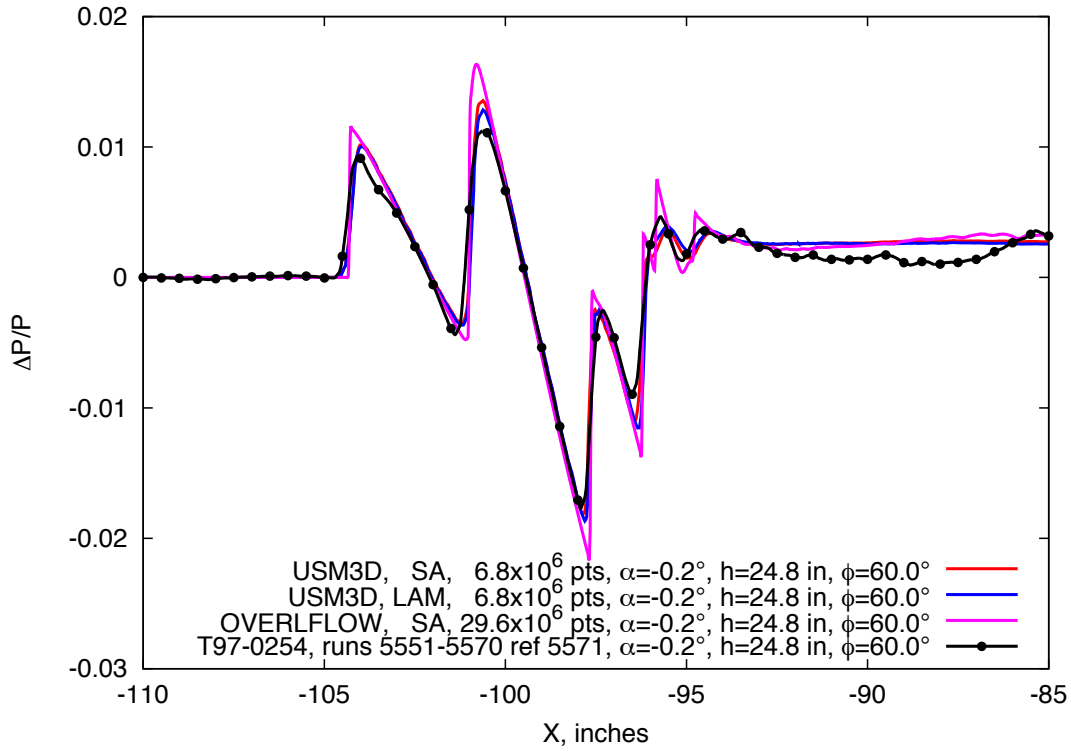

(c) ϕ=60°

Figure 9.50. 69° Delta Wing-Body, experimental data compared with USM3D and OVERFLOW solutions, M=1.7, h=25 in., Re=2.43x10^6 (continued)

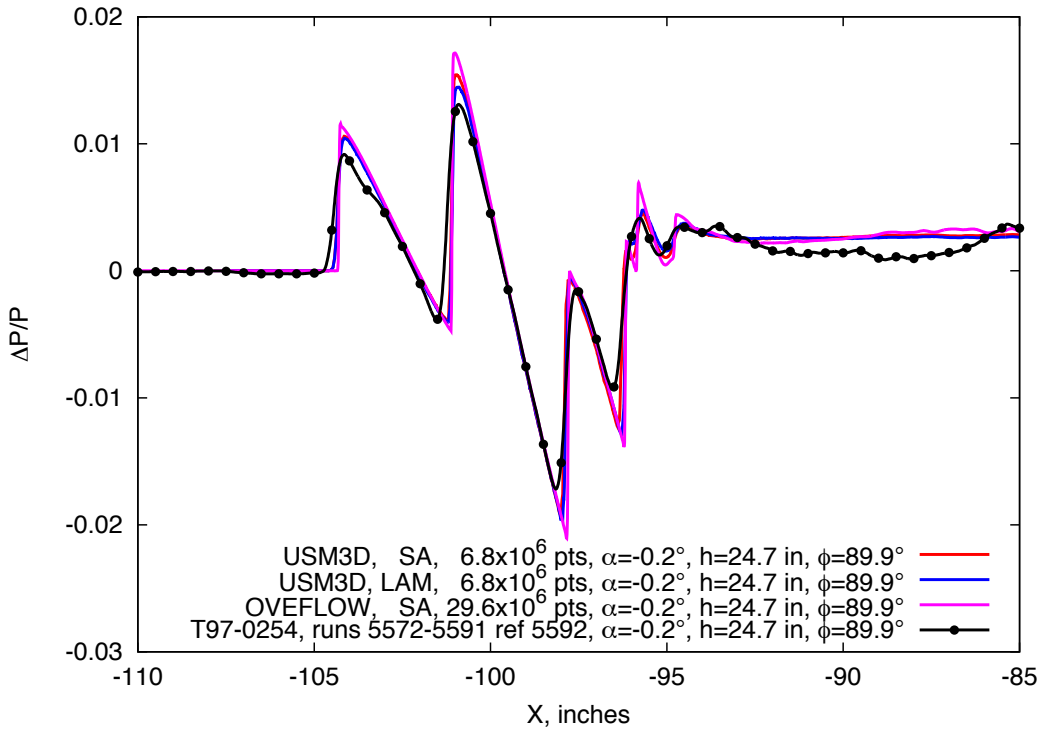

(d) ϕ=90°

Figure 9.50. 69° Delta Wing-Body, experimental data compared with USM3D and OVERFLOW solutions, M=1.7, h=25 in., Re=2.43x10^6 (concluded)

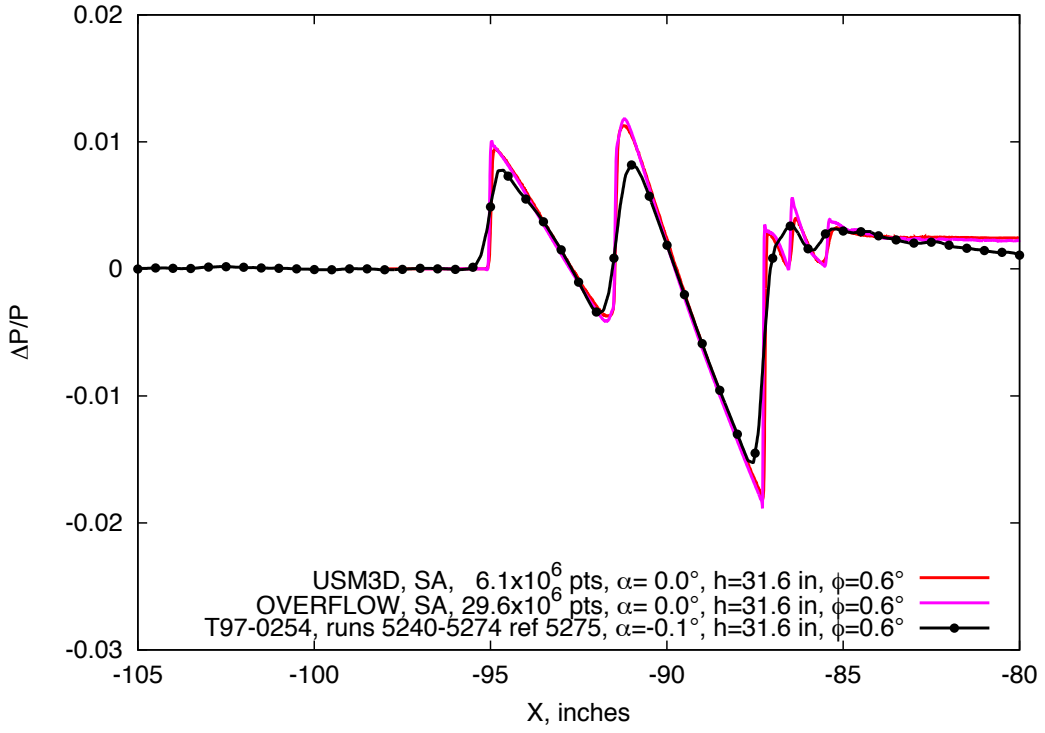

(a) ϕ=0°

Figure 9.51. 69° Delta Wing-Body, experimental data compared with USM3D and OVERFLOW solutions, M=1.7, h=32 in., Re=2.43x10^6 (continues)

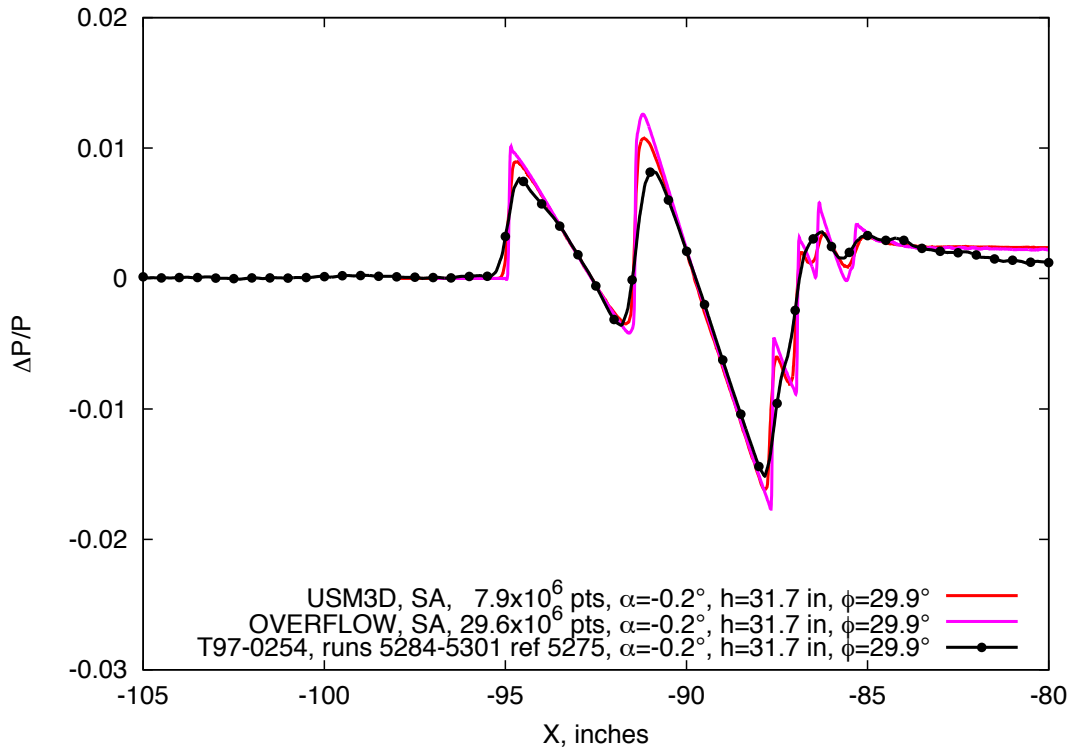

(b) ϕ=30°

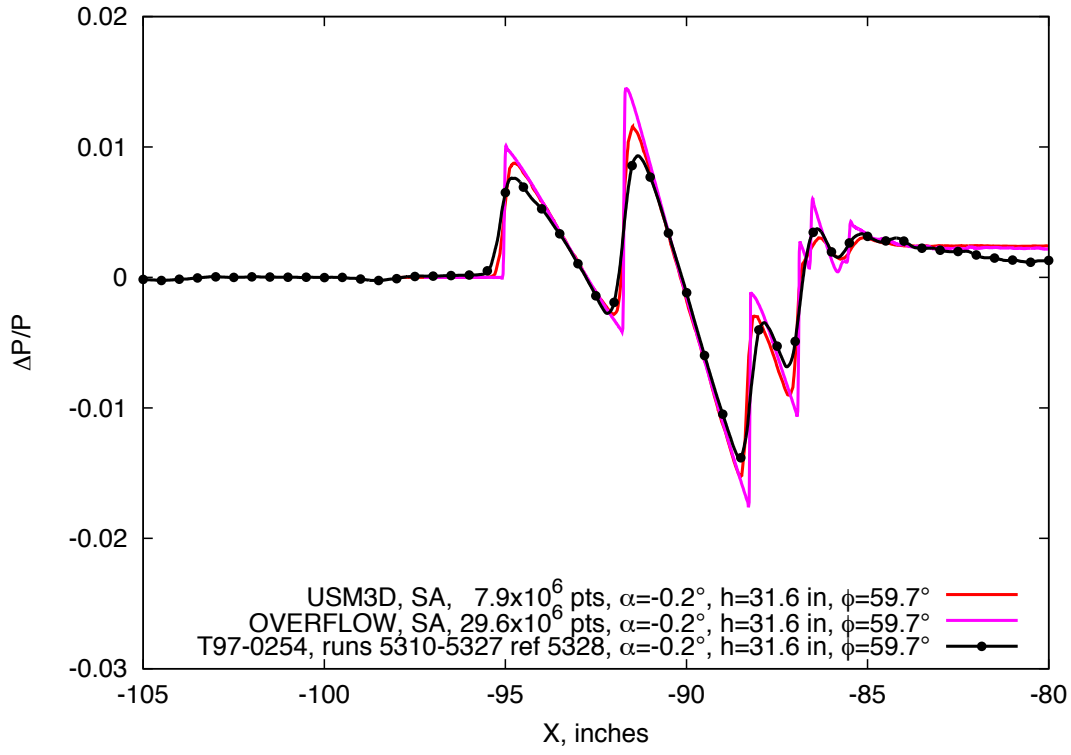

(c) ϕ=60°

Figure 9.51. 69° Delta Wing-Body, experimental data compared with USM3D and OVERFLOW solutions, M=1.7, h=32 in., Re=2.43x10^6 (continued)

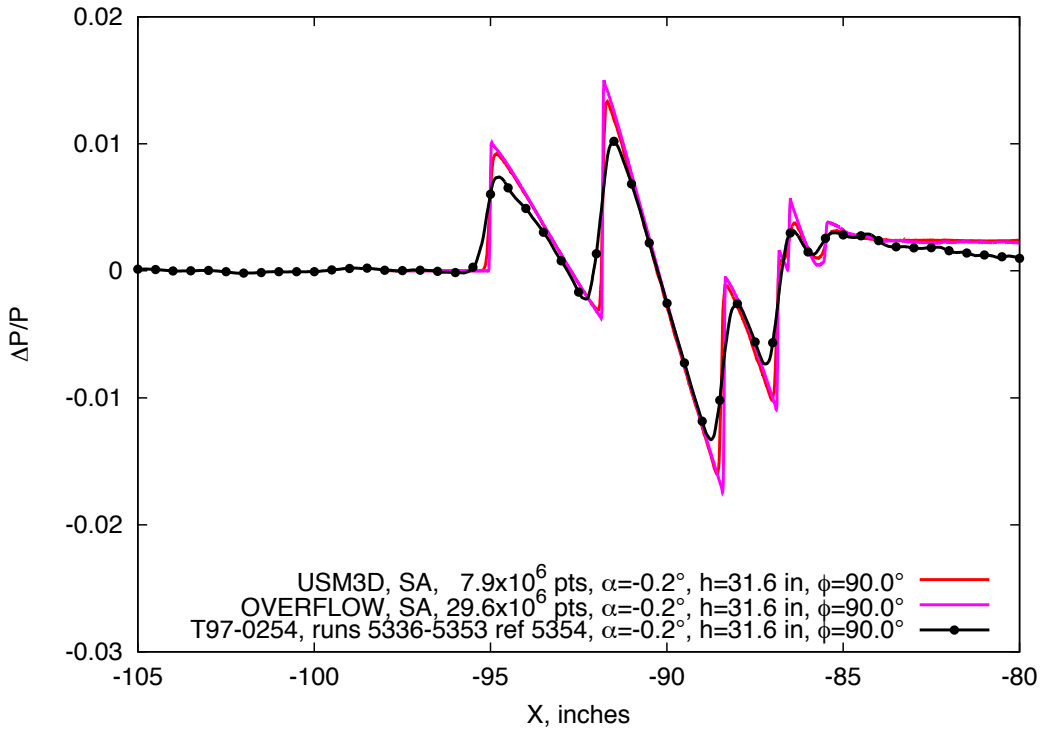

(d) ϕ=90°

Figure 9.51. 69° Delta Wing-Body, experimental data compared with USM3D and OVERFLOW solutions, M=1.7, h=32 in., Re=2.43x10^6 (concluded)

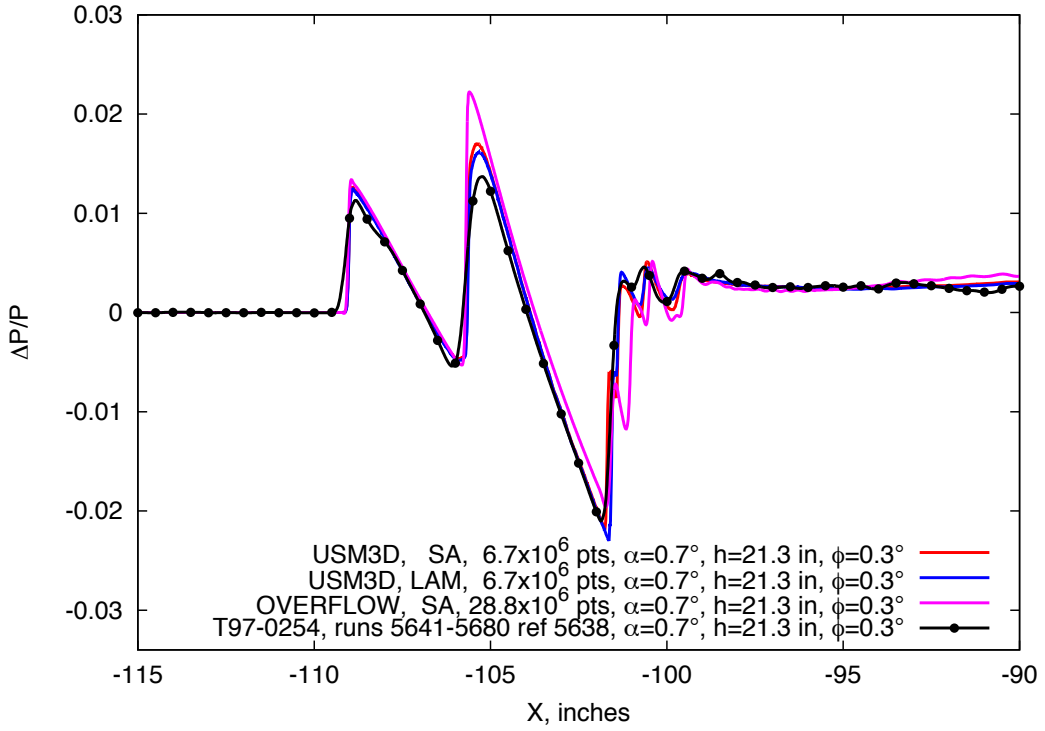

(a) α=0.7°, h=21.3 inches

Figure 9.52. 69° Delta Wing-Body, experimental data compared with USM3D and OVERFLOW computations, M=1.7, ϕ=0°, h=21- and 25-in., Re=2.43x10^6 (continues)

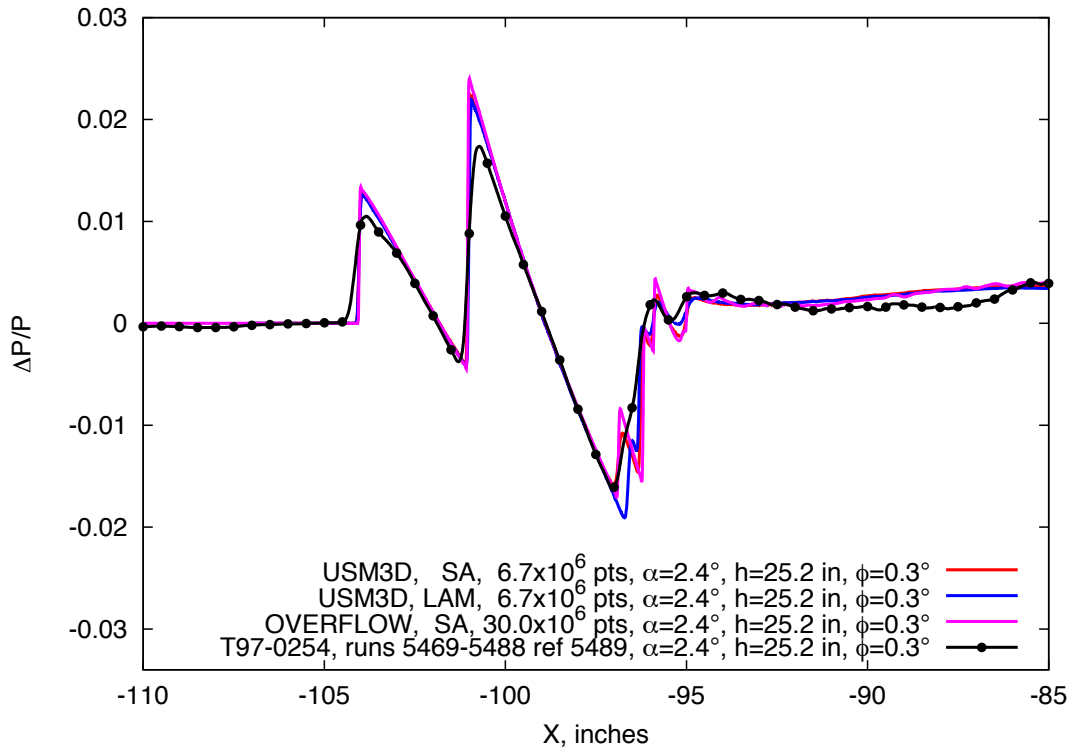

(b) α=2.4°, h=25.2 inches

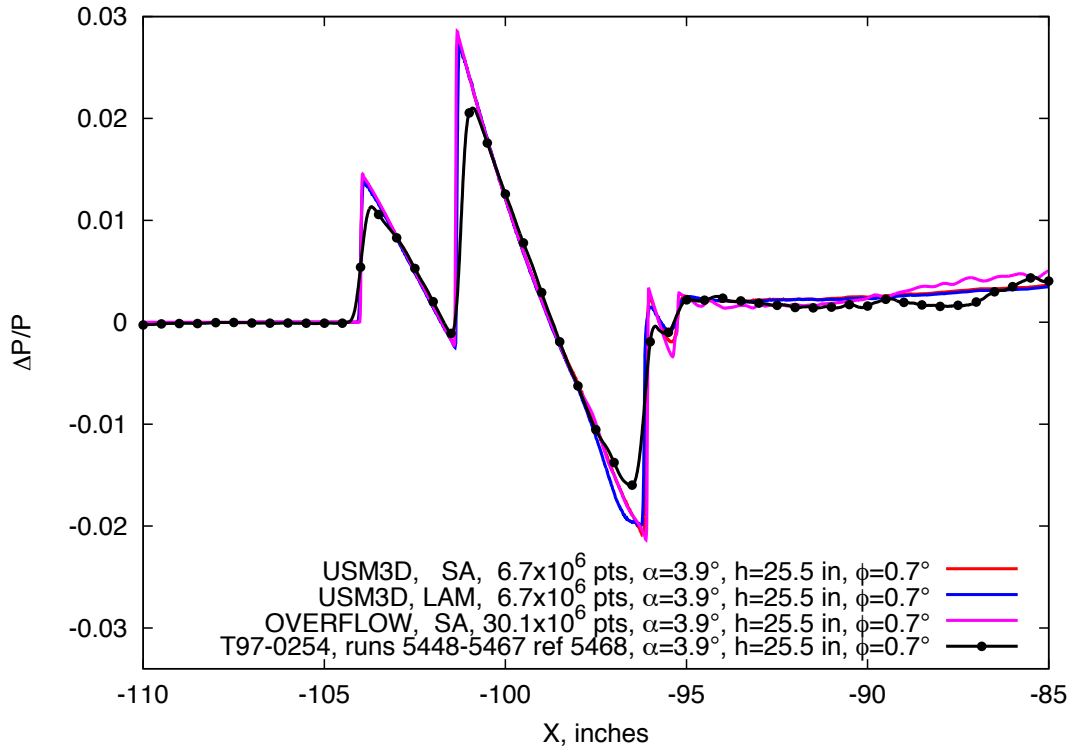

(c) α=3.9°, h=25.5 inches

Figure 9.52. 69° Delta Wing-Body, experimental data compared with USM3D and OVERFLOW computations, M=1.7, ϕ=0°, h=21- and 25-in., Re=2.43x10^6 (concluded)

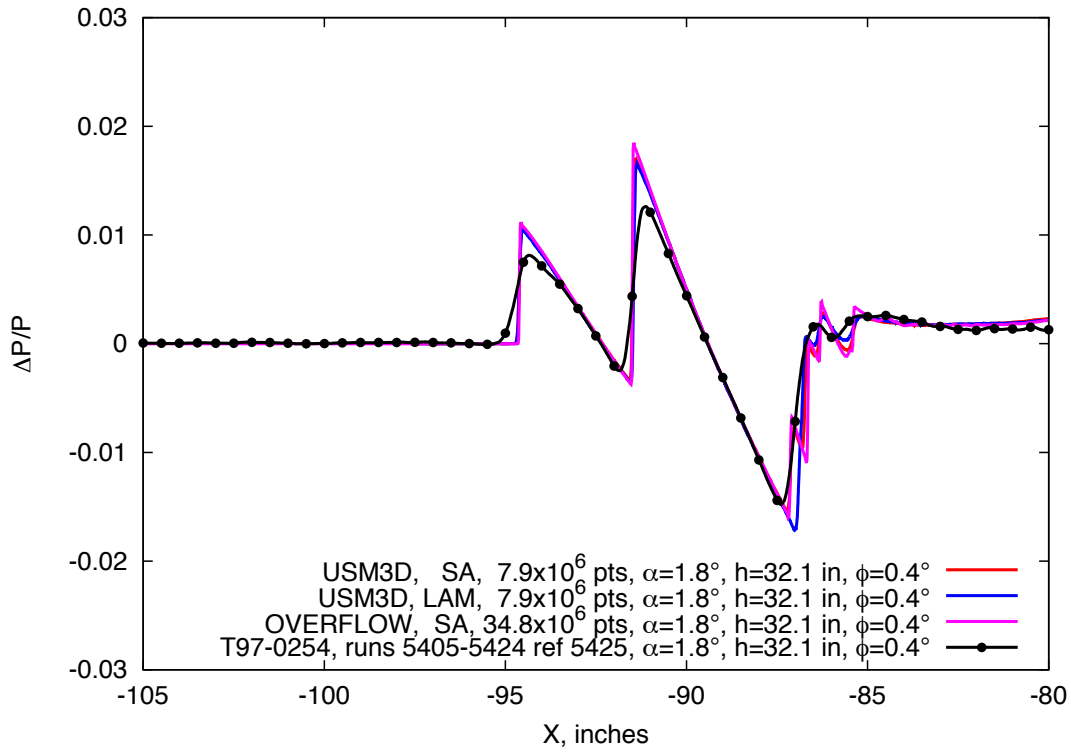

(a) α=1.8°, h=32.1 inches

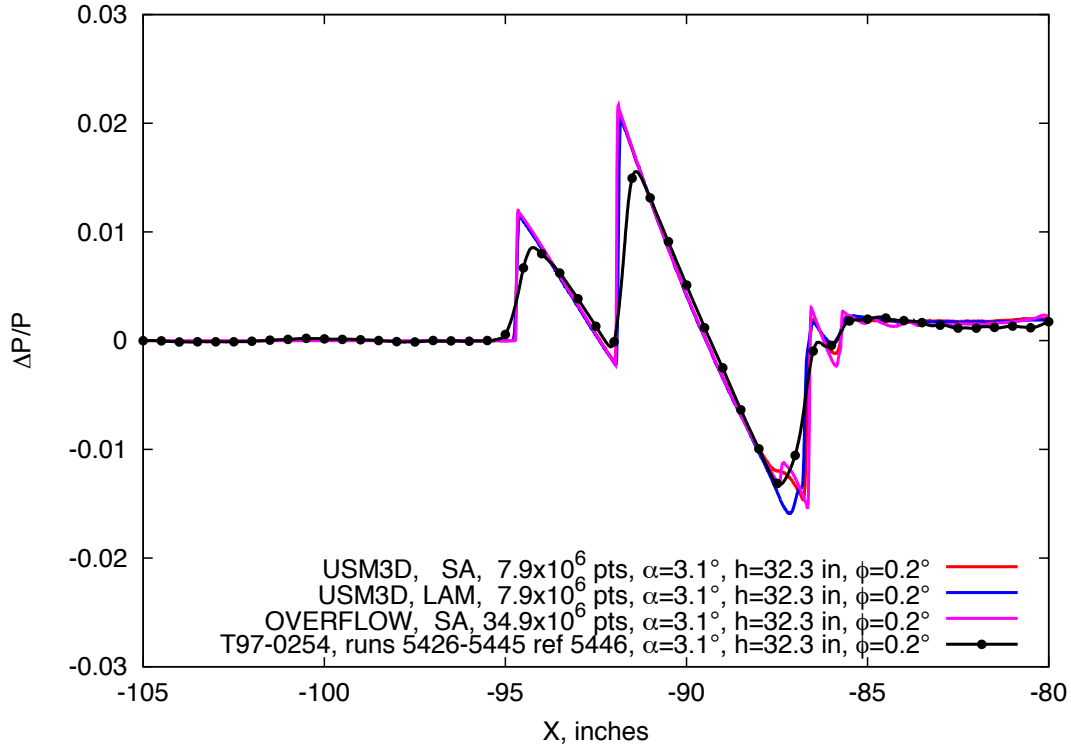

(b) α=3.1°, h=32.2 inches

Figure 9.53. 69° Delta Wing-Body, experimental data compared with USM3D and OVERFLOW computations, M=1.7, ϕ=0°, h=32 in., Re=2.43x10^6

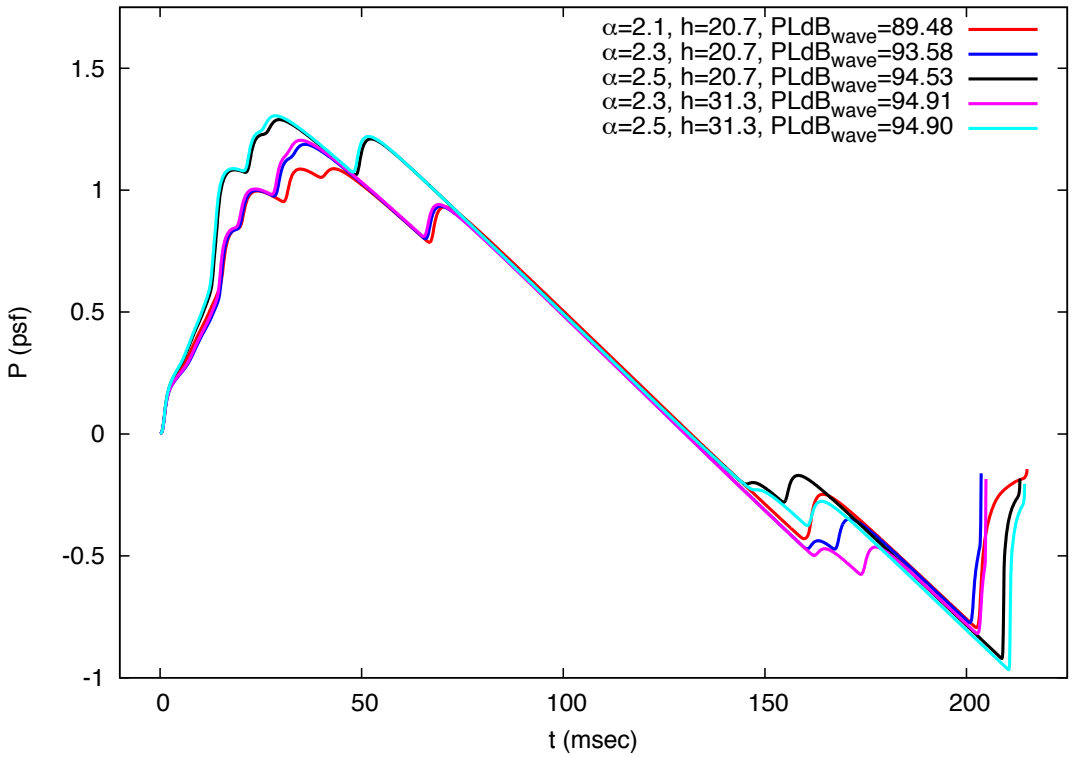

Figure 10.1. Ground level signatures of the Phase I 1021 model, extrapolated USM3D computed pressure signatures, M=1.6, h=50,000 ft. Near-field signatures taken from 20.7 and 31.3 inches at α=2.1°, 2.3°, and 2.5°

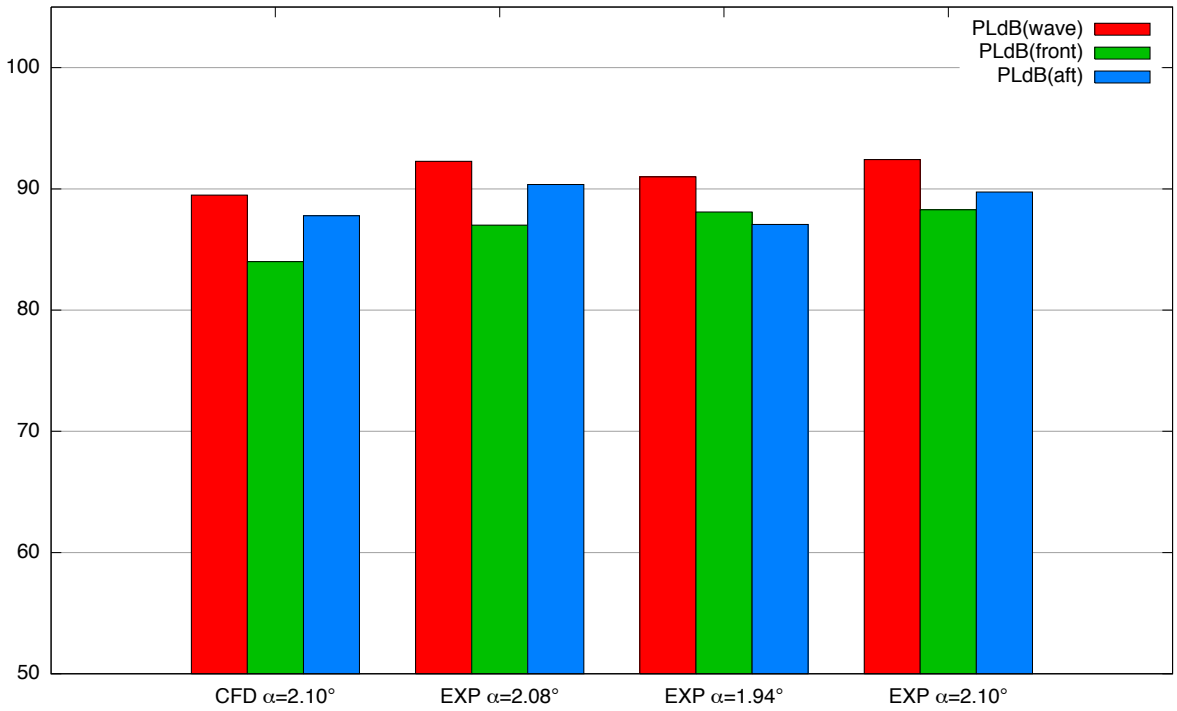

Figure 10.2. Noise level prediction from CFD and Experiment (h=21, lower α) of the Phase I 1021 model

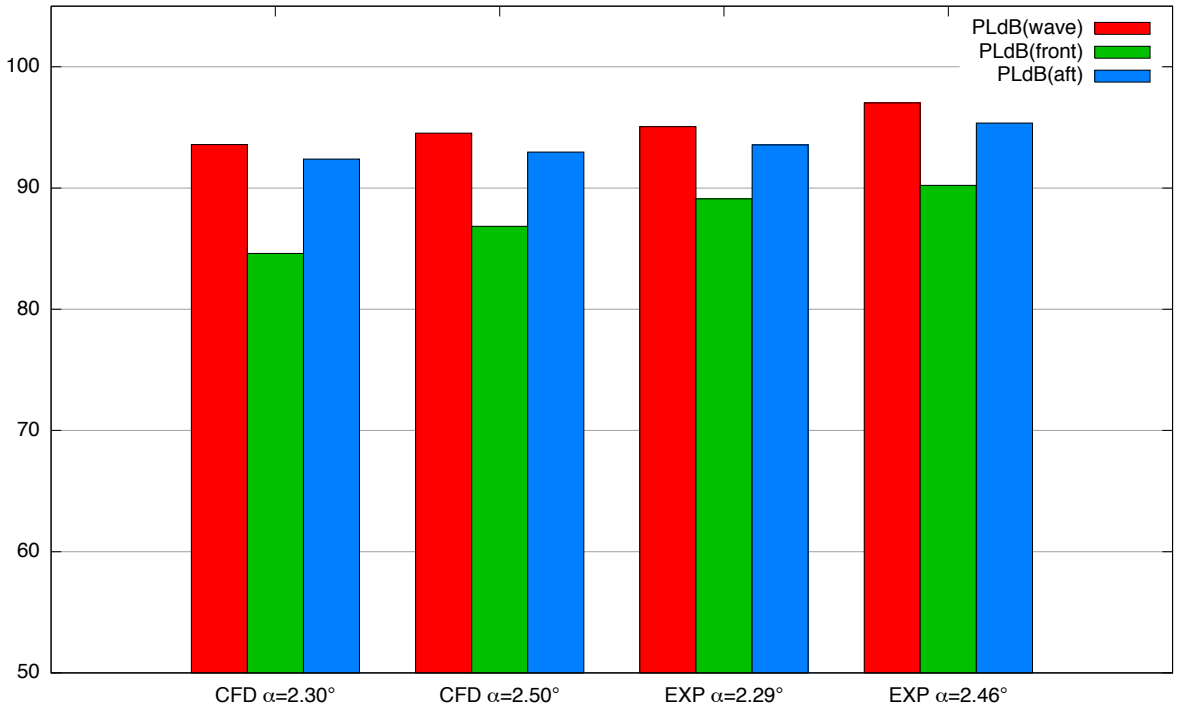

Figure 10.3. Noise level prediction from CFD and Experiment (h=21, higher α) of the Phase I 1021 model

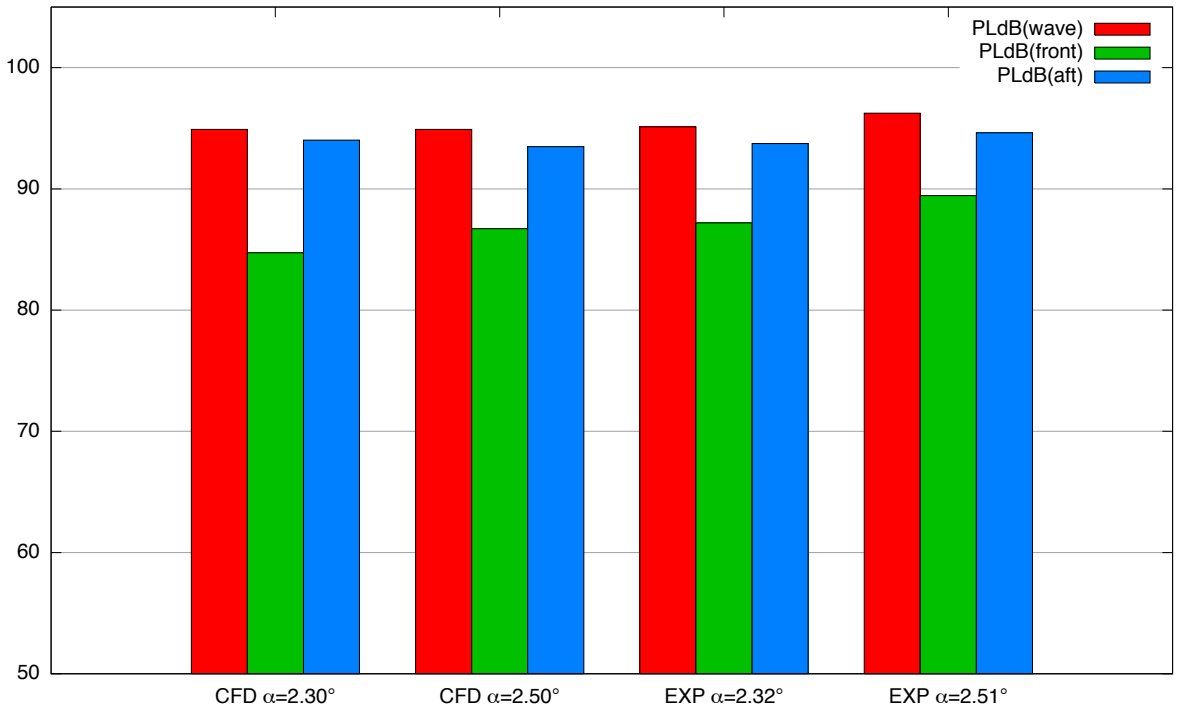

Figure 10.4. Noise level prediction from CFD and Experiment (h=31, higher α) of the Phase I 1021 model

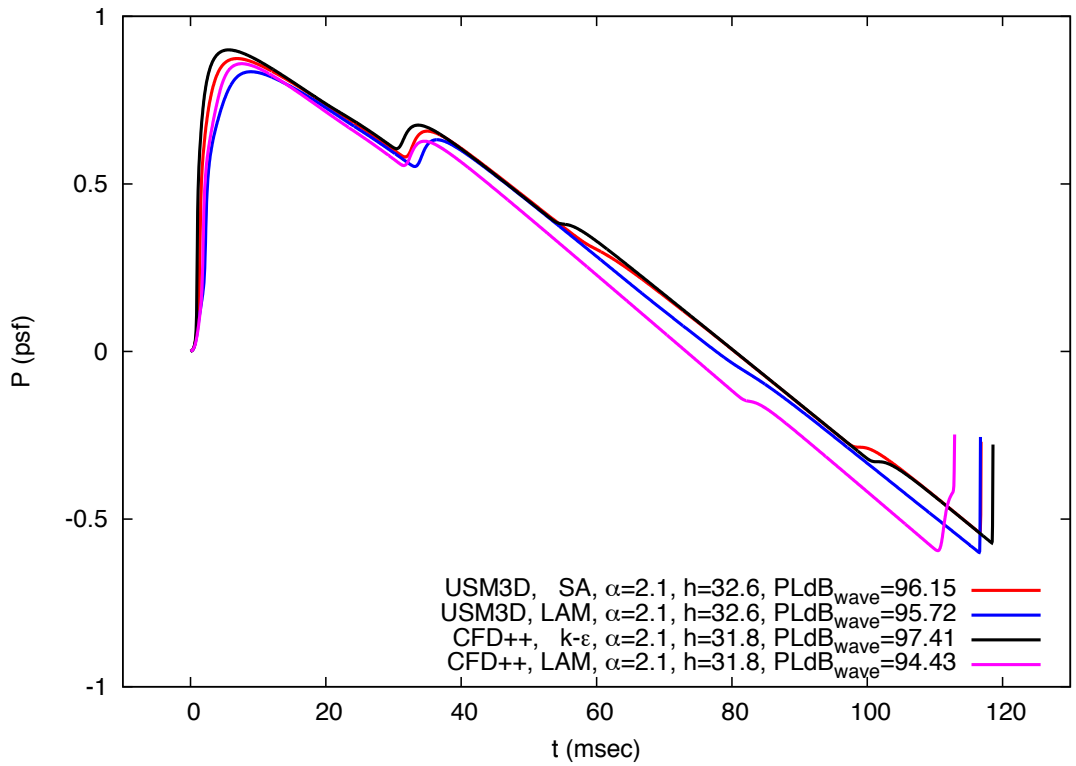

Figure 10.5. Ground level signatures of Phase II 1044 model, extrapolated USM3D and CFD++ (laminar and turbulent flow) computed pressure signatures, M=1.7, h=50,000 ft. Near-field signatures taken from 32.6 (USM3D) and 31.8 (CFD++) inches at α=2.1°

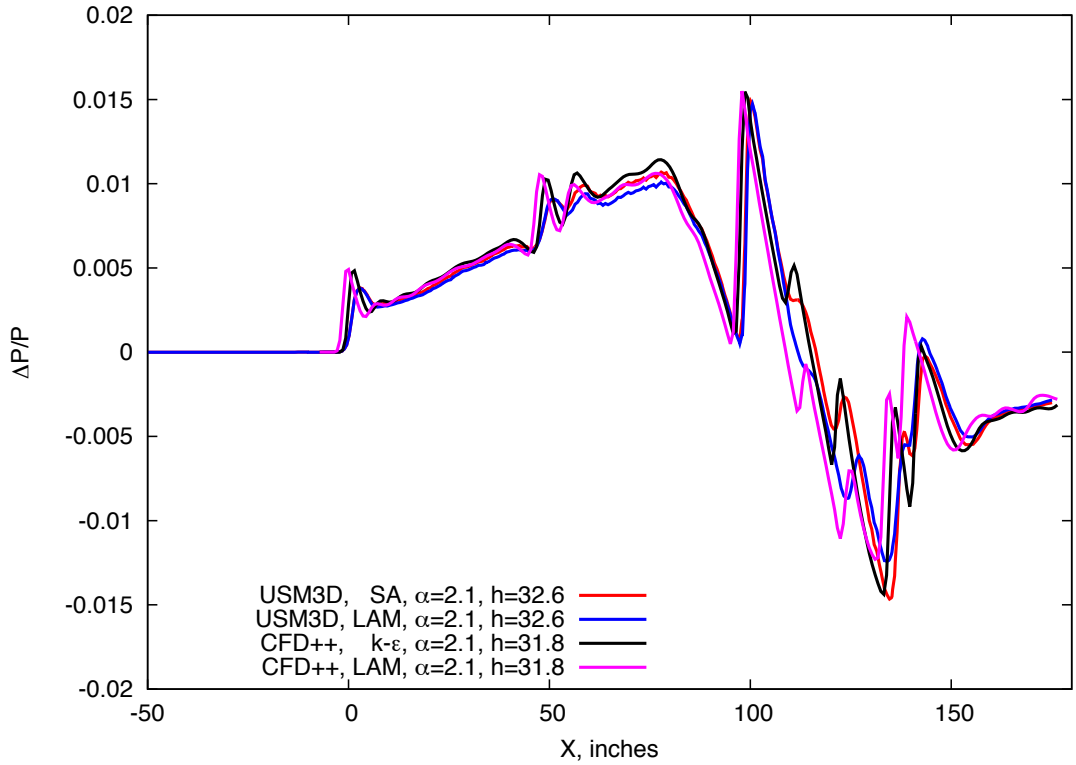

Figure 10.6. SBOOM input pressure signatures at 32 inches for the 1044 phase II 1044 wind tunnel model

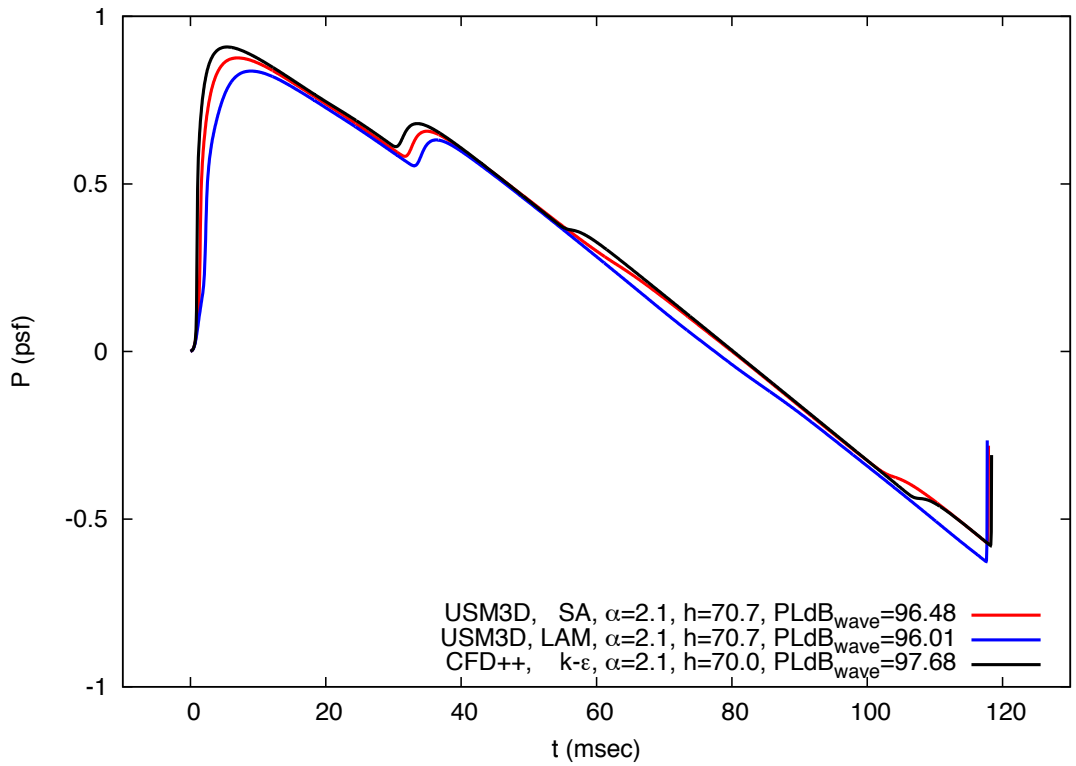

Figure 10.7. Ground level signatures for the Phase II 1044 model, extrapolated USM3D (laminar and turbulent) and CFD++ (turbulent) computed pressure signatures, M=1.7, h=50,000 ft. Near-field signatures taken from 70.7 (USM3D) and 70.0 (CFD++) inches at α=2.1°

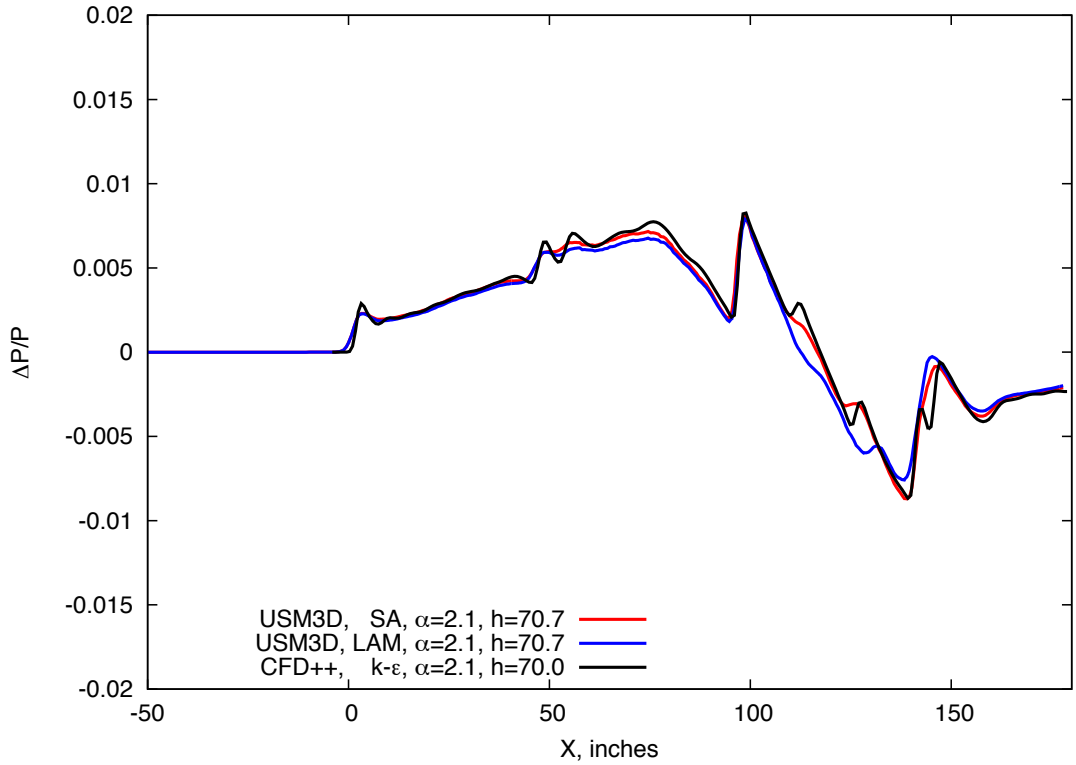

Figure 10.8. SBOOM input pressure signatures at 70 inches for the Phase II 1044 wind tunnel model

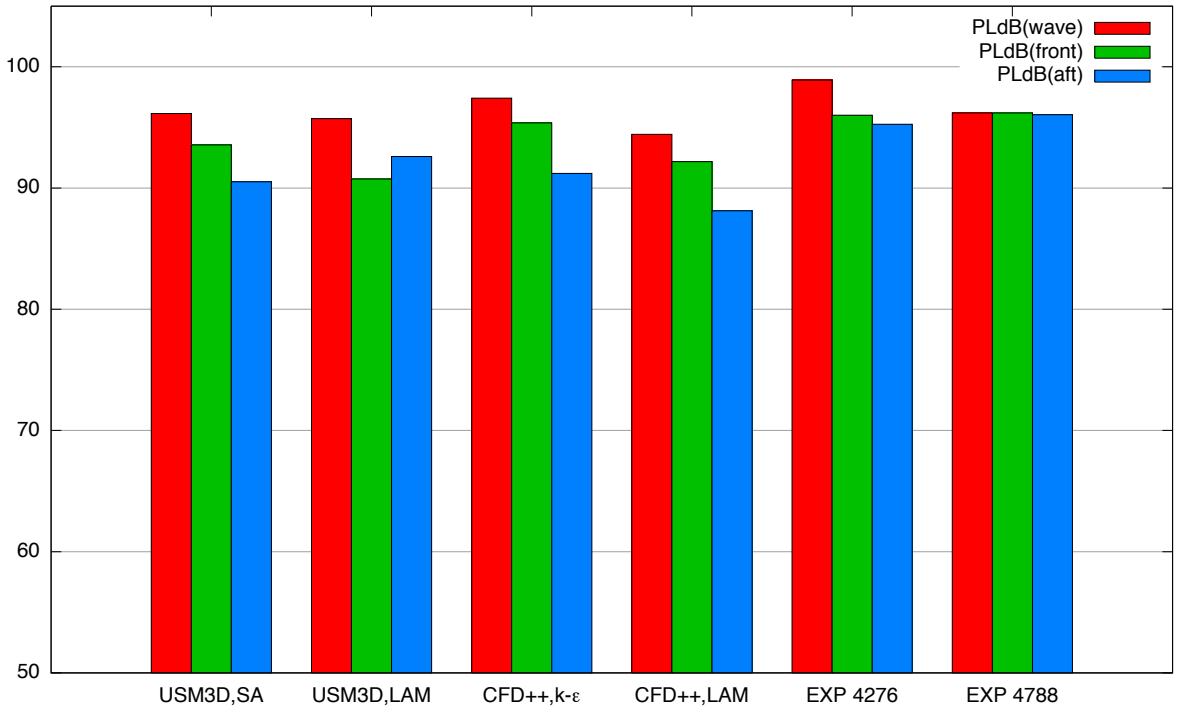

Figure 10.9. Noise level prediction from CFD and Experiment, α=2.1°, h=32 inches of the Phase II 1044 model

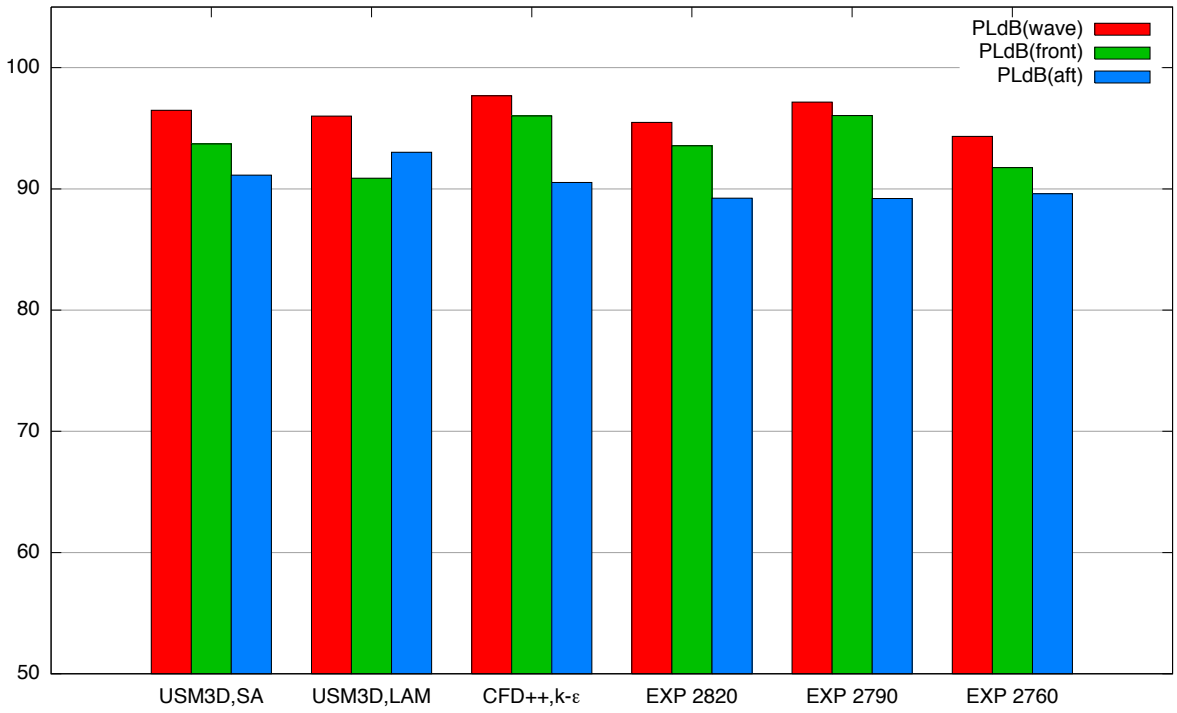

Figure 10.10. Noise level prediction from CFD and Experiment, α=2.1°, h=70 inches of the Phase II 1044 model

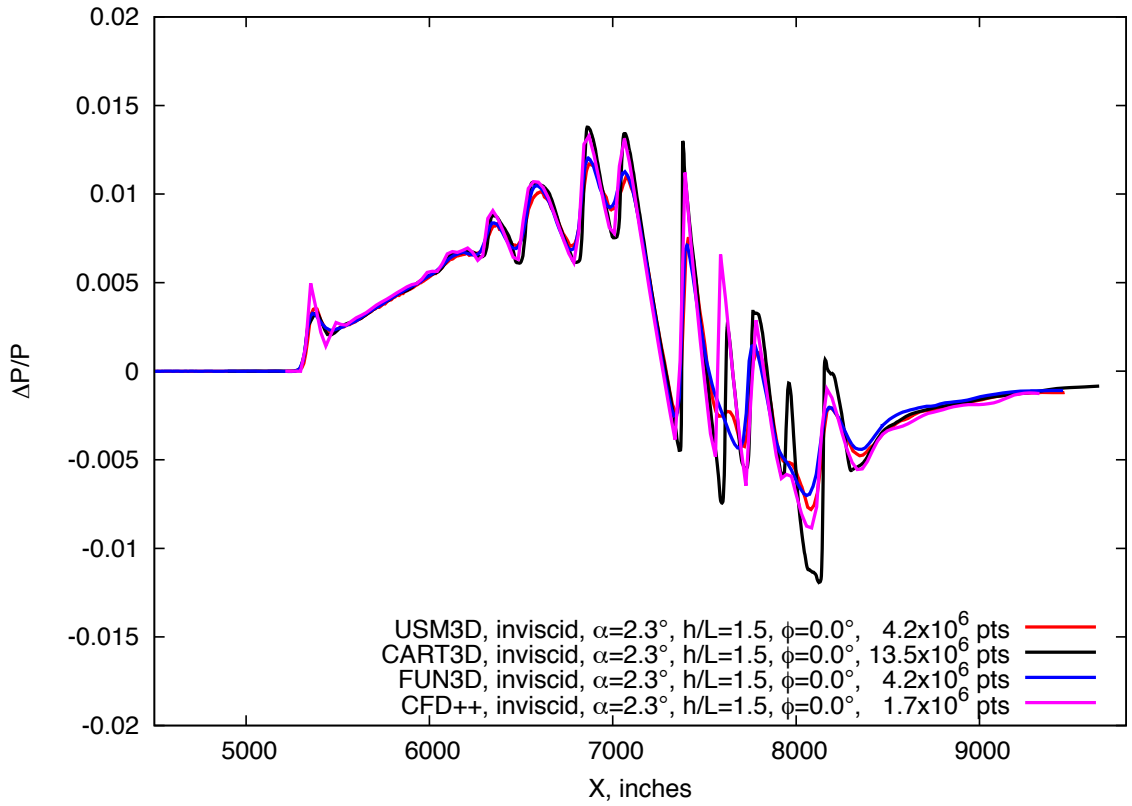

Figure 11.1. Phase I flight vehicle, Euler solutions at cruise conditions, M=1.6, h/L=1.5, ϕ=0°

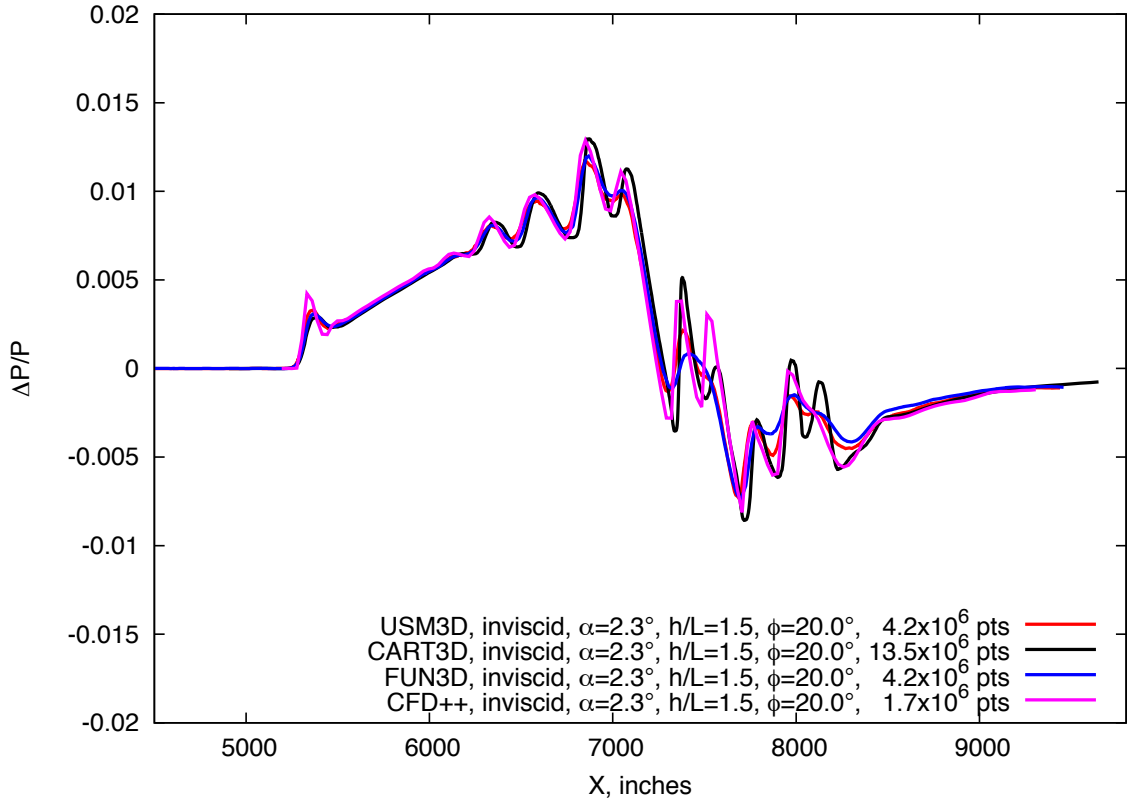

Figure 11.2. Phase I flight vehicle, Euler solutions at cruise conditions, M=1.6, h/L=1.5, ϕ=20°

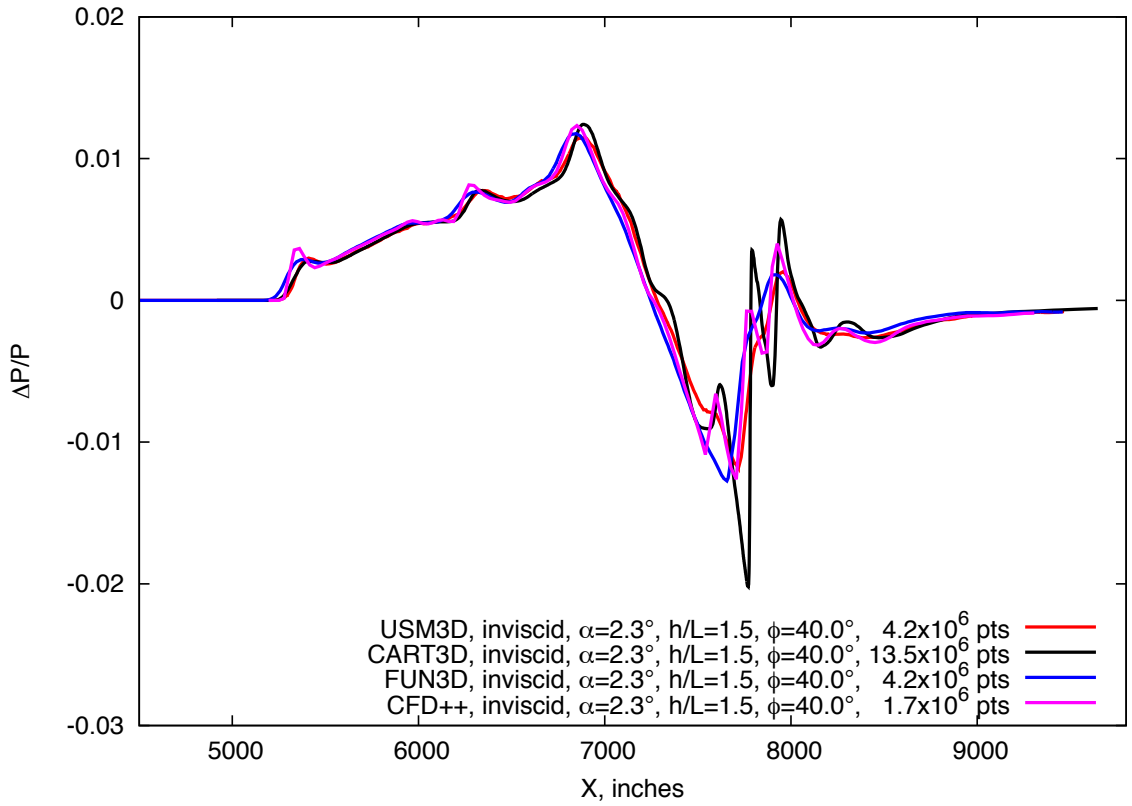

Figure 11.3. Phase I flight vehicle, Euler solutions at cruise conditions, M=1.6, h/L=1.5, ϕ=40°

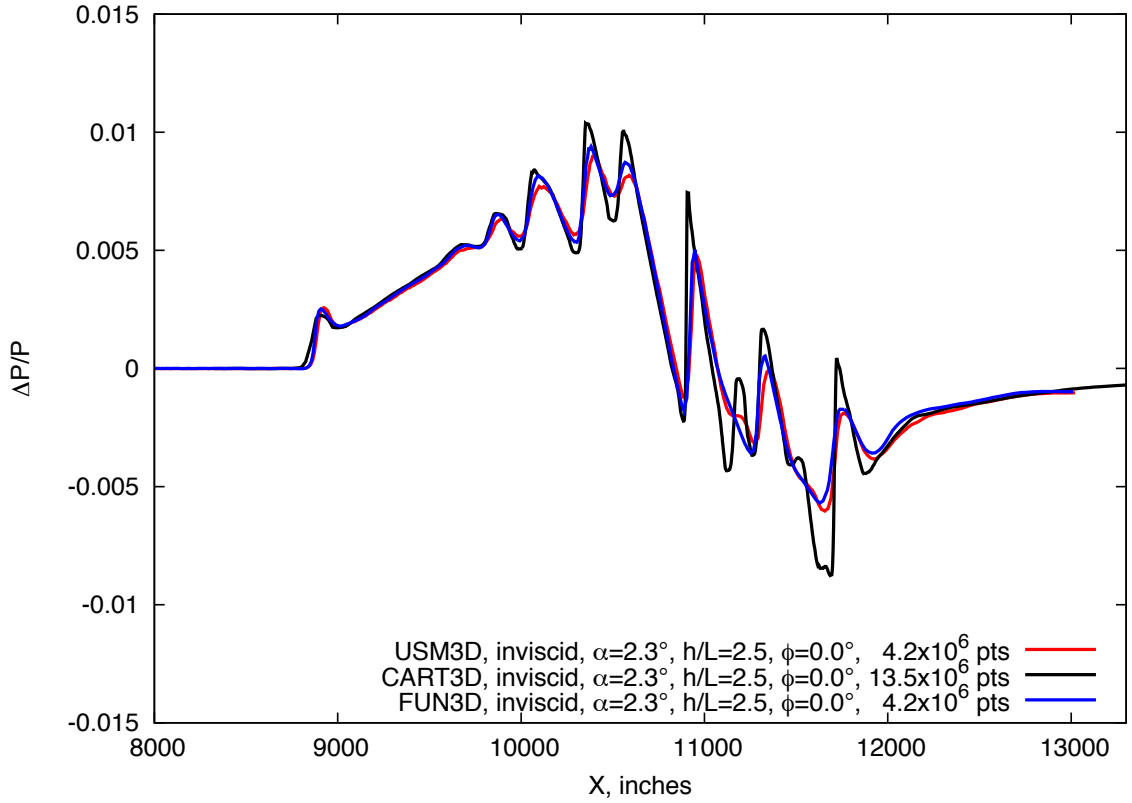

Figure 11.4. Phase I flight vehicle, Euler solutions at cruise conditions, M=1.6, h/L=2.5, ϕ=0°

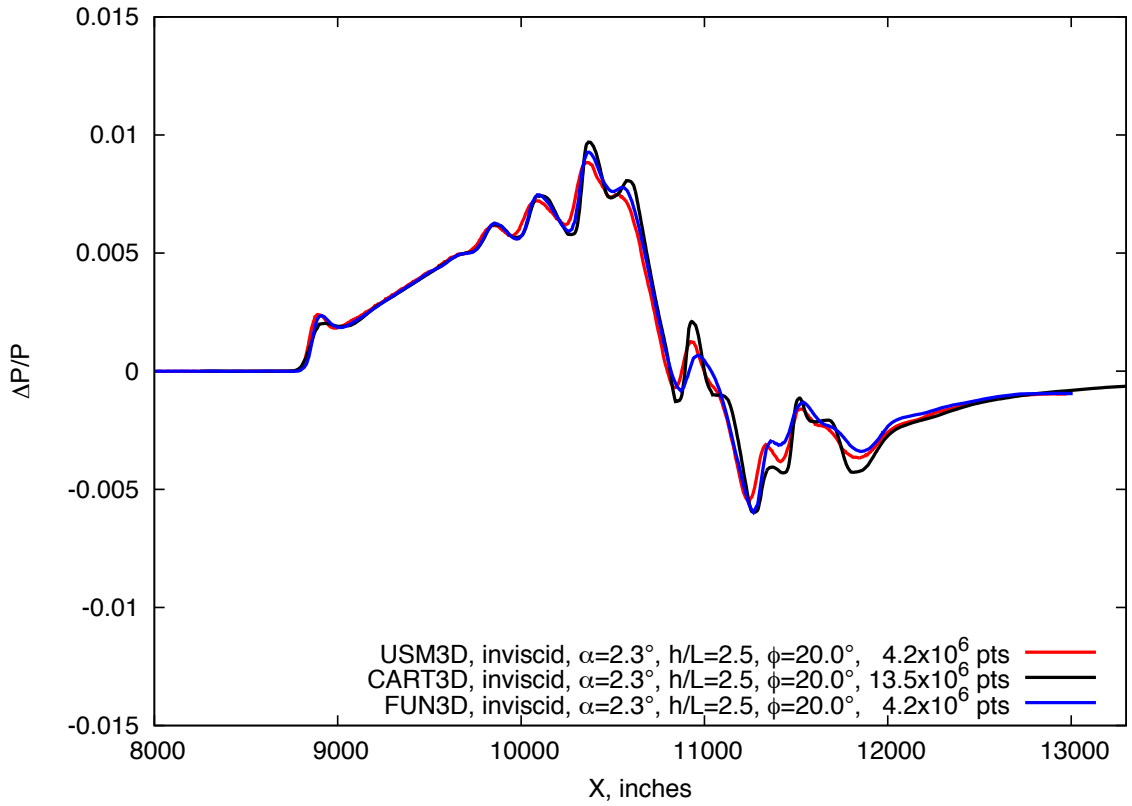

Figure 11.5. Phase I flight vehicle, Euler solutions at cruise conditions, M=1.6, h/L=2.5, ϕ=20°

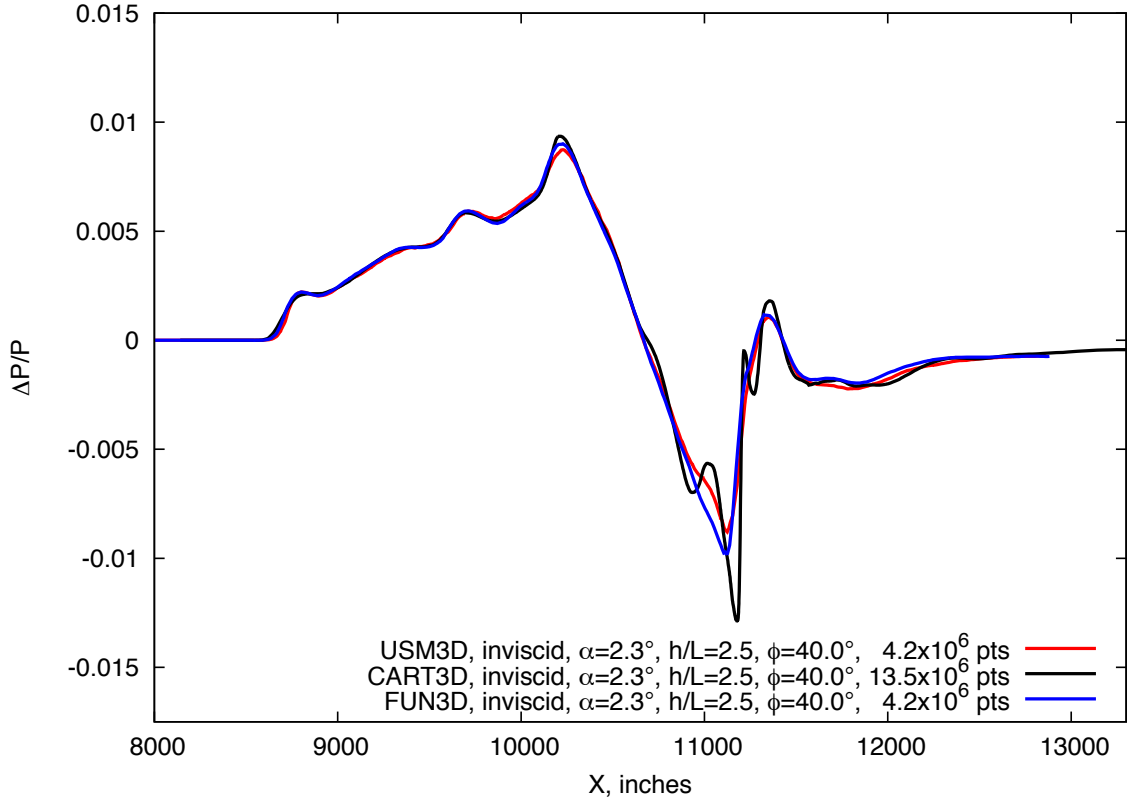

Figure 11.6. Phase I flight vehicle, Euler solutions at cruise conditions, M=1.6, h/L=2.5, ϕ=40°

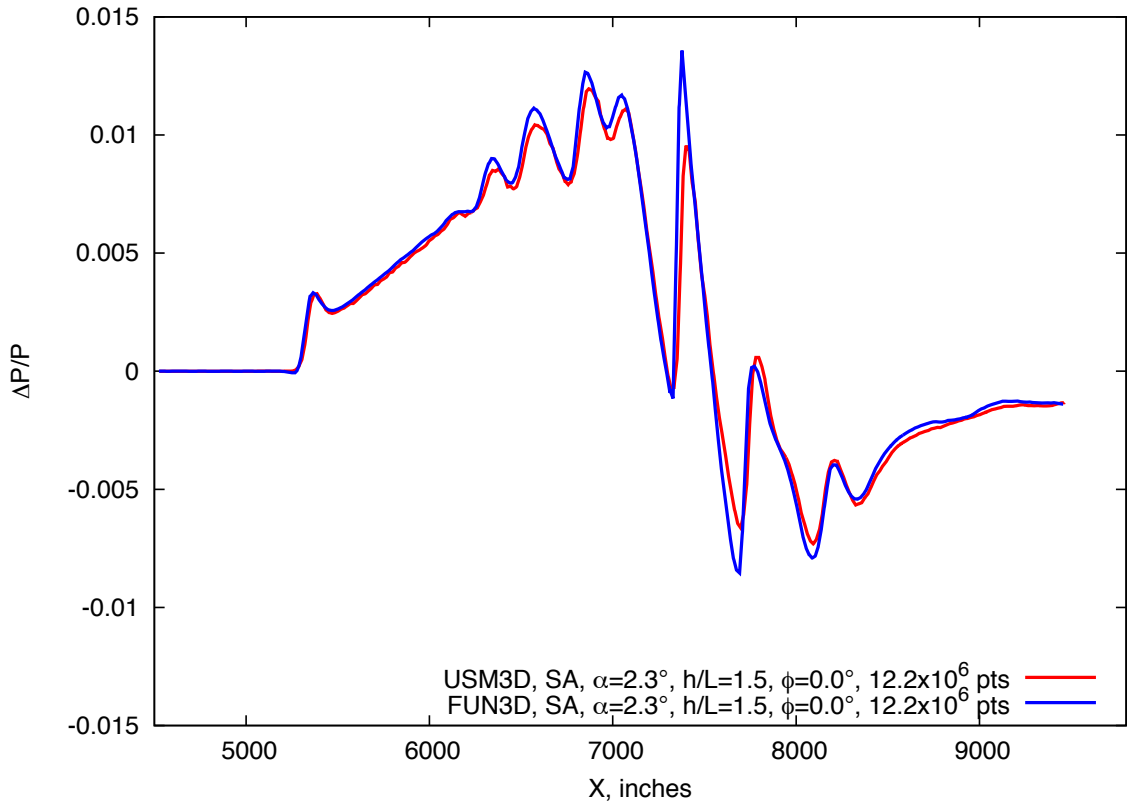

Figure 11.7. Phase I flight vehicle, Navier-Stokes solutions at cruise conditions, M=1.6, h/L=1.5, ϕ=0°

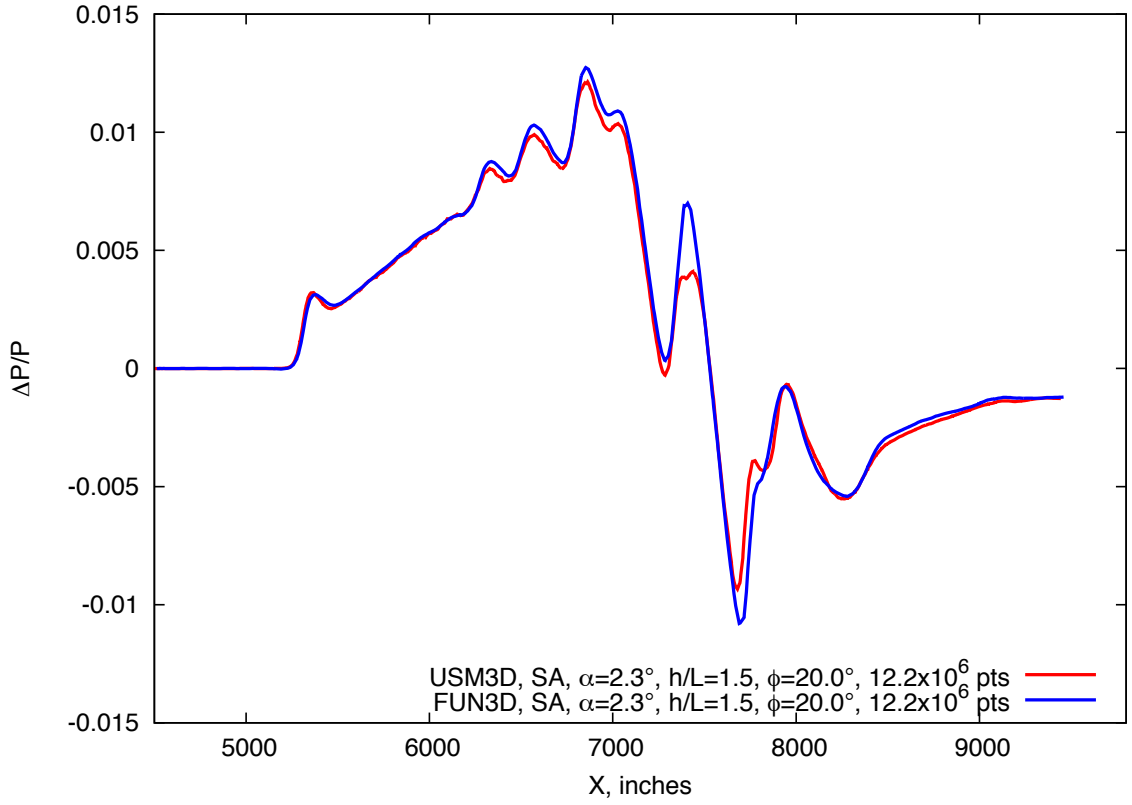

Figure 11.8. Phase I flight vehicle, Navier-Stokes solutions at cruise conditions, M=1.6, h/L=1.5, ϕ=20°

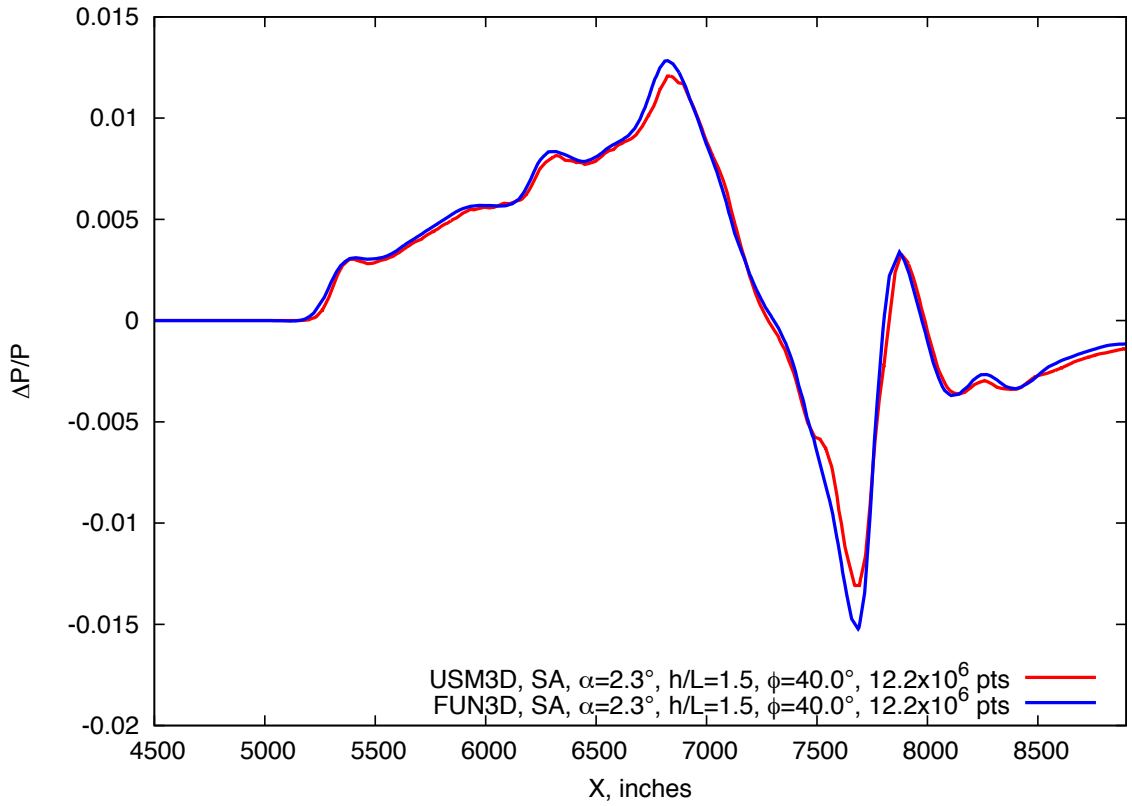

Figure 11.9. Phase I flight vehicle, Navier-Stokes solutions at cruise conditions, M=1.6, h/L=1.5, ϕ=40°

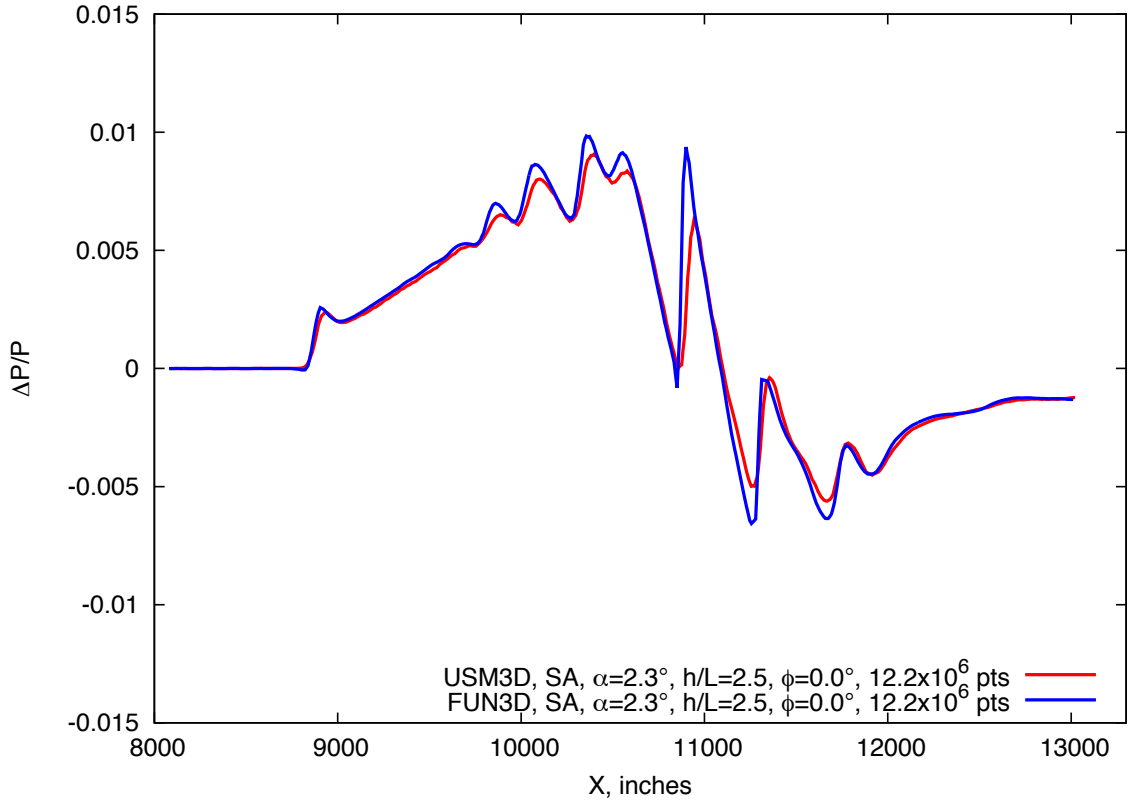

Figure 11.10. Phase I flight vehicle, Navier-Stokes solutions at cruise conditions, M=1.6, h/L=2.5, ϕ=0°

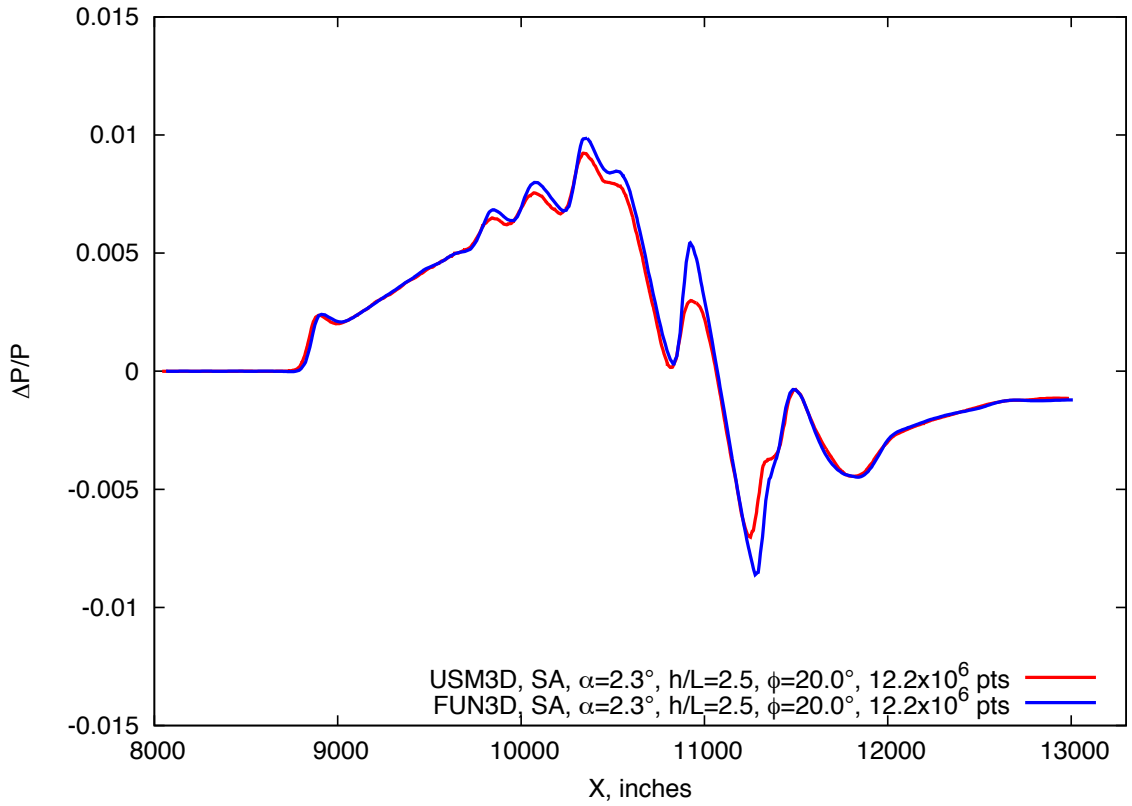

Figure 11.11. Phase I flight vehicle, Navier-Stokes solutions at cruise conditions, M=1.6, h/L=2.5, ϕ=20°

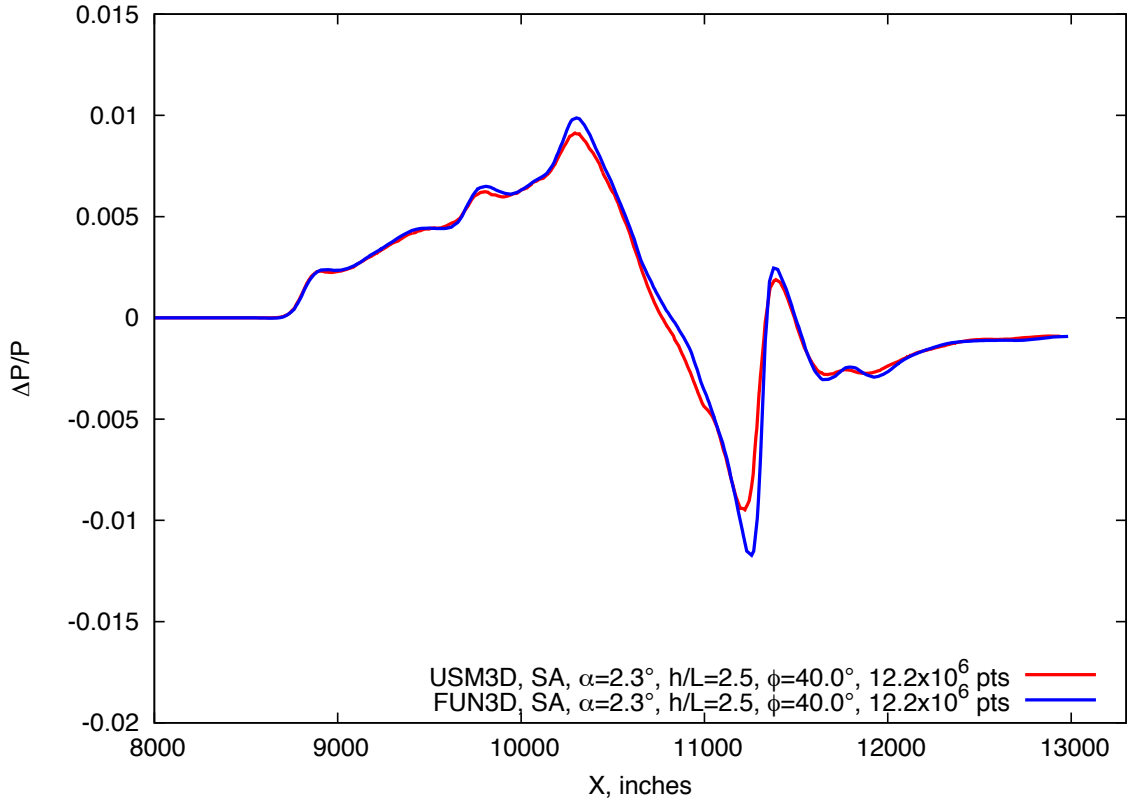

Figure 11.12. Phase I flight vehicle, Navier-Stokes solutions at cruise conditions, M=1.6, h/L=2.5, ϕ=40°

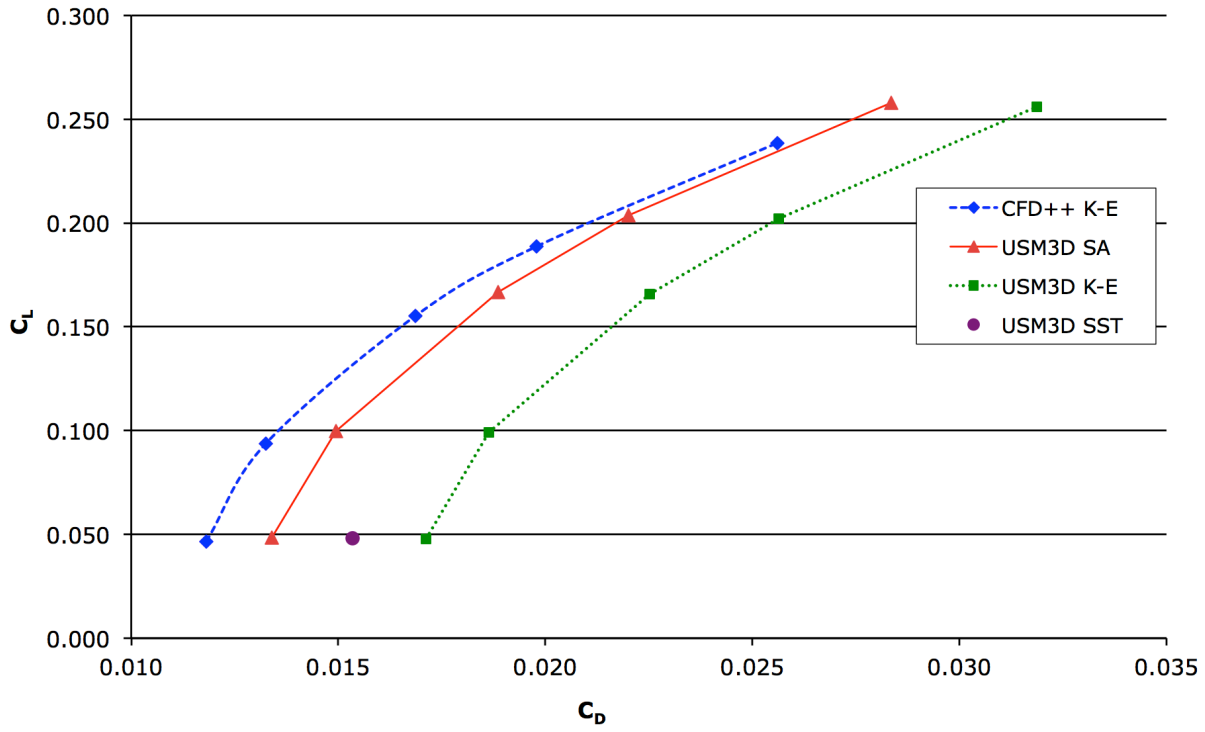

Figure 11.13. Drag polar predictions for the Phase I model with turbulence model comparisons, *M*=1.6

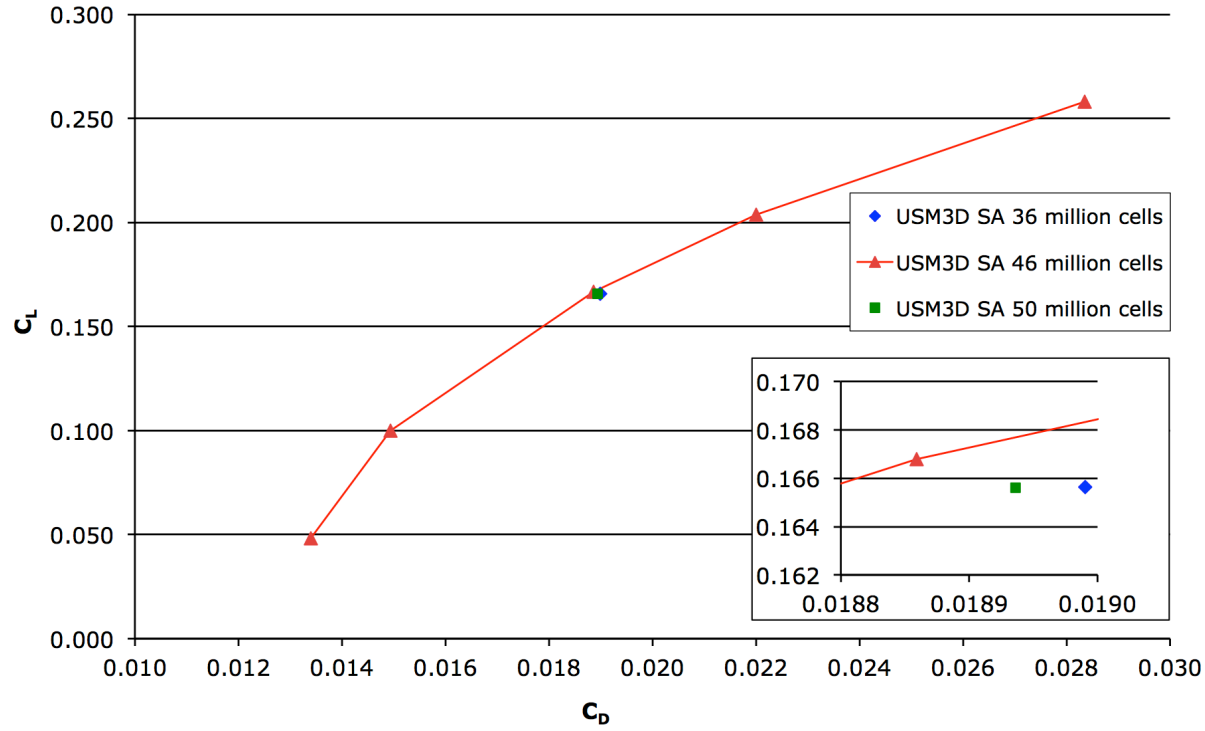

Figure 11.14. USM3D grid study for the Phase I model, *M*=1.6

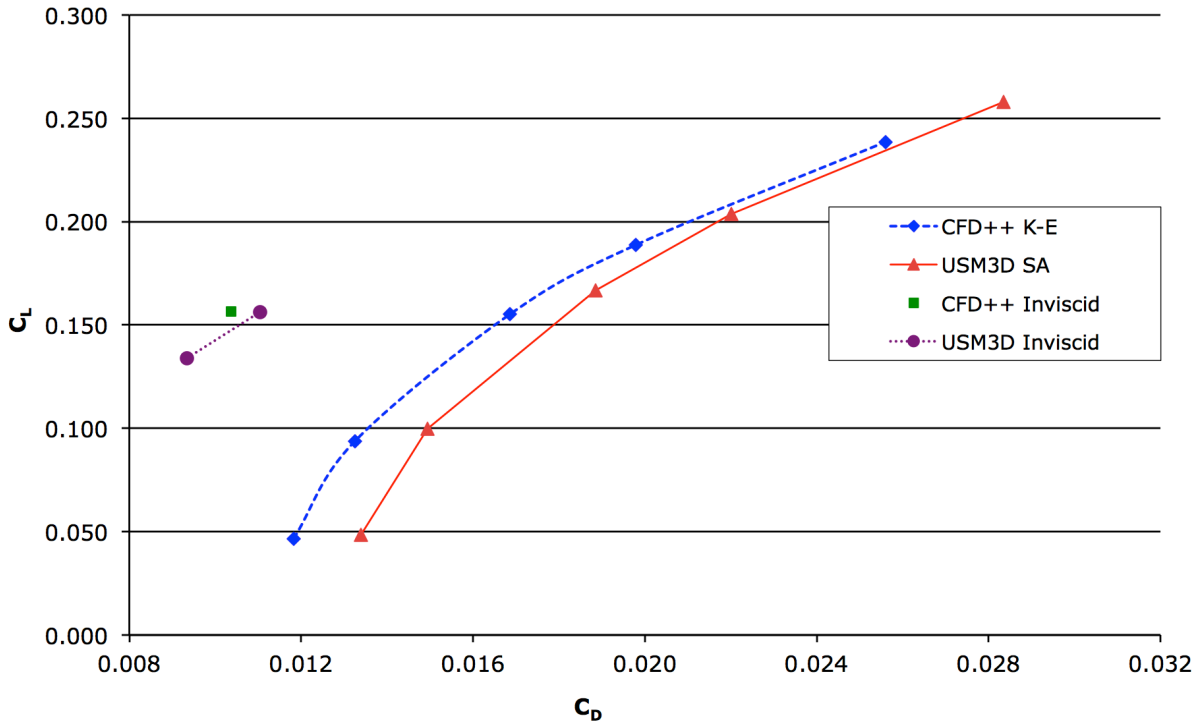

Figure 11.15. Inviscid computational results compared with the Navier-Stokes simulations Phase I model, M=1.6

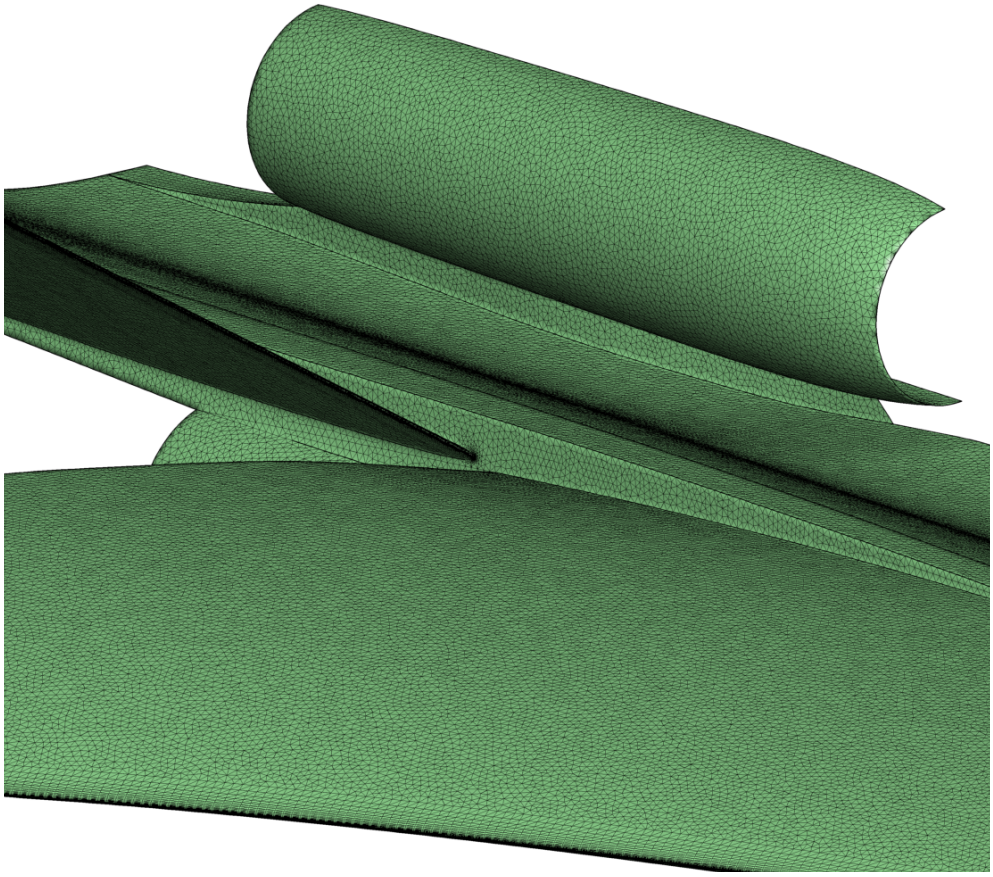

(a) Upper wing view

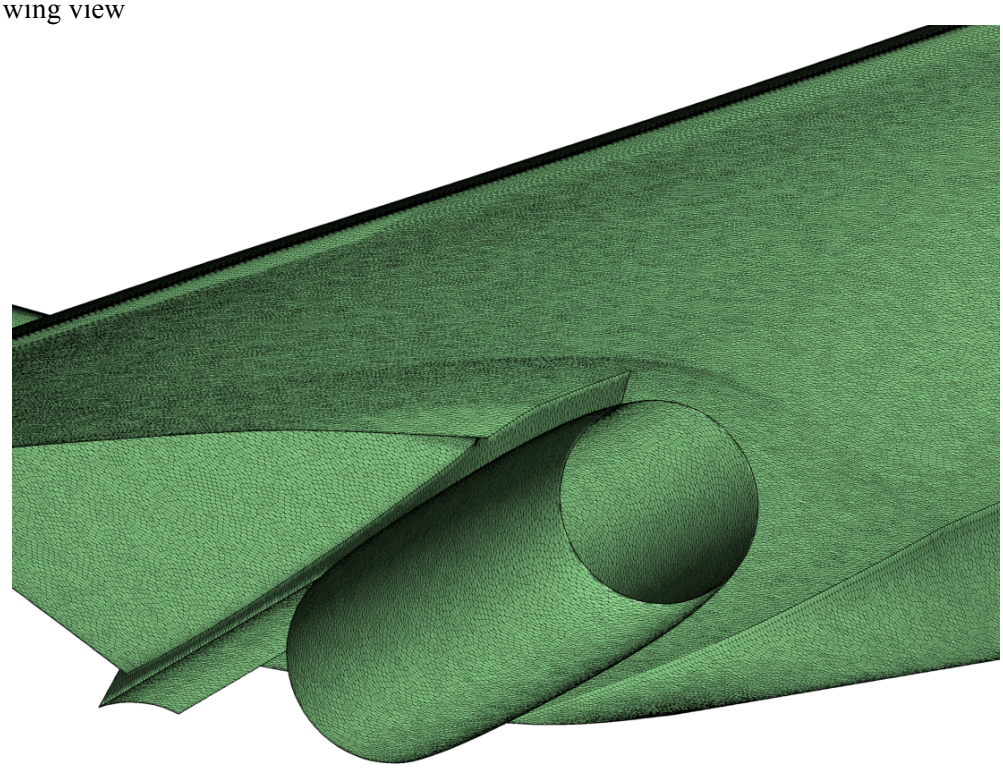

(b) Lower wing

Figure 11.16. Shaded images of the computational surface mesh of the phase II flight vehicle

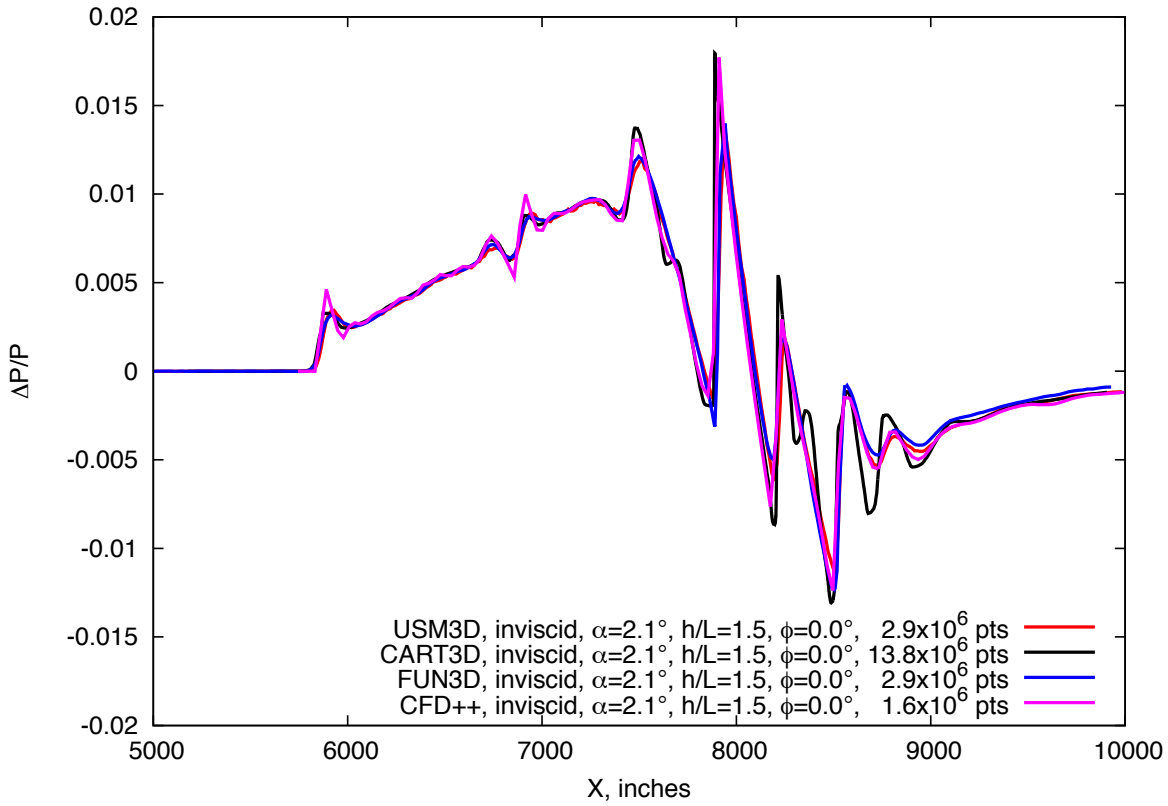

Figure 11.17. Phase II flight vehicle, Euler solutions at cruise conditions, M=1.7, h/L=1.5, ϕ=0°

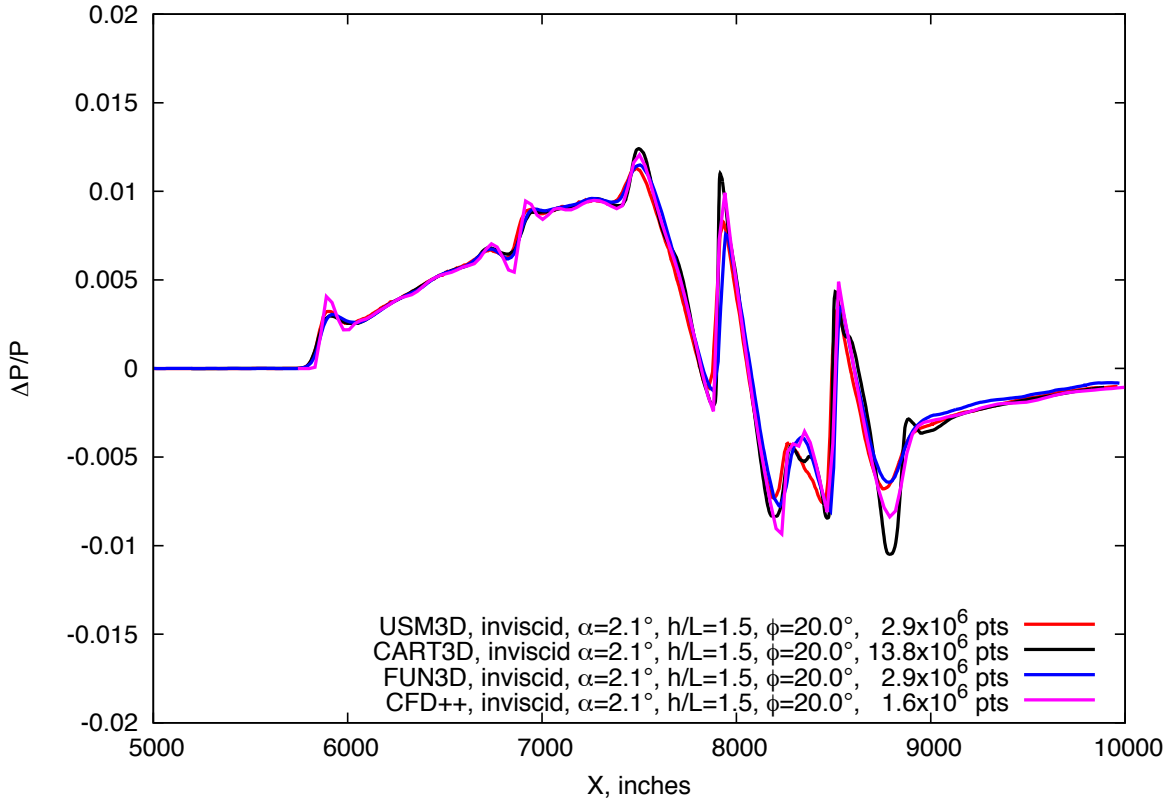

Figure 11.18. Phase II flight vehicle, Euler solutions at cruise conditions, M=1.7, h/L=1.5, ϕ=20°

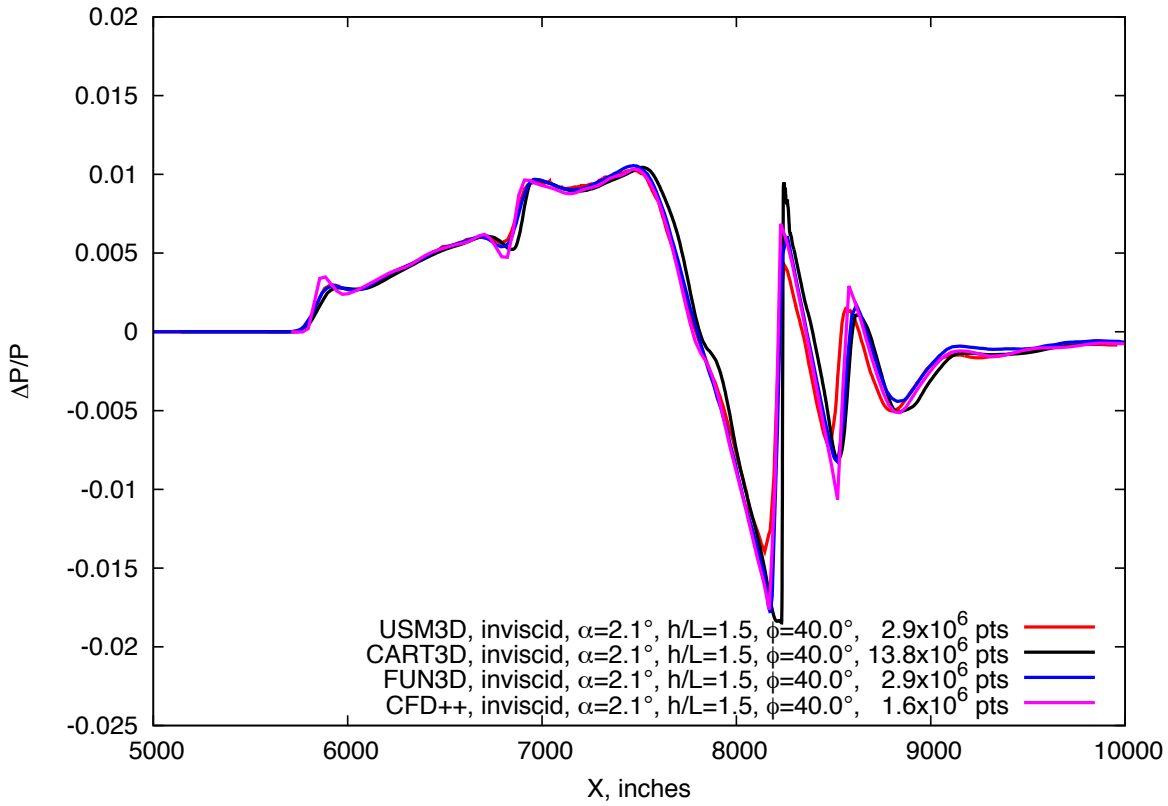

Figure 11.19. Phase II flight vehicle, Euler solutions at cruise conditions, M=1.7, h/L=1.5, ϕ=40°

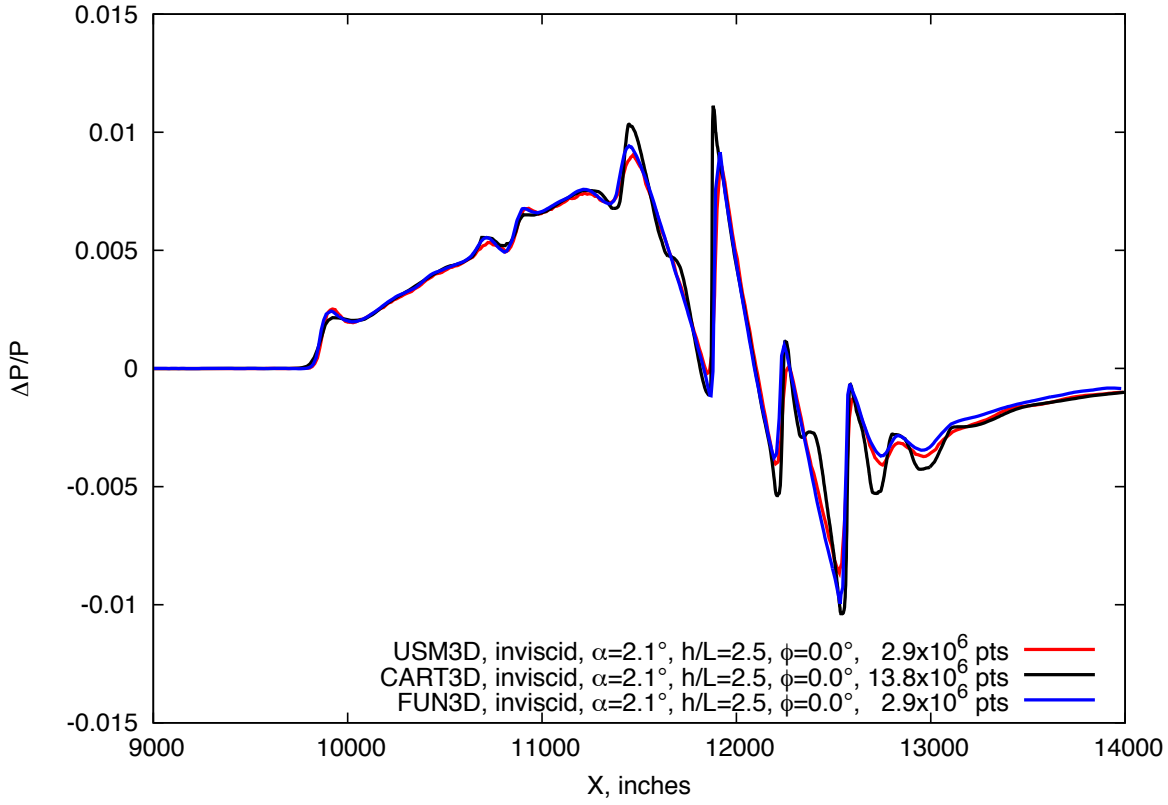

Figure 11.20. Phase II flight vehicle, Euler solutions at cruise conditions, M=1.7, h/L=2.5, ϕ=0°

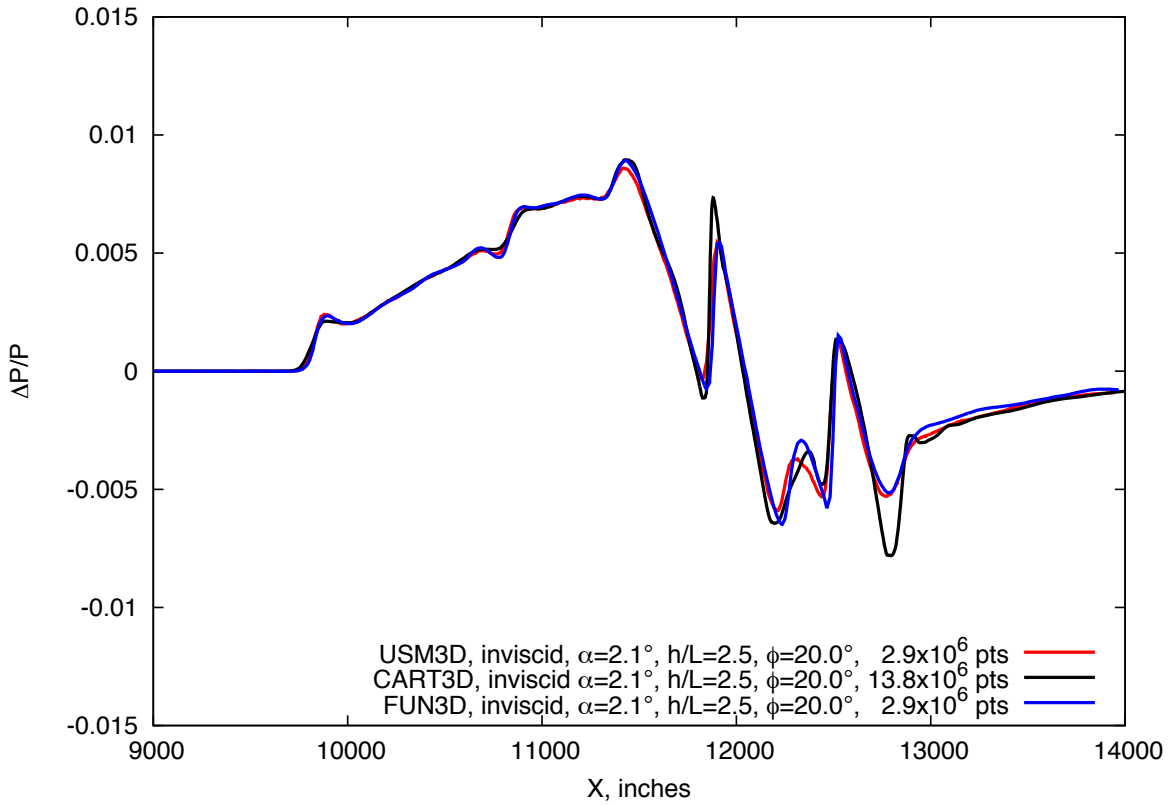

Figure 11.21. Phase II flight vehicle, Euler solutions at cruise conditions, M=1.7, h/L=2.5, ϕ=20°

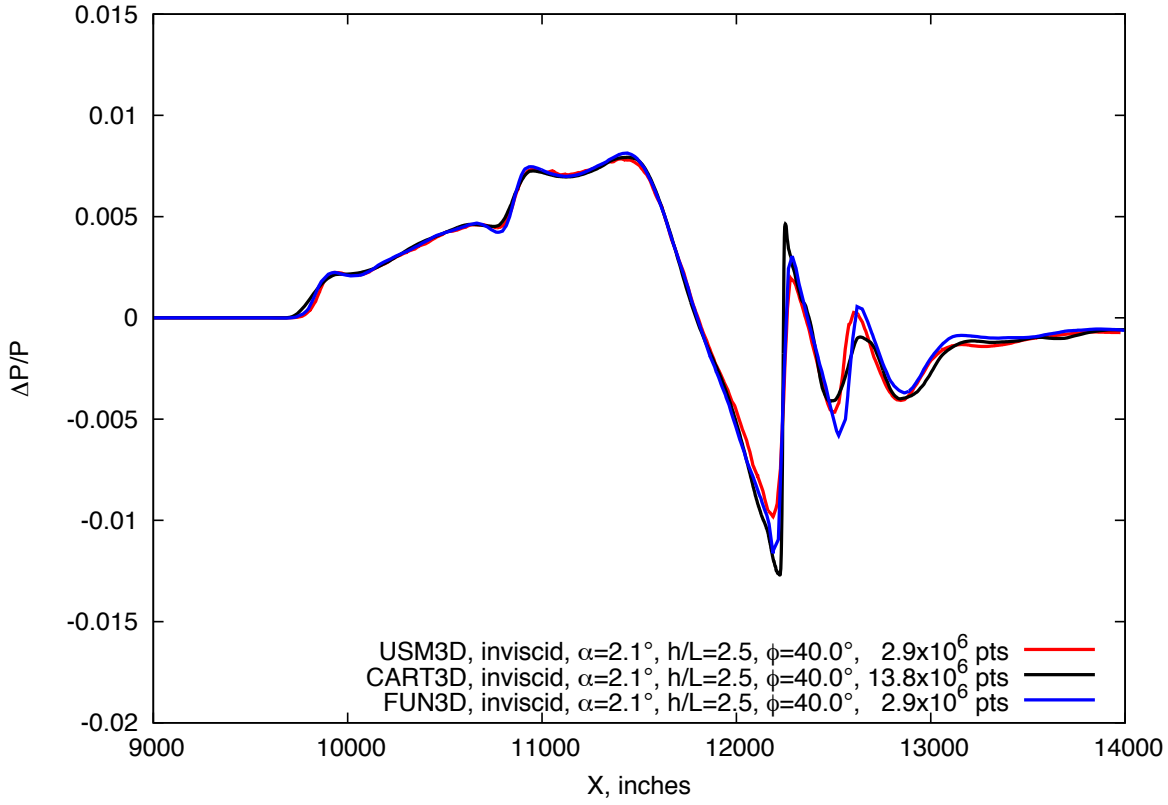

Figure 11.22. Phase II flight vehicle, Euler solutions at cruise conditions, M=1.7, h/L=2.5, ϕ=40°

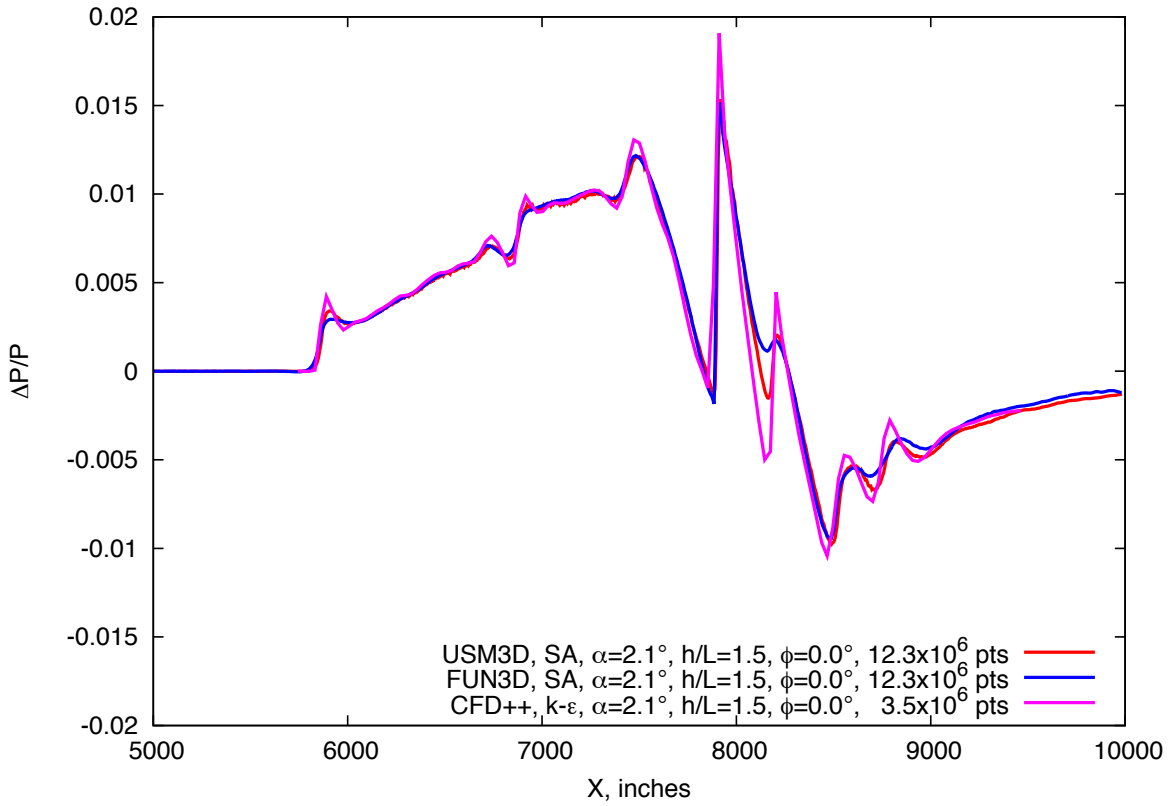

Figure 11.23. Phase II flight vehicle, Navier-Stokes solutions at cruise conditions, M=1.7, h/L=1.5, ϕ=0°

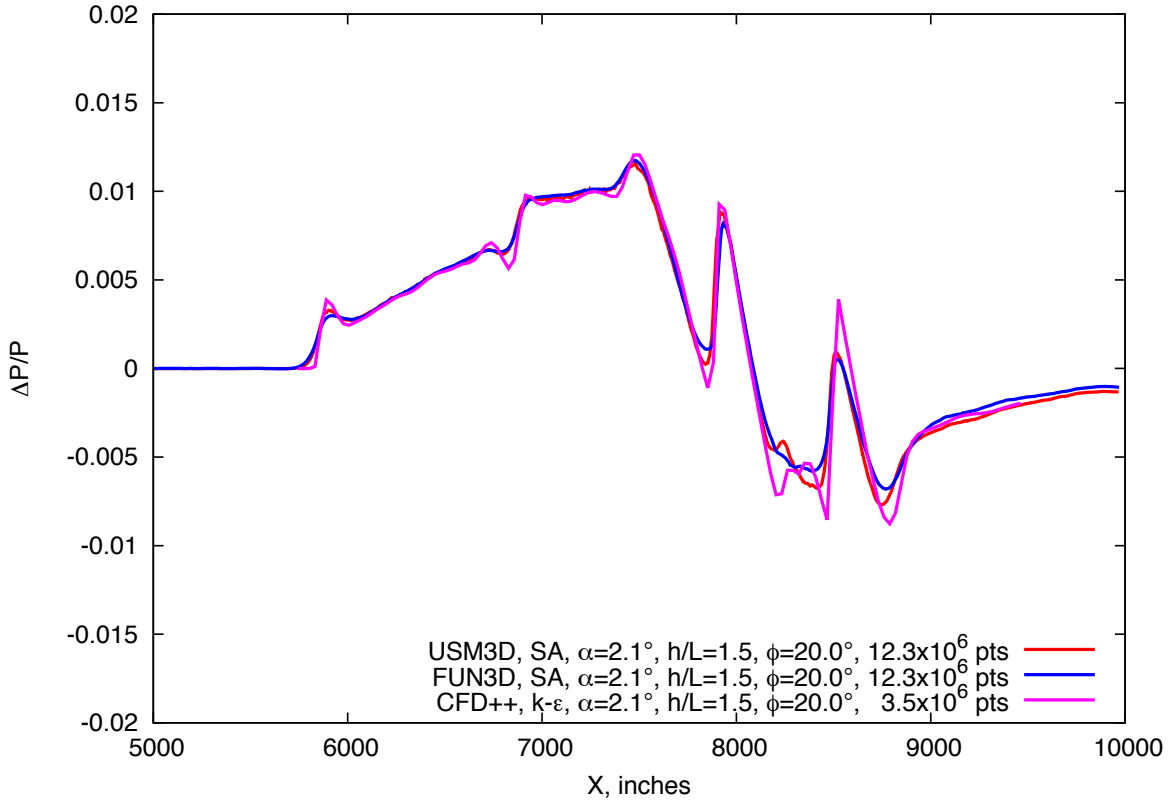

Figure 11.24. Phase II flight vehicle, Navier-Stokes solutions at cruise conditions, M=1.7, h/L=1.5, ϕ=20°

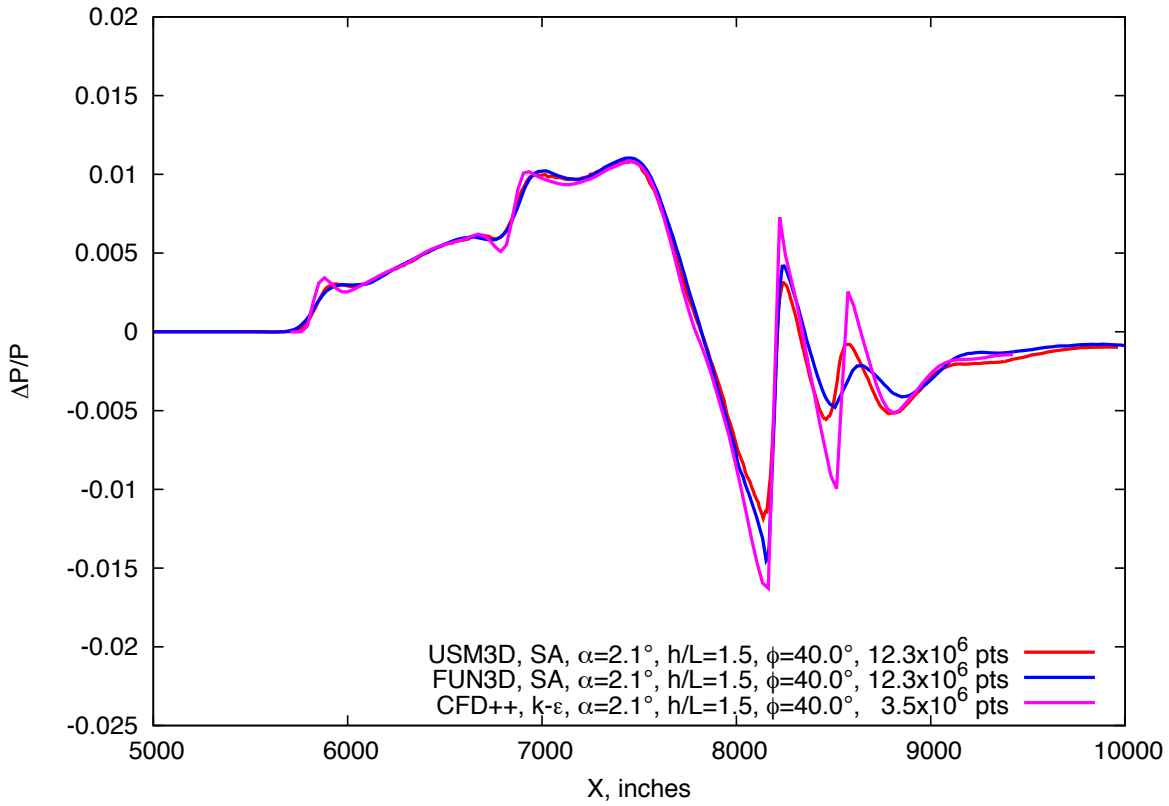

Figure 11.25. Phase II flight vehicle, Navier-Stokes solutions at cruise conditions, M=1.7, h/L=1.5, ϕ=40°

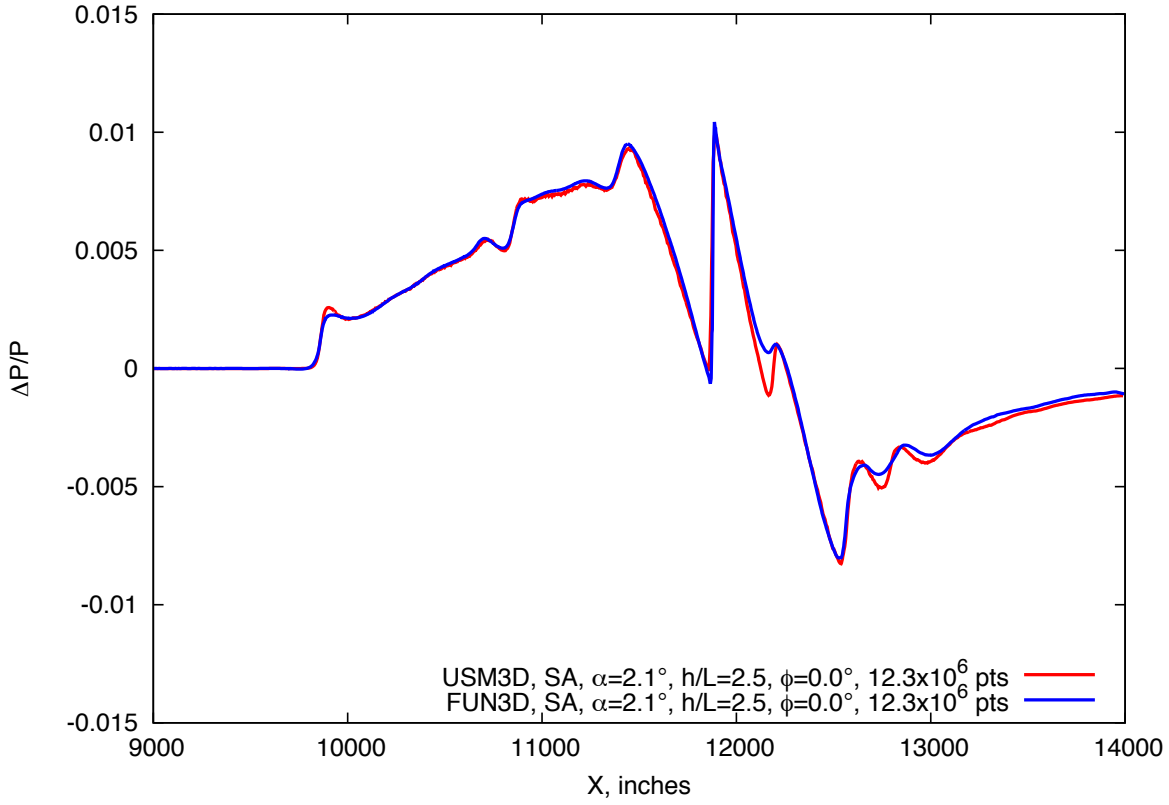

Figure 11.26. Phase II flight vehicle, Navier-Stokes solutions at cruise conditions, M=1.7, h/L=2.5, ϕ=0°

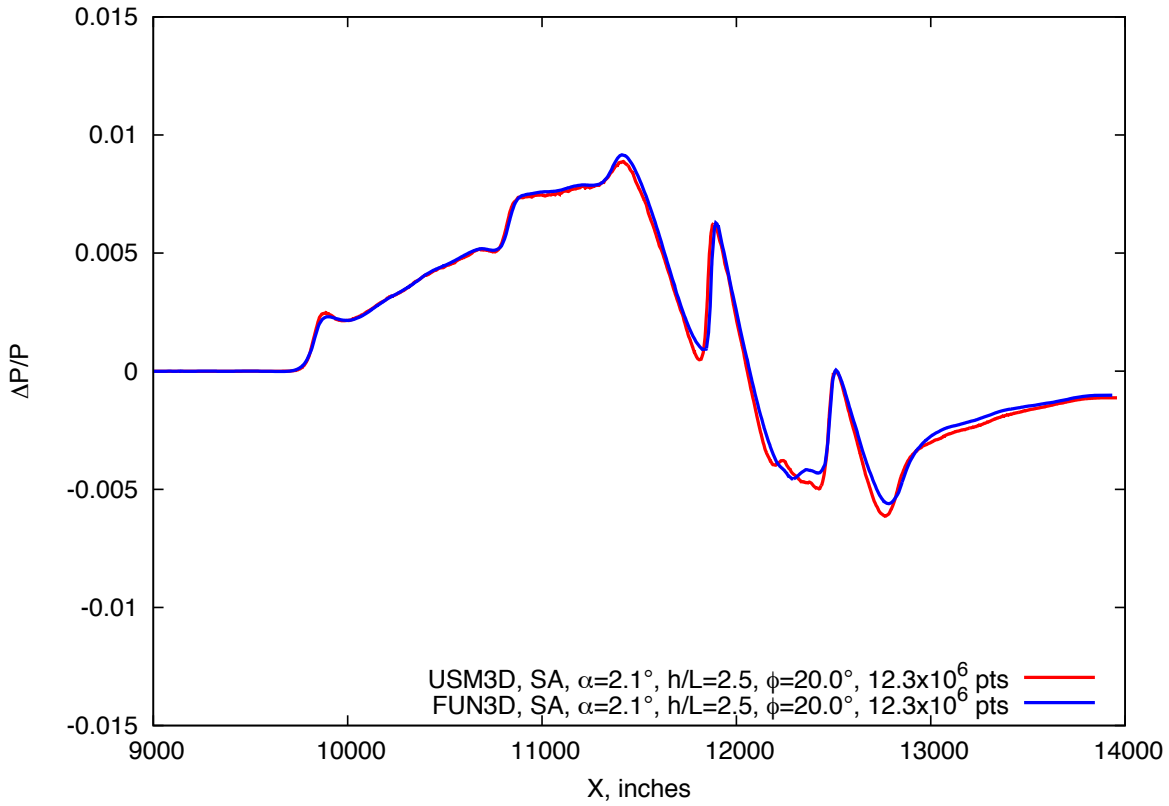

Figure 11.27. Phase II flight vehicle, Navier-Stokes solutions at cruise conditions, M=1.7, h/L=2.5, ϕ=20°

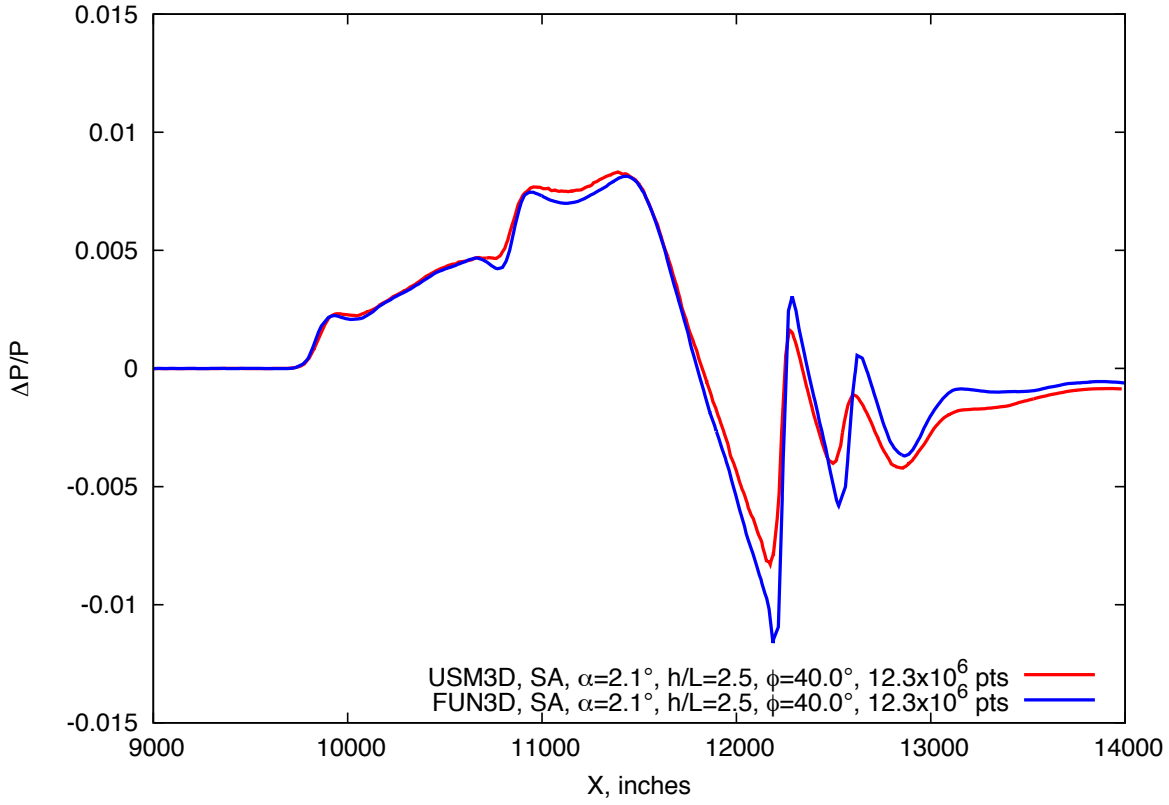

Figure 11.28. Phase II flight vehicle, Navier-Stokes solutions at cruise conditions, M=1.7, h/L=2.5, ϕ=40°

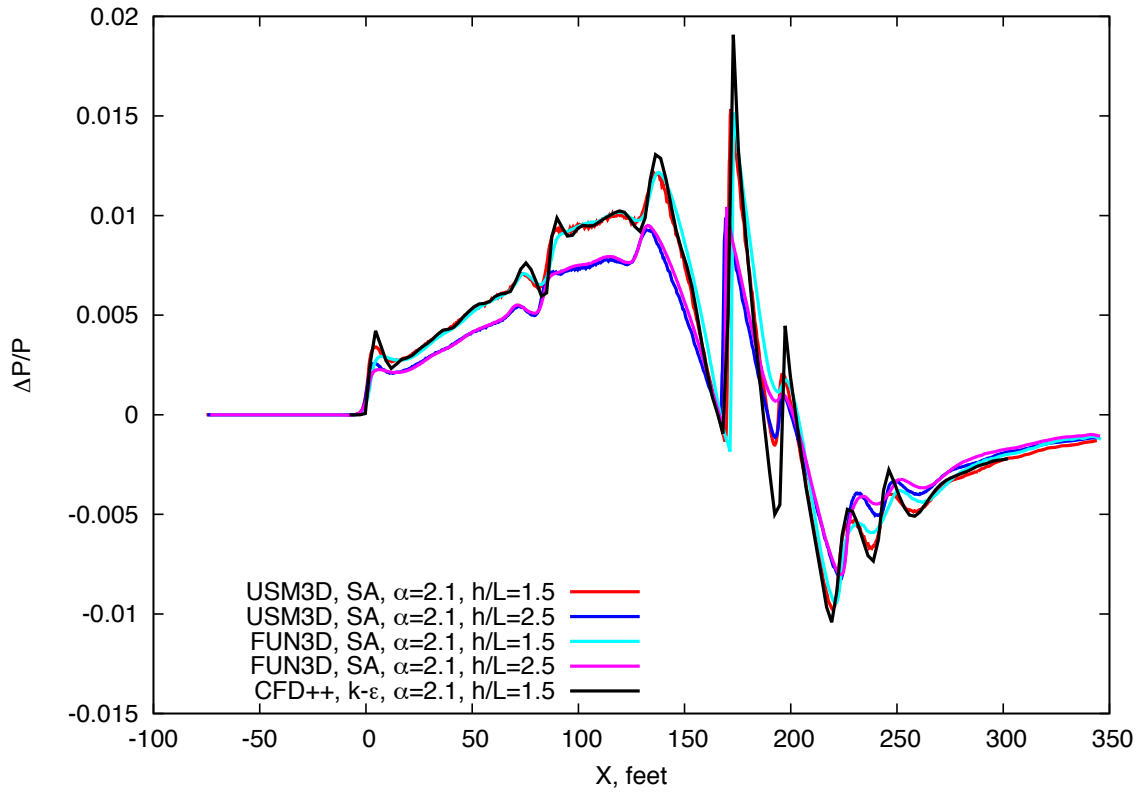

Figure 11.29. Phase II flight vehicle original CFD input signatures for SBOOM

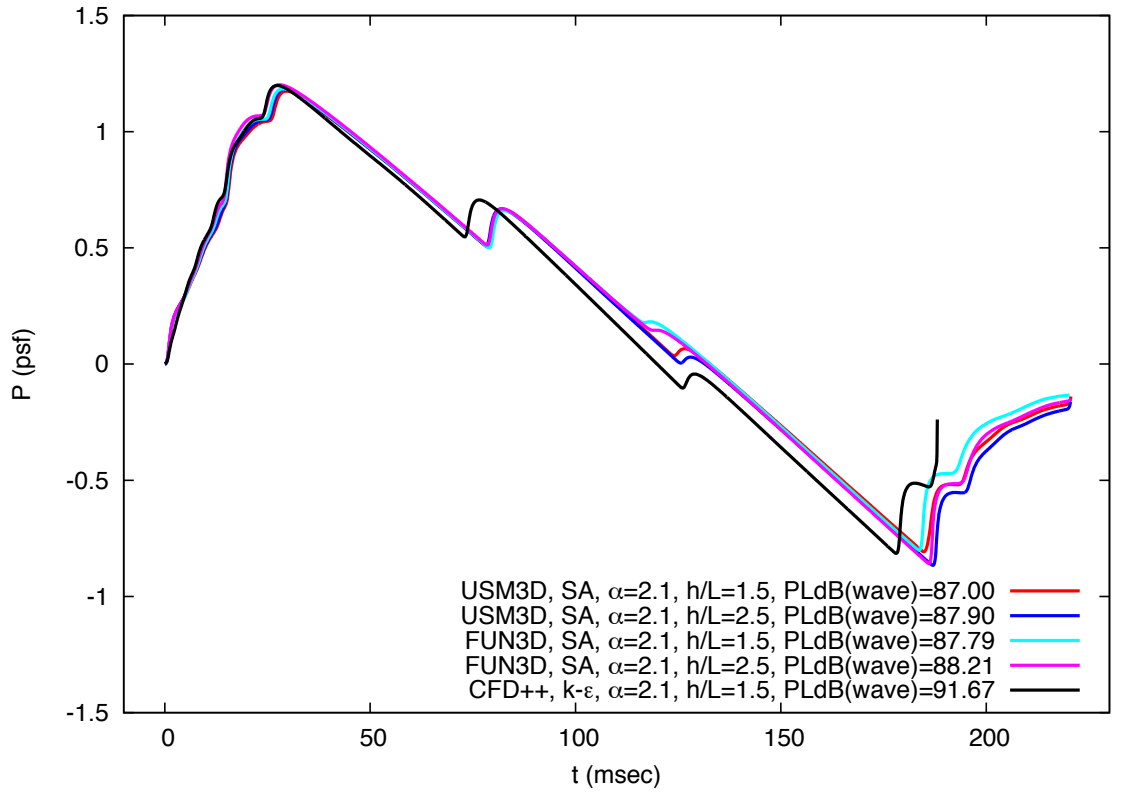

Figure 11.30. Ground level pressure signatures extrapolated from the Navier-stokes solutions of the Phase II flight vehicle, M=1.7, α=2.1°

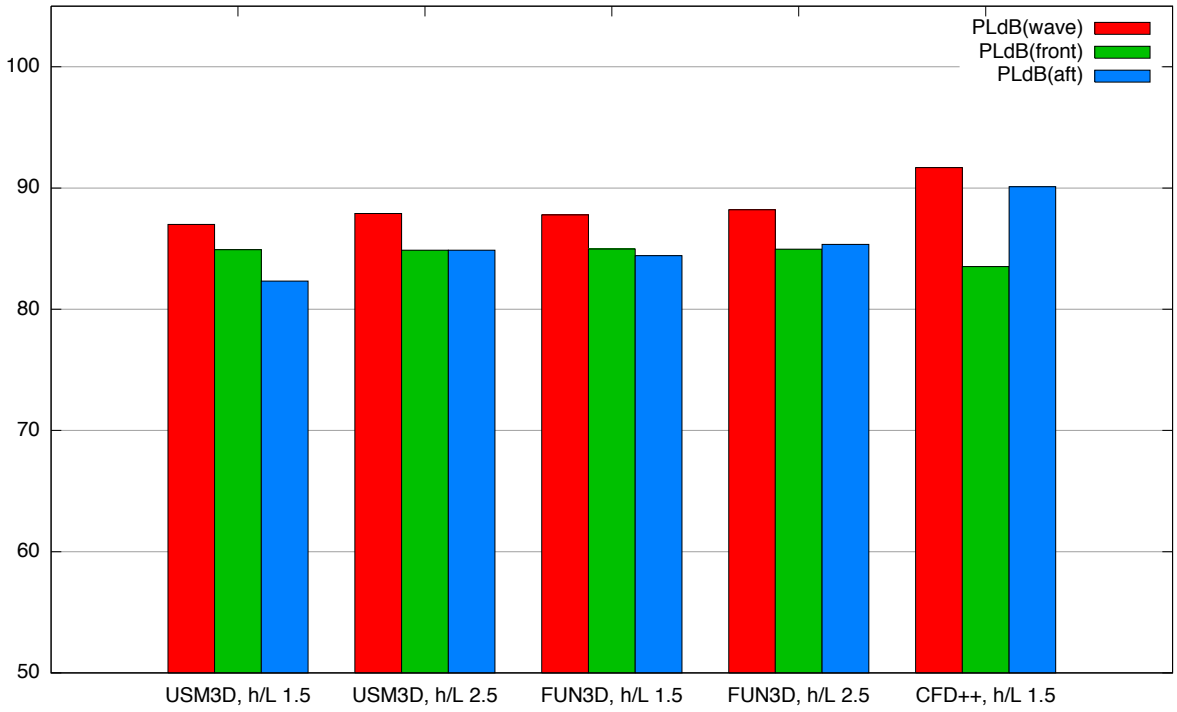

Figure 11.31. Noise level prediction from turbulent flow Navier-Stokes computations of the Phase II flight vehicle, M=1.7, α=2.1°

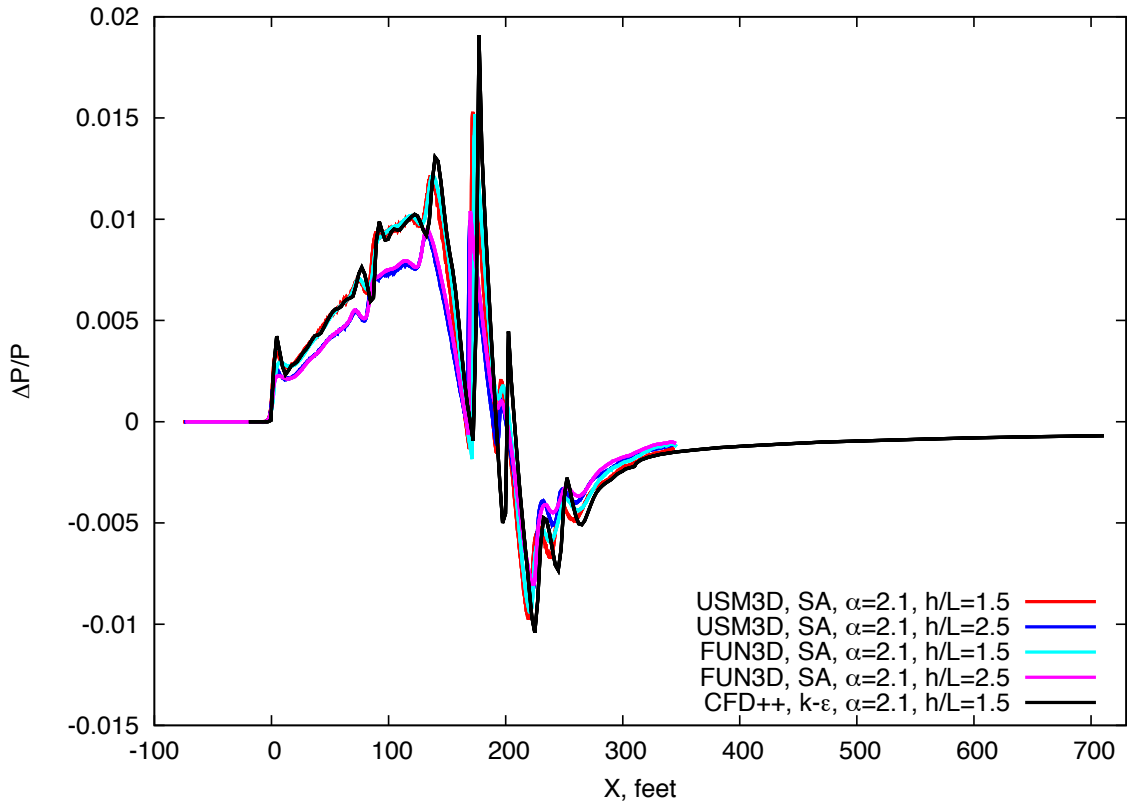

Figure 11.32. Phase II flight vehicle revised CFD input signatures for SBOOM

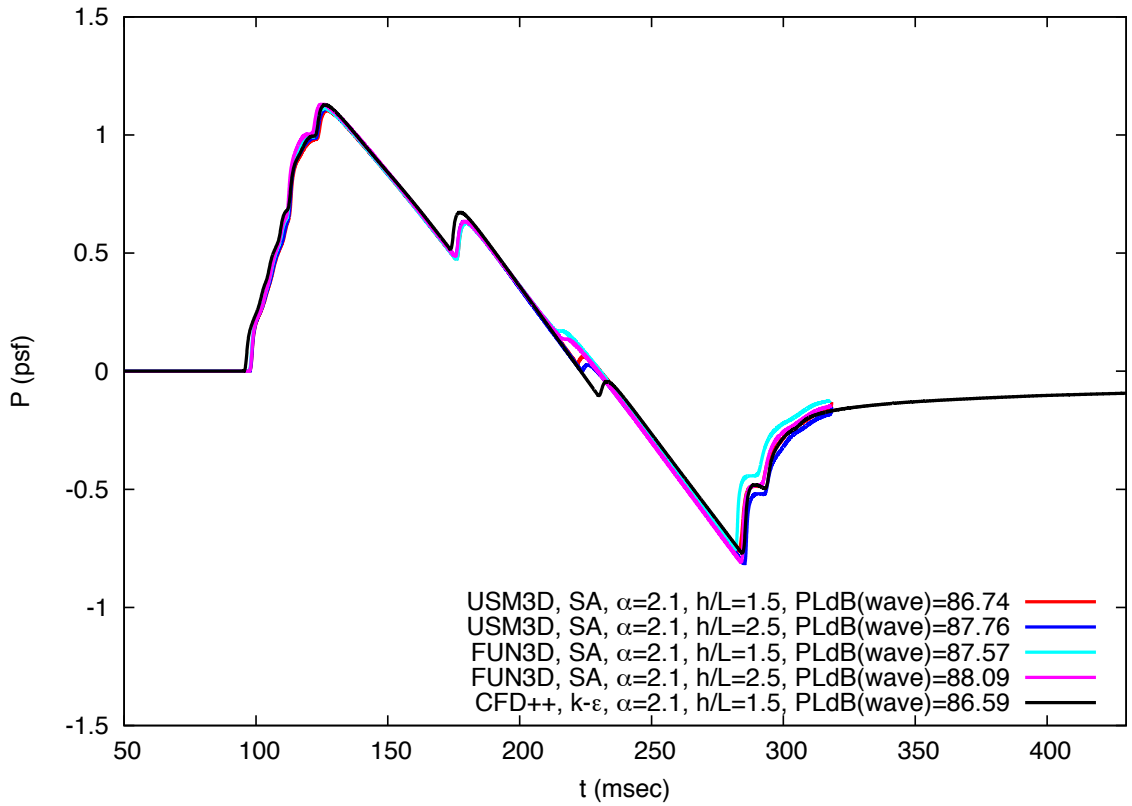

Figure 11.33. Corrected ground level pressure signatures extrapolated from the Navier-stokes solutions of the Phase II flight vehicle, M=1.7, α=2.1°

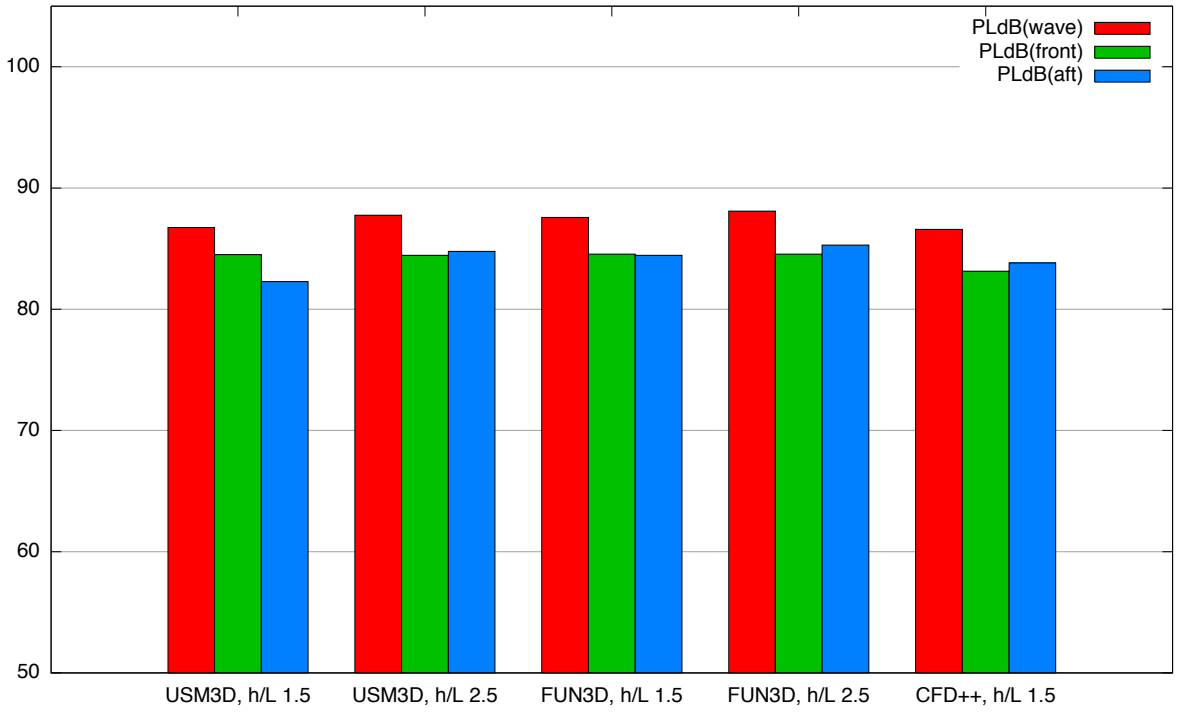

Figure 11.34. Corrected noise level prediction from turbulent flow Navier-Stokes computations of the Phase II flight vehicle, M=1.7, α=2.1°